

# Proceedings

## Microscopy Conference 2005 6. Dreiländertagung

August 28 - September 2, 2005





# Table of Contents

Preface .....	iv
Organizing Committee .....	v
Exhibitors of the MC2005 .....	vi
Advertisement .....	vii
Titles and Order of Sessions .....	viii
Author Index .....	401
Subject Index .....	408

# Preface

What has started in 1985 in Konstanz, Germany, as a convention of the three German-speaking countries Germany, Austria and Switzerland, called “Dreiländertagung”, will take place for the 6th time now in Davos. Slowly but definitely, the “Dreiländertagung“ has become a multinational event with English as the conference language and, for the first time, will have the status of a European Microscopy Society (EMS) Extension.

The Program Committee has put together a well balanced selection of Plenary Talks, Special Interest Lectures, and Regular Scientific Sessions. In addition, the program will provide plenty of room for discussing more specialized issues during Workshops. An International Scientific Advisory Board was actively involved in suggesting speakers and topics, as well as organizing and chairing sessions. Last but not least, the Poster Sessions represent an essential part of the conference where scientific results from more specific investigations will be presented. There will be ample time for discussion with the authors at the posters.

Furthermore, the Davos Congress Center provides an optimal platform for housing a large Commercial Exhibition. There will be on display the most recent developments in light-, electron-, and scanning probe microscopes, together with specimen preparation equipment and image analysis systems for both the life and materials sciences.

We have made a special effort to keep conference fees low, i.e. 60 Euros for students, in order to encourage young scientists to present their most recent findings to the more established investigators in the community.

No doubt, the world-class Davos Congress Centre will provide an excellent home for our Microscopy Conference 2005. It offers a good selection of meeting and conference rooms, all equipped with state-of-the-art audio-visual facilities. The professional staff from “Davos Tourismus” will help you with any questions or request you might have with regard to lodging, meals and travel during the meeting.

Davos, one of the largest mountain resorts in Europe, offers unforgettable encounters with nature and a broad range of delights. And anyone favoring the quiet idyll over the pulsing life in the thriving city, will find peace and tranquility in the wide Davos outdoors.

We are all looking forward to greeting you in Switzerland and wish you already now an interesting conference and a pleasant stay.

Welcome to Davos for the Microscopy Conference 2005.

Kurt Pulfer  
Chairman MC 2005 Davos

# Organizing Committee

## Finances

- \* Marcel Düggelin

## Scientific Board

- \* Ueli Aebi, Chairman
- \* Heinz Gross, Vice Chairman

## Scientific Board Representatives

- \* Ferdinand Hofer (ASEM)
- \* Peter Karnthaler (ASEM)
- \* Margit Pavelka (ASEM)
- \* Reinhard Rieger (ASEM)
- \* Hannes Lichte (DGE)
- \* Rudolf Reichelt (DGE)
- \* Paul Walther (DGE)
- \* Josef Zweck (DGE)
- \* Klaus Leifer (SSOM)
- \* Jens Gobrecht (SSOM)

## IT/Publications

- \* Daniel Mathys
- \* Stefan Dürrenberger
- \* URZ, University Basel

## General Organisation

- \* Kurt Pulfer
- \* Markus Dürrenberger

## Exhibition/Sponsoring

- \* Peter Eggli
- \* Patrick Schwarb

## Local Representant

- \* Geoff Richards

## Accommodation/Registration

- \* Davos Tourismus (<http://www.davos.ch>)

## International Scientific Advisory Board

- \* S. Daglioglu, President of the Turkish Society for Electron Microscopy
- \* M. de Lourdes Pereira, Department of Biology, University of Aveiro (Portugal)
- \* B.M. Humbel, Utrecht University, Electron Microscopy Unit, Dept. of Mol. Cell Biol (Netherlands)
- \* M. Luisa No, Departamento Física Aplicada II, Facultad de Ciencias (Spain)
- \* P. Hozak, President Czech Microscopy Society
- \* A. Czyrska-Filemonowicz, President of the Polish Society for Microscopy
- \* I. Ronchetti, Dept. Biomedical Sciences, University of Modena and Reggio Emilia (Italy)

## Contact Address

Markus Dürrenberger  
MC Davos 2005  
Universität Basel, ZMB  
Klingelbergstrasse 50  
CH-4056 Basel

Tel: +41 (0)61 267 14 04  
Fax: +41 (0)61 267 14 10  
e-mail: [duerrenberger@davos2005.unibas.ch](mailto:duerrenberger@davos2005.unibas.ch)

# Exhibitors

Alicona  
Ametec/Edax  
Atomic Force/E. A. Fischione Instruments  
BalTec RMC  
Binder Labortechnik  
Carl Zeiss AG (Lichtmikroskopie)  
Carl Zeiss SMT  
Diatome  
EO Elektronen-Optik-Service GmbH  
FEI Company  
GaLa Instrumente  
Gatan  
GIT Verlag  
Gloor Instruments  
Halcyonics GmbH  
Hamamatsu Photonics  
Hitachi  
HWL Scientific Instruments  
Imagic/Bitplane  
Jeol  
Kammrath + Weiss  
Kleindiek  
Leica Microsystem  
Microm AG  
Microscopy & Analysis  
Müller BBM GmbH / Macom II  
Nanonic  
NT-MDT  
Olympus Schweiz AG  
Oxford Instruments GmbH  
Plano  
Quantomix LTD.  
Reichert Labtec  
Renishaw  
Röntec  
SAMx/Point Electronic  
Soft Imaging System GmbH  
SPI Supplies  
Surface Imaging Systems  
Target Messtechnik  
Technoorg Linda  
Thermo Electron GmbH  
TVIPS GmbH

## Preparation to view information.

<p><b>COATING</b> CARBON, GOLD HIGH RESOLUTION • CD/DVD MASTERING</p>		 <p>SCD 050</p>
<p><b>CRITICAL POINT DRYING</b> CRITICAL POINT DRYERS</p>		 <p>CPD 030</p>
<p><b>CRYO PREPARATION</b> FREEZE • DRY • ETCH • TRANSFER</p>		 <p>VCT 100</p>
<p><b>ION BEAM MILLING</b> ION MILLING/COATING FOR TEM, SEM AND LM</p>		 <p>RES 101</p>
<p><b>MEMS PROCESSING</b> CRITICAL POINT DRYERS FOR 4", 6" AND 8" WAFERS</p>		 <p>CPD 408</p>
<p><b>CONSUMABLES</b> FULL RANGE FOR SEM AND TEM</p>		
<p><b>BAL-TEC RMG</b> ULTRAMICROTOMY AND EMBEDDING</p>		

[www.bal-tec.com](http://www.bal-tec.com)

Coating · Cryo Preparation  
Ion Etching · Solid State Preparation  
Accessories and more...

# Session and Abstract Index

## IM1: Electron optics

Chairpersons: M. Haider (Heidelberg), E. Plies (Tübingen)

- 1 Energy Width Measurements Of An Electrostatic W-Monochromator Using Thermal And Field Emitters  
J. Bärtele, E. Plies
- 2 New Multichannel Electron Energy Analyzer for Auger and Secondary Electron Analysis  
P. Cizmar, I. Müllerova
- 3 Qualification of the MANDOLINE Filter in the SESAME  
E. Essers, G. Benner
- 4 Is Parallel Illumination Possible In The TEM ?  
D. Eyidi, C. Hébert, P. Schattschneider
- 5 New Technologies to Characterize Bulk Materials  
H. Jaksch
- 6 Optical Design, Simulation, and Alignment of Present-Day and Future Aberration Correctors for the Transmission Electron Microscope  
H. Müller, S. Uhlemann, M. Haider, P. Hartel
- 7 Extended Nijboer-Zernike Aberration Retrieval for Electron Microscopy  
C. Kok, D. Maas, J. Mentink
- 8 EOD (Electron Optical Design) Program For Computations For Electron Microscopy  
B. Lencova, J. Zlamal
- 9 Optimization of Double Deflection Systems with Ray Tracing  
M. Oral, B. Lencova
- 10 Low energy focused ion beam system for TEM sample preparation  
M. Rauscher, E. Plies
- 11 In-column Corrected OMEGA Energy Filter: High-End Performance  
P. Schlossmacher, A. Orchowski
- 12 Simulation of Systematic Current Variation in a Miniaturized Electron Gun Microcolumn Applications  
B. Schröppel, D. Kern

## **IM2: Advances in TEM contrast analysis and simulation**

Chairpersons: P. Stadelmann (Lausanne), M. Lehmann (Dresden)

- 13 Ultra-Precise Measurement of Optical Aberrations for Sub-Angstrom HRTEM  
J. Barthel, A. Thust
- 14 Multi-slice Simulation of Convergent Beam Electron Diffraction Patterns  
A. Chuvilin, U. Kaiser
- 15 CBED Measurements of Thermal Expansion on Copper and Aluminum  
M. Hofmann, J. Thomas, T. Gemming, K. Wetzig
- 16 TEM Orientational Studies of  $\alpha\text{Cr}_2\text{O}_3$  Microcrystals Growing in Amorphous Films  
V. Kolosov, C. Schwamm, A. Bagmut
- 17 AFM Studies of Spots Formed in Amorphous Films by Electron Beam  
V. Kolosov, C. Schwamm, R. Gainutdinov, A. Tolstikhina
- 18 Electron Holography for Quantitative Measurements at Atomic Dimensions  
M. Lehmann
- 19 Contrast Theory for Advanced TEM Instrumentation: the Spherical-Aberration Corrector and the Wien-Filter Monochromator  
M. Lentzen, A. Thust, K. Urban
- 20 Electron Holographic Materials Analysis at Atomic Resolution  
M. Linck, H. Lichte, M. Lehmann
- 21 Ab-initio simulation of the object exit wave of ferroelectrics  
A. Rother
- 22 Special aspects on the scattering of high-energetic electrons on crystals  
A. Rother
- 23 The Frozen Lattice Model: Is it Valid to describe Thermal Diffuse Electron Scattering?  
K. Scheerschmidt
- 24 Studies and Application of Object Waves Retrieved from HRTEM Focus Series  
M. Svete, W. Mader
- 25 Phase measurements of complex scattering amplitudes by analysing diffractograms of thin amorphous foils  
A. Thesing, H. Kohl

## **IM3: Electron holography**

Chairpersons: H Lichte (Dresden), G. Pozzi (Bologna)

- 26 Electron Holography of Magnetic Nanostructures  
M. Beleggia, J. Lau, M. Schofield, Y. Zhu

- 27 Geometric vs Waveoptical Analysis of Interference Electron Microscopy Images of Reverse Biased p-n Junctions  
P. Fazzini, L. Ortolani, G. Pozzi, F. Ubaldi
- 28 Design of a test structure with wide doping range for dopant profiling with electron holography  
P. Formanek
- 29 Measurement error in phase images due to noise and limited resolution  
P. Formanek
- 30 An improved construction of electron biprism holder for the C2-aperture  
P. Formanek, B. Eienkel, H. Lichte
- 31 Biprism in condenser system for coherent two-beam illumination of an object  
P. Formanek, B. Eienkel, H. Lichte
- 32 Electron Holography with a Cs-corrected TEM at Triebenber Laboratory: Present State  
D. Geiger, H. Lichte, M. Lehmann, B. Freitag, M. Haider
- 33 Mean Inner Potential of Thin Amorphous Carbon Films  
D. Gerthsen, M. Wanner, D. Bach, R. Werner, B. Tesche
- 34 Experimental determination of the magnetic detection limit of electron holography in comparison with DPC  
C. Hurm
- 35 Electron Holography on the Way to Measuring the Weight of Atomic Columns with Single Atom Sensitivity  
M. Lehmann
- 36 Impact of Focussed Ion Beam (FIB) preparation on the measurement of electrically active dopants in silicon semiconductors using electron holography  
A. Lenk, U. Mühle, H. Lichte
- 37 Investigation of the Electrical Activity of Dislocations in GaN- and ZnO-Epilayers by Transmission Electron Holography  
E. Müller
- 38 Measurement of the Mean Inner Potential of ZnO Nanorods by Transmission Electron Holography  
E. Müller
- 39 Object Parameter Retrieval using Inverse Electron Diffraction including Potential Differences  
K. Scheerschmidt
- 40 Electron Holography on Biological Samples  
P. Simon, H. Lichte, P. Formanek, R. Wahl, M. Mertig, H. Ehrlich
- 41 Quantitative Comparison of Sideband and Centerband in Electron Holography  
D. Wolf

## IM4: SEM and LEEM

Chairpersons: R. Reichelt (Münster), L. Frank (Brno)

- 42 1D Traceable Length Measurements by Laser Interferometer in SEM  
T. Ahbe, Y. Xu, K. Hoffmann
- 43 Acquisition of signals from thin foils bombarded with very low energy electrons  
P. Hrnčirik, V. Romanovsky, I. Mullerova
- 44 Scintillation Detector in Environmental SEM  
J. Jirak, J. Skrivanek, R. Autrata
- 45 A new method for high throughput screening of cell spreading on non-transparent, nanostructured surfaces: automated processing of scanning electron microscopic images  
A. Katsen-Globa, L. Peter, M. Daffertshofer, H. Preckel, D. Schmitt, H. Zimmermann
- 46 Dynamic OIM of microstructural evolution  
R. de Kloe, S. Wright, M. Nowell
- 47 Recent Progress in Environmental and Variable Pressure SEM  
W. Knowles
- 48 Factors affecting the Collection Efficiency of Secondary Electrons in SEM  
I. Konvalina, I. Müllerová
- 49 Quantitative STEM with a High-Resolution Field Emission SEM  
V. Krzyzanek, H. Nüsse, R. Reichelt
- 50 Secondary Electron Contrast of doped Semiconductor Structures in SEM  
F. Mika, L. Frank
- 51 What can we see at very low energies in the Scanning Electron Microscope?  
I. Mullerova
- 52 Universal Heating/Cooling Device for Dynamic Experiments in a SEM  
P. Ott, J. Günter
- 53 X-Ray Microanalysis of Fully Wet Samples Using WETSEM™ Technology  
I. Ruach-Nir
- 54 A study on the crystal-orientation relationship of butterfly martensite in an Fe-30%Ni alloy by 3-D EBSD-based orientation microscopy  
H. Sato, S. Zaefferer
- 55 Extended Algorithm for Optimization of Photon Transport in Scintillation Detector  
P. Schauer, R. Autrata
- 56 Stroboscopic Low Energy Electron Microscopy - Imaging of Dynamic Processes and Transient States With Picosecond Time Resolution  
G. Schoenhense
- 57 FE-SEM, EBSD and TEM investigations of sputtered epitaxial silicon layers on different oriented substrates  
I. Sieber, I. Urben, P. Schubert-Bischoff

- 58 The Energies and Relative Intensities of M Lines  
R. Terborg, T. Eickhoff
- 59 Design of detector optics for a low energy SEM  
I. Vlcek, B. Lencova, M. Horacek
- 60 Critical Dimension Analysis of Thin (~100 nm) Gold Coatings by SEM and EDS  
S. Vynatheya, P. Ramaswamy, S. Subramanyam
- 61 Detection of Low Energy Backscattered Electrons in SEM  
P. Wandrol, R. Autrata
- 62 Topometry using a Four-Quadrant-Backscattered Electron Detector  
U. Wendt, H. Heyse, O. Kisel
- 63 3D-Orientation Microscopy in a Combined Focused Ion Beam (FIB) - Scanning Electron Microscope: A New Dimension of Microstructure Characterisation  
S. Zaefferer, J. Konrad, D. Raabe
- 64 Corrections of Magnification and Focusing in a Low Energy SEM  
J. Zobacova, F. Mika, M. Zobac, L. Frank

### **IM5: X-ray optics/microscopy**

Chairpersons: C. David (Villigen), R. Fink (Erlangen)

- 65 Biomedical Hard X-ray Phase Imaging Using a Grating Interferometer  
C. David, T. Weitkamp, T. Khan, H. Walt, F. Pfeiffer, O. Bunk, A. Diaz, T. Rohbeck, A. Groso, M. Stampanoni
- 66 Imaging Magnetic Nanostructures by Resonant X-Ray Holography  
S. Eisebitt
- 67 X-ray microscopy: beyond 2D imaging  
C. Jacobsen
- 68 TwinMic: A European twin X-ray spectromicroscopy station  
B. Kaulich
- 69 Instrumental effects in atomic resolution neutron holography  
M. Markó, L. Cser, I. Sharkov
- 70 STXM Investigations of Biological Tissues  
J. Raabe, R. Fink, A. Kilcoyne
- 71 News Trends in Synchrotron Based Hard X-Ray Microscopy and Micro-Spectroscopy  
J. Susini
- 72 3D X-ray Microscopy with Submicron Resolution Using a Laboratory Source  
A. Tkachuk, F. Diewer, S. Wang, M. Feser, H. Chang, A. Lyon, W. Yun

## IM6: Analytical TEM

Chairpersons: P. Schattschneider (Wien), H. Kohl (Münster)

- 73 High Resolution 3-D Characterization of Nanomaterials using Single and Dual Axis Tilt Tomography  
I. Arslan, T. Yates, J. Tong, N. Browning, P. Midgley
- 74 Electron Microscopy Investigation of Superconducting MgB<sub>2</sub> Tapes and Wires  
B. Birajdar, W. Pachla, A. Morawski, G. Grasso, W. Häßler, O. Eibl
- 75 Quantitative analysis of TEM (200) DF images : determination of the local Indium composition in InGaAs/GaAs quantum heterostructures.  
J. Cagnon, P. Buffat, P. Stadelmann, K. Leifer
- 76 Optimization of the positions and the width of energy windows for the recording of EFTEM elemental maps  
B. Gralla, A. Thesing, H. Kohl
- 77 Orientation-dependent EELS of TiO<sub>2</sub>: a comparison of theory and experiment  
C. Heiliger, F. Heyroth, H. Leipner, F. Syrowatka, I. Maznichenko, W. Hergert, I. Mertig
- 78 TEM Investigations of Lattice Site Occupancy of Phosphorous doped 4H-SiC  
T. Kups, A. Chuvilin, U. Kaiser
- 79 Quantitative EDX analysis of Bi<sub>2</sub>Te<sub>3</sub> in the TEM  
N. Peranio, O. Eibl
- 80 Energy-Selected Electron Diffraction Patterns of GaAs  
C. Prietzel, H. Kohl
- 81 Applications of Energy Loss Near-Edge Structures  
G. Radtke, G. Botton, S. Lazar
- 82 Energy Resolution and Spatial Resolution on a monochromated (S)TEM  
W. Rechberger, G. Kothleitner, F. Hofer
- 83 The CHIRALTEM Project: XMCD without a Synchrotron  
S. Rubino, P. Schattschneider, E. Carlino, G. Rossi, M. Fabrizioli, F. Macherozzi
- 84 High Energy Resolution Spectrum Imaging by EFTEM: Advanced Methods  
B. Schaffer, W. Grogger, G. Kothleitner
- 85 Chiral Dichroism in EELS: a New Analytical Tool  
P. Schattschneider, S. Rubino, C. Hébert, P. Formanek, H. Lichte, C. Hurm, J. Zweck
- 86 The Role Of An Alumina Membrane And Its Phase Transformations During The Layer Exchange Process  
M. Stoeger-Pollach, T. Walter, D. Eyidi
- 87 Tomographic Reconstruction of the EELS Data Cube  
W. Van den Broek, J. Verbeeck, S. De Backer, P. Scheunders, D. Schryvers

## **IM7: Advances in specimen preparation and nano structuring**

Chairpersons: H. Cerva (München), J. Mayer (Achen)

- 88 TEM Sample Preparation under SEM Observation  
E. Bugiel, V. Daniel
- 89 A new Process for Reliable and Fast In-Situ Lift-Out of TEM Samples  
C. Burkhardt, B. Holder, W. Dreher, W. Nisch
- 90 Optimization of the FIB milling conditions for RTP-processed Niobium and Tantalum nitride thin films on silicon substrates  
M. Dienstleder, M. Rogers, G. Kothleitner, F. Hofer, B. Kolbesen
- 91 Nano-fabrication with Focused Ion Beams - An innovative instrument  
J. Gierak, R. Jede, P. Hawkes
- 92 Removal of Amorphous Layers by Low Voltage FIB Preparation  
A. Graff, M. Simon, F. Altmann, H. Hoffmeister, P. Gnauck
- 93 Preparation with the RES 120 - unique ion milling system with SEM control  
W. Grünewald
- 94 New Applications of the Gatan PECS Ion Beam Cutting Tool for 3D SEM Microstructure Investigation of Heterogeneous Solids  
W. Hauffe, M. Neugebauer
- 95 Why is Selective Carbon Coating of TEM Samples so Effective?  
T. Höche, J. Gerlach, F. Heyroth
- 96 3D-Investigation of Plasma Erosion Craters using a Dual Beam Workstation  
C. Holzapfel, N. Jeanvoine, F. Soldera, A. Faundez, F. Mücklich
- 97 MFM-Probe Preparation Under Microscopic Observation Using Fe-MWCNTs  
S. Menzel, A. Winkler, J. Thomas, T. Mühl
- 98 Preparation of TEM Samples of Metallic Glass Powder  
C. Mickel, P. Schubert-Bischoff, S. Venkataraman, T. Gemming, G. Scheider
- 99 The contribution of resins to resulting image in low voltage electron microscope.  
J. Nebesarova, M. Vancova
- 100 Preparation-Dependent TEM Specimen and High-Resolution Image Quality  
T. Riedl, T. Gemming, K. Wetzig
- 101 Cross Section Preparation of Multi Layer Systems by Ion Etching (IE)  
R. Sonnleitner, C. Stocker, G. Nauer
- 102 Focused Ion Beam Micro-machining  
C. Volkert
- 103 TEM Characterization of Etched Si Nanopillars Prepared by Small Angle Cleavage Technique  
C. Zaubitzer, S. Grözinger, A. Chuvilin, U. Kaiser, R. Enchelmaier, A. Ladenburger, K. Thonke, R. Sauer

## **LS1: 3D and Cryo-Microscopy: From Molecular to Cellular Level**

Chairpersons: H. Stark (Göttingen), St. Nickell (Martinsried)

- 104 Microscopy from milli- to nanometer scale – a simple preparation protocol for multimodal imaging of tissue samples  
S. Biel, K. Wilke, K. Wittern, R. Wepf
- 105 The Outer Membrane of *Ignicoccus* - Analysis of its Structure by Cryo-fixation/Thin-Sectioning, Freeze-Etching, and Electron Tomography  
T. Burghardt, D. Näther, H. Huber, R. Rachel
- 106 Serial Block-Face Sectioning and High Resolution Imaging of Biological Samples with a Crossbeam FIB / FESEM Microscope  
C. Burkhardt, P. Gnauck, H. Wolburg, W. Nisch
- 107 Electron Tomography In Conical Geometry: 3D Reconstruction Of Tissue Sections And Metal Replicas Of Membrane Surfaces.  
F. Cantele, S. Lanzavecchia, L. Zampighi, N. Fain, E. Wright, G. Zampighi
- 108 How do adherens junctions in cellular networks of tendons change with age?  
R. Fleck, J. Claridge, R. Stanley, J. Ralphs, J. Patterson-Kane
- 109 TEM, SEM, Epifluorescence and Confocal Microscopy; Essential tools in the  
R. Fleck, M. Peyre, M. Afzal, C. Vipond, A. Rodgers, G. Stacey
- 110 Cryo-Atomic Force Microscopy (AFM) for the Study of Ice Surfaces  
M. Krzyzak, K. Techmer, S. Hacke, W. Kuhs
- 111 3d Reconstructions of Sites where Synaptic Vesicles Accumulate in Insect Larvae  
G. Leitinger, M. Pabst, P. Simmons, F. Rind
- 112 Confocal imaging of aberrant nodule ontology in legume symbiotic mutants using SYTO 13  
E. Maximova, V. Voroshilova
- 113 Vesicles of Glycosylated Cyclodextrin for Specific Recognition of Cellular Receptors as Investigated by Combination of Light Scattering and Cryo-EM  
A. Mazzaglia, A. Valerio, V. Villari, A. Rencurosi, L. Lay, L. Monsu'-Scolaro, N. Micali, N. Santo
- 114 Attempts at 3D cryo-TEM of different physiological states of arthropod hemocyanin and related hemolymph proteins  
U. Meissner, A. Martin, M. Stohr, J. Markl
- 115 Flagella of *Pyrococcus furiosus*: not only made for swimming – a correlative microscopy study  
D. Näther, G. Wanner, R. Wirth, R. Rachel
- 116 Structure of the cell-cell interaction site between two hyperthermophilic Archaea, *Ignicoccus* and *Nanoarchaeum*  
R. Rachel, T. Burghardt, D. Naether, A. Briegel, W. Baumeister
- 117 Monoglyceride Self-Assembly Particles by Cryo-TEM  
L. Sagalowicz, M. Michel, M. Leser, H. Watzke

- 118 Structural Analysis of a Newly Identified Inclusion at the Front of Blebbing Walker Carcinoma Cells  
D. Vanhecke, P. Egli, W. Graber, H. Keller, D. Studer
- 119 Cryo-SEM in Cell Biological Research  
P. Walther, M. Hagedorn
- 120 Computer Modeling of Ultrastructure of Muscle Cells  
I. Zahradnik, J. Parulek
- 121 Fine structural quantification based on 3D reconstruction of chloroplasts and mitochondria of field grown spruce and pine trees  
G. Zellnig, B. Zechmann, A. Perktold

## **LS2: Localization of Intracellular Elements and Macromolecules**

Chairpersons: H. Schwarz (Tübingen), R. Wepf (Hamburg)

- 122 Histochemical Observations on Effect of Lead in the Hepatopancreatic cells of *Palaemonetes turcorum* (Holthuis, 1961) (Crustacea, Decapoda)  
G. Aydogan, M. Kutlu
- 123 Ultrastructural Alterations in the Liver of *Aphanius chantrei* (GAILLARD, 1895) (CYPRINODONTIFORMES: CYPRINODONTIDAE) due to Acute Lead Exposure  
G. Aydogan, M. Kutlu, V. Kiliç, F. Alanyali
- 124 Observation of ice in frozen bread dough by SEM and CLSM  
A. Baier-Schenk, S. Handschin, M. von Schönau, A. Bittermann, M. Düggelin, B. Conde-Petit
- 125 Imaging Chromophores with a Post-column imaging energy filter on a 200 kV Monochromated TEM  
M. Barfels, P. Thomas, J. Hunt
- 126 Surface Localization of L-glycerol-phosphate-oxidase and of lipoprotein LppQ in *Mycoplasma mycoides* subsp. *mycoides* SC  
L. Bonvin-Klotz, P. Pilo, E. Vilei, J. Frey, M. Stoffel
- 127 Effects of Artichoke Extracts Supplementation on testis and Ovary in Cadmium Treated Rats  
H. Dogruman, E. Gurel, M. Caner, C. Demirci, U. Firat
- 128 High-fidelity ultrastructural preservation and high-efficient immunolabelling  
E. van Donselaar, B. Humbel, J. Slot
- 129 Melanosomes in Retinal Tissue: Quantitative Analysis in the TEM  
O. Eibl, S. Schultheiss, U. Schraermeyer
- 130 Diagnostic Electron Microscopy in Infectious Diseases  
H. Gelderblom

- 131 The Role of Human Cytomegalovirus UL97 Kinase in Virus Assembly: Immunofluorescence and Transmission Electron Microscopy (TEM) Analysis.  
M. Goldberg, V. Shinder
- 132 Magneto-Orientation of *Synechococcus lividus*, as demonstrated with an electron microscopic preparation technique  
J. Golecki, U. Heinen, T. Berthold, G. Kothe
- 133 Detection of the Novel Calcium-Binding Allergen Phl p 7 in Timothy Grass (*Phleum pratense*) Pollen by Immunogold Transmission Electron Microscopy  
M. Grote, R. Valenta, R. Reichelt, K. Westritschnig
- 134 Accumulation of reactive oxygen species in arbuscular mycorrhizal roots  
G. Hause, T. Fester
- 135 High-Resolution Imaging and Localization in Light Microscopy  
R. Heintzmann
- 136 Ultrastructural aspects of possible entamoebae divergention  
K. Hovnanyan, M. Hovnanyan
- 137 New view of the antitumor properties of HPMA based polymeric prodrugs  
O. Hovorka
- 138 Subcellular Location of Big Conductance Calcium-activated Potassium Channels in Cerebellar Purkinje Neurons: Targeting to Subsurface Membrane Cisternae  
W. Kaufmann, O. Ottersen
- 139 A Transmission Electron Microscope Investigation of the Lead on the Hepatopancreas of *Palaeomonetes turcorum* (Holthuis, 1961) (Crustacea, Decapoda)  
M. Kutlu, G. Aydogan
- 140 Effects of Lead on the Histopathology of Gill in *Aphanius chantrei* (GAILLARD, 1895) (CYPRINODONTIFORMES: CYPRINODONTIDAE)  
M. Kutlu, V. Kilic, G. Aydogan
- 141 Changes in the Liver Cells of Killifish *Aphanius chantrei* (GAILLARD, 1895) (CYPRINODONTIFORMES: CYPRINODONTIDAE) due to Lead Accumulation  
M. Kutlu, V. Kilic, G. Aydogan, A. Ozata
- 142 Expression of ETEC-specific surface antigens in wildtype *E. coli*, recombinant *E. coli* and *Vibrio cholerae* strains evaluated by transmission electron microscopy  
S. Luedi, J. Frei, D. Favre, J. Viret, N. Kapp, M. Stoffel
- 143 Discriminatory Staining of Budded Baculovirus  
P. Nevsten, R. Wallenberg, G. Karlsson
- 144 Comparative Quantitative Analysis of Mitochondrial Environment in Different Striated Muscle Cells  
M. Novotova, I. Zahradnik
- 145 Bacterial Spores in the Skin of a 1000-Year-Old Peruvian Mummy  
M. Pabst, I. Letofsky-Papst, E. Bock, K. Spindler, S. Guillen, F. Hofer

- 146 Structures in the Dermis of a 1000-Year-Old Mummy from Chiribaya Alta, Peru  
M. A. Pabst, I. Letofsky-Papst, E. Bock, K. Spindler, P. Wilhelm, S. Guillén, F. Hofer
- 147 Preservation of the Dermis of a 1000-Year-Old Mummy from Chiribaya Alta, Peru  
M. Pabst, I. Letofsky-Papst, P. Wilhelm, E. Bock, K. Spindler, S. Guillen, F. Hofer
- 148 Electron microscopic and X – Ray Analysis of Escherichia coli  
A. Pepoyan, K. Hovnanyan, M. Karageozyan, A. Manvelyan, M. Hovnanyan, A. Baghdasaryan
- 149 Confocal Fluorescence Microscopy: A Novel Method in Brewing  
C. Schlee, M. Miedl, G. Stewart
- 150 Improvement of freeze-fracture labeling efficiency  
W. Schlörmann, F. Steiniger, W. Richter, M. Westermann
- 151 The SNAP-tag - Labeling of Fusion Proteins in live Cells and in vitro  
M. Schwab, R. Tynes, L. Gedge, A. Brecht
- 152 Delineation of Neoplastic Human Mast Cells by Immunoelectron Microscopy  
P. Samorapoompichit
- 153 3D-reconstruction of immuno-labeled freeze-fracture replicas by electron tomography  
F. Steiniger, W. Schlörmann, M. Westermann, W. Richter
- 154 Cryofixation and Freeze Substitution combined with Tokuyasu Cryosectioning: Improved Preservation of Plant Tissue  
Y. Stierhof, H. Schwarz
- 155 Artificial elevation of glutathione by OTC is accompanied with decreased symptom development during ZYMV-infection in Cucurbita pepo plants  
B. Zechmann, G. Zellnig, M. Müller, A. Urbanek-Krajnc

### **LS3: Secretion and Endocytosis**

Chairpersons: M. Pavelka (Wien), L. Huber (Innsbruck)

- 156 Use of Energy Filtering TEM for Depiction of Organelle and Vesicle Interactions and Possible Modes of Degradation in the Green Alga *Micrasterias denticulata*  
N. Aichinger, A. Oertel, U. Lütz-Meindl
- 157 Structural and Ultrastructural Studies Concerning the Effects of Echinacea Extracts on Hemato- and Lymphopoietic Organs of Wistar Rats After Experimental Immunosuppression  
A. Ardelean, A. Hermenean, C. Craciun, G. Pribac
- 158 Atomic Force Microscopy Reveals Granulysin Induced Defects on Cholesterol Free Phospholipid Bilayers  
H. Barman, M. Walch

- 159 The Clathrin-Positive Endosomal TGN Attaches to the Golgi Stack During Transport of Cargo.  
G. Beznoussenko
- 160 Localization of the Endoplasmatic Reticulum Marker Calreticulin in the Aberrant Rodlet Cell of Teleosts  
E. Bielek
- 161 Morphological Characterization of Human Rhinovirus Infected HeLa Cells  
M. Brabec, M. Niapir, A. Ellinger, D. Blaas, R. Fuchs
- 162 Histochemical investigations of the adhesive organ of *Idiosepius* (Cephalopoda, Mollusca)  
J. von Byern, L. Rudoll, D. Gruber, W. Klepal
- 163 Ultrastructural Changes Induced by Cyclophosphamide Administration on Rats' Hepatocytes and Hepatoprotective Effects Testing of Echinacea Extracts  
C. Craciun, A. Hermenean, A. Ardelean, G. Pribac
- 164 Ultrastructure of the adhesive organ of *Idiosepius* (Mollusca, Cephalopoda)  
N. Cyran, J. von Byern, W. Klepal
- 165 Is the Plant TGN an Early Endosomal Compartment?  
J. Dettmer, Y. Stierhof, K. Schumacher
- 166 Golgi apparatus studied by advanced microscopic methods  
M. Grabenbauer
- 167 MAPK signaling from endosomes: the role of scaffolds and intracellular trafficking  
L. Huber
- 168 Prerequisites for the characterization of PKD 2 overproduction in cultivated pancreatic cancer cells using high-pressure freezing  
H. Krisp
- 169 Dynamics of Endocytic Pathways Investigated with High-Resolution 3D Microscopy  
P. Marbet, L. Landmann
- 170 Intra-Golgi transport. A way to a new paradigm?  
A. Mironov, A. Luini, G. Beznoussenko
- 171 Immuno-electron tomography studies on COPII coated vesicle formation from the endoplasmic reticulum  
J. Murk, W. Geerts, D. Zeuschner, E. van Donselaar, J. Slot, H. Geuze, B. Koster, J. Klumpermann
- 172 Glycoprotein E is involved in Coordinating Envelopment of Bovine Herpesvirus 1  
E. Schraner, C. Senn, K. Bienkowska-Szewczyk, M. Müller, P. Wild
- 173 Cytochemical Inactivation of Early and Late Endosomal Compartments. A Novel Technique for Analyses of the Endocytosis System  
M. Vetterlein, E. Scherzer, J. Neumüller, C. Meisslitzer-Ruppitsch, A. Ellinger, M. Pavelka
- 174 High temporal resolution sheds light on herpesvirus envelopment  
P. Wild, C. Senn, E. Schraner, K. Bienkowska-Szewczyk, P. Walther, U. Ziegler, M. Müller

## **LS4: Microscopy in Vascular Biology**

Chairpersons: A. Lametschwandtner (Salzburg), U. M. Spornitz (Basel)

- 175 Tumor-induced Angiogenesis: Lessons from Morphology and Molecular Biology  
S. Aharinejad
- 176 Comparison of the structures of the renal vascular system in two caudata species  
H. Ditrich
- 177 Quantification of the Layer Specific Vascular Density using anti-Collagen Fluorescence Immunohistochemistry in the Primate Striate and Extrastriate Cortex  
A. Keller, B. Weber, N. Logothetis
- 178 Weibel Palade Bodies in Close Association with Trans-Golgi Network in Progenitor Endothelial Cells  
J. Kosiuk
- 179 Scanning Electron Microscopy of Vascular Corrosion Casts and its Contribution zu Microvascular Research  
A. Lametschwandtner, B. Stoettinger, H. Bartel, B. Minnich
- 180 Cultured Human Arterial and Venous Endothelial Cells Derived from the Same Vascular Bed Differ in their Phenotypic and Genotypic Characteristics  
I. Lang, U. Hiden, M. Pabst, G. Dohr, G. Desoye
- 181 Morphodynamics of Mammalian Ovary Microvasculature. A Review by SEM of Vascular Corrosion Casts  
G. Macchiarelli
- 182 Morphological Techniques for the Demonstration of Capillary Sprouts in the Early Corpus Luteum.  
A. Ricken, K. Spanel-Borowski
- 183 Compartmentalization of Lipid Droplet Biogenesis  
M. Robenek, H. Robenek
- 184 Capillary Remodeling Permits Alveolarization after Completion of Microvascular Maturation: A 3D View of Postnatal Lung Development Using X-ray Tomographic Microscopy  
J. Schittny, S. Mund, M. Stampanoni
- 185 Epithelial and Vascular Dynamics of Rat Endometrium as Studied with SEM and Corrosion Casts  
U. Spornitz
- 186 High Resolution Analyses of Cerebral Blood Vessels and Blood Flow  
B. Weber

## LS5: Microscopy of Stem Cells, Cell Cycle and Programmed Cell Death

Chairpersons: W. Klepal (Wien), A. Ho (Heidelberg)

- 187 Typical and peculiar characters of degeneration in Cirripedia (Crustacea)  
S. Adam, D. Gruber, W. Klepal
- 188 Identification and location of bone-forming cells within cartilage canals on their course into the secondary ossification centre (SOC)  
M. Blumer, H. Fritsch
- 189 Multiple Types of Programmed Cell Death  
P. Clarke
- 190 Early postnatal apoptotic activity of mouse bladder urothelium  
A. Erman, K. Jezernik
- 191 Regeneration and Blastema Formation in Flatworms  
R. Gschwentner, B. Egger, K. Nimeth, C. Gaerber, J. Achatz, P. Ladurner, I. Philipp, R. Aufschnaiter, W. Salvenmoser, R. Rieger
- 192 Connections determine long-term fate – migration and adhesion of human adult stem cells to their niche  
A. Ho, W. Franke
- 193 Cryopreservation of Caco-2 human colon cancer cells in Fraunhofer micro- cryosubstrates: SEM and block-face- SEM for study of cell differentiation after thawing  
A. Katsen-Globa, R. Malpique, F. Ehrhart, P. Alves, H. Zimmermann
- 194 Characterization of the Totipotent Stem Cell System of the Flatworm *Macrostomum lignano*  
P. Ladurner, D. Pfister, G. Kuales, R. Gschwentner, K. Nimeth, B. Egger, Z. Adamski, W. Salvenmoser, R. Rieger
- 195 How Human Cord Blood Derived Cells Differentiate into Early Matured Endothelial Cells. A Confocal and Electron Microscopic Study Including Electron Tomography  
J. Neumüller, M. Vetterlein, S. Neumüller- Guber, J. Kosiuk, J. Huber, M. Pavelka
- 196 Regeneration and Cellular Dynamics in the Basal Bilaterian *Macrostomum lignano*  
K. Nimeth, B. Egger, R. Geschwentner, W. Salvenmoser, M. Hrouda, U. Rostek, M. Gleirscher, D. Pfister, G. Kuales, P. Ladurner, R. Rieger
- 197 Structural Characterization of a Biomolecular Nanocrystal Developed in the Crustacean *Semibalanus balanoides* (L.) Using TEM Methods and Fourier Transform Image Analysis  
C. Rentenberger, P. Karnthaler, W. Klepal
- 198 Role of stem cells in the flatworm *Macrostomum lignano* as shown by immunogold labeling of S-phase neoblasts  
W. Salvenmoser, B. Egger, K. Nimeth, Z. Adamski, A. Bode, P. Ladurner, R. Rieger
- 199 Automated Sub-Diffraction Optical Nanometry of Cell Nuclei  
U. Spöri, H. Mathee, D. Baddeley, C. Wagner, S. Martin, A. Pombo, C. Wotzlaw, J. Fandrey, C. Cremer

- 200 Effects of Curcumin on Apoptosis in “In Vivo” Solid Ehrlich Ascites Tumor  
E. Taskin, E. Taskin
- 201 Effects of Human Gonadotrophin and Growth Hormon on Ovary in Immature Rat. Light and  
electron Microscopic Study.  
T. Toparlak, S. YILMAZER, O. TOPARLAK, M. ÖZTÜRK

### **LS6: Architecture of the cell nucleus and the cytoskeleton**

Chairpersons: V. Small (Wien), I. Raska (Prague)

- 202 Qualitative Analysis of c-myc gene Domain using Confocal and Spatially Modulated Illumi-  
nation Microscopy  
C. Batram, D. Baddeley, C. Boxler, S. Stein, J. Schwarz-Finsterle, C. Cremer
- 203 High-pressure Freezing Electron Microscopy Reveals Tubular Invaginations of the Inner Nu-  
clear Membrane during Cytomegalovirus Egress  
C. Buser, P. Häberle, T. Mertens, P. Walther, D. Michel
- 204 Ultrastructure of Primordial and Primary Human Ovarian Follicles after Enzymatic Isolation  
by Collagenase and Liberase.  
A. Camboni, M. Dolmans, B. Martinez-Madrid, A. Van Langendonckt, J. Donnez, S. Not-  
tola
- 205 The Ultrastructure of Pre-60S Ribosomal Particles  
B. Maco
- 206 Electron Tomography of *C. elegans* Meiotic Spindles  
E. O’Toole, M. Srayko, J. Mäntler, T. Müller-Reichert
- 207 Involvement of Nuclear Lamins A/C in the Formation and Maintenance of Nuclear Speckles  
I. Raska, J. Vecerova, K. Koberna, J. Malinsky, E. Soutoglou, T. Misteli, T. Sullivan, C.  
Steward
- 208 Effects of humangonadotrophin and growth hormone on ovary in immature rat: light and elec-  
tron microscopic study  
T. Toparlak, S. yilmazer, O. Toparlak, M. Ozturk
- 209 Electron Tomography of the Agrobacterium DNA Transfer Complex in Transit through the  
Plant Nuclear Pore  
E. Zimmerman, E. Shimoni, M. Elbaum

## **LS7: Microscopy of Biomaterials and Extracellular Matrix**

Chairpersons: G. Richards (Davos)

- 210 Application of FIB lift out preparation for a TEM study of the in situ-interaction between CaF<sub>2</sub>-like precipitates and dental enamel surfaces  
L. Berthold
- 211 Quantitative Evaluation of Filling Restorations of Human Teeth Using Three Dimensional Scanning Electron Microscopy  
W. Dietz, S. Meineber, U. Kraft, I. Hoyer, E. Glockmann
- 212 The Use of Silver Diamine Fluoride (SDF) in Arrest of Caries Treatment - a Scanning Electron Microscopical Study  
W. Dietz, J. Schneider, B. Monse-Schneider, R. Heinrich-Weltzien
- 213 Combination of SEM and PIXE study of the in vivo biocompatibility of implants at the bone interface  
G. Guibert, F. Munnik, S. Mikhailov
- 214 High Resolution SEM imaging – Problems and Some Solutions  
I. Gwynn
- 215 Studying bacterial adhesion to biomaterials  
L. Harris, R. Richards
- 216 Detection of silversulphide deposits in the skin of patients with argyria after long-term use of silver containing drugs  
L. Jonas, C. Bloch, R. Zimmermann
- 217 Utilisation of microscopy techniques to investigate cell-biomaterial interactions  
D. Meredith, G. Richards
- 218 Additional hydration methods for observation of wet samples in ESEM  
V. Nedela, R. Autrata
- 219 Cell biological processes in articular chondrocyte-grafts – An in vivo study of a clinically applied tissue engineering method for cartilage defect treatment.  
S. Nürnberger, C. Resinger, R. Schnettler, C. Meyer, I. Wilke, D. Barnewitz, W. Klepal, V. Vécsei, S. Marlovits
- 220 Double knock-out Mice lacking Laminin a4 and Type XV Collagen show Abnormal Basement Membranes in Sciatic Nerves  
K. Rasi, R. Sormunen
- 221 Improving Imaging of Biomaterials and interfaces with FESEM  
G. Richards
- 222 SEM-Analysis of diaman-bonded burs after grinding of dental enamel and ceramics  
F. Schmidli, M. Jakubzik, C. Marinello, H. Lüthy
- 223 Mineralisation of Gelatine: Model System for Enamel  
P. Simon, P. Formanek, C. Göbel, H. Tlatlik, J. Buder, R. Kniep

- 224 The Porcellio scaber Model for Biomineralisation: Structure, Assembly and Function of the Organic Matrix in Amorphous CaCO<sub>3</sub> Deposits  
A. Ziegler, H. Fabritius

### **MS1: Spectroscopy in materials science**

Chairpersons: F. Hofer (Graz), W. Sigle (Stuttgart)

- 225 Trace Element Analysis in Presolar Stardust Grains via Spectroscopic XANES-PEEM and Full-Filed XPS-Imaging (nanoESCA)  
P. Bernhard, J. Maul, H. Elmers, G. Schoenhense, S. Merchel, C. Sudek, U. Ott
- 226 HfO<sub>2</sub> high k gate oxides by VEELS and HREM  
M. Cheynet
- 227 Probing Electron States at Surfaces, Interfaces and Nanostructures with Spatially-Resolved EELS  
C. Colliex, M. Kociak, J. Nelayah, O. Stéphan, D. Taverna
- 228 Electron Energy Loss Spectroscopy of Rare Earth-Transition Metal Compounds and Their Hydrides ReMn<sub>2</sub>(H<sub>2</sub>) (Re=Gd,Er) Aided With Ab Initio Calculations Using WIEN2k  
T. Galek, C. Hébert, D. Eyidi, P. Schattschneider, H. Figiel
- 229 Fingerprinting Mineral Phases by EFTEM  
U. Golla-Schindler, R. Hinrichs, A. Putnis
- 230 Magic Angle in EELS - the Sequel  
C. Hébert, H. Franco, P. Schattschneider
- 231 Lifetime of Hot Electrons in Copper Obtained from Low- Loss EELS  
C. Hébert, A. Satz, P. Schattschneider
- 232 STEM and ELNES investigations of Cu-rich layers and nanostructures formed on VSe<sub>2</sub> crystal surfaces by metal deposition  
S. Hollensteiner, W. Sigle, E. Spiecker, W. Jäger
- 233 The Influence of Annealing Conditions on the Precipitation Characteristics of a Martensitic 9-12 wt% Cr Steel  
F. Kauffmann, C. Scheu, H. Ruoff, K. Maile
- 234 Microstructural Studies of Early Age Hydration of Ordinary Portland Cement (OPC) using TEM  
P. Mathur, E. Gallucci, K. Scrivener, P. Stadelmann
- 235 Concentration and modulus gradients at the interface between an amine-cured epoxy and the thermoplastic PVP  
M. Munz, E. Schulz
- 236 Analytical Imaging: Complementary Methods To Microscopy  
K. Paulus

- 237 Characterization of Doped ZnO Films by Means of Analytical TEM/EELS  
H. Schmid, W. Mader
- 238 High Resolution ELNES Characterization of Chemical Bonding in Low Dielectric Constant Materials for Interconnect Isolation  
H. Stegmann, T. Walther, E. Quandt, E. Zschech, D. Schmeisser
- 239 Integrated Mineralogical and SEM/EDX Analysis: An Innovative Tool For The Identification And Source Apportionment Of Deposited Dust  
C. Trimbacher, H. Neinavaie
- 240 Combining imaging with local spectroscopy in an energy-filtered TEM/STEM  
T. Walther, J. Simon, H. Stegmann
- 241 New approach to the quantitative analysis of low loss transmission electron energy loss spectroscopy measurements  
F. Yubero, W. de la Cruz

## **MS2: Nanoparticles**

Chairpersons: P. Hoffmann (Lausanne), R. Schlögl (Berlin)

- 242 HACDF Electron Tomography: The First Example  
O. Abrosimov, A. Chuvilin, U. Kaiser
- 243 Quantitative and Chemical Study of Nano-Objects by HRTEM, HAADF and Associated Techniques  
D. Araujo, R. El Bouayadi, T. Epicier
- 244 Electron Irradiation of Carbon Nanotubes in the Electron Microscope  
F. Banhart, J. Li, M. Terrones, A. Krasheninnikov
- 245 Characterization of Au Gold nanoparticles  
B. Bártová, A. Gemperle, J. Gemperlová, M. Slouf
- 246 Magnetic Nanocrystals in Semiconductors  
J. Biskupek, U. Kaiser, H. Lichte, A. Lenk, M. Kawasaki, N. Sobolev, O. Picht, E. Wendler, W. Wesch
- 247 Dynamics of Gold Clusters on Amorphous Carbon Films Induced by Annealing in a Transmission Electron Microscope  
D. Gerthsen, M. Wanner, R. Werner
- 248 Investigation of Mechanisms of Electron Emission from Silver Cluster Films under Laser Excitation by means of Photoemission Electron Microscopy  
A. Gloskovskii, D. Valdaitsev, M. Cinchetti, S. Nepijko, G. Schönhense
- 249 Transmission Electron Microscopy Applied To The Characterization Of Gd<sub>2</sub>O<sub>3</sub> : Eu<sup>3+</sup> Nanoparticles Obtained By Spray Pyrolysis  
L. Gomez V., M. Rabanal J., A. Khalifa, J. Torralba, L. Mancic, O. Milosevic

- 250 Twin configuration of silver nanoparticles embedded in glass  
H. Hofmeister, M. Dubiel, K. Schicke
- 251 Lattice contraction and surface stress of metal nanoparticles  
H. Hofmeister, P. Miclea, M. Steen
- 252 FIB-Nanotomography: Closing the Gap between Nano- and Microstructural Imaging in 3D-Microscopy  
L. Holzer, P. Gasser, B. Muench
- 253 High-Resolution TEM Characterization of Precious Metal Nanoparticles Synthesized on Porous Substrates Using Supercritical Carbon Dioxide Approach  
D. Kang, Y. Zhang, C. Saqing, C. Erkey, M. Aindow
- 254 Titanium Disulfide Fullerene-like Nanoparticles  
A. Margolin, R. Popovitz-Biro, A. Albu-Yaron, A. Moshkovich, L. Rapoport, R. Tenne
- 255 HRTEM and EELS Investigations on Diesel Engine Soot Nanoparticles  
J. Müller, D. Su, R. Jentoft, R. Schlögl
- 256 Quantitative Particle Analysis Based on FIB-Nanotomography  
B. Münch, P. Gasser, L. Holzer
- 257 Characterization of the Core-Shell Structure in Intermetallic Nanoparticles Extracted from Ni-base Alloys  
G. Pigozzi, D. Mukherji, G. Kostorz
- 258 The influence of support materials on the morphology and properties of Pt-Sn containing catalysts  
M. Pohl, J. Radnik, D. Hoang, S. Farrage, H. Lieske, D. Herein, U. Dingerdissen
- 259 Gold nanoparticles – synthesis, characterization and influence of various additives on their size and shape  
K. Riegler, M. Rogers, B. Schaffer, G. Kothleitner, F. Hofer
- 260 Mesoporous Pure and Cr-doped WO<sub>3</sub> Synthesized by Hard SiO<sub>2</sub> Templates For Gas Sensing: image simulation and 3D reconstruction  
E. Rossinyol, F. Peiró, J. Arbiol, A. Marsal, A. Cornet, J. Morante, B. Tian, D. Zhao
- 261 Structural Investigations of Silver Nanowires by HRTEM and SAED  
H. Sauer, L. Chen, X. Bao, D. Su
- 262 Combined TEM and in situ EXAFS investigations of Ag nanoparticles in glass  
R. Schneider, M. Dubiel, H. Hofmeister, K. Schicke
- 263 PtC catalysts for the oxygen reduction reaction: Correlation of carbon support morphology and catalytic activity  
B. Tesche, B. Spliethoff, H. Schulenburg, M. Reetz

### **MS3: Nanostructured materials**

Chairpersons: D. Gerthsen (Karlsruhe), T. Waitz (Wien)

- 264 TEM Imaging of Neutron Irradiation Induced Pinning Defects in MgB<sub>2</sub> Single Crystals  
B. Birajdar, M. Eisterer, J. Karpinski, H. Weber, O. Eibl
- 265 HRTEM investigation of GdScO<sub>3</sub>/BaTiO<sub>3</sub> Multilayer  
M. Boese, M. Luysberg, J. Schubert, T. Heeg
- 266 FIB-Structuring of Photonic Elements  
V. Callegari, P. Nellen
- 267 Cr particle refinement in Cu alloy by ECAP  
M. Dadras
- 268 Microstructural Evolution of Cu Alloys During ECAP: Approach for Nanofilament Formation  
P. Egambaram Thoppay, M. Dadras, M. Leboeuf, N. de Rooij
- 269 SFM in Controlled Vapour Environment as a Tool to Observe Induced Morphology Changes of Polymer Nanostructures at Interfaces in Real Time  
M. Gallyamov, K. Albrecht, A. Mourran, A. Khokhlov, M. Möller
- 270 Features of Application of Microscopy Methods for Researches of Geological Materials  
Y. Golubev
- 271 SEM/TEM Investigations of Tungsten/Tungsten-Carbide/Carbon and MoS<sub>2</sub> Multilayers/Nanocomposites  
M. Gubisch, T. Kups, H. Romanus, L. Spiess
- 272 Quantitative TEM characterizations of complex multilayer systems on structured silicon substrates  
D. Häußler, E. Spiecker, W. Jäger, M. Störmer, C. Michaelsen, J. Wiesmann, G. Zwicker
- 273 HRTEM investigations of (Si,Ge)/Si islands in combination with FEM  
I. Häusler
- 274 Microscopic Investigation Of Native Bitumens Constitution  
O. Kovaleva, Y. Golubev
- 275 TEM-Investigation of Si(001) Modified by Pr Implantation  
A. Mücklich, R. Kögler, F. Eichhorn
- 276 TEM Study of High Pressure Torsion Plastically Deformed Cu  
B. Mingler, G. Steiner, H. Karthaler, M. Zehetbauer
- 277 Bi<sub>2</sub>Te<sub>3</sub>: Superlattices and Structural Modulations in Bulk Materials  
N. Peranio, O. Eibl, J. Nurnus
- 278 Microstructure of Fe<sub>3</sub>C-Nanowires in Damascene Sabres  
M. Reibold
- 279 TEM-studies on nanoindents with FIB-techniques  
M. Reichelt, T. Weirich, M. Bückins, J. Mayer, J. Loos, P. Gold

- 280 Refinement of the austenite structure by oscillatory compression test  
K. Rodak
- 281 Behaviour of EBID Pt/C Nanowires under mechanical stress  
M. Rogers, B. Schaffer, G. Kothleitner
- 282 AFM as a Nanomanipulation Tool for Molecular Networks: from Material Science to Life Science  
A. Schmatulla, O. Marti
- 283 Atomic Force Microscopy as a Nanomanipulation Tool from Material Science to Life Science  
A. Schmatulla, O. Marti
- 284 Investigations of LPE-grown Si<sub>1-x</sub>Gex islands by analytical TEM  
R. Schneider, I. Häusler, A. Gerlitzke, W. Neumann
- 285 Nanofold network formation on layered crystal surfaces  
E. Spiecker, S. Hollensteiner, W. Jäger, A. Schmid, A. Minor, U. Dahmen
- 286 Crystal Growth Related Investigations on the Zeolite Intergrowth System EMT/FAU Using SEM and AFM  
W. Stracke, G. Gonzalez, U. Keller, S. Gonzalez, A. Ricker, R. Reichelt
- 287 TEM study on the microstructures of Sr<sub>0.5</sub>Ba<sub>0.5</sub>NbO<sub>6</sub> thin film deposited on SrTiO<sub>3</sub> substrate  
D. Su
- 288 LaAlO<sub>3</sub>/SrTiO<sub>3</sub> interface characterization  
G. Van Tendeloo, S. Bals, S. Van Aert, J. Verbeek
- 289 TEM Study of Carbon Nanophases Grown in Carbon-Ion Implanted Quartz  
A. Tonejc, I. Djerdj, A. Tonejc, M. Bijelic, M. Buljan, U. Desnica, R. Kalish
- 290 Investigation of Brake Pad Samples before and after Squealing  
I. Urban, I. Dörfel
- 291 Nanostructured NiTi alloys studied by TEM  
T. Waitz, H. Karnthaler
- 292 Characterization of electropolymerized substituted metalloporphyrins by Atomic Force Microscopy (AFM)  
X. Zheng
- 293 Visualization of Structural State in CSD BST Thin Films  
O. Zhigalina, K. Vorotilov, A. Kumskov, O. Lebedev, A. Sigov, D. Khmelenin
- 294 Cryopreservation of cells cultured on nanostructured surfaces studied by block-face SEM in combination with freeze-substitution  
H. Zimmermann, M. Laue, S. Pflueger, N. Puetz, M. Zwanzig, S. Fiedler, P. Mestres, A. Katsen-Globa

## MS4: Alloys and intermetallics

Chairpersons: H. P. Karnthaler (Wien), W. Neumann (Berlin)

- 295 Oxidation of Tungsten Alloy  
A. Alhazza, A. Al-Omair, K. Alhazza
- 296 An Electron Microscope Study of Mechanical Twinning and Fracture in TiAl Alloys  
F. Appel
- 297 Analytical TEM of Nb<sub>3</sub>Sn multifilament superconductor wires  
M. Cantoni
- 298 Antiphase Boundaries in Ni-Al-Cr Ordered Intermetallic  
J. Elzbieta
- 299 In situ TEM Straining of bcc Twins - Unexpected Modes of Slip Transfer  
A. Gemperle, J. Gemperlova, N. Zarubova, Z. Dlabacek
- 300 TEM image simulations of nanometer-size Cu-based defects in Fe  
A. Harjunmaa, G. Yu, R. Schaeublin
- 301 Temperature Estimation Of Gas Turbine Component Service By TEM Microstructure Analysis  
A. Hessler-Wyser, F. Diologent, M. Biel, F. Bobard, P. Buffat
- 302 SEM investigations of Mg-Ag-Nd magnesium alloy  
A. Kielbus
- 303 Study of the Intermetallic compound between Steel and Al coating layer in the Hot-Dip Aluminizing Steel  
K. Kim, J. Yoon, Y. Chung
- 304 Evolution of Dislocation Boundaries in Deformed Aluminum  
P. Landau, R. Shneck, G. Makov, A. Venkert
- 305 TEM Studies of B2 Ordered Fe<sub>45</sub>at%Al Deformed by High Pressure Torsion  
C. Mangler, C. Rentenberger, H. Karnthaler
- 306 The 475°C embrittlement in 2205 duplex stainless steel  
J. Michalska, K. Rodak, M. Sozanska
- 307 TEM in situ Heating of Ultra Fine Grained Titanium  
B. Mingler, M. Peterlechner, H. Karnthaler, M. Zehetbauer
- 308 Direct Observation of Gliding Dislocations in Bi<sub>2</sub>Te<sub>3</sub> Materials  
N. Peranio, O. Eibl
- 309 An Improvement of Aluminum Alloy Properties  
S. Potrous
- 310 Microstructural investigations of extruded WE43 magnesium alloy  
T. Rzychon, A. Kielbus

- 311 TEM Weak Beam Spatial Resolution: Application to TiAl  $1/2a\langle 112 \rangle$  Superdislocation Core  
R. Schaublin
- 312 Ni<sub>4</sub>Ti<sub>3</sub> precipitates and their effects on the Ni-Ti B<sub>2</sub> matrix  
D. Schryvers, W. Tirry, Z. Yang
- 313 SEM/TEM Investigations of Nickel filled Ceramic Layers  
S. Selve, A. Knote, T. Kups, H. Krueger, L. Spiess, H. Kern
- 314 The Microstructure Of Co And Ni Binder Phases In Graded Hard Metals And Its Influence On Corrosion Resistance  
F. Sket, D. Eyidi, J. Garcia, A. Pyzalla
- 315 Study of the Microstructure of Rapidly Solidified Al-Ni-Zr Alloys by Synchrotron Tomography and Transmission Electron Microscopy  
M. Wollgarten, S. Hiller, J. Vierke, A. Haibel, P. Schubert-Bichoff, K. Sahoo, J. Banhart
- 316 Direction of Local Tensile Axis in in situ TEM strained specimens  
N. Zarubova, J. Gemperlova, A. Gemperle, Z. Dlabacek

### **MS5: Semiconductors**

Chairpersons: H. Strunk (Erlangen), P. Werner (Halle)

- 317 Studies of thin-film solar cells by transmission electron microscopy  
D. Abou-Ras, D. Mukherji, G. Kostorz, A. Tiwari
- 318 Electron Microscopy Characterization of GaN Films by ELO on Sapphire  
Y. Arroyo, P. Stadelmann
- 319 Quantitative TEM Analysis of the composition of InGaN/AlGaIn layers - Selection of the proper imaging conditions  
M. Beer, K. Engl, J. Zweck, A. Able, W. Wegscheider, M. Schowalter, A. Rosenauer
- 320 TEM Investigations of High-Quality Ge Films on Patterned Si Substrates  
E. Bugiel, T. Wietler, K. Hofmann
- 321 Mapping of Dopants in Semiconductors: The PEEM Study  
L. Frank, I. Mullerova, D. Valdaitsev, A. Gloskovskii, S. Nepijko, H. Elmers, G. Schopenhense
- 322 Interface Polarity and Shapes of Electrochemically Etched Pores in InP  
H. Föll, M. Leisner, W. Jäger, M. Rudel, E. Spiecker
- 323 Energy-Filtering TEM in Semiconductor Research  
F. Hofer, W. Grogger, B. Schaffer
- 324 Growing 1-Dimensional Semiconductor Wires inside Single-Walled Carbon  
J. Hutchison, J. Sloan, A. Kirkland, R. Carter, A. Vlandas, M. Green

- 325 Electron Tomographic Characterization of ErSi<sub>2</sub> and Ge<sub>x</sub>Si<sub>1-x</sub> Nanoparticles Prepared by Doping of 4H-SiC  
U. Kaiser, C. Kübel
- 326 Application of Electron Tomography for Semiconductor Device Analysis  
C. Kübel, T. Lee, D. Su, J. Luo, H. Lo, J. Russell
- 327 Assessment of quantum dot electronic level structure using TEM and cathodoluminescence  
K. Leifer, F. Bobard, F. Michelini, E. Pelucchi, S. Watanabe, B. Dwir, E. Kapon
- 328 Electron Holography in Combination with FIB-based “Lift-Out” Technique: Minimum Invasive 2D-Dopant Profiling of Commercial Semiconductors  
A. Lenk, U. Mühle
- 329 Structural properties of epitaxial ZnMnSe layers  
D. Litvinov
- 330 Dislocation formation in SiGe virtual substrates by He implantation and annealing: Relaxation Mechanism and Strain Transfer into Si cap layers  
M. Luysberg, N. Hueging, L. Houben, K. Urban, S. Lenk, D. Buca, B. Hollaender, H. Trinkaus, S. Mantl, M. Morschbacher, P. Fichtner, R. Loo, M. Caymax, R. Carius, P. Schäfer
- 331 TEM on Silicon-based Material: a Short Insight into a Nearly Infinitely Wide Field of Research  
E. Müller, M. Borgström, H. von Känel, D. Grützmacher
- 332 HRTEM Investigation of the Intermediate Layer Formed During MOCVD Growth of ZnO on GaAs  
J. Neethling, H. Kirmse, W. Neumann, C. Weichsel, P. Berndt, A. Leitch
- 333 TEM study of deformation mechanisms of semiconductors during nanoscratching  
M. Parlinska-Wojtan, R. Gassilloud
- 334 Grain boundaries and domain structures of ferroelectric barium titanate investigated by TEM  
M. Rössel, M. Croitoru, D. Moser, J. Ihringer, O. Eibl
- 335 Growth of Ge on graded oxide of (Sr,Ba)TiO<sub>3</sub> and Sr(Ti,Hf)O<sub>3</sub> on (001)Si  
J. Seo, C. Dieker, A. Guiller, J. Locquet, J. Fompeyrine, G. Panayiotatos, G. Marvrou, A. Dimoulas
- 336 TEM Investigation of Dislocation Characteristics in MOVPE Grown InGaN/GaN Multiple Quantum-Well Heterostructures on SiC and Al<sub>2</sub>O<sub>3</sub> Substrates  
M. Soda, M. Beer, J. Zweck, E. Zanoni, M. Peter, S. Bader, K. Engl, U. Zehnder, G. Brüderl, U. Strauss, V. Härle
- 337 Formation of compositionally ordered dots in strained GeSi alloy during in situ electron irradiation at ARM1300S  
S. Song, Y. Kim, L. Fedina, A. Gutakovskii, A. Latyshev
- 338 Quantification of the N content in Ga(NAs) and (GaIn)(NAs) by dark field TEM and refined structure factor calculation  
K. Volz, T. Torunski, O. Rubel, W. Stolz

- 339 SEM Observation of Multilayer Semiconductor Structures Using Different Detection Modes  
P. Wandrol, J. Matejkova, R. Aufrata

### **MS6: Solid State Chemistry**

Chairpersons: F. Krumeich (Zürich), D. Hesse (Halle)

- 340 TEM-Study on durability tested Anode-Supported SOFCs with LSCF Cathodes  
W. Assenmacher, W. Mader, A. Mai, M. Becker, F. Tietz, E. Ivers-Tiffée, D. Stöver
- 341 Analytical TEM Study on the Evolution of Perovskite-Type Oxides in Soft Chemical Synthesis  
A. Feldhoff, J. Martynczuk, H. Wang
- 342 TEM Investigations of Hydrothermally Treated Zircons  
U. Golla-Schindler, T. Geisler, A. Putnis
- 343 Superstructure and Domains in  $\text{La}_{0.4}\text{Sr}_{0.6}\text{CoO}_{2.71}$   
C. Gspan, W. Grogger, I. Letovsky-Papst, F. Hofer, E. Bucher, W. Sitte
- 344 Electron Energy-Loss Near-Edge Structure of Transition Metals in Crystalline, Disordered, and Amorphous Matter  
T. Höche
- 345 Crystal Structure Determination via Experimental and Calculated ELNES  
K. Hofmann, B. Albert
- 346 Characterisation of Optically Anisotropic Grandite by Electron Microscopy  
F. Kern, U. Golla-Schindler, K. Pollok, A. Shtukenberg, A. Putnis
- 347 Microstructural Implications of an Electric-Field Driven Solid State Reaction  
C. Korte, B. Franz, N. Zakharov, D. Hesse
- 348 High-Resolution STEM Characterization of Niobium Tungsten Oxides  
F. Krumeich, R. Nesper
- 349 Electron Microscopy in Solid State Sciences – A Web Tutorial  
F. Krumeich, A. Zürn, R. Nesper
- 350 HRTEM Study on the Ordered Structure of the Metastable  $\text{Ge}_2\text{Sb}_2\text{Te}_5$   
Y. Park, J. Lee, Y. Kim
- 351 Processes of Dissolution of Crystals by Atomic Force Microscopy Data  
N. Piskunova
- 352 Incommensurate metal chains in subnitrides - an ED study on  $\text{Ca}_7\text{N}_4\text{Ag}_x$   
R. Ramlau, P. Höhn, R. Kniep
- 353 The superstructure of defect clathrates studied by ED and HREM  
R. Ramlau, M. Baitinger, A. Guloy, Y. Grin

- 354 Disorder and order in zirconium arsenide selenide studied by ED and HREM  
R. Ramlau, M. Schmidt, R. Kniep
- 355 The Crystallography of Atomically Constrained 1D Crystals Formed Within Single Walled Carbon Nanotubes  
J. Sloan, R. Carter, A. Kirkland, R. Meyer, A. Vlandas, J. Hutchison
- 356 ESEM – In-Situ Heating Stage Experiments on the Sintering Behaviour of “Green Body” Ceramics  
J. Wagner, H. Schröttner, A. Reichmann, S. Mitsche, M. Schmied

### **MS7: Magnetic and dielectric materials**

Chairpersons: J. Zweck (Regensburg), H. Hug (Basel)

- 357 Structure of the Seven-fold Martensitic Phase in Ni<sub>2</sub>MnGa  
M. Aguirre
- 358 Spin-structure of magnetic domain walls in ferromagnetic ring structures  
D. Backes, L. Heyderman, F. Nolting, M. Kläui, M. Laufenberg, H. Ehrke, D. Bedau, U. Rüdiger, C. Vaz, J. Bland, T. Kasama, R. Dunin-Borkowski, S. Cherifi, A. Locatelli, S. Heun
- 359 HfO<sub>2</sub> high-k gate dielectrics grown on (001) Ge by MBE  
C. Dieker, J. Seo, G. Marvrou, A. Dimoulas
- 360 Pinning and Depinning of a magnetic vortex core in a Permalloy dot by an external magnetic field  
C. Dietrich, T. Uhlig, J. Zweck, S. Cabrini, E. Fabrizio
- 361 Imaging of fast magnetization processes within patterned magnetic materials  
J. Gruendmayer
- 362 In-situ measurements of magnetoresistive effects in ferromagnetic microstructures in the Lorentz TEM  
T. Haug, J. Gründmayer, C. Hurm, J. Zweck, C. Back
- 363 Electron Holography Investigations of Small Magnetic Particles: Single Domain States and the Superparamagnetic Limit  
M. Heumann, J. Zweck
- 364 Photoemission Electron Microscopy Imaging of Ferromagnetic Wedge Films on Substrates Pre-patterned with Micrometer-Sized Plateaus  
L. Heyderman, S. Czekaj, F. Nolting, E. Müller, P. Fischer, P. Gasser
- 365 Magnetization Pattern of Overlapping Permalloy Nanodisks  
M. Huber
- 366 Preparation and Characterisation of magnetic specimens for ChiralTEM experiments  
C. Hurm

- 367 Beam current induced changes in the crystalline structure of Ni in the TEM  
S. Hußnätter
- 368 Determination of the uncompensated spin density in antiferromagnetic/ferromagnetic multilayers by MFM  
P. Kappenberger, I. Schmid, M. Parlinska-Wojtan, H. Hug
- 369 Ferroelectric Polarization as the Gradient of Phase Shift in Electron Holography at Atomic Resolution  
C. Matzeck, H. Lichte, M. Reibold
- 370 X-Ray Magnetic Dichroism Effects and their application for magnetization dynamic studies  
J. Raabe, C. Quitmann, S. Czekaj, F. Nolting, C. Back
- 371 Ab Initio Simulations of Magnetic Chiral Dichroism in Transmission Electron Microscope  
J. Rusz, P. Novák
- 372 Analytical TEM Investigations of Electrodeposited Hard Magnetic Fe-Pt Thin Films  
J. Thomas, T. Gemming, K. Leistner, H. Schlörb, S. Fähler
- 373 Detection of Discontinuous Movements of Magnetic Vortices in Polycrystalline Magnetic Materials  
T. Uhlig, J. Zweck
- 374 Switching Characteristics of Micron Sized Symmetric and Asymmetric Magnetic Rings Using Differential Phase Contrast  
T. Uhlig, J. Zweck
- 375 Imaging Magnetization Dynamics in Ultrathin Py Rings and Synthetic GMR Spin-Valves on Picosecond Time Scale using Photoemission Electron Microscopy  
F. Wegelin, A. Krasnyuk, S. Nepijko, H. Elmers, G. Schönhense

### **WS1: EM Diagnostics of Infectious Diseases**

Chairpersons: H. Gelderblom (Berlin), S. Richter (Wien)

- 376 Ultrastructure and Morphogenesis of the Chitoor Virus. A Bunyavirus Isolated from India  
A. Basu, S. Gangodkar, A. Mishra
- 377 The Application of Scanning Electron Microscopy to the Diagnosis of Suspect White Powders  
B. Dowsett
- 378 Electron Microscopic Diagnosis in Japan  
T. Goto, R. Fujii, H. Ogura, M. Oseto, H. Nishimura, N. Sakon, E. Utagawa
- 379 Confirmation of electron microscopy results by direct testing of grids with PCR techniques  
C. Johnsen
- 380 Rapid embedding in an acrylic resin for ultrastructural pathology and diagnosis of infectious diseases  
M. Laue, H. Gelderblom, P. Mestres, N. Bannert

- 381 Diagnostic EM and PCR – positive and negative aspects of both techniques  
S. Richter, H. Gelderblom

## **WS2: Visualization of Cellular Dynamics**

Chairpersons: A. Ellinger (Wien)

- 382 The Effect of Music and Labels on Materials  
H. Bitaraf
- 383 Ultrastructural Features Of *Mimulus aurantiacus* Curtis (Section *Diplacus* Gray, subtribe *Gratiroleae*, *Scrophulariaceae*) Pollen Tube In Vivo  
F. Dane, G. Olgun, N. Ekici
- 384 Dynamics of human rhinovirus infections  
R. Fuchs, D. Blaas, U. Berka, M. Brabec
- 385 Ultrastructural localization of GFP-tagged proteins by means of DAB-photoconversion  
C. Meißlitzer-Ruppitsch, M. Vetterlein, J. Neumüller
- 386 Visualizing of Rare Intracellular Transport Events in Vivo by Combined Video Fluorescence and 3-D Electron Microscopy.  
A. Mironov
- 387 Time-resolved electron microscopy of sub-second cellular events and functional correlation with other methodologies  
H. Plattner, J. Hentschel
- 388 Electron microscopic study of cuticle differentiation in the embryo of *Drosophila melanogaster*  
C. Seifarth, H. Schwarz, U. Müller, B. Moussian
- 389 Visualization of intracellular traffic combining high time resolution with ultrastructural preservation  
P. Verkade
- 390 Cell Entry of Alpha-Herpesviruses as Revealed by High Resolution Microscopy  
P. Wild, C. Senn, W. Geerts, E. Schraner, P. Walther, M. Müller, B. Humbel

## **Plenary Lectures**

- 391 Fluorescence Nanoscopy of Cellular Structures  
C. Cremer, C. Carl, C. Karle, U. Spöri, D. Baddeley, H. Mathée, I. Upmann, L. Shopland, A. Evsikov, C. Weierich, K. Teller, I. Solovej, C. Wotzlaw, J. Fandrey, D. O'Toomre, T. Cremer

- 392 Three-Dimensional Cryo-EM of the Ribosome: What Can We Learn About the Dynamics of Translation?  
J. Frank
- 393 Bulk Nanostructured Alloys Studied by TEM  
H. Karnthaler, C. Rentenberger, T. Waitz
- 394 Electron Holography  
H. Lichte
- 395 Force microscopy on insulators  
E. Meyer
- 396 Cryo-Techniques in Cell Biology  
M. Müller
- 397 Ruska Lecture: Changing a paradigm by oscillating a knife for ultramicrotomy  
D. Studer
- 398 Focal-Series Reconstruction: An Elegant Numerical Technique for Obtaining Direct and Quantitative Information from HRTEM Images  
A. Thust, W. Coene
- 399 Atomic Resolution Transmission Electron Microscopy  
K. Urban
- 400 Nanometrology at PTB  
G. Wilkening, H. Bosse

# Energy Width Measurements Of An Electrostatic $\Omega$ -Monochromator Using Thermal And Field Emitters

Jan Bärtele and Erich Plies

Institute of Applied Physics, Auf der Morgenstelle 10, D-72076 Tübingen, Germany

One way to further enhance the resolution in modern low voltage scanning electron microscopy or spherically corrected transmission electron microscopy (SCTEM) is the incorporation of an electron monochromator into the electron optical system. This reduces the native energy width of the emitter and thus decreases the influence of chromatic aberrations. In our set-up [1] a dispersion-free electrostatic monochromator of the  $\Omega$ -type [2] is used. With a similar system integrated into a SCTEM, a reduction of the energy width of a field emission gun (FEG) from  $\Delta E_{\text{FWHM}} = 0.8$  eV down to  $\Delta E_{\text{FWHM}} = 0.3$  eV has been observed thus allowing resolution improvement to about  $1 \text{ \AA}$  [3].

Since the initial measurements [1], the set-up has been improved and measurements with thermal and field emitters have been performed. A better magnetic shielding was successfully integrated into the monochromator housing. This yields a significant improvement to alignment and performance, since the beam has an energy of only 3 keV and thus is very sensitive. A magnetic transfer lens below the monochromator and additional deflectors have also been incorporated into the system.

The system has been extensively studied using a thermal emitter for ease of use. Depending on the emitter parameters (heating current and Wehnelt voltage) typical beam characteristics were  $\Delta E_{\text{FWHM}} \approx 1$  eV @  $I_{\text{Emi}} \approx 50 \mu\text{A}$  and  $I_{\text{Probe}} \approx 25$  nA. It was possible to reduce the energy width down to  $\Delta E_{\text{FWHM}} \approx 0.5$  eV. This is in good agreement with the predicted performance of the monochromator using a reasonable assumption of the cross-over size of the thermionic gun and the magnification factor in the energy selection plane.

The system was also operated with a FEG of the ZrO/W type. Measurements were performed showing a reduction of the energy width from  $\Delta E_{\text{FWHM}} \approx 0.8$  eV down to  $\Delta E_{\text{FWHM}} \approx 0.3$  eV @  $I_{\text{Emi}} \approx 25 \mu\text{A}$  and  $I_{\text{Probe}} \approx 1$  nA. Unfortunately, a further reduction was not yet possible due to intensity problems arising from the use of a Möllenstedt analyser as a high resolution electron spectrometer [4] followed by a YAG scintillator, a light-optical transfer system and a CCD-camera [5]. Due to significant losses ( $> 90\%$ ) in both electron and photon intensity the resulting signal to noise ratio sets a limit to further improved measurements. Additional measurements using a different emitter system are performed to overcome this obstacle. A summary of the measurements and a discussion will be presented [6].

## References:

- [1] A. J. Huber, J. Bärtele, E. Plies, Proceedings of ICEM15 2002, Vol. 3, 43-44.
- [2] H. Rose, *Optik* **86** (1990) 95-98.
- [3] G. Benner, M. Matijevic, A. Orchowski, B. Schindler, M. Haider, P. Hartel, *Microsc. Microanal.* **9** (Suppl. 3), 2003, 38-39.
- [4] R. Speidel, P. Brauchle, B. Kramer and U. Schwab, *Optik* **71** (1985) 167-174.
- [5] T. Weber, Diploma Thesis, Universität Tübingen, 1997.
- [6] Support by DFG (project PL 258/1-1 and -2) and Carl Zeiss NTS is gratefully acknowledged.

# New Multichannel Electron Energy Analyzer for Auger and Secondary Electron Analysis

Petr Čižmár and Ilona Müllerová

Institute of Scientific Instruments ASCR, Královopolská 147, CZ-61264 Brno, Czech Republic

Electron spectroscopies are important methods of surface investigation. In this application, parallel energy analysis is incorporated. This makes the measurements several orders faster. One possible solution is to use a hyperbolic electrostatic field [1] for the separation of electrons with different energies. Such a field focuses the trajectories onto a row of points on the detector plane for each different kinetic energy. The cylindrically symmetrical field [2] has the same nature as the hyperbolic field and it also focuses azimuthally divergent trajectories onto a single point on the detector, which should significantly increase the detected signal. This field also must satisfy Laplace's equation. Such field can be defined by an electrostatic potential of  $\varphi = V_0 y \ln(r/R_0)$ , where  $V_0$  is a constant,  $y$  and  $r$  are coordinates,  $R_0$  is the radius of the cylindrical linear grid electrode (see FIG.).

When the potential and the outer shape of the analyzer are known, it is possible to calculate the shapes of all electrodes to reproduce the electrostatic field inside the analyzer. In this application the size is limited by the microscope chamber and other components. It consists of planar electrodes and one half-cylindrical linear grid. This setup should be easily manufacturable and inexpensive. Prior to building the electrode system its functionality was verified using the CPO [3] system.

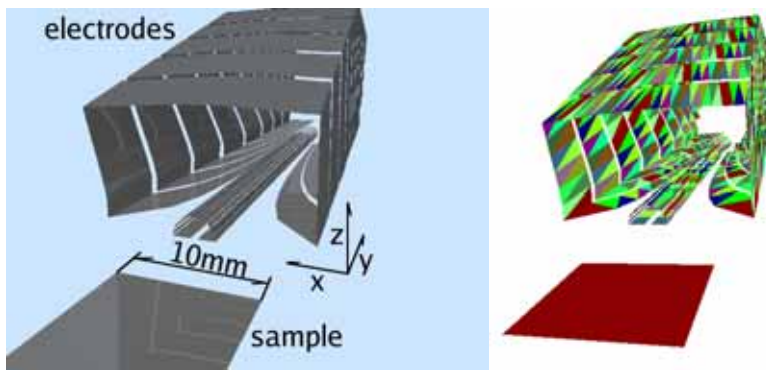


FIG. Preview of the electrode system rendered by program Povray [4] (left) and a screen-shot of the simulation of the same system in CPO [3] (right). Curved electrodes are simulated as sets of small triangle electrodes with the same potential.

The analyzer will work with electrons in the energy range 100 eV—1700 eV; the voltages on the electrodes will go from 600 V to -6473 V.

## References:

- [1] M.Jacka, M.Kirk, M.M.ElGomati, M.Prutton, *Rev. of Sci. Instrum.* 70(1999)2282
- [2] F.H. Read, *Rev. of Sci. Instrum.* 73(2002)1129
- [3] F.H. Read, CPO Programs, programs and information available at <http://www.electronoptics.com>
- [4] Povray renderer, <http://www.povray.org>
- [5] The work is supported by the ASCR Grant Agency under grant no. IAA1065304

## Qualification of the MANDOLINE Filter in the SESAME

E. Essers and G. Benner

Carl Zeiss SMT – Nano Technology Systems Division, D-73447 Oberkochen, Germany

We present performance tests of the MANDOLINE filter and first applications in the SESAME. The MANDOLINE filter [1] is designed for aberration correction up to third order. The high dispersion of more than  $6 \mu\text{m}/\text{eV}$  is very useful for energy filtering with narrow slit widths. Combined with the MANDOLINE filters unrivalled transmissivity and isochromaticity this allows Energy Spectroscopic Imaging (ESI) of large areas with energy windows down to 0.2 eV as well as measurement of radial distribution function and plasmon loss imaging with small energy windows.

The non-isochromaticity of the MANDOLINE filter is better than 5 meV (!) measured over the entire SSCCD (24 mm edge length). CBED patterns of Si  $\langle 100 \rangle$  were recorded to measure the transmissivity. Due to the spherical aberration of the objective lens, the transmissivity  $T$  is given by  $T = \pi^2 \alpha^2 (\alpha^3 C_s/4)^2$  at Lichte Focus. Fig.1 shows a CBED pattern where the FOLZ ring (104 mrad) is completely transferred through an energy slit of 1.2 eV. The apparent transmission of 108 mrad results in a transmissivity of  $T(1.2 \text{ eV}) = 15 \cdot 10^{-3} \mu\text{m}^2$ . Compared to other imaging energy filter designs (Corrected OMEGA, HR-GIF) the transmissivity is increased by a factor of more than 40.

In the spectroscopic mode first applications of the MANDOLINE filter in combination with the monochromized FE source of the SESAME also demonstrate ultimate performance. The Ti-L<sub>2,3</sub> edge of a TiO<sub>2</sub> (rutile) spectrum shows a clearly resolved pre-peak of the second peak (Fig. 2).

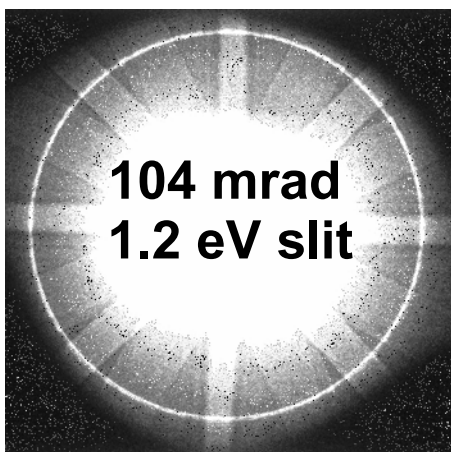


**Fig. 1:** Si  $\langle 100 \rangle$  CBED pattern with FOLZ-ring (104 mrad) taken at an energy width of 1.2 eV

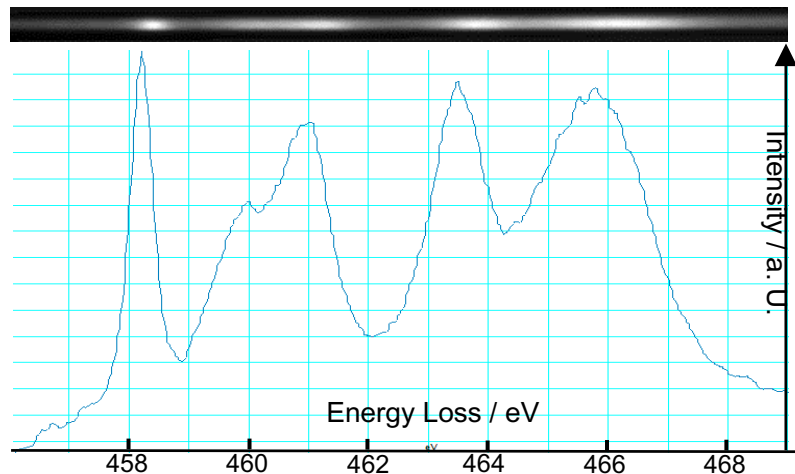


**Fig. 2:** Spectrum of Ti-L<sub>2,3</sub> edge from TiO<sub>2</sub> (rutile) (exposure time 5 s)  
Specimen courtesy of Dr. Ute Golla-Schindler, Univ. Münster

### References

- [1] S. Uhlemann, H. Rose, *Optik* **96** (1994), 163

## Is Parallel Illumination Possible In The TEM ?

Dominique Eyidi <sup>a,b</sup>, Cécile Hébert <sup>b</sup>, and Peter Schattschneider <sup>a,b</sup>

<sup>a</sup>University Service Center for Transmission Electron Microscopy, Technische Universität Wien, Wiedner Hauptstrasse 8-10, A-1040 Wien, Austria

<sup>b</sup>Institute for Solid State Physics, Technische Universität Wien, Wiedner Hauptstrasse 8-10, A-1040 Wien, Austria

Obtaining parallel illumination conditions is of paramount importance for several experiments in the transmission electron microscope (TEM) like selected area diffraction for phase identification or investigation of anisotropic materials under magic angle conditions [1].

Well-known is the image rotation induced by the helical trajectory of electrons passing through the magnetic field of the TEM lenses. The image plane rotation around the optic axis depends on both the magnetic field and the length along which the magnetic field acts.

The helical distortion of the trajectories inevitably induces a tilt angle  $\alpha$  relative to the optic axis in the object plane - even for an electron which travels parallel to the optic axis in the far field. This tilt angle is vectorially added to the convergence angle; it depends both on the distance to the optic axis and the magnetic field.

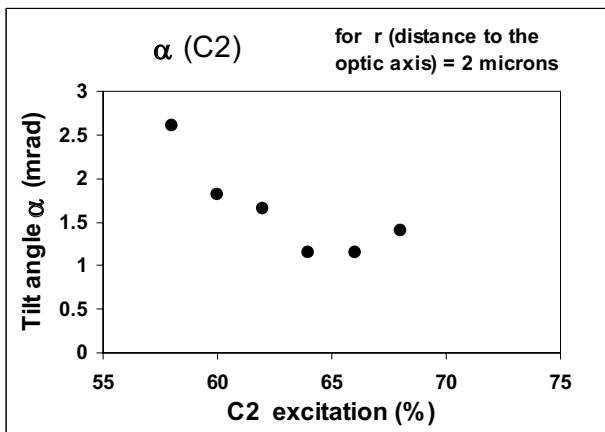


**Fig. 1.** Tilt angle as a function of the condenser lens excitation in a field of view of 2  $\mu\text{m}$ .

In the present study, we derive the tilt angle and we investigate dependences of  $\alpha$  to the distance to the optic axis and to the magnetic field. A TEM TECNAI F-20 S-Twin operating at 200 kV and a single crystalline silicon sample showing various diffraction contrast features were used for experiments. The minimum  $\alpha$  (i.e. the one corresponding to the beam with the best parallelism obtained) is found to be of the order of 1 mrad for a field of view of 2  $\mu\text{m}$ . We conclude that parallel illumination cannot be achieved in the TEM. Good agreement is found between experiments and calculations.

We also investigate the behaviour of bend extinction contours by varying the beam parallelism. The rotation and size variation of these contours according to the C2 lens excitation are analytically derived and correlated to the measured values.

References:

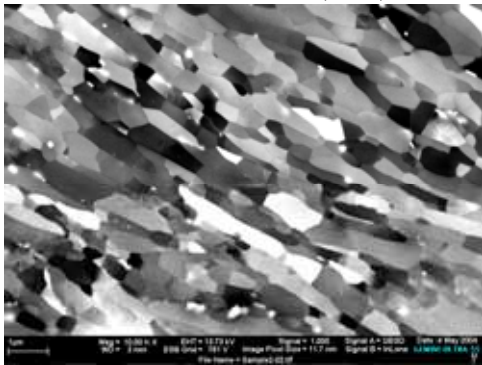
[1] P. Schattschneider, C. Hébert, H. Franco, and B. Jouffrey, Phys. Rev. B (2005) in press.

# New Technologies to Characterize Nanostructured Bulk Materials and Polymers

Heiner Jaksch

Carl Zeiss SMT–Nano Technology System Div., Carl-Zeiss-Str. 56, 73447 Oberkochen, Germany

Elastic and inelastic scattering at single atoms and excitation of electrons in solids are the fundamental processes that influence the range of electrons, the depth distribution of ionisation and the emission of SE and BSE electrons. New technologies are introduced to separate the different information coming from different scattering processes and hence better characterize nanostructured materials. Due to the GEMINI principle [<sup>1,2,3</sup>], the information, coming from the different scattering processes, is separated and projected via the GEMINI lens to different detectors (SE and *EsB*) on the beam axis, where the signal is *directly* detected without any losses from conversion plates. This principle enables the detection of very low *Z*–contrast differences, far below from a standard BSE detector. Latest tests revealed a detection limit of ppm range dopants in low *Z* material (Boron in  $\text{Al}_2\text{O}_3$ ). Even different polymers can be differentiated with this technology, due to the fact, that the signal coming from the sample, is amplified by a beam booster. The principle here is *Energy selective BSE detection (EsB)*.



New improvements come from an integrated GEMINI lens detector, selecting and separating the BSE signal via *Z* contrast and *angle* contrast. While the high angle BSE electrons, which are detected in the unique in-column energy selective *EsB* detector, the large and very large angles, coming from different scattering processes are collected in the *AsB* detector, or *Angular selective BSE* detection system.

In homogeneous crystalline bulk materials, we have strong demands to characterize this material and determine the treatment history. Chemically etching the polished surface is a common technology to describe grain structure, but sub grain information is lost. The channelling contrast, coming from mainly Mott scattered electrons, highlights the mechanism, which is used in this detector. The GEMINI lens separates the single scattered electrons from large angle *multiple* scattered BSE electrons. As a result we detect unmatched crystalline contrast, where normally nothing is visible (Fig 1 Aluminum). Very low angle changes of the lattice can be imaged.

Similar to the general GEMINI detection technology – fishing the true (interesting) signal and suppressing the noise – we separate the different scattered electrons in the *multimode* STEM detection system. Elastic (BF) and inelastic (DF) scattered electrons are separated and detected as usual. Beyond this, we image large angle scattered (LAADF) electrons and look for the orientation of crystals. Similar to the TEM imaging of a series of reflexes, different orientations, strain or defects are visible at a glance. We can detect features, absolutely not visible in normal BF or DF. The interference of Bloch waves in stressed crystals give information about growth stress or doping stress in nano particles. Altogether six basic imaging modes are used in this detection system, which is an extremely useful technology to characterize nano-structured materials.

References:

- [1] Jaksch H. et. al. *Microsc. Microanal.* (2004) 1372 CD
  - [2] Jaksch H. et. al. *Microsc. Microanal.* 9 (Suppl) (2003) 106
  - [3] Jaksch H. Field emission SEM for true surface imaging and analysis, *Materials World*, Oct. 1996
- Corresponding author: Jaksch@smt.zeiss.de

## **Optical Design, Simulation, and Alignment of Present-Day and Future Aberration Correctors for the Transmission Electron Microscope.**

Heiko Müller, Stephan Uhlemann, Peter Hartel, and Max. Haider.

Corrected Electron Optical Systems GmbH, Englerstraße 28, D-69126 Heidelberg, Germany.

The number of installed aberration-corrected transmission electron microscopes (TEM) is constantly growing. The present-day aberration correctors compensate for the spherical aberration  $C_s$  of the objective lens. For the Conventional TEM (CTEM) a corrector improves the point resolution up to the information limit without the disadvantage of affecting the information limit itself. For the Scanning TEM (STEM) a corrector allows for an increased probe semi-angle resulting in a reduced probe size and an increased probe current.

The optical design, optimization and alignment of aberration correctors requires a detailed understanding of these complex optical devices. This includes the perturbational analysis of higher-order primary aberrations and combination aberrations. The current implementation of our aberration analysis software allows to calculate the complete set of axial and off-axial aberrations up to the seventh rank, including parasitic aberrations induced by manufacturing tolerances, misalignment or electromagnetic perturbations. Based on this software we can study the behavior of a corrector system under realistic conditions w. r. t. manufacturing precision and alignment accuracy. This helps to find feasible alignment strategies sufficiently precise and stable to implement (semi-) automatic alignment procedures.

The user operates a corrector using automatic tableau methods for aberration measurement and (Auto) Alignment Tools [1] to refine the optical alignment. The microscope is considered as well-corrected if all measured residual parasitic aberrations are within the confidence interval about zero or tolerable. In this situation mainly the intrinsic residual aberrations should be limiting, e. g. in the case of a hexapole-type STEM corrector the fifth-order, six-fold astigmatism  $A_5$ . The strength of this aberration depends on  $C_s$  of the objective lens and on several design parameters of the corrector and may gain importance for an advanced  $C_s$ -corrected STEM with gun monochromator enabling a further reduction of the probe size from 80pm down to below 50pm.

Future TEM correctors envisioned by the Transmission Electron Aberration-Corrected Microscope (TEAM) project [2] will simultaneously compensate for the spherical aberration  $C_s$  and the chromatic aberration  $C_c$  of the objective lens in order to improve the information limit and the point resolution [3]. For the present-day corrector systems we obtained extensive experience with our simulation tools and alignment methods. This enables and guides the design and investigation of even more sophisticated future devices [3]. The complete set of residual aberrations, the required manufacturing precision and the feasibility of alignment procedures can be determined reliably even before the first prototype has been build.

[1] P. Hartel, H. Müller, S. Uhlemann, and M. Haider, Proc. EMC 2004, Antwerp, p. 41-42.

[2] The TEAM project homepage at <http://ncem.lbl.gov/team3.htm>.

[3] H. Müller, S. Uhlemann, and M. Haider, Microsc. Microanal. 8 (Suppl. 2), 2002, p. 12-13.

# Extended Nijboer-Zernike Aberration Retrieval for Electron Microscopy

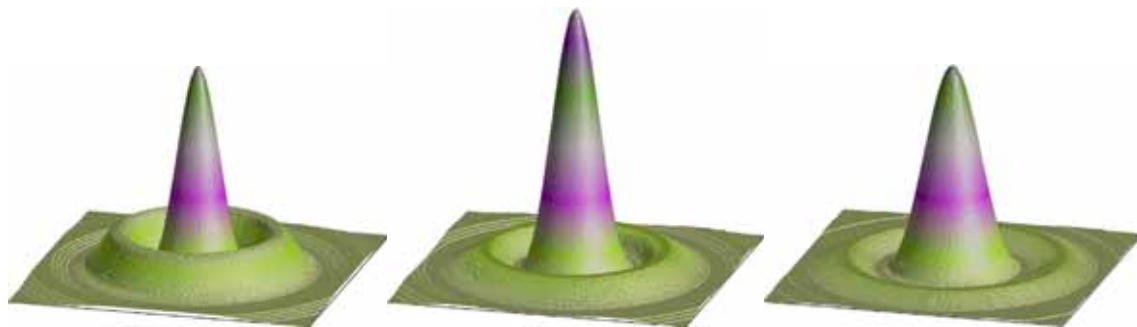
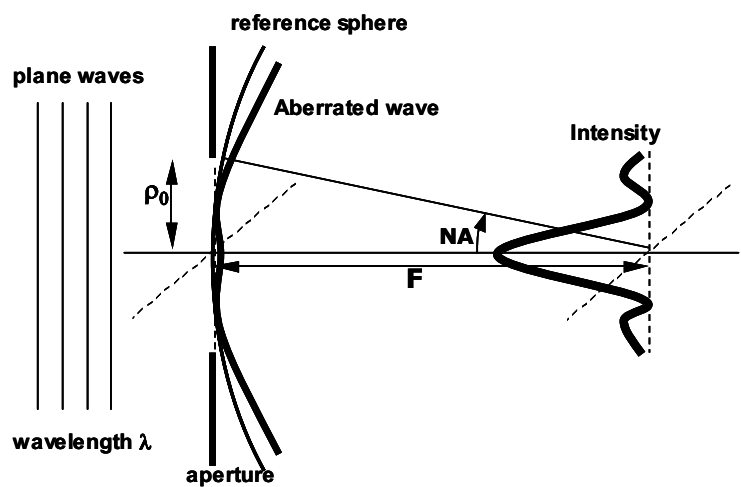
Christiaan Kok<sup>a</sup>, Diederik Maas<sup>a</sup>, Johan Mentink<sup>b</sup>

<sup>a</sup>Philips Research Eindhoven (WY-41), Prof. Holstlaan 4, 5656 AA Eindhoven, The Netherlands

<sup>b</sup>Department of physics, Eindhoven University of Technology, Den Dolech 2, 5612 AZ Eindhoven, The Netherlands

The Extended Nijboer-Zernike Aberration Retrieval (ENZAR) method is a method to calculate the aberrations of the probe forming system from a through-focus series of measured probe intensity distributions. ENZAR was originally developed for use in lithography (light optics)[1,2].

The basis of the algorithm stems from wave optics which describes the relation between the aberrations in the pupil and the observed intensity close to the focal plane. An expression has been derived which makes it possible to *quickly* and *accurately* evaluate the intensity close to the focal plane (see lower figures) in terms of aberrations represented by Zernike-coefficients[2]. Due to the properties of this representation it is also possible to estimate accurately the aberrations from a through-focus series of the observed probe intensity[3].



ENZAR has been implemented and evaluated for SEM and STEM. For SEM and STEM the probe intensity distribution can be reconstructed from scanned images. For STEM it is also possible to magnify the probe and observe the probe intensity directly.

## References:

[1] A.J.E.M. Janssen, J. Opt. soc. Am. A (19, 2002), pp. 849-857

[2] for more information see: <http://www.nijboerzernike.nl>

[3] P. Dirksen et al, J. Microlith., Microfab., Microsys., (2, 2003), pp. 61-68

## **EOD (Electron Optical Design) Program For Computations For Electron Microscopy**

B. Lencová<sup>a</sup> and J. Zlámal<sup>b</sup>

<sup>a</sup> Institute of Scientific Instruments AS CR, Královopolská 147, 612 64 Brno, Czech Republic

<sup>b</sup> Institute of Physical Engineering, Faculty of Mechanical Engineering, Brno University of Technology, Technická 2, 619 69 Brno, Czech Republic

Software for Particle Optics Computations (SPOC) has been developed in the course of many years mostly at ISI Brno and TU Delft. Valuable for the users are graphical input and display DOS interfaces introduced in 1990, allowing the input of data and display of results [1]. SPOC consists of 5 packages, each with 5-6 separate interlinked programs. The interfaces have become obsolete and an off-line external 2D plotting program is no more supported.

To improve and simplify this situation, we showed in 2000 at EUREM in Brno [2] that all FEM programs and their interfaces as well as newly programmed ray tracing had been successfully integrated in a single program called EOD and demonstrated its use by computing a compound lens. EOD is a modular program, compiled in Visual Fortran, which allows one to program all Windows graphics, use mouse and pull-down menus, on-line Help, and so on. EOD uses a clearly defined project structure to analyze complex systems with many elements, lenses, deflectors and multipoles. Optimization procedures allow excitations to be adjusted to achieve given image position or size.

Field computation by the first order FEM is no more critical issue; by using a large number of points (one minute is needed for 200000 point meshes), error of field is small and it can be analyzed. Unique features of EOD include an unlimited size of coarse and fine meshes for FEM by dynamic memory allocation, FEM meshes with graded step are used and there is more freedom in automatic fine mesh generation. SPOC data can be imported; in the background the geometry of other data can be shown as well as DXF or PLT files, to which the coarse mesh can snap. The program displays axial potential or field and/or color-coded saturation of iron or map of potentials or fields. Later a module for space charge computations in electron guns and ion optical systems was added [3]. Recently we added a module for the computation of optical properties from paraxial trajectories and aberration integrals for systems with lenses and deflectors. Let us stress that, in accurately computed fields, the ray tracing of suitably chosen set of rays provides paraxial properties as well as aberrations of any order [4]. Future development of EOD will be aimed at improving the input and output of ray tracing, to extracting aberration coefficients from ray tracing results, analyzing spot profiles and emittance diagrams; subsequently, the optics of correctors and other multipole systems will be added as well as an optical module for the dynamic corrections of aberrations and the analysis of misaligned systems, and even stochastic interactions.

### References:

- [1] B. Lencová, G. Wisselink, Nucl. Instr. Meth. **A298** (1990) 56-66.
- [2] B. Lencová, J. Zlámal, Proc. EUREM 2000, Brno, Vol. I, 101-102.
- [3] P. Jánký, B. Lencová, J. Zlámal, Proc. MC2003, Dresden, 22-23.
- [4] Supported by the Institutional Research Plan No. AV0Z20650511 of AS CR.

# Optimization of Double Deflection Systems with Ray Tracing

Martin Oral, Bohumila Lencová

Institute of Scientific Instruments ASCR, Královopolská 147, 612 64 Brno, Czech Republic

The resolution in SEMs is determined by the size and shape of the particle probe. The most frequently used deflection system is the prelens double deflection system. In a standard design, the first deflector deflects the beam by an angle  $\alpha$ , the second by  $-2\alpha$ , so that the central trajectory intersect the optical axis in the final lens. Provided that the deflection aberrations are negligible, the preferred intersection (and a possible aperture) is in the object nodal point of the lens [1]. In practice, the aberration of the deflectors must be also taken into account. Then the deflection and lens aberrations mix and some of them can even be eliminated by selecting the sizes, excitations and positions of deflectors [2].

Ray tracing programs, such as Trasys [3], enable fast and accurate calculation of a high number of real particle trajectories. The performance of the deflection system and the lens in a given setup can be determined by the ray tracing. Optimum system configuration (when the illuminated area on the specimen is as small as possible) can be found in the set of possible settings. It is also possible to analyze beam shapes at different positions on the axis or affected by the position of an aperture.

A test system consists of an asymmetric "axial-gap" lens (bore diameters 21 and 5 mm, gap width 6.5 mm) and two identical saddle coils (length 20 mm, diameter 12 mm) placed 90 and 30 mm from the lens center. Fig. 1 shows the variation of the beam shape in the Gaussian image plane for three excitations of the first stage (producing the deflection of 0.8 mm) and for different ratios of their excitations. The shapes are formed by a conical beam with a half-angle of 10 mrad starting on the axis (object and image distances 260 and 15 mm, respectively).

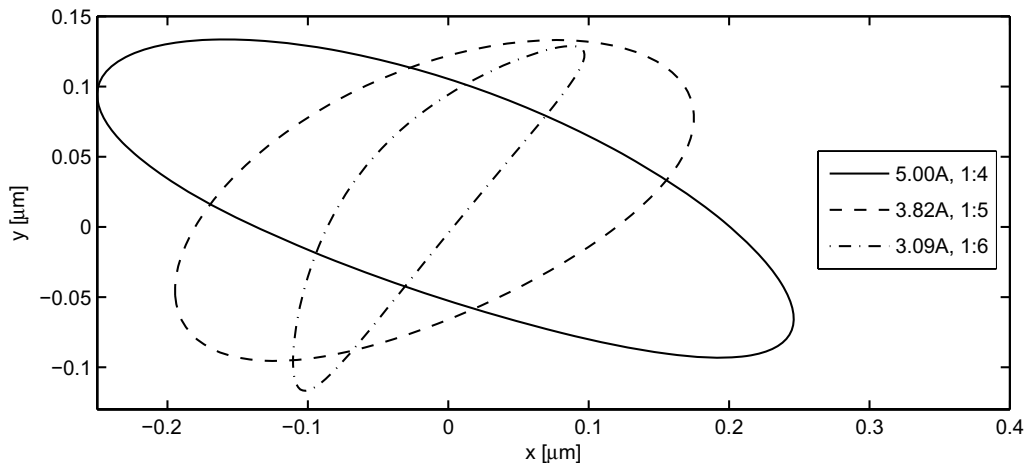


Fig. 1: Beam shapes in the Gaussian image plane for 0.8 mm deflection and different excitations of the deflectors, given as the excitation of the first stage and a ratio of excitation for the second one.

## References:

- [1] P. W. Hawkes, E. Kasper: Principles of Electron Optics, Volume 2, Academic Press 1996.
- [2] B. Lencová: On the design of electron beam deflection systems, *Optik* **79** (1988), 1-12.
- [3] B. Lencová: Trasys 3.70 user manual, SPOC Brno, April 2002.
- [4] Supported by the Institutional Research Plan No. AV0Z20650511 of AS CR.

# Low Energy Focused Ion Beam System For TEM Sample Preparation

Michael Rauscher, Bernhard Degel, Erich Plies, and Karin Marianowski

Institute of Applied Physics, University of Tübingen,  
Auf der Morgenstelle 10, D-72076 Tübingen, Germany

As a consequence of the continuing downsizing of semiconductor devices, transmission electron microscopy is becoming increasingly important in integrated circuit failure analysis. With modern FIB systems, high quality site-specific cross-section samples of layered materials may be prepared within only a few hours, thus allowing rapid failure identification and analysis. However, compared to conventional sample preparation techniques employing low energy (broad) ion beams the use of high energy (30-50 keV) focused ion beams inevitably leads to an increase in sample damage. Consequently, the removal or diminution of this has been an issue for some time [1-3]. One more recent approach is the utilisation of lower milling energies within the framework of the FIB method [4,5] - ideally utilising optically optimised systems for the low energy regime.

The basic design of the dedicated low energy ion beam column currently under test in our laboratory is shown in Fig. 1 [6]. Ions from a Gallium liquid metal ion source (LMIS) are accelerated using a

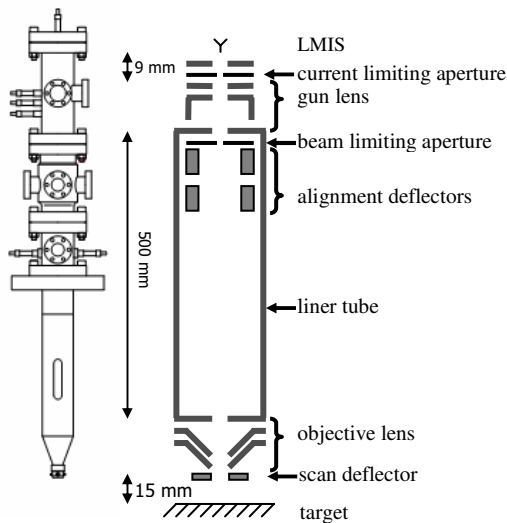


FIG. 1: Outline drawing of the experimental low energy ion-optical column.

three electrode gun lens. The source distance, i.e. the distance from the emitter tip to the first gun lens electrode, is 9 mm. An electrically insulated liner tube allows setting the drift space between the lenses on high potential. The beam is focussed to the grounded target by means of a three electrode objective lens with the last electrode being set on ground potential in order to keep the target region field-free. The clear working distance is 15 mm and the impact energy range is 1-3 keV.

The performance of the ion beam system will be discussed on the basis of classical particle-optical calculations, i.e. based on the determination of aberration coefficients, as well as on the basis of data from direct ray-tracing that includes the effects of Coulomb interactions. Initial experimental data on the ion optical system performance will also be presented [7].

## References:

- [1] N.I. Kato *et al.*, J. Vac. Sci. Technol. A 17 (1999) 1201.
- [2] R.M. Langford and A.K. Petford-Long, J. Vac. Sci. Technol. A 19 (2001) 982.
- [3] B. Arnold and H.D. Bauer, Practical Metallography 40 (2003) 109.
- [4] P. Gnauck, PhD thesis, University of Tübingen, 2000.
- [5] F. Altmann, Workshop "Präparative Aspekte der TEM", May 18<sup>th</sup> 2005, Oberkochen.
- [6] M. Rauscher and E. Plies, J. Vac. Sci. Technol. B 22 (2004) 3004.
- [7] Funding of part of this work by Bal-Tec AG Liechtenstein is gratefully acknowledged.

## In-column Corrected OMEGA Energy Filter: High-End Performance

G. Benner, E. Essers, B. Huber, G. Lang, A. Orchowski, A. Thesen, and P. Schlossmacher

Carl Zeiss SMT – Nano Technology Systems Division, D-73447 Oberkochen, Germany

The new 200 kV FE-TEM of Carl Zeiss NTS, the LIBRA<sup>®</sup> 200FE, houses the In-column Corrected OMEGA filter which goes back on a paper of Lanio, Krahl and Rose [1]. In the LIBRA<sup>®</sup> 200FE this filter was realized for the very first time as a commercial product and is the only in-column energy filter on the market with aberration correction [2]. The performance of the Corrected OMEGA filter was further investigated in special instruments as the ultra-high resolution TEM (UHRTEM) as well as in LIBRA<sup>®</sup> 200FE TEMs equipped with monochromized field emission (FE) source.

The UHRTEM, as a dedicated high-resolution 200 kV FE-TEM, has recently achieved a new record milestone in ultra-high imaging resolution [3,4]. Young's fringes extend to 0.8 Å isotropic in all direction and even to 0.7 Å in some directions. In an In-column energy filter TEM (EFTEM) the electron beam path goes through the energy filter in all operation modes (imaging, diffraction, spectroscopy). The ultra-high resolution performance clearly demonstrates that the Corrected OMEGA filter has no limiting effect on imaging quality consistent with theoretical estimations.

In spectroscopy mode with a monochromized FE source the Corrected OMEGA filter shows ultimate performance. ZLPs with FWHM values below 0.2 eV can easily be recorded: typically the FWHM is around 135 meV for an acquisition time of 1 sec. It should be noted that this is achieved with the same Corrected OMEGA filter and its current supplies which are built in the LIBRA<sup>®</sup> 200FE. Due to the superior performance of the Corrected OMEGA filter the energy resolution of this EFTEM is determined solely by the energy spread of the source and not by the energy filter itself. Thus, a monochromator upgrade instantly provides the better energy resolution of the monochromized source.

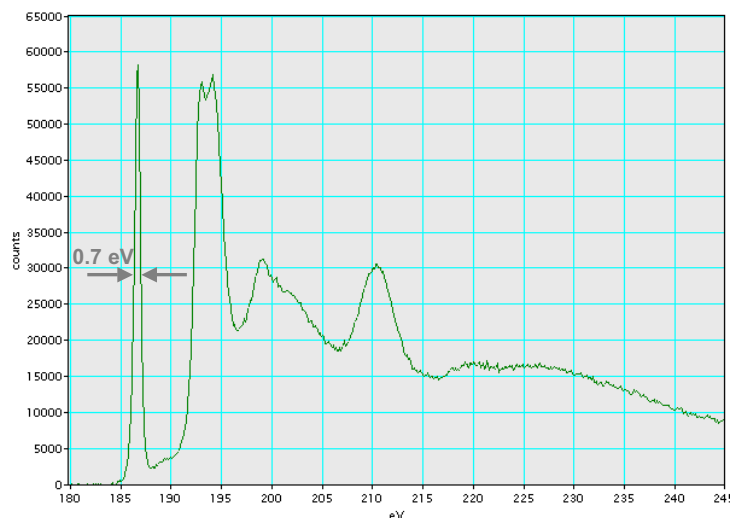


Figure: EELS spectrum of boron nitride recorded. HV supply of a monochromator FEG was used (but MC off);  $\pi^*$ -peak exhibits FWHM of 0.7 eV.

### References:

- [1] S. Lanio, H. Rose, D. Krahl, *Optik* **75** (1986) 56.
- [2] G. Benner et al., *Microsc. Microanal.* **10** (Suppl. 2), 2004, p. 860
- [3] Carl Zeiss SMT Press Release # 006/05 (19/01/2005); refer to <http://www.smt.zeiss.com/nts>
- [4] P. Schlossmacher, A. Thesen and G. Benner, *European Semiconductor*, Mid-March 2005, Vol. 27, No. 3, pp. 22-24

# Simulation of Systematic Current Variation in a Miniaturized Electron Gun Microcolumn Applications

Birgit Schröppel and Dieter P. Kern

Institute of Applied Physics, University of Tübingen,  
Auf der Morgenstelle 10, D-72076 Tübingen, Germany

Simulations are presented for a miniaturized field emission electron gun for systematic and rapid current variation to be used in an electrostatic microcolumn [1]. A rotationally symmetric tetrode system consisting of a self-aligned field emitter [1], an extractor, a current control electrode and an anode has been investigated for finding a suitable setup to allow fast variation of the beam current by approximately a factor of 10.

The variation of the beam current is achieved by changing the focusing voltage applied to the control electrode. To achieve high beam currents (e.g. 100 nA), the electron beam is strongly focused while for low currents (e.g. 10 nA) focusing is weak and a large fraction of the electron bundle is removed by the last gun electrode/anode.

Simulations of the tetrode system were performed using the SOURCE program package [2]. The influence of a variation of several electron gun parameters such as distances between electrodes, thicknesses of electrodes, radii of electrode apertures, and applied voltages was investigated. With respect to electrode/insulator design the range of variation was limited by the requirements of the intended microfabrication technique of the electron gun (employing conventional semiconductor technology) as well as electron optical considerations. Limitations for the applied voltages were set by the dielectric strength as well as the upper limit for the tolerable total emission current of the chosen tungsten field emitter.

Depending on the specific geometry one or two possible voltage settings were found for realizing the intended change in beam current. These settings correspond to real and virtual crossovers for the high beam current case, respectively. Details on the possible beam current variation, aperture angle of the resulting electron beam, as well as the characterization of the generated electron bundle by appropriate aberration coefficients for further electron optical calculations will be presented. From that the most favorable tetrode design for the miniaturized electron gun will be identified and discussed together with possible alternatives.

## References:

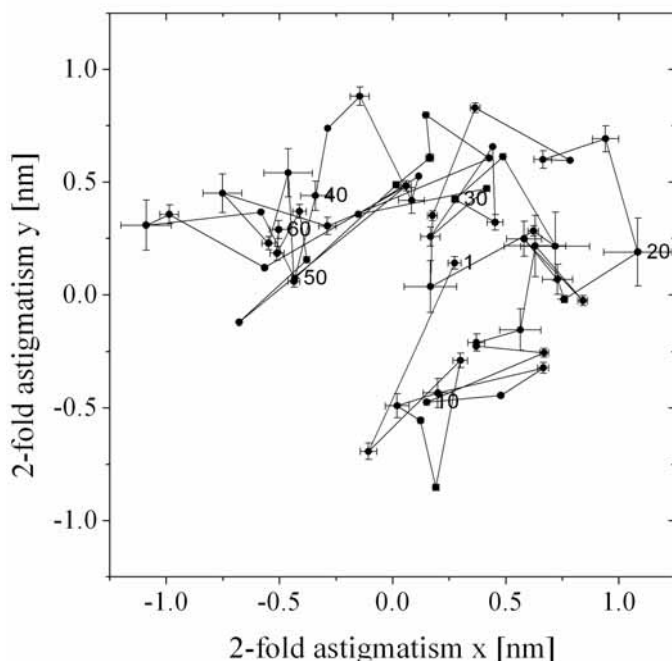
- [1] T.H.P. Chang, D.P. Kern, and L.P. Muray, J. Vac. Sci. Technol. B 6 (1990) 1698-1705
- [2] Program used for calculation: SOURCE by MEBS Ltd.
- [3] We gratefully acknowledge the support by Intel<sup>®</sup>

# Ultra-Precise Measurement of Optical Aberrations for Sub-Angstrom HRTEM

Juri Barthel and Andreas Thust

Institut für Festkörperforschung, Forschungszentrum Jülich GmbH, D-52425 Jülich, Germany

In the near future high-resolution transmission electron microscopes will be available, which provide an information limit well below one Angstrom on a routine basis. However, in order to perform reliable and reproducible materials science investigations on this length scale, the mere availability of the appropriate information limit is only a necessary but not a sufficient development stage. To obtain reliable and interpretable results, many more higher-order optical aberrations than presently usual have to be measured and controlled. The ultra-precise measurement of higher-order aberrations is a mandatory prerequisite for their consecutive correction either by hardware [1] or by software via phase retrieval methods [2]. For this purpose we started the ATLAS software project with the goal to obtain an aberration measurement solution, which satisfies extreme requirements with respect to (1) robustness, (2) precision, and (3) speed. Based on the well-known diffractogram tableau method [3], where the defocus and the 2-fold astigmatism induced by intentional beam tilts are observed as a variation of Thon rings, we gained new theoretical insights into the optimum choice of beam tilts, into coherence effects under strongly tilted illumination, and into the error propagation analysis of aberration parameters. Most important, we developed highly efficient software algorithms for the fast and ultra-precise recognition of diffractogram patterns.



The ATLAS software allows us to measure the low-order aberrations defocus and 2-fold astigmatism with nearly Angstrom precision. This is more than one order of magnitude more precise than existing solutions known to us. With the achieved precision it is for the first time possible to derive sufficiently accurate all higher-order aberrations, which are necessary to gain a controlled access to the sub-Angstrom regime. Moreover, the stability of a microscope can be diagnosed by a time-resolved high-precision measurement of the defocus and the 2-fold astigmatism.

Fig. 1: Time-resolved measurement of the 2-fold astigmatism over two minutes (60 images) at the spherical-aberration corrected CM 200 microscope installed in Jülich.

## References:

- [1] S. Uhlemann, M. Haider, *Ultramicroscopy* 72 (1998) 109.
- [2] A. Thust, M.H.F. Overwijk, W.M.J. Coene, M. Lentzen, *Ultramicroscopy* 64 (1996) 249.
- [3] F. Zemlin, K. Weiss, P. Schiske, W. Kunath, K.-H. Herrmann, *Ultramicroscopy* 3 (1978) 49.

# Multi-slice Simulation of Convergent Beam Electron Diffraction Patterns

Andrey Chuvilin and Ute Kaiser

Materialwissenschaftliche Elektronenmikroskopie, Universität Ulm, 89069 Ulm, Germany

Convergent Beam Electron Diffraction (CBED) is a technique with a wide range of unique capabilities. It can be applied for crystal symmetry determination, polarity determination of non-centrosymmetric crystals, temperature factors and charge density refinement, dislocations and interface study, lattice parameter determination and local strain analysis. Only a few tasks, such as symmetry group or polarity determination, can be solved by direct interpretation of CBED patterns. However, for most of the tasks, especially if quantitative results are required, dynamical calculations of CBED patterns have to be performed, which are mainly based on the Bloch-wave approach [1, 2] so far. However, if the crystal to be investigated is defective or interfaces have to be studied, the Bloch wave theory can not be applied without further approximations, because of a huge number of Bloch states in this case, which requires enormous computational effort.

The multislice method was suggested as an alternative for calculating nanodiffraction [3]. The advantage of the multislice method is that it does not require particular approximations for imperfect crystals and thus electron scattering for the distorted crystals can be calculated to the same accuracy as for the perfect crystals. Muller et al. [4] applied the multislice method to calculate correlated phonon background in CBED patterns. Thus it was shown, that real-space information is present in experimental CBED patterns and can be reproduced using the multislice method. Also using the multislice method, Spence et al. [5, 6] simulated successfully superstructural Laue rings from dislocation cores.

Here, we show that the multislice approach is capable to calculate deficient HOLZ lines in the central CBED disk correctly and fast even for large models by implementing our new slicing scheme [7]. Consequences of this approach seem to be of general value for the understanding of the process of CBED pattern formation and in particular to answer the question of how local a CBED pattern can be.

## References

- [1] K. Tsuda, M. Tanaka, *Acta Cryst. A* 51 (1995) 7.
  - [2] J.M. Zuo, J.C. Mabon, WebEMAPS software, University
  - [3] J.C.H. Spence, *Acta Cryst. A* 34 (1978) 112.
  - [4] D.A. Muller, B. Edwards, E.J. Kirkland, J. Silcox, *Ultramicroscopy* 86 (2001) 371.
  - [5] C. Koch, J.C.H. Spence, C. Zorman, M. Mehregany, J. Chung, *J. Phys.: Condens. Matter* 12 (2000) 10175.
  - [6] J.C.H. Spence, C. Koch, *Phil. Mag. B* 81 (11) (2001) 1701.
  - [7] A. Chuvilin and U. Kaiser *Ultramicroscopy* 104, 2005,73
- This work has been supported by the DFG KA 1295/2-3

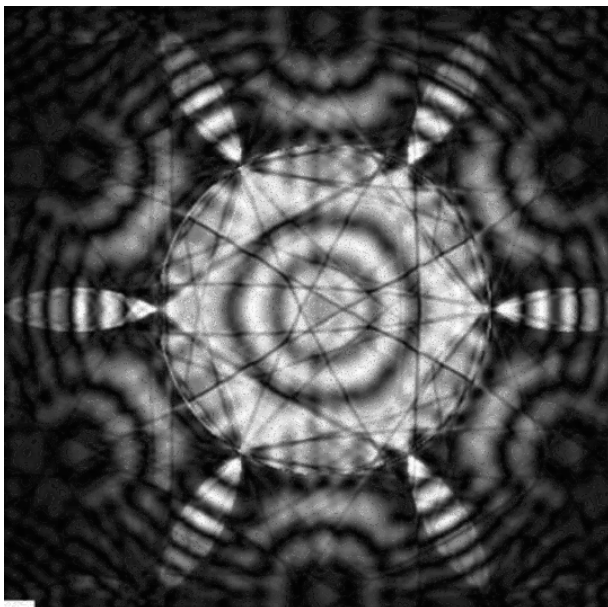


Figure: CBED pattern calculated for a probe position near Si edge simulated by the Multislice Method [7]

## CBED Measurements of Thermal Expansion on Copper and Aluminum

M. Hofmann, J. Thomas, T. Gemming, K. Wetzig

IFW Dresden, Leibniz Institute for Solid State and Materials Research Dresden, P.O. Box 270116, D-01171 Dresden, Germany

In the field of surface acoustic wave devices (SAW) higher frequencies and operation power lead to a higher load of the SAW device electrodes. This results in a stress-induced material transport, called acoustomigration. This material transport is connected with local stress gradients and can cause the failure of the SAW device [1].

Recently, the material of the metallizations of electronic circuits changes from Al to Cu. Besides the higher conductivity, the higher resistance of Cu against migration processes is the reason for that.

To understand the mechanism of acoustomigration the measurement of local stresses with a lateral resolution better than 100 nm is necessary. The convergent beam electron diffraction (CBED) seems to be suitable method. It allows the measurement of lattice parameters up to the high accuracy of  $\Delta a/a = 2 \cdot 10^{-4}$  [2]. The stress state can then be derived from the lattice parameters.

Especially the CBED measurements on Cu need the well-defined consideration of dynamical effects with passable time for doing that. The simulation procedures and the achievable accuracy have been checked by measurements of the thermal expansion of Al und Cu single crystals.

The measured single crystals were electrochemically and conventionally (ion milling) thinned. The measurement of the lattice parameters changed by thermal expansion needs the accurate determination of the HOLZ line positions. The Hough transformation is a well-known method to determine the position of lines in diffraction patterns [3]. Software based on the package of Krämer [3] was used for the determination of the HOLZ line positions and the fit of the experimental patterns. The lattice constants were calculated by comparison of the differences in the HOLZ line intersections between the experimental patterns and the kinematical simulations with dynamical correction terms of each used HOLZ line. These dynamical correction terms were calculated by comparison of the kinematical and dynamical HOLZ line positions and stored in a database. Thereby, the fit procedure works faster without loss of accuracy. To reduce the number of fit parameters it is necessary to assume a model for the strain state. A first simple model, the uniform contraction of all lattice axes, leads to unexpected values. A modified model bases on a two-dimensional stress-state. The thinned samples are small disks with a hole in the center. In the x-y-plane the contraction is equal in all directions. But in the normal z-direction the Poisson dilatation is superposed with a thermal contraction. This assumption led to significant lower deviations from the expected values. The measurements of the thermal expansion on aluminum and copper single crystals show that the needed accuracy of  $5 \cdot 10^{-4}$  for the measurements of the stresses in the SAW metallizations is reached not only in Al but also in Cu, despite the larger dynamical effects due to higher Z in the latter case.

[1] S. Menzel, K. Wetzig in "Metal Based Thin Films for Electronics", ed. K. Wetzig, C.M. Schneider, (Wiley-VCH, Weinheim) (2003), 245.

[2] D.B. Williams, C.B. Carter in "Transmission Electron Microscopy II", (Plenum Press, New York) (1996), 338.

[3] S. Krämer, J. Mayer, C. Witt, A. Weickenmeier and M. Rühle, Ultramicroscopy 81 (2000), 245.

Financial support by the DFG under contract GE 1037/6-1 is gratefully acknowledged.

# TEM Orientational Studies of $\alpha\text{Cr}_2\text{O}_3$ Microcrystals Growing in Amorphous Films

V.Yu. Kolosov<sup>1</sup>, C.L. Schwamm<sup>1</sup>, A.G. Bagmut<sup>2</sup>

<sup>1</sup>Physics Dept., USUE, 8 Marta str., 620219 Ekaterinburg, Russia, vladkol@usue.ru

<sup>2</sup>National Technical University "KhPI", Kharkiv, Ukraine.

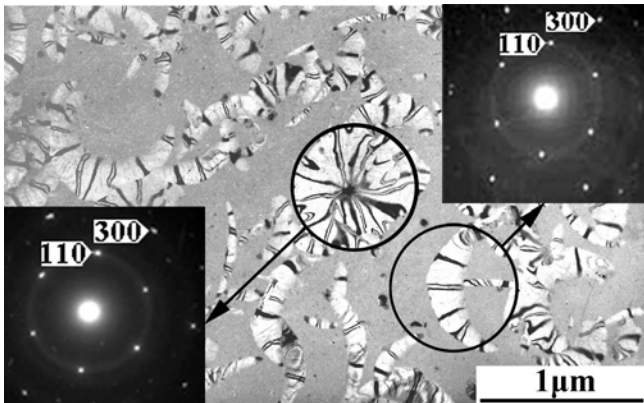


Fig. 1 Amorphous matrix with  $\alpha\text{Cr}_2\text{O}_3$  round and crescent-like crystals with SAD images.

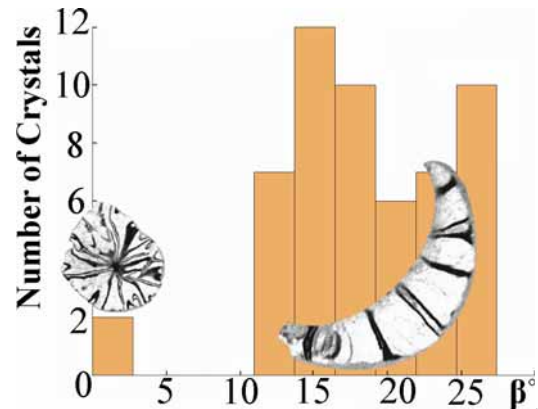


Fig. 2 The distribution of  $\alpha\text{Cr}_2\text{O}_3$  crystals by orientation angle  $\beta$

Bend contour technique [1] is very useful for *transmission electron microscopy* studies of lattice orientation, in particular for "transrotational" [2] crystals with *strong internal lattice bending*. The  $\alpha\text{Cr}_2\text{O}_3$  crystals grown (400°C, 5 min.) in laser evaporated substrate-free amorphous films are of two main morphology types: round and crescent-like, Fig.1. The [001] direction in the nucleus is, correspondingly normal and declined from the normal (through angle  $\beta$ , Fig. 2) to the film plane. Contrary to selected area diffraction (SAD), giving the point patterns of the same lattice orientations, (Fig. 1), detailed analysis of "transrotational" crystals based on bend contour patterns refines lattice orientations of crescent-like crystals ( $\beta = 13 \div 27^\circ$ , Fig. 2). The value of local internal lattice planes bending, peaks at about 180° (measured for {300}) per micrometer of crystal length, misorientation in crystal boundaries  $\sim 10\text{-}70^\circ$ , (in average around 30°).

Also we observe that internal lattice plane bending depends on initial crystal orientation and crystal size: the more [001] is declined from normal to the film plane, the more is bending of internal lattice of this crystal as well as crystal length. The radius of morphological curvature of crescent-like crystals is roughly independent from other morphological and orientational parameters — it determines on the early stages and stay constantly during crystal growth.

Thus TEM bend contour method makes it possible to study the relationship between parameters of internal lattice bending and parameters of crystal morphology for a crystals. We suppose that it is the strong internal lattice bending (around the axis lying in the film plane) revealed from the bend contour patterns, that determines most of the regularities observed.

This work is partially supported by INTAS (00-100), pending support from RFBR (04-02-96072).

[1] V.Yu. Kolosov Proc. XII ICEM, Seattle, San Francisco Press, v.1 (1990), p. 574.

[2] V.Yu. Kolosov and A.R. Thölen, Acta Mater. 48 (2000), p. 1829.

## TEM and AFM Studies of Spots Formed in Amorphous Films by Electron Beam

V.Yu. Kolosov<sup>1</sup>, C.L. Schwamm<sup>1</sup>, R.V. Gainutdinov<sup>2</sup> and A.L. Tolstikhina<sup>2</sup>

<sup>1</sup>Physics Dept., USUE, 8 Marta Str. 62, 620219 Ekaterinburg, Russia, VladKol@usue.ru

<sup>2</sup>Institute of Crystallography RAS, Leninskii prospekt 59, 119333 Moscow, Russia

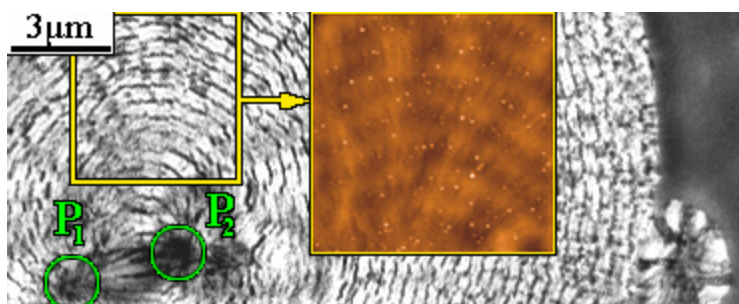


Fig. 1 TEM of Se crystal in amorphous matrix.  
AFM of selected area on insert.

At the present paper we use transmission electron microscopy (TEM), including *in situ* studies and video-records analysis, combined with atomic force microscopy (AFM) to study the internal (TEM) and surface (AFM) structure of some, concrete transrotational [1] crystals. Two different kinds of crystals — Se and  $\alpha\text{Fe}_2\text{O}_3$  were produced by electron beam annealing in amorphous films prepared by vacuum condensation (Se, with Te doping) and pyrolysis ( $\text{Fe}_2\text{O}_3$ ).

Complicated regular change in lattice orientations are indicated by regular bend contour patterns (presented earlier for both Se [2, 3] and  $\alpha\text{Fe}_2\text{O}_3$  [1, 2]). It is the basis for the present combined studies, where the interrelation of crystal lattice orientation and surface relief has been of prime interest.

The macro relief of the crystal as a whole - usually Se spherulites ( $\varnothing\sim 20\text{-}50\ \mu\text{m}$ ) having form of a hat, lying upside down with maximal deflection  $\sim 0.5\text{-}1\ \mu\text{m}$ , and being flat for  $\text{Fe}_2\text{O}_3$ . The central region with 2 poles, separated by a distance about 3  $\mu\text{m}$  is studied for Se spherulite. Orientation [001] is almost normal to the film plane at the poles (Fig. 1) and is parallel to this plane in between (TEM data). It corresponds to AFM data: the poles are the lowest points of the crystal; an area including 2 poles has the form of a boat (width  $\sim 1.5\ \mu\text{m}$ ). Concentric zones of different orientations and imperfection revealed by TEM are also seen in AFM, based on the variations in mean height (for Se, Fig. 1) and on the character of fibrous structure ( $\text{Fe}_2\text{O}_3$ ) which differs for two types of spherulites. Both spherulites have also radial elongated nodes and hollows of different character revealed by AFM.

Probably most important observation for the amorphous-crystalline interface made for crystallization of  $\alpha\text{Fe}_2\text{O}_3$  phase: there are strong variations in crystal height, probably associated with variations of lattice orientations, which should be taken into account for advanced models of crystal growth in amorphous films. Anyway it is evident, that simple concept: flat crystal growing along the inside of amorphous film, powered primarily by tensile stresses (caused by the density changes) in parallel with various imperfections at the crystal growth front, is inadequate.

This work is partially supported by INTAS (00-100), pending support from RFBR.

[1] V.Yu. Kolosov and A.R. Tholen, *Acta Mater.*, v. 48 (2000), p. 1829.

[2] V.Yu. Kolosov *Proc. XIII ICM*, Seattle, San Francisco Press, v.1 (1990), p. 574.

[3] I.E. Bolotov and V.Yu. Kolosov, *Phys. Stat. Sol.* v. 69a (1982), 85.

# Electron Holographic Materials Analysis at Atomic Resolution

Martin Linck, Hannes Lichte and Michael Lehmann

Triebenberg Laboratory, University of Dresden, 01062 Dresden, Germany

Electron holography is a promising method to contribute to the question “Which atom is where?”. Previous investigations on GaAs in 110-orientation have shown that different atomic numbers are distinguishable on the basis of their specific phase shift [1]. Since the contrast in the phase of the object exit wave does not suffer from the Stobbs factor [2], electron holography offers a direct and quantitative interpretation which can be used for materials analysis.

Interpretation of data in terms of atomic species only makes sense, if the relationship between phase shift  $\varphi$  and atomic number  $Z$  is known. In literature a coarse dependence of  $Z^{0.6}..Z^{0.7}$  has been given [3]. A closer look at the dependence reveals new problems for direct interpretation (fig. 1). The phase shift, measurable from the aberration-free image wave at the center of the projected atom, was simulated at a resolution of 0.1 nm by a multislice algorithm in EMS [4] using a cubic supercell of 5 nm length with a centered single atom. Consulting the periodic table of elements, an increasing phase shift can be found for neighbouring main group elements while adjacent subgroup elements only show weak differences. In particular, the lanthanides (4f) show inversions. So, although the components of the specimen are known, different atom columns cannot be easily distinguished in every case. Additionally the  $\varphi(Z)$ -dependence changes with specimen thickness, when dynamic interactions gain influence. Thus comparison with simulations is still very important.

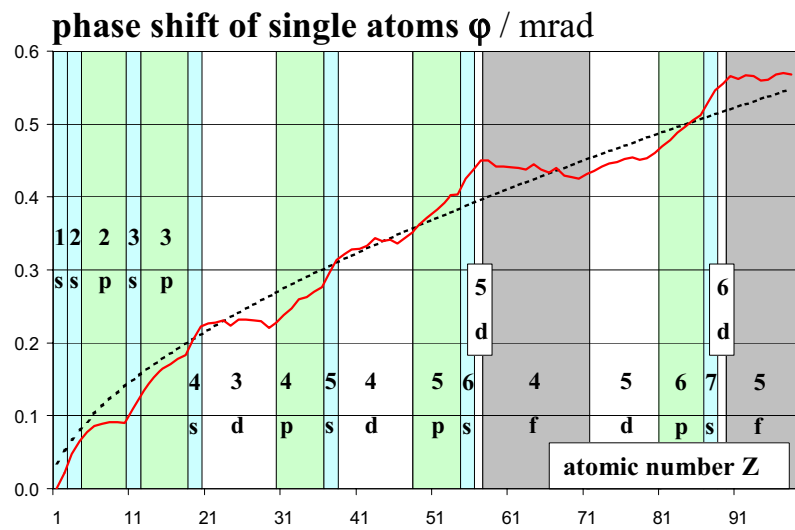


Fig. 1: Single atom phase shift (solid line), computed by EMS [4] with scattering factors of Weickenmeier and Kohl for 0.1 nm resolution.  $Z^{0.6}$  (dotted line) only gives a coarse approximation. The background indicates the partially occupied outer electron orbitals.

With improvements in resolution and phase detection limit, one should think about simulation techniques, which contain also more accurately the influence of bonding orbitals instead of assuming only spherically symmetric scattering factors. Simulation results of an element in different compositions then might vary from each other depending on the bonding and the structure. [5]

[1] M. Lehmann and H. Lichte, Cryst. Res. Technol. (2005) 149-160.

[2] M. Lehmann, Microsc. Microanal., Vol.9 (Suppl.3) (2003) 046.

[3] E.J. Kirkland, Advanced Computing in Electron Microscopy, Plenum Press (1998).

[4] P.A. Stadelmann, Ultramicroscopy 21 (1987), 131-146.

[5] Discussions on Triebenberg esp. with Dr. D. Geiger and A. Rother are gratefully acknowledged.

# Contrast Theory for Advanced TEM Instrumentation: the Spherical-Aberration Corrector and the Wien-Filter Monochromator

Markus Lentzen, Andreas Thust, and Knut Urban

Institut für Festkörperforschung, Forschungszentrum Jülich GmbH, 52425 Jülich, Germany

In transmission electron microscopy attempts are made today to improve high-resolution imaging through the combined use of spherical-aberration correctors [1] and gun monochromators. The proper tuning of the objective lens defocus  $Z$  and the now variable spherical aberration  $C_S$  extends the interpretable resolution of structure images up to the information limit  $g_{\max}$  of an instrument [2, 3]. If the scattered part of the exit wave function, carrying the structure information, advances the unscattered part by a phase of  $2\pi\chi_0$ , then the optimum values for bright-atom contrast are [4]:

$$Z = \frac{8\chi_0}{\lambda g_{\max}^2}, \quad C_S = -\frac{40\chi_0}{3\lambda^3 g_{\max}^4}, \quad R = \frac{16|\chi_0|}{3g_{\max}},$$

with the wavelength  $\lambda$ , and the delocalisation in the image plane,  $R$ .

The information limit is improved substantially by the use of gun monochromators, which filter a small energy interval from the source distribution by a slit in an energy-dispersive plane, and thus reduce the deleterious effect of the chromatic aberration of the objective lens. For one of these monochromators, of the Wien-filter type [5], the dispersion is still present in the illumination cross-over acting as the virtual source: electrons of different energy  $E$  appear to impinge from different directions  $\mathbf{Q}(E)$  onto a certain point in the object plane. A detailed recalculation of the contrast transfer under partially coherent illumination yields, besides the established envelopes for spatial and temporal coherence,  $E_S$  and  $E_F$  [6], a new damping envelope  $E_D$  reflecting the dispersion:

$$E_S = \exp\left(-\pi^2 q_0^2 |\nabla\chi|^2\right), \quad E_F = \exp\left(-\pi^2 \Delta_F^2 \left(\frac{\partial\chi}{\partial Z}\right)^2\right), \quad E_D = \exp\left(-\pi^2 \Delta_M^2 \left(\frac{\partial\mathbf{Q}}{\partial Z} \nabla\chi \cdot \vec{e}_Q + \frac{\partial\chi}{\partial Z}\right)^2\right),$$

with the aberration function  $\chi$  of the objective lens, defocus  $Z$ , semi-convergence  $q_0$ , defocus spread  $\Delta_F$  due to high-voltage and lens-current instabilities, defocus spread  $\Delta_M$  due to the remaining energy spread, and a unit vector  $\mathbf{e}_Q$  along the dispersion axis. The dispersion parameter  $\partial\mathbf{Q}/\partial Z$  is the direction change per energy divided by the defocus change per energy, due to the chromatic aberration. The envelope  $E_D$  introduces an asymmetric damping of spatial frequencies  $\mathbf{g}$  and  $-\mathbf{g}$ , and hence an inevitable asymmetric contrast transfer, which has to be considered in any high-resolution contrast analysis, either by image simulation or by wave function reconstruction methods.

## References:

- [1] M. Haider, H. Rose, S. Uhlemann, E. Schwan, B. Kabius, K. Urban, *Nature* 392 (1998) 768.
- [2] M. Lentzen, B. Jahnen, C.L. Jia, A. Thust, K. Tillmann, K. Urban, *Ultramicroscopy* 92 (2002) 233.
- [3] C.L. Jia, M. Lentzen, K. Urban, *Microscopy and Microanalysis* 10 (2004) 174.
- [4] M. Lentzen, *Ultramicroscopy* 99 (2004) 211.
- [5] P.C. Tiemeijer, *Inst. Phys. Conf. Ser.* 161 (1999) 191.
- [6] K. Ishizuka, *Ultramicroscopy* 5 (1980) 55.

# Electron Holography for Quantitative Measurements at Atomic Dimensions

Michael Lehmann

Triebenberg Lab, Institute of Structure Physics, Dresden University, D-01062 Dresden, Germany

In high-resolution transmission electron microscopy (HRTEM), there is large quantitative mismatch (factor 3..5) of lattice fringe contrasts, when experimental image intensities are compared with simulated ones. This discrepancy is widely known as Stobbs-factor. In HRTEM however, the hunt for the grounds of the Stobbs-factor is not straightforward because of mainly two reasons: Firstly, only the intensity of the aberrated image wave is recorded, hence the phase information is lost, which only allows pseudo wave optical analysis. Secondly, the image intensity is formed by both elastically and inelastically scattered electrons, which hampers the quantitative comparison with simulations.

Off-axis electron holography is intrinsically a full quantitative method for recording and reconstruction of the electron wave in amplitude and phase. This is accomplished by means of recording two holograms, the object hologram and the empty hologram for reference. Both holograms are reconstructed with the same parameters, and the resulting aberrated image waves are divided with each other. This yields the normalized amplitude and the corrected phase free from artificial modulations caused by distortions of projector lenses, biprism filament, and fiber optics of the CCD-camera. Subsequent correction of the coherent wave aberration yields the object exit-wave, which corresponds to the elastic electron wave at the exit surface of the sample in the electron microscope. This object exit-wave is a two-dimensional data array, which offers the possibility of sophisticated wave optical analysis in both real and reciprocal space:

- The measurement of reflection intensities in the holographic sideband (Fourier transform of the image wave) allows an accurate zone-axis alignment of the crystal, which is the ground for quantitative analysis.
- Local variations of thickness and crystal tilt can easily be identified by holographic nanodiffraction.
- The reconstruction in the light of single reflections allows the quantitative analysis of their contribution to the object exit-wave in real space. This is of special interest for wedge-shaped samples, where the excitation of reflections can be measured in amplitude and phase depending on specimen thickness and quantitatively compared with corresponding object exit-wave simulations.
- Measuring amplitude and phase of the object exit-wave at atom positions and plotting as "argand-plot" permits studying absorption, i.e. the loss of electrons from the coherent wave field. With increasing signal-to-noise ratio, counting the number of atoms in an atomic column is within reach.

Luckily, all holographic investigations show that the reconstructed object exit-wave is hardly affected by the Stobbs-factor opening the possibility for sophisticated material analysis with atomic resolution.

## Ab-initio simulation of the object exit wave of ferroelectrics

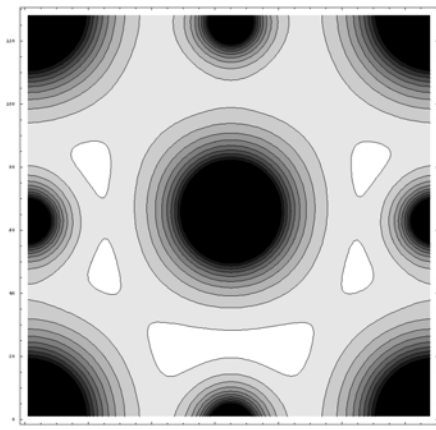
Axel Rother<sup>a</sup>, Sibylle Gemming<sup>b</sup> and Hannes Lichte<sup>a</sup>

<sup>a</sup> Triebenberg Laboratory, Institute of Structure Physics, Dresden University, Dresden, Germany

<sup>b</sup> Institute of Physical Chemistry and Electrochemistry, Dresden University, Dresden, Germany

Ferroelectrics are unique in that, below the Curie temperature, they transform from a cubic unit cell to a tetragonal one, giving rise to an inner electric polarization along the tetragonal axis. In [1], it is shown that High Resolution Electron Holography reveals electric dipoles in the unit cells of e.g. BaTiO<sub>3</sub>, which are the basic assumption in solid state physics for understanding ferroelectricity. To interpret these findings accurately and, at the end, quantitatively, it is indispensable to model the potential distribution in the unit cell, which gives rise to the phase modulation of the object exit wave analyzed by holography.

Simulations with parameterized atomic potentials (e.g. [2]) cannot provide the needed data about the electric potential distribution. For accurate potential calculations, we chose the following way: In a first step, ab-initio calculations are performed to obtain the charge-density distribution in a tetragonally distorted unit cell of BaTiO<sub>3</sub>. The valence electron density is calculated within the framework of DFT (Density Functional Theory), as implemented in the plane-wave pseudo-potential program package ABINIT [3]. The core-valence interaction is described by non-conserving soft-core potentials, which allow the explicit treatment of the semi-core states of Ti and Ba. For generation of the required total electron density, the core electron density derived from the resulting pseudo-potential is added to the core-valence density. In a second step, the Coulomb potential distribution in the unit cell is determined by solving the Poisson-equation for the resulting charge-density distribution. Since all the involved distributions are periodic in real space, the Poisson equation is solved preferably in Fourier space. Finally, the potential distribution is used for computing the object exit wave, e.g. by means of a Multi-Slice Method.



The analysis of the data clearly reveals a dipole component in the projected potential of the BaTiO<sub>3</sub> unit cell (fig.1) hence confirms the findings of [1]: The atomic dipoles in ferroelectrics can be characterized from the phase image reconstructed from a high-resolution electron hologram.

Fig.1: Projected potential of tetragonally distorted barium titanate

### References:

- [1] Ch. Matzeck, H. Lichte, M. Reibold, *Ferroelectric Polarization as the Gradient of Phase Shift in Electron Holography at Atomic Resolution*, this Conference
- [2] A. Weickenmeier, H. Kohl (1991), *Computation of Absorptive Form Factors for High-Energy Electron Diffraction*, Acta Cryst. A47, 590-597
- [3] The ABINIT code is a common project of the Universite Catholique de Louvain, Corning Inc., and other contributors.
- [4] Support from DFG in the Framework of FOR 520 is gratefully acknowledged

## Special aspects on the scattering of high-energetic electrons on crystals

Axel Rother<sup>a</sup>, Kurt Scheerschmidt<sup>b</sup>, and Hannes Lichte<sup>a</sup>

<sup>a</sup>Triebenberg Laboratory, Institute of Structure Physics, Dresden University, 01062 Dresden, Germany

<sup>b</sup>Max Planck Institute of Microstructure Physics, Weinberg 2, 06120 Halle, Germany

Quantitative analysis becomes more and more important in High-Resolution-Transmission-Electron-Microscopy (HRTEM). The current task of HRTEM-development is expanding the method from the sole characterization of the periodic structure to the determination of position and species of atoms within the specimen. Electron Holography is a unique technique capable of recording a 2-dimensional electron wave. In order to interpret this electron wave quantitatively, it is crucial to understand the interaction process between electron and specimen. Several methods have been developed to describe the scattering process. They offer a good qualitative description, although quantitatively they suffer from inaccuracy, which may contribute to the Stobbs-factor [1]. The problem has not been solved yet, although several proposals have been made.

In this work, some of those proposals have been compared analytically and quantitatively: The influence of the backscattered electrons, the singular structure of the scattering potential, and the thermal movement of the atoms within the solid. Firstly, the influence of the backscattered electrons is examined through the general solution of the stationary Schrödinger-Equation of a crystal as proposed by Lamla [2]. The only restrictions within that approach are posed to the geometry of the 3-dimensional crystal: The crystal is infinite in the directions perpendicular to the optical axis and finite along the optical axis. Within this geometry, the wave-function can be found by using a plane-wave-expansion in the vacuum region and a general Bloch-wave-expansion with complex Bloch-vectors in the crystal region. The solution does not incorporate approximations. The result raises questions with respect to the correct incorporation of the boundary conditions and hence the influence of the backscattered electrons, which are usually neglected. Secondly, the multislice method [3] is utilized to analyze the singular structure of the scattering potential. It is shown that screened atomic potentials with and without singularity produce a different behaviour in the simulation, especially at high sampling rates. The results are additionally compared with experimental data. Thirdly, concerning the thermal movement of the atoms it is shown that in electron holography an averaged 2-dimensional wave is measured and that the attenuation of the reflexions in Fourier-Space is not fully described by using the Debye-Waller-approach [4] originally developed for X-ray scattering.

It is demonstrated that all these factors produce effects, which might be not fully understood until now. This suggests that they probably contribute to the Stobbs-factor. Further investigations and developments are needed for a more appropriate consideration in image simulations.

### References:

- [1] C.B. Boothroyd (1998), *Why don't high-resolution simulations and images match?*, Journal of Microscopy, Vol. 190, 99-108
- [2] E. Lamla (1938), *Zur Theorie der Elektronenbeugung bei Berücksichtigung von mehr als 2 Strahlen und zur Erklärung der Kikuchi-Enveloppen. I*, Annalen der Physik, 5. Folge, Band 32
- [3] J.M. Cowley, A.F. Moodie (1957), *The Scattering of Electrons by Atoms and Crystals. I. A New Theoretical Approach*, Acta Cryst. 10, 609-619
- [4] e.g. J.C. Slater (1967), *Insulators, Semiconductors and Metals Vol.3*, McGraw-Hill Book Company

## The Frozen Lattice Model: Is it Valid to describe Thermal Diffuse Electron Scattering?

K. Scheerschmidt

Max Planck Institute of Microstructure Physics, D-06120 Halle, Germany, [schee@mpi-halle.de](mailto:schee@mpi-halle.de)

Molecular dynamics simulations solving Newton's equations of many particle systems and using enhanced empirical potentials are performed to obtain frozen lattice (FL) models suitable for electron microscope image simulations [1, 2]. Snapshots of the atomic structures [3] are taken at equidistant times from a constant volume simulation (NVE ensemble), slightly rescaling all particle velocities to control the temperature up to the thermal equilibrium (cf. Fig. 1 for energy equilibration in a [100]-40x40x40GaAs-supercell with 216000 atoms). The simulated exit wave functions based on the FL's are transferred through the microscope with Gaussian distributed defoci describing the instabilities. Incoherent collection (cf. Fig.2, defocus half width 10nm around Scherzer, 200kV, Cs=1.2mm) of the intensities yields the phenomenon of thermal diffuse scattering (TDS). The semi-classical FL approach is justified because the atomic vibrations in a crystal (energies  $\leq 0.1\text{eV}$ , velocities  $\approx 10^3\text{m/s}$ ) are much slower than the incident fast electron (100keV,  $10^8\text{m/s}$ ). If the incoherence is suitably considered and the specimen is thicker than the free mean phonon excitation path it is equivalent to a rigorous quantum approach [4]. However, by analyzing the vibrational spectrum a direct influence of the different phonon modes can be revealed in the images. A contrast mismatch between FL-simulated TDS and the usual approach using Debye-Waller factors corresponding to  $\langle u^2 \rangle$  (cf. Fig. 1 and 2 insets), indicates whether phonon scattering is sufficiently considered [5,6]

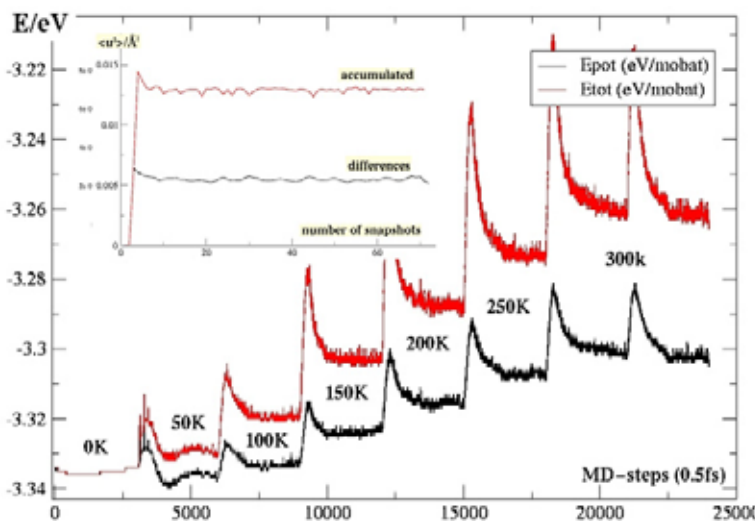


**Fig.1** Total and potential energy during MD equilibration at different temperatures (in K). Inset: mean atomic square displacements of 300K.

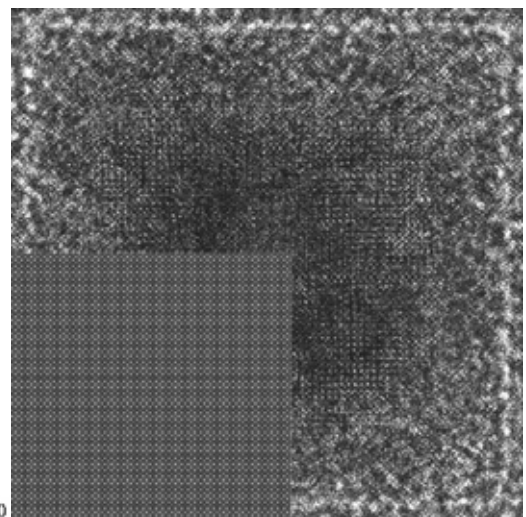


**Fig.2** Comparison of TDS simulation with FL-approach and Debye-Waller description (inset).

### References:

- [1] K. Scheerschmidt, D. Conrad, and A. Belov, *Comput. Mater. Sci.* **24** (1997) 108-115.
- [2] D. Timpel, K. Scheerschmidt, and S. Garofalini, *J. Non-Cryst. Solids* **221** (1997) 187-198.
- [3] How to simulate TDS with MD relaxed frozen phonon states was discussed at the International Triebenberg Workshop in September 2003 near Dresden. All participants, but especially Harald Rose, are kindly acknowledged.
- [4] Z.L.Wang, *Acta Cryst.* **A54** (1998) 460 and *Phil. Mag.* **B79** (1999) 37.
- [5] K. Omoto, K. Tsuda, and M. Tanaka, *J. Electron Microscopy* **91** (2002) 67.
- [6] L.M. Peng, S.L. Dudarev, and M.J. Whelan, *Monographs on the Physics and Chemistry of Materials*, Oxford Sci. Publ. 2004.

## Studies and Application of Object Waves Retrieved from HRTEM Focus Series

M. Svete, W. Mader

Institut für Anorganische Chemie der Universität Bonn, Römerstraße 164, D-53117 Bonn, Germany

The contrast in single HRTEM images is formed by the electron wave perturbed in the imaging system of the electron microscope and hence contains artefacts. The interpretation of HRTEM contrast is substantially improved on the basis of the electron wave at the exit face of the object. One alternative to retrieve the object wave is the reconstruction from a set of HRTEM images taken with varying focus [1,2]. In the present contribution we investigate restored object wave functions from different materials by means of simulated images taking into account the specimen parameters thickness  $t$  and crystal tilt ( $\tau_1, \tau_2$ ) off the exact zone axis. The aim of the study is to obtain information on the specimen parameters depending on the crystal system and as a function of the image resolution. Furthermore, it is possible to obtain diffraction patterns of nanometre-sized regions from the electron wave, and the patterns can be used to monitor thickness variations as well as bending of the imaged crystal.

HRTEM images are acquired with a Philips CM300 UT FEG electron microscope with spherical aberration coefficient  $C_s = 0.6$  mm. Exit wave reconstructions are performed using the TrueImage software (FEI company), and the EMS program package [3] is used for image simulations. Materials investigated include Si in zone axes such as [001], [110], and [103] and  $\beta$ - $\text{Si}_3\text{N}_4$  in [0001]. Fig. 1 shows the amplitude and phase of the reconstructed wave of Si in [001] with the simulated image and atom positions as insets. The crystal thickness increases from top right to bottom left, which is also displayed in the fading amplitude at the very thin crystal region. The square dot pattern of the amplitude and the phase image show little variations which allows thickness determination with accuracy not better than approx. 1 nm. However, reversals of the contrast of amplitude and/or phase are well observed at other crystal thicknesses.

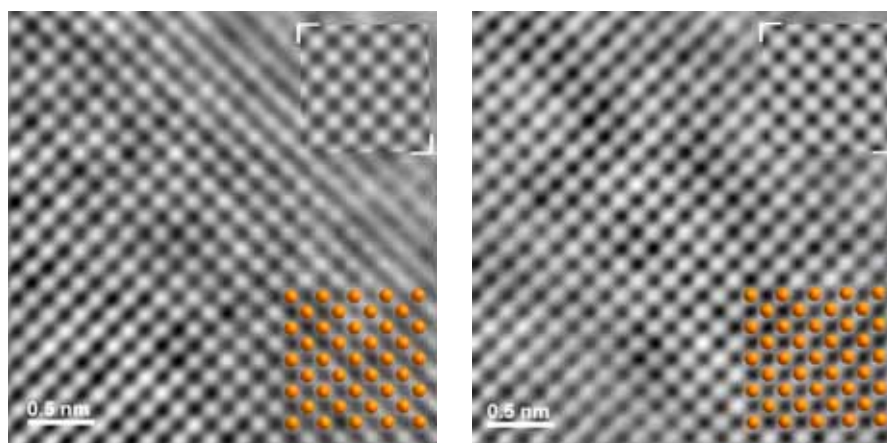


**Fig. 1:** Reconstructed exit wave of Si in [001] with insets of simulated wave and structure model. Simulation is exactly in the [001] zone axis and for crystal thickness  $t = 8.15$  nm.

### References:

- [1] M. Op de Beeck, D. Van Dyck, W.M.J. Coene, Ultramicroscopy 64 (1996) 167.
- [2] A. Thust, M.H.F. Overwijk, W.M.J. Coene, M. Lentzen, Ultramicroscopy 64 (1996) 249.
- [3] P.A. Stadelmann, Ultramicroscopy 21 (1987) 131.

Andreas Thesing and Helmut Kohl

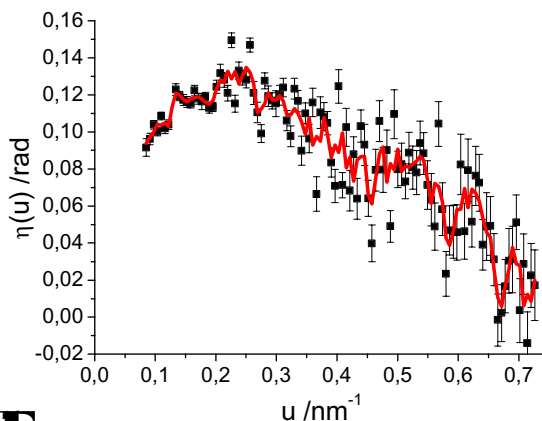
Physikalisches Institut und Interdisziplinäres Centrum für Elektronenmikroskopie,  
Westf. Wilhelms-Universität Münster, Wilhelm-Klemm-Str. 10, 48149 Münster, Germany

We investigated diffractograms of elastically filtered images of thin amorphous foils of C, Si and Ge using the weak object approximation [1]. In this approximation the contrast transfer function in diffractograms contains a phase  $\eta$ , which can be attributed to complex scattering amplitudes due to the breakdown of the first-order Born approximation. With the spatial frequency  $u$  the atomic scattering amplitude  $f_a(u)$ , the two-particle structure factor  $S(u)$ , the phase shift  $\chi(u)$  caused by the lens aberrations and the defocus  $\Delta f$ , the diffractogram of an elastically filtered image of a weak object consisting of one element “a” can be written as [2, 3]

$$|\mathcal{C}(f, \Delta)|^2 f_a(u) S(u) E_a(u) E_c(u) |a| u f^2 \cdot \sin u(\chi(u, \Delta) - \eta(u)). \quad (1)$$

The damping envelopes  $E_a(u)$  and  $E_c(u)$  are caused by partial coherence of the electron beam due to the energy spread of the incoming electrons and the slight convergent illumination respectively.

A method of determining constant phases  $\eta$  using diffractograms was presented in [4]. To measure the phase  $\eta(u)$  as a function of the spatial frequency we analysed contrast transfer characteristics (CTCs). These are grey-tone illustrations of the diffractogram intensities of eq. (1) with the vertical and horizontal axis representing the defocus and the spatial frequency respectively. They have been analysed e. g. in [2] to evaluate the chromatic contrast transfer envelope. Here we used diffractograms of focal series of elastically filtered images and corrected them for the background and the modulation transfer function of the used CCD camera to calculate CTCs. Eq. (1) has been fitted to the experimental data of the CTCs in each discrete spatial frequency using a least squares fit yielding  $\eta(u)$  for acceleration voltages of 80 kV and 297 kV and for  $u < 1/\text{nm}$ . Fig. 1 shows the measured  $\eta(u)$  for a Ge foil of 8 nm thickness at 297 kV using elastic filtering with an energy slit width of 10 eV as an example. We are currently performing calculations to understand the origin of the measured decay and oscillations in  $\eta(u)$ .



Measured phase  $\eta(u)$  for a Ge foil

elastic filtering with an energy slit width of 10 eV as an example. We are currently performing calculations to understand the origin of the measured decay and oscillations in  $\eta(u)$ .

#### References:

- [1] K.-J. Hanszen, Adv. Opt. Electr. Micr. (1971), 1-84.
- [2] G. Möbus and M. Rühle, Optik (1993), 108-118.
- [3] R. Knippelmeyer, A. Thesing and H. Kohl, Zeitschrift für Metallkunde (2003), 282-289.
- [4] D. Typke and M. Radermacher, Ultramicroscopy (1982), 131-138.

# Electron Holography of Magnetic Nanostructures

M. Beleggia, J.W. Lau, M.A. Schofield, Y. Zhu

Center for Functional Nanomaterials, Brookhaven National Laboratory, Upton, NY 11973, USA.

Phase-sensitive techniques in Transmission Electron Microscopy allow us to access a great deal of physical information on natural and artificial structures at the nanoscale. Several open problems still exist in micromagnetics, such as the determination of phase diagrams, energetics, histeretic properties, thermal stability and spin-wave dynamics on magnetized nanostructures of non-ellipsoidal shape. Electron Holography, with its high spatial resolution and phase sensitivity, is probably the most suitable technique for nanoscale characterization of magnetic materials. A correct image interpretation, however, is achieved only with the interplay between experiments and theoretical modeling. The Fourier-space approach which has been developed recently for the computation of electromagnetic fields and phase shifts [1,2], provides the necessary support to the experimental methods in order to reach unprecedented capabilities in nanoscale characterization.

We have approached the study of magnetic ground-states in nanostructures as a function of shape and material parameters. As the overall dimensions decrease, shape anisotropy becomes important in determining the magnetic response of a given nanostructure. Single-domain limits, critical sizes for vortex nucleation, appearance of domain walls, low-frequency dynamic response...on the nanoscale everything is affected by shape anisotropy and by the dipolar energy associated to a general magnetization topography. For nano-rings, we have determined a phase diagram which allows us to locate the expected magnetization state for a given set of external parameters (shape, material). With Electron Holography, we have measured the ground state in a Permalloy nano-ring with inner radius of 58 nm, outer radius of 104 nm, and thickness of 4.7 nm, finding, as expected, a vortex closure-domain magnetization topography. The study is in progress and dynamical in-situ observations of the magnetic response of the ring to an external applied field are now being carried out [3].

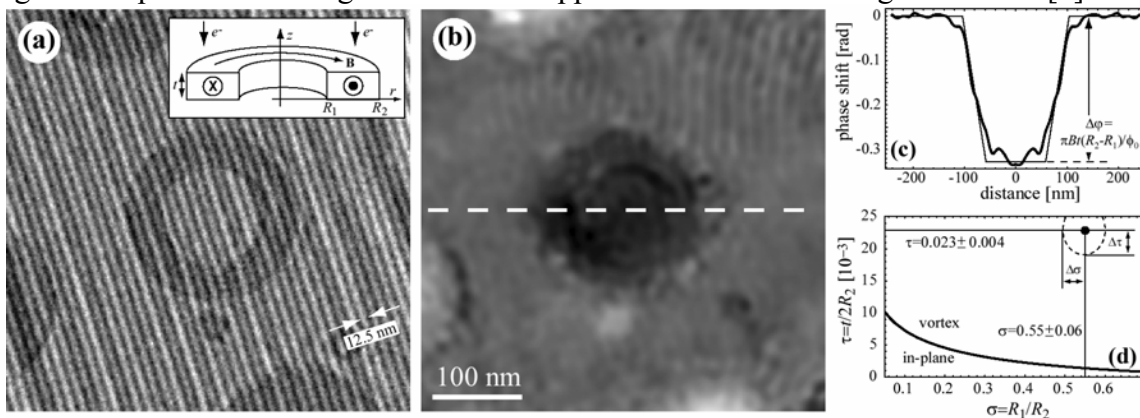


Fig.1: (a) Hologram of an artificially patterned Permalloy ring; (b) reconstructed magnetic phase shift; (c) phase profile along the dashed line in (b) showing a 1 T field in the ring; (d) section of the phase diagram with the location of the experimental point well inside the vortex region.

[1] M. Beleggia, P.F. Fazzini and G. Pozzi, *Ultramicroscopy* **96** (2003) 93

[2] M. Beleggia and M. De Graef, *J. Magn. Magn. Mater.* **263** (2003) L1

[3] This work was supported by by U.S. DOE (BES), under contract No. DE-AC02-98CH10886.

# Geometric vs Waveoptical Analysis of Interference Electron Microscopy Images of Reverse Biased p-n Junctions

P.F. Fazzini<sup>a</sup>, L. Ortolani<sup>a</sup>, G. Pozzi<sup>a</sup>, and F. Ubaldi<sup>a</sup>

<sup>a</sup>Department of Physics, I.N.F.M. and C.N.I.S.M., University of Bologna Viale B. Pichat 6/2, 40127 Bologna, Italy

Recently interference electron microscopy observations of reverse-biased p-n junctions [1] show that this method can be usefully employed for extracting reliable information as the object can be considered as a one-dimensional phase object. In this particular case, the phase difference between interfering points is directly displayed in the trend of the fringes, making their interpretation easier and more quantitative than that obtainable from out-of-focus observations [2].

However, owing to the fact that interferometric experiments are carried out with a narrow interference field and relatively low number of fringes, it turns out that also the shadow effects on the biprism edges, linked to the derivative of the phase shift, are playing a relevant role.

The shape of the interference field can be strongly modified by the presence of the specimen while the diffraction fringes originating at biprism edges, can influence both in amplitude and phase the resulting interferogram [3].

In order to take into account these effects properly, the image wavefunction in the interference mode has been formerly calculated by means of an asymptotic approximation [3]. The obtained results show that the geometric optical results are recovered at the first order, whereas the effect of diffraction is taken into account by the following terms of the asymptotic expansion. Although the resulting picture is quite satisfactory and able to explain the main features of the experimental results, unfortunately its validity range is restricted.

Today, thank to the improved computer performances and the availability of high level programming languages like Mathematica, the complete waveoptical numerical analysis of the image formation in the interference mode is easier. As a consequence the results of the geometrical and full waveoptical analysis can be compared to clarify the range of validity of the geometric optical approximation. In the particular case of p-n junctions, this kind of analysis has been carried out employing both a simplified analytical model, valid for a bulk specimen, and numerical simulations including the influence of surface effects and oxide charging. In both these cases the presence of external fields is unambiguously revealed by the long range bending of the interference fringes far from the junction.

[1] P. F. Fazzini, P.G. Merli, G. Pozzi and F. Ubaldi, to be published in the MSM-XIV conference proceedings

[2] M. Beleggia et al., Phys. Rev. B 67 (2003) 045328.

[3] G. Matteucci et al., Advanc. Imag. Electron. Phys. 99 (1997) 171.

[4] This work was supported by MIUR, FIRB funding RBAU01M97L. Useful discussions with Dr P.G. Merli are gratefully acknowledged.

# Design of a test structure with wide doping range for dopant profiling with electron holography

Petr Formánek

Speziallabor Triebenbergl, TU Dresden, Zum Triebenbergl 50, D-01328 Dresden, Germany

For potential mapping by electron holography, electrically inactive “dead layers” [1] at the surfaces of the specimen have to be taken into account. The thickness of dead layers was measured with holography on specimens doped to about  $10^{19} \text{ cm}^{-3}$  [1, 2]. However, it is reasonable to assume that the dead layer thickness depends on doping [3]. A suitable test structure is necessary for an experimental proof. In order to reduce influence of specimen preparation on measurements, layers with wide doping range ( $10^{16} \text{ cm}^{-3} - 10^{20} \text{ cm}^{-3}$ ) should be present in a single specimen, e.g. in a sequence  $p(20)/n(20)/p(19)/n(19)/p(18)/n(18)/p(17)/n(17)/p(16)/n(16)/\text{substrate}$ , where numbers in braces express the dopant concentration. In such a simple sequence, there is a problem due to the width of space charge region (SCR) at lower dopings. For example, SCR of a symmetric abrupt  $p-n$  junction with  $10^{16} \text{ cm}^{-3}$  doping is  $\sim 250 \text{ nm}$  wide, while hologram width is at most a couple of micrometers. Thus the complete stack would be too wide for holography.

In this report we present a modified sequence that minimizes space charge region. Simple  $p-n$  junctions are replaced by the sequence  $pp^+n^+n$ . Highly doped layers (“buffer” layers) at the interface serve as a reservoir for mobile carriers that remain in the buffer instead of spilling into the lowly doped layers. The effect of buffer layers is demonstrated in Fig. 1 for the case of a symmetric  $p-n$  junction with doping of  $10^{16} \text{ cm}^{-3}$ . Using a buffer layer of 21 nm with doping of  $10^{18} \text{ cm}^{-3}$  reduces SCR from 250 nm to less than 50 nm compared to a junction without the buffer.

Usual geometry of TEM specimens, i.e. a plan-parallel lamella, does not enable to probe the structure of a dead layer because electron holography measures only projected potential  $V_{\text{projected}}$  along the electron beam (Fig. 2):  $\varphi(x, y) = C_E \int V(x, y, z) dz = C_E V_{\text{projected}}(x, y)t$ , where  $C_E$  is the interaction constant and  $t$  is the specimen thickness. We propose a new geometry – a cylinder. In case of a cylinder and under assumption of constant potential at the surface, the potential is rotationally symmetric, and then the phase is

$\varphi(x) = 2C_E \int_{r=x}^R V(r) \frac{r}{\sqrt{r^2 - x^2}} dr$  (Fig. 2). We propose an iterative algorithm to solve the equation for  $V(r)$ .

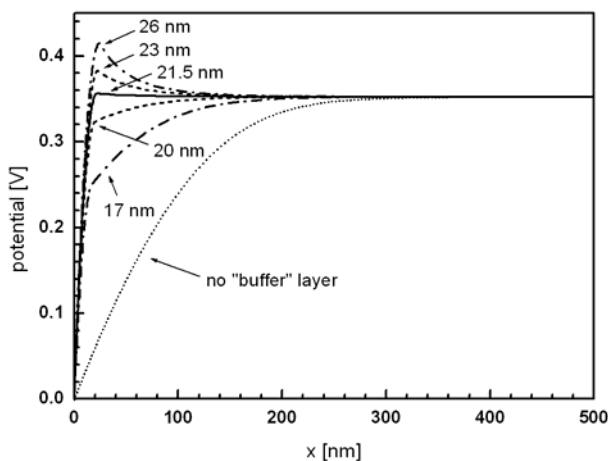


**Fig. 1:** Potential in  $n$ -side of the  $pp^+n^+n$  structure with  $p(n)$  doping of  $10^{16} \text{ cm}^{-3}$  and  $p^+(n^+)$  doping of  $10^{18} \text{ cm}^{-3}$ . The thickness of the “buffer”  $p^+, n^+$  layers is indicated.

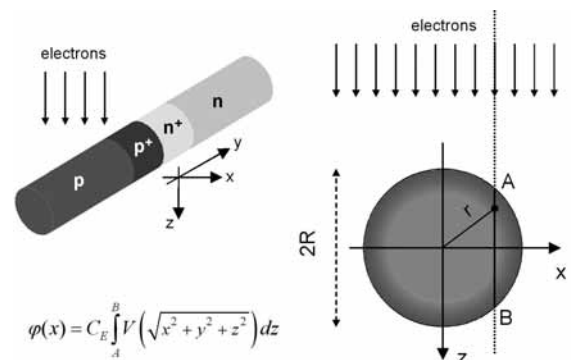


**Fig. 2:** Cylindrical geometry of specimen for measurement of potential in “dead layers”.

References: [1] Rau et al, Phys. Rev. Lett. 82 (1999) 2614, [2] Twittchet et al, Phys. Rev. Lett. 88 (2002) 238302, [3] Somodi et al, Mater. Res. Soc. Symp. Proc. Vol. 839 (2005) P3.2.1

# Measurement error in phase images due to noise and limited resolution

Petr Formanek\*

IHP, Im Technologiepark 25, D-15236 Frankfurt(Oder), Germany

Electron holography is a promising method for metrology of semiconductor devices, especially for p-n junction delineation and dopant mapping. The question arises, what the precision and accuracy of holographic measurement is, taking into account noise and limited resolution of the hologram.

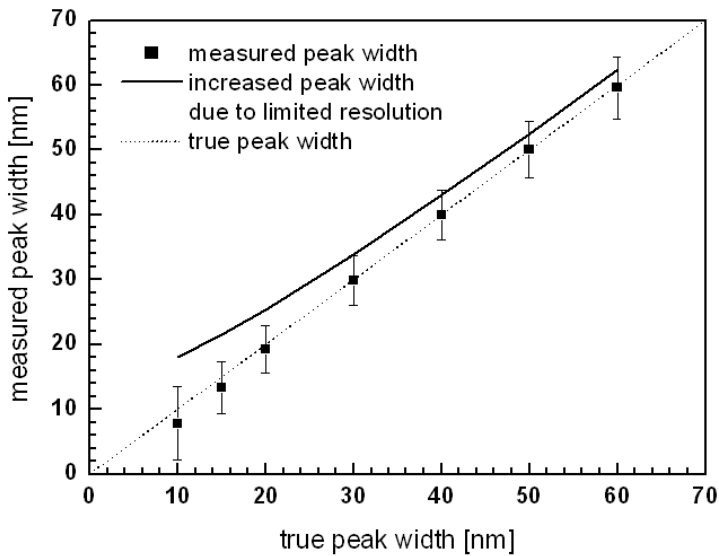


**Fig. 1:** Simulation of peak width measurement at a resolution of 20 nm and a signal-to-noise ratio of 13. The true peak width is on x-axis, the measured peak width on y-axis. The solid line denotes direct measurement in phase image. The squares denote measurement according to our method. The error bars are caused by noise in phase images.

a resolution of 20 nm and a signal-to-noise ratio of 13. The solid line denotes the peak widths as measurable directly from a noiseless phase image. Due to the limited resolution, the peaks are broadened and thus the measurement would be biased. An evaluation procedure using model fitting as described above deliver the mean values denoted in Fig. 1 by the squares, which lie more closely to the true values. The noise causes scatter of the measured values denoted by the error bars. The conclusion is: peak width of 15 nm can be reliably measured even at a resolution of 20 nm with the same random error as measurement of peak widths greater than 30 nm.

Our method is suitable for study of measurement errors of any kind, not just base width. The simulations provide a *lower limit* of measurement precision and accuracy, if no further artefacts, e.g. due to charging or dynamical diffraction show up.

We acknowledge the European Commission's project HERCULAS for financial support.

\* Present address: Speziallabor Triebenber, TU Dresden, Zum Triebenber 50, D-01328 Dresden, Germany, [www.triebenber.de](http://www.triebenber.de)

We investigate this issue by Monte-Carlo simulation at the example of a base width measurement from a phase image of a bipolar transistor. The phase profile across the base is approximated by a Gaussian peak of known position, width and height. A noisy hologram is simulated and a model of the phase profile (i.e. a Gaussian peak) is fitted to the phase reconstructed from the simulated hologram. The free parameters for fitting are peak position and width. The best-fit parameters are compared to the initially known parameters. The hologram is simulated 512 times to get enough data for a statistical analysis. In the simulation, resolution and noise level can be set arbitrarily.

The results for a concrete example are presented in Fig. 1. Simulated measurement of peak widths in the range of 10 nm to 60 nm was performed at a

# An improved construction of electron biprism holder for the C2-aperture

Petr Formánek, Bernd Eienkel, Hannes Lichte

Speziallabor Triebenberg, TU Dresden, Zum Triebenberg 50, D-01328 Dresden, Germany  
www.triebenberg.de

The Möllenstedt electrostatic biprism [1] is often used as a beam splitter in electron interferometry and holography. The biprism holder used in Philips CM-series microscopes for electron holography, i.e. biprism placed in the selected-area diffraction (SAD) plane, has dimensions of 5.2 mm x 2.5 mm. A new microscopy phenomenon – circular dichroism in TEM [2] – would be measurable using the biprism in the second condenser (C2) aperture plane. The maximum allowed dimensions for the biprism holder in the C2 plane are 4.0 mm x 2.0 mm. A simple shrink of dimensions of the SAD holder is hardly manufacturable. That is why we designed an improved construction that has got several advantages: (1) smaller dimensions, (2) reduced risk of flashover, (3) only one contacting point, and (4) easier assembly.

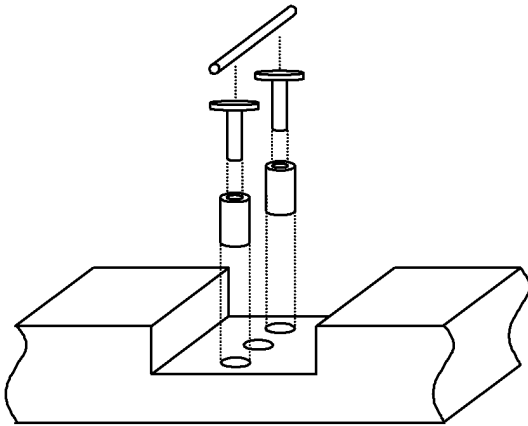


**Fig. 1:** Old biprism holder construction

In the old construction of the holder for SAD plane (Fig. 1) the biprism is soldered by means of a silver paste on 2 rivets cemented into isolation cylinders. The holes in the holder, necessary for the isolation, weaken the stiffness of the holder, which is only 1 mm thick at the biprism. Each rivet is contacted on the bottom of the holder. Flashovers often happen at the contact points.

The new construction (Fig. 2) for a C2-biprism is based on a rectangular block (fastened with a screw to the holder body) with two holes parallel to the axis of the holder. A U-shaped electrode is lead through the block in isolation cylinders. The electrode is contacted in one point only at the crook of the 'U'. All parts of the holder are relatively easy to manufacture and quick to assemble. The minimum voltage on the biprism when flashovers occur is 1000 V, three times as much as for the old down-scaled construction.

We acknowledge European Commission's project CHIRALTEM for financial support.

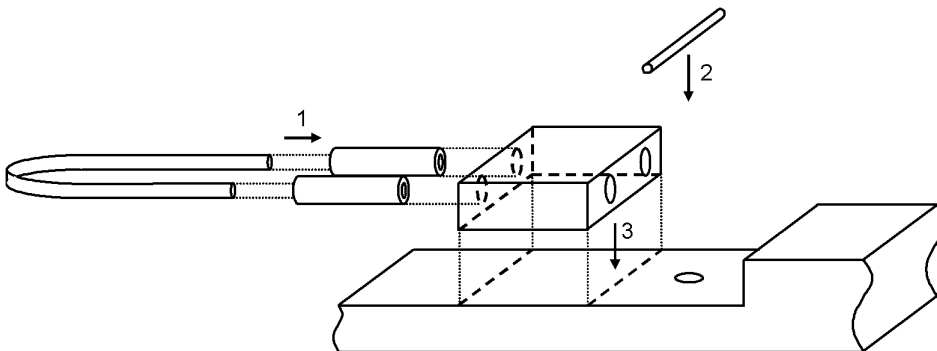


**Fig. 2:** New biprism holder construction

## References

- [1] G. Möllenstedt, H. Düker, Zeitschr. für Physik 42 (1955) 41
- [2] C. Hébert, P. Schattschneider, Ultramicroscopy 96 (2003) 463

## Biprism in condenser system for coherent two-beam illumination of an object

Petr Formánek, Bernd Eienkel, Hannes Lichte

Speziallabor Triebenberg, TU Dresden, Zum Triebenberg 50, D-01328 Dresden, Germany  
www.triebenberg.de

A new microscopy phenomenon, circular dichroism in TEM [1], would be measurable in various setups. One of them is realized with an illumination consisting of two coherent waves impinging at the specimen at a certain mutual angle, producing interference fringes of a certain spacing and position (phase). This can be achieved with a Möllenstedt electrostatic biprism [2] mounted in the second condenser (C2) aperture plane. We report on optical characteristic of this system.

The biprism splits the incoming wave and creates two partial waves that are deflected by the electrical field of the biprism. The two waves interfere and create a fringe pattern at the specimen. The fringe spacing achieved ranges from 5 nm to 40 nm. The deflected waves can be also observed in the back focal plane of the objective lens, where they produce two diffraction patterns (Fig. 1) of the specimen. The mutual lateral shift of the two diffraction patterns  $\Delta K$  is directly proportional to the biprism volage  $U_{bp}$ :

$$\Delta K = 0.018 \text{ nm}^{-1}/V U_{bp}. \quad (1)$$

Further, we investigate the influence of the illumination setup (C2 lens excitation, spot size, gun lens) on the fringe spacing.

We acknowledge European Commission's project CHIRALTEM for financial support.

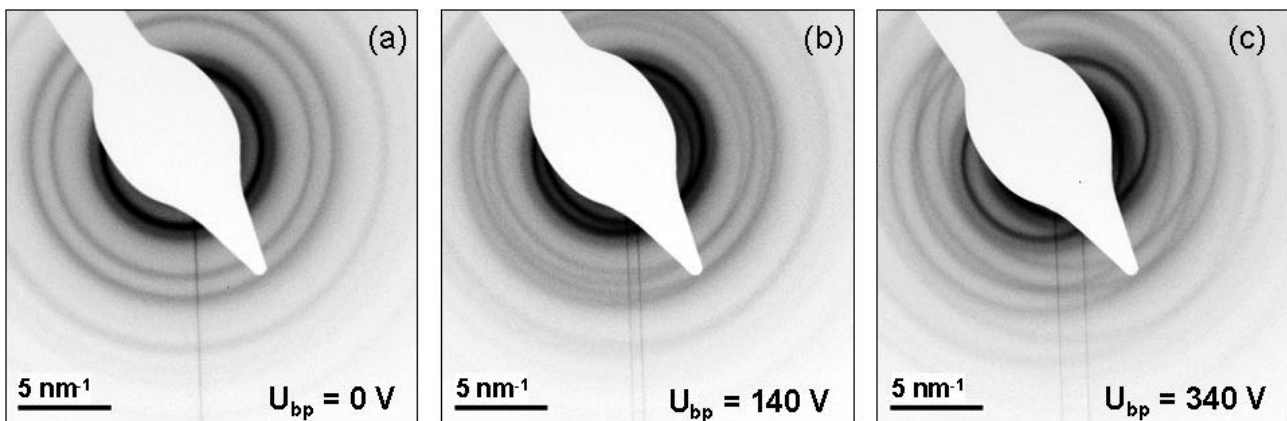


**Fig. 1:** Diffraction patterns (inverted) of nanocrystalline gold at biprism voltages (a)  $U_{bp} = 0 \text{ V}$ , (b)  $U_{bp} = 140 \text{ V}$ , and (c)  $U_{bp} = 340 \text{ V}$ ,

### References

- [1] C. Hébert, P. Schattschneider, Ultramicroscopy 96 (2003) 463
- [2] G. Möllenstedt, H. Düker, Zeitschrift. für Physik 42 (1955) 41

## Electron Holography with a Cs-corrected TEM at Triebenberg Laboratory: Present state

Dorin Geiger<sup>a</sup>, Hannes Lichte<sup>a</sup>, Michael Lehmann<sup>a</sup>, Bert Freitag<sup>b</sup> and Maximilian Haider<sup>c</sup>

<sup>a</sup>Triebenberg Laboratory, ISP, Dresden University, D-01062 Dresden, Germany, [www.triebenberg.de](http://www.triebenberg.de)

<sup>b</sup>FEI Eindhoven, The Netherlands, <sup>c</sup>CEOS GmbH, D-69126 Heidelberg

Cs-corrected TEM [1] extends the point resolution up to the information limit given by chromatic aberration. The point-spread-function (PSF) shrinks to a diameter of about 0.1nm hence also delocalisation disappears. Despite the huge progress, usual imaging is still conventional; therefore, the phase of the electron image wave is still lost hence cannot be used for retrieval of neither the object wave or the object structure. Likewise, large area object structures like electric/magnetic domains or biochemical specimens are still invisible. Furthermore, the practical work with the Cs-corrected microscope shows that small residual aberrations cannot be avoided, and hence for accurate interpretation of the findings, a-posteriori fine-tuning of residual aberrations is necessary. Consequently, electron holography is the matter of choice for a Cs-corrected TEM.

Also for holography, a Cs-corrected TEM offers strong advantages: For successful aberration corrections by off-axis electron holography [2] with a conventional TEM we need a detection camera with high pixel number allowing sufficient sampling of the steep wave aberration function, also at highest spatial frequencies. The large number of aberration parameters, which have to be accurately known for numerical corrections, makes the aberration corrections under prevalence of Cs-value very difficult. Last but not least, the quantum noise increases proportional to Cs hence limits signal detectability and resolution. Consequently, a Cs-corrected TEM is the matter of choice for electron holography.

Within the framework of a common project, a FEI Tecnai F20 TEM with Cs-corrector (CEOS company), equipped in the SA-aperture holder with a Möllenstedt biprism for electron holography, is in operation in the Triebenberg laboratory. First tests show the following performance: higher magnification than for CM200 with a factor of about 1.2, and a remarkable enhancement of the fringe contrast by a factor of about 5 [3] with a corresponding improvement of the phase detection limit. For example, at the spacing of 0.7Å, the hologram fringe contrast amounts to about 19%, i.e. improved by a factor 3. The phase detection limit at the Signal/Noise ratio  $S/N = 3$  was estimated from the standard deviation of the phase noise (0.03rad) in vacuum as  $2\pi/70$  rad. This is substantially lower than the phase signal  $2\pi/50$  rad expected from a single oxygen atom.

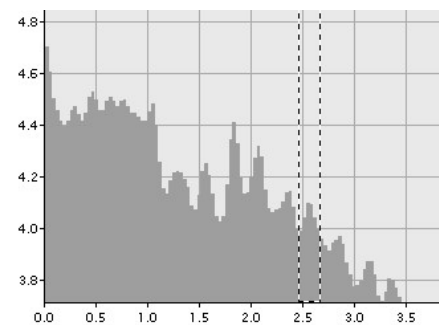


**Fig.1** Phase distribution in a very thin gold cluster, phase linescan across lattice planes. The phase gap between two gold atom columns is about 0.15rad and hence 5 times the phase noise. (Tecnai F20-Cs)

### References:

- [1] M. Haider, H. Rose, S. Uhlemann, E. Schwan, B. Kabius, K. Urban, Ultramicroscopy 75 (1998) 53–60.
- [2] H. Lichte, Advances in Optical and Electron Microscopy 12 (1991) 25–91.
- [3] D. Geiger, H. Lichte, M. Lehmann, M. Haider, B. Freitag, Proc. Of the 13th EMC, Antwerp 2004.
- [4] Financial support from Deutsche Forschungsgemeinschaft is gratefully acknowledged.

## Mean Inner Potential of Thin Amorphous Carbon Films

Matthias Wanner<sup>a</sup>, David Bach<sup>a</sup>, Dagmar Gerthsen<sup>a</sup>, Ralph Werner<sup>b</sup>, and Bernd Tesche<sup>c</sup>

<sup>a</sup>Laboratorium für Elektronenmikroskopie, Universität Karlsruhe (TH), D-76128 Karlsruhe, FRG

<sup>b</sup>Institut für Theorie der Kondensierten Materie, Universität Karlsruhe (TH), D-76128 Karlsruhe, FRG

<sup>c</sup>Max-Planck-Institut für Kohlenforschung, Kaiser-Wilhelm-Platz 1, D-45470 Mülheim/Ruhr, FRG

The mean inner Coulomb potential (MIP) of thin amorphous carbon films  $V_0$  was measured by transmission electron holography evaluating the phase shift  $\Delta\phi$  of the transmitted beam of the object wave with respect to the vacuum reference wave. The films with a density of approximately  $1.75 \text{ g/cm}^3$  are prepared by means of a special impact evaporation technique. The film thickness  $t$  in the range of 1 nm up to about 16 nm was determined by electron energy-loss spectroscopy.

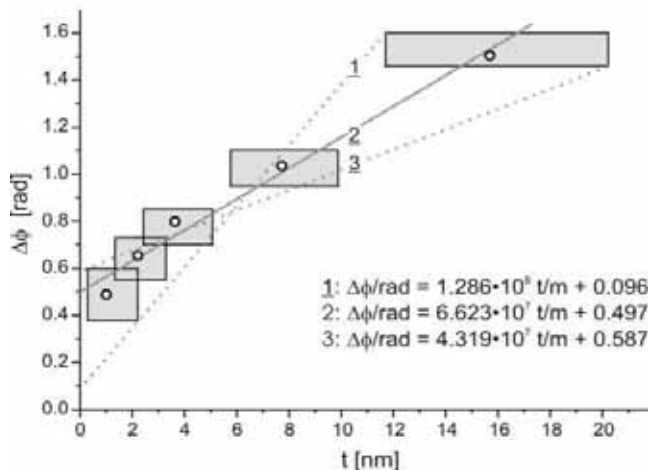


**Fig. 1:** Phase shift plotted as a function of the film thickness. The grey regions indicate the experimental and statistical errors.

shif because the exposure of the regions where holograms were taken was limited to  $< 1$  min and a systematic increase of the phase shift during a microscopy session was not observed. We suggest that the offset is related to a surface-induced electrostatic potential, which could result from adsorbate molecules with a dipole moment.

### References:

[1] M. Schowalter, J. T. Titantah, D. Lamoen, P. Kruse, *Appl. Phys. Lett.* 86 (2005) 112102

[2] A. Harscher, H. Lichte, *Proceedings of the International Conference on Electron Microscopy ICEM14 (1) (1998) 553.*

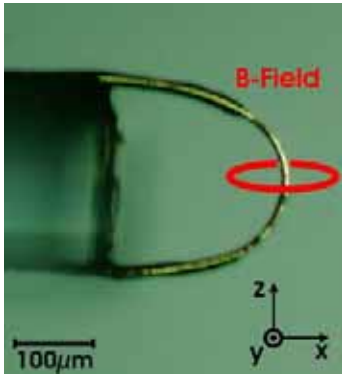
[3] We thank M. Schowalter for numerous instructive discussions. The work was supported by the Center for Functional Nanostructures (CFN) funded by the Deutsche Forschungsgemeinschaft (DFG).

## Experimental determination of the magnetic detection limit of electron holography in comparison with DPC

C. Hurm<sup>1</sup>, M. Heumann<sup>1</sup>, T. Uhlig<sup>1</sup>, J. Zweck<sup>1</sup>

<sup>1</sup>NWF II - Physik, Universität Regensburg, D-93040 Regensburg, Germany

Electron holography and differential phase contrast (DPC) can serve as two elegant variants of Lorentz microscopy with a high spatial resolution of about 10nm for both techniques, if applied in Lorentz mode and dependent on the specific experimental conditions [1],[2]. Besides the well-known lateral resolution one has also to consider the magnetic resolution, i.e. what is the smallest amount of induction that gives still a significant signal. To deal with this question, it is best to investigate the imaging properties using a well-known specimen which acts as a standard.



The standard specimen consists of a gold wire loop bent across a 250μm silicon plate and a finely adjustable constant current source. The setup is assembled onto a specimen holder which is electrically wired and which can be inserted into the TEM in both of the operating states, holography and DPC. The current through the gold loop generates a magnetic field around the wire, which deflects the electron beam. The lowest current and thus the lowest created induction which causes a visible effect in the image plane corresponds to the magnetic detection limit of the measured technique. If the wire is segmented properly, a calculation of the integral  $\int B_{x,y} dz$  of the magnetic field passed by the

electron beam is possible. This integral is directly proportional to the differential phase detected by DPC. From our calculations, a detection limit of  $(2.5 \pm 0.5) Tnm$  is found at a confidence level of 95%. A permalloy ( $Ni_{80}Fe_{20}$ ) specimen with saturation induction of 1.08 T therefore requires a minimum specimen thickness of  $(2.3 \pm 0.4) nm$ .

In electron holography, the electron wave is split in two partial waves which interfere in the image plane. In our setup, both of the partial waves pass through areas of different magnetic field, so according to Aharonov-Bohm the phase difference is given by the magnetic flux enclosed between the two partial waves [1]. As the theoretic detection limit for the phase shift mainly depends on statistics [3], a desired spatial resolution requires a specific enclosed magnetic flux to be detectable. If magnetic structures are to be recorded at a 10 nm resolution level, a phase difference of  $(0.45 \pm 0.09) rad$  (equivalent to  $\frac{1}{7} \pi$ ) or an enclosed flux of  $(290 \pm 60) Tnm^2$  is needed for a visible effect at our experimental conditions. If, however, a magnetic structural resolution of 100nm is sufficient, the detection limit is given by a phase difference of  $(0.17 \pm 0.03) rad$  (equivalent to  $\frac{1}{18} \pi$ ) or a flux of  $(110 \pm 20) Tnm^2$ , both at a confidence level of 95%. The corresponding specimen thickness (permalloy) is about  $(27 \pm 5) nm$  at 10nm spatial resolution and  $(1.0 \pm 0.2) nm$  at 100nm spatial resolution.

[1] Uhlig T., Dissertation, Regensburg (2004), ISBN 3-8325-0752-3

[2] Heumann M., Dissertation, Regensburg (2005), ISBN 3-8325-0870-8

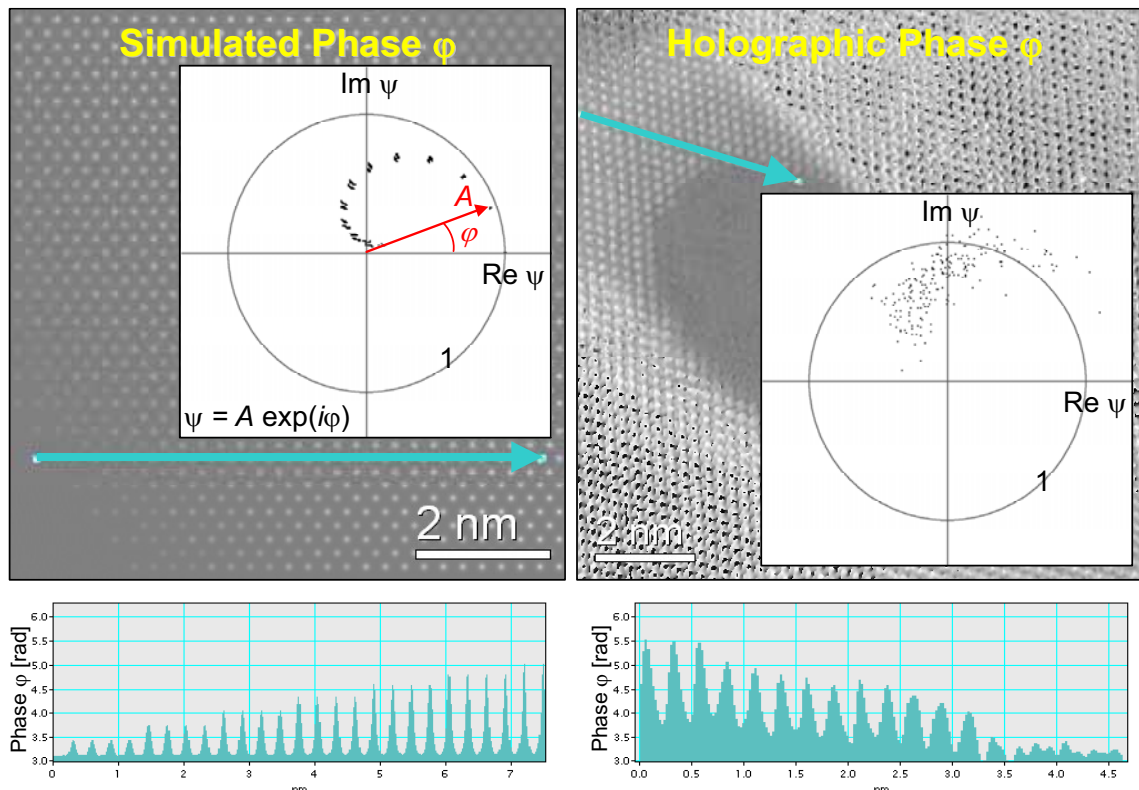
[3] Harscher A., Lichte H., Ultramicroscopy Aug 1996; 64(1-4): 57-66

# Electron Holography on the Way to Measuring the Weight of Atomic Columns with Single Atom Sensitivity

Michael Lehmann

Triebenberg Lab, Institute of Structure Physics, Dresden University, D-01062 Dresden, Germany

After correction of the coherent wave aberration, off-axis electron holography provides the object exit-wave  $\psi$  in amplitude  $A$  and phase  $\varphi$  at the exit-surface of the sample, only modified by damping of higher spatial frequencies due to limited spatial and temporal coherence. For thin samples with light elements, the phase shift is proportional to the number of atoms within a column. For heavy elements, the proportionality does not hold anymore because "absorption" from the coherent wave field and dynamical scattering reduce the phase shift increment, when the number of atoms within a column is increased. The weight of an atomic column is best measured by means of so-called "argand-plots", where amplitude and phase of each atomic column is plotted as real and imaginary part of the object exit-wave [1]. In the simulation of Au [110], this results in a spiral with discrete phase steps according to the monoatomic steps in the simulated object. In the corresponding holographic experiment considering only the thin area, these steps are currently not resolved because of noise; however, the spiral due to "absorption" is well reproduced without rescaling the measured values. This is a further hint that electron holography is hardly affected by the Stobbs-factor. [2]



[1] J.R. Jinschek, Ch. Kisielowski, D. Van Dyck, P. Geuens, Proc. of SPIE, Vol. 5187

[2] These investigations are the result of discussions with Prof. Dirk Van Dyck from EMAT, Antwerp University. The specimen was kindly provided by Dr. Christian Kisielowski, NCEM, Berkeley. The financial support by the Deutsche Forschungsgemeinschaft DFG is gratefully acknowledged.

# Impact of Focussed Ion Beam (FIB) preparation on the measurement of electrically active dopants in silicon semiconductors using electron holography

Andreas Lenk<sup>a</sup>, Uwe Mühle<sup>b</sup>, and Hannes Lichte<sup>a</sup>

<sup>a</sup> Institute of Structure Physics, Triebenberg Laboratory, Dresden University, 01062 Dresden, Germany

<sup>b</sup> Infineon Technologies Dresden GmbH & Co OHG, Germany

Electron holography in a transmission electron microscope (TEM) delivers 2D-projected potential images of a 3D-object. Therefore, it allows the measurement of electrically active doped areas in semiconductive materials [1]. With the steady development of semiconductor technology towards continuously shrinking device dimensions, the combination of electron holography and FIB target preparation has become increasingly important over the last years [2]. However, for an exact quantitative evaluation, it is necessary to understand the potential distribution in a FIB-specimen along the electron beam (z-direction). Neglecting the structure along z can lead to a misinterpretation of the measured data, which are inevitably averaged in the 2D-projection.

This usually lost information can be accessed in a new experiment: A standard FIB-lamella is further micro-machined with a second FIB cut, perpendicular to the original lamella. The result is a freestanding needle with four equally treated lateral sides (Fig.1). The special specimen geometry is used to gain cross-section phase images of FIB lamellae. The symmetrical shape of the needle also allows calculating the true curvature of the electrical potential from the 2D-projected image.

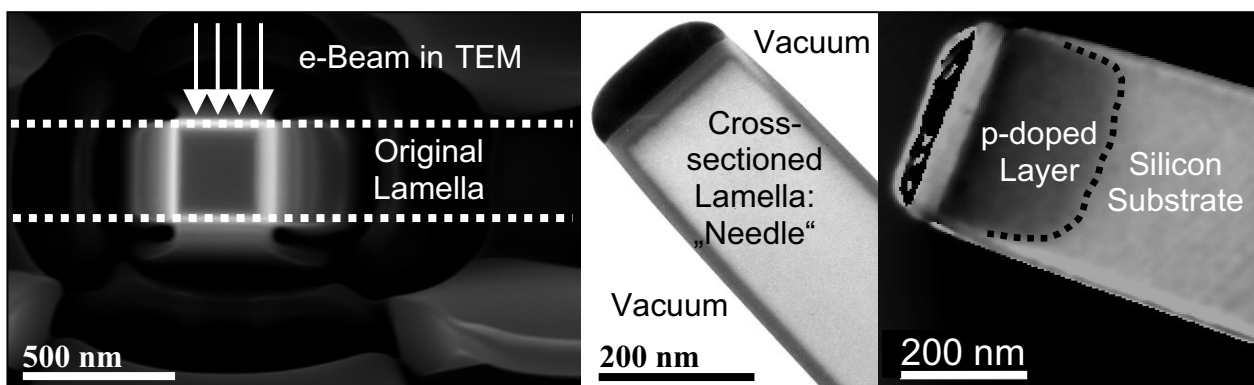


**Fig. 1:** **Left:** Topview of needle (Scanning Electron Microscope); **Center:** Lateral view of needle (TEM bright field); **Right:** Phase image of needle with p-n junction (dotted line)

The investigated needles were prepared from differently doped wafers. In all cases, three adjacent zones can be distinguished along z: An electrically dead surface layer, a transition zone with increasing electrical activity, and finally a fully active inner core. The transition zones are remarkably different for p- and n-doped structures, which can explain the stronger signal measured at p-doped structures. Furthermore, the potential generally drops towards the lamella surface.

## References:

- [1] W D Rau, P Schwander, F H Baumann, W Hoppner and A Ourmazd “Two-dimensional mapping of the electrostatic potential in transistors by electron holography” *Phys Rev Lett* **82** (1999) 2614-2617.
- [2] M R. McCartney, “Quantitative analysis of one-dimensional dopant profile by electron holography” *Applied Physics Letters* **80/17** (2002) 3213 - 3215

# Investigation of the Electrical Activity of Dislocations in GaN- and ZnO-Epilayers by Transmission Electron Holography

E. Müller<sup>a</sup>, P. Kruse<sup>a</sup>, D. Gerthsen<sup>a</sup>, R. Kling<sup>b</sup>, and A. Waag<sup>b</sup>

<sup>a</sup>Laboratorium für Elektronenmikroskopie, Universität Karlsruhe, D-76128 Karlsruhe, Germany

<sup>b</sup>Abteilung Halbleiterphysik, Universität Ulm, D-89069 Ulm, Germany

<sup>c</sup>Institut für Halbleitertechnik, Universität Braunschweig, D-38106 Braunschweig, Germany

Epitaxial layers frequently contain high densities of threading dislocations, which exceed typically values of  $10^9 \text{ cm}^{-2}$  for ZnO. If the dislocations are electrically active, the overall charge balance of the material can be influenced significantly and the charge-carrier mobility is strongly reduced. Previous studies [1] have already shown that dislocations which are generated during plastic deformation are electrically active in many semiconductors.

In our study the electrical activity of single threading dislocations in epitaxial ZnO- and GaN-layers was investigated by electron holography in a transmission electron microscope. By reconstructing the phase of the image wave in the vicinity of dislocations, the electrostatic potential associated with the dislocation line charge can be detected. Indications for charged dislocations in GaN were already found by applying electron holography [2].

A key point of our work is the analysis of dislocations in cross-section samples where the dislocations lines are oriented perpendicular to the electron beam. This geometry provides several advantages although the phase shift is not maximized. Thus, the formation of pits at the intersection of the dislocation line with the surface due to ion etching of the sample can be avoided. The determination of the thickness of the sample is not necessary due to the measurement of relative phase shifts compared to the undisturbed regions of the sample. Additionally, dynamical contributions to the phase shift are easier to control.

A theoretical model for the electrostatic potential of a charged dislocation was already calculated [3]. Comparing the measured and theoretically expected potential, a line charge density of  $2 \text{ e/nm}$  was found at threading dislocations in GaN- and ZnO-epilayers. These charges can result either from intrinsic dislocation states and/or from point defects which are accumulated in the dislocation strain field.

## References:

[1] Yu.A. Osip'yan, V.F. Petrenko, A.V. Zaretski and R.W. Whitworth, *Adv. Phys.* **35** (1986) 115

[2] D. Cherns and C.G. Jiao, *Phys. Rev. Lett.* **87** (2001) 205504

[3] W.T. Read, *Theory of Dislocations in Germanium*, *Phil. Mag.* **45** (1954) 775

# Measurement of the Mean Inner Potential of ZnO Nanorods by Transmission Electron Holography

E. Müller<sup>a</sup>, P. Kruse<sup>a</sup>, D. Gerthsen<sup>a</sup>, A. Rosenauer<sup>b</sup>, M. Schowalter<sup>b</sup>, D. Lamoen<sup>c</sup>, R. Kling<sup>d</sup>, and A. Waag<sup>e</sup>

<sup>a</sup>Laboratorium für Elektronenmikroskopie, Universität Karlsruhe, D-76128 Karlsruhe, Germany

<sup>b</sup>Institut für Festkörperphysik, Universität Bremen, Otto-Hahn-Allee 1, D-28359 Bremen, Germany

<sup>c</sup>Departement Fysica, Universiteit Antwerpen, B-2020 Antwerpen, Belgium

<sup>d</sup>Abteilung Halbleiterphysik, Universität Ulm, D-89069 Ulm, Germany

<sup>e</sup>Institut für Halbleitertechnik, Universität Braunschweig, D-38106 Braunschweig, Germany

The mean inner potential (MIP) is known as the volume average of the Coulomb potential of a solid [1]. Besides being of fundamental importance, precise values of the MIP are required for quantitative image analysis and simulation in transmission electron microscopy (TEM) and electron holography.

In the past few years ZnO has been considered as a promising material for the fabrication of optoelectronic devices and different sensors. However only one experimental value for the MIP of ZnO ( $V_0 = 21$  V) measured by electron holography in a transmission electron microscope was published so far [2]. It differs significantly from the theoretical value of  $V_0 = 16.1$  V which was calculated using the EMS program package [3]. Due to the discrepancy between the experimental and theoretical value of the MIP and the technological importance of ZnO we have performed measurements of the MIP using off-axis transmission electron holography.

Accurate measurements of the mean inner potential by transmission electron holography are often hampered by an imprecise knowledge of the sample thickness. To overcome this problem, ZnO nanorods with a well-defined geometry and diameter were used in our study. Likewise artefacts due to typical specimen preparation procedures could be avoided. The absence of dislocations or other extended defects was verified by analysing dark-field images with different imaging vectors under two-beam conditions. Holograms were taken under kinematical diffraction conditions. High-resolution transmission electron microscopy images were used for magnification calibration. The phase and amplitude of the image wave were extracted numerically from the sideband of the digitised hologram. The phase shift of the transmitted beam of the image wave with respect to the reference wave travelling through the vacuum yields the mean inner potential which was determined to be  $V_0 = (15.9 \pm 1.4)$  V for ZnO. This experimental value is in good agreement with the calculated value of  $V_0 = 15.8$  V using ab initio density functional theory computations [4] and  $V_0 = 16.1$  V from Doyle Turner electron scattering factors computed for isolated atoms.

## References:

[1] M. O'Keefe and J.C.H. Spence, *Acta Cryst. A* **50** (1994) 33

[2] M. Elfving and E. Olson, *J. Appl. Phys.* **92** (2002) 5272

[3] P. Stadelmann, *Ultramicroscopy* **21** (1987) 131

[4] M. Schowalter, D. Lamoen, A. Rosenauer, P. Kruse and D. Gerthsen, *Appl. Phys. Lett.* **85** (2004) 4938

# Object Parameter Retrieval using Inverse Electron Diffraction including Potential Differences

K. Scheerschmidt

Max Planck Institute of Microstructure Physics, D-06120 Halle, Germany, [schee@mpi-halle.de](mailto:schee@mpi-halle.de)

Object data can be directly retrieved from the electron microscope exit wave function without using trial-and-error iterative matching [1]. The retrieval of local data, e.g. thickness, orientation, potential, as a basis of a general object reconstruction, can be gained by linearizing the scattering problem and constructing regularized and generalized inverse matrices. Starting e.g. from a hologram, where all reflections  $\mathbf{g}$  are separately reconstructed, the moduli ( $A$ ) and phases ( $P$ ) of the exit plane wave  $\Phi^{\text{exp}}$  are determined for each  $\mathbf{g}$  (cf. Fig. 1, Fouriertransform of the hologram and selected  $\mathbf{g}$ ). Theoretical waves  $\Phi^{\text{th}}$  are then calculated using the dynamical scattering matrix  $M$  for an a priori model characterized by the number of beams and the scattering potential. With a suitable experimentally predetermined trial average beam orientation  $\mathbf{K}_{\text{Oxy}}$  and a sample thickness  $t_0$  as a free parameter, a perturbation approximation yields both  $\Phi^{\text{th}}$  and  $M$  as linear functions of parameters to be retrieved. The analytic form of the equations enable the inverse solution  $[t, \mathbf{K}_{xy}, \dots] = M_{\text{inv}} \cdot (\Phi^{\text{exp}} - \Phi^{\text{th}})$ , thus yielding directly for each image pixel  $(i,j)$  the local thickness  $t(i,j)$  and the local beam orientation  $\mathbf{K}_{xy}(i,j)$ . Generalizing of  $M_{\text{inv}}$  avoids the ill-posedness, the problem, however, is now ill-conditioned. As pointed out in different previous analyses (cf. e.g. [2]) a regularization of the retrieval procedure requires the control of the confidence and stability region. As shown in the retrieved  $t$  and  $\mathbf{K}_{xy}$  of Fig.1, the modeling errors because of the potential difference are the remaining fault.

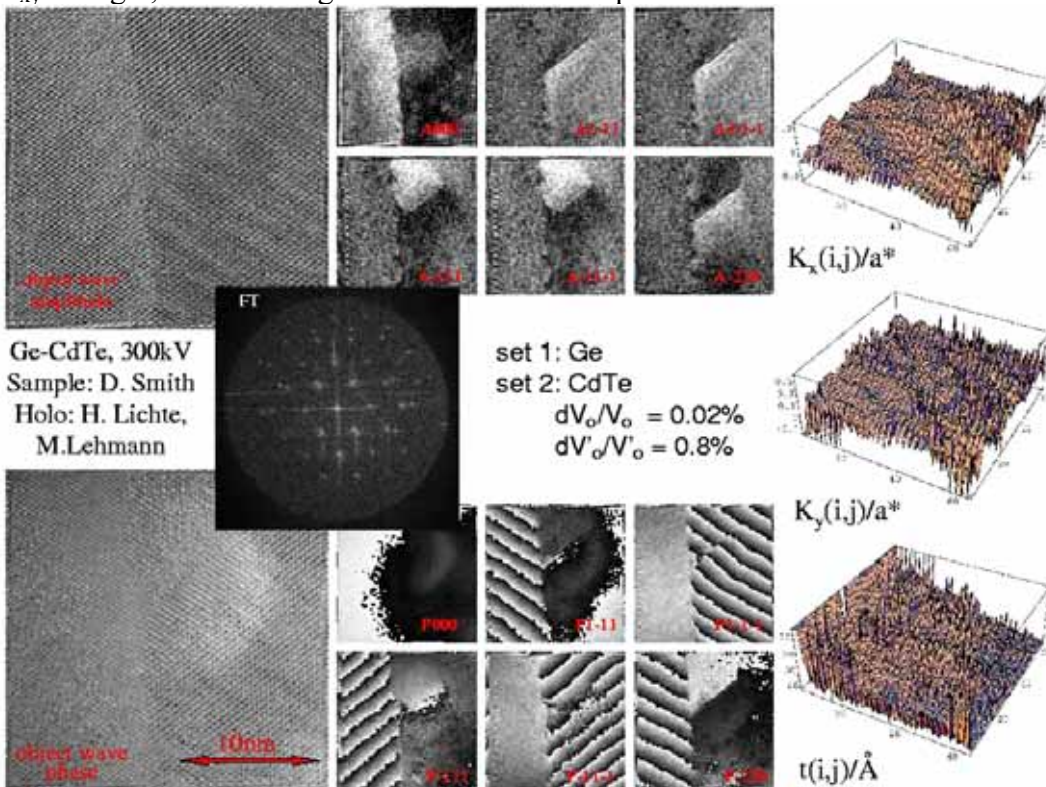


**Fig.1:** Retrieval of local thickness  $t$  and orientation  $\mathbf{K}_{xy}$  for an Ge-CdTe interface including different potential parameters

**References:**[1]. K. Scheerschmidt, Lecture Notes in Physics **486** (1997) 71 and Journal of Microsc. **190** (1998) 238-248. [2] K. Scheerschmidt, Microsc. Microanal. **9**, Suppl.6 (2003) 56 and WAVES 2003, Proc. 6<sup>th</sup> Int. Conf. Math. Num. Aspects Wave Prop., Eds.: G.C. Cohen and P. Joly, Springer Vlg., 2003, 607.

## Electron Holography on Biological Samples

Paul Simon<sup>a</sup>, Hannes Lichte<sup>b</sup>, Petr Formanek<sup>b</sup>, Rainer Wahl<sup>c</sup>, Michael Mertig<sup>c</sup> and Hermann Ehrlich<sup>c</sup>

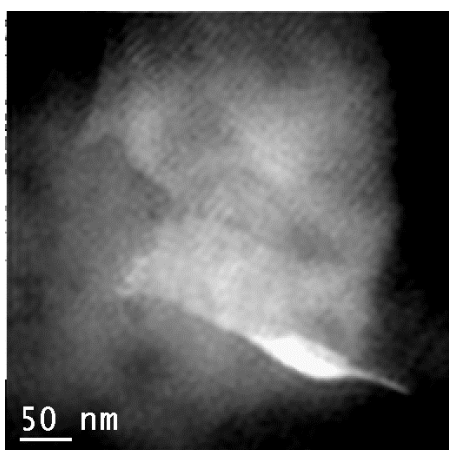
<sup>a</sup>Max-Planck-Institut für Chemische Physik fester Stoffe, 01187 Dresden, Germany

<sup>b</sup>Triebenberglaboratory, Institute of Structure Physics, Dresden University, 01062 Dresden,

<sup>c</sup>Max Bergmann Center of Biomaterials and Institute of Materials Science, Dresden University, 01069 Dresden, Germany

Our recent work deals with regular bacterial surface proteins (S-layer) of *Bacillus sphaericus* NCTC 9602 [1, 2]. They are quasi two dimensional crystals with different lattice symmetries of periodically arranged protein or glyco proteins, which form the outermost part of the cell envelope of various bacteria and archaee. We investigated as-dried, freestanding samples on a holey carbon film and evaporated a protective thin carbon layer onto the S-layer in order to avoid charging. In this way, the S-layer could be investigated without disturbing support film and vacuum beneath the sample for the reference wave is assured.

We obtained the phase micrograph at just focus, thus we were able to image the edges of the crystal sheet without blurring (fig. 1). The topography is nicely reproduced showing a strong waviness of the crystal sheet as indicated by the bright areas corresponding to thicker sample regions and darker regions which represent the thinner parts. The processed diffraction pattern (power spectrum) of the phase features four spots corresponding to a square lattice with a spacing of 11 nm, which is to some extent smaller than measured by the negative staining method of 12.5 nm.



Additionally, we show new results of electron holography of collagen fibres with 7.5 nm resolution. Collagen is a broad spread fibre protein, occurring in all kind of living systems e.g. in glassy sponges, bone or tendon of vertebrates [3].

**Fig. 1:** Reconstructed phase image of the unstained crystal lattice of surface layer protein.

It plays a key role in bone formation, however, till now, it is not clear in detail at which sites of the collagen fibres mineralisation by apatite takes place. Therefore, it would be helpful to image the morphology and topography of the protein before and after mineralisation without staining in order to avoid artefacts by chemical treatment. Here, we report of a collagen I of calf skin. The reconstructed phase image of the non-stained crystal lattice of collagen I protein fibre shows a chessboard-like structure. Cross striation with period of 60 nm and even finer structural details up to 7 nm are clearly imaged. Height variation amounts to about 5nm.

### References:

- [1] P. Simon, H. Lichte, R. Wahl, M. Mertig, W. Pompe, BBA (Biomembr.) 1663 (2004) 178-187.
- [2] P. Simon, H. Lichte, J. Drechsel, P. Formanek, A. Graff, R. Wahl, M. Mertig, R. Adhikari, H. G. Michler, Adv. Mater. 15, (2003) 1475-81.
- [3] Ehrlich, H., Ereskovsky, A.V., Molodtsov, S.L., M. Mertig, M., Goebel, C., Simon, P., Hanke, T., Krylova, D.D., Pompe, W., Worch H. (2005) to be published.

## Quantitative Comparison of Sideband and Centerband in Electron Holography

D. Wolf, M. Lehmann, H. Lichte

Triebenberg Laboratory, Institute of Structure Physics, University of Dresden, D-01062 Dresden, Germany

The lattice fringe contrast mismatch between experimental high-resolution transmission electron microscope (HRTEM) images and corresponding image simulations, which is commonly referred to as “Stobbs factor”, has been discussed for about 10 years, e.g. [1]. Using off-axis electron holography, the main suspect contribution to the Stobbs factor, namely the electrons inelastically scattered by the specimen, can be studied [2].

An off-axis electron hologram intrinsically contains the image intensity as well as the aberrated image wave. Therefore, both parts of information, gained from the same object position in one experiment, can quantitatively be compared. In Fourier space, both are well separated as centerband (Fourier transform of the intensity) and sideband (Fourier transform of the image wave). According to [3], the reconstructed image wave only consists of elastically scattered electrons, whereas the intensity consists of both, elastically as well as inelastically scattered electrons. Consequently, electron holography provides a unique access to the intensity distribution of inelastically scattered electrons.

However, the non-perfect imaging process in the electron microscope influences centerband and sideband in a different manner. The main points of consideration are, firstly, the modulation transfer in the charged coupled device (CCD) camera, described by the spatial frequency dependent Modulation Transfer Function (MTF). The MTF influence on the electron hologram Fourier spectrum has to be corrected by the MTF, which is obtained by the “knife edge method” [4].

Secondly, the influence of partial coherence on the non-linear centerband is included in the (rather complicated) Transmission Cross Coefficient (TCC) [5]. On the other hand, in case of the linear sideband, this leads to a simple damping by the spatial envelope and the chromatic envelope [6]. In order to compare centerband and sideband, however, it is not sufficient to calculate the absolute square of the image wave, because non-linear contributions are wrongly taken into account. A more accurate calculation is the application of the so-called Explicit Focal Integration [7] on the reconstructed image wave. Then, the quantitative comparison is mainly limited by the signal-to-noise ratio, which is about 5-times worse in the intensity determined from the sideband than the one from the centerband.

After careful consideration of all points discussed above, an electron hologram of a wedge shaped GaAs sample in [110] orientation shows an about 2.5 higher lattice fringe contrast in the intensity, determined from a sideband, than in the intensity recovered from the centerband. These results strongly suggest a major contribution of inelastically scattered electrons to the Stobbs factor.

[1] C. B. Boothroyd: *Journal of Microscopy* 190 (1998) 99-108.

[2] C. B. Boothroyd, R.E. Dunin-Borkowski: *Ultramicroscopy* 98 (2004) 115-133.

[3] H. Lichte: *Advances in Optical and Electron Microscopy* 12 (1991) 25-91.

[4] R.R. Meyer, A.I. Kirkland, R.E. Dunin-Borkowski, J.L. Hutchison: *Ultramicrosc.* 85 (2000) 9-13.

[5] J. Frank: *Optik* 38 (1973) 519-536.

[6] H. Lichte: *Ultramicroscopy* 20 (1986) 293 – 304.

[7] W.M.J. Coene, A. Thust, M. Op de Beeck, D. van Dyck: *Ultramicroscopy* 64, 109-135.

# 1D Traceable Length Measurements by Laser Interferometer in SEM

Thomas Ahbe<sup>a</sup>, Yunfei Xu<sup>b</sup>, and Klaus-Peter Hoffmann<sup>a</sup>

<sup>a</sup> Physikalisch-Technische Bundesanstalt Braunschweig and Berlin, Bundesallee 100,  
38116 Braunschweig, Germany

<sup>b</sup> University of Shanghai for Science and Technology, Shanghai, China

Because of their high magnification scanning electron microscopes are used to measure very fine structures and thin layers of prepared cross-section. Thickness measurements of thin films and coatings on samples are important for the functionality of many devices, where the thickness has to be in the right range. Deviations could cause a failure of the device. This and others are reasons for the need of traceable thickness measurements. To achieve this in a SEM, a direct link to the wavelength of a laser is necessary, e.g. by using a laser based displacement interferometer. For the measurement task, a measuring range of about 80  $\mu\text{m}$  and an uncertainty, which is adequate to the reachable resolution of the sample in the SEM, should be reached.

Parts of the set-up are already described in [1]. Inside the SEM chamber there is a piezo driven table with a stroke of 100  $\mu\text{m}$  in one axis. The movement of the table along this axis is now measured and controlled by a laser interferometer. This become possible by using a high-speed DSP-board for direct processing of the analogue signals from the interferometer [2]. Compared to the former set-up [1] the acquisition rate thereby was increased by a factor of eight. Now it is possible to work at SEM magnifications between 3,000 and 75,000 times, which corresponds to a measuring range for a single image between 25  $\mu\text{m}$  and 1.5  $\mu\text{m}$ .

Additionally, by this procedure firstly the calibration of the magnification of the SEM can be obtained from the measured data directly, as there is no need of a separate calibration. Secondly, it should be possible to measure large distances in a so-called step-image-modus. Hereby two small features separated by a larger distance can be measured by two SEM-images at high magnifications at each position and a fast moving between the two positions, because all positions are continuously measured by laser interferometer.

The new set-up will mainly be used for thickness measurements of layers of cross sections. The requirements given by the ISO-Standard [3] will be considerably surpassed, with the quality of the material border lines on the cross section being the main contribution to the uncertainty.

- [1] T. Ahbe, N. Haft, K. Hasche, K.-P. Hoffmann, Micro System Technologies 98, Sixth International Conference on Micro Electro, Opto, Mechanical Systems and Components, Potsdam/Germany, December 1-3,1998, pp. 627-629
- [2] G. Dai, F. Pohlenz, H.-U. Danzebrink, K. Hasche, G. Wilkening, Measurement Science and Technology 15 (2004) pp. 444-450.
- [3] International Standard ISO 9220: metallic coatings - Measurement of coating thickness Scanning electron microscope method, 1988

## Acquisition of signals from thin foils bombarded with very low energy electrons

Petr Hrnčířík, Vladimír Romanovský, Ilona Müllerová

Department of Electron Optics, Institute of Scientific Instruments, Academy of Sciences of the Czech Republic, Královopolská 147, 612 64 Brno, Czech Republic

A Scanning Low Energy Electron Microscope (SLEEM) in its multifunctional version has been put into operation (Fig. 1). It is equipped with a Schottky-emission gun and a cathode lens enabling one to acquire micrographs throughout the full energy scale from 10 keV down to zero energy (the mirror mode) at high resolution [1].

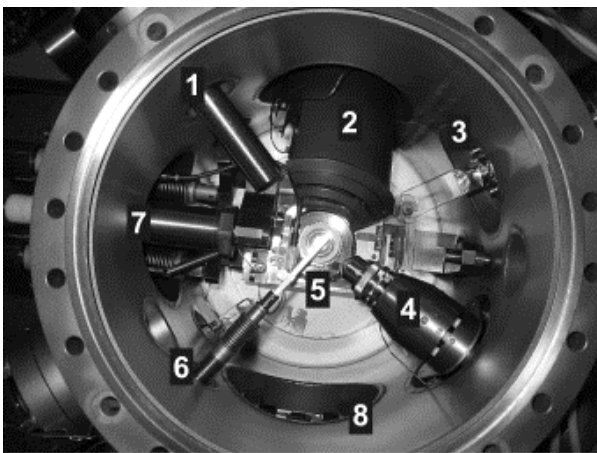


Fig. 1: Photograph of the specimen chamber (1-detector of secondary electrons, 2-analyser of Auger electrons, 3-detector of backscattered or low energy electrons, 4-ion gun, 5-detector of transmitted electrons, 6-aperture of the objective lens, 7-specimen stage, 8-air-lock entrance.

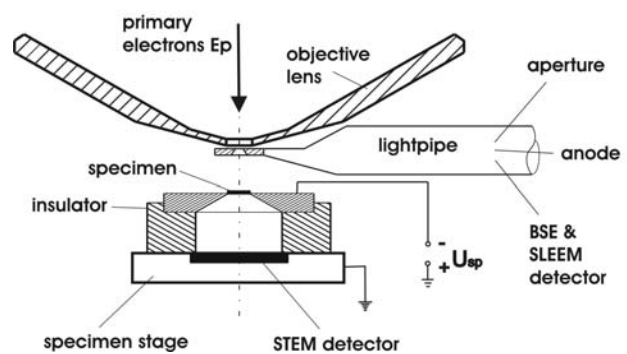


Fig. 2: BSE&SLEEM - detector of backscattered and low energy electrons (YAG crystal), STEM-detector of transmitted electrons (PIN structure). Primary electrons of a high energy (10 keV) are decelerated in front of the specimen by a negative potential  $U_{sp}$  while both detectors are grounded. The specimen-absorbed current can also be measured on the high potential.

Because the inelastic mean free path of electrons is known to rapidly increase below about 50 eV of electron energy, the very low energy electrons are thought to penetrate very thin foils [2-4]. In order to verify this, an STEM method for very low energies has been elaborated and is being proved with carbon and metallic foils. The experimental device includes a range of the above-mentioned complementary techniques that enable all electron signals excited (reflected, transmitted and absorbed) to be detected simultaneously. The first experimental results have confirmed the new possibilities of examining the scattering of the very low energy electrons in matter.

- [1] Müllerová I, Frank L, in: *Advances in Imaging and Electron Physics* **128**, ed. P.W. Hawkes, Elsevier Academic Press (2003) 309.
- [2] Spence JCH, *Micron* 28 (1997) 101.
- [3] Hrnčířík P, Křivánek O, Müllerová I, in: *Proc. of EMC 2004, Antwerp, Belgium, Vol. I.*, IM9.P02.
- [4] Hrnčířík P, Müllerová I, *GIT I&M* 6 (2004) 47.
- [5] This work is supported by research project no. KJB 2065405 of the Grant Agency of AS CR.

## Scintillation Detector in Environmental SEM

J. Jirak<sup>a,b</sup>, J. Skrivanek<sup>a</sup> and R. Aufrata<sup>b</sup>

<sup>a</sup> Department of Electrotechnology, Faculty of Electrical Engineering and Communication, Brno University of Technology, 602 00 Brno, Czech Republic

<sup>b</sup> Institute of Scientific Instruments of the Academy of Sciences, 612 00 Brno, Czech Republic

What makes the environmental scanning electron microscope (ESEM) so interesting for many scientific branches such as material sciences, biology or medicine, is that the ESEM allows us to observe wet specimens or nonconductive specimens in their nature state without any previous preparation. Nevertheless the creation of high quality artifact-free secondary electron image is a nontrivial process. This article deals with the possibility of secondary electrons detection at increased pressure conditions in the specimen chamber of ESEM.

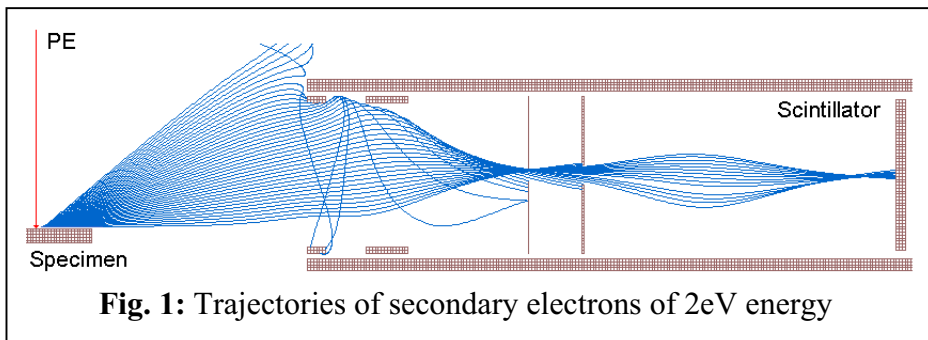


**Fig. 1:** Trajectories of secondary electrons of 2eV energy

There exist one major way for the secondary electrons detection in the ESEM. This way is based on the usage of ionization detector [1].

The scintillation detector seems to be another way for this detection. At the

Everhart – Thornley detector [2] the secondary electrons passed through the collector grid are accelerated to the scintillator with a voltage of about several kV. This voltage is applied to the conductive surface of the scintillator and accelerates secondary electrons in order to give them sufficient energy for efficient scintillation.

This principle is useful for conditions of conventional SEM which operates at vacuum at least  $10^{-2}$  Pa in the specimen chamber but it is impossible at increased pressure conditions of the ESEM because of gas discharge problems. Our new design of secondary electron detector is based on location of the scintillator of the detector in a scintillator room with low pressure. This room is separated from the specimen chamber by the system of pressure-limiting apertures which work also as the electron lens for secondary electrons. Fig. 1 shows the trajectories of secondary electrons of 2 eV energy, accelerated by potential of 50 V and focused by the electron lens into the scintillator room. The trajectories of secondary electrons were simulated by Simion 3D ver. 7.0 program. This method is rather new and is under development. The modified Everhart - Thornley detector seems to be a progressive way for detection of secondary electrons in the ESEM.

### References:

[1] Meredith, P., Donald, A., M., Thiel, B.: Scanning, 18 (1996) 467 – 473

[2] Reimer, L.: Scanning electron microscopy, (1998) 527

[3] This research is supported by project of GACR No. 102/05/0886 and project MSM 002163051.

## A New Method for High Throughput Screening of Cell Spreading on Non-Transparent, Nanostructured Surfaces: Automated Processing of Scanning Electron Microscopic Images.

A. Katsen-Globa<sup>a</sup>, L. Peter<sup>a</sup>, M. Daffersthofer<sup>b</sup>, H. Preckel<sup>b</sup>, D. Schmitt<sup>a</sup>, H. Zimmermann<sup>a</sup>

<sup>a</sup>Fraunhofer IBMT, Ensheimer Str. 48, 66386 St. Ingbert, Germany

<sup>b</sup>Evotec Technologies GmbH, Schnackenburgallee 14, 22525 Hamburg, Germany

The use of nanostructured materials may improve the survival of adherent cells during cryopreservation. For this purpose, screening of new suitable nanostructures and biocompatibility testing must be performed. One of the important criteria is cell adhesion and spreading on the substrate [1]. However, the quantitative high throughput analysis of cell spreading on the nanostructured surfaces is a major problem. These substrates are generally non-transparent and conventional light microscopy cannot visualize cell spreading. An alternative is scanning electron microscopic (SEM) imaging [1]. We propose a new method for the automated quantitative screening of cells grown on non-transparent, nanostructured surfaces by analyzing SEM images with Acapella software from Evotec Technologies GmbH.

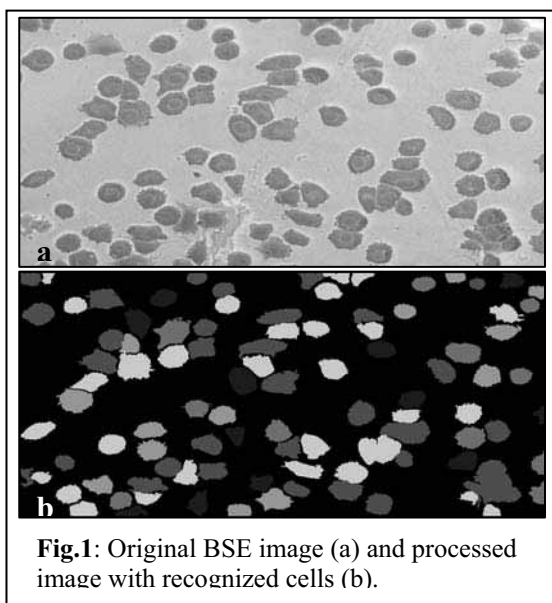


**Fig.1:** Original BSE image (a) and processed image with recognized cells (b).

L929 cells were cultivated on the different nanostructured surfaces. At different times during culture, the cells were stained using a viability fluorescence assay, examined by stereo microscopy and fixed and treated for SEM with tannic acid and heavy metals as previously described [2]. After dehydration and critical point drying, the cells were coated with carbon and examined in environmental SEM using secondary electron (SE)- and backscattered electron (BSE)-modes. For quantitative analysis of cell spreading, the pictures were taken at low magnification (200x). Each substrate was investigated at every time point of cell cultivation by analyzing at least 4 images with a total number of approx. 300 cells. Image processing includes creating a reverse image, generating of background image information, subtraction of background information from image, applying of threshold segmentation (for each image), calculation of cell area, deletion of non-cell objects, splitting

of cells by distance, removing of fragmentary border cells, calculation of several figures of merit as cell count, total area of cells, etc. The results of the analysis have shown that the best SEM-images eligible for analysis are BSE- or mixed (90:10) BSE/SE-images. The high contrast achieved by heavy metal impregnation in combination with the described algorithm permits not only automated cell counting but also the estimation of the shape and area of cell spreading (Fig. 1). We present time resolved quantitative analysis of adhesion processes on different surfaces used for cryopreservation of adherent cells. The method can be used in material science for different quantitative analysis of SEM-images.

### References:

- [1] Baxter L, Frauchiger V, Textor M, ap Gwynn I, Richards R.G. *Europ. Cells Mat.* 4, (2002), 1-17.
- [2] Katsen A.D., Andrushkevich V.V., Tregubova N.A., Rovensky Yu.A. *Scanning*, 14, (1992), 225-230.
- [3] Grants: 03N8707 by BMBF and NMP4-CT-2004-500039 by EU.

## Dynamic OIM of microstructural evolution

René de Kloe<sup>a</sup>, Stuart I. Wright<sup>b</sup>, and Matthew M. Nowell<sup>b</sup>

<sup>a</sup> EDAX BV, PO Box 4144, 5004 JC Tilburg, The Netherlands

<sup>b</sup> EDAX-TSL, 392 East 12300 South, Suite H, Draper, UT 84020 USA

While electron backscatter diffraction (EBSD) has become an established technique within materials characterization labs around the world, the technique is still relatively young and new applications are continuing to emerge. Improved acquisition speeds and automation of EBSD scan acquisition in combination with other equipment within the scanning electron microscope (SEM) have enabled the use of Orientation Imaging Microscopy (OIM) systems to study dynamic in-situ experiments. Such dynamic experiments include observations of microstructural evolution during plastic deformation with tensile stages, while heating stages can be used to study recrystallisation, grain growth, and phase transformations. In addition to these temporal three-dimensional studies, spatial three-dimensional studies can be performed by in-situ serial sectioning in microscopes equipped with both electron and focused ion beams (fig. 1). From such datasets grain and crystallographic information can be obtained in three dimensions. In this contribution, data collection and processing procedures together with examples of both temporal and spatial three-dimensional experiments will be presented.

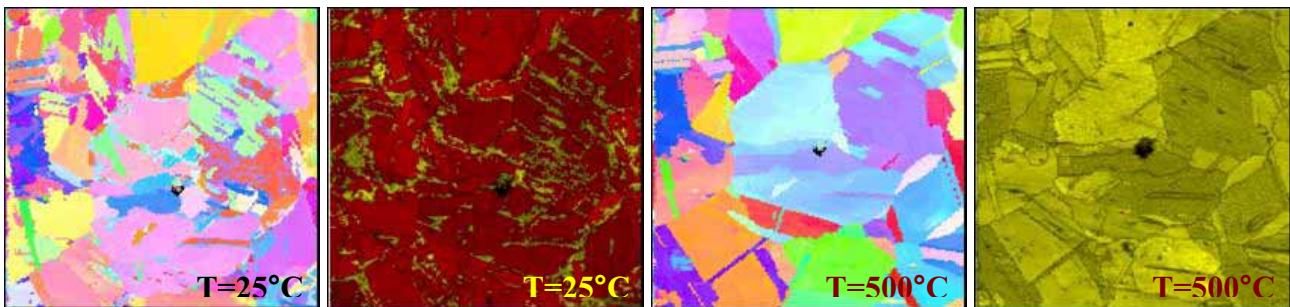


**Fig. 1:**

EBSD IPF and phase maps of identical areas in cobalt before and after phase transformation.

Left: IPF crystal direction maps, right: phase maps.

Yellow phase: beta cobalt; red phase: alpha cobalt.

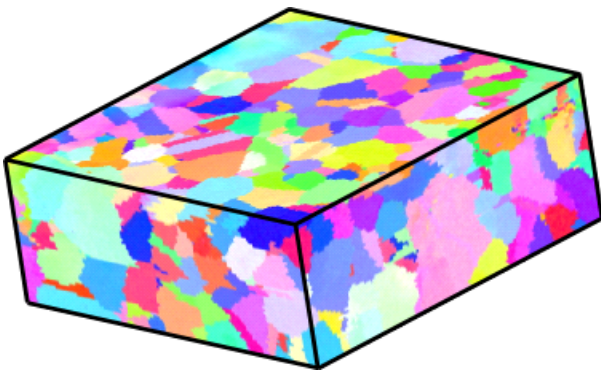


**Fig. 2:**

3D EBSD datacube of nickel superalloy after FIB serial sectioning.

## Recent Progress in Environmental and Variable Pressure SEM

W. Ralph Knowles

FEI Company, Peabody, MA10960, USA

Environmental and variable pressure scanning electron microscopy (SEM) offers two distinct capabilities that are lacking in conventional high vacuum SEM. One is the ability to image uncoated insulating samples using a wide range of beam energies, and the other to perform *in situ* dynamic experiments. The latter include hydration/dehydration, heat induced phase changes and gas-sample reactions. The capabilities of specific instruments are limited by the detector types available for imaging, and the range of gas types and pressures available for dynamic experimentation. This paper reviews the evolution of these capabilities, and describes the recent developments, including the novel use of the environmental gas for gas-assisted electron beam etching and deposition.

Secondary electron (SE) imaging is typically performed using the charge carriers (electrons and ions) or photons produced in the SE-gas interaction. The usefulness of a given detector is defined by the range of accessible operating parameters, such as the maximum gas pressure, field of view and minimum beam energy. Low beam energy, ultra high resolution imaging has been achieved using a gaseous SE detector that utilizes the magnetic field of an immersion lens to enhance the SE amplification process [1]. This method yields high quality SE images at gas pressures and working distances as low as 10Pa and 2mm, respectively, whilst preserving the high degree of charge control characteristic of variable pressure SEM.

At the other end of the spectrum, the maximum pressure accessible by gaseous SE detectors has recently been increased to approximately 2500Pa, using the technique described by Toth and Baker [2] in 2004. This method allows for the imaging of fully hydrated samples at room temperature (previously, hydration required cooling of the sample to temperatures on the order of 2°C, due to the inability of SE detectors to produce high quality images at gas pressure in excess of approximately 1000Pa). The characterization of hydrated materials can be extended further using scanning transmission electron microscopy (STEM). A novel environmental STEM detector will be described. It facilitates sample cooling and concurrent surface imaging using gaseous SE and solid state BSE detectors.

For many years, environmental SEM has been used for dynamic experimentation (hydration, heating and tensile testing) where the sample is observed in a gaseous environment that may be part of the experiment. A new field is emerging for electron beam induced chemistry. The electron beam is used to dissociate gaseous precursors, giving rise to highly localized etching or deposition, while retaining the charge control capabilities of environmental SEM. Beam induced chemistry will be discussed with emphasis on technologically significant applications such as the repair of photolithographic masks.

### References:

- [1] Thiel, et al, *Microscopy and Microanalysis* (2004) 158-159
- [2] Toth, Baker, *Microscopy and Microanalysis* (2004) 1062-1063

# Factors affecting the Collection Efficiency of Secondary Electrons in SEM

Ivo Konvalina, Ilona Müllerová

Department of Electron Optics, Institute of Scientific Instruments, Academy of Sciences of the Czech Republic, Královopolská 147, 612 64 Brno, Czech Republic

The Everhart-Thornley (ET) detector [1] is the most often used type of secondary electron (SE) detector in the Scanning Electron Microscope (SEM). While the overall quality of the final image is influenced by all components of the detection channel, the collection efficiency (CE), which is defined as a ratio of collected SEs to all emitted ones, governs the image contrast and its signal to noise ratio. The detective quantum efficiency (DQE) of such detector has been found significantly below one [2]. The main reason is in complicated distribution of electrostatic and magnetic fields in the specimen vicinity, which strongly influences the secondary electrons trajectories [3].

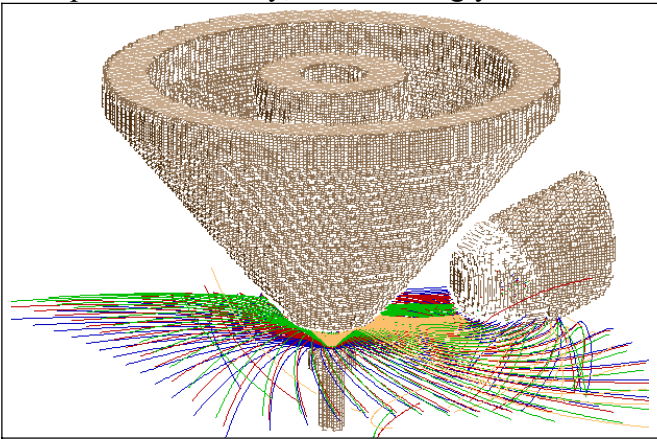


**Fig. 1:** 3D view of a bundle of simulated SE trajectories. Energy of emitted electrons is 5 eV, working distance is 10 mm, grid potential is +300 V, scintillator potential is +10 kV, polar angles of emission are 80, 70, 60, and 50°, and azimuthal emission angles vary from 0 to 360° in 5° steps.

The SE trajectories were simulated by the SIMION 7.0 software [4], which allows for handling 3D arrangements without rotational symmetry under simultaneous affect of electrostatic and magnetic fields. In Fig. 1 one example is shown of a simulation chart with the specimen holder and pole-piece of the objective lens (OL) on ground potential. It is clearly visible that only a small part of emitted SEs reaches the detector. We have performed a lot of simulations and established that CE is strongly influenced with the shape of the whole specimen chamber and all its parts on ground potential. The CE also significantly varies with the specimen diameter and the working distance [5]. Further important roles play the detector position and the potential of its front grid, as well as the electron transport through a realistically shaped grid toward the scintillator. Surprisingly, in most setups no increase in grid potential is able to enlarge CE above 0.5. Influence of the OL magnetic field on SE trajectories was studied for the specimen immersed in strong (in-lens system) or in weak (standard SEM) magnetic fields. Some moderate magnetic field at the specimen surface can even enhance the CE of the side-attached ET detector.

## References:

- [1] T.E. Everhart, R.F.M. Thornley, *J. Sci. Instrum.* **37** (1960) 246.
- [2] D.C. Joy, C.S. Joy, R.D. Bunn, *Scanning* **18** (1996) 533.
- [3] M. Balasubramanyam, E. Munro, J. Taylor, *Nucl. Instrum. Meth. Phys. Res.* **A363** (1995) 270.
- [4] D. A. Dahl, *Int. J. Mass Spectrom.* 200 (2000) 3.
- [5] I. Konvalina, I. Müllerová, *Microscopy and Microanalysis* **9** [Suppl. 3] (2003) 108.
- [6] The study is supported by FEI Czech Republic, Ltd., and by GA ASCR under no. A1065304.

## Quantitative STEM with a High-Resolution Field Emission SEM

Vladislav Krzyzanek, Harald Nüsse, and Rudolf Reichelt

Institute of Medical Physics and Biophysics, University of Muenster, D-48149 Muenster, Germany

Quantitative measurements, e.g., of the sample thickness, molecular masses or mass distributions, can be obtained from thin samples using scanning transmission electron microscopes (STEMs). Since more than two decades dedicated STEMs equipped with an annular dark-field (ADF) detector capable of single-electron counting are very successfully used for quantitative work in the biophysical research (e.g., [1-3]). STEMs are very expensive, difficult to operate and therefore not widespread in laboratories. Commercial high-resolution field emission scanning electron microscopes (HR-FESEM) also possess the potential for quantitative work in STEM mode. The extension of HR-FESEM for quantitative microscopy requires modifications of the commercial hardware as well as specific software packages for digital data acquisition and subsequent image processing as shown recently with an “out-lens” FESEM S-800 (Hitachi Ltd., Japan) [4].

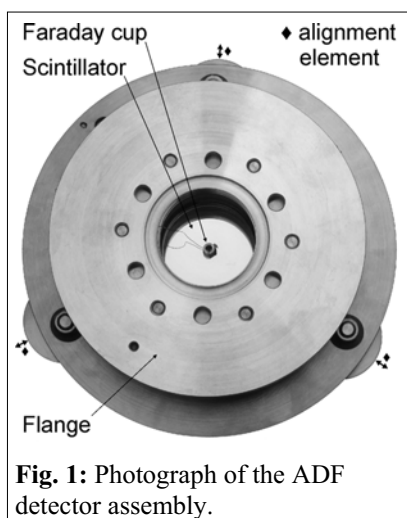


**Fig. 1:** Photograph of the ADF detector assembly.

We extended an “in-lens” S-5000 (Hitachi Ltd., Japan) HR-FESEM with a specified resolution of 0.6 nm in SE mode at 30 kV for quantitative SEM/STEM which requires: (i) knowledge of the actual probe current (to be measured indirectly using the objective aperture current); (ii) any very low beam current needed (hardware modification); (iii) very fast single-electron counting detector and fast counting electronics. The detector consists of a plastic scintillator BC-404 (Saint-Gobain Crystal & Detectors, USA) glued onto a short quartz glass light pipe which transfers the generated light pulses directly to a high gain photomultiplier BURLE 8850 (BURLE Technologies, USA). The detector is mounted in an assembly adjustable perpendicular to the optical axis by about 3 mm. A small Faraday cup located at the centre of the detector enables the direct measurement of the probe current (Fig. 1).

The digital ADF-signal and the analogue objective aperture current are simultaneously acquired by a modified digital image scanning system DISS5 (Point Electronic, Germany). The system includes a digital scan generator for electron beam control and an interface for acquiring specific SEM settings. The shortest pixel-time of our setup amounts about 10  $\mu$ s. All data are stored in a multipage TIFF. The relationship between mass thickness and ADF-detector signal can be calculated using Monte Carlo simulations MONCA [5]. Specifically for the mass determination, a complex MASDET software package was developed [6], which allows the display of micrographs, selection of particles and background areas in the micrograph, automatic processing of data, and the statistical analysis.

### References:

- [1] A. Engel, Ultramicroscopy 3 (1978), 273.
- [2] J.S. Wall, Scanning Electron Microscopy 2 (1979), 291.
- [3] S.A. Müller, A. Engel, Micron 32 (2001), 21.
- [4] V. Krzyzanek, H. Nüsse, R. Reichelt, Proc. 13<sup>th</sup> Europ. Micros. Congress, vol. 1 (2004), 391.
- [5] V. Krzyzanek, R. Reichelt, Microsc. Microanal. 9 (Suppl. 3) (2003), 110.
- [6] V. Krzyzanek, R. Reichelt, Microsc. Microanal. 9 (Suppl. 3) (2003), 112.
- [7] Helpful discussions with Prof. A. Engel & Dr. S.A. Müller (Biocenter, Basel/CH) are greatly acknowledged.

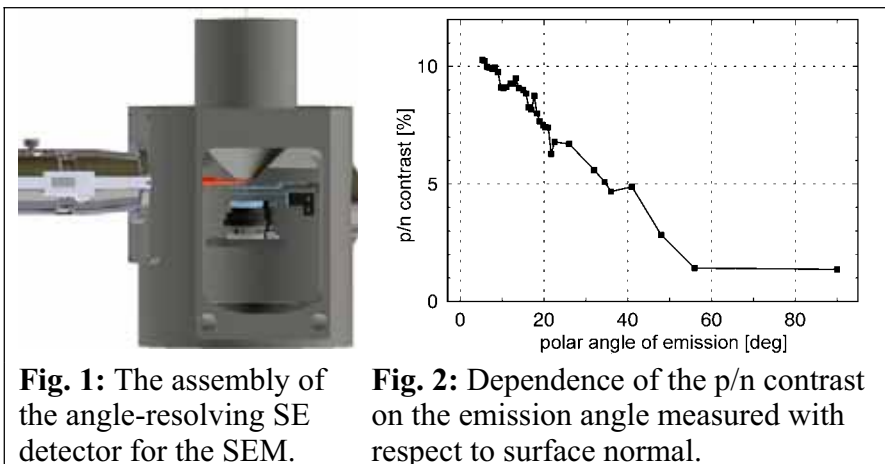
## Secondary Electron Contrast of doped Semiconductor Structures in SEM

Filip Mika and Luděk Frank

Institute of Scientific Instruments AS CR, Královopolská 147, CZ-61264 Brno, Czech Republic

Although the dopant contrast in SEM has now been studied for more than a decade, a clear explanation of it remains a matter for the future. Present discussions particularly concern the role of electric fields above the surface [1] or below it [2], while the angular dependence of the contrast [2, 3] has also not been fully clarified. Generally, p-type silicon appears brighter in the secondary electron (SE) emission than n-type. This study aims to examine the contrast behaviour with the emission angle, for which purpose a special detector assembly has been designed.

The system contains a three-electrode cathode lens with the outermost electrode grounded and the second electrode held at -7 kV. The specimen itself has a bias determining the landing electron energy. The whole assembly fits between the pole-piece of the objective lens and the specimen holder, causing the working distance to be extended to 35 mm (see Fig. 1). The special detector, based on a single-crystal YAG scintillator, is retractable with an extremely finely adjustable lateral position measured to an accuracy of 0.01 mm. The active scintillator area is restricted to a rectangle. The width of the rectangle, which is oriented along the detector axis, measures only 280  $\mu\text{m}$  and defines the angular resolution. The geometrical set-up and electrode potentials have been designed on the basis of SIMION 7.0 software simulations, aiming for the maximum broadening of the signal beam in the detection plane. The detector acquires some combination of secondary and backscattered electron signals [2], of which only SE mediate the contrast. The system was verified on patterned n-type doped areas ( $1 \times 10^{18} \text{ cm}^{-3}$  of phosphorus atoms) made into an Si (100) p-type substrate ( $1 \times 10^{15} \text{ cm}^{-3}$  of boron atoms) with a landing electron energy of 1 keV and primary energy of 10 keV. The first results (Fig. 2) show the p/n contrast as primarily borne with SE emitted near the optical axis and steeply decreasing with the emission angle.



The study should explain the contrast mechanism active in the SE imaging mode. Various dopant concentrations shall be compared in both p- and n-type doping to substrates of an opposite conduction type.

### References:

- [1] Sealy C. P., Castell M. R., Wilshaw P. R., J. Electron Microsc. 49 (2000) 311.
- [2] Müllerová I., El-Gomati M. M., Frank L., Ultramicroscopy 93 (2002) 223.
- [3] Schönjahn C. et al., Appl. Phys. Lett. 83 (2003) 293.
- [4] The work was supported by GA CR project no. GA102/05/2327.

## What can we see at very low energies in the Scanning Electron Microscope?

Ilona Müllerová

Department of Electron Optics, Institute of Scientific Instruments, Academy of Sciences of the Czech Republic, Královopolská 147, 612 64 Brno, Czech Republic

The Scanning Electron Microscope (SEM) is a widely used instrument, which is normally optimised to a primary beam energy of about 15 keV, in contrast to the Low Energy Electron Microscope (LEEM) operated below 50 eV. There are great differences between these instruments, both in their illumination and detection parts. Nevertheless, contrast types can be expected in SEM similar to those observed in LEEM (Bauer 1994) when the cathode lens (CL) principle, inherent to LEEM, is incorporated into the SEM (Müllerová and Frank, 2003). To detect all emitted electrons, auxiliary fields have to be used to divert the signal beam (accelerated to nearly the same energy as the primary electrons) from the optical axis [3]. In our simple detection system the anode of the CL is formed by a YAG crystal with a tiny central opening, so that the slowest signal electrons can escape through the bore, but a small specimen tilt can secure acquisition even of specularly reflected slowest electrons. For an example see Fig. 1.

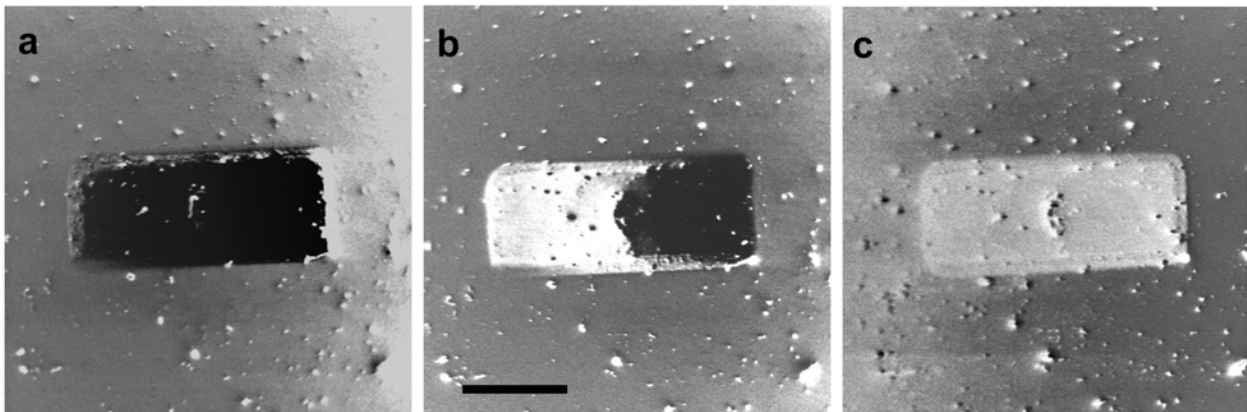


Fig. 1: Boron-diffused P<sup>+</sup> type patterns into a phosphor-doped N type Si (111) substrate. The dopant concentrations in the P<sup>+</sup> and N types were  $1 \times 10^{19} \text{ cm}^{-3}$  and  $4 \text{ to } 6 \times 10^{14} \text{ cm}^{-3}$  respectively. The tilt dependence of the total reflection effect is shown with tilts of (a) 0°, (b) 0.45°, (c) 0.72°; the length of the scale bar is 20  $\mu\text{m}$ , the landing energy 1.5 eV.

In the range of units of eV all known mechanisms of radiation damage, including formation of carbonaceous contamination, already drop in activity, the inelastic mean free path increases and the transmitted electrons can again be detected behind very thin foils [4]. The diffraction contrast in the SLEEM mode has been observed [3] and the quantum size contrast is now our subject of interest.

[1] Bauer E, Rep. Progr. Phys. 57 (1994) 895.

[2] Müllerová I, Frank L, Advances in imaging and electron physics 128 (2003) 309.

[3] Vlček I, Lencová B, Horáček M, in: Proc. 13th Eur. Microsc. Congr. Vol. 1 (2004) 337.

[4] Hrnčířík P, Romanovský V, Müllerová I, in: these proceedings.

[5] The work is supported by the Grant Agency of the Czech Republic, grant no. GA102/05/2327.

# Universal Heating/Cooling Device for Dynamic Experiments in a SEM

Ott Philipp and Günter John Ralph

EMOTT AG, c/o Universität Zürich, Winterthurerstrasse 190, CH-8057 Zürich

A certain demand for control of the specimen temperature existed since the very beginning of scanning electron microscopy (SEM) to prevent an outgassing or the decomposition of the specimen. This was however limited by the need of the dehydration of biological or humid samples. It has rapidly increased with the advent of microscopes operating under less stringent vacuum conditions. With the development of these SEM's it is now possible to investigate biological or humid samples directly without any preparation, but this is only a small extract of the possible uses. There are much more sophisticated applications such as controlled dehydration, solvation of chemical substances, crystallisation, decomposition, and many more. A SEM, equipped with such a device is not any more just a device to produce images, it is a lab in the lab. As a consequence, now most microscope providers offer commercially available temperature control stages. These however frequently do not meet all needs of the users. For instance the stages can induce image distortions (Fig. 1) produced by the cooling device or the desired temperature range does not match the demands. Therefore we have developed a new design of a cooling/heating stage which uses the Peltier [1] effect. In this way the temperature setting is achieved much faster and more accurately than by conventional means. Our design is shielded from magnetic fields of the Peltier unit, as any change of the fields in the stage distorts the image, be it continuously or alternatingly varied (Fig. 2-4).

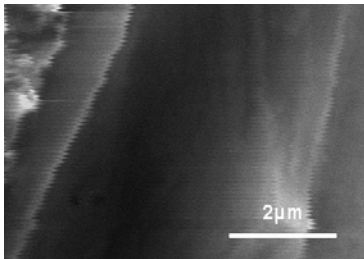


Fig. 1: Image distortion induced by a commercial Peltier stage

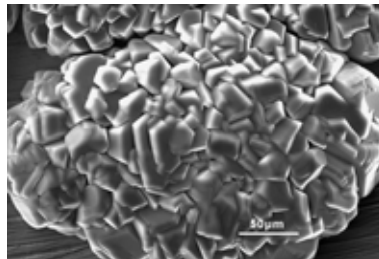


Fig. 2: Crystallisation of water

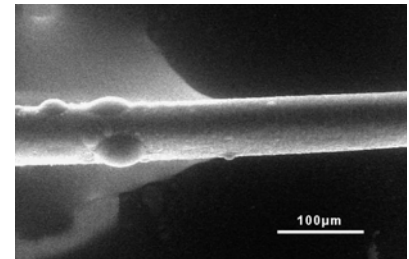


Fig. 3: Condensation of water (left) on a human hair in a temperature gradient

The figures 2 - 4 are taken by a SEM equipped with our newly developed Heating/Cooling devices.

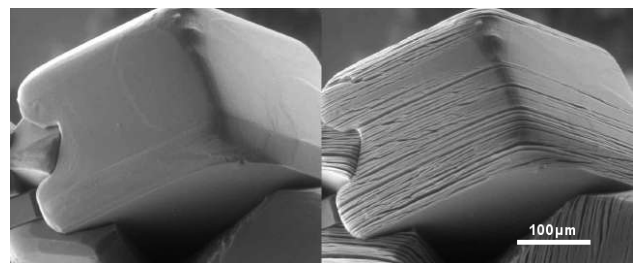


Fig. 4: Dehydration of Copper-formiate

Reference:

[1] Peltier M., Annales de Physique et Chimie, Série 2, Tome 56, 371-386 (1834).

## X-Ray Microanalysis of Fully Wet Samples Using WETSEM™ Technology

Irit Ruach-Nir

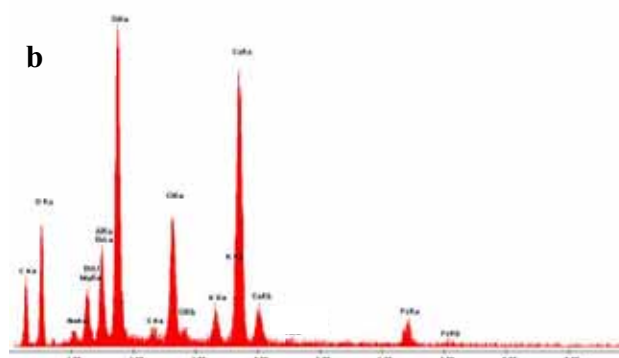
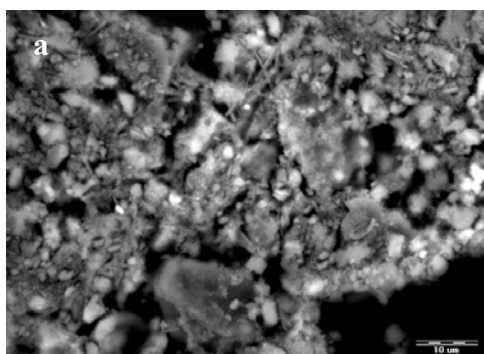
Quantomix ltd. PO Box 4037, Nes-Ziona 70400, Israel

Characterization of chemical microstructures is one of the most important applications of the scanning electron microscope (SEM) equipped with an energy dispersive x-ray spectrometer (EDS). However, one of the challenges this technique was facing is the ability to apply it to wet samples, due to the high vacuum requirements of the SEM. Typical examples include creams, solutions, suspensions and other liquid containing samples.

In this work we show that the recently developed WETSEM™ technology, provided a solution and enabled direct observation and chemical analysis of samples in their native wet state. WETSEM™ uses conventional scanning electron microscopes equipped with a standard EDS detector. The technology was used to study the chemical composition of samples from a variety of fields of use including material science and bio-science. Samples of creams, solutions, and other liquid containing specimens such as suspensions of metal, ceramics and mineral particles were analyzed.

When using WETSEM™ technology, the sample is placed in a sealed specimen capsule (the QX capsule), and is isolated from the vacuum by a thin, electron-transparent membrane. A metal grid mechanically supports the membrane. The thin membrane is used as a window through which imaging and x-ray analysis is carried out. The contribution of the membrane to the sample EDS spectrum was investigated and shown to be negligible. Since the thickness of the membrane is a few hundreds of nanometers and the x-ray signal comes from a much thicker layer the membrane does not interfere with the EDS measurement and its contribution to the EDS spectrum is manifested only by a carbon peak. The grid consists of 330x330 μm windows. When an EDS spectra is generated from an area within such window the elemental signature of the grid is negligible. This work shows results that validates these conclusions

The figure below shows the WETSEM image (a) and the full frame EDS spectrum (b) of dead sea mud courtesy of AHAVA®. The full frame spectrum provides the average chemical composition of the area seen in the image. The elements detected are: C, O, Mg, Br, Al, Si, Cl, Ca and Fe.



# A study on the crystal orientation relationship of butterfly martensite in an Fe-30 % Ni alloy by 3-D EBSD-based orientation microscopy

Hisashi Sato, Stefan Zaeferrer

Max-Planck Institut für Eisenforschung, 40237, Düsseldorf, Germany

The crystal-orientation relationship (OR) between martensite ( $\alpha$ ) and austenite ( $\gamma$ ) in Fe alloys has been intensively investigated. In previous studies on Fe-Ni alloys both the Kurdjumov-Sachs (K-S) and the Nishiyama-Wassermann (N-W) ORs have been reported [1,2,3]. The measurements have been usually carried out by TEM or XRD. However, TEM allows only very localised observations while XRD yields only average information. In the current study, the local OR along the  $\alpha$ - $\gamma$  interface of butterfly-type martensite has been investigated on large areas in 3-dimensions by electron backscatter diffraction (EBSD) on serial sections created by means of a high resolution focused ion beam (FIB)-SEM (Zeiss Crossbeam XB 1560).

The material, a Fe-30mass%Ni alloy was cast, homogenised and hot rolled. Subsequently a specimen of 15×10×5 mm was austenitized at 900°C for 6 h and then water quenched. The sample was mechanical and electrochemically polished. Serial sectioning was carried out by removing thin layers of approximately 300 nm of material by means of a focused ion beam. On each section the microstructure was observed by orientation microscopy using a step size of 50 nm .

Figure 1 shows the microstructure observed on planes at increasing distances from the surface,  $d$ . ( $d = 0, 530, 1080$  nm). Most of the  $\alpha$ - $\gamma$  interface shows either K-S or N-W OR. In some  $\alpha$  lamellae narrow twins are visible close to one interface. The width of the martensite plate (A) increases with increasing  $d$ . At the thin area of the plate (fig. (a)) the interface only exhibits K-S OR. With increasing plate width an increasing amount of NW OR is observed on one side of the plate while the other keeps the KS OR. From the observations we propose the following mechanism: martensite plates nucleate with a KS OR. During growth the transformation shear stresses deform the parent austenite and rotate its crystal lattice by dislocation pile-ups. The piled-up dislocations are subsequently inherited into the martensite which, consequently, also acquires an orientation change. The rotations of  $\alpha$  and  $\gamma$  are responsible for the observed change of the OR from KS to NW.

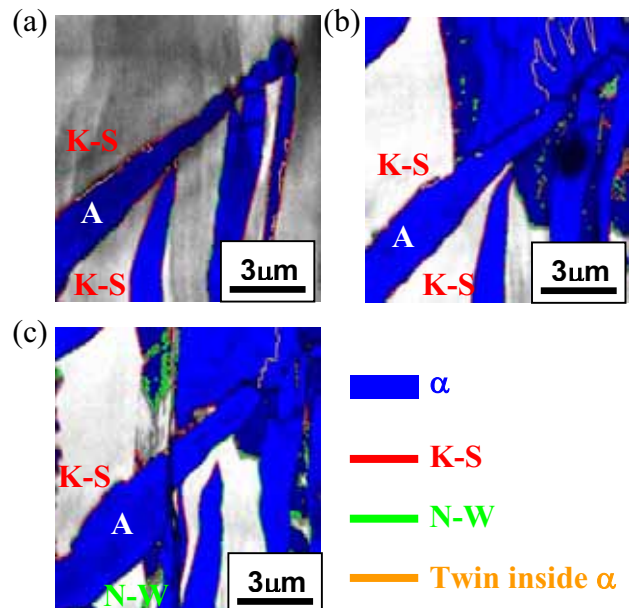


**Fig. 1:** Orientation maps obtained from sections on the surface (a) and at  $d=530$  nm (b) and  $d=1080$  nm (c) below the surface.

## References:

- [1] W.P.Liu, H.J.Bunge, Mater. Lett. 10 (1991) 343.
- [2] T. Maki, C. M. Wayman, Acta metall. 25 (1977), 681
- [3] X.M. Zhang, E. Gautier, A. Simon, Acta metall. 37 (1989), 487

# Extended Algorithm for Optimization of Photon Transport in Scintillation Detector

Petr Schauer and Rudolf Aufrata

Institute of Scientific Instruments, Academy of Sciences of the Czech Republic, Královopolská 147, CZ-61264 Brno, Czech Republic

To avoid inefficiency and inhomogeneity of BSE scintillation detection systems, efficient transport of photons from luminescent centres in a scintillator to a photocathode of a photomultiplier tube must be provided. Optimization of the photon transport of a rotationally symmetric Everhart-Thornley detector is quite a feasible task, because a code for the Monte Carlo (MC) simulation is based on the system geometry which is a function of one variable coordinate. For such a rotationally symmetric detection system the previous MC code Scintil [1] was developed in our laboratory. The Scintil code includes photon generation in a point source, mirror reflection by a metal coated surface, Fresnel reflection by a metal uncoated surface, Fresnel passage through the boundary of different materials, diffusion reflection and passage through a matted surface and optical absorption in material.

Unfortunately, BSE scintillation detectors have no rotational symmetry. Therefore, it was necessary to rebuild the algorithm of Scintil for the optimization of BSE detection systems. Such an extended algorithm has been used in our SciUni code for practically any geometry. The main difference between the algorithms of SciUni and Scintil is in the description of detector surfaces and subsequently in the determination of the position of the photon interaction with the surfaces mentioned. Using SciUni, any surface can be described as:

$$\sum_{i=1}^3 k_i \frac{(x_i - x_{0i})^2}{A_i^2} = P \quad (1)$$

where  $x_1, x_2$  and  $x_3$  are the x, y and z intersection point coordinates, respectively,  $x_{01}, x_{02}$  and  $x_{03}$  are the x, y and z surface body origin coordinates, respectively, and  $k_1, k_2, k_3, A_1, A_2, A_3$  and  $P$  are geometrical coefficients of the surface as described for different bodies in Table 1. Using the extended SciUni code and the Fortran 77 compiler a SciUni program for different computer platforms (including PC) has been developed, and the MC light-guiding simulation as the basic method for the computer optimized design (COD) of new BSE scintillation detectors is available at our laboratory,

**Table 1.** Some examples of coefficients for different lateral areas for equation (1)

body \ coefficient	$A_1$	$A_2$	$A_3$	$k_1$	$k_2$	$k_3$	$P$
Sphere (any axis)	$r$	$r$	$r$	1	1	1	1
Cone (y axis)	$r$	$v$	$r$	1	-1	1	0
Cylinder (x axis)	1	$r$	$r$	0	1	1	1
Plane ( $\perp$ z axis)	1	1	1	0	0	1	0
Plane (defl. from z axis)	$k$	1	1	1	0	-1	0
Ellipsoid (y axis)	$a$	$c$	$a$	1	1	1	1
Hyperboloid (x axis)	$c$	$a$	$a$	-1	1	1	1

*r* - radius, *v* - body high, *k* - slope of deflection, *a* - half-axis (plane of symmetry), *c* - half-axis (along body axis)

## References:

- [1] Schauer, P.; Aufrata, R.: *Scanning* **14** (1992), 325-333.

# Stroboscopic Low Energy Electron Microscopy – Imaging of Dynamic Processes and Transient States with Picosecond Time Resolution

Gerd Schönhense

Institut für Physik, Johannes Gutenberg-Universität, D-55099 Mainz, Germany

Time resolution in the nanosecond range has previously been achieved in SEM via fast beam-blanking combined with synchronized operation of an electric circuit for e-beam testing of the temporal operation of ICs [1]. Nanosecond-laser pulsed metal films have been studied using a high-speed TEM technique [2]. In several fields of high current interest, even higher time resolution is mandatory. Ultrafast remagnetization, e.g. precessional motion of the magnetisation in magnetic memory elements or spinwave eigenmodes in confined structures, happen on a sub-ns timescale. Transient states like “hot-electron” states in metals and semiconductors exist in the femtosecond range. New concepts have to be developed that allow “real-time” imaging of such fast processes using electron microscopy.

A promising technique with potential for very high time resolution is low energy electron microscopy. The diffraction contrast in LEEM as well as the various contrast mechanisms of photoemission electron microscopy PEEM can be combined with high time resolution by using pulsed excitation sources. Pulsed electron beams for LEEM can be obtained using pulsed laser excitation of a photocathode (for GaAs pulse lengths shorter than 30 ps have been achieved). Pulsed photon beams from lasers (fs pulses) or the natural time structure of Synchrotron radiation (down to few-ps pulses) can be exploited in PEEM. A recent example using magnetic circular dichroism contrast and Synchrotron radiation is shown in figure 1. Fast magnetic field pulses are generated by current pulses  $I$  through a coplanar waveguide (a), the magnetic response is imaged by a stroboscopic technique (b). Here, a magnetic flux-closure structure (seen at 0 ps) is driven into a striped domain phase (blocking pattern) [3].

The state of the art of stroboscopic imaging using low-energy electrons will be discussed and principal limitations will be outlined. Last but not least, the pulsed beam in low energy electron microscopes bears the potential of a novel approach of aberration correction [4].

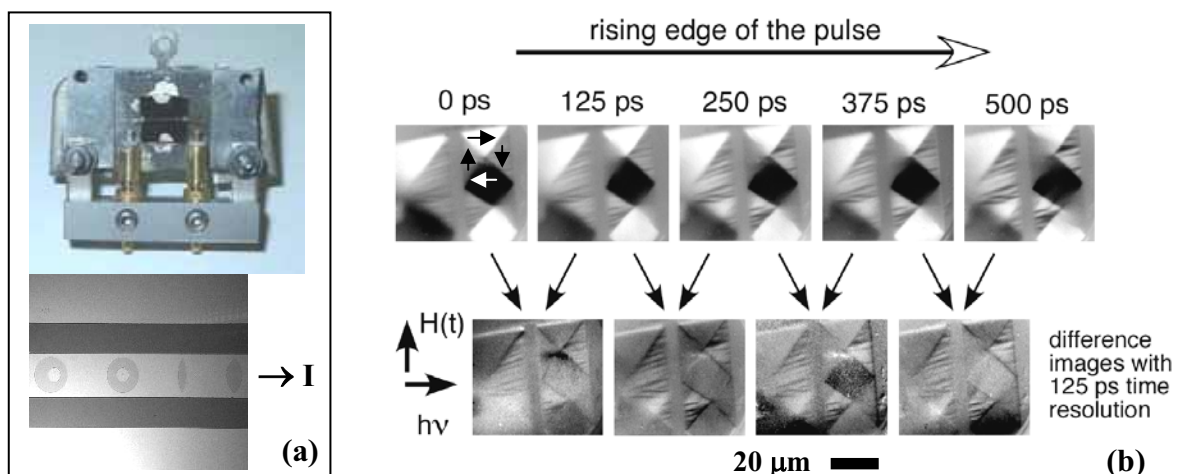


**Fig. 1:** Exchangeable sample holder with waveguide (a); series of snapshots at 0 – 500ps (b)

[1] H.P. Feuerbaum, *Scanning* **5** (1) (1982) 14-24

[2] H. Dömer, O. Bostanjoglo, *Rev. Sci. Instrum.* **74** (2003) 4369-4372

[3] C.M. Schneider et al., *Appl. Phys. Lett.* **85** (2005) 2562

[4] G. Schönhense and H. Spiecker, *J. Vac. Sci. Technol. B* **20** (2002) 2526-2534

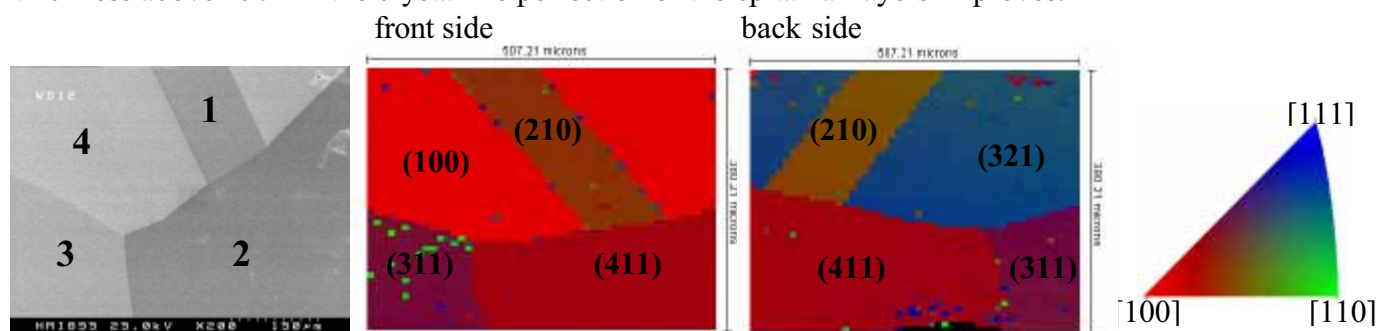
## FE-SEM, EBSD and TEM investigations of sputtered epitaxial silicon layers on different oriented substrates

Ina Sieber<sup>a</sup>, Peter Schubert-Bischoff<sup>a</sup>, Ingrid Urban<sup>b</sup>

<sup>a</sup> Hahn-Meitner-Institut, Abteilung Silizium-Photovoltaik, Kekuléstr. 5, D-12489 Berlin, Germany

<sup>b</sup> Bundesanstalt für Materialforschung und -prüfung, Unter den Eichen 87, D- 12205 Berlin, Germany

We have investigated epitaxial silicon layers deposited by pulsed magnetron sputtering at 500°C on (100)-, (111)- and (311) oriented silicon substrates and on SILSO wafers with different orientation. Up to now, a limited epitaxial growth on mainly (100) oriented substrates was reported at temperatures up to 600°C. With deviation from the (100) orientation, the density of defects and inclusions in the epitaxial layers increase up to the transition to fine-crystalline growth on (111) oriented substrates. For layers deposited by sputtering, epitaxial growth with high crystalline perfection is not only observed on (100) oriented substrates, but also on other substrate orientation, as shown by the example of an epitaxial layer on four differently oriented domains of a SILSO wafer (see figure). The SEM investigations (left image) reveal the smooth surface of an epitaxial layer with only slight morphological differences on differently oriented domains. EBSD investigations of the epitaxial layer and the substrate measured from the back side (middle and right image, respectively) show that on (311), (411) and (210) oriented domains, the epitaxial layers maintain the substrate orientation during growth, while for the (321) oriented substrate region, the orientation in the layer changes to a direction close to (100). The change to the (100) orientation also is found for the growth on (110) and defined (111) oriented substrates. For these orientations, transmission electron microscopic investigations show defects such as stacking faults and small amorphous inclusions in a region starting at the substrate-film interface up to a thickness of 150 nm. With increasing film thickness above 150 nm the crystalline perfection of the epitaxial layers improves.



SEM micrograph of epitaxial silicon layer on four differently oriented domains of SILSO wafer and crystal orientation mappings of front and back side (reversed) in normal direction and the inverse polefigure.

Acknowledgement: The authors thank F. Fenske for the deposition of layers.

[1] D.J. Eaglesham, J. Appl. Phys. (1995) 3597

[2] T.A. Wagner, L. Oberbeck, R.B.Bergmann, J.H. Werner, Solid State Phenom. 80-81 (2000)95

[3] B. Rau, I. Sieber, B. Selle, S. Brehme et al., Thin Solid Films 451- 452(2004)644

## **The Energies and Relative Intensities of M Lines**

Ralf Terborg, Thorsten Eickhoff

RÖNTEC AG, Schwarzschildstraße 12, D-12489 Berlin

Within recent years some new atomic databases were published in the internet. These contain – besides other fundamental parameters – line energies and intensities of K, L and M lines. However, these databases show considerable differences, a lack of accuracy, line intensities which are varying by three orders of magnitude and missing lines when compared to measured spectra, especially in the low energy area. This is also true for some widely used but old publications.

These discrepancies, especially in the relative line intensities, cannot be explained only by errors in the measurements or uncertainties of depending fundamental parameters. In truth, line energies and intensities were interpolated or even estimated as roughly constant for a wide range of elements in the periodic system. Additionally, some significant lines like the  $M\zeta$  line were neglected in the databases or publications.

Even for elements with M lines greater than 2keV atomic databases show significant differences. For example for the common element gold some databases show only three lines which agree with experimental spectra in line energy and intensity, whereas at least five lines are significant and clearly visible in experimental spectra.

RÖNTEC, in co-operation with Prof. Wendt from the Institute for Physical High Technology Jena, investigated L and M line spectra and revised and extended the RÖNTEC database. Results of this work will be presented and some examples will be compared with other databases.

## Design Of Detector Optics For A Low Energy SEM

I. Vlček, B. Lencová and M. Horáček

Institute of Scientific Instruments AS CR, Královopolská 147, 61264 Brno, Czech Republic

A LESEM using cathode lens allows imaging with very low energy electrons. Although many adaptations of existing SEMs work satisfactorily with a cathode lens, for surface physics applications we need UHV and related sample preparation methods [1]. In order to produce images of competitive quality/information contents to a LEEM, we need an objective lens of similar quality as that used there [2] as well as a better utilization of all the information contained in the signal electrons. The cathode lens not only determines the optical properties of LESEM but it also accelerates the signal electrons into the column, where they have to be separated and detected.

We have decided to modify our UHV SLEEM using a commercial electrostatic two-lens column with a Schottky cathode (2LE of FEI) [1]. This column will be used as an illumination part of a low energy SEM. The crucial element in the new electron-optical setup is the weak Wien filter [3], which separates the signal electrons by deflecting them by 15 degrees from the primary beam. The signal from the SEM will be spread over the detector area of a fast 80x80 pixel back-side illuminated CCD detector [4], and so it will allow the utilization of the angular and energy distribution of the signal beam. The optimum energy at the detector is 4.2 keV, and so we made all elements electrostatic and working close to this beam energy. Because of the energy dispersion of the Wien filter, we have to position the beam crossover into the center of the filter for high resolution imaging with an auxiliary condenser lens. The objective lens resembles the design of LEEM by Adamec et al [2].

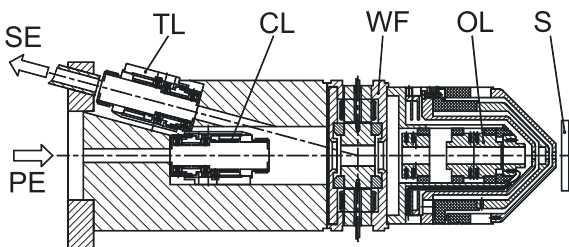


Fig. 1. The setup of the lower part of the LESEM.

Figure 1 shows the critical part of the system. The primary beam electrons (PE) are focused by an auxiliary condenser lens (CL) into the center of the Wien filter (WF); the objective lens (OL) with electrostatic deflectors can be combined with a cathode lens if the primary electrons are decelerated by an electrostatic field between OL and the specimen (S). The signal electrons (SE) are deflected from the primary beam and with an electrostatic transfer lens (TL) they are transferred in the direction of the detector; its ground electrode

is split into four sections that allow centering of the beam. Because of the small deflection, the CL and TL lenses must be close to the beam axis, as shown in Fig. 1 [5].

### References:

- [1] I. Müllerová and L. Frank, *Adv. Imag. Electron Phys.* **128** (2003), 309-443.
- [2] P. Adamec, E. Bauer and B. Lencová, *Rev. Sci. Instrum.* **69** (1998), 3583-7.
- [3] I. Vlček and B. Lencová, *Proc. 12th EUREM, Brno 2000*, I87-I88.
- [4] M. Horáček, *Rev. Sci. Instrum.* **74** (2003), 3379-84.
- [5] Support by Grant Agency of the Czech Republic, grant number 202/03/1575, is acknowledged.

## **Critical Dimension Analysis of Thin (~100 nm) Gold Coatings by SEM and EDS**

Parvati Ramaswamy, S.Vynatheya , S.Seetharamu

Materials Technology Division, Central Power Research Institute, P.B.No. 8066,  
Prof. Sir C.V.Raman Avenue, Bangalore – 560 080, India

The abilities of scanning electron microscope (SEM) equipped with an attachment for energy dispersive spectrometry (EDS) which allows viewing the structure of the specimen, identification of the elements in them and visualization of their lateral distribution as X-ray maps is undisputed. However, understanding the nature of analysis required, specimen preparation methods and the analytical capabilities of the instrument should be viewed critically together in order to arrive at a completely accurate and reliable solution to the problem being studied. This becomes highly essential typically in cases where thin coatings (~100nm) are being analysed for thickness alongwith chemical composition and defects. The various electronic, eddy current and X-ray based gauges available for plating thickness measurements are likely to be sensitive to changes in substrate material and part geometry. The substrate material and small sized components may offer a challenge for non-destructive thickness gauges. Further, while there are a few non-destructive optical methods based on principles of ellipsometry and reflectometry for measuring the thickness of thin films, they are not combined with the special abilities of ascertaining the chemical composition simultaneously at the inner regions of measurement. These analyses are performed efficiently by SEM and EDS system and this method is the referee method for quality control. However, stress is laid on the criticality of the need of adequate method of sample preparation and analysis.

Gold coatings (varying in thickness between 100nm and submicron range) on nickel coated metallic as well as non-metallic substrates were analyzed using SEM (both in the secondary and back scattered detection mode) and EDS. Disagreement on the coating composition, thickness, uniformity in coating characteristics (with specified allowable range), minimum and maximum thickness etc. can lead to discrepancies to be solved only by analysis of the problem with high level of accuracy and reliability and the issues are being addressed in the present paper. [1]

1. The Authors gratefully acknowledge the management of CPRI for approving the publication of this paper in MC-2005 conference.

## Detection of Low Energy Backscattered Electrons in SEM

Petr Wandrol<sup>a</sup>, Rudolf Aufrata<sup>a</sup>

<sup>a</sup>Dep. of Electron Optics, Institute of Scientific Instruments AS CR, 61264 Brno, Czech Republic

Application of the low accelerating voltage of the primary electron beam became due to its obvious advantages very popular in last decade. Instruments which are able to work with accelerating voltage of 3 keV and lower are called Low Voltage Scanning Electron Microscopes (LV SEMs). Detection of the backscattered electrons (BSEs) in LV SEM is because of their low energy very questionable. The planar YAG backscattered (BSE) detector installed under the pole piece that is the most efficient BSE detection system [1] in SEM can not be used in LV SEM because the low energy BSEs do not produce sufficient number of photons in the scintillator and therefore signal provided by this detector is low as well as the quality of the image. This problem is adequately solved in the newest types of LV SEMs equipped by an immersion objective lens where the BSE detection performs in the objective lens by scintillation detector [2] or by transformation of BSE to SE3 [3]. This contribution offers a solution of the BSE detection problems in LV SEMs which are not equipped by the in-lens BSE detection systems.

It is necessary to accelerate the low energy BSEs before they reach the scintillator. This acceleration can be carried by a bias of at least 4 kV applied on the electrode which is created on the scintillator surface. The high bias accelerates both, the BSEs and the secondary electrons (SEs). There are two ways of the SEs filtration. First possibility is an energy filter created by a grid on a negative bias transparent for BSEs. Second way is the detector installation under the immersion objective lens where SEs are focused into this lens. The grid is in this case grounded and serves only to limitation of the high bias.

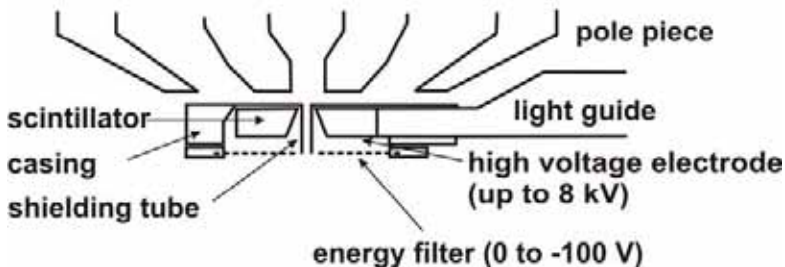


**Fig. 1:** Low voltage BSE detector under the pole piece

trajectories of signal electrons in the software Simion 3D [4] and Trasys [5]. In both above mentioned ways of SEs filtration a hundred percent of SEs with energy of 5 eV are deflected from their trajectories and doesn't reach the scintillator. Approximately 50% of BSEs with energy of 1.5 keV reach the scintillator and create the signal. According to realized computations it is possible to create a high-quality BSE image using designed detector in LV SEM.

### References:

- [1] Aufrata R., Schauer P.: In Proceedings of 13<sup>th</sup> European Microscopy Congress (2004), p. 75-76
- [2] Steigerwald M. G. D.: Microscopy Today vol. 11, (2003), p. 26-28
- [3] Hitachi Scientific Instrument Technical Data, sheet no. 98
- [4] Lencová B., Wisselink G.: Nucl. Instrum. Meth. Res. A298 (1990), p. 56-66
- [5] Dahl D. A.: In Proceedings of 43<sup>rd</sup> Conf. on Mass Spectroscopy and Allied Topics (1995), p. 717
- [6] This work is supported by the Academy of Sciences of Czech Rep., grant no. KJB200650501

# Topometry using a Four-Quadrant-Backscattered Electron Detector

Ulrich Wendt, Hartmut Heyse, Olga Kisel

Otto-von-Guericke-University Magdeburg, Dep. of Materials Science;  
Universitaetsplatz 2, D-39106 Magdeburg; [wendt@mb.uni-magdeburg.de](mailto:wendt@mb.uni-magdeburg.de)

Topometry of surfaces generated by very different processes (e.g. coating, fracture, wear, machining, electro erosion) and of different materials contain information on the generation processes and on the relationship between topography and properties. To extract this information a quantification of the surface topography (topometry) is necessary.

For quantitative 3D-microscopy several methods with specific performances (lateral and axial resolution, height range, vacuum etc.) are available to deliver a data set containing the x, y, z coordinates for each sample point. Topometry based on images obtained by a four-quadrant backscattered electron detector in a SEM has certain advantages, e.g. wide-spread availability of SEM's, high resolution, large field of depth, imaging of specimens with great height differences. Specimen tilting is not necessary, as is the case in SEM-stereophotogrammetry.

The applicability and limitations of 4Q-BSE-topometry was tested using a four-quadrant semiconductor BSE detector system (point electronic GmbH). Four BSE-images were simultaneously registered on a PC-based image acquisition system (DISS/point electronic GmbH) (Fig. 1) The topographical image (Fig. 2) was reconstructed from the image set (Still creator module of the Mex software; Alicona GmbH) based on the "shape from shading" principle [1].

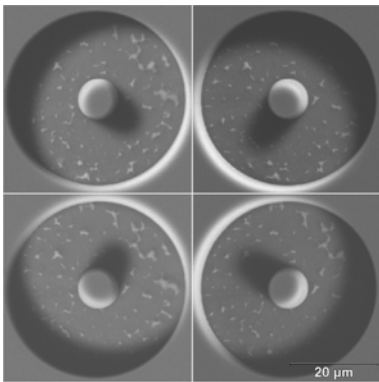


Fig. 1: 4-Quadrant-BSE- images of a FIB pattern in Si

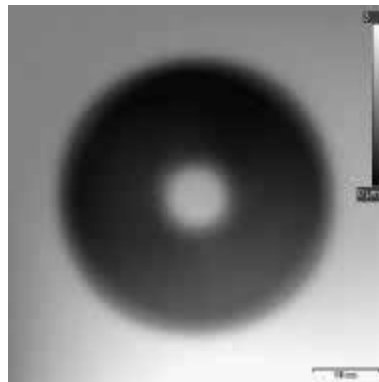


Fig. 2: Topo image obtained from the images in Fig. 1

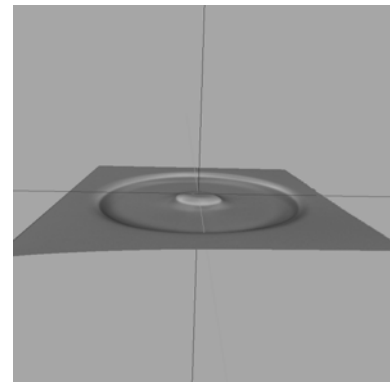


Fig. 3: Parallel projection of the topo image in Fig. 2

The results obtained with different specimens (ceramic beads, FIB-manufactured patterns in Si, hardness indentations, and brittle fracture surfaces) show that the influence of accelerating voltage, specimen current, working distance, and specimen tilt have to be considered. These influences limit the application of the 4Q-BSE-topometry to certain specimen topographies. Suggestions for modifications of the reconstruction algorithm, that consider also the angular distribution of the BSE emission [2], are given to improve the performance of this very useful topometry method.

## References:

- [1] K. Ikeuchi, B.K.P. Horn; Artificial Intelligence, 17(1981)141–184
- [2] L. Reimer; Scanning Electron Microscopy, Springer Berlin 1998

## 3D-Orientation Microscopy in a Combined Focused Ion Beam (FIB) - Scanning Electron Microscope: A New Dimension of Microstructure Characterisation

Stefan Zaefferer, Joachim Konrad, Dierk Raabe

Max-Planck-Institut für Eisenforschung, 40237 Düsseldorf, Germany

Orientation microscopy (OM) by means of automatic analysis of electron backscatter diffraction (EBSD) patterns and mapping of the determined crystallographic results is a well established technique for the characterisation of crystalline materials by scanning electron microscopy. Surfaces with low radiation defect density, suitable for the formation of clear EBSD patterns, can be produced by sputtering the surface under grazing incidence with a  $\text{Ga}^+$  ion beam in a focused ion beam (FIB) microscope. It is therefore possible to combine EBSD-based OM with well-controlled serial sectioning by FIB and obtain in this way 3-dimensional microstructure and microtexture data. The full palette of microstructure information offered by OM, including grain size and form, type of crystallographic phase, dislocation density, grain and phase boundary type, local texture and so on is then available in 3 dimensions. A combination with compositional data from x-ray spectroscopy (e.g. EDS) gives even more information.

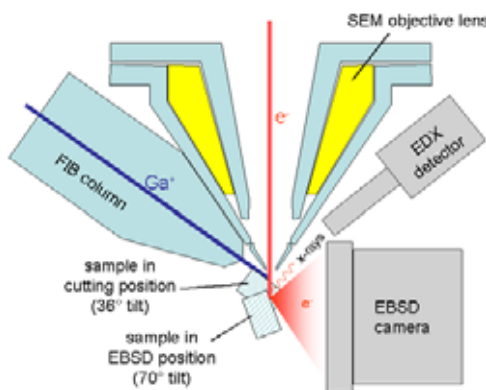


**Fig. 1:** Schematic set-up of the combined FIB-SEM for orientation microscopy

alloys containing Laves-phase particles.  $\text{Fe}_3\text{Al}$  alloys have a good potential for the use at high temperatures in corrosive atmospheres. One problem, however, is their low strength at high temperatures. Laves-phase particles are added as potential strengtheners. Large particles, however, lead to recrystallisation by particle stimulated nucleation (PSN). 3D OM allows to analyse the PSN process in great detail (direction of maximum orientation gradient, occurrence of large angle grain boundaries). In principle, every feature that can be rendered by EBSD OM can be used for 3D reconstruction.

We recently acquired a combined FIB-SEM (Zeiss Crossbeam XB 1560) which is particularly optimised for 3D-orientation microscopy. EBSD camera and EDS detector are positioned on the side opposite to the FIB column, thus allowing a very easy change between the milling position (sample at  $36^\circ$ ) and the EBSD position ( $70^\circ$ ). A schematic is shown in figure 1. Together with the companies EDAX/TSL and Zeiss we are currently developing an automatic "slice and analyse" system.

A first result is presented in figure 2. It shows the 3-dimensional microstructure of a hot rolled  $\text{Fe}_3\text{Al}$ -based

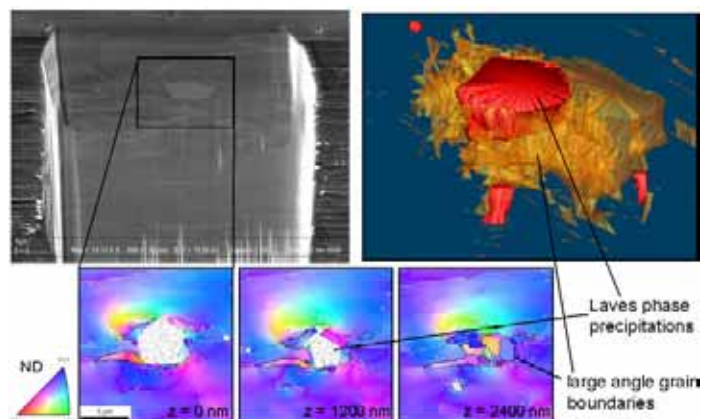
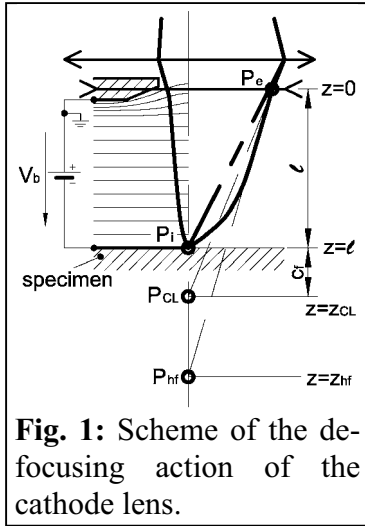


**Fig. 2:** Some orientation maps obtained by serial sectioning and the 3-D reconstruction of the microstructure rendered from 8 sections using the public domain program IMOD (J.R. Kremer et al., J. Struct. Biol. 116 (1996), 71).

## Corrections of Magnification and Focusing in a Low Energy SEM

J. Zobačová, F. Mika, M. Zobač, L. Frank

Institute of scientific instruments AS CR, Královopolská 147, CZ-612 64 Brno, Czech Republic



A very low energy impact of primary electrons is an advantage of the SEM equipped with a retarding field element below the pole-piece of the objective lens (OL). The specimen alone is used as the negatively biased electrode, i.e. cathode of the cathode lens (CL). Scintillator disc with a particular shape of the bore serves both as anode of CL and detector. The electric field of the cathode lens penetrating the central opening of the anode acts as a diverging lens, see Fig. 1. An accurate analytical expression for the focal length of such lens  $f_{AL}$ , assuming the field steeply changes in the aperture plane, is derived in [1]. The optical power of the cathode

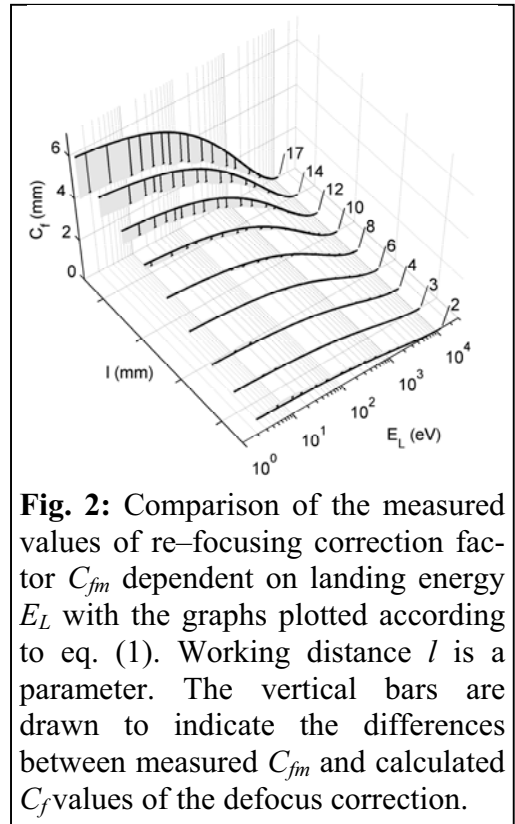
lens modifies some of the standard optical parameters. Use of geometrical optics laws makes possible to find correct expressions for the objective lens excitation (defining the working distance) [1] and the image magnification [2] once the cathode lens is excited and retards the primary beam in front of the specimen. In computer-controlled electron microscopes these parameters, particularly as regards focusing and magnification, can be corrected automatically. Derivation of algorithms for such corrections, (e.g. eq. 1), and their experimental verifications, (see Fig. 2), are presented in this paper.

For illustration, see the focus correction  $C_f$ , which is determined according to the excitation of the OL as the relation:

$$C_f = -l \frac{2l\sqrt{k} + f_{AL}(\sqrt{k} - 1)}{2l\sqrt{k} - f_{AL}(\sqrt{k} + 1)} > 0, \text{ where } f_{AL} \text{ depends on the immersion ratio } k. \quad (1)$$

### References:

- [1] J. Zobačová, M. Zobač, M. Oral, I. Müllerová, L. Frank: Corrections of magnification and focusing in a cathode lens equipped SEM. Scanning, submitted.
- [2] Müllerová I, Frank L: Very low energy microscopy in commercial SEMs. Scanning 15 (1993) 193-201.
- [3] Support of the GA ASCR under grant no. KJB 2065301 is gratefully acknowledged.



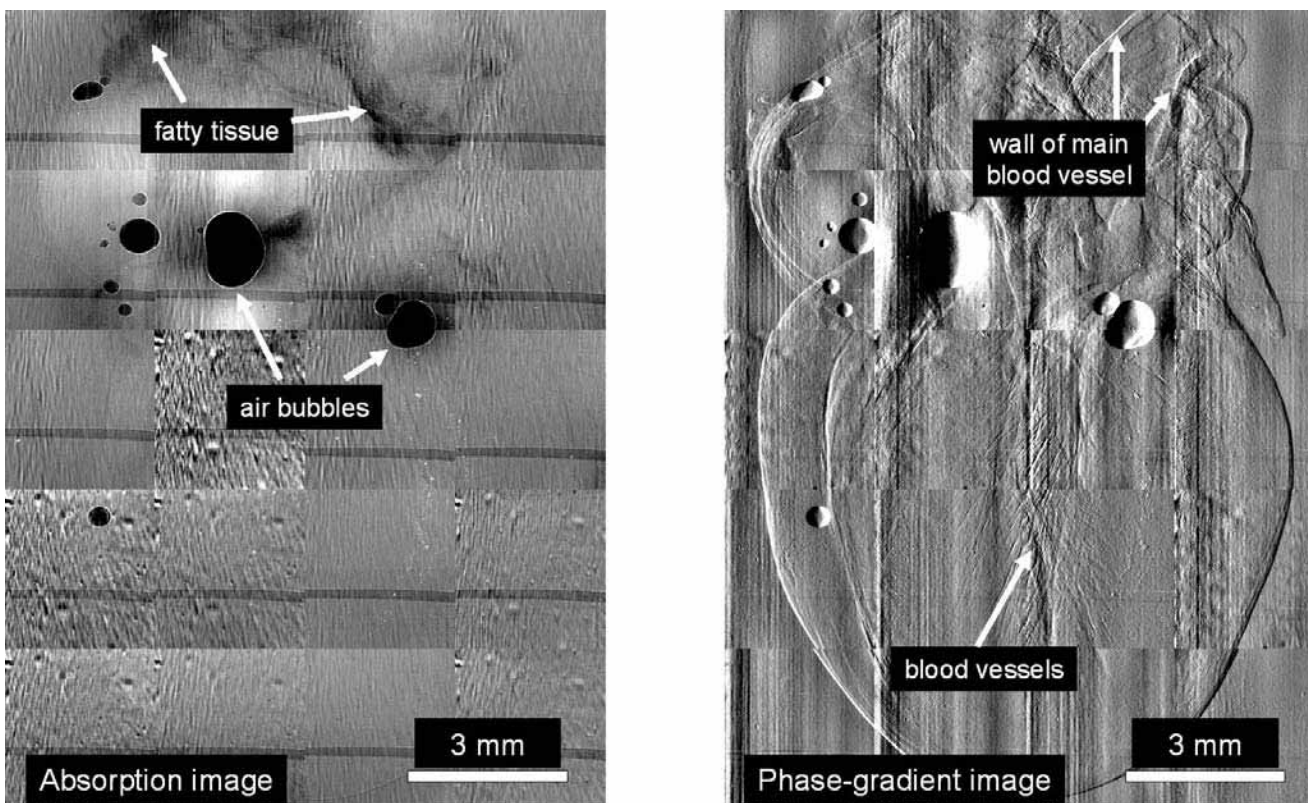
## Biomedical Hard X-ray Phase Imaging Using a Grating Interferometer

C. David, T. Weitkamp, T. Khan\*, H. Walt\*, F. Pfeiffer, O. Bunk, A. Diaz, T. Rohbeck, A. Groso, M. Stampanoni

*Paul Scherrer Institut, CH 5232 Villigen-PSI, Switzerland*

*\* Forschung Gynäkologie, Universitätsspital, Frauenklinikstr. 10, 8091 Zürich, Switzerland*

The imaging of biological or medical tissue samples in the hard x-ray range is problematic due to the low absorption coefficient of light elements. We have recently developed a grating interferometer that allows us to visualize the phase shift gradient, which can greatly increase the contrast of such samples. As an example the figure below shows x-ray images of an animal organ which was put in a container with water. We have used synchrotron radiation of 17 – 18 keV photon energy for imaging. Due to the limited size of the synchrotron beam of 3mm, the image has been stitched together from 20 sub-frames. In absorption contrast, only air bubbles and some fatty tissue are visible, whereas the complete organ with many details can be seen in the differential phase contrast image. We expect that the technique can be useful to reduce the dose applied in medical examinations, especially in mammography.



X-ray micrographs of a rat heart in water taken with polychromatic radiation of 17-18 keV energy.

## Imaging Magnetic Nanostructures by Resonant X-Ray Holography

S. Eisebitt

*BESSY m.b.H., Albert-Einstein-Str. 15, 12489 Berlin, Germany; eisebitt@bessy.de*

While holography has evolved to a powerful technique in the visible spectral range, it is difficult to apply at shorter wavelength as no intrinsically coherent (soft) x-ray laser is yet available as a light source. The progression from visible light towards shorter wavelength is motivated by the increase in spatial resolution that can be achieved. Of equal importance is the possibility to exploit special contrast mechanisms provided by scattering in resonance with transitions between electronic core and valence levels.

We demonstrate magnetic imaging by x-ray spectro-holography, exploiting x-ray circular dichroism as a contrast mechanism. Images of magnetic domain patterns in thin film magnetic multilayers with perpendicular anisotropy are presented. Such materials are of importance in high density recording media for current and future generation hard drives. The images are obtained by direct Fourier inversion of the small angle scattering pattern, without the need of phase retrieval or an iterative computing process. Currently, we achieve a spatial resolution of 50 nm at an x-ray wavelength of 1.59 nm. [1]

Holography at this wavelength is made possible by combining the sample with a nanostructured mask. An advantage of this approach is that there are no severe space constraints around the sample, making it easy to realize extreme sample conditions such as high magnetic fields or low/high temperature, which is of particular interest for applications in material science. Here, we present domain images in applied magnetic fields for magnetic multi-component systems and discuss future opportunities for single shot imaging experiments at free electron x-ray lasers.

[1] S. Eisebitt, J. Lüning, W. F. Schlotter, M. Lörger, O. Hellwig, W. Eberhardt, J. Stöhr, Lensless Imaging of Magnetic Nanostructures by X-ray Spectro-Holography, *Nature*, **432**, 885 (2004).

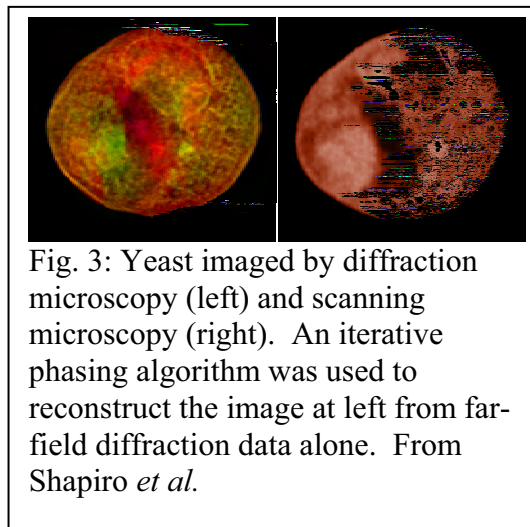
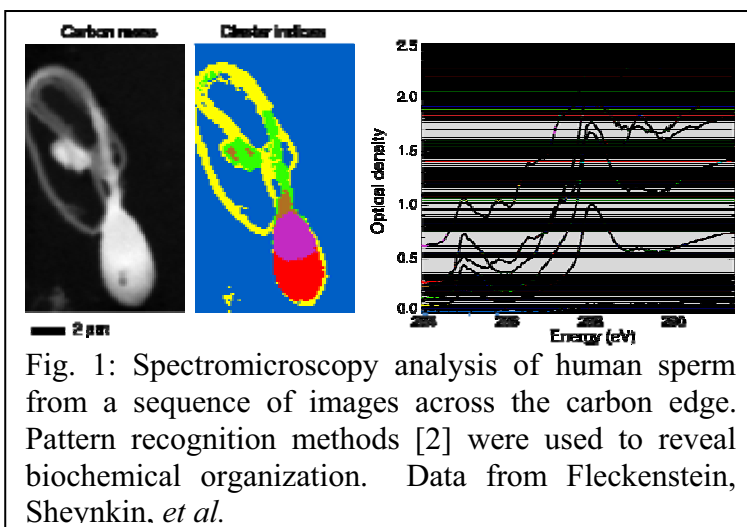
## X-ray microscopy: beyond 2D imaging

Chris Jacobsen<sup>a</sup>

<sup>a</sup>Department of Physics & Astronomy, Stony Brook University, Stony Brook, NY 11794-3800, USA

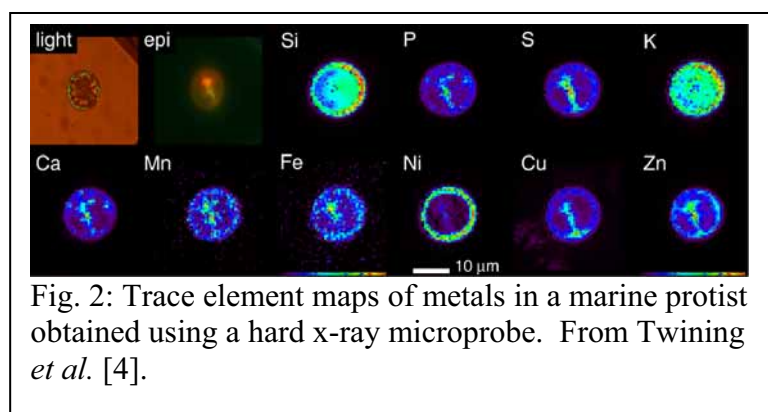
X-ray microscopes are providing new capabilities for a number of studies. Soft x-ray microscopes operating between the carbon (290 eV) and oxygen (540 eV) absorption edges are able to image wet or frozen hydrated specimens at 30 nm resolution or better on specimens several micrometers thick. Because soft x rays do not suffer multiple elastic or inelastic scattering, spectromicroscopy studies using near-edge absorption offer excellent chemical state sensitivity for studying polymers or biomaterials (Fig. 1). At higher energies, x-ray microprobes can be used to map elemental concentration with sensitivity better than a tenth of a part per million (Fig. 2). While impressive gains are being made in the development of high resolution x-ray optics, additional possibilities include the reconstruction of images from x-ray diffraction data with no optics-imposed resolution limits (Fig. 3).

These and other examples of present capabilities of x-ray microscopes will be presented, along with a perspective on future possibilities.



### References:

- [1] See *e.g.*, papers in *Journal de Physique IV* **104** (2003).
- [2] M. Lerotic *et al.*, *Ultramicroscopy* **100**, 35 (2004).
- [3] J. Miao *et al.*, *Nature* **400**, 342 (1999).
- [4] B. Twining *et al.*, *Anal. Chem.* **75**, 3806 (2003).



## **TwinMic: A European twin X-ray spectromicroscopy station**

Burkhard Kaulich

ELETTRA – Sincrotrone Trieste, Strada Statale 14, km 163.5 in Area Science Park, I-34012 Trieste-Basovizza, Italy

The potential for development of X-ray microscopy is part of the scientific case for the construction of third and higher generation synchrotron light sources. The unique capability of X-ray microscopes to explore heterogeneous phenomena has increasing impact in microcharacterization of solid and liquid matter. Two types of X-ray microscopes, scanning and full-field imaging with different imaging capabilities, are worldwide in operation or under construction.

A novel approach used in a RT&D project of the European Commission aimed at integrating both X-ray microscope types in a single, compact instrument. For the first time, a X-ray microscope is constructed by the united effort of European groups that have mastered in X-ray instrumentation, optics and detectors, nanotechnology, imaging and X-ray spectroscopy using different contrast mechanisms.

The expected potential and capability of such a twin microscope station is the combination of complementary microscope modes with versatile contrast techniques into a *single* instrument to perform: (i) X-ray imaging for morphological characterization combined with dynamical studies and tomography; (ii) spectromicroscopic analysis including elemental mapping and determination of specimen's chemistry on microscopic scale; and (iii) specimen characterization in their natural, solid or liquid environment.

Essential strength of the instrument is its wide working energy range from 250 - 3500 eV preserving the performance of individual microscopes. The photon energy range covers the water window between the C, N and O absorption edges and L-edges of Fe, Ni, Co with particular importance for characterization of magnetic materials. Access to K-absorption edges of elements opens up the opportunity for advanced studies in biology, medicine, pharmacology, geochemistry, environmental and earth sciences, and material research.

The TwinMic station is temporary hosted by the ELETTRA BACH beamline, where it past successfully first commissioning experiments.

References:

<http://www.elettra.trieste.it/twinmic>

## **Instrumental effects in atomic resolution neutron holography**

László Cser<sup>a</sup>, Márton Markó<sup>a,b</sup>, Ivan Sharkov<sup>c</sup>

<sup>a</sup> Neutron Spectroscopy Department, Research Institute for Solid State Physics and Optics, H-1122 29-33 Konkoy-Thege M. str Budapest Hungary

<sup>b</sup> Nuclear Technical Institute, Budapest University of Technology and Economics, H-1111 3-9 Műegyetem rkp. Budapest Hungary

<sup>c</sup> Physical Institute, St.Petersburg State University, 198904 1 Uljanovskaja str. St.Peterhof, St.Petersburg, Russia

Neutron holography is a direct method for imaging the local three-dimensional structure at atomic resolution level. We have investigated the effect of the instrumental resolution. It is analytically proven that the finite measurement domain in the scattering space causes broadening of the atomic spots in the reconstructed image, the wavelength distribution and detector resolution determine the size of the visible space around the source or the detector atom. As consequence of these effects the tales of images of farther atoms shifts the spots of the nearer atoms. This shift can be decreased by choosing a worse resolution but cannot be decreased by numerical convolution. Finally, to increase the accuracy of the measurement, model calculation should be made.

## STXM Investigations of Biological Tissues

Jörg Raabe <sup>a</sup>, Rainer Fink <sup>b</sup>, A.L.D. Kilcoyne <sup>c</sup>

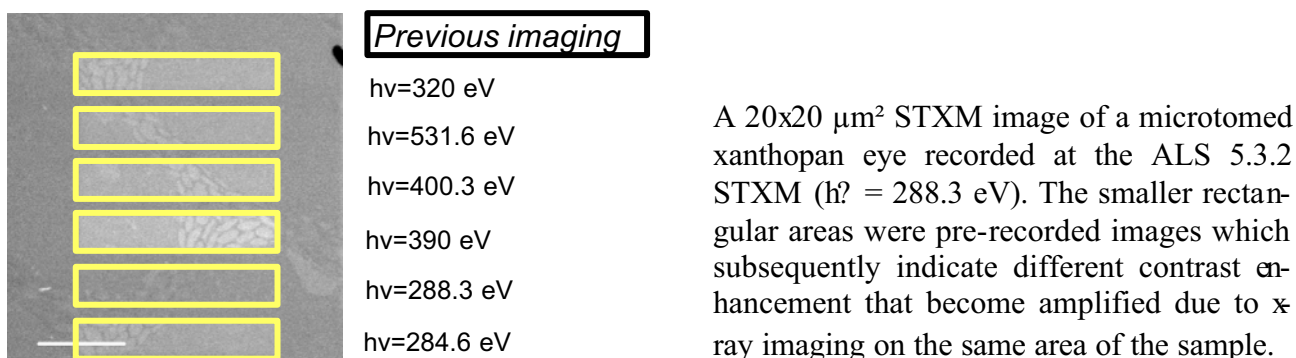
<sup>a</sup> Paul Scherrer Institut, WSLA/224, CH-5232 Villigen-PSI, Switzerland

<sup>b</sup> University Erlangen, Physikal. Chemie 2, Egerlandstrasse 3, 91058 Erlangen, Germany

<sup>c</sup> Adv. Light Source, 1 Cyclotron Rd., MS 7R0222, LBNL, Berkeley, CA 94720-8225, USA

In contrast to the conventional use of scanning transmission x-ray microscopy as an analysis tool for materials, especially extending to “soft materials”, we have investigated some biological tissues to ascertain an alternative and promising avenue of the application of zone-plate based scanning x-ray microspectroscopy.

We have investigated several biological samples taking advantage of the polymer STXM (BL5.3.2) at the Advanced Light Source. A set of experiments focused on the investigation of biological fibers, in particular the spectroscopic properties of spider webs. Preliminary energy dependent line scans across the fibres yielded no distinct dichroism mechanism and thus no direct evidence for a preferential orientation of the monomers. Another interesting biological area is the analysis of human hair. Although the lateral resolution in STXM (< 35 nm) is currently about an order of magnitude less than in transmission electron microscopy (TEM), the resolution achieved was sufficient in recognizing the internal structure and morphology of human hair. However, no specific spectral signatures were distinguished which would have allowed identification of distinct chemical species.



Radiation damage or in-situ chemical changes due to the high photon flux density are often a disadvantage in x-ray microscopy. However, in some cases it may be advantageous as we have demonstrated for insect eyes.

The talk will furthermore present the POLLUX STXM at the Swiss Light Source POLLUX Beamline, which is a further development of the ALS STXM. This instrument will open new experimental possibilities in zone-plate based microspectroscopy in various fields in the natural and material sciences or environmental science and will be open for external users in summer 2006.

This project is funded by the BMBF under contract 05 KS4WE1/6.

## **News Trends in Synchrotron Based Hard X-Ray Microscopy and Micro-Spectroscopy**

Jean Susini

European Synchrotron Radiation Facility, BP220, F-38043 Grenoble Cedex, France

The unique properties of X-rays make them a powerful probing radiation for use in microscopy techniques. For example, soft X-ray microscopes have established capabilities in absorption contrast imaging of thick hydrated biological material in near-native environments at spatial resolutions well beyond those achievable with visible light microscopy. In the past decade there has been a strong tendency in X-ray microscopy to develop alternative contrast mechanisms and spectroscopic methods, which can provide both valuable complementary information on the sample nature and/or reduce the necessary radiation doses. Simultaneously, the development of high brilliance high energy X-ray sources coupled with advances in manufacturing technologies of focusing optics has led to significant improvements in sub-micrometer probes for spectroscopy, diffraction and imaging applications in the multi-keV 'hard' X-ray range. Both by extrapolation of the experience gained in the soft X-ray regime and by the development of new techniques, 'hard' X-ray microscopes now offer a complementary analytical tool which can contribute to a wide range of existing and new applications of X-ray microscopy.

The main fields of applications are driven by the unique attributes of X-ray microscopy in the multi-keV energy range: i) access to K-absorption edges and fluorescence emission lines of medium-light elements and L,M - edges of heavy materials for micro-spectroscopy, chemical or trace element mapping; ii) higher penetration depths compared to soft X-rays allowing imaging of thicker samples; iii) favorable wavelengths for diffraction studies and iv) generally large focal lengths and depths of focus which are advantageous for the use of specific sample environments (in-situ, high pressure, controlled temperatures....). Typical experiments can be broadly divided into two categories: i) morphological studies which require high spatial resolution and are therefore well adapted to 2D or 3D transmission full-field microscopy. ii) studies dealing with co-localization and/or speciation of trace elements in heterogeneous matrices at the micron scale. Scanning X-ray microscopy, in transmission and/or fluorescence modes, tends to be better suited for the latter cases, which often require both low detection limits and spectroscopic analysis capabilities

This presentation will be biased towards sub-micron microscopy developed on the X-ray microscopy beamlines at the European Synchrotron Radiation Facility (Grenoble). Following a brief account on the characteristics of these instruments, strengths and weaknesses of X-ray microscopy and spectro-microscopy techniques in the 1-20keV range will be discussed and illustrated by examples of applications. The main technical developments, involving new focusing lenses, novel phase contrast geometry or 3D imaging, will be presented.

### 3D X-ray Microscopy with Submicron Resolution Using a Laboratory Source

A. Tkachuk, F. Duewer, S. Wang, M. Feser, H. Chang, A. Lyon, W. Yun

Xradia Inc., 5052 Commercial Circle, Concord, CA 94597, USA

X-ray microscopy has evolved into a powerful tool for material and biological research during the last decade [1]. Utilization of Fresnel zone plates as imaging optics opens up new avenues to explore the internal structures of the optically opaque solids with submicron resolution previously inaccessible by other analytical techniques. X-ray computed tomography (XCT) with Fresnel lenses offers powerful nondestructive 3D full field imaging technique, which was previously confined to synchrotron radiation centers. This is due to the need for a bright and intense source of x-rays, which severely limits the availability and accessibility of x-ray microscopes. Large scale studies using x-ray microscopy require laboratory based instruments that provide easy access and reliable operation.

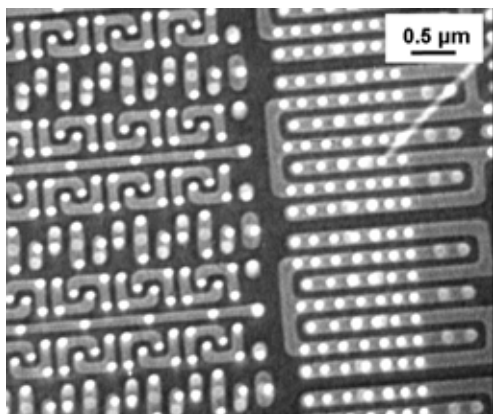


Fig.1 Transmission x-ray microscope image of a copper integrated circuit (IC).

We have developed an x-ray microscope system operating at 5.4 keV and 8 keV x-ray energies based on a commercially available laboratory x-ray source [2]. In-house fabrication of Fresnel zone plates with outermost zone widths as small as 35 nm enables us with spatial resolution better than 50 nm (see Fig. 1), with the promise of substantial improvements in the near future. Optimizing the laboratory source, the throughput of the imaging Fresnel zone plate and the efficiency of the detector, exposure times on the order of 10 min per 2D cross-section image are achieved in absorption and Zernike phase contrast [3] modes. The system is automated for data collection and computer reconstruction.

Applications and experimental results obtained with the XCT microscope in the fields of materials science and biology will be presented.

[1] X-ray Microscopy 2002 Conference Proceedings, J. Susini, D. Joyeux and F. Polack Editors, J. Phys. IV 104 (2003).

[2] S. Wang, F. Duewer, S. Kamath, C. Kelley, A. Lyon, K. Nill, D. Scott, D. Trapp, W. Yun, "A transmission x-ray microscope (TXM) for nondestructive 3D imaging of IC's at sub 100-nm Resolution", Proceedings of 28<sup>th</sup> ISTFA Conference, Phoenix, AZ (2002) 227-233.

[3] F. Zernike, Das Phasenkontrastverfahren bei der mikroskopischen Beobachtung, Z. tech. Phys., 36 (1935) 36.

## High Resolution 3-D Characterization of Nanomaterials using Single and Dual Axis Tilt Tomography

Ilke Arslan<sup>a</sup>, Timothy Yates<sup>a</sup>, Jenna Tong<sup>a</sup>, Nigel Browning<sup>b,c</sup>, and Paul Midgley<sup>a</sup>

<sup>a</sup>Department of Materials Science and Metallurgy, University of Cambridge, CB2 3QZ, Cambridge, UK.

<sup>b</sup>Department of Chemical Engineering and Materials Science, University of California, 95616, Davis, USA.

<sup>c</sup>National Center for Electron Microscopy, Lawrence Berkeley National Laboratory, 94720, Berkeley, USA.

Over recent years, nanotechnology has become a key component in the field of materials science. Rather than analyzing and determining the properties of bulk single or poly-crystals where the third dimension is assumed to be uniform, we must now analyze materials that have a finite size and shape in three dimensions, and not necessarily uniform in any of the directions. This new demand on materials characterization has led to the development of electron tomography for inorganic materials using Z-contrast imaging in the scanning transmission electron microscope (STEM).

This technique involves taking a series of images of the sample at different tilt angles, normally ranging between  $-70^\circ$  to  $+70^\circ$  every 1 to 2 degrees, and using these two dimensional images to reconstruct a three dimensional volume of the sample. This tilt range may increase depending on the sample geometry and the holder used. However, as we can never achieve the full  $\pm 90^\circ$  tilt range due to shadowing from the grid bars or the sample itself, an artefact is induced in the reconstruction from what is called “the missing wedge” of information. In order to minimize this effect, a second tilt series may be taken at  $90^\circ$  to the first tilt series such that the missing wedge is reduced. This is called dual axis tomography.

Here we present high resolution single and dual axis STEM tomography of quantum dots and tetrapods. The results from Sn quantum dots in a Si matrix illustrate the ability to identify the size, shape and distribution of embedded dots in a layer in three dimensions. Furthermore, we are able to identify how the quantum dots are actually formed by observing a dot that has formed outside of the embedded layer. These results indicate 1nm resolution in all three dimensions using single axis tomography.

Dual axis tomography is demonstrated for the first time in materials science using a newly developed holder from Fischione. CdTe tetrapod samples are analyzed using single and dual axis tomography. Tetrapods are the perfect test specimen for dual axis tomography as they have long thin arms in a tetrahedral geometry, meaning at least one of the arms may be pointing in the direction of the missing wedge during acquisition of the data, and hence missing from the reconstruction. A comparison of the single and dual axis reconstructions will be shown and implications for resolution will be discussed.

# Electron Microscopy Investigation of Superconducting MgB<sub>2</sub> Tapes and Wires

B.Birajdar<sup>a</sup>, W.Pachla<sup>b</sup>, A.Morawski<sup>b</sup>, G.Grasso<sup>c</sup>, W.Häßler<sup>d</sup>, O.Eibl<sup>a</sup>

<sup>a</sup> Institute of Applied Physics, University of Tübingen, D-72076 Tübingen, Germany

<sup>b</sup> High Pressure Research Center, Sokolowska 29/3701-142, Poland

<sup>c</sup> INFN LAMIA Corso Perrone 24, 16152 Genova, Italy

<sup>d</sup> IFW, Institute of Metallic materials, Helmholtzstrasse 20, D-01069 Dresden, Germany

MgB<sub>2</sub> has a T<sub>c</sub> of (~39 K), which is higher than that of NbTi (~9.5 K). Its critical current density (J<sub>c</sub>) and upper critical field (B<sub>c2</sub>) however need to be improved by optimising the microstructure. Grain boundaries in MgB<sub>2</sub> do not act as weak links. Microstructure of a number of MgB<sub>2</sub> tapes and wires subjected to different processing techniques namely hydrostatic extrusion, bi-axial rolling, and varying annealing temperature has been investigated using SEM, EPMA (electron probe microanalysis) and TEM, in the framework of the HIPERMAG project.

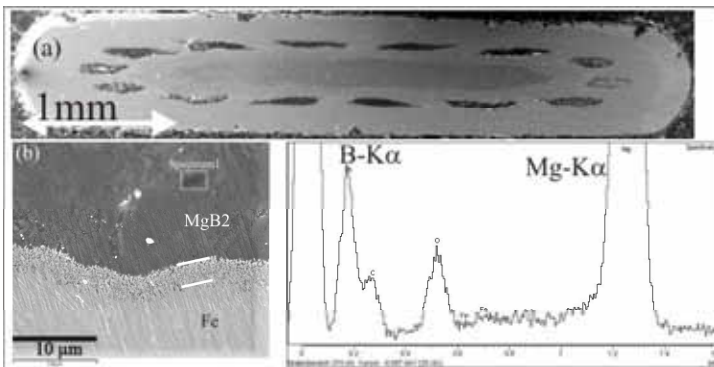


Fig. 1: SEM secondary electron image showing cross-section of a multifilamentary tape (a) and MgB<sub>2</sub>-sheath interface in a monofilamentary tape (b). SEM-EDX spectrum of MgB<sub>2</sub> core (c).

SEM and EPMA are used to analyse the secondary phases of higher boride compounds, SiC and diamond additives and the MgB<sub>2</sub>-sheath interfaces. Fig.1 shows a secondary electron image of a multi-filamentary tape (a), and of the MgB<sub>2</sub>-sheath interface of a monofilamentary tape (b). SEM-EDX enables qualitative chemical analysis of the MgB<sub>2</sub> tapes (Fig. 1(c)). The most reliable quantitative boron analysis is available by EPMA [1].

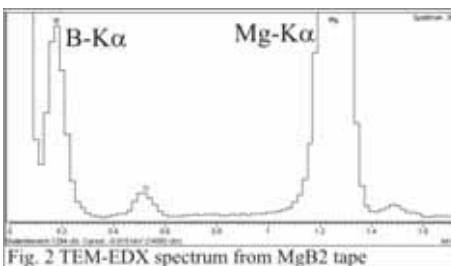


Fig. 2 TEM-EDX spectrum from MgB<sub>2</sub> tape

Chemical analysis of MgB<sub>2</sub> and higher borides can be performed in the TEM by EELS but also by quantitative EDX analysis. Fig. 2 Shows an EDX spectrum of MgB<sub>2</sub> tape acquired with TEM with a large B-peak yielding an excellent signal-to-background ratio. Quantitative analysis of B requires absorption correction by parameter less methods [2]. Defects on the nanometer scale are imaged by diffraction contrast under two-beam conditions in bright and dark-field images. Dislocations, grain boundaries, MgO precipitates, SiC and diamond nano-inclusions in the MgB<sub>2</sub> tapes and wires have been analysed using a LEO 912 TEM equipped with an EDX detector and an Omega energy spectrometer. The size of these defects is comparable to the superconducting coherence length of MgB<sub>2</sub> (~5 nm) and these can pin the magnetic vortices effectively

## References:

1. Wenzel T, Nickel K G, Glaser J, Meyer H-J, Eyidi D, Eibl O *phy. stat. sol. (a)* **198** (2003) 374
2. Eibl O, *Ultramicroscopy* 50 (1993) 179

# Quantitative analysis of TEM (200) DF images : determination of the local Indium composition in InGaAs/GaAs quantum heterostructures.

J. Cagnon<sup>a</sup>, P.A. Buffat<sup>a</sup>, P.A. Stadelmann<sup>a</sup> and K. Leifer<sup>b</sup>

<sup>a</sup>Interdisciplinary Centre for Electron Microscopy - CIME, EPFL, CH-1015 Lausanne, Switzerland

<sup>b</sup>Institute of Electron Microscopy and Nano-Engineering, Ångström Laboratory, SE-751 21 Uppsala, Sweden

In this work, we have analyzed quantitatively the contrasts evolution in (200) dark-field images of strained InGaAs/GaAs planar quantum wells. Therefore we have optimized sample preparation, the observation techniques and the parameters influencing the (200) dark-field image intensities. By the exploration of the parameter space permitted we determined the possibilities and limits of the quantitative analysis of chemical composition from (200) dark-field images. To understand the observed contrasts quantitatively, we developed a simulation tool based on the finite element calculations of the 3D strain fields and their integration in a dynamical contrast calculation. These simulations were compared with the experimental observations. Based on these results, we developed a method for the quantitative analysis of the chemical composition of  $\text{In}_x\text{Ga}_{1-x}\text{As}/\text{GaAs}$  heterostructures [1]. This method relies on the determination of calibration curves of chemical and strain contrasts. The obtained precision is better than  $\Delta x = 0.015$  in an Indium concentration range of  $0.0 < x < 0.35$  and a spatial resolution of about one nanometre.

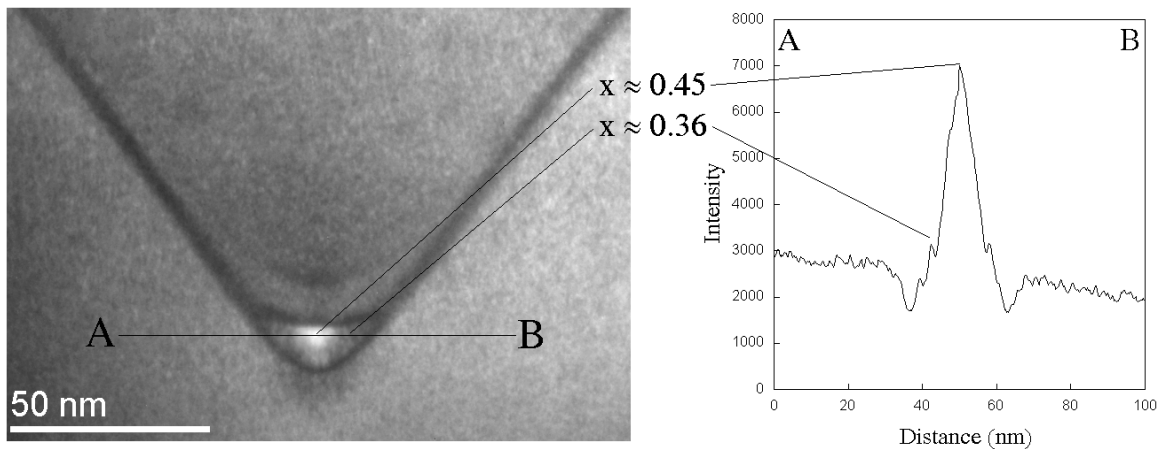


Fig. 1: (200) dark-field image of an  $\text{In}_{0.35}\text{Ga}_{0.65}\text{As}$  – 5nm V-groove heterostructure and corresponding intensity profile showing nanometric fluctuations of indium composition in the quantum wire.

This method was also extended to the characterization of non-planar nanostructures which can not be tilted to the two beam conditions without loss of spatial resolution due to the projection of interfaces. We determined the experimental conditions allowing chemical mapping of indium in these heterostructures (Fig. 1). Our results were confirmed by simulations.

## References:

[1] J. Cagnon, P.A. Buffat, P.A. Stadelmann, K. Leifer, *Microscopy of Semiconducting Materials*, Proceedings of the Royal Microscopical Society Conference. IOP Publishing, Bristol, UK, (2003), 203-206.

## Optimization of the positions and the width of energy windows for the recording of EFTEM elemental maps

Benedikt Gralla, Andreas Thesing and Helmut Kohl

Physikalisches Institut und Interdisziplinäres Centrum für Elektronenmikroskopie, Westfälische Wilhelms-Universität Münster, Wilhelm-Klemm-Str. 10, 48149 Münster, Germany

Due to the small cross-sections for inner-shell excitations, the detection limit in elemental maps is determined by the signal-to-noise ratio (SNR). Therefore it is vital to choose the instrumental parameters as to optimize the SNR. Following earlier work by Kothleitner [1] and Berger [2], we have investigated the influence of the positions and the widths of energy loss windows for recording elemental maps. In order to be able to easily obtain reliable data for arbitrary energy loss windows, we acquired electron energy loss spectra (EEL spectra) with an energy dispersion of about 0.5 eV/channel and determined the intensity values for energy loss windows of larger widths by summing the spectral data over the corresponding energy losses. In particular we are using four windows: three below and one above the characteristic energy loss.

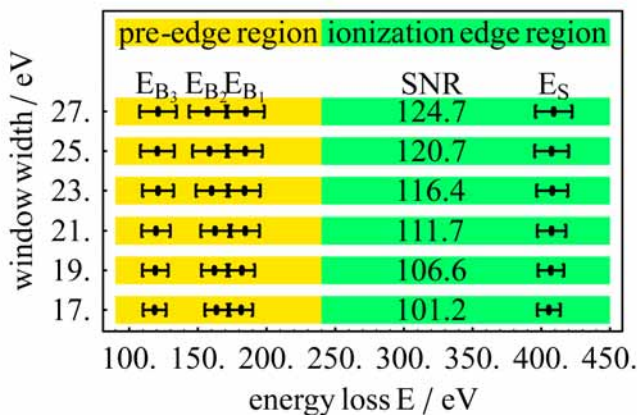


**Fig. 1:** Results for the optimal positions in order to get the optimal SNR of molybdenum.

we obtained an improvement of the SNR of 37 % using the optimized energy loss window positions and an energy slit width of 21 eV.

We compared these results for the improvement of the SNR with those obtained from experimental elemental maps. Each pixel of this image series can be considered to be part of an EEL spectrum of the corresponding part of the specimen. Every image series contains three inelastically filtered images with energy losses below the ionization edge and one energy filtered image with an energy loss above the characteristic energy loss of the element of interest. The use of the optimized parameters led to an experimental improvement of the SNR of 36 % in the case of Mo.

References:

- [1] G. Kothleitner and F. Hofer, *Micron* **29** (1998) 349-357
- [2] A. Berger and H. Kohl, *Optik* **92** (1993) 175-193

## Orientation-dependent EELS of TiO<sub>2</sub>: a comparison of theory and experiment

Christian Heiliger<sup>a,b</sup>, Frank Heyroth<sup>b</sup>, Hartmut S. Leipner<sup>b</sup>, Frank Syrowatka<sup>b</sup>, Igor Maznichenko<sup>c,a</sup>  
Wolfram Hergert<sup>a</sup>, and Ingrid Mertig<sup>a</sup>

<sup>a</sup> Department of Physics, Martin-Luther University, D-06099 Halle, Germany

<sup>b</sup> Interdisciplinary Center of Materials Science, Martin-Luther University, D-06099 Halle, Germany

<sup>c</sup> Theoretical Department of Inst. of Physics, Rostov State Univ., 344090 Rostov-on-Don, Russia

Highly resolved electron energy loss spectra are widely used for fingerprint chemical analysis. For this purpose, reference spectra are averaged over all crystallographic orientations. Based on that, the aim of the presented investigations is the determination of the orientation dependence of the spectra and the theoretical analysis of this influence. For it we present a comparison of calculated and measured orientation-dependent core loss EEL spectra of the three modifications of TiO<sub>2</sub> rutile, anatase, and brookite having slightly different bonding conditions. The measurements of the O-*K* and Ti-*L* edges were carried out in the HB501 UX scanning transmission microscope equipped with the Gatan Enfina parallel EELS detector with an energy resolution of about 0.45 eV. Different excitation conditions were chosen for the collection of EEL spectra using the imaging and diffraction mode of the microscope. The orientation dependence was clearly visible in the O-*K* edge.

The calculations are based on density functional theory [1]. Spin-orbit coupling is included in the theoretical description of the core levels to distinguish the *L*<sub>2</sub> and *L*<sub>3</sub> edges. Many body corrections for the core hole effect are included by a *Z* + *x* approximation. A very good agreement with the calculated spectra was achieved in the peak positions by considering the oxygen core hole within a *Z* + 1, and the titanium core hole within a *Z* + 2 approximation. The relative intensities were not reproduced (Fig. 1). To compare the conventional core hole approximation with our *Z* + *x* approach, atomic calculations of the scattering phase were performed for both cases. As a result, titanium with the core hole and chromium without core hole leads to nearly the same d-resonance energy, which was taken as a confirmation of our *Z* + *x* approximation.

References:

[1] P. Rez, J. Bruley, P. Brohan, M. Payne, and L. A. J. Garvie, *Ultramicroscopy* **59**, (1995) 159.

[2] The authors gratefully acknowledge the collaboration of Kalevi Kokko (Univ. of Turku, Finl.).

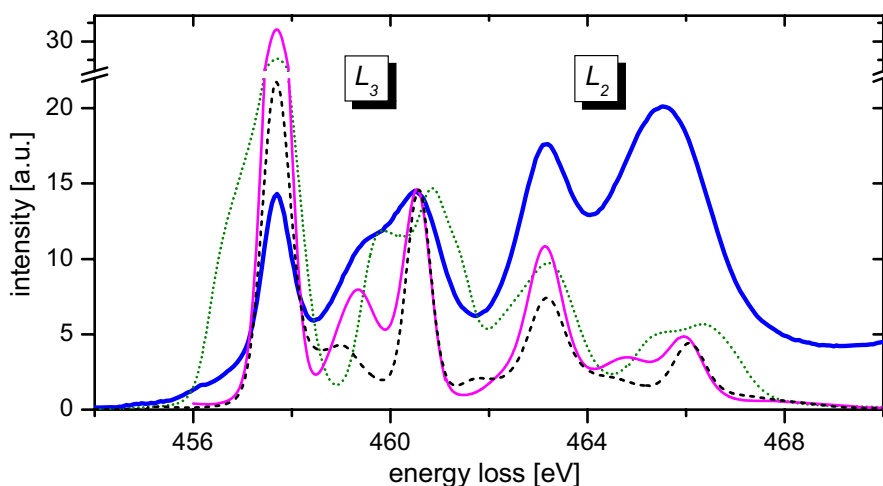


**Fig. 1:** Calculations of the titanium *L*-edges of rutile without consideration of the core hole (dotted green line), using a *Z* + 1 approximation (dashed black line) and using a *Z* + 2 approximation (thin solid magenta line) in comparison to experimental data (thick solid blue line). The sample surface is oriented in [100].

# TEM Investigations of Lattice Site Occupancy of Phosphorous doped 4H-SiC

Th. Kups<sup>a</sup>, A. Chuvilin<sup>b</sup> and U. Kaiser<sup>b</sup>

<sup>a</sup> Department of Material Engineering, Center for Micro and Nanotechnologies, Technical University Ilmenau, 98693 Ilmenau, Germany

<sup>b</sup> Materials Science Electron Microscopy, University of Ulm, 89069 Ulm, Germany

High power electronic devices based on SiC require a high concentration of dopants. This can be achieved preferentially by ion implantation because of the small diffusion coefficients of dopants in SiC. After implantation, a thermal post-implantation annealing process is necessary to electrically activate the implanted dopants and to reduce the lattice damage. High temperature annealing (>1600°C) reduces implantation-induced defects, however in the case of high foreign atom concentration, the SiC matrix remains defective always [1]. The site occupancy of highly p- and n doped SiC is one important question, which is not fully understood yet.

We addressed this question to phosphorous doped SiC by using the channelling technique ALCHEMI (atomic location by channelling enhanced microanalysis) and by using Convergent Beam Electron Diffraction (CBED). By means of ALCHEMI, the site occupancy of atoms within a matrix lattice can be distinguished ([2], [3]) by the different x-ray excitation when tilting the electron beam (or the specimen) around a pre-defined zone axis. In the zone used the excitation of Bloch states is very different for the possible site occupancy (Si-, C- or interstitial position) of dopants. Different site occupancies create different strains on the matrix lattice. Lattice parameter changes can be determined very precisely using CBED when evaluating the positions of higher order Laue zone (HOLZ) lines [4].

P implanted 4H-SiC (concentrations:  $1 \cdot 10^{19} \text{ cm}^{-3}$  and  $5 \cdot 10^{19} \text{ cm}^{-3}$ , energy: 160keV, annealed 2min@1600°C at 160mbar Ar atmosphere) has been investigated using a TEM TECNAI S20 operating at 200kV. EDX analysis was made on [01-10] zone axis incidence for tilts of  $\pm 1/2g$  to  $\pm 5/2g$  with  $g=0004$ . The CBED pattern were obtained at [120 80 1] zone axis incidence in the region of the maximum of dopant concentration.

ALCHEMI results show the tendency that phosphorous is located preferentially on interstitial sites for both dopant concentrations.

The high indexed line (2 -1 -20) of the [120 80 1]-4H-SiC zone axis incidence is very sensitive to lattice parameter changes in c-axis direction. The CBED patterns obtained from the strained region of maximal dopant concentration show a line splitting of the weak line (2 -1 -20). To reproduce this line splitting by calculation, we used our newly developed multislice program [5]. A bent model based on [6] was built with lattice bending perpendicular to the beam direction between 0.01nm and 0.06 nm. The simulated line splitting reproduces the observed experimental rather well.

## References:

- [1] U. Kaiser et al. Nature Materials 1 (2002), 102,
- [2] J.C.H. Spence, J. Taftø, J. of Microscopy 130 (1983) 147
- [3] U. Kaiser, J. Electron Microscopy 50 (2001) 251,
- [4] A. Chuvilin, Th. Kups, U. Kaiser J. Electron Microscopy 53 (3), (2004) 237
- [5] A. Chuvilin and U. Kaiser Ultramicroscopy 104 (1) (2005) 73
- [6] L. Clément, R. Pantel, L.F. Tz. Kwakman, J.L. Rouvière, J. Appl. Lett 85(4), (2004), 651

Acknowledgements: This work has been supported by the DFG KA 1295/2-3

## Quantitative EDX analysis of $\text{Bi}_2\text{Te}_3$ in the TEM

N. Peranio<sup>a</sup> and O. Eibl<sup>a</sup>

<sup>a</sup> Institut für Angewandte Physik, Universität Tübingen, Auf der Morgenstelle 10, D-72076 Tübingen, Germany

The chemical composition of n-type  $\text{Bi}_2(\text{Te},\text{Se})_3$  Peltier devices was investigated by energy-dispersive X-ray spectroscopy (EDX) in a Zeiss 912 $\Omega$  TEM equipped with an Omega filter. The advantage of EDX analysis in a transmission electron microscope (TEM) is the higher lateral resolution of about 50 nm compared to a resolution of 1 $\mu\text{m}$  by wavelength-dispersive X-ray spectroscopy (WDX) in an electron probe microanalysis (EPMA). Preliminary results yielded artifacts due to Bi fluorescence radiation and hole counts significantly beyond zero. Hole count measurements and measurements in non-electron transparent specimen regions yielded stray electrons. Therefore, we inserted a stray aperture in the TEM to absorb the stray radiation which yields a high-precision quantitative chemical analysis. With this aperture inserted we obtained local mole fraction ratios of  $40.1 \pm 1.1$  at% for Bi. The hole counts decreased by a factor of 5 and the scatter of the data decreased by a factor of 4. Also, our investigations showed a slightly changing stoichiometry on the micrometer scale and thus confirmed the inhomogeneous chemical composition found by WDX [1]. The mole fraction ratios of Se and Te vary by 1.5-2 at%. Variations of stoichiometry are smaller on the sub-micrometer level and increases with increasing length scale.

References:

[1] Eyidi D. et. al., Phys. Stat. Sol. (a), Vol.187, No.2 (2001), pp. 585-600

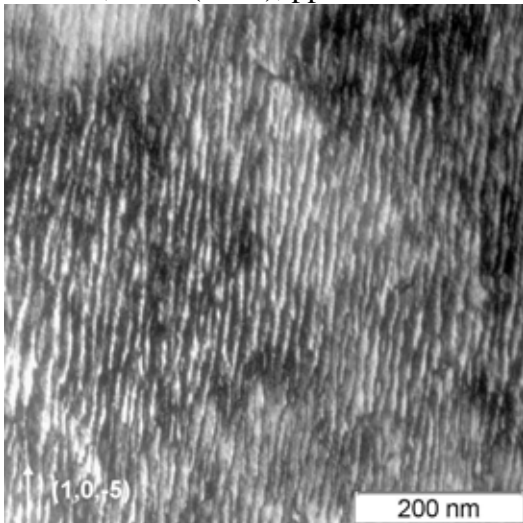


**Fig. 1:** TEM (1,0,-5) dark field image of the structural modulation in  $\text{Bi}_2(\text{Te},\text{Se})_3$  with a wave length 10 nm. Several EDX spectra were acquired within such an area of  $1\mu\text{m}^2$  to verify the homogeneity on the sub-micrometer scale.

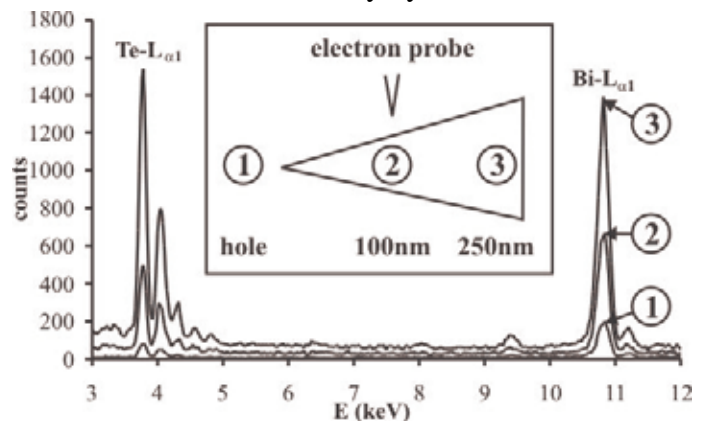


**Fig. 2:** EDX spectra of a n-type  $\text{Bi}_2\text{Te}_3$  sample. Stray electrons are responsible for the hole counts .

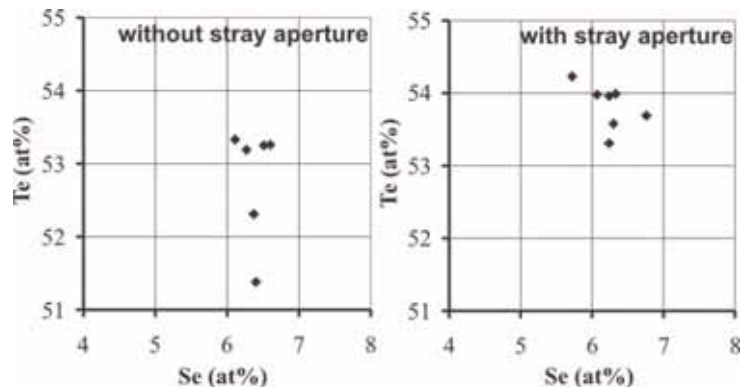


**Fig. 3:** Te-Se correlation diagrams obtained in n-type  $\text{Bi}_2(\text{Te},\text{Se})_3$  within an area of  $1\mu\text{m}^2$ . The scatter of data is reduced by a factor of 4 with inserted stray aperture.

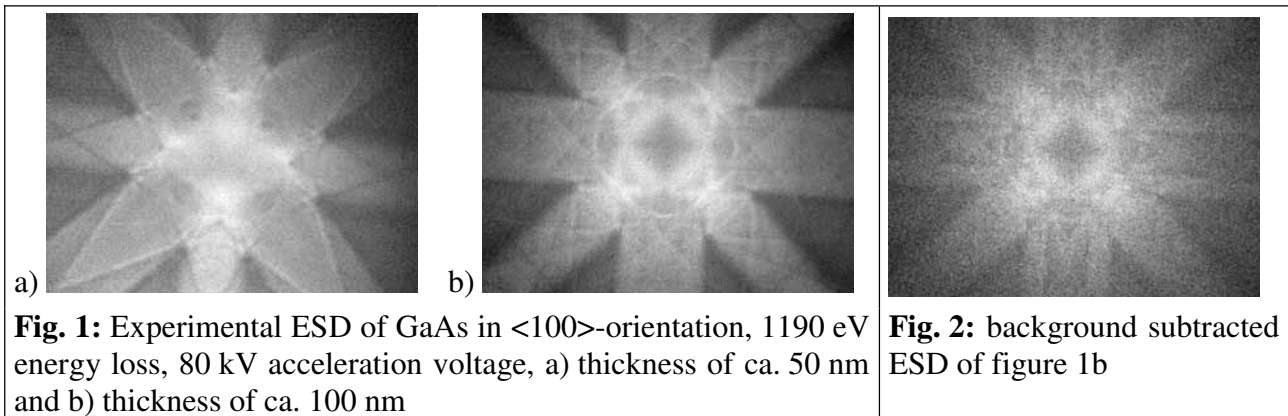
# Energy-Selected Electron Diffraction Patterns of GaAs

Claudia Prietzel and Helmut Kohl

Physikalisches Institut und Interdisziplinäres Centrum für Elektronenmikroskopie (ICEM),  
Westfälische Wilhelms-Universität Münster, 48149 Münster, Germany

Energy-selected diffraction patterns (ESD) contain site-specific information about the specimen and about the distribution of elements within the unit cell. For an interpretation of these patterns it is necessary to compare the experiment with corresponding simulated inelastically filtered diffraction patterns. For the experiments we used TEM's with integrated energy filters and acceleration voltages of 80 kV and 200 kV. The simulation of ESD is based on the Bloch wave method [1,2].

In this work we present studies of a GaAs single crystal in the  $\langle 100 \rangle$ -zone axis orientation. In this orientation the diffraction patterns have a four-fold symmetry with mirror planes. So it is sufficient to calculate a  $45^\circ$ -triangle and reconstruct the other parts of the ESD by reflection and rotation. Many parameters (crystal thickness, orientation, acceleration voltage and energy loss) are predetermined by the experiment and influence the diffraction patterns.



In figure 1 two experimental results are shown for an acceleration voltage of 80 kV. The diffraction patterns show strong dependence on crystal thickness. Therefore it is necessary to use parallel sided samples and to determine the thickness exactly. Increasing the thickness from 50 nm to 100 nm the ESD structures are becoming sharper. So the optimal thickness is about 100 nm for an acceleration voltage of 80 kV. However, for thick specimens the exposure time is high and contamination influences the ESD. To compare the experiment with the simulation, we use the 3-window method for background subtraction [3]. Figure 2 shows the background subtracted Ga signal at 1190 eV for a thickness of ca. 100 nm. In the next step we have to calculate the diffraction pattern for GaAs, considering the experimental parameters, and compare it with the experiment.

## References:

- [1] Weickenmeier A., PhD Thesis, Technische Hochschule Darmstadt, D17 (1991).
- [2] Weickenmeier A., Kohl H., Phil. Mag. B60 (1989) 467.
- [3] Overbeck N., PhD Thesis, Westfälische Wilhelms Universität Münster, (1999).

## Applications of Energy Loss Near-Edge Structures

Gianluigi A. Botton<sup>a,b</sup>, Guillaume Radtke<sup>a</sup>, and Sorin Lazar<sup>b</sup>

<sup>a</sup>Brockhouse Institute for Materials Research, McMaster University, Hamilton, L8S 4M1 Canada

<sup>b</sup>Kavli Institute of Nanoscience, Delft University of Technology, Delft, The Netherlands.

The technique of electron energy loss spectroscopy (EELS) in the transmission electron microscope makes it possible to probe the chemical environment of atoms in a solid with a spatial resolution below 1nm. Arguably, the most powerful features in EELS spectra are the near-edge structures. These provide information on the chemical environment of the probed atoms and the local electronic structure. The capability of probing the chemical environment details at very high spatial resolution combined with energy dispersive microanalysis, make it possible to provide direct information on properties of materials. With the advent of monochromators available in commercial transmission electron microscopes [1,2] the improvements in energy resolution for near-edge structure analysis, now approaching the capabilities of dedicated X-ray absorption beam lines in synchrotrons, are providing additional information to be used to gain insight into a range of properties of solids, including excitation effects, magnetism and interactions at interfaces.

In this presentation we will discuss the approaches to obtain improvements in energy resolution (hardware and software), the limitations of the technique, the use of detailed spectroscopic modeling techniques to retrieve information on the electronic structure and properties of materials. Examples related to the study of different types of metal-insulator transitions [3] and magnetism are presented. We will also discuss the limits of EELS for the study of very low energy loss spectroscopy to retrieve information on the bandgap of materials. We will present systematic studies related to bandgap measurements and the required conditions to obtain data for a range of materials. Examples related to the characterization of materials at high spatial resolution as well as studies of the anisotropy of materials [4] will be presented [5].

### References:

[1] Mitterbauer *et al.* *Ultramicroscopy* **96** (2003) 469.

[2] Lazar *et al.*, *Ultramicroscopy* **96** (2003) 535.

[3] Safa-Sefat A. *et al.*, *J. Solid State Chemistry* (2005),

[4] Botton GA, *J. Electron Spectroscopy and Rel. Phen.*, **143**, (2005), 129,

[5] We are grateful to the NWO (The Netherlands) and NSERC (Canada) for supporting this research.

## Energy Resolution and Spatial Resolution on a monochromated (S)TEM

W. Rechberger, G. Kothleitner and F. Hofer

Institute for Electron Microscopy, Graz University of Technology, Steyrergasse 17, A-8010 Graz, Austria

The energy resolution in Electron energy-loss spectroscopy (EELS) is largely limited by the stability of the high voltage supply, by the resolution of the spectrometer and by the energy spread of the source. To overcome this limitation a Wien filter monochromator was recently introduced with commercially available transmission electron microscopes (TEM) [1], offering the advantage to better resolve EELS fine structures, which contain valuable bonding information. The method of Z-contrast imaging within an (S)TEM, utilizing a high-angle annular dark-field (HAADF) detector can perfectly complement the better energy resolution, since both can be collected simultaneously. In combination with a monochromator microscope not only high spatial resolution images can be recorded but also high energy resolution EELS spectra are attainable.

In this work we investigated the STEM performance of a 200 kV monochromated Tecnai F20 with a high resolution Gatan Imaging Filter (HR-GIF). As a test sample, we have chosen an ODS-niobium alloy [2] with embedded  $\text{TiO}_x$  precipitates. The spherical titanium-oxide particles offer large enough Z difference to the matrix and have diameters ranging from 2 to 10nm, hence are well suited to test the spatial resolution. In unfiltered STEM (monochromator off, no dispersion of the beam, 0,55 eV energy resolution) the microscope is in nanoprobe-mode and the probe diameter can be as small as 0,2 nm which allows atomic resolution imaging. In filtered STEM, however, (monochromator on, dispersion of the beam, 0,25 eV energy resolution) the probe size is enlarged to approximately 2 nm as there is not enough demagnification of the source. Titanium-oxides are known to display a variety of different EELS fine structures, which can only be adequately resolved in monochromated EEL-spectra as shown in [3] and therefore are suitable candidates for challenging the monochromator also in terms of energy resolution.

### References:

- [1] P.C. Tiemeijer, *Ultramicroscopy* **78** (1999), p. 53.
- [2] F. Hofer, P. Warbichler, W. Grogger, *Ultramicroscopy* **59** (1995), p. 15.
- [3] C. Mitterbauer, PhD Thesis (2003), TU-Graz, Austria
- [4] The author would like to thank the “Steirischer Zukunftsfonds”

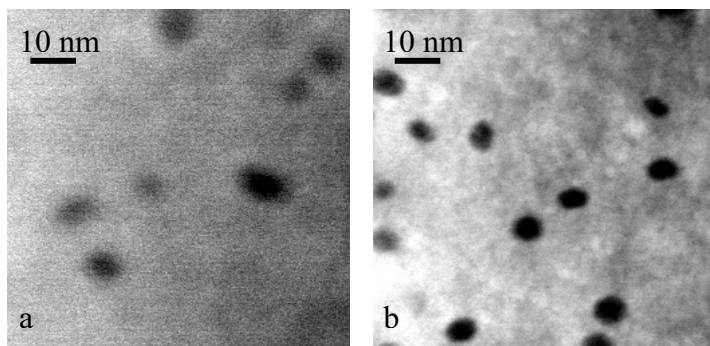


**Fig. 1:** HAADF images generated with a **a.)** monochromated and a **b.)** conventional STEM probe of  $\text{TiO}_x$  particles (dark spots) in Nb (bright matrix)

## The CHIRALTEM Project: XMCD without a Synchrotron

S. Rubino<sup>a</sup>, P. Schattschneider<sup>a</sup>, E. Carlino<sup>b</sup>, G. Rossi<sup>b</sup>, M. Fabrizioli<sup>b</sup>, F. Macherozzi<sup>b</sup>

<sup>a</sup>Institute for Solid State Physics, Vienna University of Technology, A-1040 Vienna, Austria

<sup>b</sup>TASC-INFN National Laboratory, 34012 Trieste, Italy

X-rays Magnetic Circular Dichroism (XMCD) is the circular polarization dependence of the X-Rays absorption spectra (XANES) when the sample is magnetized. Whereas the similarities between XANES and energy loss near edge structures (ELNES) in the Transmission Electron Microscope (TEM) succeeded to export Linear Dichroism to the TEM, a similar task for Circular Dichroism was considered impossible with present technology. A recent discovery [1] shows that this is not true.

A 10 nm thick layer of Iron was deposited on a GaAs (001) disk previously thinned to electron transparency. Measurements of transverse and longitudinal Magneto Optic Kerr Effect showed evidence of residual in-plane magnetisation. XMCD measurements have been performed by aligning

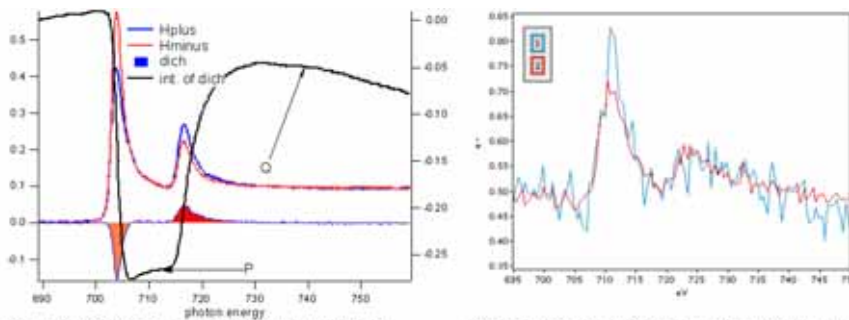


Fig 1.: XMCD detected as difference in the peak intensities of Fe  $L_{2,3}$  edge (shaded areas).

Fig 2.: EMCD as difference in normalised EEL spectra of Fe  $L_{2,3}$  edge under different excitations.

the residual magnetisation of the sample and the photon spin parallel and antiparallel. The dichroic signal is obtained by scanning in energy over the Fe  $L_{2,3}$  edges and either by reversing the circular polarisation handedness from the undulator radiation source, or by rotating the sample of  $180^\circ$ ,

i.e reversing the magnetization vector in the experimental geometry. XMCD signal with typically 33% asymmetry at the  $L_3$  edge were obtained on several samples and locations on each sample. The lateral resolution of the XMCD measurements was  $50 \mu\text{m}$  (fig. 1).

To measure the Energy-loss Magnetic Chiral Dichroism (EMCD) in the TEM, an interferometric technique, already tested for Ni [2], is used: the polarisation vector  $e$  of light corresponds to the momentum transfer  $q$  of the electron to the target. The crystal itself serves as a beam splitter and dephaser, to obtain an excitation corresponding to left- or right-handed circularly polarised light. This can be achieved by choosing two particular electron energy loss spectrometer detector positions in the diffraction plane (fig. 2). EMCD and XMCD have been detected on the same Fe sample. This not only proves the EMCD effect for a material other than Ni, but also establishes the first direct comparison with the X-rays technique. However, the interferometric technique presents several limitations and some merits that will be discussed.

### References:

- [1] C. Hébert, P. Schattschneider: *Ultramicroscopy* **96** (2003) 463-468.
- [2] S. Rubino, P. Schattschneider, C. Hébert: *Tem experiment on Circular Dichroism in Ni*, 13. European Microscopy Congress (EMC2004), 22. - 27. 8. 2004, Antwerp.
- [3] Work supported by the European Commission, FP6-2003-NEST-A / contract # 508971.

# High Energy Resolution Spectrum Imaging by EFTEM: Advanced Methods

B. Schaffer, W. Grogger, G. Kothleitner

Research Institute for Electron Microscopy, Graz University of Technology, Steyrergasse 17, A-8010 Graz, Austria

Spectrum imaging in an energy-filtering transmission electron microscope (EFTEM SI) is a method of collecting an almost complete data set in both the spatial and the electron energy-loss (EEL) dimension by combining a series of closely spaced EFTEM images on energy-loss axis [1]. In this work we show that modern imaging filters, which are higher order aberration corrected, allow energy resolutions less than 1 eV to be achieved if ultra small energy selecting slit widths down to 0.1 eV are used. An adaptive acquisition routine becomes necessary to compensate for strongly varying intensity conditions to achieve reasonable total acquisition times at an optimal signal-to-noise ratio (SNR). Approaching resolution limits in both the spatial and the energy-loss dimension makes more sophisticated data correction necessary as the remaining spectral aberration of the filter (non-isochromaticity) becomes more influential. We will present a new improved spatial drift correction scheme [2] and demonstrate that a full data correction concerning non-isochromaticity (Fig.1A) and energy drift (Fig.1B) can be performed. It will be shown that the correction has to be performed simultaneously with the spatial drift correction [3]. The improved energy resolution of the EFTEM SI increases contrast in ratio images of energetically closely spaced spectral features (FIG.1C). More importantly, the full spectral information in good energy resolution allows methods previously developed for EELS analysis now to be applied also to mapping spectral features over a larger field-of-view at good spatial resolution.[4]

## References:

- [1] J.L. Lavergne et al., *Microsc. Microanal. Microstruct.* 3 (1992) 517.
- [2] B. Schaffer et al., *Ultramicroscopy* 102 (2004) 27.
- [3] B. Schaffer et al., *Ultramicroscopy* (in press).
- [4] Thanks to Dr. A. Trampert (Paul Drude Institute Berlin, Germany) for providing the sample and to the SFB „Electroactive Materials”, Austrian Science Fund, Vienna for financial support.

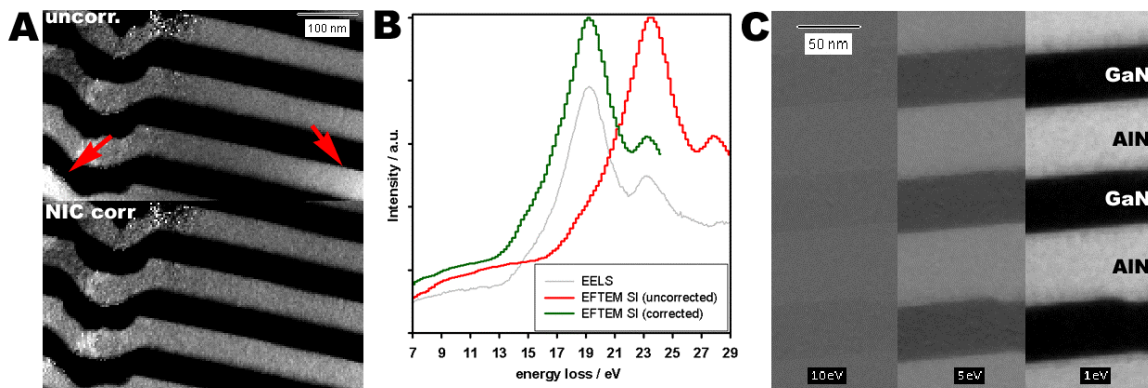


Fig.1: A: Plasmon ratio images of a GaN/AlN multilayer before (top) and after (bottom) non-isochromaticity correction. B: Extracted EELS spectra from the EFTEM SI before and after energy drift correction compared to a STEM EELS spectrum; C: Contrast enhancement in plasmon ratio images due to a smaller slit. Data was acquired with a 10 eV, 5 eV and 1 eV slit, respectively.

## Chiral dichroism in EELS: a New Analytical Tool

P. Schattschneider<sup>a</sup>, S. Rubino<sup>a</sup>, C. Hébert<sup>a</sup>, P. Formanek<sup>b</sup>, H. Lichte<sup>b</sup>, C. Hurm<sup>c</sup>, J. Zweck<sup>c</sup>

<sup>a</sup> Institute for Solid State Physics, Vienna University of Technology, A-1040 Wien, Austria

<sup>b</sup> Institute of Structure Physics, Dresden University, D-01062 Dresden, Germany

<sup>c</sup> Institute for Magnetism and Magneto-electronics, University of Regensburg, D-93040 Regensburg, Germany

The theoretical possibility to detect chiral transitions with EELS [1] was recently demonstrated in an experiment [2]. This makes ELNES in the TEM a strong competitor of the synchrotron for X-ray Magnetic Circular Dichroism (XMCD) studies. In analogy to XMCD we introduce the term EMCD: Energy loss Magnetic *Chiral* Dichroism. We choose the adjective *chiral* instead of *circular* in order to stress that there is no (circular) polarization of the probe electron involved. Rather, it is the chirality of the allowed transitions that is detected in the experiment when the scattering geometry is chosen properly.

In the experiment, a coherent superposition of two momentum transfer vectors perpendicular to each other is set up, tuning the phase difference between the two interactions to  $\tilde{\Gamma}_1$  as sketched in fig. 1.

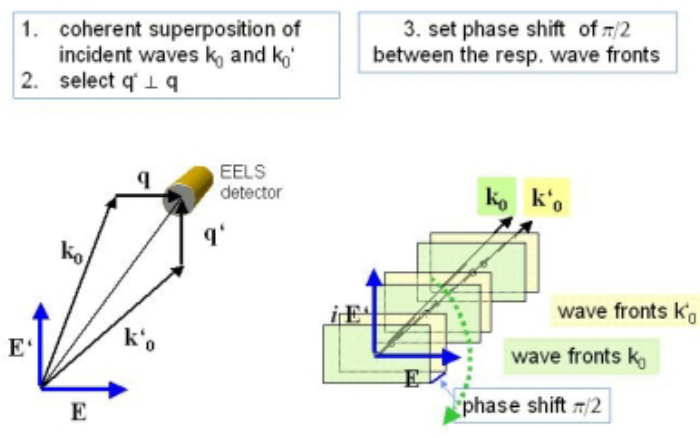


Fig. 1: Chiral dichroic conditions for electrons are set up in 3 steps: 1. creation of a coherent superposition of two plane waves on the specimen; 2. positioning of the EELS detector in the diffraction plane such that  $q \perp q'$  and  $q = q'$ ; 3. setting the phase shift between the two incident electron waves to  $\tilde{\Gamma}_1$ . Since  $q \perp E$  (the electric field) this corresponds to a circularly polarised photon with positive helicity.

The inelastic interference term carries the dichroic signature. The proper tool for description of inelastic interference, and as such also for EMCD is the mixed dynamic form factor (MDFF). More precisely, it turns out that chiral transitions show up in the imaginary part of the MDFF. In the dipole approximation, a particularly simple expression is obtained.

An overview of the several possible experimental approaches to set up the coherent superposition of electron waves and to measure the dichroic signal is given. First experiments show the feasibility of the new technique. Possible applications as well as the complementarity to synchrotron experiments are discussed.

### References:

[1] C. Hébert, P. Schattschneider, *Ultramicroscopy* 96 (2003) 463.

[2] P. Schattschneider *et al.*, EDGE EELS workshop, 1. - 5. May 2005, Grundlsee, Austria.

[3] This research was supported by the European Commission, contract nr. 508971 (CHIRALTEM)

# The role of an alumina membrane and its phase transformations during the layer exchange process

Michael Stöger-Pollach<sup>a</sup>, Thomas Walter<sup>b</sup>, Dominique Eyidi<sup>b</sup>, Jens Schneider<sup>c</sup>, and Stefan Gall<sup>c</sup>

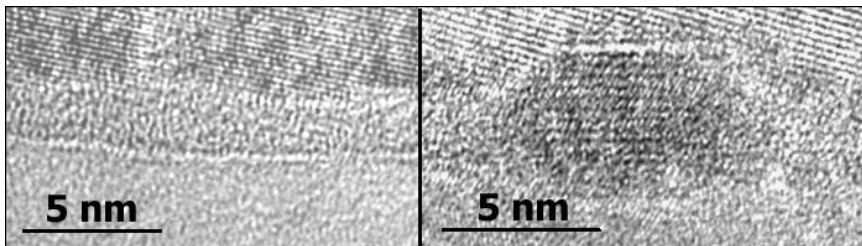
<sup>a</sup>University Service Center for TEM, Technische Universität Wien, A-1040 Vienna, Austria

<sup>b</sup>Inst. für Festkörperphysik, Technische Universität Wien, A-1040 Vienna, Austria

<sup>c</sup>HMI Berlin, SE 1 Si-Photovoltaik, D-12489 Berlin, Germany

For cost reduction in processing of thin film solar cells, crystallization of seed layers on inexpensive foreign substrates and their subsequent epitaxial thickening is a promising approach [1]. Due to the use of glass substrates the process temperatures are limited to less than 600 °C. A specific form of aluminium-induced crystallization (AIC) of amorphous silicon (a-Si) is the aluminium-induced layer exchange (ALILE) process. In the ALILE process an initial glass/Al/a-Si stack is transformed into a glass/poly-Si/Al(+c-Si) stack by annealing at temperatures below the eutectic temperature of the Al-Si-system ( $T_{eu}=577$  °C). Oxidation of the aluminium film prior to a-Si deposition is required to form a thin permeable membrane at the Al/a-Si-interface, which controls the mass transport across the interface but stays in place.

Due to the fact, that the role and behavior of the membrane is still not completely understood, we investigated membranes produced at 25 °C in air and at 400 °C, and 500 °C in oxygen atmosphere



before and after the layer exchange. Using high resolution transmission electron microscopy (HRTEM) we observed that during the heat treatment of the layer exchange process the metastable amorphous alumina membrane – which was grown at 25°C – partly crystallizes. The membrane produced at 400°C contains small crystallites but is predominantly amorphous and shows this phase transformation during the layer exchange, too. This effect opens many channels for the exchange of material between the top and the bottom layers. The membrane grown at 500 °C is already large grained. A phase transformation could therefore not be observed.

**Fig. 1:** Membrane before (left) and after (right) layer exchange. After the exchange process small crystallites can be identified.

Using energy filtered TEM (EFTEM) the membrane/Al interface was determined to be an important diffusion path for Si. This supplies Si for the grains to grow further, which all nucleate at the membrane/Al interface at multiple Al-grain boundaries.

## References:

[1] S.Gall et. al., Thin Solid Films (2005) submitted.

[2] financial support was given by the European Commission (Contr. Nbr. ENK5-CT-2001-00543)

## Tomographic Reconstruction of the EELS Data Cube

Wouter Van den Broek<sup>a,b</sup>, J. Verbeeck<sup>a</sup>, S. De Backer<sup>b</sup>, P. Scheunders<sup>b</sup>, and D. Schryvers<sup>a</sup>

<sup>a</sup>EMAT, University of Antwerp, Groenenborgerlaan 171, B-2020 Antwerp, Belgium

<sup>b</sup>Vision lab, University of Antwerp, Groenenborgerlaan 171, B-2020 Antwerp, Belgium

Two of the major methods of acquiring the EELS data cube are image-spectroscopy [1] (or an Energy Filtered Series or EFS) and spectrum-imaging [2]. We propose a novel method. In imaging mode the energy filter produces an image that is a superposition of images with different energy losses, a suitable defocus of the filter will shift these images with respect to each other, see Fig. 1. In spectroscopy mode the energy filter produces a spectrum that is a superposition of spectra stemming from different parts of the sample, a defocus will also shift these spectra, see Fig. 2. The resulting images can be seen as projections of the data cube. A sufficient number of these projections can be used to reconstruct the data cube using tomographic techniques [3].

If the filtered back projection algorithm is assumed, the Nyquist theorem predicts that with sufficient projections the resolution of the reconstruction equals that of the projections [3,4], yielding a better spectral and the same spatial resolution as an EFS. A Monte Carlo simulation proved that the novel method needs a lower acquisition time than an EFS, to acquire a data cube with the same resolution and mean signal to noise ratio. It was respectively 1.5, 1.9, 3.0, 3.9 and 6.0 times faster for data cubes of 100 by 100 pixels and 25, 51, 101, 201 and 401 energy channels [3]. We believe this will lead to a faster recording of the data cube with higher resolution, greatly reducing beam damage and drift problems. The defocus might be possible by an alternative setting of the lenses in a commercial spectrometer, eliminating the need for additional hardware, but more research is needed. [5]

[1] J.-L. Lavergne, J.-M. Martin, M. Belin, *Microscopy Microanalysis Microstructures* 3 (1992) 517 – 528.

[2] C. Jeanguillaume, C. Colliex, *Ultramicroscopy* 28 (1989) 252 – 257.

[3] W. Van den Broek, J. Verbeeck, S. De Backer, P. Scheunders, D. Schryvers, Submitted to *Ultramicroscopy*.

[4] R. N. Bracewell, A. C. Riddle, *Astrophys. J.* 150 (1967) 427 – 434.

[5] W. Van den Broek is supported by a Concerted Action project, University of Antwerp, 2002/1, “Characterisation of nanostructures by means of advanced electron energy spectroscopy and filtering”.

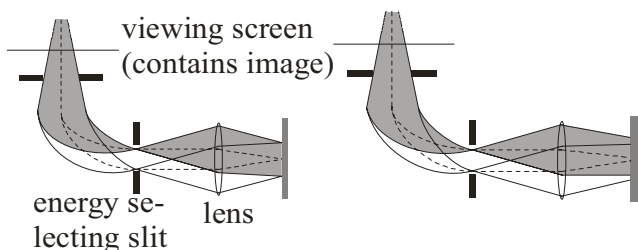


Fig. 1: A focused (left) and defocused (right) energy filter in imaging mode.

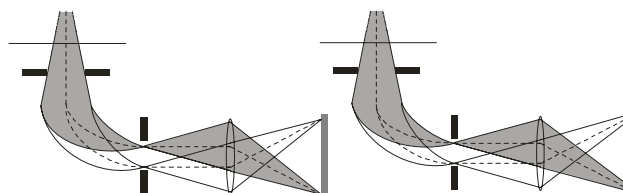


Fig. 2: A focused (left) and defocused (right) energy filter in spectroscopy mode.

## TEM Sample Preparation under SEM Observation

Eberhard Bugiel and Daniel Voss

Institute for Semiconductor Devices and Electronic Materials, University of Hannover, Appelstr. 11A, D-30167 Hannover, Germany, Phone: +49-511-762-4226, Fax: +49-511-762-4229, E-mail: bugiel@ihw.uni-hannover.de

For more than 30 years, ions have been used for TEM sample preparation. The ion thinning procedure was the prerequisite for a breakthrough in XTEM investigations. In this method, a broad ion beam with a diameter of about  $0.5\ \mu\text{m}$  is directed toward the sample. In the past, the electron microscopists have learned to prepare successfully different materials. However, a target preparation is normally not possible in an easy way. But on the other hand, we can prepare sufficiently thin regions of several  $100\ \mu\text{m}$  diameter. During the last 10 years, the FIB technique has been developed into a powerful tool for target preparation. But also that method has some disadvantages, namely we can investigate only regions of several microns. In addition, the ion energy is quite high (about 30 keV). We can improve the preparation results of conventional ion thinning by observing the etching process in a SEM mode. In such mode, target preparation becomes possible.

We upgraded an older Cambridge Stereoscan 200 SEM (Fig.1 a) with an additional ion source (Fig.1 b) operating in the range of several 100 V up to 12.5 kV. We used a specially designed saddle field ion gun.

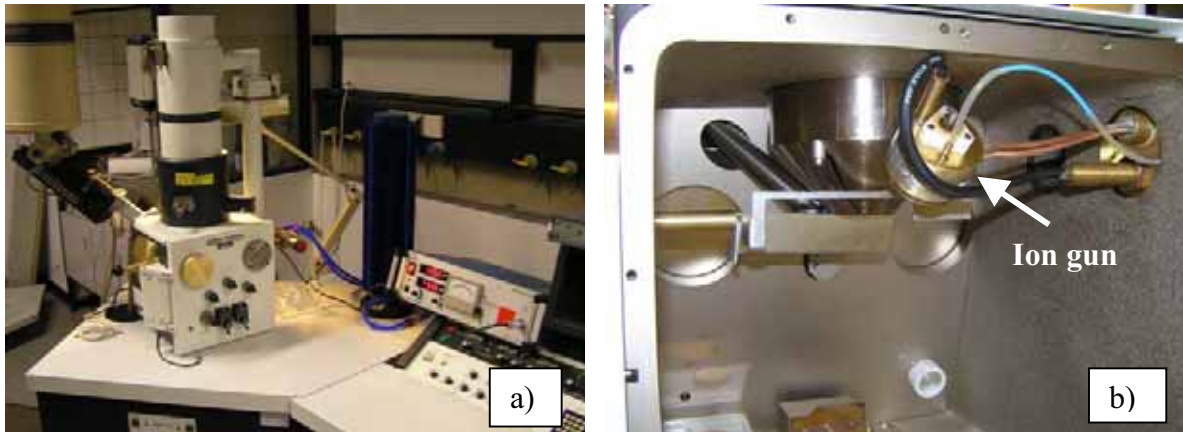


Fig. 1: A Cambridge Stereoscan 200 (a) is equi

Besides TEM sample preparation, we can use this technique also for many other sample preparations and modifications using ions, like e.g., bevel etch techniques.

## A new Process for Reliable and Fast In-Situ Lift-Out of TEM Samples

C. Burkhardt, B. Holder, W. Dreher, W. Nisch

NMI Natural and Medical Sciences Institute, Markwiesenstr.55,  
72770 Reutlingen, Germany

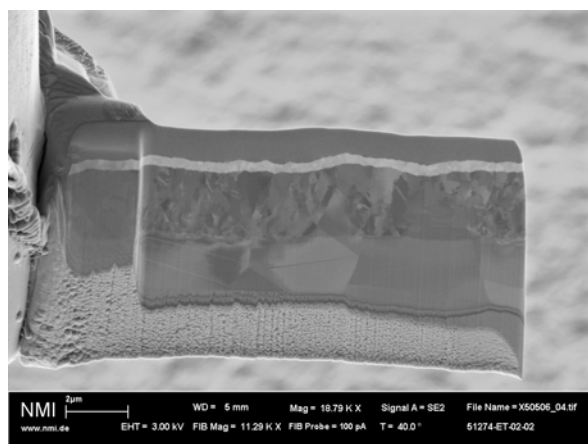
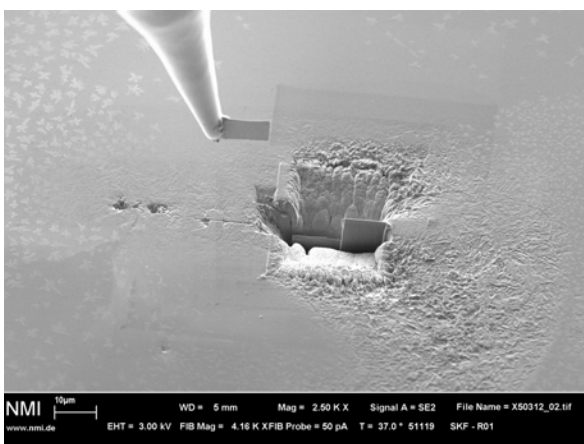
A new process for in-situ lift-out of focused ion beam (FIB) prepared transmission electron microscopy (TEM) lamella inside a scanning electron microscope has been developed some time ago [1]. By local electron beam induced metal organic vapor deposition (MOCVD) of a tungsten or platinum layer, the fine lamella is connected to a sharp needle. This needle itself is integrated on a TEM grid, which is moved by a micromanipulator to the lamella. After fixing the lamella to this needle, the lift-out process is finished. This is a main advantage in comparison to other in-situ lift-out procedures, where the lamella has to be transported to a TEM grid after attaching to the manipulation needle [2]. This second manipulation step is critical and damage or loss of the lamella is possible.

We have now adapted this new process to a crossbeam FIB / FESEM microscope. After milling the lamella to a thickness of 1 to 2  $\mu\text{m}$ , the lamella is attached to the TEM grid by electron and ion beam induced MOCVD and finally cut out from the substrate by the ion beam. In a next step, the lamella is polished to a final thickness below 100 nm. In the last step, the TEM grid with the finished lamella is attached to a scanning transmission electron microscope (STEM) holder for in-situ STEM analysis in the crossbeam microscope or to a TEM holder for TEM imaging.

Beside secure manipulation, the needle grid allows low energy argon milling for final polishing. This final polishing can be performed in a classical broad beam ion miller or inside the TEM. In-situ milling in the TEM allows secure thinning and removing of amorphous layers under direct observation and analytical examination within the transmission electron microscope.

### References

- [1] Burkhardt C, Nisch W. Pract. Metallogr. (2004) 41:190-198
- [2] Langford RM, Clinton C. Micron. (2004) 35(7):607-11



Lift-out sample attached to the special needle grid (left) and after polishing (right).

## Optimization of the FIB milling conditions for RTP-processed Niobium and Tantalumnitride thin films on silicon substrates

M. Dienstleder<sup>a</sup>, M. Rogers<sup>a</sup>, G. Kothleitner<sup>a</sup>, F. Hofer<sup>a</sup> and B.O. Kolbesen<sup>b</sup>

<sup>a</sup>Institute for Electron Microscopy, Graz University of Technology

<sup>b</sup>J.W. Goethe-Universität Frankfurt, D-60439 Frankfurt am Main, Germany

In this work we use a dual beam focused ion beam instrument (FIB) for the preparation of thin electron transparent foils suitable for electron energy-loss spectroscopy (EELS) and energy – filtering transmission electron microscopy (EFTEM) from various types of thermally grown Niobium and Tantalum nitrides. Rapid thermal processing (RTP) has been utilized to a large extent in mainstream semiconductor manufacturing for implant anneals, silicidation, oxidation, nitridation and other processes. These metal nitrides have stimulated commercial interest because of their extreme hardness, wear and corrosion resistance, and thermal and electrical properties. Although the fast heating and cooling rates of RTP may be used to optimize process conditions, the formation of a defined nitride layer chemistry, being uniform within some nanometers, is still object for research and requires the use of versatile preparation tools and characterization possibilities featuring high spatial (and energy) resolution together with chemical sensitivity. The aim of this study is to determine the best approach to the preparation of various RTP processed Nb and Ta–nitride thin films on SiO<sub>2</sub> substrates.

Common to all preparation steps is the pre-conditioning of the sample, by depositing at least a 50 nm thick Au/Pd layer on the specimen to protect the surface against ion implantation into the top surface layers and to prevent material removal during the initial phase of FIB milling.

The following steps will be discussed in detail: What are the relative advantages and disadvantages of fast script milling vs. manual milling? Can the milling be improved by using XeF<sub>2</sub> reactive gas for insulator enhanced etching? What are the critical steps during the in-situ lift out with the “Omniprobe™” micromanipulator (Fig.1)? And finally, what are the optimal FIB parameters with respect to milling-induced amorphization of the sample surface (Fig.2)?

Fig:1

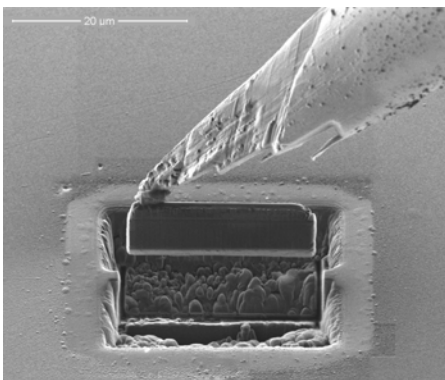
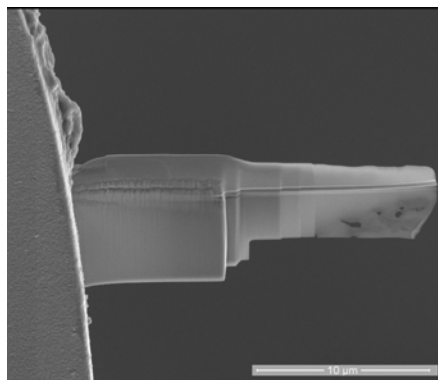


Fig.2



References:[1] M. Rogers et al., Prakt. Metallogr. 42 (2005) 172-187

## Nano-fabrication with Focused Ion Beams An innovative instrument

Jacques Gierak<sup>a</sup>, Ralf Jede<sup>b</sup>, Peter Hawkes<sup>c</sup> and the Nano-FIB partners<sup>d</sup>

<sup>a</sup>Laboratoire de Photonique et de Nanostructures

Route de Nozay, 91460 Marcoussis, France email: jacques.gierak@lpn.cnrs.fr

<sup>b</sup>Raith GmbH, Hauert 18, Technologiepark, 44227 Dortmund, Germany

<sup>c</sup>CEMES/CNRS, 29 rue Jeanne Marvig, 31055 Toulouse, France

<sup>d</sup>[http://europa.eu.int/comm/research/industrial\\_technologies/](http://europa.eu.int/comm/research/industrial_technologies/)

Focused Ion Beam (FIB) technology today plays an important role in IC manufacturing processes such as failure analysis and thin magnetic head trimming. We will describe our specific iterative effort carried out under the Nano-FIB EC project (*Contract No. G5RD-CT2000-00344*) combining developments in liquid metal ion source geometries and research in ion optics specifically for high-resolution applications, with characterization of ion induced damage in FIB patterned structures. Our objective was to demonstrate that the Focused Ion Beam technique is now a challenging technique for nanotechnology. This is because the lateral patterning of structures having one nanometre-sized dimension (thickness) with FIB no longer relies on sputtering effects with high local incident dose ( $> 10^{16}$  ions/cm<sup>2</sup>), but rather on local defect injection and surface modifications of high crystallinity substrates. In the present case the selectivity of the ion probe becomes of major importance to induce extremely low dose effects ranging from  $10^{14}$  ions/cm<sup>2</sup> to  $10^{12}$  ions/cm<sup>2</sup> [1].

We will present our work aiming to explore the nano-structuring potential of a highly focussed pencil of ions. We will show that Focused Ion Beam technology (FIB) is capable of overcoming some basic limitations of current nano-fabrication techniques and to allow innovative patterning schemes for nanoscience. In this work, we will first detail the very high resolution FIB instrument we have developed specifically to meet nano-fabrication requirements. Then we will introduce and illustrate some new patterning schemes we propose for next generation FIB processing. These patterning schemes are (i) Nano-engraving of membranes as a template for nano-pores and nano-masks fabrication. (ii) Local defect injection for magnetic thin film direct patterning. (iii) Functionalisation of graphite substrates to prepare 2D-organized arrays of clusters. (iv) Selective epitaxy of III-V semiconductors on FIB patterned surfaces. Finally we will show that FIB patterning is fully compatible with “bottom-up” or “organisation” processes.

We will conclude this presentation by introducing some emerging concepts and principles we have started to explore for next-generation FIB processing and systems.

[1] Exploration of the ultimate patterning potential achievable with high resolution focused ion beams, J. Gierak, D. Mailly, P. Hawkes, R. Jede, L. Bruchhaus, L. Bardotti, B. Prével, P. Mélinon, A. Perez, R. Hyndman, J.-P. Jamet, J. Ferré, A. Mougín, C. Chappert, V. Mathet, P. Warin, J. Chapman: *Appl. Phys. A*, 10.1007/s00339-004-2551-z (2004)

## Removal of Amorphous Layers by Low Voltage FIB Preparation

Andreas Graff, Michél Simon, Frank Altmann, Hilmar Hoffmeister\*, Peter Gnauck\*

Fraunhofer Institut für Werkstoffmechanik Halle, Heideallee 19, 06120 Halle, Germany

\*Carl Zeiss NTS GmbH, Carl-Zeiss-Straße 56, 73447 Oberkochen, Germany

For HRTEM investigations and EBSD pattern the quality of the FIB prepared samples is often not sufficient. To improve the quality of the FIB polished surfaces detailed experiments have been performed. The influence of the Ga ion beam of the formation and the shape of amorphous layers on silicon was studied depending on the ion beam accelerating voltage and its incident angle by SEM and TEM.

A FIB (Crossbeam 1540, Carl Zeiss NTS) is used to expose silicon single crystals and structured silicon wafers by Ga ions and to prepare cross-sections for TEM. Some of the amorphous layers were investigated by TEM (CM 20 Twin, CM 20 FEG, Philips).

The irradiation of silicon by high energy Ga ions produces thick amorphous layers at the surface of the target. During shaping of trenches for cross-sections and TEM samples the side walls are affected by the ion beam as well (Fig.1). To remove back sputtered material and the amorphous layer formed by the Ga implantation ions with 2kV accelerating voltage can be applied. The amorphous layer on the surface and the sidewalls nearly vanishes by irradiation with low energy Ga ions under  $10^\circ$  tilt to the surface normal (Fig. 2).

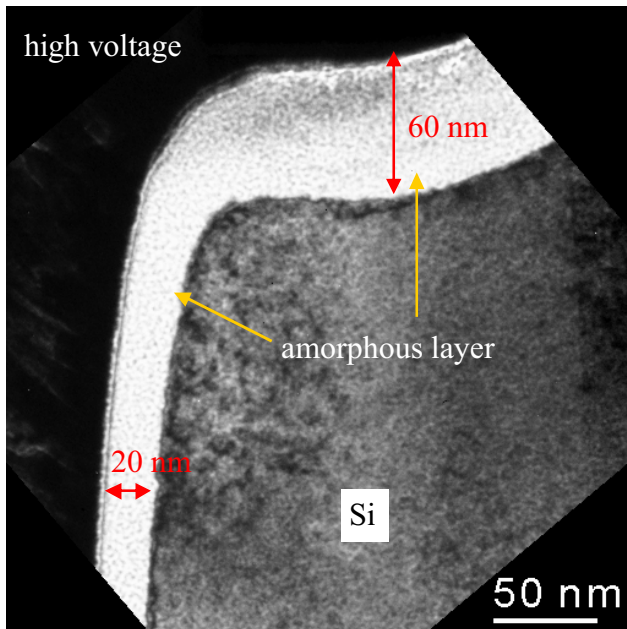


Fig. 1 TEM image of FIB prepared crystalline silicon. Thick amorphous layer at the surface and the sidewalls. (accelerating voltage 30kV)

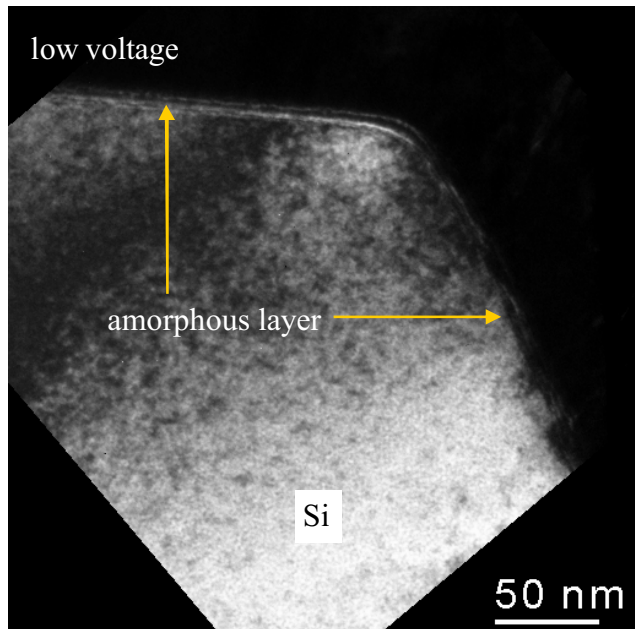


Fig. 2 TEM image of a FIB prepared crystalline silicon. Removal of amorphous layer due to low energy Ga ions. (accelerating voltage 2kV)

## **Preparation with the RES 120 – unique ion milling system with SEM control**

Wolfgang Gruenewald

BAL-TEC Innovation GmbH, D-09119 Chemnitz, Neefestraße 82, Germany

### **Introduction**

In recent years ion milling devices have been advanced in most of their features. Nevertheless today's ion milling systems are still limited in their specimen observation system that is used during the milling process. Conventional devices use light microscopes with magnifications in the range of multiple hundreds. Under these conditions an evaluation of the thinning process is impossible. The combination of a standard ion milling system with a scanning electron microscope allows precise and reliable sample preparation for electron microscopy.

### **RES 120 – The new SEM controlled ion milling system**

The RES 120 is a unique fully computer controlled ion beam sample preparation system that uses a SEM for process observation. The development of this new milling device was driven to overcome the sample observation difficulties of conventional ion milling systems. The vacuum chamber configuration contains a SEM with SE, TE and BSE detector, a five axis stage and two ion guns. The SEM column sits on top of the vacuum chamber. The sample holder is fixed on a five axis stage and can be moved between two positions, the milling and the observation position. All motions are motor driven, very fast and of highest precision. The sample imaging occurs via three detectors, SE, BSE and TE. The SE detector is positioned to allow high resolution investigation. The TE detector is mounted right underneath the sample so that it can move with the sample. A BSE detector enables sample observation during the milling process.

Two infra-red (IR) cameras admit chamber observation, of which one of them is used for beam alignment. The camera principle even allows visualisation of low energy ion beams. All parameter settings for the milling and the SEM system are operated via one touch screen.

### **Results and Conclusions**

The wide range of applications of the RES 120 is supported by a variety of sample holders for TEM and SEM sample preparation. Ion gun and sample holder tilting possibilities enable milling angles from 0° to 90°. The high degree of freedom of parameter setting ensures the preparation of a very wide range of materials such as semiconductors, metals, ceramics and even polymers.

Direct observation of the sample during the milling process is possible with the BSE and TE detector in a maximum resolution of 50 nm. The sample can be moved into the optimum working distance of the SEM for the in situ evaluation of the preparation results in high resolution (15 nm). This enables a site specific sample preparation of very small structures down to nano-structures.

Because the surface modification of SEM samples can be followed via live image the process can be stopped on time. This is very useful for applications like contrast enhancement, slope cutting and surface cleaning.

All live images viewed with the SEM or IR camera can be stored. Due to the unique assembly the RES 120 has no limitation regarding the applications. The main advantage of the RES 120 is a permanent monitoring of the ion milling process under optimum conditions. Thanks to the optimum sample observation the RES 120 ensures a time saving sample preparation with an almost 100 % sample yield.

## New Applications of the Gatan PECS Ion Beam Cutting Tool for 3D SEM Microstructure Investigation of Heterogeneous Solids

W. Hauffe and M. Neugebauer

Physics Department, Dresden University of Technology, D-01062 Dresden, Germany

Various ion beam processing procedures are well established for preparation of SEM samples: Polishing, cleaning, milling, etching and cutting. The general processes together with standard applications have been described earlier and led to methodical developments [1, 2]. The Gatan Precision Etching Coating System (PECS) allows all these processes in one single apparatus additionally combined with the coating capability [3]. The ion beam cutting tool allows combined with the other ion beam processing steps manifold applications on nearly all materials [4]: Heterogeneous solid samples consisting of metals, insulators, semiconductors, polymers, biomaterials etc. with any roughness, porosity, and hardness differences. The technique does not require embedding and therefore as an additional advantage the perpendicular or inclined cut area can be observed simultaneously with the initial surface microregion. Cutting alone allows the observation in the SEM material contrast combined with elemental analysis. Fig. 1 shows such example of a heterogeneous material with carbon fibres and PTFE in a fuel cell cut with 7 keV Ar ions. With additional ion beam processing steps the information gain can be extended. By selective ion etching the internal grain and phase structure will be visible. Fig. 2 shows a perpendicular cutting plane through IC structures cut and selectively etched with 7 keV Kr ions and coated with AuPd. The high ion beam cutting quality requires the FESEM inspection (Zeiss Gemini/IFWDresden) to resolve all details up to nanometer dimensions.

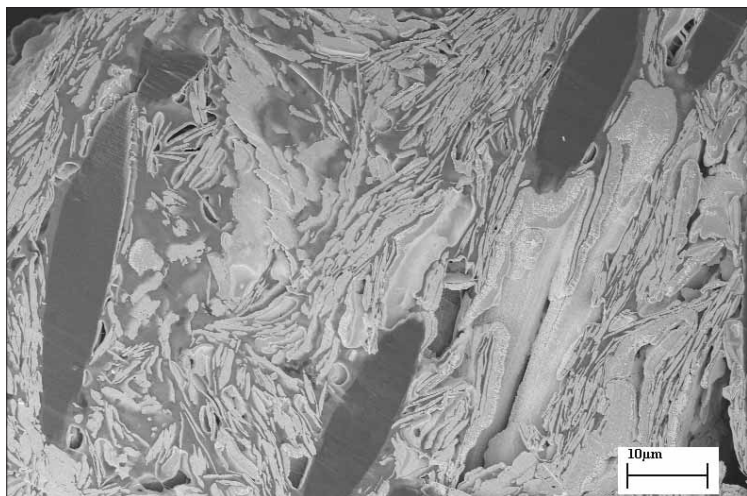


Fig.1: Ion beam cut through the heterogeneous backing layer of a fuel cell containing carbon fibres and PTFE (FESEM image: S. Menzel)

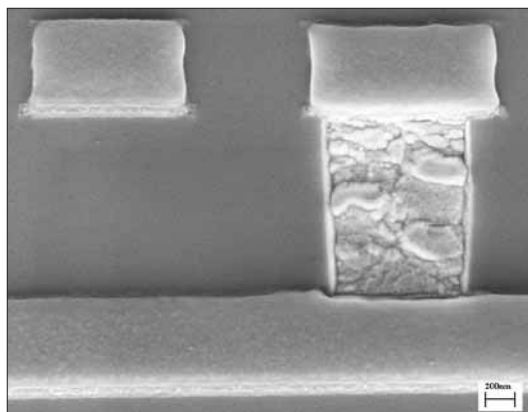


Fig. 2: Perpendicular ion beam cut through IC structures after selective ion etching and AuPd coating (FESEM image: H. Wendrock)

### References:

- [1] W. Hauffe, "Production of Microstructures by Ion Beam Sputtering" in *Sputtering by Particle Bombardment III* (Eds. R.Behrisch, K.Wittmaack), Springer Ser. Topics in Applied Physics, Vol. 64 (Springer-Verlag, Berlin, Heidelberg, New York, 1991) p. 305
- [2] W. Hauffe, Patents DD 139670 (1977), DD 152232 (1980) and DD 218954 (1982)
- [3] Gatan product information PECS 2004
- [4] W. Hauffe, D. Glöß, R.J. Mitro, Proc. ICEM 15, Durban/SouthAfrica 2002, Vol. I, p. 273

## Why is Selective Carbon Coating of TEM Samples so Effective?

Thomas Höche<sup>1,2</sup>, Jürgen W. Gerlach<sup>1</sup>, and Frank Heyroth<sup>3</sup>

<sup>1</sup> Leibniz-Institut für Oberflächenmodifizierung e.V., D-04318 Leipzig, Germany

<sup>2</sup> 3D - Micromac AG, D-09114 Chemnitz, Germany

<sup>3</sup> IWZ Materialwissenschaften, Martin-Luther-Universität, D-06120 Halle, Germany

Electrostatic charging of non-conducting specimens occurs in the transmission electron microscope due to highly complex inelastic-scattering processes of impinging electrons resulting in ionisation and subsequent emission of secondary electrons and Auger electrons [1].

The accumulation of positive charge in the sample can be significantly reduced by e.g. preparing powdered samples onto an electrically conducting support film such as carbon. However, if bulk samples are to become studied, the deposition of a conducting thin film covering the *entire* sample has the disadvantage that this film is both deteriorating image quality (in high-resolution TEM) and enhance contamination (in all electron nanoprobe related techniques including all kinds of analytics, convergent electron beam diffraction, Z-contrast etc.).

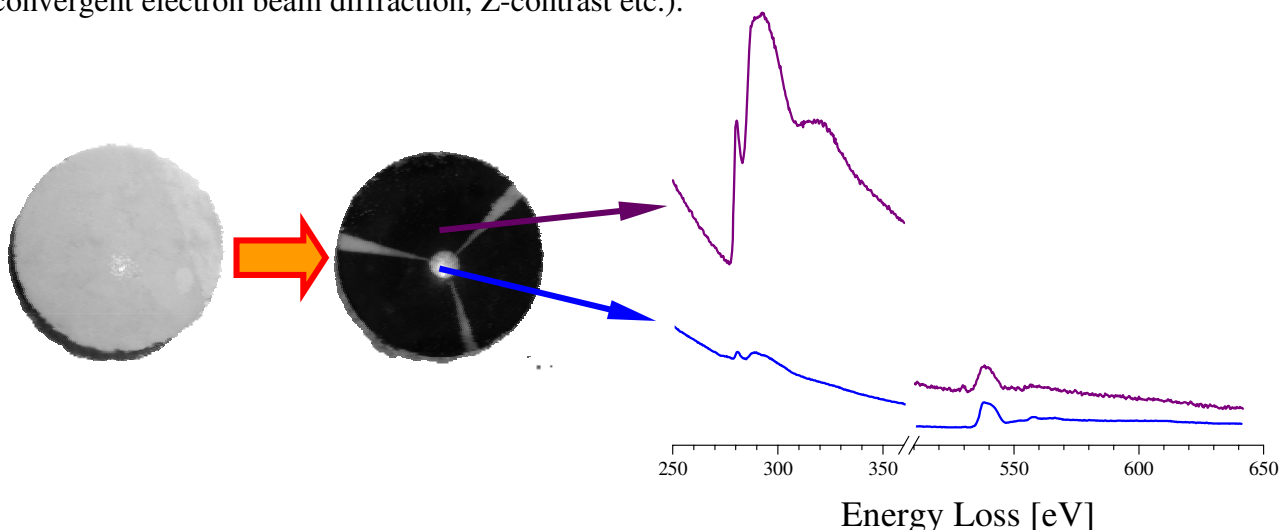


Fig. 1 Effect of selective coating on the carbon-layer thickness (C-K and O-K EEL spectra).

It was hence proposed to rather use *selective coating* utilising an adapted blind [2]. The latter mask is shielding the areas of interest from direct deposition with the conducting thin film. With this technique, for example, a beam of 3 nm diameter was kept fix for five minutes at one position of a sapphire sample without any indication of contamination in a 400 kV electron microscope.

Electron energy-loss spectroscopy and secondary ion mass spectroscopy are combined to explain the mechanisms making this preparation technique so excellent for both the suppression of charging and the avoidance of contamination.

### References:

[1] J. Cazaux, *Ultramicroscopy* 60 (1995) 411.

[2] T. Höche & T. Petsch, German Patent (2003), filed. The CoatMaster kit for selective coating of TEM samples is available through 3D-Micromac AG of Chemnitz, Germany.

### 3D-Investigation of Plasma Erosion Craters using a Dual Beam Workstation

C. Holzapfel, N. Jeanvoine, F. Soldera, A.E. Faundez, F. Mücklich

Institute for Functional Materials, Saarland University, P Box 15 11 50, D-66041 Saarbrücken, Germany, <http://www.uni-saarland.de/fak8/fuwe/index.html>, email: c.holzapfel@mx.uni-saarland.de

In this study, the potential of the focused ion beam (FIB) technique for target preparation of plasma erosion craters is evaluated. Plasma erosion is a fundamental process in many processes and industrial applications, for example spark plugs or electrical contacts. Due to the localized high energy input, plasma discharge leads to the formation of localized erosion craters. Because of the small size of these craters (Fig. 1A), only on the order of a few tens of microns or less, conventional metallographic preparation is difficult or even impossible. Therefore, a well suited characterization technique which is able to analyze both the surface structure, as well as the structural variation with depth is required. The most straightforward approach is using a combination of electron microscopy and FIB. The FIB enables to investigate the change in microstructure with depth by precisely oriented cross-sections. Using the automated “slice and view” technique a full 3D-reconstruction of the erosion craters can be achieved (Fig. 1B,C). In addition, samples can be prepared for further TEM analyses.

In this study, different materials were characterized in a dual beam workstation in order to understand the plasma erosion process. Samples consisting of metallic thin layers provide a measure of the depth of interaction by observing the interaction of the layers resulting from melting during the high-temperature stage as well as recrystallization (Fig. 1). High-resolution chemical analysis in STEM mode further helps in constraining the depth of interaction. Plasma erosion experiments employing preoxidized Ni samples show that due to the non conducting nature of the oxide layer a much larger crater is observed. On the other hand, samples consisting of single phase RuAl show a much thinner oxide scale. Thus this material exhibits a high potential for future use as electrode material. As demonstrated in this study, 3D-FIB investigations clearly are a big step forward in order to understand the physical principals of microstructural changes on the nano- and micrometer scale.

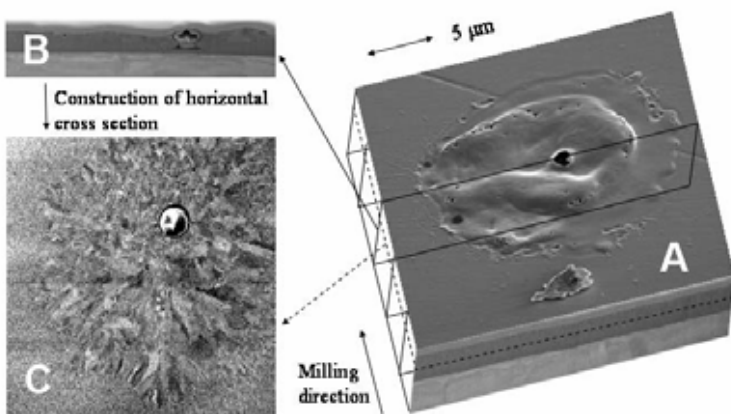


**Figure 1.** The 3D-diagram displayed in A shows a plasma erosion crater on the surface (original picture at 52° tilt). With the focused ion beam slices are subsequently milled into the crater as indicated (the first slice is shown in A as well). A slice cutting through the central hole of the crater is shown in B. In total 300 slices were milled. By recombining corresponding pixel lines in these slices the horizontal cross-section 350 nm below the unmodified reference surface shown in C can be reconstructed.

Clearly, radially-directed grains crystallized from a high temperature melt can be identified.

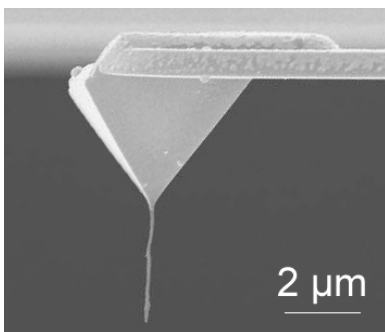
## MFM-Probe Preparation Under Microscopic Observation Using Fe-MWCNTs

S.B. Menzel, A. Winkler, J. Thomas, and T. Mühl

IFW Dresden, Leibniz Institute for Solid State and Materials Research Dresden, P.O.Box 270116, D-01171 Dresden, Germany

Carbon Nanotubes (CNTs) are expected to play an important role in the technology of tomorrow. Their strong potential has already been demonstrated in conductors, transistors, rectifiers, actuators, and also electron sources for microscopy application. Beside attempts to control the properties of the CNTs, one of the present challenges is the development of techniques for their precise manipulation or even self-alignment [1-3].

In the present paper iron filled multiwalled CNTs (Fe-MWCNTs) were transferred from substrates to AFM cantilevers using a 3-axis nanomanipulator (Kleindiek). Vertically grown Fe-MWCNTs were placed on a tungsten wire tip and transferred onto an AFM cantilever tip. Manipulation was done inside a scanning electron microscope (Gemini 1530/ZEISS) as well as inside a focussed ion beam workstation (FIB 200/FEI). The advantage when using the FIB is that the CNT can be pasted to the W-tip or to the cantilever tip by platinum deposition which is much stronger than the fixing by electron beam induced contamination inside the SEM. Firstly, one end of the CNT was fixed onto the cantilever or the W tip, then the other end was separated from the substrate by ion beam cutting, considering that the free end was filled with an Fe-nanowire. In the case of CNT transfer inside the SEM the tubes were removed from the substrate only by tractive force. However, because the adjustment of the CNTs towards the cantilever tip is difficult to realize, in other experiments the cantilever was affixed to the nanomanipulator directly, and approached to the CNTs which had been deposited on razor blade edges by electrophoresis [2]. For these purposes, CNTs were dispersed in a solution of 1,2-Dichlorethane (DCE) and then the solution was dropped between two razor blades aligned parallel to each other with a gap of about 400  $\mu\text{m}$ . By applying a sinusoidal voltage (100 V<sub>p</sub>, 1 MHz) the CNTs were aligned in electric field direction. By this way, an alignment of the Fe-MWCNTs along magnetic flux lines was also investigated. After evaporation of the solvent the Fe-MWCNTs adhere on the surface by van-der-Waals interactions. Microscopic characterization of the MFM-probes showed that nanotubes are aligned on the tips under different angles which is caused by both the geometry of the pyramidal tip and the bow of the CNT. This problem was avoided by drilling a hole into a Si<sub>3</sub>N<sub>4</sub> cantilever tip by Ga<sup>+</sup>-ion etching. Then the Fe-MWCNTs were thread into the hole and fixed by Pt. The figure shows an example of a fabricated MFM-probe which was successfully used for MFM-measurement.



### References:

- [1] T. Arie et al.: in: Journal of Vacuum Science and Technology B, Vol. 18 (2000), p. 104
- [2] Y. Nakayama and S. Akita: in: New Journal of Physics, Vol. 5 (2003), p. 1281
- [3] T. Ono et al.: in: Nanotechnology, Vol. 13 (2002) p. 62
- [4] Authors are grateful for collaboration with S. Hampel, C. Täschner, B. Arnold, D. Lohse, and A. Leonhardt.

**Figure:** Example of a MFM cantilever tip with Fe-MWCNT

## Preparation of TEM Samples of Metallic Glass Powder

C. Mickel <sup>a</sup>, P. Schubert- Bischoff <sup>b</sup>, S. Venkataraman <sup>a</sup>, T. Gemming <sup>c</sup>, G. Scheider <sup>a</sup>

<sup>a</sup> IFW Dresden, Institut für Metallische Werkstoffe, Postfach 270016, D- 01171 Dresden, Germany

<sup>b</sup> Hahn- Meitner- Institut Berlin, Glienicker Straße 100, D- 14109 Berlin, Germany

<sup>c</sup> IFW Dresden, Institut für Festkörperanalytik und Strukturforchung, Postfach 270016, D- 01171 Dresden, Germany

We report on a new method to prepare TEM samples from  $\text{Cu}_{47}\text{Ti}_{33}\text{Zr}_{11}\text{Ni}_8\text{Si}_1$  metallic glass powders.

Studies of the crystallization process of metallic glasses are important for understanding the glass formation in metallic systems. It helps to design new metallic glass systems and to optimise their properties .

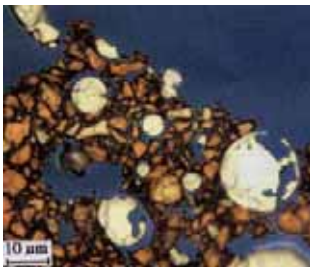
In our case, the metallic glass powder was prepared by gas atomisation. This process allows for rapid solidification of the melt with a cooling rate of about  $10^5$ -  $10^6$  K/s. The resulting glassy powders exhibit a fairly large supercooled liquid region prior to crystallization (1). The powder particles have a spherical shape with diameters of less than  $40\mu\text{m}$ .

The powder was subjected to different heat treatments in order to investigate the crystallization process by TEM.

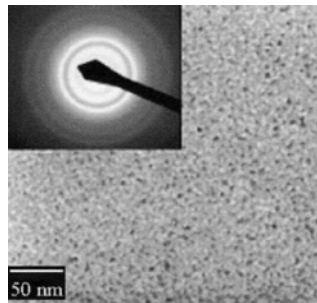
In order to make sure that the TEM results are representative, a large variety of TEM samples has been prepared. For a large field of view it was essential to prepare large electron transparent areas. Since all conventional preparation methods failed, a new method was developed: The powder particles were embedded in a medium with a sputter yield equal or lower to the one of the powder particles. Therefore an epoxy resin was mixed with a filler powder (graphite, boron or titanium nitride with grain sizes of  $2\text{...}5\mu\text{m}$ ) until it became a compact, ductile and kneadable paste. To this paste about 30% of its volume of the metallic glass powder were added. The mixture was cured at  $80^\circ\text{C}$  for 30 min, given a compact and well machinable block. From this block thin slices of  $5\text{...}8\mu\text{m}$  thickness were prepared by polishing. They were further thinned down by ion milling .

Each in this way prepared powder sample contained divers transparent powder particles.

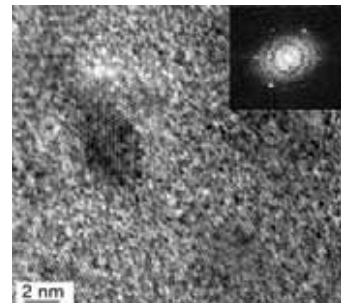
TEM and HRTEM investigations offered clear crystallisation differences in the powders with different heat treatments.



LM: Powder embedded in epoxy resin and TiN



TEM Bright Field



HRTEM Bright Field

(1) S. Venkataraman, et al., manuscript submitted to Acta Mater.

## **The contribution of resins to resulting image in low voltage electron microscope.**

Jana Nebesářová<sup>1,2</sup> and Marie Vancová<sup>1,3</sup>

<sup>1)</sup> Institute of Parasitology, Academy of Sciences of the Czech Republic, Branišovská 31, 370 05 České Budějovice, Czech Republic

<sup>2)</sup> Faculty of Science, Charles University in Prague, Viničná 7, 128 08 Praha 2, Czech Republic

<sup>3)</sup> Faculty of Sciences, University of South Bohemia at České Budějovice, Branišovská 31, 370 05 České Budějovice, Czech Republic

The low voltage electron microscope LV EM 5 (DeLong Instruments) is a new type of a table-size microscope specially designed for the observation of biological specimens [1]. The microscope consists of two parts: the image originates in the small electron microscope, then it is converted to the light image on a high-quality yttrium-aluminium garnet (YAG) crystal, which serves as a fluorescent screen and closes the electron microscopic part. The standard light microscope effects next magnification of the image. More information about a construction of the low-voltage electron microscope is possible to find on <http://www.dicomps.com/micro/mwin.htm>.

The main advantage of LV EM consists in the use of an accelerating voltage around 5 kV, which brings an enhancement of image contrast nearly twenty times higher than for high voltage electron microscope using the accelerating voltage 100 kV [2]. Therefore staining procedures could be omitted and the specimen could be observed closer to its native state. On the other hand so low accelerated primary electrons are able to pass only through the extra ultra thin sections with the thickness about 20 nm. Atoms with low atomic number, which form biological specimens, are able to scatter so low energy primary electrons. Even atoms of resins which the specimen is embedded in, can contribute in scattering and contribute to image formation [3].

The aim of this work was to evaluate a contribution of resin atoms to the resulting image. We compared: 1/ the appearance of 20 nm ultrathin sections cut from pure resins PolyBed 812 and Spurr in LV EM 5. 2/ the ultrastructure appearance of a few types of mouse tissues prepared by the same way and embedded in PolyBed 812 and Spurr. 3/ because the image contrast in LV EM 5 is very sensitive to the section thickness [4,5], we tried to show the influence of the section roughness, which was caused by different kinds of knives (diamond and oscillating diamond [6]), on the resulting image.

1. DeLong A.: Electron Microscopy 1992, Vol.1, 79-82, 1992
2. Coufalová E., DeLong A.: Proc. EUREM 12, I183, 2000
3. Nebesářová J., Vancová M.: Microscopy 2002. Proceedings of the 2<sup>nd</sup> Annual Meeting of the Czechoslovak Microscopy Society (Ed. L. Frank), GRAPHICAL Brno, Czech Republic, 35-36, 2002
4. Nebesářová J., Vancová M.: Proceedings of 13<sup>th</sup> EMC, I.403, Antwerp 2004
5. Drummy L.F., Yang J.Y., Martin D.C.: Ultramicroscopy, 99 (4): 247-256, 2004
6. Studer D., Gnaegi H.: J. Microscopy, 197: 94-100, 2000

# Preparation-Dependent TEM Specimen and High-Resolution Image Quality

T. Riedl<sup>1</sup>, T. Gemming<sup>1</sup>, and K. Wetzig<sup>1</sup>

<sup>1</sup> IFW Dresden, Leibniz Institute for Solid State and Materials Research Dresden, Helmholtzstr. 20, D-01069 Dresden, Germany

Many studies of crystalline thin films using HRTEM and EELS have been published, but few exist about the quantification of specimen and high-resolution image quality which are strongly influenced by the applied preparation scheme. In particular for HRTEM applications ideally flat, artifact-free specimens are required to obtain valuable image data [1].

In this contribution we analyze TEM specimens of pulsed laser deposited  $\text{La}_{0.7}\text{Sr}_{0.3}\text{MnO}_3$  (LSMO) thin films on  $\text{SrTiO}_3$  (STO) substrate, a promising material for magnetoelectronics [2].

Important specimen quality parameters are the thickness, its lateral homogeneity, and the width of the amorphized rim indicating the thickness of amorphous surface layers. Concerning the quality of atomic column images we distinguish between position and intensity homogeneity. The first can be measured by the peak width of Fourier transforms, the latter by the lateral variations of the mean intensity per unit cell normalized to the primary illumination and that of the integral contrast per unit cell [3] normalized to the mean intensity. The mentioned quantities have been evaluated for STO of TEM specimens prepared [4] by Gatan PIPS, Bal-Tec RES ion milling machines, and by the focussed ion beam (FIB) technique. Preparation influences on quality parameters will be discussed. In particular, the effect of low-energy  $\text{Ar}^+$  milling has been studied: It leads to a reduction of amorphized surfaces and hence to a remarkable enhancement of atomic-column contrast in HRTEM images.

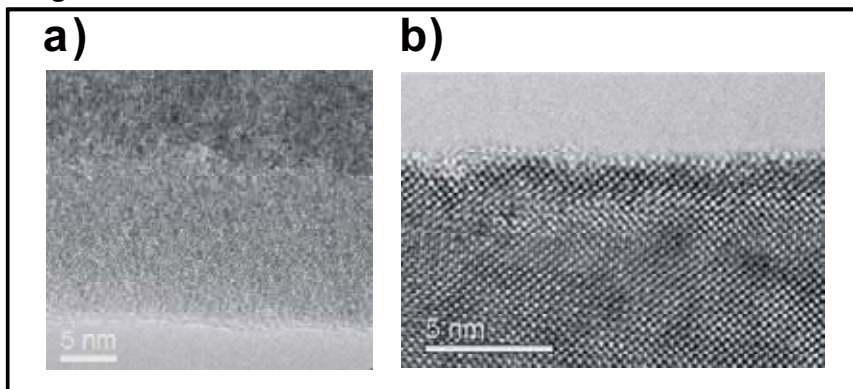


**Fig. 1:** Amorphized rim before (a, ~13nm) and after (b, ~0nm) low-energy milling of a FIB specimen

## References:

- [1] C.B. Carter and D.B. Williams, Transmission Electron Microscopy Vol. III (1996).
- [2] J.S. Noh et al., Appl. Phys. Lett. 79 (2001) 233.
- [3] K. von Hochmeister, dissertation at Univ. Stuttgart, MPI Metallforschung (2004).
- [4] We kindly acknowledge B. Arnold and D. Lohse (IFW Dresden) for TEM preparation.
- [5] We kindly acknowledge financial support by the Deutsche Forschungsgemeinschaft via Forschergruppe 520/ B3 (project GE 1037/ 8).

## Cross Section Preparation of Multi Layer Systems by Ion Etching (IE)

R. Sonnleitner<sup>a</sup>, Ch. Stocker<sup>a</sup> and G.E. Nauer<sup>a,b</sup>

<sup>a</sup>ECHEM – Centre of Competence in Applied Electrochemistry, 2700 Wiener Neustadt, Austria

<sup>b</sup>Institute of Physical Chemistry, University of Vienna, 1090 Vienna, Austria

Multi coating or multi material systems are widely used in many different kinds of industrial applications. For the evaluation of the quality of those composites, microstructural investigations (phase identification and determination of the chemical composition of the layers as well as the grain structure) are important. In order to perform SEM investigations on those composites, the first step is to prepare a cross section using classic metallographic preparation including cutting, grinding and polishing. This way of preparation may not be sufficient if: (1) grain structure in each material has to be visualised and (2) layers are very thin ( $\ll 1 \mu\text{m}$ ) and/or fairly weak. One possibility to produce “clean” cross sections of even thin layers and to reveal information about the grain structure in each layer is ion etching (IE) of the grinded and polished cross section.

During IE, noble gas ions (for example  $\text{Ar}^+$ ) are accelerated at energies in the range between 1 to 10 keV. The ions hit the sample surface [1] and atoms of the sample surface are removed. The amount of material removed depends on the one hand on the parameters of the ion beam (the mass of ions, acceleration voltage/ energy of the ions, ion current, orientation of the surface relative to the ion beam..) and on the other hand on etched material(s) (crystal system and the grain orientation, phases,...) [2]. The corresponding preparation was performed with a GATAN-Precision Etching Coating System (PECS<sup>TM</sup>)–Model 682. For the SEM investigations a Philips XL 30 FEG ESEM was used. In the following the advantages and potentials of this preparation method in terms of revealing microstructural features for a subsequent microscopical investigation will be illustrated by the examples of 2 different materials/coating systems.

References:

[1] H. Schumann, H. Oettel(Hgst); „Metallographie“, 14. Auflage, WILEY-VCH Verlag GmbH, 2005

[2] I. Gräf; „Anwendung des Ionenstrahlätzens in der Materialcharakterisierung“; GATAN GmbH, 2001

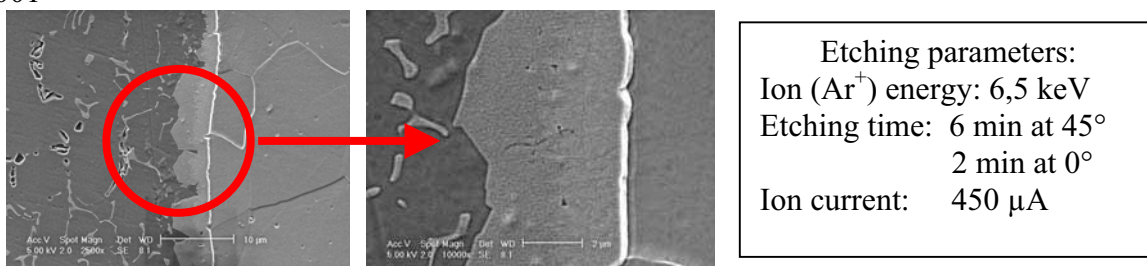


Figure 1 Al-Steel composite

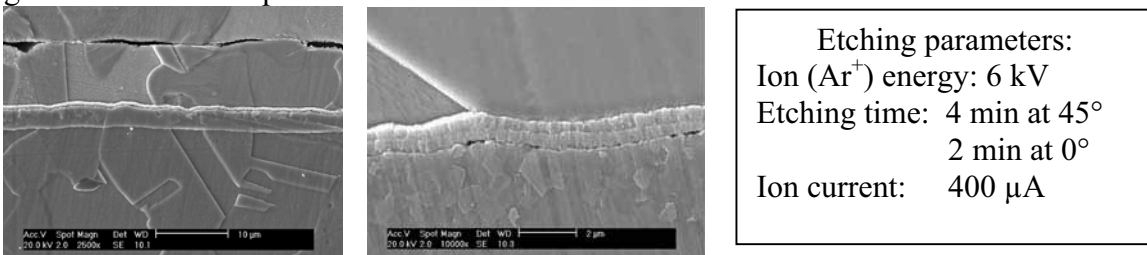


Figure 2 Cu-Ni-Ag-multilayer-system

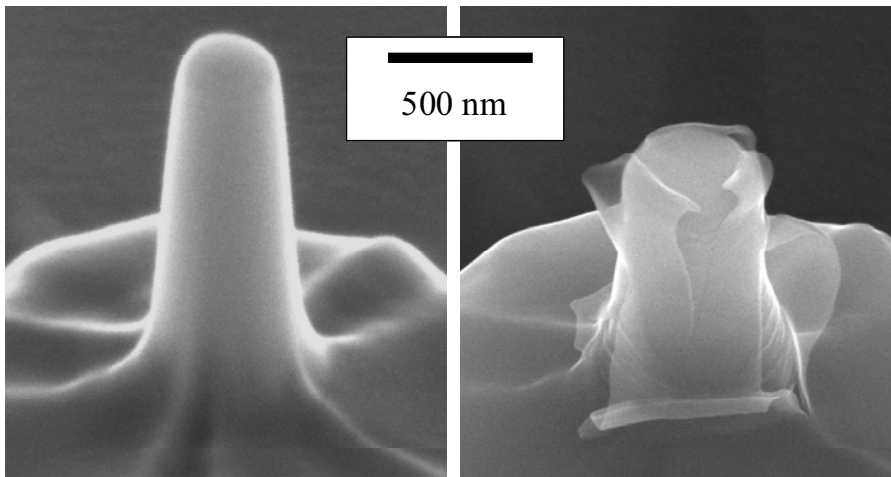
## Focused Ion Beam Micro-machining

C.A. Volkert

Forschungszentrum Karlsruhe, P.O. Box 36 40, 76021 Karlsruhe Germany

The focused ion beam (FIB) microscope is a powerful tool for characterization and micro-machining of samples. The finely focused Ga ion beam allows high resolution imaging (resolution  $\sim 10$  nm) and precise cutting (minimum feature size  $\sim 20$  nm) and is thus ideally suited for a number of applications including preparation of site-specific TEM samples. In this talk, a number of examples will be presented, with particular emphasis placed on the use of the FIB for 3D material characterisation and machining of sub-micron samples for mechanical testing.

Three-dimensional information can be obtained from the surface region of a sample by successive milling of cross-sections using the focused ion beam and then imaging with either the ion beam or the electron beam. Through the use of 3D reconstruction techniques, these images can provide quantitative information about sample morphology, grain structure, and elemental distributions. In one example, the grain boundary orientations in a 300 nm thick thermal fatigued Cu film are investigated. In a second, void size and morphology in a 480 nm wide Cu interconnect after electromigration is measured and quantitatively correlated with grey scale images obtained by backscattered electrons in an SEM. In general, the FIB allows volumes from  $(1 \mu\text{m})^3$  up to  $(100 \mu\text{m})^3$  to be investigated with a spatial resolution of roughly 50 nm.



*A FIB machined 300 nm diameter single crystal Al column before and after compressing with a flat punch in a nanoindenter*

The micro-machining capabilities of the FIB can also be used to great advantage in preparing samples for mechanical testing. Results from sub-micron compression tests and fracture toughness tests on samples machined from a variety of materials will be discussed. A clear effect of sample size on deformation is observed, as are some artefacts which are attributed to FIB-induced damage and Ga contamination. These

artefacts limit the minimum feature size that can be milled while still maintaining mechanical integrity, and place important constraints on the use of the FIB for prototyping.

## TEM Characterization of Etched Si Nanopillars Prepared by Small Angle Cleavage Technique

Christian Zaubitzer<sup>a</sup>, Sabine Grözinger<sup>a</sup>, Andrey Chuvilin<sup>a</sup>, Ute Kaiser<sup>a</sup>  
Rainer Enchelmaier<sup>b</sup>, Andreas Ladenburger<sup>b</sup>, Klaus Thonke<sup>b</sup>, Rolf Sauer<sup>b</sup>

<sup>a</sup>Materialwissenschaftliche Elektronenmikroskopie, Universität Ulm, 89069 Ulm, Germany

<sup>b</sup>Abteilung Halbleiterphysik, Universität Ulm, 89069 Ulm, Germany

Silicon nanopillars were produced by CF<sub>4</sub> based highly anisotropic reactive ion etching (RIE), utilizing a sub-monolayer coverage of gold colloidal particles with 50 nm diameter as etching mask. The shrinkage of these nanopillars by subsequent dry thermal oxidation enables the fabrication of silicon nanostructures in the sub-10 nm regime. Such structure sizes are required for semiconductor devices, which make use of quantization effects. Silicon nanowires (SiNWs) are promising candidates for future device applications, e.g. in single-electron devices. The electrical properties of these nanostructures are strongly affected by etching-created defects and by their surface properties.

To characterize the defect structure of such nanopillars they are studied by means of transmission electron microscopy (TEM) in cross-sectional view. Applying the usual preparation technique by gluing pieces face-to-face, etching-related defects such as amorphization around the nanopillars can not be distinguished from the amorphous glue. Here we apply the Small Angle Cleavage Technique (SACT), which allows preparing cross-sections without the usage of glue. Another advantage is that no ion-beam thinning is needed, reducing the risk of artefact production.

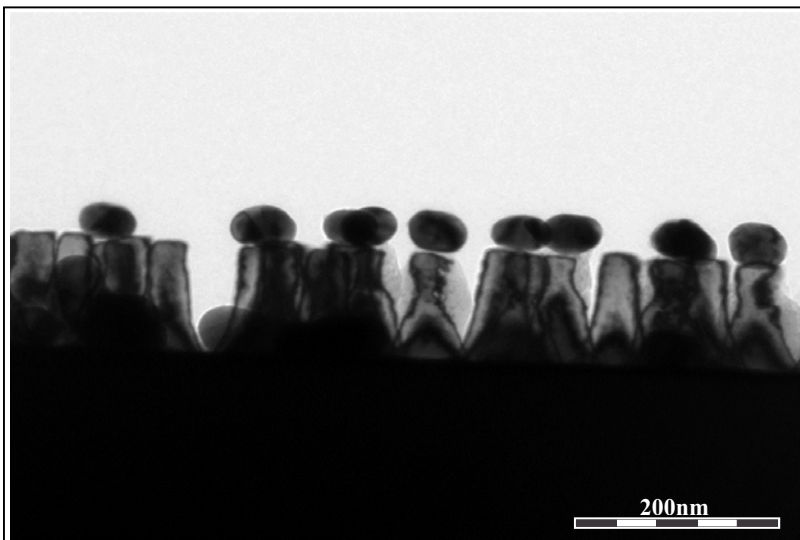


**Fig. 1:** TEM bright-field image of etched Si needles. The Au colloids were used as etching mask.

The TEM investigations are performed using a Philips CM 20 operating at 200kV. They show that the nanopillars are crystalline. Not all needles are capped by a gold particle, what could be the result of the TEM sample preparation. It was found that the Au particles are randomly oriented on the needles. A thin amorphous layer of about 2-4 nm thickness covers the whole needle. Further electrical measurements will be interpreted in the light of these results

### Acknowledgements:

The work has been supported by the DFG, Sonderforschungsbereich 569.

## Microscopy from milli- to nanometer scale – a simple preparation protocol for multimodal imaging of tissue samples

Stefan S. Biel, Katrin Wilke, Klaus-Peter Wittern, Roger Wepf

R&D Beiersdorf AG, Research Microscopy, 20245 Hamburg, Germany

Histochemical investigation of tissue biopsies ideally requires an optimal structure preservation at the light (LM) and electron microscopic (EM) level. Although cryo-immobilisation by high-pressure freezing provides the best structural preservation, it is routinely used only for EM investigations. For light microscopy chemical fixation or cryo-fixation protocols with low structural preservation have been established. These invasive fixation protocols have the drawback of introducing unpredictable fixation artefacts. Therefore, comparative histopathological (LM) and ultrastructural (EM) results are usually obtained from parallel sample preparations that have not been prepared identically and only allows to compare similar, but never exactly the identical structure.

To overcome these limitations, we modified a freeze-substitution protocol (FS), in order to investigate resin-embedded cryo-immobilised tissue by confocal laser scanning microscopy (CLSM) prior to EM examination. This is facilitated by the addition of specific fluorescent dyes during the FS exchange step. Using selective binding properties of various dyes to different cellular structures, specific structures of the tissue block can be depicted by CLSM. Subsequently, these specific structures are selectively prepared for follow-up investigation by EM. Antibody binding is not impaired by this modification and hence allows histochemical investigation at LM and EM level.

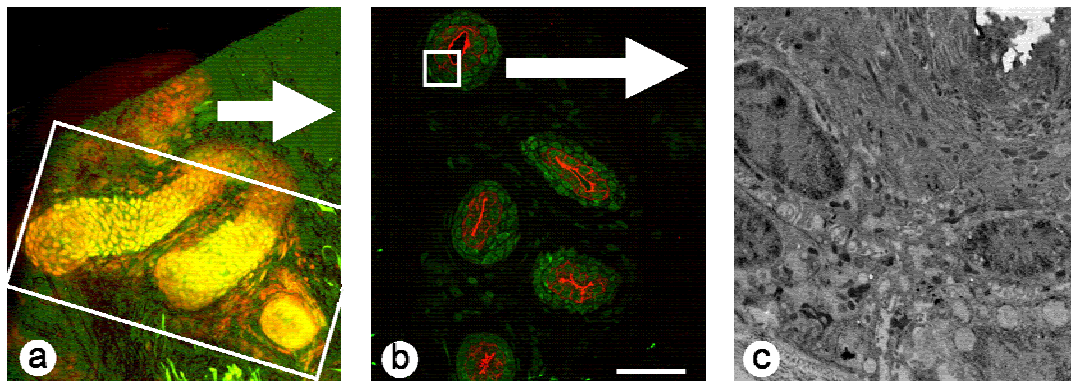


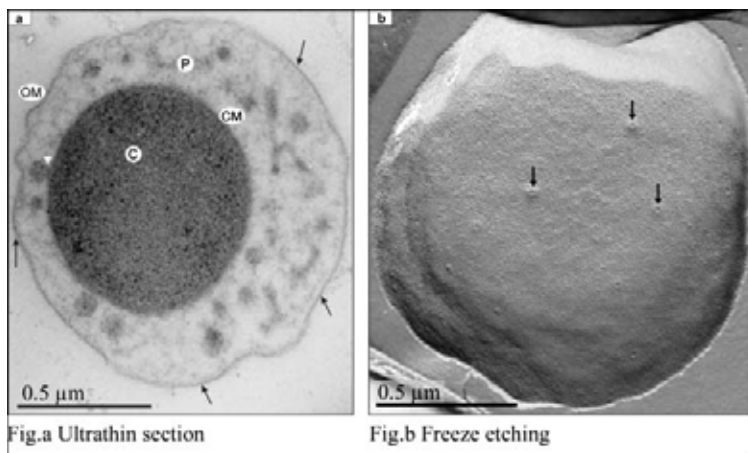
Figure 1: Investigation of the same sweat duct at different microscopic levels. (a) CLSM imaging of the area of interest. (b) Immunolabelling for milk fat globule. The milk fat globule label (red) is restricted to the luminal part of the sweat duct while the phosphine signal (green) is visible in the nuclei of all cell layers in the duct. (c) TEM investigation shows that also the ultrastructural details of the sample are well preserved. Scale bar: 50  $\mu\text{m}$

## The Outer Membrane of *Ignicoccus* – Analysis of its Structure by Cryo-Fixation/Thin-Sectioning, Freeze-Etching, and Electron Tomography

T. Burghardt, D. J. Näther, H. Huber and R. Rachel

University of Regensburg, Lehrstuhl für Mikrobiologie, Universitätsstr. 31, D-93053 Regensburg, Germany

Cells of the Crenarchaeot *Ignicoccus* are strict chemolithoautotrophs, using H<sub>2</sub> as electron donor and S<sup>0</sup> as electron acceptor, at T = 90°C. The outermost sheath of *Ignicoccus* cells does not contain a cell wall polymer, but is a novel type of outer membrane, the first and only one described for an archaeal cell [1,2]. This membrane is of special interest, as it is involved in cell-cell interaction and metabolite transport to *Nanoarchaeum equitans*. *Nanoarchaeum equitans*, the smallest archaeon known today (diameter: about 0.4 µm), only grows in a kind of symbiosis with *Ignicoccus* [3].



We have analysed the structure and (bio-) chemistry of the outer membrane of *Ignicoccus*: it was identified by electron microscopy in freeze-etch experiments where the two membrane leaflets become separated. In ultrathin sections following high-pressure freezing, this membrane is asymmetric, with a densely stained outer leaflet and a weakly stained inner one. It contains archaeal lipids, derivatives of glycerol phytanyl di-ether lipids but no tetra-ether lipids [4], and, in addition, two kinds of protein complexes:

- (a) numerous tightly packed copies of a protein complex, each 7 nm in diameter;
- (b) few large pores, 24 nm in diameter (Fig.b, arrows), structurally reminiscent to Secretin complexes of Gram-negative Bacteria.

The 7nm-complexes have an apparent mass of about 50 kDa [5] and can be dissociated into their monomers (M<sub>r</sub>: 6.2 kDa) in 2% SDS at T ≥ 110°C. A 3D reconstruction of the negatively stained outer membrane by electron tomography revealed that these particles are transmembrane complexes, arranged in small quasi-crystalline patches in which each complex contains a 2nm-pore. Further studies will focus on the possible function of these complexes, the structure of the large pores, and the interaction of the membrane with the S-layer of *Nanoarchaeum equitans*.

### References:

- [1] H. Huber et al, *IJSEM* **50** (2000) 2093-2100
- [2] R. Rachel et al, *Archaea* **1** (2002) 9-18
- [3] H. Huber et al, *Nature* **417** (2000) 63-67
- [4] U. Jahn et al, *Arch.Microbiol.* **182** (2004) 404-413
- [5] D.J. Näther and R. Rachel *Biochem.Soc.Trans.* **32** (2004) 199-203

## Serial Block-Face Sectioning and High Resolution Imaging of Biological Samples with a Crossbeam FIB / FESEM Microscope

C. Burkhardt<sup>1</sup>, P. Gnauck<sup>2</sup>, H. Wolburg<sup>3</sup>, W. Nisch<sup>1</sup>

1 NMI Natural and Medical Sciences Institute, Markwiesenstr.55,  
72760 Reutlingen, Germany

2 Carl Zeiss SMT, Nanotechnology Systems Division, Carl Zeiss Str.56,  
73447 Oberkochen, Germany

3 Institute of Pathologie, University of Tuebingen, Germany

Surface imaging of the block-face of embedded cells or tissue offers new possibilities for the investigation of ultrastructural details of biological samples [1]. By milling embedded samples inside a crossbeam microscope using a focused ion beam (FIB), it is possible to prepare a micro block-face at defined positions [2]. This micro block-face may be observed in-situ by low voltage field emission scanning electron microscopy (FESEM) at high resolution. Contrast and resolution are comparable to transmission electron microscopy (TEM) analysis of ultra-thin sections. SEM imaging is possible even while the ion beam is polishing the sample (live milling). In this way layers as thin as 10 nm may be removed sequentially by the ion beam and the new block-face may be imaged and added to a 3D image stack. The serial block face imaging can also be recorded in real-time and captured as video in an avi-file. From this data a 3D reconstruction of the sample may be obtained.

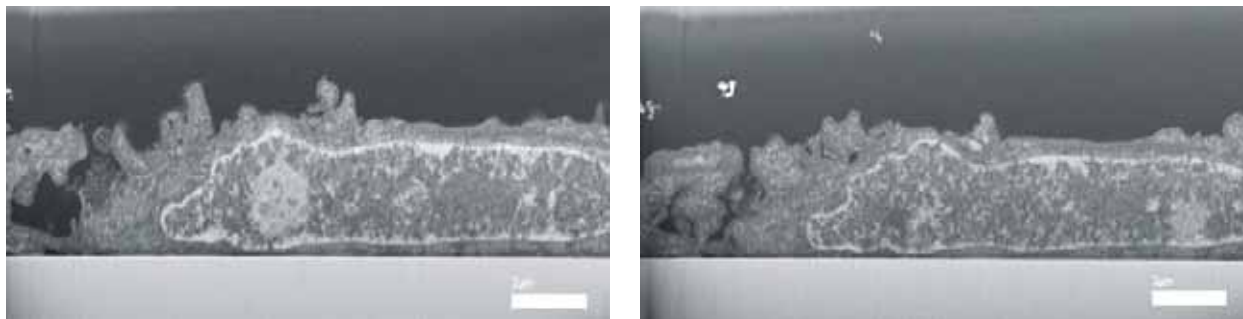
Beside site specific preparation of micro block-faces, the FIB technique allows to prepare the interface between hard materials of technical surfaces and adjacent layers of single cells or tissue. We present first results of this new technique of serial sectioning of different cells (osteoblasts, fibroblasts) grown on hard surfaces of implants and biochips. The samples were prepared with a standard EM protocol (fixation, staining, embedding) [3], which was modified to obtain a flat embedding, a prerequisite for the FIB technique.

### References

[1] N. Matzko, M. Mueller, *J Struct Biol.* (2004) 146(3):334-43.

[2] C. Burkhardt, W. Nisch, *Pract. Metallogr.* (2005) 42:161-171.

[3] F. Pfeiffer, B. Herzog, D. Kern, L. Scheideler, J. Geis-Gerstorfer, H. Wolburg, *Microelectronic Eng.* (2003) 67-68:913-922.



Secondary electron micrograph of the block face of an embedded fibroblast cell grown on a thin titanium film deposited on a silicon substrate. The sample was cross-sectioned and imaged in two different layers, scale bar: 2  $\mu\text{m}$ .

## **Electron Tomography In Conical Geometry: 3D Reconstruction Of Tissue Sections And Metal Replicas Of Membrane Surfaces.**

Francesca Cantele<sup>a</sup>, Salvatore Lanzavecchia<sup>a</sup>, Lorenzo Zampighi<sup>b</sup>, Nicholas Fain<sup>c</sup>, Ernest Wright<sup>b</sup> and Guido A. Zampighi<sup>c,d</sup>

<sup>a</sup>Dept. of Structural Chemistry, University of Milano, via G. Venezian 21, 20133 Milano, Italy

<sup>b</sup>Dept. of Physiology, UCLA, CA, USA

<sup>c</sup>Dept. of Neurobiology, UCLA, CA, USA

<sup>d</sup>Jules Stein Eye Institute, Los Angeles, CA, USA

In an effort to explore the limit and potential of electron tomography we have developed a reconstruction strategy based on conical geometry, a method that has been described theoretically, but never used because of technical and computational limitations. To resolve these problems, we used a rotating/tilting stage (designed and built by Gatan) to collect conical series, and developed a strategy for 3D reconstruction and the software to implement it [1]. The alignment strategy was based on the manual tracking of particles, followed by angular refinement (up to 0.1 degree), which uses projection matching. 3D reconstruction was performed by using weighted back projection (WBP) in different implementations. We tested R\* weighting for conical geometry and algorithm for arbitrary geometry [2]. We also developed a new strategy to subdivide the target volume into small regions that were reconstructed separately. With arbitrary geometry, this contrivance affects the weighting scheme in such a way that high frequency components are not under-weighted, as happens when the standard algorithm is applied to large volumes. Auxiliary tasks include filling the missing region by means of projection onto a convex set (POCS), and estimating the resolution using Fourier shell correlation of independent reconstructions from odd and even projections of the conical series.

First, we reconstructed metal replicas of liposomes reconstituted with small (120 kDa) aquaporin-0 (AQP0) tetramers that function as water channels. 3D reconstructions of these thin (~1.5 nm) and highly scattering metal replicas permitted us to describe the size and shape of functional AQP0 tetramers inserted in phospholipid bilayers. In replicas of lens fibers, we reconstructed nuclear membranes and demonstrated the organization of the nuclear pores as well as the intra-membrane particles embedded in the nuclear membranes.

We also applied conical tomography for reconstructing plastic sections of rat somato-sensory cortex (~50 nm in thickness). Using series comprised of 72 projections spaced by 5 degree azimuths, we obtained reconstructions of chemical synapses that permitted resolving the tri-layer structure of membranes (~4 nm) resulting from the bilayer organization of phospholipids [3].

Finally, in an effort to understand the relationship between geometry and resolution in electron tomography, we are comparing reconstructions from single axis, dual axis and conical geometry using experimental and computer simulations methods.

References:

[1] Lanzavecchia S. *et al.*, J. Struct. Biol. 149 (2005) 87-98.

[2] Radermacher M., J. Electron Microsc. Tech. 9 (1988) 359-394.

[3] Zampighi G.A. *et al.*, J. Struct. Biol. (2005) *in press*.

## How do adherens junctions in cellular networks of tendons change with age?

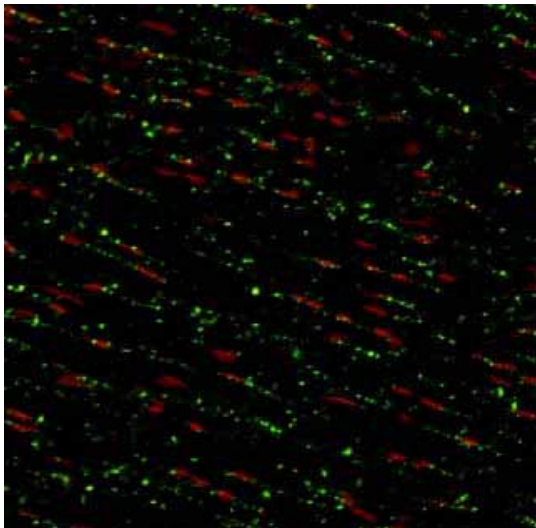
R. Fleck\*, J. Claridge, R. Stanley, J. Ralphs and J.C. Patterson-Kane

\*NIBSC, Blanche Lane, South Mimms, Herts, EN6 3QG; The Royal Veterinary College, Hawkshead Lane, Hatfield, Herts, AL9 7TL

Confocal scanning laser microscopy (CSLM) has been used rarely to examine tendon structure. Adherens Junctions (AJ) are cell-to-cell adhesion junctions which contribute to tissue integrity maintenance and mechanotransduction in many tissues, although their role in tendon is poorly defined. We have shown the presence of discrete, punctate foci of two component proteins of AJs: vinculin - a cytosolic adapter protein - and n-cadherin - a glycoprotein anchor which binds cells together - in equine flexor and extensor tendons. The incidence of equine tendon injury increases significantly with age, and thus there is a need to understand the age-related changes in the cellular populations of these structures.

Cryosections of equine tendon were labelled using an indirect immunofluorescence technique and visualised by CSLM using a Leica TCS SP2 confocal on a Leica DMRE microscope, connected to a computer running Leica Qwin Image Processing and Analysis software, version 3.0.0. A x20 objective lens and dual channel fluorescence using fluorescein (FITC) and rhodamine (TRITC) filter settings (laser wavelength 488nm and 543nm) was used. Five 10 $\mu$  Z-stacks were taken of each cryosectioned sample.

Image Pro-Plus 5.0 (Media Cybernetics, MD, USA) was used to analyse two pictures from each channel per Z-stack, giving a total number of 10 repeats per channel per sample.



Green vinculin and red nuclei of tendon

Numbers and sizes of tenocyte nuclei and vinculin and n-cadherin plaques within a fixed area of interest (AOI) (408pixels wide, 303pixels high; 0.1983mm<sup>2</sup> area per picture; 1.983mm<sup>2</sup> per sample) were calculated using a custom-designed macro to ensure repeatability. Accurate tenocyte and plaque counts were achieved by selecting an appropriate intensity range of 50-255. Images were then pseudo-coloured and a specific threshold value for pixel intensity was selected for tenocytes and plaques. An automated function was chosen to eliminate random single red pixels, to ensure the nuclear count was accurate.

Detailed examination of the microscopic organization of tendons by this technique allows quantitative analysis of age-related changes in expression of junction proteins.

## **TEM, SEM, Epifluorescence and Confocal Microscopy; Essential tools in the Standardisation and Control of Biological Medicines – Three Case Studies.**

Roland A. Fleck, Marisa Peyre, Mohammad A. Afzal, Caroline Vipond, Angela Rodgers and Glyn Stacey

National Institute for Biological Standards and Control, Blanche Lane, South Mimms, Potters Bar, EN6 3QG. E-mail: [rfleck@nibsc.ac.uk](mailto:rfleck@nibsc.ac.uk)

As biological medicines have developed so have the challenges of ensuring their safety. Even today emerging and postulated therapies continue to represent a moving target with ever changing safety concerns and needs. Multi-component and conjugate vaccines are becoming common and there is a general expectation that gene therapy and stem cell therapies will emerge, each requiring effective procedures for demonstrating and testing safety, effectiveness and efficacy if they are to become widely available.

Micro-spheres (MS) based on biodegradable poly-lactic or poly-lactic-co-glycolic acid polymers (PLA and PLGA) represent a promising technology for new vaccine delivery systems. However, some essential criteria have to be met before these vaccines could reach the clinical development stage. Key issues are the maintenance of formulation consistency ensuring the safety and the efficacy of every batch and their *in vivo* mode of action. Imaging techniques have been employed to evaluate formulation parameters, degradation kinetics and the uptake of a fluorescent PLGA model vaccine. We were able to assess the quality of the model vaccines by SEM and monitor their physical properties including polymer type, particle sizes and formulation stability. Furthermore, TEM and confocal microscopy allowed us to move on from the *in vitro* to the *in vivo* model gaining a better understanding of the mechanisms involved in the uptake and processing of MS by phagocytes.

Isolation of mumps virus on the continuous Vero cell line has proven convenient in a laboratory setting. However, they may not be very sensitive and may select for particular variants adapted from clinical specimens. This may adversely affect research relating to virulence, attenuation and pathogenesis. CaCo-2, PLC/PRF/5, MDCK, L-929, BCL-CF003 and MCF-7 cell lines were investigated for their sensitivity to infection with mumps virus. Immunofluorescent staining of the mumps nucleocapsid protein residues indicated that mumps was abundantly expressed in CaCo-2, PLC/PRF/5, MCF-7 and Vero cells. L-929, MDCK and BCL-CF003 showed only weak reactivity with the mumps antibody with differences in the expression pattern when compared with Vero. TEM revealed; cytoplasmic zones of nucleocapsid, viral budding and free virus. Of the cells tested CaCo-2, PLC/PRF/5 and Vero produced infectious virus with Vero and CaCo-2 the most permissive.

Imaging techniques including; confocal-, freeze drying- and electron-microscopy clearly allow detailed studies of biological medicines to be performed, often with the added value of immuno-specific labelling. These techniques also play a routine part in vaccine safety/efficacy testing, including; BCG, Flu and Meningococcal B outer membrane vesicle vaccines.

## **Cryo-Atomic Force Microscopy (AFM) for the Study of Ice Surfaces**

Marta Krzyzak, Kirsten Techmer, Susanne Hacke, Werner F. Kuhs

Dept. of Crystallography, Goldschmidtstrasse 1, 37077 Göttingen, Germany

The properties of ice surfaces are of interest in physics, chemistry, geosciences and for various technical applications. Consequently, the surface of ice has been subject to various experimental investigations: SEM, optical ellipsometry, NMR, Raman spectroscopy, measurements of interfacial electrical conductivity, measurements of adhesion strength and of the interface viscosity. More recently, Atomic Force Microscopy (AFM) was added to study synthetic ice surfaces with a high vertical resolution at the few nanometer-scale. Our interest is in surface studies of ice and snow to obtain information about crystallization and alteration processes, in particular the study of the formation and metamorphosis of natural snow. Beyond the high vertical resolution further advantages of AFM are the in-situ tests of some physical properties of ice like viscosity, micro-hardness or electric and ionic conductivity, all relevant to ice surfaces.

For our studies we used a PicoScan instrument of Molecular Imaging. Several technical problems needed to be solved to investigate the surface of ice in air at temperatures down to  $-30\text{ }^{\circ}\text{C}$ . A permanent temperature control near the ice surface including the neighbouring environment (to gauge sublimation and condensation artefacts) was fundamental to obtain useful surface images. Problems were also encountered with a freezing and/or a breaking of the tip caused by frost along the ice surface. To prevent water condensation upon the surface, the AFM investigations were performed in an environment of dry nitrogen gas inside a glove box. The air humidity was determined with an analogue hygrometer. The ice used was formed from distilled water. For the precise control of the ice temperature a regulated sample stage was used: Under the sample plate with a central hole a Peltier cooler was mounted, whose temperature was permanently controlled. The copper plate was fixed in the hole on the Peltier cooler with a thermally conductive paste. The samples were frozen onto the copper plate. The temperature on the ice surface was measured with an additional thermal sensor. The maximum temperature difference between the Peltier cooler and the ice surface in the range from  $-10$  to  $-25\text{ }^{\circ}\text{C}$  after 1 h amounted to  $0,1\text{ }^{\circ}\text{C}$ . The whole set-up was installed in a room of about  $20\text{ }^{\circ}\text{C}$ . The AFM investigations were made in contact mode using different types of cantilevers such as  $\text{Si}_3\text{N}_4$  with spring constants  $< 1\text{ N/m}$  as well as silicon cantilevers with spring constants of  $3\text{ N/m}$  and of  $< 1\text{ N/m}$ . At higher resolution, especially in non-contact mode, AFM-measurements were partly disturbed by vibrations within the building. Vibration problems also occurred during cooling of the glove box by an additional external cooling loop. Presently, an improved anti-vibration stage is under construction.

First AFM images of ice crystals were made in contact mode. Structures like grain boundaries between individual ice crystals and etch pits could be seen. Comparative surface investigations were made by SEM indicating that etch pits of up to some hundred nanometer in depth are a typical feature of the ice studied. The beginning of sample heating due to the scanning with the tip can be detected after some minutes which finally leads to melting of the surface. This process is most likely provoked by the heat emission of the cantilever chip as indicated by the fact that the effect depends on the length of the cantilevers used.

### 3d Reconstructions of Sites where Synaptic Vesicles Accumulate in Insect Larvae

Gerd Leitinger<sup>a</sup>, Maria Anna Pabst<sup>a</sup>, Peter J. Simmons<sup>b</sup>, and F. Claire Rind<sup>b</sup>

<sup>a</sup>Institute of Cell Biology, Histology and Embryology, Centre for Molecular Medicine, Medical University of Graz, 8010 Graz, Austria

<sup>b</sup>School of Biology, University of Newcastle upon Tyne, Newcastle upon Tyne, UK

To track changes in the location of the sites where synaptic vesicles accumulate, we labelled specific synaptic proteins in larvae of the locust *Schistocerca gregaria*.

We used primary antibodies directed against two synaptic proteins of the fruit fly, *Drosophila*: synapsin [1] (a protein responsible for the formation of the reserve pool of synaptic vesicles), and synaptotagmin [2] (a protein of the vesicle membrane thought to be a calcium sensor of the synapse). We applied these antibodies to parts of the locust brain that contain the ocellar nerves and ocellar tracts (parts of the visual system) and visualised them using fluorescent secondary antibodies. Fluorescence was detected using a Leica confocal microscope. We then used image restoration software (SVI Huygens), and 3d-reconstructed stacks of optical sections with Amira software.

The results show that both antigens mostly co-localise within the ocellar nerves and ocellar tracts in both larvae and adult locusts; this indicates that both molecules accumulate early at presumed synaptic sites. There are, however, changes in the distribution of these sites within the ocellar visual system during postembryonic development. In early instars, most immunoreactivity is found in the ocellar nerves, which connect the single eyes (ocelli) with the brain, and the two proteins appear evenly distributed throughout the ocellar tracts (extensions of the ocellar nerves within the brain). In contrast, in later instars and adult locusts, there appear to be more presumed synaptic sites within the ocellar tracts and fewer sites within the ocellar nerves.

#### References:

[1] BR Klagges, G Heimbeck, TA Godenschwege, A Hofbauer, GO Pflugfelder, R Reifegerste, D Reisch, M Schaupp, S Buchner, E Buchner, J Neurosci 16 (1996) 3154-65.

[2] JT Littleton, HJ Bellen, and MS Perin, Development 118 (1993) 1077-88.

Funded by the Austrian Science Foundation (Project P17874-B05).

## Confocal imaging of aberrant nodule ontology in legume symbiotic mutants using SYTO 13.

E. Maximova<sup>1</sup>, V. Voroshilova<sup>2</sup>, N. Sandal<sup>3</sup>, J. Stougaard<sup>3</sup>, and M. Udvardi<sup>2</sup>

<sup>1</sup>Institute of Plant Physiology, MD 2002 Chisinau, Republic of Moldova

<sup>2</sup>Max Planck Institute of Molecular Plant Physiology, 14476 Golm, Germany

<sup>3</sup>University of Aarhus, Aarhus, Denmark

Symbiotic nitrogen fixation (SNF) in legumes results from a series of signal exchanges that trigger development of root nodules, which eventually contain millions of nitrogen-fixing rhizobium bacteroids [1]. A variety of plant mutants are known that are impaired at different stages of nodule development/differentiation. Confocal laser-scanning microscopy (Leica, Germany), using the fluorescent nucleic-acid stain SYTO 13 (Molecular Probes, Inc., Eugene, OR, USA) [2] was employed in this study to reveal ontological defects in three symbiotic mutants of *Lotus japonicus*: *sym6*; *sym11*; and *sst1-1* (*sym13*). SYTO 13 enabled visualization of the bacterial infection process as well as plant cell meristematic activity and cellular differentiation during nodule development in wild-type and mutant plants. The *sym6* mutant formed only a few small nodule-like structures (bumps) on the root after inoculation with rhizobia. Microscopic analysis revealed that the plant cells in these structures were not infected by bacteria. This was confirmed using a rhizobial strain constitutively expressing the *GusA* gene. In contrast, *sym11* formed small white ineffective nodules, which underwent premature senescence. Finally, *sst1-1* developed pinkish nodules, which also senesced prematurely. By 28 days post-inoculation, *sst1-1* contained degrading symbiotic structures in the central part of the nodule (Fig. 1). This study indicates that multiple plant genes are required for nodule development and persistence. Map-based cloning of these genes [3] will clarify their exact roles in the future.

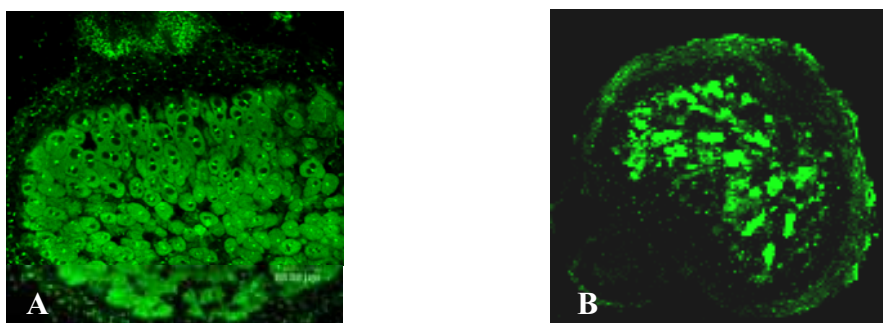


**Fig.1. Morphology of root symbiosis in *Lotus japonicus* at 28 days post-inoculation in wild-type (A) and *sst1-1* mutant plants (B).**

### References

- [1] Limpens E., Bisseling T. 2003. Current Opinion in Plant Biology 6:343-350.
- [2] Guindulain T., Comas J., Vives-Rego J. 1997. Applied and Environmental Microbiology. 63: 4608-4611.
- [3] Krussel L., Krause K., Ott T., Desbrosses G. et al. 2005. The Plant Cell. 17: 1625-1636.

## Vesicles of Glycosylated Cyclodextrin for Specific Recognition of Cellular Receptors as Investigated by Combination of Light Scattering and Cryo-EM

Antonino Mazzaglia<sup>ab</sup>, Antonio Valerio<sup>c</sup>, Valentina Villari<sup>d</sup>, Anna Rencurosi<sup>e</sup>, Luigi Lay<sup>c</sup>, Luigi Monsù Scolaro<sup>b</sup>, and Norberto Micali<sup>d</sup>, and Nadia Santo<sup>f</sup>

<sup>a</sup>ISMN-CNR, Unità di Messina, 98166 Messina, Italy

<sup>b</sup>Dipartimento di Chimica Inorganica, Chimica Analitica e Chimica Fisica, 98166 Messina, Italy

<sup>c</sup>Dipartimento di Chimica Organica ed Industriale, 20133 Milano, Italy

<sup>d</sup>IPCF-CNR, Sezione di Messina, 98166 Messina, Italy

<sup>e</sup>ISTM-CNR, 20133 Milano, Italy

<sup>f</sup>Interdepartmental Centre of Advanced Microscopy, 20133 Milano, Italy

Specific recognition of cell-targeting systems (e.g. host carrier, self-aggregated species) is a major ambition in the applications of supramolecular science to pharmaceuticals. One of the main challenge is to create self optimising cooperative systems having a controlled number of components, shape, and size able to target complexed drugs to the their biological site of action. As host carrier molecules, in the past decade, cyclodextrins (CDs) have also been modified with glycosyl groups (i.e. epitopes) for binding to saccharide-specific protein as cell-wall lectins. Recently, some of us demonstrate that specially designed amphiphilic  $\beta$ - CDs are capable of forming micellar aggregates or bilayer vesicles as less immunogenic (due to their oligo-ethylene oxide exterior) and more versatile drug encapsulators than a single CD molecule [1-3]. Vesicles of amphiphilic  $\beta$ - CDs with alkylthio chains of different length (alkyl is hexyl or hexadecyl) at the primary-hydroxyl side and glycosylthio-oligo-(etyleneglycol) units at the secondary-hydroxyl side were prepared and their multivalent effects in binding with lectins was assessed [4]. Above cmc, they form vesicles, as indicated by the scattered intensity profile from Elastic Light Scattering measurements (ELS), in the range of 150-250 nm as measured in dilute solutions through Quasi-Elastic Light Scattering (QELS). The hydrodynamic radius of more hydrophobically substituted CD are similar to that of thiohexyl CDs, as well as the radius obtained from the fit of the intensity profile with the model of a spherical vesicles. By ELS a substantial difference is observed in the value of the absolute intensity: at the same CD mass concentration. The most hydrophobically substituted CDs vesicles are more massive than the shortest ones. Cryo-electron microscopy confirmed this result. A dispersion of CDs, prepared at the same condition of ELS procedure, was rapidly frozen by immersion in liquid ethane and observed at the transmission electron microscope Leo 912ab (Zeiss) under low-electron dose irradiation. These results would get more insights on the lyotropic properties of investigated systems: no perturbations such as immobilization and staining were introduced. Besides selectivity in molecular recognition of glycosyl-CD versus specific cellular receptors would be modulated by hydrophobic and hydrophilic balance of the glycol-carrier.

<sup>1</sup>Ravoo B.J., Darcy R., *Angew. Chem., Int.Ed.* **2000**, 39, 4324.

<sup>2</sup>Lombardo D., Longo A., Darcy R, Mazzaglia A., *Langmuir*, **2004**, 20,1057-1064.

<sup>3</sup> Mazzaglia A., Donohue R., Ravoo B.J., Darcy R, *Eur.J.Org.Chem.* **2001** 1715-1721.

<sup>4</sup> Mazzaglia A.; Forde D.; Garozzo D.; Malvagna P.; Ravoo B.J and Darcy R., *Org. Biom. Chem.*, **2004**, 2, 957.

## Attempts at 3D cryo-TEM of different physiological states of arthropod hemocyanin and related hemolymph proteins

Ulrich Meissner, Andreas Martin, Michael Stohr, Jürgen Markl

Department of Zoology, Johannes Gutenberg University, 55099 Mainz, Germany

The investigation of meaningful physiological states of large proteins such as enzyme complexes by electron microscopy is well established. Nevertheless, 3D reconstruction from TEM images is mainly directed to the structure of intact molecules, rather than the precise functional states that a protein can adopt. That structural details can correlate with the physiological state of a protein has been described for the hemocyanin from the tarantula *Eurypelma californicum* by SAXS investigation [1] [2], and from cryo-TEM data for the *E. coli* chaperone GroEL [3].

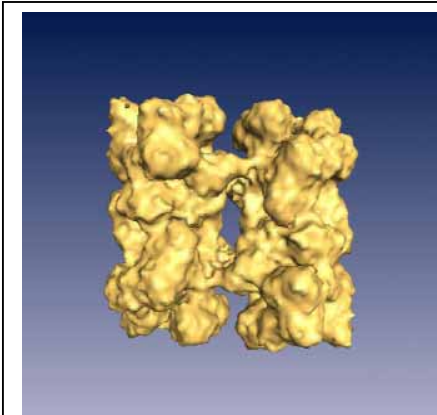


**Fig. 1: Oxygenated form of Tarantula hemocyanin**  
Reconstructed from micrographs prepared and taken under defined physiological conditions

The transport of oxygen in the hemolymph of many arthropod or molluscan species is facilitated by large copper-containing respiratory proteins known as hemocyanins. Arthropod hemocyanins and related proteins are members of the hemocyanin superfamily, such as phenoloxidases and insect storage proteins, which are hexamers (1x6-mers) or oligo-hexamers (2x6- to 8x6-mers) of a 75 kDa subunit. Recently, we have published an 8 Å reconstruction of the 1x6 hemocyanin of *Palinurus elephas* (PeH) [4]. Currently we are studying the larval serum proteins LSP1 and LSP2 from *Drosophila melanogaster*; they lack a copper active site. The reconstructions of these “storage proteins” show similarities, but also significant differences to the PeH molecule. 3D data of resolutions better than 15 Å (10 Å using 3-sigma criterion) on the 4x6-mer hemocyanin of the tarantula *Eurypelma californicum* (Fig. 1) and the 8x6-mer hemocyanin of the horseshoe crab *Limulus polyphemus* are now also available. Both hemocyanins are currently being examined under oxy and deoxy conditions.

Here we will present selected data of our recent studies on several members of the arthropod hemocyanin superfamily, obtained by cryo-electron microscopy and single particle analysis.

### References:

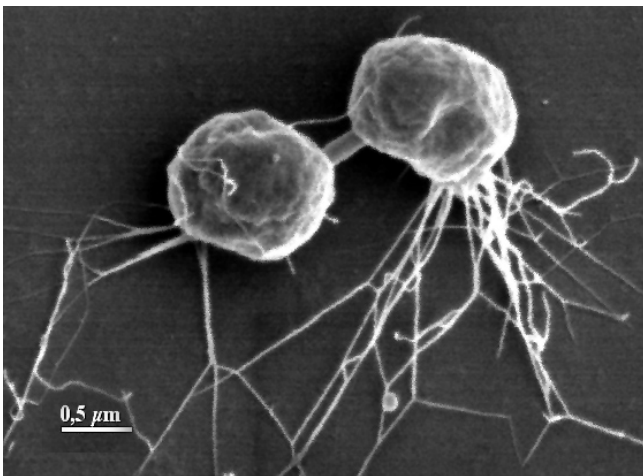
- [1] Decker et al., FEBS Lett. 393 (1996) 226-230.
- [2] Hartmann et al., Eur. Biophys. J. 30 (2001) 471-475.
- [3] Ludtke et al., Structure 12 (2004) 1129-1136.
- [4] Meissner et al., J. Mol. Biol. 325 (2003) 99-109.
- [5] Supported by grants to J.M. from the DFG (Ma843) and the Stiftung Rheinland-Pfalz für Innovation (15202386261548)

## Flagella of *Pyrococcus furiosus*: not only made for swimming – a correlative microscopy study

D. J. Näther, \*G. Wanner, R. Wirth, and R. Rachel

University of Regensburg, Lehrstuhl für Mikrobiologie, Universitätsstr. 31, D-93053 Regensburg;  
\*Institute for Botany, University of Munich, D-80638 München, Germany

*Pyrococcus furiosus* has been described in 1986 as a representative of a new archaeal genus [1]. This marine hyperthermophilic archaeum was named for its ability of rapid swimming and growth at about 100°C ('rushing fireball'). Numerous surface appendages, up to 50 per cell, have been observed to be inserted monopolarly on the coccoid cell and were, accordingly, named 'flagella'. In a correlative approach using high temperature (95°C) light microscopy under oxygen-free conditions, as well as scanning electron microscopy and transmission electron microscopy of cryo-fixed, freeze-etched cells, we show striking micrographs demonstrating that these 'flagella' are multi-functional organelles: We observe:



*The establishment of cell-cell connections:*  
'Flagella' can assemble into cable-like structures which interconnect cells. Such cell connections are observed by high temperature fluorescence light microscopy and by electron microscopy, especially in cultures at stationary growth phase, and are not rare. Up to 2 to 5% of cells can form such connections, resulting normally in pairs of cells. In few cases, also triplets have been observed.

*The adherence to surfaces:*  
'Flagella' are expressed especially on cells growing on various (but not all) surfaces

provided in culture bottles. They allow the adherence and establishment of biofilms, e.g. on sand grains from the beach of Porto di Levante, Vulcano, Italy – the place from which *P. furiosus* originally was isolated – and also on carbon films.

The flagella of *P. furiosus* cells are, therefore, multifunctionally cell surface organelles. They may be used for swimming [2]. As shown here, the cocci also use them for formation of cell-cell connections and for adherence to surfaces.

### References:

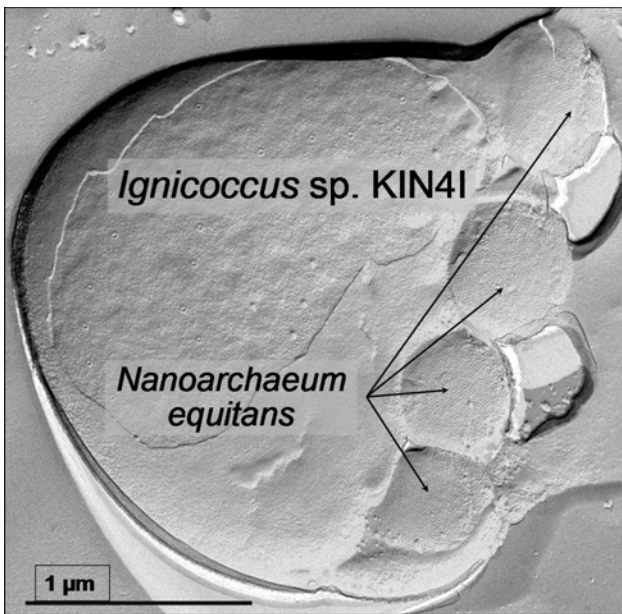
- [1] Fiala G. and Stetter K.O., Arch.Microbiol. 145 (1986) 56-61
- [2] Bardy S. et al., Microbiol. 149 (2003) 295-304

## Structure of the cell-cell interaction site between two hyperthermophilic Archaea, *Ignicoccus* and *Nanoarchaeum*

R. Rachel, T. Burghardt, D. J. Näther, A. Briegel\*, W. Baumeister\*

University of Regensburg, Lehrstuhl für Mikrobiologie, Universitätsstr. 31, D-93053 Regensburg;  
\*MPI for Biochemistry, Molecular Structural Biology, D-82152 Martinsried, Germany

*Nanoarchaeum equitans* is the smallest archaeon known today, with a cell diameter of about 0.4  $\mu\text{m}$  and a volume at about 0.034  $\mu\text{m}^3$  (~1% of an *E.coli* cell). It can only be cultivated at a temperature of 80 to 90°C under anoxic conditions in the presence of and in contact to a member of the genus *Ignicoccus*, *I. sp.* strain KIN4I [1]. In the analysis of the *N.equitans* genome, genes for several basic biosynthetic and metabolic pathways could not be identified, and are possibly missing at all [2]. Mutagenesis studies for understanding the kind of the interaction are not feasible, at present. Therefore, we have started to study the interaction by physiological experiments, i.e. by providing *Ignicoccus* cells with labelled substrates and tracing the fate of the metabolites.



In a second approach, we analyze the ultra-structure and composition of the molecules involved in the physical interaction. To this end, we have studied the dominant surface structures of both cells by electron microscopy and (bio-) chemical methods. *N.equitans* cytoplasmic membranes contain glycerol phytanyl di-ether and tetra-ether lipids [2]. The lipid composition is very similar to *Ignicoccus*, supporting the view that the lipids are taken up from the host, in order to compensate the lack of biosynthetic capabilities of *N.equitans* [3]. *N.equitans* cells are covered by an S-layer with hexagonal symmetry as shown by electron crystallography. It is composed of a 100 kDa glycoprotein. In contrast, the outermost sheath of *Ignicoccus sp.* KIN4I is an outer membrane, the first (and so far only one)

described for an archaeal cell [4]. Ultrathin sections of high-pressure frozen, freeze-substituted cells show a tight contact between the *Ignicoccus* outer membrane and the *N.equitans* S-layer at the site of interaction. Further studies will focus on the detailed analysis of the cell-cell interaction site by tomography and on the biochemistry of the membrane proteins which might be involved in the physical interaction and the exchange of metabolites.

### References:

- [1] Huber H. et al, Nature 417 (2002) 63-67
- [2] Jahn U. et al, Arch.Microbiol. 182 (2004) 404-413
- [3] Waters E. et al, PNAS 100 (2003) 12984-12988
- [4] Rachel R. et al, Archaea 1 (2002) 9-18

## Crystallography of Self-Assembly Particles Studied by Cryo-TEM

*L. Sagalowicz\*, M. Michel, M. E. Leser and H. J. Watzke.*

Nestlé Research Center, Vers-Chez-Les-Blanc, CH-1000 Lausanne 26, Switzerland

\*E-mail: [Laurent.Sagalowicz@rdls.nestle.com](mailto:Laurent.Sagalowicz@rdls.nestle.com)

Amphiphilic molecules such as monoglycerides, phospholipids form spontaneously self-assembly structures when present in an aqueous and/or oleic environment. Due to their hydrophilic/hydrophobic compartmentalisation these self-assembly structures can incorporate at the same time hydrophilic and lipophilic molecules of various sizes, molecular structure and polarity. Monoglyceride self-assembly structures were shown to be an excellent entrapment medium for flavor molecules and can be used as carrier systems for nutritionally active compounds. Self-assembly nanostructures were used to control flavor formation occurring during Maillard reaction. The yield in Maillard reaction products from amino-acids and sugars in a monoglyceride w/o microemulsion ( $L_2$  phase) and in a bi-continuous cubic phase was shown to be remarkably higher and different than in water [1].

For practical applications, bulk self-assembly structures have to be dispersed into water in form of sub-micron particles. Homogenizing a mixture of monolinolein [2] or monoolein [3], and Pluronic F127 in water using ultrasound leads to the formation of dispersed reversed bicontinuous cubic phases.

In this study, it is shown that cryo-TEM (Fig.1) and tilting experiments can be used to identify the internal structure and the space group of dispersed self-assembly structures. In particular the presence of the 111 reflection enables to differentiate between two different types of cubic structures having the space group  $Pn3m$  or  $Im3m$ . In addition, mechanisms of particle stabilization are proposed.

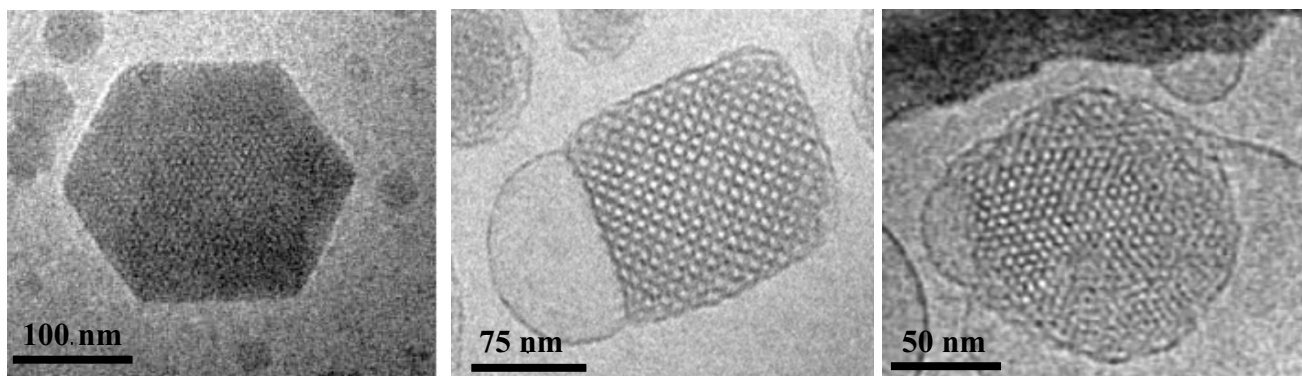


Figure 1: Particles with different internal self-assembly structures, (left) reversed hexagonal, (center) reversed bicontinuous cubic with a space group  $Im3m$  and (right) reversed bicontinuous cubic phase with a space group  $Pn3m$

### References

1. S. Vauthey, Ch. Milo, N. Garti, M. E. Leser, and H. J. Watzke. *J. Agric. Food Chem.*, 2000. **48**(10): p. 4808-4816.
2. L. de Campo, A. Yagmur, L. Sagalowicz, M. E. Leser, H. J. Watzke and O. Glatter, *Langmuir*, 2004 **20**(13): 5254-5261.
3. J. Gustafsson, H. Ljusberg-Wahren, M. Almgren and K. Larsson. 1997, *Langmuir* 13: 6964-6971.

## **Structural Analysis of a Newly Identified Inclusion at the Front of Blebbing Walker Carcinosarcoma Cells**

D. Vanhecke, Eggli, P., Graber, W., Keller, HU., Studer, D.

Institute of Anatomy, University of Bern, 3000 Bern 9, Switzerland

The development of a new specimen preparation system results in a faster and gentle transfer of samples to a Leica EMPACT high-pressure freezer (Leica, Vienna, Austria) is accomplished. The native structure is better preserved due to this technical breakthrough (commercialised by Leica, Vienna, Austria), since sample preparation can be performed faster before cryo-immobilization. The ultrastructure of Mammalian cells was improved compared to that of conventionally fixed specimens when using this sampling method.

Here, we describe a large frontal inclusion in the non-adherent metazoan Walker carcinosarcoma cell line. Initially observed by differential interference contrast (DIC) an entity at the front of the cell is observed, typically in the neighbourhood of blebs. The inclusion is vacuole-like, but fluorescent dyes, as well as transmission electron microscopy failed to show a surrounding membrane. The term “pseudovacuole” (PV) was chosen for its resemblance with a vacuole and to emphasize the difference from it. Light scanning microscopy (LSM) of living cells stained with fluorescent trackers showed high levels of the positively charged amino acid lysine, while a marker for nucleic acids revealed the pseudovacuoles as a nucleic acid-free cytoplasmic region.

Transmission electron microscopic (TEM) micrographs showed unstained almost empty zones in chemical fixed Walker carcinosarcoma cells. Our sampling system allowed specimen preparation before cryofixation of cell pellets within 30 seconds. TEM micrographs of high pressure frozen, freeze-substituted and resin embedded samples revealed similar zones as seen in chemically fixed cells. However, in the latter case the zones are not empty. Albeit faintly stained, a loose structured organization, unrelated to membranes, is recognizable. Cell organelles (e.g. mitochondria and vesicles) are absent in these zones. By labelling the cells with the lysine tracker prior to the cryotreatment, a co-localisation between the fluorescent pseudovacuoles (in LSM) and the organelle free zones (TEM) is found. Therefore, the faintly stained zones in TEM are pseudovacuoles.

We can only hypothesize about the function of the pseudovacuoles. It's location, content, and behaviour points in the direction of a possible involvement in bleb formation, e.g. as an osmotic tool regulating intracellular pressure prior to bleb protrusion. The data gathered so far suggest that this entity would act according to Ling's fixed charge hypothesis.

## Cryo-SEM in Cell Biological Research

Paul Walther<sup>a</sup>, and Monica Hagedorn<sup>b</sup>

<sup>a</sup>Central Electron Microscopy Facility, University of Ulm, D-89069 Ulm, Germany

<sup>b</sup>Department of Biochemistry, University of Geneva, CH-1211 Geneva-4, Switzerland

In a cryo-field emission SEM (**cryo-FESEM**) biological structures can be investigated in a near life-like state with a few nm resolution. Many artifacts of conventional chemical fixation and dehydration techniques can, thereby, be prevented. After being immobilized by cryo-fixation, the samples can be investigated in the cryo-SEM in the fully frozen-hydrated or in the partially freeze-dried (“deep-etched”) state. Bulk samples can be observed, since in the SEM the sample does not need to be transparent for the electron beam. This makes the SEM more versatile than the TEM since no thin-sectioning and no replica cleaning is necessary. Two approaches to investigate biological systems with cryo-FESEM are shown here: Investigation of cells and tissue (Figure 1) and investigation of macromolecular complexes *in-vitro* (Figure 2).

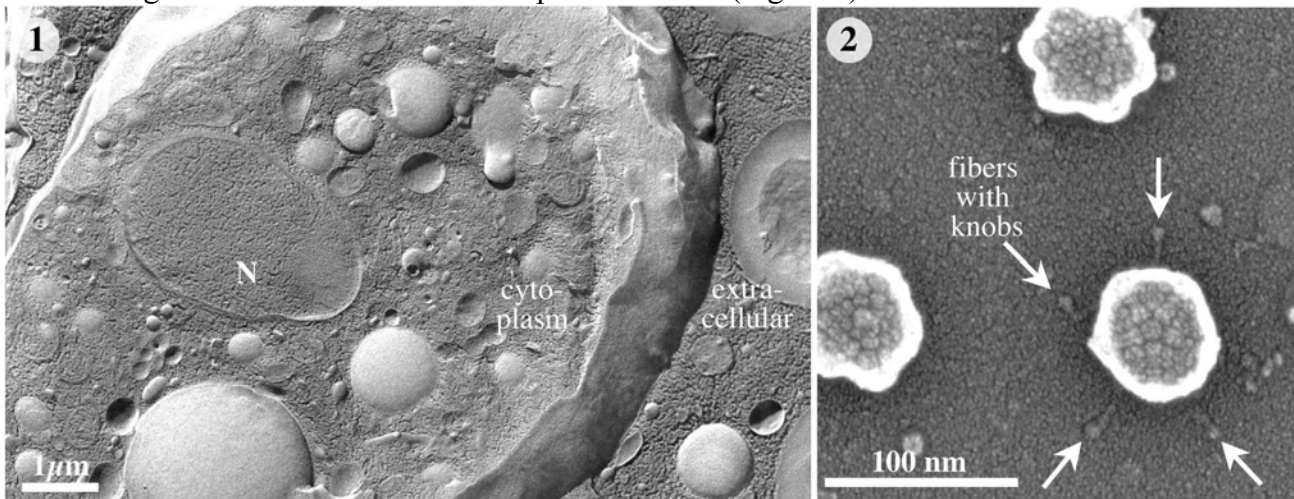


**Figure 1.** *Dictyostelium discoideum* was **high pressure frozen** in an **HPM compact 01** (Engineering Office M. Wohlwend GmbH, Sennwald, Switzerland). In order to visualize intracellular structures, the frozen cells were cryo-fractured. Then the samples were double-layer coated [1]. Platinum-carbon (3 nm) was electron beam evaporated at an angle of 45°. A backing layer of 5 nm carbon was evaporated perpendicularly. The carbon coat mechanically stabilizes the tissue pieces and enhances electrical conductivity. The frozen samples were mounted onto the Gatan cryo-holder 626. Specimens were investigated in the hydrated state at a temperature of 143 K in the Hitachi S-5200, in-lens field emission SEM using the **backscattered electron signal** in order to penetrate the carbon layer and to obtain an image of the underlying platinum that is in close contact with the biological structures of interest [2]. Both, the cytoplasm as well as the extracellular medium with very high water content, occur well frozen with no ice-crystal segregation patterns.

**Figure 2.** Adenoviruses were adsorbed on a carbon coated EM-grid and plunge-frozen, partially freeze dried at a temperature of 177 K and rotary coated with about 1 nm of tungsten by electron beam evaporation [3]. These samples were imaged with the **secondary electron signal** at 173K.

[1] P. Walther, *J. Microsc.* 212 (2003), 34-43.

[2] P. Walther, and J. Hentschel, *Scanning Microsc.* (1989) 3, (Suppl. 3), 201-211.

[3] R. Hermann, and M. Müller, *Scanning* 19 (1997) 337-342.

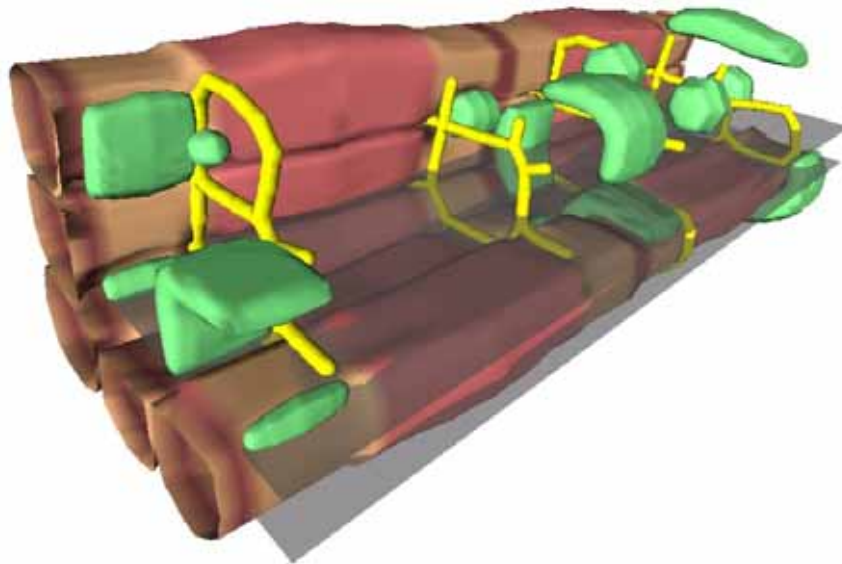
## Computer Modeling of Ultrastructure of Muscle Cells.

Ivan Zahradník<sup>a</sup> and Július Parulek<sup>b</sup>

<sup>a</sup> Institute of Molecular Physiology and Genetics, SAS, Vlárská 5, 833 34 Bratislava, Slovakia

<sup>b</sup> Department of Applied Informatics, Faculty of Mathematics Physics and Informatics, Comenius University, Mlynská dolina - pavilon M, 842 48 Bratislava, Slovakia

A computer modeling tool allowing construction of 3D geometrical models of living cells and their organelles with very high spatial resolution would facilitate understanding of physiological processes at cellular level. Here we describe an original approach to construction of models of skeletal muscle cells and their organelles such as myofibrils, mitochondria, t-tubules, sarcoplasmic reticulum, and sarcolemma at the ultrastructural level (resolution 1 nm, size of about 1000  $\mu\text{m}^3$ ).



Construction of the model is based on the theory of implicit surfaces and of their binary operations. Geometry of the muscle fibre and of its constituents is defined by means of parallel modeling planes perpendicular to the longitudinal axis of the fiber. In each modeling plane, the number, shape and topology of organelles is defined by means of skeleton elements and functionally represented polygons. The 3D model is obtained by implicit shape transformations of the defined objects between the modeling planes. This approach allows generation of the surfaces of organelles and explicit association of each model voxel with only one of the organelles. As a result, the condition of organelle exclusivity is fulfilled and the volume and surface densities of each organelle type in the model can be estimated. A simulated electron microscopic experiment can be performed using specific tools of the modeling application that allow generation of ultra-thin sections of specified thickness through the created model along any specified sectioning plane, and their projection to the image plane. A set of random sections can be used for a simulated stereological experiment. Visualization of the model and its components can be achieved at various levels of detail and complexity according to user's requirements.

*Supported by APVT – 51-31104*

# Fine Structural Quantification Based on 3D Reconstruction of Chloroplasts and Mitochondria of Field Grown Spruce and Pine Trees

Zellnig G., Zechmann B. and Perktold A.

Institute of Plant Sciences, University of Graz, Schubertstraße 51, 8010 Graz, Austria, Europe

Chloroplasts and mitochondria are central cytoplasmic organelles of plant cells participating in many metabolic processes associated with photosynthesis and respiration. Their structure is affected by different biotic and abiotic factors, however, in ultrastructural analyses the evaluation of the condition of the organelles is usually based on the 2D information of a limited number of ultrathin sections. Applying conventional transmission electron microscope (TEM) techniques it is not possible to specify the relations and amount of fine structures in the cell because ultrathin sections are too thin (80 nm) for evaluation of complete organelles in the TEM. 3D reconstructions of small organelles can be made by electron tomography but this method is restricted to a cell volume of about  $5 \mu\text{m}^3$  [1]. With the method applied in this work a 500-fold higher volume can be investigated, though section thickness restricts the resolution in z-direction to 80 nm. 2D measurements and 3D reconstructions of ultrathin serial sections showed that spinach chloroplasts react very sensitive to drought stress [2] and revealed significant differences in the content of fine structures depending on the daytime. Precise quantitative ultrastructural data of complete cell organelles are still missing or very rare, however, they proved to provide important information considering the biogenesis of chloroplasts or the heterogeneity of plant mitochondria.

In the present study mesophyll cell chloroplasts and mitochondria of one year old needles of field grown *Picea abies* and *Pinus canariensis* plants are investigated by ultrathin serial sectioning, TEM and digital image analyses. These procedures allow 3D reconstructions of complete organelles and the quantification of their fine structures on a very high level of resolution.

The investigated chloroplasts show a characteristic internal organization with differences in their average size and also in their internal structures. Chloroplasts of spruce needles have a mean volume of  $37 \mu\text{m}^3$  with a starch content of  $1.7 \mu\text{m}^3$ , a thylakoid volume of  $9.9 \mu\text{m}^3$  and a content of plastoglobuli of  $0.4 \mu\text{m}^3$ . In pine needles chloroplasts are significantly bigger ( $60 \mu\text{m}^3$ ) containing a higher volume of plastoglobuli ( $5.4 \mu\text{m}^3$ ) but less starch ( $1.3 \mu\text{m}^3$ ) in comparison to spruce chloroplasts. The differences in the starch and plastoglobuli content are even more pronounced when calculated as relative shares of the total chloroplast volume. 3D reconstruction and measurements also reveal differences in the mitochondria of both species indicating higher volumes ( $0.8 \mu\text{m}^3$ ) and surface areas ( $3.9 \mu\text{m}^2$ ) in pine when compared to spruce mitochondria ( $0.4 \mu\text{m}^3$  and  $2.8 \mu\text{m}^2$ , respectively).

The results obtained in this study supply quantitative and morphological fine structural data of complete chloroplasts and mitochondria of field grown plants, which enable a detailed comparison of the variation and distribution of fine structures.

## References:

- [1] Otegui M.S. & Staehelin L.A. 2004. *Planta* 218: 501-515.
- [2] Zellnig G., Zechmann B. & Perktold A. 2004. *Protoplasma* 223: 221-227.
- [3] Acknowledgement: This work was supported by the Austrian Science Fund, Project P15374-B03.

## Histochemical Observations on Effect of Lead in the Hepatopancreatic cells of *Palaemonetes turcorum* (Holthuis, 1961) (Crustacea, Decapoda)

Gözde Aydoğan, Mehtap Kutlu

Anadolu University, Faculty of Science, Department of Biology, 26470, Eskişehir, Turkey

The biological impact of heavy metals in aquatic systems has become a major concern in recent years. In the present study, effects of acute lead toxicity were investigated on different cell types of hepatopancreatic ceca in *Palaemonetes turcorum* since hepatopancreas could be a potential indicator organ for heavy metal toxicity.

The experiment consisted two groups; control group and experimental group. There were four replicates per group with five animals with an average body weight each of  $1.21 \pm 0.1$  g in each replicate. Animals were starved for 96 hr. Pb solutions were prepared by dissolving lead acetate in distilled water. The animals in experimental group were exposed to lead acetate at a single toxicant concentration  $LC_{50}$  (96 hr.) 0.394 mg/L. This concentration of  $LC_{50}$  was determined for *Gammarus pulex*, another freshwater organism sensitive to environmental pollution from Crustacea, by Kutlu and Sümer (1998) [1].

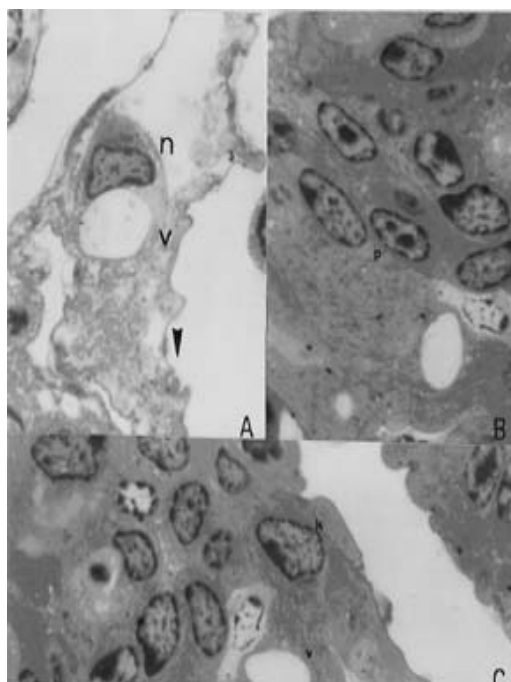


**Figure. 1:** Light micrographs of the hepatopancreatic cells in experimental group animals.

The crustacean hepatopancreas is composed of blind tubules, which are internally lined with a single epithelial layer delimiting the lumen and consisting of at least four cell types: E (embryonic), R (resorptive), F (fibrillar) and B (blister-like) cells. All the other cells are derived from E cells and have different functions in metabolic processes [2]. Different cell types in the hepatopancreas of *P. turcorum* were characterized. Effects of lead were observed in the hepatopancreatic cells after 96 hr exposure. There were loss of the cell outline, karyolysis in the nucleus (n) and enlarged vacuoles (v) in B cell (Fig.1 A). Changes in E cell were characterized with karyolysis (k) and vacuolation (v) in the cytoplasm (Fig.1C). Pyknosis (p) was observed in F cell (Fig.1 B). Dilation of cellular membran was observed in all cell types (Fig.1). Lead exposure results in serious damage on hepatopancreatic cells of *P. turcorum*. The major findings of this study rings up the importance of the hepatopancreas of *P. turcorum* as an accumulator of lead and an indicator organ for acute lead toxicity.

### References:

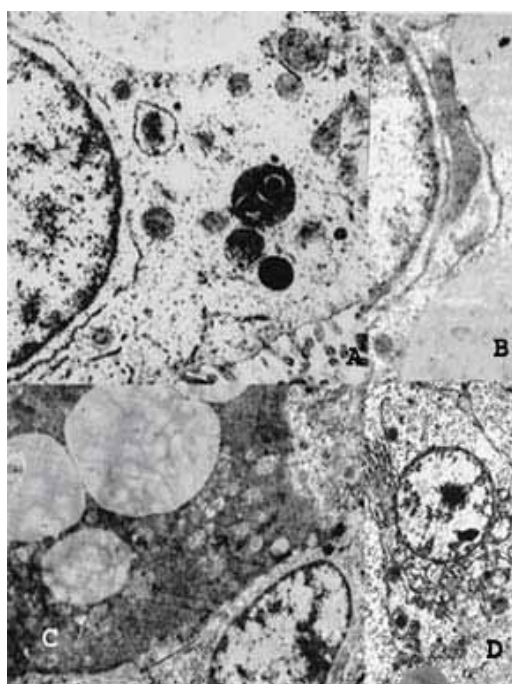
- [1] Kutlu M, Sümer S, Bull Environ Contam
- [2] Zilli L, Schiavone R, Scordella G, Zonno V, Verri T, Storelli C, Vilella S J Comp Physiol B 173 (2003), 355-363

## Ultrastructural Alterations in the Liver of *Aphanius chantrei* (GAILLARD, 1895) (CYPRINODONTIFORMES: CYPRINODONTIDAE) due to Acute Lead Exposure

Gözde Aydoğan, Mehtap Kutlu, Volkan Kılıç, Filiz Susuz

Anadolu University, Faculty of Science, Department of Biology, 26470, Eskişehir, Turkey

Ultrastructural changes in the liver have been used as biomarkers of toxic chemicals in environmental risk assessment. The ultrastructure of fish livers have proved to be valuable as a sensitive indicator of toxicant induced injury [1,2]. But relatively few investigations have defined the morphological effects of acute lead exposure on freshwater fish.



Ultrastructural alterations in the liver of Killifish, *Aphanius chantrei* (Cyprinodontiformes: Cyprinodontidae) after lead exposure were studied by transmission electron microscopy (TEM). One group of fish was exposed to a lead concentration 0.394 mg/L (acute) for 96 h in a static system. The hepatocytes in the control fish were characterized by a central rounded nucleus with a very distinct single nucleolus with high electron density and a small amount of heterochromatin. The granulated endoplasmic reticulum (GER) was arranged in parallel stacks of cisternae, usually adjacent to the nucleus and cell membrane. Spherical ovoid mitochondria were preferentially found around the nuclei. A variable amount of glycogen randomly located throughout the cytoplasm and lipid bodies were also observed in control individuals (Fig 1D).

**Fig.1:** Electron micrographs of hepatocytes

Acute lead exposure caused changes in the shape and location of the nucleus. The number and size of the lipid droplets were also increased (Fig 1C). Some changes in the organelles such as the dilation and degranulation of granulated endoplasmic reticulum (GER) and morphological changes in the mitochondrial cristae were observed (Fig 1A, Fig 1B). There were formations of myelin bodies and secondary lysosomes in the cytoplasm (Fig 1A). Our results were in parallel with some other authors reports which suggests that the morphological perturbations on mitochondria and GER are results of adaptive changes to heavy metal contamination in fish hepatocytes [3,4].

### References:

- [1] Gašpić ZK, Zvonarić T, Vroč T, Odžak N, Barić A, Water Res 36 (2002) 5023-5028
- [2] Thopon S, Pokethitiyook P, Chalermwat K, Upatham ES, Sahaphong S, Environ Toxicol 19 (2003) 11-19.
- [3] Ferreira AG, Melo EJT, Carvalho CEV, Acta Microscopica 12 (1) (2003) 49-54.
- [4] Yang JL, Chen HC Zool Stud 42 (2003) 455-461.

## Observation of ice in frozen bread dough by SEM and CLSM

Astrid Baier-Schenk<sup>a</sup>, Stephan Handschin<sup>a</sup>, Marina von Schönau<sup>a</sup>, Anne Greet Bittermann<sup>b</sup>, Marcel Düggelein<sup>c</sup>, Béatrice Conde-Petit<sup>a</sup>,

<sup>a</sup>Institute of Food Science and Nutrition, Swiss Federal Institute of Technology (ETH) Zurich, CH-8092 Zurich, Switzerland

<sup>b</sup>Center of microscopy (EMZ), University of Zurich, CH-8006 Zurich, Switzerland

<sup>c</sup>ZMB, Center for Microscopy, Bio-/Pharmacenter, CH-4056 Basel, Switzerland

Freezing of bread dough is widely applied in the bakery industry since it presents advantages in terms of logistics, preservation and convenience. However, prolonged frozen storage impairs the baking performance as manifested by a low loaf volume and an irregular pore structure of the crumb. One factor which is thought to contribute to the deterioration of dough structure is the formation of ice. In the present investigation ice formation in foamed bread dough was monitored with CLSM, and the growth, morphology and distribution of ice crystals was investigated by cryo-SEM.

An upright CLSM with a freezing stage was used to visualize ice formation and wheat dough with air inclusions served as model for proofed bread dough. Ice formation initiated at the gas pore interface where large ice crystals were formed after a freezing time of 4h at -15°C. To further analyze the ice fraction in dough, bread dough was frozen after proofing, stored at -22°C ±3°C and analyzed without previous thawing in the cryo-SEM. Ice crystals could be observed after a freezing time of 1h at the gas pore interface. Crystal growth and rounding off by recrystallization was observed upon frozen storage, and after 149 days the crystals reached a size of several 100 micrometers and were located in the pores of frozen dough.

It is concluded that upon freezing of proofed bread dough ice is preferentially formed at the gas pore interface. A salient feature of frozen dough is the accumulation of water in form of ice in the gas pores of dough. It is hypothesized that this redistribution of water in bread dough by ice crystal growth in the pores contributes to a cryo-dehydration of the polymeric compounds in dough which, in turn, impairs the baking performance of frozen dough.

### References:

A. Baier-Schenk et al 2005. In situ observation of the freezing process in wheat dough by confocal laser scanning microscopy (CLSM): Formation of ice and changes in the gluten network. *Journal of Cereal Science* 42: 255-260.

A. Baier-Schenk et al 2005. Ice in prefermented frozen bread dough – An investigation based on calorimetry and microscopy. *Cereal Chem.* 82 (3): 251-255.

# Imaging Chromophores with a Post-column Imaging Energy Filter on a 200 kV Monochromated TEM

M.M.G. Barfels, P. Thomas, and J.A. Hunt

Gatan Research & Development, Pleasanton 94588, USA

An imaging energy filter can extract chemical and molecular information for a variety of materials including biological samples, polymers, semiconductors and geological specimens, that in combination with a (S)TEM can be mapped with unparalleled spatial resolution [1,2,3]. In the case of chromophores, molecules that absorb light in the visible region and reflect or transmit the remaining colors, the low energy loss signal corresponding to the visible region of the spectrum can be used to localize dyes or fluorescent markers in a biological matrix. The possibility of obtaining sub-cellular chromophore localization using electron microscopy includes revealing ultrastructural information on the binding of dyes, a highly sensitive localization of immuno-labelled proteins and membrane receptors with a bound chromophore or fluorophore label, or sub-cellular localization of chromophore like drugs such as adriamycin, used as a therapeutic agent for cancer.

Imaging chromophores, has largely remained in the purview of photon microscopy techniques since mapping energy loss electrons corresponding to the electron optical excitation of chromophores is at the threshold of what can be done with a 1 eV energy resolution. The tail of the highly intense zero loss peak adds a high background diminishing the signal in the visible region of the spectrum. Reducing the width of the zero-loss peak with a mono-energetic electron source and a high-resolution spectrometer to 0.070 eV FWHM can reveal signal into the far-infrared region [4].

Figure 1 shows the electron energy loss signal of Acid Fuchsin with features that can be used to identify and distinguish this compound in a biological matrix. Spectra and maps of different types of histological stains such as acid fuchsin, eosin and Nile red will be presented.

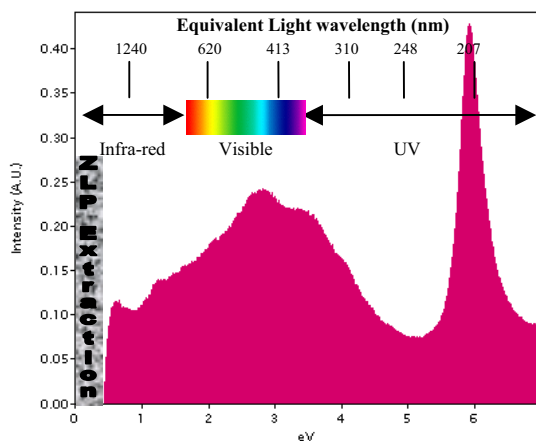


Figure 1: Acid Fuchsin suspended on a holey carbon film acquired on a monochromated TF20 at 200 kV with a GIF Tridiem-ERS over a 1 second exposure. The molecular absorption energy of the visible spectrum is 1.6 – 3.4 eV or  $\lambda = 770 \text{ nm} - 370 \text{ nm}$  respectively. Strong absorption can be seen in the UV region followed by absorption in the visible region of the spectrum. The zero-loss peak of 0.18 eV FWHM on the specimen has been extracted resulting in an onset energy of 0.45 eV.

## References:

- [1] H. Kohl, H. Rose, *Adv. Electronics Electron Phys.* 65 (1985) 173.Z
- [2] D. Muller, J. Silcox, *Ultramicroscopy* 59 (1995) 195.
- [3] M.M.G. Barfels et al., *Micron* 29 (1998) 97.
- [4] H.A. Brink and M.M.G. Barfels et al., *Ultramicroscopy* 96 (2003) 367.

## Surface Localization of L- $\alpha$ -glycerol-phosphate-oxidase and of lipoprotein LppQ in *Mycoplasma mycoides* subsp. *mycoides* SC

Laetitia Bonvin-Klotz<sup>1</sup>, Paola Pilo<sup>2</sup>, Edy M. Vilei<sup>2</sup>, Joachim Frey<sup>2</sup>, Michael H. Stoffel<sup>1</sup>

<sup>1</sup>Division of Veterinary Anatomy, University of Berne Veterinary School, 3012 Bern, Switzerland

<sup>2</sup>Institute of Veterinary Bacteriology, University of Berne Veterinary School, 3012 Bern, Switzerland

*Mycoplasma mycoides* subsp. *mycoides* small colony type (*Mmm* SC) is the etiological agent of contagious bovine pleuropneumonia (CBPP), a disease being included in the A-list of the *Office International des Epizooties*. Despite their devastating effect, these smallest self-replicating organisms lack typical primary virulence factors such as toxins, cytolysins and invasins. However, highly virulent strains of *Mmm* SC possess the enzyme L- $\alpha$ -glycerol-phosphate-oxidase (GlpO) which metabolizes glycerol-3-phosphate to di-hydroxy-acetone-phosphate, a reaction yielding hydrogen peroxide (H<sub>2</sub>O<sub>2</sub>) as a highly cytotoxic by-product [1]. As H<sub>2</sub>O<sub>2</sub> is potentially harmful to the pathogen as well, the location of the enzyme is of prime interest. The goal of the present study, therefore, was to localize GlpO in *Mmm* SC. LppQ-total is a known transmembrane lipoprotein which is specific to *Mmm* SC. Whereas its N-terminal domain (LppQ-N) is surface-exposed, its C-terminus is not accessible from the outside as it is an integral membrane domain (LppQ-C) [2].

Polyclonal monospecific sera directed against recombinant GlpO, LppQ-N, LppQ-C and LppQ-total protein were generated and used for immunogold labelling. *Mmm* SC were grown on poly-L-lysine-coated cover slips which had been previously sputtered with gold or platinum. Immunogold-labelling was performed and specimens were processed for scanning electron microscopy (SEM). Secondary electron and corresponding backscattered electron signals were examined in a high-resolution field emission scanning electron microscope DSM 982 Gemini (Zeiss, Oberkochen, Germany). Control experiments with pre-immune sera and an anti-calcitonine antibody instead of specific antisera were negative.

Immunogold labelling yielded a strong signal with anti-LppQ-total and a somewhat weaker signal with anti-LppQ-N. But for a faint background, no labelling was detected with anti-LppQ-C. These findings provided evidence, that the protocol used revealed epitopes being exposed at the extraplasmatic surface only. Dense labelling with anti-GlpO disclosed the enzyme to be homogeneously distributed at the cell surface.

Our findings support the contention that GlpO is membrane-bound and, thus, is liable to play a crucial role in the pathogenesis of CBPP. In addition, localization of this virulence factor at the cell surface may pave the ground for the development of new vaccines.

[1] Pilo, P., Vilei, E. M., Peterhans, E., Bonvin-Klotz, L., Stoffel, M. H., Dobbelaere, D., Frey, J. 2005. A metabolic enzyme as a primary virulence factor of *Mycoplasma mycoides* subsp. *mycoides* Small Colony. *J. Bact.*, in press.

[2] Abdo, E. M., Nicolet, J., and Frey, J. 2000. Antigenic and genetic characterization of lipoprotein LppQ from *Mycoplasma mycoides* subsp. *mycoides* SC. *Clin. Diagn. Lab. Immunol.* 7:588-95.

## Effects of Artichoke Extracts Supplementation on Testis and Ovary in Cadmium Treated Rats

Husniye Dogruman<sup>a</sup>, Ebru Gurel<sup>b</sup>, Metin Caner<sup>c</sup>, Cihan Demirci<sup>b</sup> and Umay Fırat<sup>d</sup>

<sup>a</sup>Medical Biology, Veterinary Medicine Faculty Istanbul University, 34310 and Istanbul, Turkey

<sup>b</sup>Zoology, Science Faculty Istanbul University, 34310 and Istanbul, Turkey

<sup>c</sup>General Surgery, Cerrahpasa Medicine Faculty Istanbul University, 34310 and Istanbul, Turkey

<sup>d</sup>Technology Institute, Istanbul University, 34310 and Istanbul, Turkey

Cadmium (Cd) is a toxic heavy metal of considerable environmental and occupational concern. It has extremely long biological half life. Cd is recognised as a parameter promoter of pathophysiological changes in humans and animals. It has been shown to affect reproductive organs. Also rat testes are extremely sensitive to Cd. High doses of Cd rapidly induces an extensive haemorrhagic necrosis in testes of male rats[1]. Cd has been found to influence ovarian function both directly and indirectly in mammals. In this study we have used antioxidative and hepatoprotective potential of artichoke (*Cynara scolymus L.*) extracts to prevent harmful effects of Cd in rats[2].

Project was planned with 6 experimental and 2 control groups. 8 weeks old Wistar albino rats with the average weight of 80-100 g were chosen for the study. The study groups were prepared as follows

**Group 1:** 10 male rats were used. CdCl<sub>2</sub> dissolved in 0,9% NaCl was injected subcutaneously to rats with the dosage of 1mg/100 g of body weight every other day.

**Group 2:** CdCl<sub>2</sub> was injected to 10 male rats as in Group 1 and artichoke dissolved with distilled water was given orally with the dosage of 3 mg/100 g of body weight every day.

**Group 3:** Artichoke was given orally to 10 male rats with the dosage of 3 mg/100 g of body weight every day. **Group 4, Group 5, Group 6** are formed by female rats. The same administration was done as in Group 1, Group 2 and Group 3. **Control 1** was formed by male rats, **Control 2** was formed by female rats. 0,1 ml distilled water every day orally and 0,1 ml 0,9 % NaCl each following day subcutaneously were given to the rats in Control 1 and Control 2.

After 4 weeks, rats were sacrificed under ether anaesthesia and testes and ovaries were prepared for a histological examination. By microscopic examinations, it was observed that in the samples of testes which were injected Cd (Group 1), Spermatogonia were damaged and destroyed. Similar damages were detected in Leydig cells. In the group 2 which were injected both Cd and artichoke, the damage in both spermatogonia and leydig cells were less. In Control 1 and Group 3 which were injected only artichoke, testes views were similar. In Ovarium samples of female rats, there was no damage observed in testes due to Cd. Immunoreactive iNOS and eNOS were increased in the interstitial aerea in testis in Group 1 on the otherhand in Group 2 they were localized less than Group 1 in the interstitial aerea in testis. In this study, it is concluded that, artichoke can have a protective effect against the damage in testes resulted by Cd.

### References:

[1] Ronojoy Sen Gupta, Jisun Kim, Molecular and Cellular Endocrinology 221 (2004) 57-66.

[2] R. Gebhardt, M. Fausel, Toxicology in Vitro 11 (1997) 669-672.

[3] This work was supported by Research Fond of The University of Istanbul

## High-fidelity ultrastructural preservation and high-efficient immunolabelling

E.G. van Donselaar<sup>1,2</sup>, B.M. Humbel<sup>2</sup>, J.W. Slot<sup>1</sup>

<sup>1</sup>Department of Cell Biology, University Medical Center Utrecht, NL-3584 CX Utrecht, The Netherlands

<sup>2</sup>Electron Microscopy & Structure Analysis, Department of Molecular Cell Biology, Utrecht University, NL-3584 CH Utrecht, The Netherlands

In the last 40 years cryofixation has gained the reputation and convincingly proven to be the method of choice to prepare biological samples with the least alteration to their native structure. Straight forward imaging techniques like cryoSEM [1] or CEMOVIS [2] most reliably reveal those structures. To localise cellular components by e.g., immuno gold labelling, however, different strategies have to be applied.

The most successful and efficient method for immuno gold labelling is the cryosectioning method pioneered by Tokuyasu [3] and refined in our laboratory in Utrecht [4]. Here, the samples are chemically fixed and embedded in an ice/sucrose matrix. The sections are cut with a cryo-ultramicrotome, thawed and labelled. In contrast to all the other techniques the cellular structures remain in their 'water' environment until the labelling procedure is completed.

To combine cryofixation with immunolabelling techniques, cryofixed samples were dehydrated and if needed chemically fixed by freeze-substitution and low-temperature embedded in metacrylates, e.g. Lowicryls [5]. After polymerisation the resin blocks were warmed to room temperature and thin sections are cut on a standard microtome. In general, the morphology of these samples is excellent and localisations studies can be done. Proteins of low copy number or in low concentrations, however, are easily missed in resin embedded material.

In this communication we propose an alternative hybrid preparation technique: cryofixation by HPF, chemical fixation during freeze-substitution, rehydration and embedding in ice/sucrose for Tokuyasu cryosectioning. Several different substitution protocols were used to find recipes, which result in high membrane contrast and high label efficiency.

### References:

- [1] Walther, P. & Müller, M. Biological ultrastructure as revealed by high resolution cryo-SEM of block faces after cryo-sectioning. *J. Microsc.* **196**, 279-287 (1999).
- [2] Al-Amoudi, A. et al. Cryo-electron microscopy of vitreous sections. *EMBO J.* **23**, 3583-3588 (2004).
- [3] Tokuyasu, K. T. Cryosections for immunohistochemistry. *J. Electron Microsc.* **35**, 1977-1978 (1986).
- [4] Liou, W., Geuze, H. J. & Slot, J. W. Improving structural integrity of cryosections for immunogold labeling. *Histochem. Cell Biol.* **106**, 41-58 (1996).
- [5] Humbel, B. & Müller, M. in *The Science of Biological Specimen Preparation 1985* (eds. Müller, M., Becker, R. P., Boyde, A. & Wolosewick, J. J.) 175-183 (SEM Inc., AMF O'Hare, 1986).

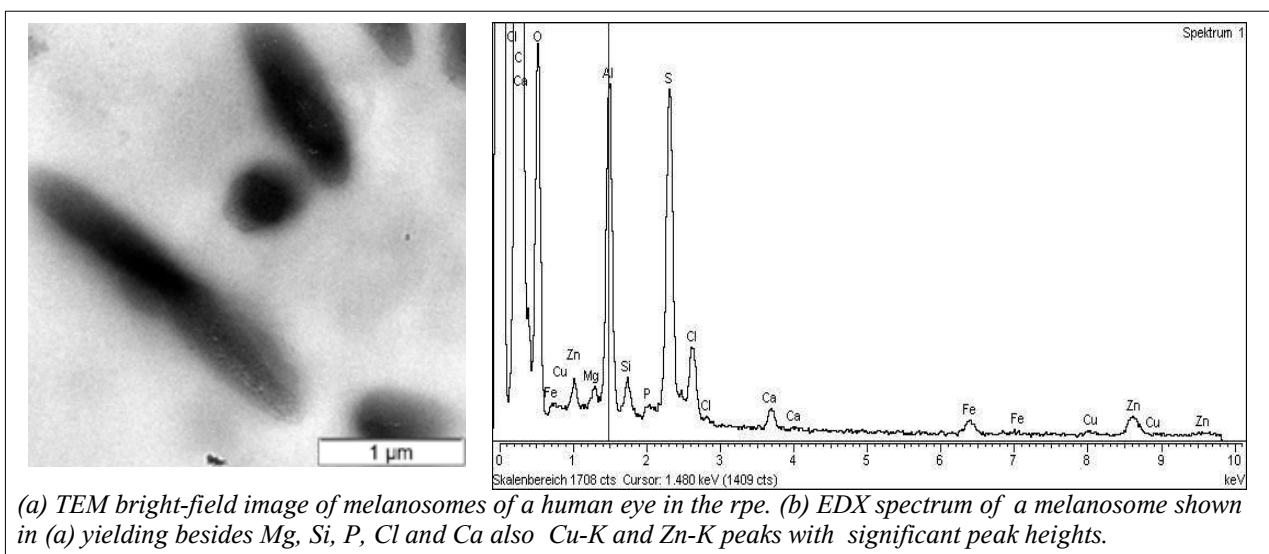
## Melanosomes in Retinal Tissue: Quantitative Chemical Analysis in the TEM

O. Eibl<sup>1</sup>, S. Schultheiss<sup>2</sup>, U. Schraermeyer<sup>2</sup>

<sup>1</sup> Insitutit für Angewandte Physik, Eberhard Karls Universität Tübingen, Auf der Morgenstelle 10, 72076 Tübingen

<sup>2</sup> Sektion für Experimentelle Vitreoretinale Chirurgie, Universitätsaugenklinik Tübingen, Schleichstr. 12/1, 72076 Tübingen

Melanosomes in retinal tissues of a human, monkey and rat were analysed by EDX in the TEM. Samples were prepared by ultramicrotomy at different thicknesses. The material was mounted on Al grids and samples were analysed in a Zeiss 912 TEM equipped with an Omega filter and EDX detector with ultrathin window. Melanosomes consist of C and O as main components, mole fractions are about 90 at% and 3-10 at% respectively, and small mole fraction ratios, between 2 and 0,1 at%, of Na, Mg, K, Si, P, S, Cl, Ca. All elements were measured quantitatively by standardless EDX with high precision. Mole fractions of transition metals Fe, Cu and Zn were also measured. For Fe a mole fraction ratio of less than 0,1 at% was found and gives the melanin its paramagnetic properties. Its mole fraction is however close to or below the minimum detectable mass fraction of the used equipment. Only in the human eye and only in the retinal pigment epithelium (rpe) the mole fractions of Zn (0,1 at% or 5000 µg/g) and Cu were clearly beyond the minimum detectable mass fraction. In the rat and monkey eye the mole fraction of Zn was at or below the minimum detectable mass fraction and could not be measured. The obtained results yielded the chemical composition of the melanosomes in the choroidal tissue and the retinal pigment epithelium (rpe) of the three different species. The results of the chemical analysis are discussed by mole fraction correlation diagrams. Similarities and differences between the different species are outlined. Correlation behaviour was found to hold over species, e.g. the Ca-O correlation. These are the first quantitative analyses of melanosomes by EDX reported so far. The quantitative chemical analysis should open a deeper understanding of the metabolic processes in the eye that are of central importance for the understanding of a large number of eye-related diseases. The chemical analysis also allows a correlation with structural changes observed at the various regions of the eye.



(a) TEM bright-field image of melanosomes of a human eye in the rpe. (b) EDX spectrum of a melanosome shown in (a) yielding besides Mg, Si, P, Cl and Ca also Cu-K and Zn-K peaks with significant peak heights.

## Diagnostic Electron Microscopy in Infectious Diseases

Hans R. Gelderblom

c/o Robert Koch-Institut, Nordufer 20, D-13353 Berlin, Germany E-mail: Gelderblomh@rki.de

Viruses, bacteria and other germs can induce specific diseases in their hosts - be them human, livestock or plants – causing health impairment, even death, and/or economic losses or changes in the ecological balance. Infectious agents are rapidly spread by man-made, agent-specific and other factors, e.g. global mobility of men and goods, microbial adaptation, changing climate and ecosystems. The burden of emerging infections (HIV, SARS, Ebola-, Nipahvirus etc.) as well as old, re-emerging threats (e.g. yellow fever, drug-resistant bacteria, human monkeypox, bird flu) recently increased by the threats of bio- and agro-terrorism (BAT). BAT, the deliberate release of naturally occurring or specifically bio-engineered pathogens – some of which easily deployable and highly lethal – can cause major problems as indicated by the 2001 anthrax letter attacks in the US [1].

Control and specific treatment of infections require the causative agent(s) to be known. A respective lab diagnosis should be achieved with speed and certainty. Electron microscopy can deliver this service even today – in the presence of highly specific ELISA- and PCR techniques - as exemplified in 2003 when the cause of SARS was rapidly identified as a coronavirus and during the human monkeypox outbreak in the US [reviewed in 1]. Both events underline that electron microscopy should be performed front-line in order to make full use of its specific advantages: the resolution and undirected “open view” can visualize even the smallest agents. As a “catch-all-method” it can visualize all agents in a sample, even unexpected ones - without the need for agent-specific reagents. The morphology observed assigns the germ directly to a specific family of agents and at the same time serves as an internal positive control. An early “family-diagnosis” is most often sufficient to start anti-viral therapy, barrier nursing, etc.: it will often exclude a more dangerous agent and can determine also the next steps for a type-specific lab diagnosis.

Samples may come directly from a patient’s lesion or body excretions, from diagnostic cultures or environmental samples. The preparation of choice, due to its speed, is negative-staining. A sample can be evaluated within 15 min after arrival in the lab. Particle concentrations of  $>10^6$  /ml are required [2], a condition met in many instances. The use of enrichment methods and of especially adhesive grids will enable rapid and reliable results. Advice on proper procedures is given by the Consultant Lab of the Robert Koch-Institut in a series of Hand-Outs, specific references etc. [3]. As other lab methods, diagnostic electron microscopy must be performed in a quality-controlled way. For this an External Quality Assurance scheme (EQA-EMV) - free of charge - is run twice a year by the Consultant Lab (with 114 participants in 32 countries in the recent EQA-18). Workshops and Basic Lab Courses help for continuous exchange, education and training [3]. Together, these means will help also in the future to keep electron microscopy indispensable as a lab diagnostic method in infectious diseases emergencies and BAT.

References: [1] Morens, DM, Folkers, GF, Fauci, AS (2004) Nature 430, 242-249  
[2] Biel, SS, Nitsche, A, Kurth, A. et al. (2004) Clin Chemistry 50, 306-312  
[3] [www.rki.de](http://www.rki.de) click: >English >The Institute >Departments and .. >National Reference Centres and .. >Consultant Laboratory for Diagnostic Electron Microscopy

## **The Role of Human Cytomegalovirus UL97 Kinase in Virus Assembly: Immunofluorescence and Transmission Electron Microscopy (TEM) Analysis.**

Miri D. Goldberg<sup>1,2</sup>, Vera Shinder<sup>3</sup>, Alik Honigman<sup>2</sup>, Maysa Azzeh<sup>1,2</sup>, Albert Taraboulos<sup>2</sup>, Alexander Rouvinski<sup>2</sup>, Dana G. Wolf<sup>1</sup>

<sup>1</sup>Department of Clinical Microbiology and Infectious Diseases, Hadassah University hospital, and Departments of <sup>2</sup>Virology & Molecular Biology the Hebrew University-Hadassah Medical School, Jerusalem, <sup>3</sup>Electron Microscopy Unit, Weizmann Institute of Life Sciences, Rehovot, Israel

Human cytomegalovirus (HCMV), a betaherpesvirus, is a major cause of disease in immunocompromised individuals and a common cause of congenital infection leading to developmental abnormalities. The HCMV UL97 kinase plays a crucial role in viral propagation, and has been shown to affect late replication steps involving capsid maturation and nuclear egress. Using the UL97 deletion mutant (UL97<sup>-</sup>), we have demonstrated by immunofluorescence microscopy that the absence of UL97 kinase activity results in a modified subcellular distribution of the viral structural protein assembly sites, from compact structures impacting upon the nucleus to diffuse perinuclear structures punctuated by large immunonegative vacuoles. Infection by either wild type (wt) HCMV or UL97<sup>-</sup> viruses induced a profound reorganization of wheat germ agglutinin (WGA)-positive Golgi-related structures. Importantly, the viral-induced Golgi remodeling along with the reorganization of the nuclear architecture were substantially altered in the absence of UL97 kinase activity.

We have employed TEM ultrastructural analysis of cells infected by either the wt or the UL97<sup>-</sup> viruses; infected human foreskin fibroblasts, grown on saphir discs, were subjected to high pressure freezing fixation and analyzed at 96 hours post infection. Ultrastructural EM analysis showed differences in the morphology and localization of wt and UL97<sup>-</sup> virus particles in the nucleus and cytoplasm. While in the wt virus - capsids appeared mostly diffused through nucleus, in UL97<sup>-</sup>-intranuclear inclusions, composed of clusters of empty capsids, appeared in the periphery of the nucleus. In the cytoplasm, the wt virus particles bud into Golgi-derived vacuoles with following accumulation in bigger vacuoles. These big intracytoplasmic vacuoles did not appear in UL97<sup>-</sup>-infected cells, which rather demonstrated multiple small Golgi-related vacuoles containing limited virus particles, scattered in the cytoplasm. Immuno-EM analysis, following immuno-gold labeling of the HCMV pp28 tegument protein, showed pp28 staining of Golgi-related vacuoles in both the wt and the UL97<sup>-</sup> viruses.

These findings reveal a role for the UL97 kinase in critical nuclear and cytoplasmic steps of HCMV assembly and in the remodeling of the cellular secretory pathway that takes place during HCMV infection.

## Magneto-Orientation of *Synechococcus lividus*, demonstrated with an Electron Microscopic Preparation Technique

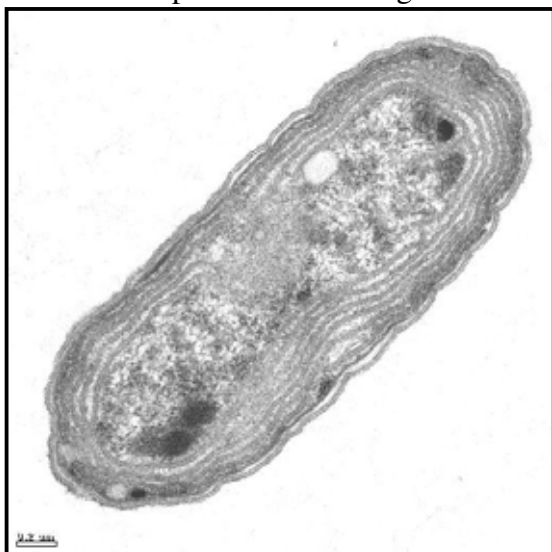
J. R. Golecki<sup>a</sup>, U. Heinen<sup>b</sup>, T. Berthold<sup>b</sup>, and G. Kothe<sup>b</sup>

<sup>a</sup> Microbiology, Institute Biology 2, University of Freiburg, D-79104 Freiburg, Germany

<sup>b</sup> Department of Physical Chemistry, University of Freiburg, D-79104 Freiburg, Germany

The primary processes of photosynthesis, especially the composition of the reaction center proteins and their structural organisation inside the photosynthetic membranes are of great interest. One investigation method is to study time-resolved Electron Paramagnetic Resonance (EPR) of the secondary radical pair in photosystem I formed by photoexcitation. Spin-correlated radical pairs are the short-lived intermediates of the primary energy conversion steps.

Recently, in EPR studies [1] a magneto-orientation of the cyanobacterium *S. lividus* in the magnetic field of the spectrometer was demonstrated. The knowledge of the exact orientation of the cell with its photosynthetic apparatus in the magnetic field during EPR studies is important for the correct interpretation of the EPR-spectra. The aim of our electron microscopic study was to verify the magneto-orientation of *S. lividus* with a second independent method. We developed a special microscopic preparation method preserving the original orientation of *S. lividus* in the magnetic field inside the spectrometer. For this reason we suspended deuterated and <sup>15</sup>N-substituted cells of *S. lividus* in a solution of 2% liquid agar with a low gelling temperature of < 30°C. The mixture was filled in a sample tube and then quickly placed into the field of a spectrometer. The magnetic field direction was parallel to the long axis of the sample tube. Magnetic field induced alignment of the



cells was achieved in the liquid agar at 35°C with a field of 7 T for 30 min. After 30 min. the sample was cooled down within 10 min. to 4°C where the agar solidified. After removal of the sample from the spectrometer, the closed end of the sample tube was cut off and the solidified agar rod was pushed out using a metal stick. The agar rod containing the *S. lividus* cells was prepared for electron microscopy by fixation with glutaraldehyde and embedding in epoxy resin. The agar rod with *S. lividus* was placed into a flat embedding mould with the long axis parallel to the long axis of the embedding form. To guarantee exact placement of the samples, this procedure was performed using a binocular. This arrangement ensured that during the preparation of

thin sections in the microtome the section plane was always perpendicular to the magnetic field direction in the spectrometer. Thus, a precise evaluation of the cell alignment relative to the magnetic field direction is possible. In thin sections we could demonstrate that the *S. lividus* cells were cut to 98 % in their long axes (Fig.) indicating a magneto-orientation perpendicular to the magnetic field. Morphometric measurements of the cell shape and the area of the photosynthetic and cytoplasmic membranes confirmed the spectroscopic results.

[1] Heinen, U., Poluektov, O., Stavitski, E., Berthold, Th., Ohmes, E., Schlesselman, S.L., Golecki, J.R., Moro, G.J., Levanon, H., Thurnauer, M.C., and Kothe, G.: J. Phys. Chem. B, **108** (2004) 9498-9504

## Detection of the Novel Calcium-Binding Allergen Phl p 7 in Timothy Grass (*Phleum pratense*) Pollen by Immunogold Transmission Electron Microscopy

Monika Grote<sup>a</sup>, Rudolf Valenta<sup>b</sup>, Rudolf Reichelt<sup>a</sup>, Kerstin Westritschnig<sup>b</sup>

<sup>a</sup>Institute of Medical Physics and Biophysics, UKM, University of Münster, Germany

<sup>b</sup>Institute of Pathophysiology, General Hospital, University of Vienna, Austria

In order to localize Phl p 7, a novel calcium-binding allergen in timothy grass pollen, we used a rabbit antibody raised against the C-terminal fragment of the Phl p 7 allergen molecule [1] followed by 10 nm colloidal gold coupled goat anti-rabbit IgG antibody. Pollen grains from timothy grass were collected in spring 2003 and used directly without storing. A strictly non-aqueous preparation technique was employed as described earlier in detail [2]. Phl p 7 allergens were detected in the pollen wall (exine), in the cytoplasmic matrix between the reserve materials (amyloplasts and polysaccharide particles), and in the mitochondria (**Figure 1**). In control experiments replacing the specific rabbit antibody by the pre-immune antibody a very low amount of non-specific labeling was observed in **Figure 2**.

When comparing the distribution pattern of the novel timothy grass pollen allergen Phl p 7 to that of a formerly studied another calcium-binding two EF-hand allergen, Bet v 4 in birch pollen [3], we find similar locations for the two allergens in the pollen grains as regards their occurrence in the wall and in calcium-rich cellular sites (mitochondria). Since pollen germination is a calcium-dependent process, we assume that these calcium-binding allergens might be involved in the regulation of calcium metabolism during pollen tube formation and pollen-stigma interactions.

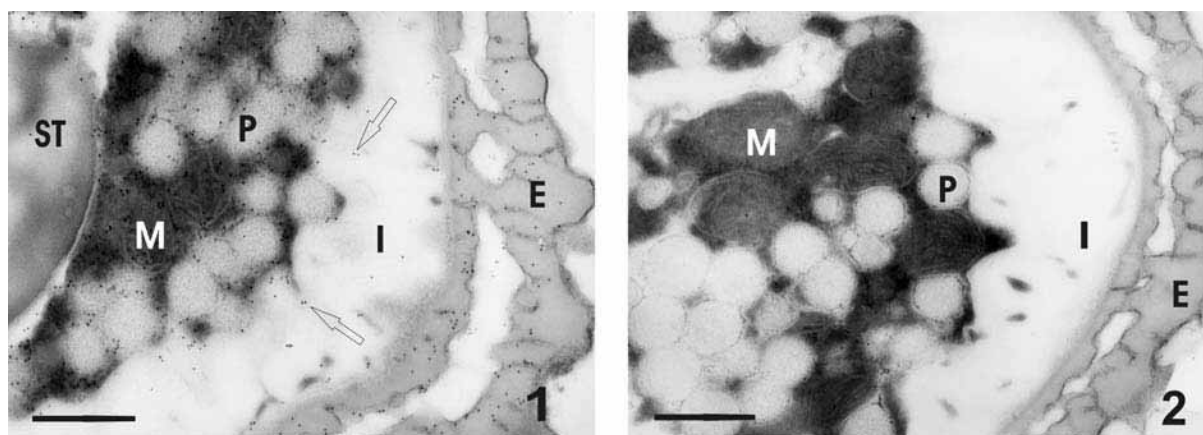


**Fig. 1.** Timothy grass pollen after incubation with rabbit anti-Phl p 7 antibodies followed by 10 nm colloidal gold coupled goat anti-rabbit antibodies. **Fig. 2.** Control experiment using the pre-immune antibodies instead of the anti-Phl p 7 antibodies. Abbreviations: E, exine; I, intine; M, mitochondrion; P, polysaccharide particle; ST, starch. Bars = 0.5  $\mu$ m. Arrows point to gold particles. References:

[1] Westritschnig K, Focke M, Verdino P et al. *J Immunol* 172(2004)5684-5692

[2] Grote M, Dolecek C, van Ree R, Valenta R. *J Histochem Cytochem* 42(1994)427-431

[3] Grote M, Hayek B, Reichelt R et al. *Int Arch Allergy Immunol* 120(1999)287-294

[4] Acknowledgement: The expert technical assistance of Ms U Malkus in preparation of the specimens and Ms G Kiefermann in photography is gratefully acknowledged.

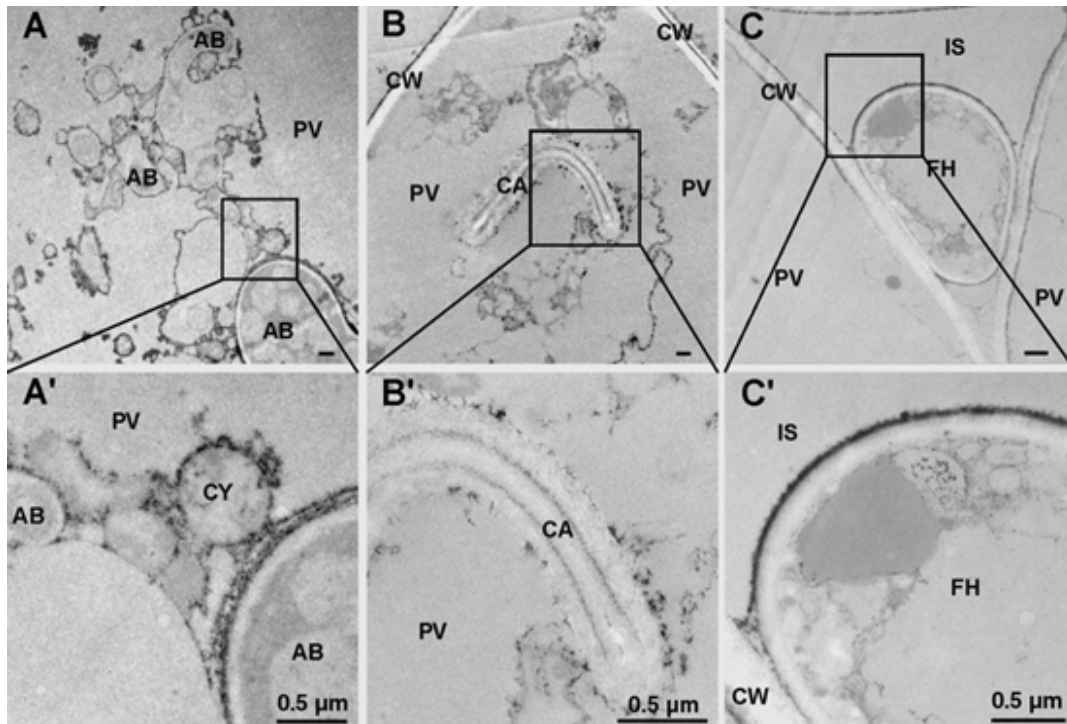
## Accumulation of reactive oxygen species in arbuscular mycorrhizal roots

Gerd Hause<sup>a</sup>, and Thomas Fester<sup>b</sup>

<sup>a</sup>Biozentrum, Martin-Luther-Universität Halle-Wittenberg, D-06120 Halle, Germany

<sup>b</sup>Abteilung Sekundärstoffwechsel, Leibniz-Institut für Pflanzenbiochemie, D-06120 Halle, Germany

We investigated the accumulation of reactive oxygen species (ROS) in arbuscular mycorrhizal (AM) roots from *Medicago truncatula*, *Zea mays* and *Nicotiana tabacum* using three independent staining techniques. Colonized root cortical cells as well as the symbiotic fungal partner were observed to be involved in the production of ROS. Extraradical hyphae and spores from *Glomus intraradices* accumulated small levels of ROS within their cell wall and produced ROS within the cytoplasm in response to stress. Within AM roots, we observed a certain correlation of arbuscular senescence and H<sub>2</sub>O<sub>2</sub> accumulation after staining by diaminobenzidine (DAB) and a more general accumulation of ROS close to fungal structures when using dihydrorhodamine-123 (DHR-123) for staining. According to electron microscopical analysis of AM roots from *Zea mays* after staining by CeCl<sub>3</sub>, intracellular accumulation of H<sub>2</sub>O<sub>2</sub> was observed in the plant cytoplasm close to intact and collapsing fungal structures, whereas intercellular H<sub>2</sub>O<sub>2</sub> was located on the surface of fungal hyphae. These characteristics of ROS accumulation in AM roots suggest similarities to ROS accumulation during the senescence of legume root nodules.



Localization of H<sub>2</sub>O<sub>2</sub> in AM roots of *Zea mays* after staining by CeCl<sub>3</sub>. General views (A-C) and corresponding details (A'-C'). Signals specific to staining by CeCl<sub>3</sub> were observed within the plant cytoplasm (CY) close to intact arbuscular branches (AB, A, A') and collapsing arbuscular branches (CA, B, B') as well as on the surface of intercellular fungal hyphae (FH, C, C').

## **High-Resolution Imaging and Localization in Light Microscopy**

Rainer Heintzmann; King's College London, Randall Division Guy's Campus,  
London SE1 1UL, United Kingdom; Email:rainer.heintzmann@kcl.ac.uk

After an introduction on 4Pi microscopy the concept of non-linear structured illumination techniques is discussed. Finally the novel method of separating and localizing overlapping images of quantum dots using their blinking statistics is presented. Quantum dots are visible also in electron microscopy due to their cores containing high amounts of cadmium.

The non-linear approach of saturating optical transitions (for structured illumination as well as beam-scanning approaches) is discussed, which has a great potential especially in combination with photo-switchable dyes such as the newly released DRONPA molecule by Atsushi Miyawaki's group. The nonlinear concepts such as STED and saturated structured illumination can be combined with the aperture enhancing concepts 4PI and I<sup>5</sup>M respectively.

Quantum dots blink individually. This property can be used to identify their individual contribution to the image and subsequently localize them at high resolution. To this aim the statistical tool of Independent Component Analysis (ICA) is used. For the localization, a Maximum Likelihood fit based on the Poisson statistics of single photon counting is advantageous.

## **Ultrastructural aspects of possible entamoebae divergence producing the four-nuclear cysts**

Karlen O. Hovnanyan, Margarita K. Hovnanyan

Institute Molecular biology of NAS RA, Yerevan , 375014, Republic of Armenia

It's well known that eukaryotes, particularly protists, come of prokaryotes and have many common genetic, metabolic, regulatory processes. Compartmentalization of eukaryote cell within the evolution process came of prokaryote by the way of prokaryote cytoplasmic membrane invasion in cytoplasm and formation of nuclear membrane as well as another cellular compartments. What about the mitochondria, in given case we prefer the mitochondria production from symbiobacterial bacteria [1]. For the examination of systematics and parasitism of protists taking into account the evolutionary development it's very important the choice of the model divergent features. We consider it to be well-founded the comparative investigation on macromolecular and molecular levels of morpho-functional features of prokaryotes and protists divergent lines representatives which passed their own evolution development way. Considering it we thought that entamoebae producing four-nuclear cysts, having no mitochondria, granular endoplasmic reticulum are more identical models. In our work we used parasitical and free-living entamoebae: *Entamoeba histolytica* strains excreted from the patients with intestinal amebiasis, *Entamoeba invadens* excreted from the snakes with amebiasis and *Entamoeba moshkovskii* excreted from sewage. All entamoebae kinds have been cultivated in Pavlov's medium. Electronic-microscopical investigation of *Entamoeba histolytica*, *Entamoeba invadens* and *Ent. moshkovskii* morphogenesis revealed the identity of entamoebae morphogenesis (vegetative forms and cysts) ultrastructural characteristic. One of the important structural systematic feature for entamoebae we consider it to be the virus-like endosymbiont which are like rabdoviruses by their submicroscopical organization. Their length is 140-200nm, diameter is 60nm. After the  $\gamma$ -ionizing radiation on entamoebae the membrane of viral particles as three-layer membrane is distinctly revealed. Virus-like particles of entamoebae are like sigma viruses – symbionts by their ultrastructural characteristic which are meet in *Drosophila melanogaster* and which are hereditary [2, 3]. Virus sigma containing RNA is the extranuclear genetic determinant of sensitivity *Drosophila* regarding CO<sub>2</sub>. Parasitical and free-living four-nuclear cyst which form entamoebae and which we investigated as we think evolutionally are the divergence of entamoebae one branch living isolated in different natural habitat.

### References:

1. Gibbs S.R. (1981), *Int. Rev. Cytol.*, 72, P.49.
2. Bul J., Noulis J. (1981) *Extranuclear a heredity. M.*, "Mir", P. 831-836.
3. Bauriiller R.C. (1967). *Mutat. Res.* 4, P. 831-836.

## New view of the antitumor properties of HPMA based polymeric prodrugs

O. Hovorka<sup>a</sup>, J. Strohalm<sup>b</sup>, V. Šubr<sup>b</sup>, K. Ulbrich<sup>b</sup>, B. Říhová<sup>a</sup>

<sup>a</sup> Institute of Microbiology, ASCR, Vídeňská 1083, Prague 4, 142 20, Czech Republic

<sup>b</sup> Institute of Macromolecular Chemistry, ASCR, Heyrovsky sq. 2, Prague 6, 162 06, Czech Rep.

### INTRODUCTION

Polymeric conjugates based on N-(2-hydroxypropyl)methacrylamide (HPMA), were designed as carriers for anticancer drugs, e.g. doxorubicin (Dox) [1-4]. Despite the fact that some of them are in clinical trials, we are still far away from understanding the mechanism of their action. Cleavability of the drug from the oligopeptidic side-chains of polymeric carriers was regarded as a key mechanism ensuring pharmacological activity. In view of the newest results, this seems to be a mistake and intracellular cleavage of doxorubicin is not a necessary prerequisite for the pharmacological activity of HPMA-based conjugates [5].

### RESULTS AND DISCUSSION

Because of the intrinsic fluorescence of the active component doxorubicin, we could directly track and quantify the intracellular pathway of the tested conjugates. Immediately after being added to the cell culture, non-targeted conjugates of HPMA with doxorubicin bound through proteolytically cleavable (GFLG) or non-cleavable (GG or LL) spacers [7] enter the cells very quickly (detectable in seconds) without the need of any active mechanism. The conjugates penetrate through the plasma membrane and are detectable in all associated cellular membranes - membranes of the endocytic compartment, nuclear membrane, Golgi and endoplasmic reticulum membranes. Immediately after washing the cells with fresh media (after 1 minute), the intracellular fluorescence of the conjugates significantly decreases, while the fluorescence of endosomes loaded with Alexa-488 labeled transferrin remains unchanged. This suggests that the conjugates are accumulated mainly due to their physico-chemical interactions with cellular membranes. Active accumulation is also involved, but it is detectable only as a residual fluorescence of washed cells.

The intensity of accumulation of the conjugates is different in different cellular types. CD4<sup>+</sup> and CD8<sup>+</sup> populations of mouse T-lymphocytes are divided into two subsets, based on the intensity of accumulation of the drugs. Treg cells (CD4<sup>+</sup>CD25<sup>+</sup>) that dampen the antitumor immune response [7], have always been classified as Dox<sup>high</sup> population. This suggests a completely new, unexpected mechanism by which the polymeric conjugates could positively influence cancer treatment.

### REFERENCES

1. Kopeček J. Polym. Med 7(3): 191-221 (1977)
2. Kopeček J. et al. US Patent 5 037 883 (1991)
3. Říhová B. et al Clin Immunol Immunopathol 46(1): 100-14. (1988)
4. Říhová B. Drugs in the Future 28, 1 – 22, (2003)
5. Hovorka O. et al. J. Cont. Rel. 80(1-3): 101-17 (2002)
6. Ulbrich, K. Materials structure 10, 3-4 (2003)
7. Emens, LA. et al. Endocr. Relat. Cancer. Mar;12(1):1-17. (2005)

### ACKNOWLEDGEMENTS

This research was supported by the GAČR grants no. 305/04/P004 and 305/05/2268

## Subcellular Location of Big Conductance Calcium-activated Potassium Channels in Cerebellar Purkinje Neurons: Targeting to Subsurface Membrane Cisternae

Walter A. Kaufmann<sup>a</sup> and Ole Petter Ottersen<sup>b</sup>

<sup>a</sup>Institute of Pharmacology, Innsbruck Medical University, AT-6020 Innsbruck, Austria

<sup>b</sup>Centre for Molecular Biology and Neuroscience, Department of Anatomy, University of Oslo, N-0317 Oslo, Norway

The physiological impact of each ion channel strongly depends on the site where it is expressed: in which type of neurons and exactly in which subcellular domain within each neuron [1]. Thus detailed information on the precise localization of ion channels is of paramount importance in order to understand their function. So far, little is known about the subcellular localization of most K<sup>+</sup> channels and this gap in our knowledge hampers the understanding of neuronal signaling mechanisms and functions.

This study addressed the precise subcellular localization of big conductance calcium-activated potassium channels (BKs) in cerebellar Purkinje cells. Affinity purified rabbit antisera directed against the channel principal subunit alpha 1 (encoded by the KCNMA1 or mSlo1 gene) were used for immunodetection. The ultrastructural location was studied by means of pre-embedding peroxidase and post-embedding immunogold electron microscopy as performed before [2]. In the present study, we found BK channels unevenly distributed over the surface membrane of cerebellar Purkinje cells and targeted to specific subcellular domains. At Purkinje cell dendritic spines, channels were localized to the plasma membrane of spine head and neck, sparing postsynaptic specializations. Also at the plasma membrane of the cell soma, BK channels were detected. They were absent from symmetric as well as asymmetric synaptic junctions, and they could be classified into two pools. One pool was evenly distributed over the somatic membrane, and the other was clustered at areas of subsurface membrane cisterns, also called hypolemmal cisternae. These cisterns, originally described by Rosenbluth [3], were also reactive to inositol 1,4,5-triphosphate receptor (InsP3) immunolabeling [4].

InsP3 mediates the effects of several neurotransmitters, hormones and growth factors by mobilizing Ca<sup>2+</sup> from intracellular stores. Ca<sup>2+</sup> release through these channels may raise local Ca<sup>2+</sup> concentrations to levels high enough for BK channel activation. Coupling of Ca<sup>2+</sup> release through InsP3 and activation of Ca<sup>2+</sup> sensitive potassium channels may thus present a novel functional microdomain within neurons.

### References:

- [1] Cooper EC, Harrington E, Jan YN and Jan LY: *J Neurosci.* 21;24 (2001) 9529-40.
- [2] Hu H, Shao LR, Chavoshy S, Gu N, Trieb M, Behrens R, Laake P, Pongs O, Knaus HG, Ottersen OP and Storm JF: *J Neurosci.* 21;24 (2001) 9585-97.
- [3] Rosenbluth J: *J. Cell Biol.* 13 (1962) 405-421.
- [4] Ross CA, Meldolesi J, Milner TA, Satoh T, Supattapone S and Snyder SH: *Nature* (1989) 468-470.

## A Transmission Electron Microscope Investigation of the Lead on the Hepatopancreas of *Palaemonetes turcorum* (Holthuis, 1961) (Crustacea, Decapoda)

Mehtap Kutlu, Gözde Aydoğan

Anadolu University, Faculty of Science, Department of Biology, 26470, Eskişehir, Turkey

The liver and pancreas in vertebrate animals are the main sites of both organic and inorganic reserve material. In crustaceans, the hepatopancreas has the function of both the liver and pancreas of vertebrates and therefore is involved in the secretion of digestive enzymes and the absorption and storage of lipid material. Hepatopancreas could also be a potential indicator organ for heavy metal toxicity [1].

The common prawn *Palaemonetes spp.* is an ecologically important and widely distributed shallow water species which has a potential economic importance. In this study effects of heavy metal lead were investigated in hepatopancreatic cells of *Palaemonetes turcorum* by transmission electron microscopy.

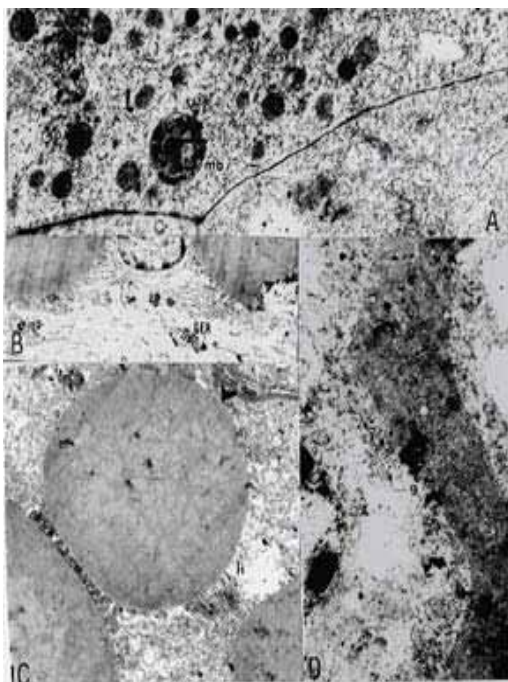


**Fig. 1:** Transmission electron micrographs of hepatopancreatic cell of *P. turcorum*

Control group was not exposed to lead but experimental group was for 96 h at a single toxicant concentration  $LC_{50}$  0.394 mg/L. This concentration of  $LC_{50}$  was determined for *Gammarus pulex*, another freshwater organism sensitive to environmental pollution from Crustacea, by Kutlu and Sümer (1998).

Ultra structural changes of the hepatopancreatic cells were studied in these two groups by electron microscopy techniques. Some changes in the organelles such as the dilation and degranulation of granulated endoplasmic reticulum, changes in the shape and location of the nucleus occurred. Dilation of membranous structures such as morphological changes in the mitochondrial cristae were observed. There were formations of myelin bodies, secondary lysosomes, glycogen particles and there was an increase in the number and size of lipid droplets.

### References:

- [1] Papathanassiou E, King PE, Comp Biochem Physiol 77 (1984) 243-249.
- [2] Kutlu M, Sümer S, Bull Environ Contam Toxicol 61 (1998) 816-821.

## Effects of Lead on the Histopathology of Gill in *Aphanius chantrei* (GAILLARD,1895)(CYPRINODONTIFORMES:CYPRINODONTIDAE)

Mehtap Kutlu, Volkan Kılıç, Gözde Aydoğan

Anadolu University, Faculty of Science, Department of Biology, 26470, Eskişehir, Turkey

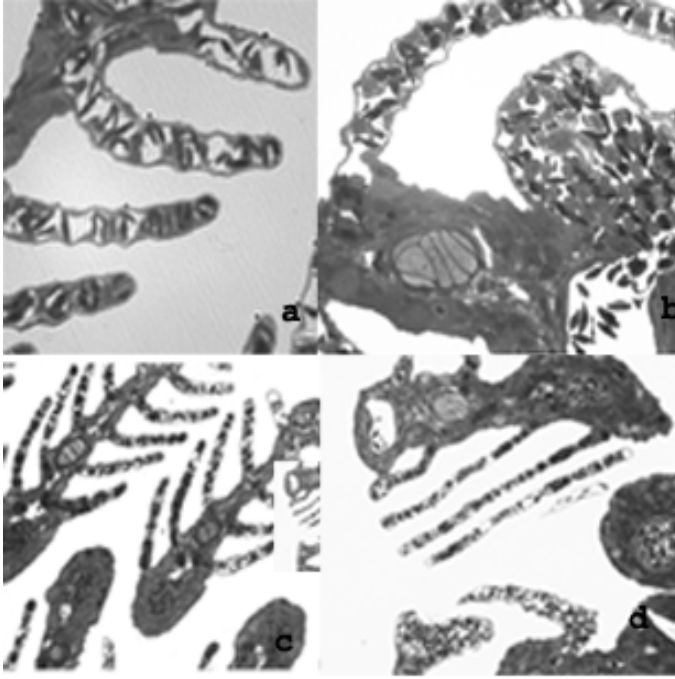


**Fig. 1:** Light micrographs of the gill of *A. chantrei* after 96 h. lead exposure.

a- control group b-experimental group  
c- control group d-experimental group

### References:

[1] Soeginato A, Charmantier-Daures M, Trilles JP, Charmantier G, Aquat. Living. Resour. 12 (1) (1999) 57-70

Cadmium is a heavy metal which is bio-available as a free divalent cation,  $Cd^{+2}$  which is the main agent of toxicity to fish. Cadmium appears to enter mainly through gill ionocytes and accumulates mainly in kidney, liver and gill tissue of fish. An investigation on the effect of the heavy metal cadmium (Cd) on the gill of *Aphanius chantrei*, sensitive organism for environmental pollution, was carried out. The fish were exposed to sub-lethal concentrations (5500 g/l) Cd for a period of four days. Observations of histological structures found that most of the secondary lamella have degenerated,. There were deformation of the gill tissue and traces of pigmentation.

## Changes in the Liver Cells of Killifish *Aphanius chantrei* (GAILLARD,1895) (CYPRINODONTIFORMES:CYPRINODONTIDAE) due to Lead Accumulation

Mehtap Kutlu, Volkan Kılıç, Gözde Aydoğan, Ahmet Özata

Anadolu University, Faculty of Science, Department of Biology, 26470, Eskişehir, Turkey

Lead is considered a major toxicant to several aquatic organisms. The aquatic biota is the main pathway of toxic trace metals from a contaminated environment to humans, since some metals such as lead, mercury and cadmium suffer biomagnification through food chains, presenting their highest concentration in higher trophic level organisms like fish [1,2].

Lead absorption is distributed to two main compartments. The readily exchangeable compartment comprises blood and soft tissues such as liver, kidney and brain. As an important organ involved in metabolic processes and in detoxification of xenobiotics, the liver may have pathological alterations due to the accumulation of lead to toxic levels [3].

The Killifish, *Aphanius chantrei* (Cyprinodontiformes: Cyprinodontidae) is a freshwater organism which is endemic in streams, rivers and lakes in Turkey [4,5]. Several populations of *Aphanius spp.* are now considered extinct or endangered due to environmental pollution [6].

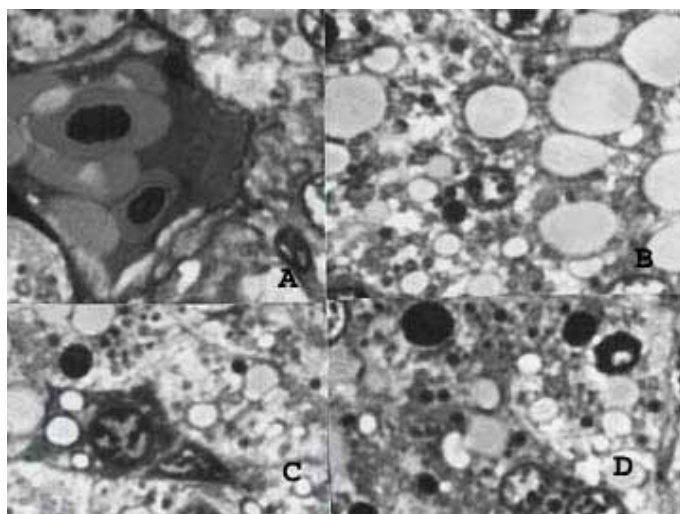


**Fig. 1:** Light micrographs of the hepatocytes in *A. chantrei* after 96 h. lead exposure

The experiment consisted two groups: control group and experimental group. There were 4 replicates per group with 5 animals in each replicate. Animals in experimental group were exposed to lead for 96 h .

After 96h. Lead exposure, changes in the shape and chromatin dense of the nucleus in the hepatocytes was observed. There was an increase in the number and size of the lipid droplets (Fig 1B) and granular change in the cytoplasm (Fig 1D). Changes towards apoptosis were observed in some hepatocytes (Fig 1A, Fig 1C).

### References:

- [1] Ferreira AG, Melo EJT Carvalho CEV, Acta Microscopica 12 (1) (2003) 49-54.
- [2] Gašpić ZK, Zvonarić T, Vroč T, Odžak N, Barić A, Water Res 36 (2002) 5023-5028.
- [3] Schmitt JC, Finger SE, Arch Environ Contam Toxicol 16 (1987) 185-207.
- [4] Gaillard C, Arch Mus Hist Nat Lyon (1895) 2-15.
- [5] Balık S Ege Üniversitesi Basımevi Bornova-İzmir (1988) 422.
- [6] Wildekamp RH, Küçük F, Ünlüsayın M, Neer WV, Tr J of Zoology 23 (1999) 23-44.

## **Expression of ETEC-specific surface antigens in wildtype *E.coli*, recombinant *E.coli* and *Vibrio cholerae* strains evaluated by transmission electron microscopy**

Stefan Lüdi<sup>1,2</sup>, Joachim Frey<sup>2</sup>, Didier Favre<sup>3</sup>, Jean-Francois Viret<sup>3</sup>, Nadine Kapp<sup>1</sup>, Michael H. Stoffel<sup>1</sup>

<sup>1</sup>Division of Veterinary Anatomy, University of Bern Veterinary School, 3012 Bern, Switzerland

<sup>2</sup>Institute of Veterinary Bacteriology, University of Bern Veterinary School, 3012 Bern, Switzerland

<sup>3</sup>Berna Biotech Ltd, Rehhagstrasse 79, 3018 Bern, Switzerland

Enterotoxigenic *Escherichia coli* (ETEC) are an important cause of diarrhea in infants in less-developed countries and in travelers. Adhesion to the small intestine mucosa is dependent on specific Colonization Factor Antigens (CFA) and Coli Surface (CS) Antigens, which form so-called pili or fimbriae [1]. CFA/I, CS3 and CS6 are the most prevalent fimbrial antigens found in clinical isolates. These specific surface structures are potent immunogens and, thus, are promising candidates for vaccine generation.

The goal of this study was to visualize the morphology of CFA/I, CS3 and CS6 pili in wildtype and recombinant *E. coli* strains as well as in recombinant *V. cholerae* strains. Therefore, corresponding ETEC genes were cloned into *E.coli* K12 strain DH10B as well as into *V. cholerae* strain CVD 103-HgR in order to investigate the expression of pili using transmission electron microscopy in conjunction with negative staining and immunolabelling.

Expression of fimbriae was dependent on culture conditions and sample handling. Negative staining was effective in revealing CFA/I and CS3. Differences in the morphology of genetically and immunologically identical pili in wildtype and recombinant ETEC strains as well as in recombinant *V.cholerae* could clearly be demonstrated using negative staining. Notwithstanding, specific immunolabelling of pili unambiguously demonstrated the presence of all three types of surface antigens investigated including CS6.

The present study provides evidence that specific ETEC surface antigens can adequately be expressed in recombinant *E.coli* strains as well as in an attenuated *V. cholerae* vaccine strain. Although pili may take on a different morphology, they seem to remain immunologically unaltered and, therefore, may be expected to elicit a proper immune response. This study provides a basis for the assessment of recombinant vaccines.

### References

[1] Jonson, A. B., S. Normark, and M. Rhen. 2005. Fimbriae, pili, flagella and bacterial virulence. *Contrib Microbiol* 12:67-89.

The technical support of Cynthia Furer, Yvonne Schlatter, Corinne Hug and Simon König is gratefully acknowledged. This work was financially supported by....

## Discriminatory Staining of Budded Baculovirus

Pernilla Nevsten<sup>a</sup>, Gunnel Karlsson<sup>b</sup>, and Reine Wallenberg<sup>a</sup>

<sup>a</sup>nCHREM, Lund University, P.O. Box 124, SE-221 00 Lund, Sweden

<sup>b</sup>Biomicroscopy unit, Lund University, P.O. Box 124, SE-221 00 Lund, Sweden

Immunogold labeling of budded baculovirus was used as a step to prove surface expression of enhanced green fluorescent protein, EGFP. The EGFP had been introduced by a new method based on the baculovirus/insect cell expression system [1]. When using a PTA staining procedure, both negatively and positively stained virus particles appeared (Figure 1a) but the immunogold label only attached to the positively stained virus (Figure 1b and c).

We suggest that the membrane of the budded baculovirus is degraded and a fraction of the virus particles lose the membrane during storing or during the immunolabeling procedure. The fraction lacking membrane, as shown in Figures a and c, is negatively stained while the virus particles that still are membrane coated are positively stained as PTA stains glycoproteins [2] at the membrane surface. In addition there is a possibility for stain to penetrate underneath the membrane if the membrane is ruptured [3]. [4]

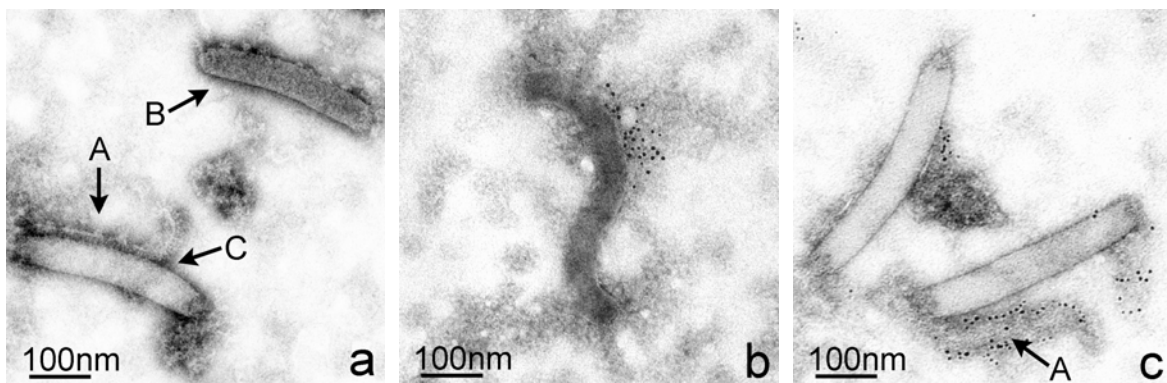


**Fig 1** a) Non-modified baculovirus was used to control grids. On these grids there were no immunogold labeling. The negatively stained virus particles (marked A) have lost the coating membrane while virus particles with membrane are positively stained due to staining of glycoprotein (marked B). b) Some virus particles partially lost their membrane through peeling off (C). b) On the grids with the modified baculovirus immunogold specific labeling appears only on positive stained virus particles. c) Apparently unspecific labeling on the surrounding area was seen. However, on closer scrutiny, it is clear that this is labeling of shedded membranes, thus explaining the absent of labeling of the (negatively stained) naked particles.

### References:

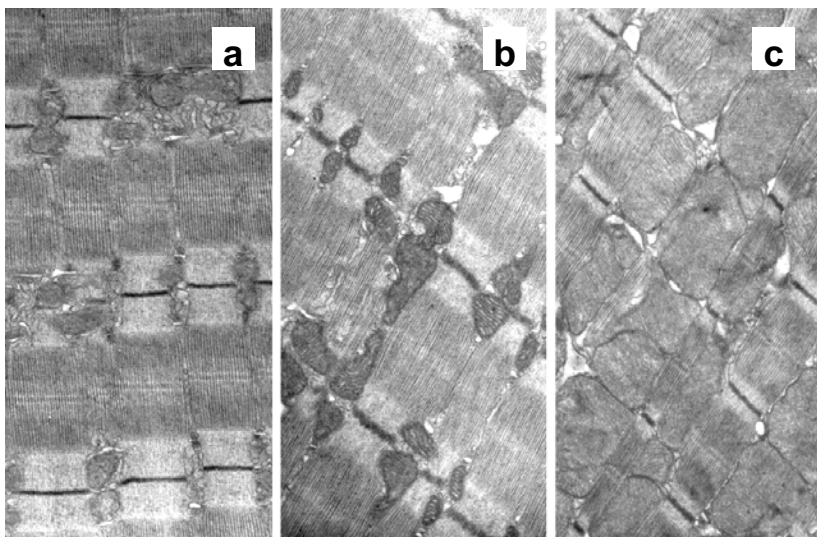
1. J. Borg, P. Nevsten, R. Wallenberg, C. Falkenberg, C. Holm, *Journal of Biotechnology*, submitted
2. G.W. Bernard and M. E. Barkin, *Archives of Oral Biology* **17(6)** (1972), p 983-6.
3. J. R. Finlay, D. S. Teakle, *Journal of General Virology* **5** (1969), 93-6
4. Support from the Swedish Research Council and the Knut and Alice Wallenberg foundation is gratefully acknowledged. Dr. Jörgen Borg is acknowledged for providing the virus.

## Comparative Quantitative Analysis of Mitochondrial Environment in Different Striated Muscle Cells.

Marta Novotová and Ivan Zahradník.

Institute of Molecular Physiology and Genetics SAS, Vlárská 5, 833 34 Bratislava, Slovak Republic

The amount and localization of mitochondria in muscle cells is a result of continuous adaptation of cell function to various stimuli that shape muscle contractility. Here we compare topology of mitochondria from the point of their spatial relations to neighbouring organelles in three functionally distinct muscle fibre types - the fast (a), the slow (b) and the cardiac muscle (c) fibres.



We have used a stereological method of vertical sections applied to electron microscopic images of gastrocnemius, soleus, and ventricular muscles. Muscle samples were prepared from five adult male mice. The environment of mitochondria was estimated as the relative contact area of the mitochondrial surface with the surface of individual neighbouring organelles.

In the three muscle types, the differences in relative

mitochondrial volume were found to translate into differences in the environment of mitochondria. Both the subsarcolemmal and intermyofibrillar mitochondria communicated most frequently with the surface of myofibrils and with the sarcoplasmic reticulum. In cardiac muscle, however, contact area of mitochondria with the A-band was larger than in skeletal muscles, while in skeletal muscles contact area with the I-band was larger than in cardiomyocytes. The surface of mitochondria surrounded with cisterns of sarcoplasmic reticulum in triads was larger in skeletal types of muscle fibres than in cardiac muscle. In slow muscle fibres, a relatively large coverage of mitochondria with t-tubules of triads was noticeable .

On the basis of measurements of the mitochondrial environment we conclude that in cardiac muscle the mitochondria support primarily contractility, while in skeletal muscles their role is mainly in support of calcium release and uptake.

*Supported by APVT – 51-31104*

## Bacterial Spores in the Skin of a 1000-Year-Old Peruvian Mummy

M.A.Pabst<sup>1</sup>, I.Letofsky-Papst<sup>2</sup>, E.Bock<sup>1</sup>, K.Spindler †<sup>3</sup>, S.Guillén<sup>4</sup>, F.Hofer<sup>2</sup>

<sup>1</sup>Department for Cell Biology, Histology and Embryology, Medical University of Graz, A-8010 Graz, Austria, <sup>2</sup>Research Institute for Electron Microscopy, Graz University of Technology, <sup>3</sup>Institute for Pre-and Protohistory, University of Innsbruck, Austria, <sup>4</sup>Centro Mallqui, Ilo, Peru

A mummy found in the Atacama desert in South Peru was investigated. In the dermis of the skin of this mummy from the necropolis of Chiribaya Alta, numerous bacterial spores (Fig.1) have been found. Bacterial spores are dormant stages of the microorganisms, which are formed in response to starvation and can withstand extreme conditions of heat, radiation, toxic chemicals, dehydration and time [1]. The TEM investigation of these spores exhibits that in these ovoid spores a core, a cortex, a lamellar inner and an outer spore coat still can be distinguished. In the core phosphate as constituent of the DNA, which is localized in this area of the spores, could be detected as well as carbon, oxygen and nitrogen indicating the presence of proteins, were found by electron energy-loss spectroscopy (EELS). Especially in the spore coat along with proteins higher amounts of sulfur could be found. Here, a cystein rich protein is described, whose disulfide bonds are responsible for their radiation resistance. In all three layers of the bacterial spores calcium could be detected by x-ray spectrometry (EDXS). Large amounts of dipicolinic acid are known to be present as Ca-chelate in bacterial spores, which is thought to be the reason for heat resistance. On the border of the cortex to the inner spore coat, electron dense patches were observed frequently, which were analysed using EDXS. The electron dense structures consist of carbon, oxygen, iron, aluminium, phosphorus, calcium and zinc or in other patches silicon instead of zinc.

The bacterial spores found in the dermis seem to belong to the spore-forming genera *Bacillus* or *Clostridium* [2]. SEM studies of possibly other species of bacterial spores reveal a special surface structure. Closely packed ridges extend along the longitudinal axis of the spore and on one end a kind of collar can be seen (Fig.2). Because only spores seem to be present, one can assume that when the corpse dried out, the “nutrition” for the bacteria was no longer present and so they formed spores, which were preserved for 1000 years along with the mummy.

### References:

- [1] Ingraham JL, Ingraham CA, Prentiss H., Introduction to Microbiology (1995) USA: Wadsworth Publishing Company
- [2] Perrin C, Nolly V, Mourer R, Schmitt D, Ann Dermatol Venerol, 121 (1994) 470-475

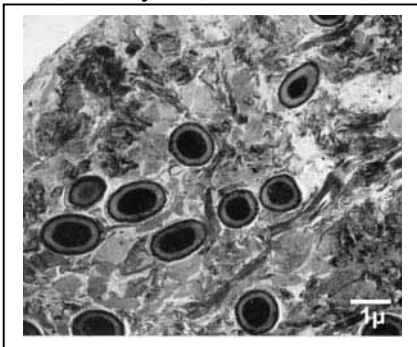


Fig.1 Bacterial spores

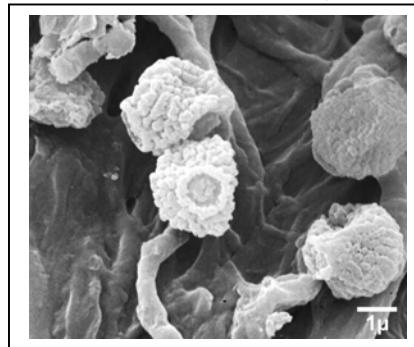


Fig.2 Bacterial spores

## Structures in the Dermis of a 1000-Year-Old Mummy from Chiribaya Alta, Peru

M.A.Pabst<sup>1</sup>, I.Letofsky-Papst<sup>2</sup>, E.Bock<sup>1</sup>, K.Spindler<sup>3</sup>, P. Wilhelm<sup>2</sup>, S.Guillén<sup>4</sup>, F.Hofer<sup>2</sup>

<sup>1</sup>Department for Cell Biology, Histology and Embryology, Medical University of Graz, A-8010 Graz, Austria, <sup>2</sup>Research Institute for Electron Microscopy, Graz University of Technology, <sup>3</sup>Institute for Pre-and Protohistory, University of Innsbruck, Austria, <sup>4</sup>Centro Mallqui, Ilo, Peru

In the Atacama desert in South Peru a mummy from the necropolis of Chiribaya Alta was found lying unwrapped in the sand. The skin of the mummy has a leather-like texture and a light brown colour. Microscopical investigations reveal that the epidermis was not present any more. In the dermis, however, many cross striated collagen fibrils and elastic fibers could be detected with TEM. Darkly stained cells could be found in the dermis between connective fibers. In these cells putative membrane bound cellular organelles can be seen. Some of which look like mitochondria.

The hot and dry climate dries out the corpses quickly. Rapid postmortem desiccation commonly results in long-term, spontaneous soft tissue preservation. Since the dermal structures are in such an excellent preserved state the question arises if the studied mummy was additionally artificially preserved. However, no traces of embalming substances could be detected on the studied mummy using infrared spectroscopy.

In the dermis numerous bacterial spores have been found. Bacterial spores are dormant stages of the microorganisms, which are formed in response to starvation and can withstand extreme conditions of heat, radiation, toxic chemicals, dehydration and time <sup>1</sup>. The TEM investigation of these spores exhibits that in these ovoid spores a core, a cortex, a lamellar inner and an outer spore coat still can be distinguished. On the border of the cortex to the inner spore coat, electron dense patches were observed frequently. In these different areas various elements could be detected by EDXS and EELS. SEM studies of possibly other species of bacterial spores reveal a special surface structure.

The bacterial spores found in the dermis seem to belong to the spore-forming genera *Bacillus* or *Clostridium* <sup>2</sup>, and they might have been preserved for 1000 years along with the mummy.

### References:

- 1 Ingraham JL, Ingraham CA, Prentiss H., Introduction to Microbiology (1995) USA: Wadsworth Publishing Company
- 2 Perrin C, Nolly V, Mourer R, Schmitt D, Ann Dermatol Venerol, 121 (1994) 470-475

## Preservation of the Dermis of a 1000-Year-Old Mummy from Chiribaya Alta, Peru

M.A.Pabst<sup>1</sup>, I.Letofsky-Papst<sup>2</sup>, P. Wilhelm<sup>2</sup>, E.Bock<sup>1</sup>, K.Spindler †<sup>3</sup>, S.Guillén<sup>4</sup>, F.Hofer<sup>2</sup>

<sup>1</sup>Department for Cell Biology, Histology and Embryology, Medical University of Graz, A-8010 Graz, Austria, <sup>2</sup>Research Institute for Electron Microscopy, Graz University of Technology, <sup>3</sup>Institute for Pre- and Protohistory, University of Innsbruck, Austria, <sup>4</sup>Centro Mallqui, Ilo, Peru

In the Atacama desert in South Peru a mummy from the necropolis of Chiribaya Alta was found lying unwrapped in the sand, obviously a victim of tomb looters.

The skin of the mummy has a leather-like texture and a light brown colour. Microscopical investigations reveal that the epidermis was not present any more. In the dermis, however, many cross striated collagen fibrils and elastic fibers could be detected with TEM (Fig 1). Cells which are darkly stained by uranyl acetate and lead citrate could be found in the dermis between connective fibers, (Fig. 2). In these cells putative membrane bound cellular organelles can be seen. Some of which look like mitochondria. They have a diameter of ~ 0.6 µm. Two membranes are visible, the inner one folded like to cristae. The membranes are in negative contrast, meaning that they look bright whereas the cytoplasm of the cell is dark. Additionally, a putative nucleus was observed.

In this hot and dry climate corpses dried out quickly. Rapid postmortem desiccation commonly results in long-term, spontaneous soft tissue preservation. Presumably due to these conditions, the oldest mummy reported to date – about 9000 years old - was found here [1]. Since the dermal structures are in such an excellent preserved state the question arises if the hot and dry climate was the only reason for tissue preservation on the studied mummy. It is also known that elite individuals of importance for the society have been artificially preserved in South Peru [2]. However, no traces of embalming substances could be detected on the studied mummy using infrared spectroscopy.

### References:

- [1] Aufderheide AC, Muñoz I and Arriza B, *Am J Phys Anthropol* 91 (1993) 189-201.
- [2] Vreeland JM, JR, In: Cockburn A, Cockburn E, and Reyman TA, eds. *Mummies, Disease & Ancient Cultures*. Cambridge: Cambridge University Press. (1998) 154-189.

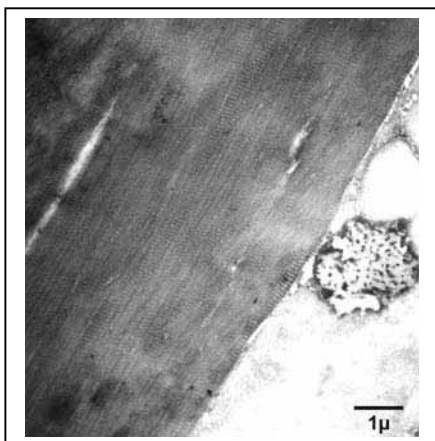


Fig.1 connective tissue

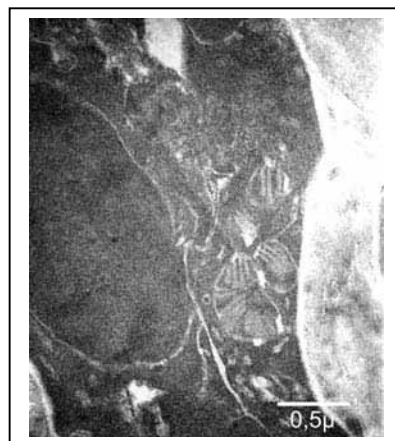


Fig.2 dermal cell

## **Electron microscopic and X-Ray Analysis of *Escherichia coli***

Astghik Pepoyan, Karlen Hovnanyan, Maria Karagyozyan, Anahit Manvelyan,  
Margarita Hovnanyan, Anna Baghdasaryan

Institute of Molecular Biology of NAS RA, Yerevan, 375014, Armenia

The surface structures and membranes of bacteria play an important role in intercellular interaction and establishment of dynamic stable balance in parasitocenosis in intestine and in external medium.

The aim of the present research was to study morphologic properties of *E. coli* pathogenic and commensal strains and its membranes by the electron microscopy and X-ray diffraction method. The cellular filamentation of these strains as well as comparative role of LPS from their membrane on bacterial cell wall biophysical properties such as hydrophobicity and adhesion were investigated.

The transmission electronic microscope Tesla – 500 was used for investigating 39 *E. coli* strains' cellular filamentation. For studying the bacterial external structure it was used the method of negative contrast coloring by using 1% salt solution of phosphor-wolfram. pH of solution was 6,0-7,0. After drying bacterial preparation was colored in the drop of phosphowolframics' acid solution. For the comparative ultrastructural analysis of *E. coli* culteres the bacteria were fixed in 2,5% glutaraldehyde on 0,1M cacodylate buffer (pH-7,2) and postfixed in 1% osmiumtetraoxide on 0,1M cacodylate buffer (pH-7,2). After dehydration in and saturation the bacteria fall-out was enclosed in aralditis. Ultrathin sections were colored in uranyl acetat and by lead citrate.

The electron microscopic investigations of morphology of *E. coli* strains have not revealed any salience peculiarities connected with their pathology. On the same time, as showed the results of X-ray diffraction method, the reflexes from the investigated *E. coli* cell walls after LPS removal are different. Also it was revealed the difference of *E. coli* strains by their hydrophobicity and adhesion. On ultrathin sections *E. coli* has ultrastructure and division type, typical for Gram- bacteria L-transformed specimen like spheroplasts.

The role of LPS on bacterial cell wall biophysical properties was investigated by using the X-ray diffraction method under the small and big angles. The reflexes from the bacterial cell walls in the 0.01 M phosphate-buffer on untreated cells and on a sample of *E. coli* treated with 100 mM ethylenediaminetetraacetic acid (EDTA), which removes approximately 80% of the LPS molecules, were obtained. For finding out the legitimacies of changes of midline distances of small-angle reflexes and the definition of membrane's both characteristics and intermembrane distances /d/ for more expressed reflexes, the dependence from the ratio of the water concentration and membranes were obtained.

As showed the investigations the structure of *E. coli*' membranes can be decisive for finding out new probiotic strains and the X-ray diffraction method can be used for revealing efficient probiotic strains.

## Confocal Fluorescence Microscopy: A Novel Method in Brewing

Cornelia Schlee<sup>a</sup>, Michaela Miedl<sup>a</sup>, Graham G. Stewart<sup>a</sup>

<sup>a</sup>ICBD, Heriot-Watt University, Riccarton, Edinburgh EH14 4AS, United Kingdom

Using confocal imaging and fluorescence microscopy it is possible to gain important information about the physiological state of a yeast population by visualising cell compounds such as glycogen, neutral lipids, trehalose and bud scars. This knowledge is a fundamental requirement to achieve stability throughout the fermentation process. Disturbances that are caused by a change in the physiological state of the yeast population can be determined and corrective actions taken.

Glycogen is accumulated in the yeast cell in the adaption phase and the beginning of early exponential growth phase during the supply of nutrients. It is metabolised at the end of fermentation, at times of nutrient limitation. The chance of a yeast cell starting a new round of cell cycle decreases with increasing consumption of glycogen. The fluorescence dye acriflavine stains glycogen in yeast cells [1].

Neutral lipids act as energy storage compounds and perform protective functions against high ethanol and sugar concentrations. They are synthesised mainly at the beginning of fermentation and in situations of stress. The highly lipophilic benzophenoxazone dye Nile Red intercalates in lipid droplets and stains neutral lipids [2].

The disaccharide trehalose is a stress protectant during storage and plays a role in the initiation of the cell cycle as it quickly supplies a carbohydrate- and energy source. Trehalose is incorporated in the cell as soon as the proliferation activity of the yeast decreases. The trehalose content can be determined using the lectin-fluorochrome-conjugate concanavalin A-fluorescein [3].

Bud scars consist of crater like chitin-rings on the cell surface that are not flexible enough to ensure sugar and gas exchange. They are stained by the fluorescent dye wheat germ agglutinin-fluorescein [4]. The higher the number of bud scars, the less the remaining cell surface that allows the transport of gas and sugar molecules. High fluorescent signals imply the existence of many old or dead cells in the cell population whereas low fluorescence indicates a young and dynamic cell population.

### References:

[1] Hutter, K.-J., Remor, M. and Müller, S.: Biomonitoring der Betriebshefen in praxi mit fluoreszenzoptischen Verfahren. VII. Mitteilung: Untersuchungen zur flusszytometrischen Bestimmung des Glykogengehaltes der Betriebshefe, Brauwissenschaft 53 (2000) 68-76

[2] Hutter, K.-J., Müller, S., Herber, M.: Biomonitoring der Betriebshefen in praxi mit fluoreszenzoptischen Verfahren, III. Mitteilung: Funktionalitätstests an Hefezellen, Brauwissenschaft 49 (1996) 164-170.

[3] Hutter, K.-J., Kliemt, C., Nitzsche, F., Wießler, M.: Biomonitoring der Betriebshefen in praxi mit fluoreszenzoptischen Verfahren. IX. Mitteilung: Trehalose – Stressprotektant der Saccharomyces-Hefen. Brauwissenschaft 56 (2003) 121-125.

[4] Hutter, K.-J., Nitzsche, F.: Untersuchungen über die Alterung der Bierhefen mit Hilfe der flusszytometrischen Analyse, Brauwissenschaft 55 (2002) 196-199.

## Improvement of freeze-fracture labeling efficiency

Wiebke Schlörmann, Frank Steiniger, Walter Richter, Martin Westermann

Elektronenmikroskopisches Zentrum, Klinikum der Friedrich-Schiller-Universität,  
Ziegelmühlenweg 1, 07743 Jena, Germany

In the 90ties Kazushi Fujimoto [1] developed a new freeze-fracture replica immuno-labeling technique using sodium dodecyl sulfate (SDS) to clean the replicas. The replicas were obtained from chemically unfixed, rapidly-frozen cells. The detergent dissolves rests of cellular components with the release of material that is in direct contact to the replica film. Thus membrane lipids, transmembrane protein complexes as well as peripheral proteins remain bound to the replica. The crucial advantage of this method is the large-area, cytochemical detection of protein-and lipid distribution-patterns on protoplasmic and exoplasmic fracture faces of freeze-fractured membranes with electron microscopical resolution.

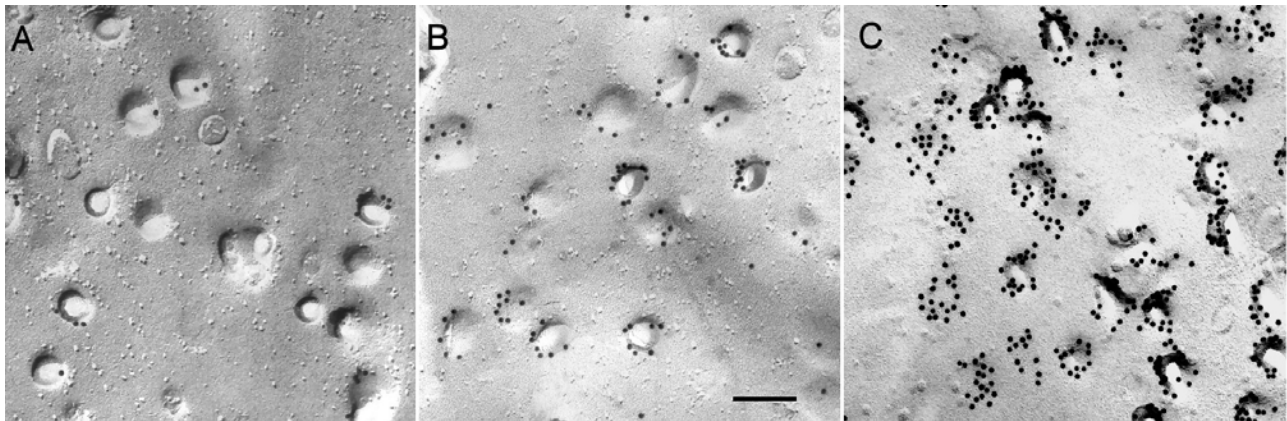


**Fig. 1.** Freeze-fracture immuno-labeling efficiency of plasma membrane caveolin-1 in chemically unfixed 3T3 mouse fibroblast cells. **A**, Pt-C replication, thickness of the Pt layer 2.5 nm. **B**, Pt-C replication, thickness of the Pt layer 1.5 nm. **C**, the best labeling efficiency was achieved by an reversed evaporation of carbon as first and platinum as second layer (C-Pt replication). Bar, 100 nm

Labeling the membrane protein caveolin-1 of caveolae [2] we often found variations in labeling efficiency. Higher labeling rates were detected in replica areas with thin or no platinum. We studied this effect by variation of the evaporation parameters. Labeling Pt-C replica with platinum layer thickness of 2.5 nm we counted 0-4 gold particles/caveola. A thinner platinum layer of 1.5 nm resulted in labeling rates of  $5.8 \pm 2.4$  gold particles/caveola and a replication in reverse order (C-Pt) lead to high labeling rates of  $14 \pm 4.4$  gold particles/caveola. As result freeze-fracture labeling efficiency of caveolin-1 is enhanceable by evaporation of thin platinum layers but the highest labeling rates were achieved evaporating carbon as first replication layer. Further research on the cause of this evaporation effect is in work.

### References:

- [1] Fujimoto K., Histochem. Cell Biol. 07 (1997) 87-96
- [2] Westermann M., Steiniger F., Richter W. Histochem. Cell Biol. (2005) Epub ahead of print

## **The SNAP-tag - Labeling of Fusion Proteins in live Cells and *in vitro***

Schwab M., Tynes R., Gedge L., Kindermann M., Brecht A.

Covalys Biosciences AG, Benkenstr. 254, CH-4108 Witterswil

Covalys recently introduced a protein labeling technology which offers an elegant way to label proteins in cells or in a cell-free environment with high specificity under biological conditions. This technology relies on the fusion of the target protein with the SNAP-tag, which is a single domain protein that reacts covalently with benzylguanine derived substrates. In this one-step reaction a label is transferred from the substrate to a cysteine thiol group of the SNAP-tag, forming a stable thioether bond between label and target protein. The SNAP-tag technology can be used for labeling of proteins in living cells, as well as for labeling *in vitro* and for covalent immobilization of SNAP-tag fusion proteins to solid supports, such as for protein arrays, surface plasmon resonance or to beads.

We will present data from the use of cell permeable SNAP-tag substrates that allow the labeling of fusion proteins inside or outside living cells. SNAP-tag fusion proteins can be labeled within intracellular compartments using a cell permeable substrate or the extracellular portion of a membran protein can be labeled selectively using a non cell permeable dye. This allows to study receptor trafficking from the membrane through the endocytotic pathway without observing interfering signals from the secretory pathway. The exposure of cells to the SNAP-tag substrate can be controlled in time thus allowing pulse/chase labeling experiments by using different fluorescent labels. In contrast to some autofluorescent proteins, SNAP-tag labels are not affected by fixation, expanding the range of possible experimental approaches. Currently we are offering green and red fluorescent SNAP-tag substrates and a biotin probe for intracellular labelling. One of the fluorescent dyes is compatible with a standard fluorescein filter set and the other one can be used with rhodamine filters. For selective extracellular labeling four dyes are available of which the excitation peaks are at 488, 547, 632 and 647 nm, respectively. We are constantly broadening available labels for intra- and extracellular applications. Furthermore we are establishing an orthogonal SNAP-tag system that will allow the simultaneous labeling in live cells of two different proteins fused to one of two SNAP-tag variants.

An important consideration for industrial users is the sales model which does not require an explicit licensing agreement and related payments.

## Delineation of Neoplastic Human Mast Cells by Immunoelectron Microscopy

Puchit Samorapoompichit<sup>1,2</sup>, Marianne Steiner<sup>1</sup>, Gerit-Holger Schernthaner<sup>2,3</sup>, Christof Worda<sup>4</sup>, Wolfgang R. Sperr<sup>2</sup>, Peter Valent<sup>2</sup>

<sup>1</sup>Center of Anatomy and Cell Biology, Institute of Histology & Embryology,

<sup>2</sup>Department of Internal Medicine I, Division of Hematology and Hemostaseology,

<sup>3</sup>Department of Internal Medicine II, Division of Angiology, and

<sup>4</sup>Department of Obstetrics and Gynecology,

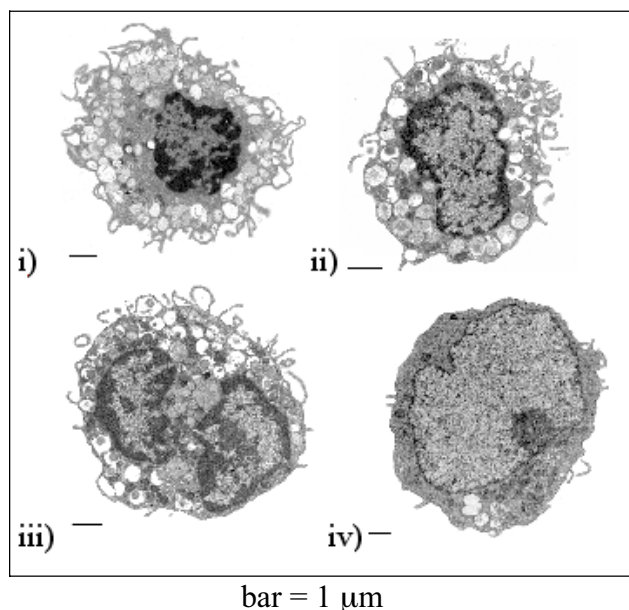
Medical University of Vienna

Schwarzspanierstrasser 17,

A-1090 Vienna,

Austria

Depending on the stage of cell maturation and disease-variant, histomorphological properties of neoplastic mast cells (MC) vary in systemic mastocytosis (SM) and related myeloid neoplasms. We have examined ultrastructural and cytomorphological features of normal tissue MC and neoplastic bone marrow MC in patients with SM (n=4), myelomastocytic leukemia (MML, n=2), mast cell leukemia (n=2), and tryptase-positive acute myeloid leukemia (AML, n=4). Based on their ultrastructure and morphology, four distinct cell types could be delineated:



i) mature well-granulated tissue MC exhibiting a round central nucleus, ii) atypical MC type I with oval nuclei, hypogranulated cytoplasm, and prominent surface projections, iii) immature atypical MC with bi- or poly-lobed nuclei (atypical MC type II = promastocytes), and iv) metachromatic blasts. Type I atypical MC were detected in patients with indolent SM, whereas type II MC and metachromatic blasts were primarily found in MML, MCL, and tryptase-positive AML. In all samples examined, the identity of MC could be reconfirmed by immunoelectron microscopy. As a matter of fact, irrespective of the stage of cell maturation or the disease-variant, all types of MC contained tryptase in their cytoplasmic granules. Taken together, immunoelectron microscopy may be a helpful approach in confirming the identity of neoplastic MC in myeloid neoplasms.

### 3D-reconstruction of immuno-labeled freeze-fracture replicas by electron tomography

Frank Steiniger, Wiebke Schlörmann, Martin Westermann, Walter Richter

Elektronenmikroskopisches Zentrum, Klinikum der Friedrich-Schiller-Universität Jena,  
Ziegelmühlenweg 1, D-07743, Germany

The SDS-freeze-fracture immuno-labeling technique [1] is a proper tool to investigate the distribution of biomolecules in chemically unfixed, native biological samples. For the immunogold-labeled plasma membrane domain structure “caveola” we have shown that the true shape can only be analysed by stereoscopic viewing or goniometer tilt series [2]. To reconstruct the three-dimensional structure more precisely here we tested the method of electron tomography after variation of Pt-C-replication and immuno-labeling. Concerning replication we compared the standard evaporation procedure (at first Pt followed by C) and the replication in reverse order (at first C followed by Pt). As different labeling methods we compared immunogold-labeling and immunophosphatase-cerium-labeling of caveolin-1 in 3T3-mouse-fibroblast cells. Whereas immunogold-labeling results in a deposition of distinct gold grains immunophosphatase-cerium-labeling results in a sheet-like deposition of cerium phosphate. Tomography was done by manual processing with help of goniometer tilt series in the range of angle from  $-60^\circ$  to  $+60^\circ$  and IMOD-software (Bolder Laboratory of 3D-Electron Microscopy of Cell).

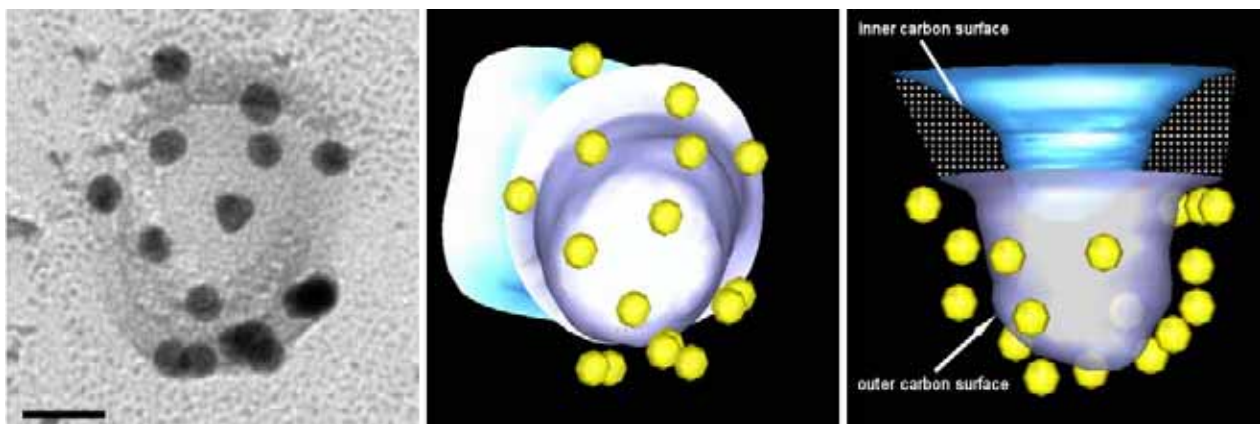


**Fig. 1.** Electron tomography of caveolin-1 freeze-fracture immunogold-labeled caveola from 3T3-mouse fibroblast cell. **A**, single micrograph of the tilt series at  $0^\circ$ . **B**, three-dimensional model, top view. **C**, three-dimensional model, side view. Bar 20 nm.

As a result we show that electron tomography is an appropriate method to analyse three-dimensional, composed structures as result from freeze-fracture preparation. Furthermore, we anticipate better insights into the process of replica-immuno-labeling and possible artefact formations.

#### References:

- [1] Fujimoto K., Histochem. Cell Biol. 07 (1997) 87-96
- [2] Westermann M., Steiniger F., Richter W. Histochem. Cell Biol. (2005) Epub ahead of print

# Cryofixation and Freeze Substitution Combined with Tokuyasu Cryosectioning Improved Preservation of Plant Tissue

York-Dieter Stierhof<sup>a</sup> and Heinz Schwarz<sup>b</sup>

<sup>a</sup>Zentrum für Molekularbiologie der Pflanzen, Universität Tübingen, D-72076 Tübingen

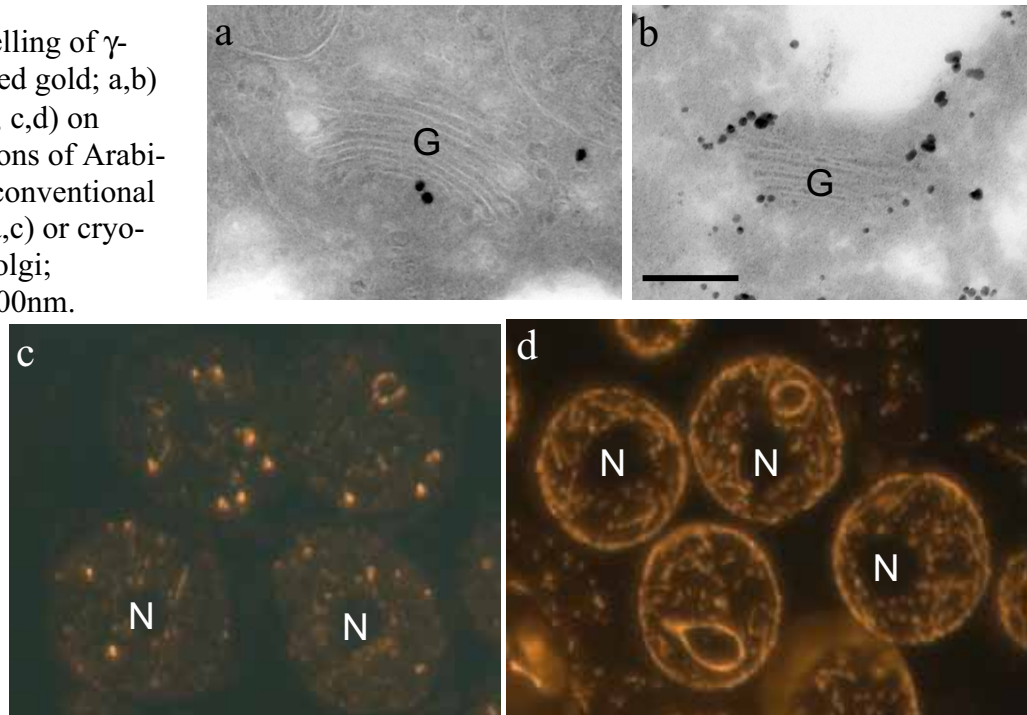
<sup>b</sup>Max-Planck-Institut für Entwicklungsbiologie, D-72076 Tübingen, Germany

Immunogold labelling on ultrathin cryosections prepared according to Tokuyasu is one of the most powerful methods for ultrastructural localization of intracellular antigens [1]. The initial chemical fixation step is a prerequisite in order to stabilize the ultrastructure prior to cryoprotection (sucrose infiltration), freezing, cryosectioning, thawing and immunolabelling. Conventional chemical fixation is a relative slow and selective process and therefore a possible source of artifacts. Slot and colleagues [2] have shown that it is possible to use native cryosections of high pressure frozen samples, chemically fixed during thawing, for immunocytochemistry. However, cryosectioning of high pressure frozen cells is technically demanding. Here we present another possibility to circumvent conventional chemical fixation: after cryofixation, the sample was freeze-substituted and rehydrated prior to conventional cryoprotectant infiltration, freezing, cryosectioning and labelling. Immunofluorescence and immunogold labelling demonstrate that distinct antigens/structures in plant tissue like ovules and anthers, cannot be fixed fast enough by conventional chemical fixation. However, they are preserved after cryofixation, freeze substitution and rehydration; e.g.,  $\alpha$ -tubulin (microtubule skeleton) and  $\gamma$ -COP (Golgi derived vesicles) in pollen grains and embryos (Fig. 1).

[1] Tokuyasu KT. *J Cell Biol* **57** (1973) 551-565.

[2] Möbius W, Ohno-Iwashita Y, van Donselaar EG, Oorschot VMJ, Shimada Y, Fujimoto T, Heijnen HFG, Geuze HJ, Slot JW. *J Histochem Cytochem* **50** (2002) 43-55.

**Fig. 1:** Immunolabelling of  $\gamma$ -COP (silver enhanced gold; a,b) and  $\alpha$ -tubulin (Cy3; c,d) on Tokuyasu cryosections of Arabidopsis pollen after conventional chemical fixation (a,c) or cryofixation (b,d). G, Golgi; N, nucleus. Bar = 500nm.



## **Artificial Elevation of Glutathione by OTC is Accompanied with Decreased Symptom Development during ZYMV-infection in *Cucurbita pepo* Plants**

Zechmann B., Zellnig G., Urbanek-Krajnc A. and Müller M.

Institute of Plant Sciences, University of Graz, Schubertstraße 51, 8010 Graz, Austria, Europe

Plants react to pathogen attack with changes in levels of antioxidants (e.g. ascorbate, glutathione etc.) and its related enzymes due to the pathogen induced oxidative stress and activation of defense genes. Increased levels of glutathione have been demonstrated to be involved in the development of resistance, mainly during incompatible plant microbe interactions [1]. Therefore the aim of the present study was to investigate whether artificially increased levels of glutathione are able to induce resistance in plants during compatible *Zucchini Yellow Mosaic Virus* (ZYMV)-infection.

Styrian oil pumpkin seedlings (*Cucurbita pepo* L. subsp. *pepo* var. *styriaca* GREB.) were treated for 48 hours with 1mM OTC (L-2-oxothiazolidine-4-carboxylic acid) to artificially increase cellular glutathione contents and infected with ZYMV 10 days later. The impacts of OTC-treatment on glutathione levels were tested on the subcellular level by immunogold labeling of glutathione with the transmission electron microscope (TEM) and on the whole leaf level with high performance liquid chromatography (HPLC). Testing was done a) for roots, cotyledons and the first true leaves after OTC-treatment to analyze to which extent OTC increases glutathione levels in different cell compartments and on the whole leaf basis and b) in roots, older and younger leaves three weeks after ZYMV-inoculation to study how possible signs of resistance correlate with glutathione levels on the subcellular level and on the whole leaf basis. Additionally, symptom severity was evaluated at this time.

Immunocytological and biochemical investigations revealed that two days after OTC-treatment glutathione contents were increased in all investigated organs (roots, cotyledons and the first leaves) of up to 145.5% in peroxisomes of cotyledons. Three weeks after ZYMV-infection glutathione labeling density was found to be significantly increased on the cellular level with the TEM in intact cells of infected leaves of up to 121.35 % in the cytosol of younger leaves and decreased in roots. However, no difference was found between 1mM OTC-treated and control plants. In contrast, biochemical studies showed that ZYMV-infection induced significant decreased glutathione-levels within the whole leaf. Nevertheless, OTC-treatment resulted in elevated glutathione contents in ZYMV-infected leaves.

Evaluation of symptom development at this point revealed that 70% of ZYMV-infected plants treated with 1mM OTC prior to infection showed no signs of symptoms although virus particles were detected in leaves and roots with negative staining methods. Only 30% of the plants showed signs of ZYMV-infection like yellowing, minor stunting and first signs of mosaic patterns. Therefore we can conclude that elevated glutathione contents within Styrian pumpkin plants might have been involved in the development of resistance during compatible ZYMV-infection.

### References:

[1] de Gara L., de Pinto M. C. & Tommasi F. 2003. *Plant Physiology and Biochemistry* 41: 863-870.

[2] Acknowledgement: This work was supported by the Austrian Science Fund, Project nr.: P16273-B06.

## Use of Energy Filtering TEM for Depiction of Organelle and Vesicle Interactions and Possible Modes of Degradation in the Green Alga *Microsterias denticulata*

N. Aichinger, A. Oertel and U. Lütz-Meindl

Cell Biology Department, Plant Physiology Division, 5020 Salzburg, Austria

The unicellular green alga has served as a model system for growing plant cells since several decades [1]. Details on cell growth, morphogenesis and on subcellular organization are well known. In the present study several organelle interactions and possible degradation pathways in growing and non-growing *Microsterias denticulata* cells are shown by the use of high pressure freeze fixation, cryosubstitution and energy filtering transmission electron microscopy (EFTEM). For EFTEM analyses ultrathin sections of a thickness of about 50 nm were mounted on uncoated copper grids with narrow hexagonal mesh. Images were filtered at zero loss energy (Fig. 1) or at an energy range of about 250 eV (energy window = 20 eV) below the carbon specific absorption edge (high contrast images, HCIs). HCIs produce a more “three dimensional” impression and are distinctly superior to images taken by conventional TEM techniques both in contrast generation and in providing structural information [2].

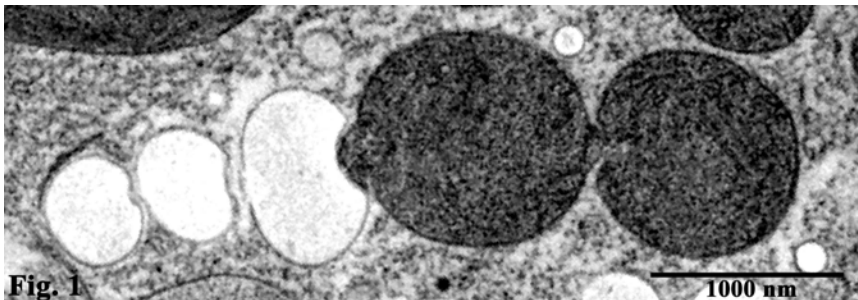


Fig. 1  
Contacts between mitochondria and mucilage vesicles filtered at zero loss energy.

Contacts among mitochondria or between mitochondria and mucilage vesicles always occur by formation of a cone-shaped protuberance of a mitochondrion that penetrates into its fusion partner (Fig. 1). Similar cone-shaped protuberances are also formed by microbodies when contacting mucilage vesicles or other organelles. In the same way lytic compartments interact with mitochondria, microbodies or vesicles by extending their contents into the respective compartment. Detached portions of mitochondria are found inside these lytic organelles. The frequent attachments of mitochondria and microbodies with the plasma membrane and their structural disintegration upon this contact may point towards another degradative process.

Marked contacts are also observed between vesicles that are involved in mucilage excretion. Vesicular structures appearing at the dictyosomal rim fuse with empty mucilage vesicles, suggesting that they discharge their contents. Together with subsequent fusions between mucilage vesicles during transport from the centrally located dictyosomes to the cortical cytoplasm, these observations may explain the functioning of an efficient and highly dynamic local mucilage excretion machinery [3].

### References:

- [1] Meindl, U., Microbiol. Rev. 57 (1993) 415-433.
- [2] Lütz-Meindl, U. & Aichinger, N., Protoplasma 223 (2004) 155-162.
- [3] The study has been supported by the Austrian Science Fund, project P15849 to U.L.-M.

## Structural and Ultrastructural Studies Concerning the Effects of Echinacea Extracts on Hemato- and Lymphopoietic Organs of Wistar Rats After Experimental Immunosuppression

Ardelean A., Anca Hermenean, Craciun C., Pribac G.C.,

Department of Cell Biology and Histology, "Vasile Goldis" Western University, Faculty of Medicine, 310396, Arad, Romania

The majority of the cytostatics used in chemotherapy induce most of the time pronounced immunosuppressive states and lymphotoxic effects, characterized by the alteration of hematic and lymphopoietic organs. In this experiment we have chose to investigate the effect of *Echinacea purpurea* extract administration, respectively *Echinacea pallida* on some hematic and lymphopoietic organs (bone marrow, thymus and spleen) after inducing experimental immunosuppression by the administration of cyclophosphamide.

Cyclophosphamide therapy (40 mg/kg/zi) administred on rats by i.p. injections for a period of 3 days, determined morphological and structural alterations of studied organs, characterized by profound disruption of cellular and vascular component: cell depletion (by blocking of mitotic divisions) with massive depopulation followed by fibrosis, blood stasis and vascular congestion, perivascular edemas and sometimes haemorrhagic zones. Although they're high extensive, structural and ultrastructural modifications induced by cyclophosphamide are reversibile, that proves the function reconstruction of studied organs. Even so, after 10 days from the last dose of cytostatic, the morphological and functional parameters are much more inferior than those of the control group.

Both of the Echinacea extracts administred by intragastric gavage of the rats treated with cyclophosphamide, determined a stimulation of structural and functional reconstruction of studied organs: bone marrow, thymus and spline, the restoration on cellular and subcellular level of these organs are much more rapid than self-reconstruction, fact proved by our light and electron microscopy images.

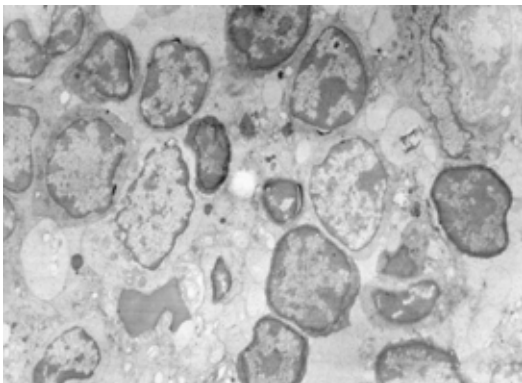


**Fig. 1** Thymus cortex from CFA group, x 5.600

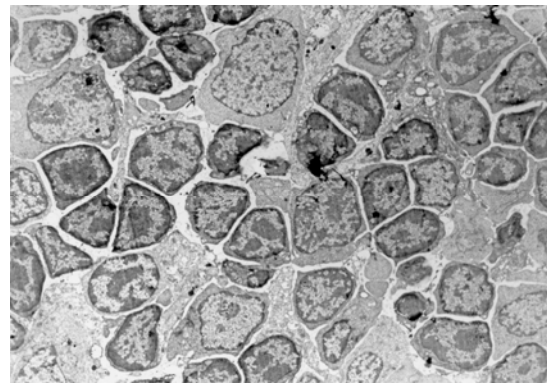


**Fig. 2** Thymus cortex from group treated with CFA and Echinacea extract, x 6.930

## **Atomic Force Microscopy Reveals Granulysin Induced Defects on Cholesterol Free Phospholipid Bilayers**

H. K. Barman, M. Walch, S. Latinovic, C. Dumrese, P. Groscurth and U. Ziegler

Division of Cell Biology, Institute of Anatomy, University of Zurich, Winterthurerstrasse 190, CH-8057 Zurich, Switzerland

The release of lytic proteins from granules of cytotoxic effector cells plays an important role in the immune system. Perforin and granzyme B are well known constituents found in cytotoxic granules together with granulysin, a 9 kD protein active against microbial pathogens. Granulysin is taken up via lipid raft mediated endocytosis and subsequently lyses intracellular bacteria without affecting the target cell. The mechanism by which granulysin binds to eukaryotic cells and lyses intracellular bacteria is not well understood [1, 2].

We have studied the binding and the effect of granulysin on liposomal phospholipid bilayers with uncharged, negatively charged and lipid raft like composition. Immunoblotting techniques showed binding of granulysin only to lipid bilayers with negative charges or lipid raft like composition. In contrast to binding, only negatively charged bilayers, but never bilayers with lipid raft like composition revealed a granulysin induced increase in permeability as shown by fluorescence release assays. Using atomic force microscopy the binding and changes in permeability of lipid bilayers with negative charges could be visualized as irregularly shaped defects through the whole bilayer. By adding specific antibodies to the bilayers with defects, the binding of granulysin could be observed. Defects did not appear in bilayers with uncharged or lipid raft like composition.

Based on these results we conclude that granulysin interacts with negatively charged cholesterol free membranes typically found in bacteria and causes defects by binding to the negatively charged phospholipids using electrostatic interactions. In contrast, granulysin is able to bind to lipid rafts in eukaryotic cell membranes from where it is taken up by the endocytotic pathway leaving the cell intact.

### References:

- [1] S. V. Pena, D. A. Hanson, B. A. Carr, T. J. Goralski, A. M. Krensky, *J Immunol* **158** (1997) 2680.
- [2] M. Walch, E. Eppler, C. Dumrese, H. Barman, P. Groscurth, U. Ziegler, *J Immunol* **174** (2005) 4220.

## **The Clathrin-Positive Endosomal TGN Attaches to the Golgi Stack During Transport of Cargo.**

Galina V. Beznoussenko<sup>1</sup>, Josef Neumuller<sup>2</sup>, Monica Vetterlein<sup>2</sup>, Daniele Di Giandomenico<sup>1</sup>, Irina S. Sesorova<sup>2</sup>; Oliviano Martella<sup>1</sup>, Nuria Jimenez-Gil<sup>3</sup>, Koert Burger<sup>3</sup>, Alberto Luini<sup>1</sup>, Alexander A. Mironov<sup>1</sup> and Margit Pavelka.

<sup>1</sup>Department of Cell Biology and Oncology, Consorzio Mario Negri Sud, Via Nazionale 8, 66030 Santa Maria Imbaro (Chieti), Italy. <sup>2</sup>Institute of Histology and Embryology, University of Vienna, Schwarzschanerstrafle 17, A-1090 Vienna, Austria. <sup>3</sup>Department of Biochemical Physiology, Institute of Biomembranes, Utrecht University, Padualaan 8, 3584 CH Utrecht, The Netherlands

The mechanisms of secretory transport through the Golgi remain an issue of debate. Several transport schemes are under consideration in the search for a new paradigm in the field of intracellular secretory transport. Here, using different protocols for synchronization of cargo progression through the Golgi, we have examined the predictability power of different models of intra-Golgi transport, to determine the mechanisms of the exit of cargo from the Golgi. The last clathrin-positive cisterna is absent in resting stacks, where the last medial cisterna is covered by the ER cisterna. During a transport wave through the Golgi, the endosomal TGN forms this clathrin-positive cisterna, which is introduced between the ER cisterna and the last medial cisterna replacing the ER cisternae attached to the medial Golgi. Most of the procollagen and the temperature sensitive variant of the G protein of vesicular stomatitis virus being transported through the Golgi stack bypasses the last clathrin-positive Golgi cisterna. After synchronization, procollagen aggregates appear simultaneously in *cis* and medial cisternae, and during emptying of the Golgi with an outgoing wave, the medial and *trans* cisternae are emptied simultaneously. The arrival of cargo at the endosomal TGN induces the augmentation of the latter. Our preliminary data suggest that Golgin-97 regulates attachment of clathrin-positive cisternae of the endosomal TGN to the Golgi. Altogether these data support the carrier maturation model of intra-Golgi transport.

## **Localization of the endoplasmic reticulum marker calreticulin in the aberrant rodlet cell of teleosts**

Edith Bielek

Center for Anatomy and Cell Biology, Dept. for Nuclear and Developmental Biology, Medical University of Vienna, Schwarzschanierstrasse 17, A-1090 Vienna, Austria

**OBJECTIVE:** The peculiar “rodlet cell” (RC) occurs in varying numbers in nearly all tissues of teleosts but preferentially in epi- and endothelia, blood and hemopoietic organs. Its conspicuous morphology - rodlet-shaped inclusions with a dense, rodlike core and a thick fibrous capsule – led to varying controversial interpretations. Currently, it is mainly described as a special secretory cell probably of leucocytic origin. A defensive function is assumed because of its increase in multiple stress conditions [1]. However, the organelle development follows only partly the classic secretory pathway and several features indicate continuous endoplasmic reticulum (ER) – hypertrophy, resulting in vesiculation of the cytoplasm and ending with confluent ER lacunae displacing the other organelles. Moreover, ER-membrane undulations reminiscent of (micro-) tubulo-reticular structures known in ER - overproduction and the occurrence of tubular elements (especially along expelled cores) have been observed [2]. Therefore, the distribution of the evolutionary conservative calreticulin, a luminal ER – protein with multiple modulating functions [3,4], was investigated in two teleostean families, Salmonidae (trout) and Cyprinidae (goldfish, carp).

**MATERIAL AND METHODS:** Samples of gill and intestinal epithelium from adult trout (*Oncorhynchus mykiss*), goldfish (*Carassius auratus* L.) and carp (*Cyprinus carpio* L.) were processed for normal morphology after routine methods: double fixation (glutaraldehyde and OsO<sub>4</sub>), embedding in epoxy resin, staining with Uranyl-acetate/lead citrate. Blocs for immunocytochemistry were embedded without postfixation in LR White and stained with rabbit polyclonal anti-calreticulin (600-101-ab4; Abcam) followed by a 10 nm gold conjugate (GαR Auro Probe RPN-421).

**RESULTS AND CONCLUSION:** RCs of all investigated species showed a strong positive reaction in rodlet sacs. In immature stages the signal was weaker and localized in the fine fibrillar material in the rodlet sacs, sometimes with concentrations along the developing (condensing?) cores. Weak to moderate reaction was observed in small vesicles in cytoplasm and along the cis – Golgi face, and also in the nucleus. For comparison, adjacent mucous cells displayed a strong reaction at the cis – Golgi face and none in the granules. One of the main functions of calreticulin is the prevention of the aggregation of misfolded proteins [3,4]. Defective proteins usually recycle in the ER-intermediate compartment but might get segregated if irreparable. Therefore, the presence of calreticulin in the presumed secretory product, the rodlets, supports the hypothesis of a surplus production of unknown protein(s) under cellular stress, representing possibly a pathological reaction instead of a regular secretion with defensive function.

### **REFERENCES:**

- [1] MANERA M., DEZFULI B.S. *J. Fish Biol.* 65, (2004), 597-619.
- [2] BIELEK E. *Anat. Rec.* 283A, (2005) 239-249
- [3] JOHNSON S. ET AL. *Trends in Cell Biol* 11, (2001), 122-129.
- [4] MA Y., HENDERSHOT L.M. *Cell Stress & Chaperones* 7, (2002), 222-229.

## Morphological Characterization of Human Rhinovirus Infected HeLa Cells

Marianne Brabec<sup>1</sup>, Majid Niapir<sup>2</sup>, Adi Ellinger<sup>2</sup>, Dieter Blaas<sup>3</sup> and Renate Fuchs<sup>1</sup>

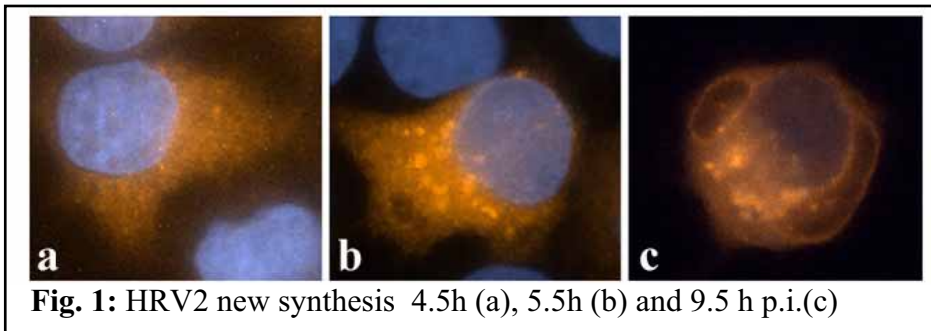
<sup>1</sup>Dept. Pathophysiol., Med. Univ. Vienna, A-1090 Vienna, Austria

<sup>2</sup>Dept. Histol. Embryol., Med. Univ. Vienna, A-1090 Vienna, Austria

<sup>3</sup>Dept. Med. Biochem., Med. Univ. Vienna, A-1030 Vienna, Austria

Human rhinovirus serotype 2 (HRV2) is a non-enveloped, positive-strand RNA virus that belongs to the picornavirus family. It is internalized by LDL-receptor family members and undergoes a conformational change of its capsid proteins in the low pH environment ( $\text{pH} \leq 5.6$ ) of late endosomes. This results in RNA release into the cytoplasm [1] where translation of the viral polyprotein is initiated. The polyprotein is cleaved autocatalytically by viral proteases, which also cleave cellular proteins such as eIF4G and thereby initiate the shut off of host cell protein synthesis [2]. So far, it is unknown where HRV protein and RNA synthesis take place. Replication of minus and plus strand RNA of other picornaviruses occurs on the outside of endoplasmic reticulum (ER)-derived membrane vesicles induced by the viral non-structural proteins 2BC/2C [3].

To characterize HRV2 proteins synthesis and its effects on cellular processes we applied indirect immunofluorescence microscopy using antibodies against viral proteins, cellular compartments and the cytoskeleton. At 4.5 h post infection (p.i.) viral proteins were found in the entire cytoplasm (Fig.1a), whereas protein aggregates had formed in the juxtannuclear area at 5.5 h p.i. (Fig.1b). About 9.5h p.i.HRV2 synthesizing cells revealed alterations typical for apoptosis (Fig.1c).



Already early during infection ( $> 5.5$  h) morphological alterations were evident: disorganization of intermediate filaments and microtubules, depolymerization of actin filaments, disassembly of the Golgi apparatus and rearrangement of the ER. We currently investigate the time-dependent sequence of these alterations. In summary, virus-induced effects on the cytoskeleton and the secretory pathway are assumed to facilitate HRV replication, cell killing and virus release.

### References:

- [1] Brabec, M., D. Schober, E. Wagner, N. Bayer, R. F. Murphy, D. Blaas, and R. Fuchs. *J. Virol* 79 (2005) 1008-1016.
- [2] Seipelt, J., H. D. Liebig, W. Sommergruber, C. Gerner, and E. Kuechler. *J Biol Chem* 275 (2000) 20084-9.
- [3] Egger, D., and K. Bienz. *J Gen Virol* 86 (2005) 707-18.

Acknowledgement: Supported by Austrian Science Fund P17590.

## Histochemical investigations of the adhesive organ of *Idiosepius* (Cephalopoda, Mollusca)

Janek von Byern<sup>a</sup>, Livia Rudoll<sup>b</sup>, Daniela Gruber<sup>a</sup> and Waltraud Klepal<sup>a</sup>

<sup>a</sup> University of Vienna, Cell Imaging and Ultrastructure Research, 1090 Vienna, Austria

<sup>b</sup> University of Vienna, Department of Theoretical Biology, 1090 Vienna, Austria

*Idiosepius* is the smallest member of the cephalopods, attaching during the day to the lower leaf surfaces of sea grass or algae for camouflage by means of special glue glands [1]. The adhesive system (also termed adhesive organ) is restricted to the posterior part of the fin region of the dorsal mantle side and can easily be distinguished based on structural features from normal epithelium [2]. Histological and histochemical procedures were determinate to elucidate the nature of the epithelial secretion of two *Idiosepius* species. The adhesive organ of both species possesses four different cell types (columnar, granular, goblet and interstitial cells), which can be distinguished morphologically and according to of their secretory composition. The first three cell types contain periodate-reactive substances (neutral hexose sugars) and basic protein, whereas the interstitial cells lack any secretory material. Several histochemical tests (PAS, PAD, Diamine, Mixed Diamine, Colloid Iron, Biebrich Scarlet and Fast Green test) indicate that the ratio of protein and polysaccharides varies strongly between the glandular cells, forming different protein-polysaccharide complexes. Columnar cells have a high ratio of glucose sugar units and a protein fraction. The granular cells show a balanced ratio of different sugar units and protein whereas the goblet cells exhibit higher protein fractions and a lower ratio of hexose sugar units other than glucose. Acidic and sulphated substances, tested by Alcian Blue 8GX, Azure A and Toluidine blue O, are absent in *Idiosepius*. Next to the glandular cells the surface layer of the adhesive organ also contains sugar units, presumably secretion products of the cells.

The histochemical nature of the secretory products suggests that adhesion and de-adhesion is not evoked by a duo-gland adhesive system such found as that in *Euprymna scolopes* [3] and gastropods [4]. *Idiosepius* may rather exhibit the “Stefan-type” of adhesion [5]. This form of adhesion may be related to habitat choice and behavior.

### Reference List

- [1] NESIS, K., 1982. Cephalopods of the World: 1-351.
- [2] SASAKI, M., 1921. On an adhering habit of a pygmy cuttlefish, *Idiosepius pygmaeus* Steenstrup. *Annotationes Zoologicae Japonenses*, 10,21: 209-213.
- [3] SINGLEY, C. T., 1982. Histochemistry and fine structure of the ectodermal epithelium of the sepiolid Squid *Euprymna scolopes*. *Malacologia*, 23,1: 177-192.
- [4] GRENON, J. F. and WALKER, G., 1978. The histology and histochemistry of the pedal glandular system of two limpets, *Patella vulgata* and *Acmaea tessulata* (Gastropoda: Prosobranchia). *J.Mar.Biol.Assoc.UK.*, 58: 803-816.
- [5] STEFAN, M. J., 1874. Versuche für die scheinbare Adhäsion. *Sitzungsberichte der Kaiserlichen Akademie der Wissenschaften Wiens.Mathematisch-Naturwissenschaftliche Klasse*, 69: 713-735.
- [6] Acknowledgements: This project was enabled by the Austrian Science Fund (FWF), Project No. P 17 193 – B 12 and Japan Society for the Promotion of Science (JSPS), Grant No. 04567.

## Ultrastructural Changes Induced by Cyclophosphamide Administration on Rats' Hepatocytes and Hepatoprotective Effects Testing of Echinacea Extracts

Crăciun C., Anca Hermenean, Ardelean A., Pribac G.C.

Department of Cell Biology and Histology, "Vasile Goldis" Western University, Faculty of Medicine, 310396, Arad, Romania

In the current experiment we have tested the possible hepatoprotective effects of vegetal extracts from two species of Echinacea on Wistar rats, previously treated with cyclophosphamide.

Knowing that cyclophosphamide (CFA) has a hepatic metabolism, we have focused on the subcellular modifications of hepatocytes induced by cyclophosphamide, administered for 3 days (40 mg/kg/day) and also the ultrastructural features of hepatocytes belonging to rats that were subject to cyclophosphamide therapy followed by 10 days of vegetal extracts administration obtained from species of *Echinacea purpurea* or *Echinacea pallida*.

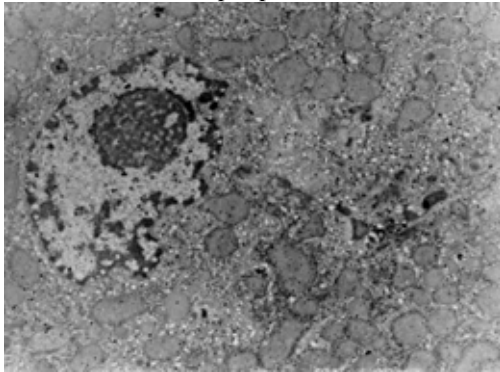


**Fig. 1** Hepatocyte, group treated with Cyclophosphamide, x 12.600

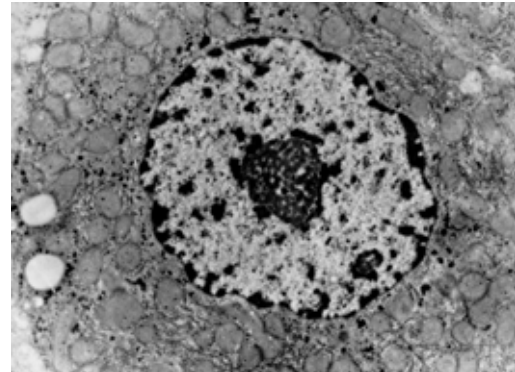


**Fig. 2** Hepatocyte, group treated with *E. pallida* extracts, x 12.600

The administration of cyclophosphamide determined severe morphological and functional alterations of the liver, fact proved by ultrastructural images from the treated group exclusively with the cytostatic.

Ultrastructural analysis of the liver belonging to both of the treated groups with CFA and Echinacea extracts, reveals the fact that both of the extracts had an antihyperlipidemic effect, more evident in the case of the *E. pallida* group. Also, the proteic metabolism is reestablished, fact proved by the normal ultrastructure of nucleoli, mitochondria and increased electron density of the cytoplasmic matrix. The quantity of SER is high, that suggests an increased detoxifying activity, against negative action induced by CFA. We observe high number of Kupffer cells, fact that confirms our previous statements, respectively the capacity of vegetal extracts to annihilate the modifications induced by cyclophosphamide and to maintain a normal metabolic activity of hepatocytes.

Our results demonstrated that the administration of *Echinacea purpurea* and *Echinacea pallida* extracts had a ultrastructural and functional reconstruction effects on the liver affected by CFA treatment, that suggests the hepatoprotective action of these vegetal extracts.

# Ultrastructure of the adhesive organ of *Idiosepius* (Mollusca, Cephalopoda)

Norbert Cyran, Janek von Byern and Waltraud Klepal

University of Vienna, Cell Imaging and Ultrastructure Research, 1090 Vienna, Austria

The genus *Idiosepius*, found in South Africa, Indo-Pacific and Australia, comprises the smallest species of cephalopods [1]. As a characteristic feature they possess an adhesive organ on the dorsal mantle side near the fin base [2]. The animals use the secretion of the adhesive glands to stick to sea grass leaves or algae for camouflage when threatened by predators. The present study describes the morphology of the adhesive organ focusing on the ultrastructure of the gland cells.

The epithelium of the adhesive organ is about 80  $\mu\text{m}$  thick (Fig. 1a and 1b) and it is densely covered by microvilli. Four cell types (columnar, granular, goblet and interstitial cells) can be distinguished morphologically and on account of their secretory products. The numerous columnar cells have a stretched pear-like shape and contain globular granula with a diameter of 1  $\mu\text{m}$ . They occur in groups of 5-8 cells forming a hump on the surface. Approximately 8 granular cells surround this aggregate. This cell type contains closely packed spherical granula of 3-5  $\mu\text{m}$  in diameter. The goblet cells are numerous in the boundary and fin adhesive region but less present in the middle part. They are filled with homogeneous finely granular material. Interstitial cells contain strands of filaments but no granular material.

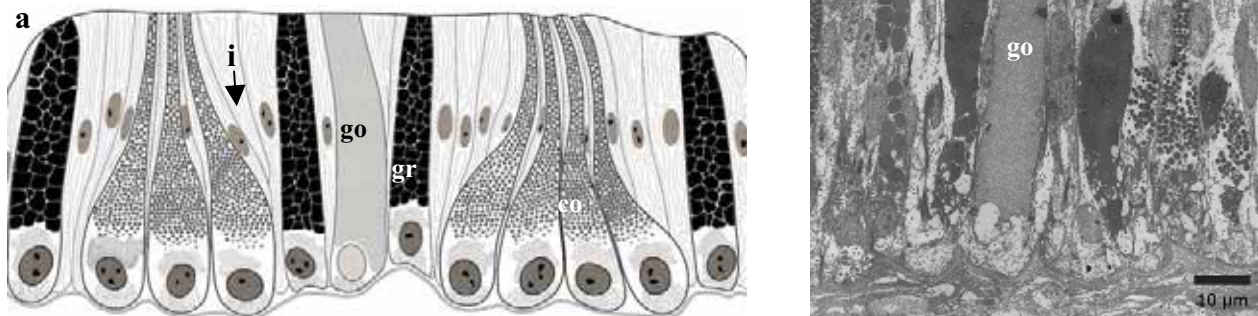


**Fig. 1:** Adhesive organ of *Idiosepius*. **a:** Schematic drawing of the cell types. **b:** TEM picture of the epithelium. co columnar cell, go goblet cell, gr granular cell, i interstitial cell.

While the columnar and granular cells show high secretory activity, there is little evidence for metabolic activity in the goblet cells. The nuclei in all glandular cells are located basally, while the nuclei of the interstitial cells are central.

## Reference List

1. NORMAN, M. D., 2000. Tintenfischfuehrer. 1st: 1-320.
2. SASAKI, M., 1921. On an adhering habit of a pygmy cuttlefish, *Idiosepius pygmaeus* Steenstrup. *Annotationes Zoologicae Japonenses*, 10,21: 209-213.
3. Acknowledgements: This project was enabled by the Austrian Science Fund (FWF), Project No. P 17 193 – B 12. The authors like to mention Sylvia Nürnberger for her helpful comments and constructive criticism.

## Is the Plant TGN an Early Endosomal Compartment?

Jan Dettmer<sup>a</sup>, York-Dieter Stierhof<sup>b</sup>, and Karin Schumacher<sup>a</sup>

<sup>a</sup>Zentrum für Molekularbiologie der Pflanzen, Pflanzenphysiologie, Universität Tübingen,

<sup>b</sup>Zentrum für Molekularbiologie der Pflanzen, Mikroskopie, Universität Tübingen,  
D-72076 Tübingen, Germany

The exact pathways of endocytosis in plant cells are not well understood. In particular, the knowledge about early endosomal compartments is fragmentary. The V-ATPase is a highly conserved multiheteromeric protein complex, which uses ATP to pump H<sup>+</sup> from the cytosol into the lumen of endocompartments. Here we report that the three Arabidopsis isoforms of subunit a (VHA-a) fused to GFP differ in their subcellular localization. VHA-a2-GFP and VHA-a3-GFP are present at the tonoplast, whereas VHA-a1-GFP localizes to a compartment in close vicinity to the trans-Golgi region. Immunogold and immunofluorescence labelling of VHA-a1-GFP as well as ultrastructural studies on cryofixed samples reveal labelled vesicles of different size (Fig. 1) which are also positive for the V-ATPase subunit E and the TGN marker AtSyp41/AtTLG2a, but negative for  $\gamma$ -COP/Sec21 (COPI coat) and sialyltransferase (Golgi stacks). The endocytosis marker FM4-64 rapidly colocalizes with VHA-a1-GFP-positive compartments prior to Ara6-, Ara7- and AtSyp21/ - AtPEP12-positive compartments suggesting that the TGN is an early endosomal compartment. VHA-a1-GFP labelled vesicles are also negative for rabs Ara6 and Ara7 (putative early endosome), and AtSyp21/AtPEP12 (prevacuolar compartment).

This project is funded by the Deutsche Forschungsgemeinschaft DFG through SFB446.

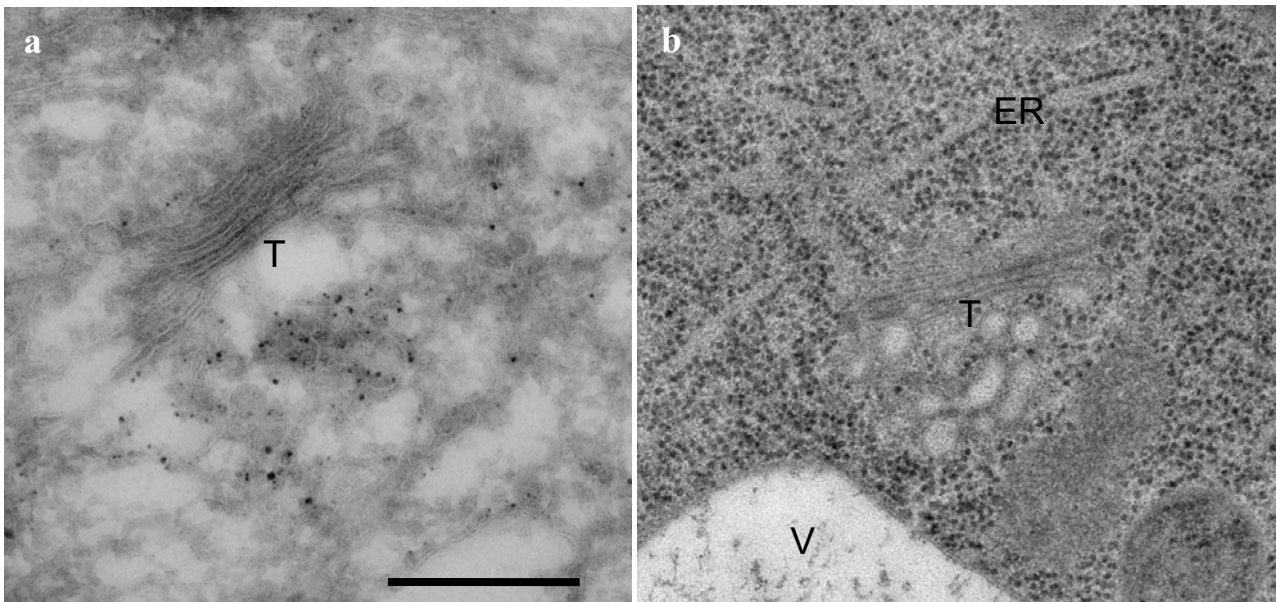


**Fig.1:** (a) Immunogold labelling of VHA-a1-GFP on ultrathin cryosections (Arabidopsis root tip). (b) Ultrathin resin section showing Golgi and TGN (Arabidopsis root tip) after high pressure freezing and freeze substitution. ER, endoplasmic reticulum; T, trans-Golgi; V, vacuole. Bar = 500 nm.

## Golgi apparatus studied by advanced microscopic methods

Markus Grabenbauer

EMBL Heidelberg, 69117 Heidelberg, Germany

The Golgi apparatus morphology and structure is investigated by three different novel microscopic approaches : Correlative light and electron microscopy using green fluorescent protein (GFP) as a molecular marker, 4 Pi-microscopy for enhanced resolution in light microscopy and cryo-electron microscopy of vitrified sections (CEMOVIS) for enhanced effective resolution in electron microscopy.

Correlative light and electron microscopy combines the advantages of *in vivo* fluorescence microscopy and the resolution of electron microscopy and tomography. A new method was developed and named GRAB (GFP Recognition After Bleaching), which uses oxygen radicals generated during the GFP bleaching process to photo-oxidize diaminobenzidine (DAB) into an electron dense precipitate. This allows the direct detection of GFP by electron microscopy and electron tomography at ~8 nm resolution. GRAB was performed using GFP tagged to the Golgi-resident enzyme N-acetylgalactosaminyltransferase 2 (GalNAc-T2<sup>GFP</sup>) and other Golgi associated proteins. GalNAc-T2<sup>GFP</sup> was localized to cisternal membranes showing a clear gradient across the Golgi stack. Using electron tomography, we detected GalNAc-T2<sup>GFP</sup> in COP coated buds and peri-Golgi vesicles supporting the “cisternal maturation model” of Golgi function. Aware of the presence of GalNAc-T2<sup>GFP</sup> in at least 2 adjacent Golgi cisternae separated by ~80 nm, we engaged 4 Pi confocal microscopy, aiming to discern cisternae by improving light microscope resolution. A third approach involved performing cryo-electron microscopy of vitrified sections (CEMOVIS) combined with electron tomography, which provides further insights into structural details of Golgi apparatus under close to physiological conditions.

## **MAPK signaling from endosomes: the role of scaffolds and intracellular trafficking**

Teis D., Morandell, S., Araujo M.E.G., Taub, N., Stasyk T., Kurzbauer, R\*., Clausen T\*., Hekman, M.\*\* , Rapp, U.\*\* and Huber L.A.

\*Institute for Molecular Pathology (IMP), Dr. Bohrgasse 7, A-1030 Vienna, Austria

\*\*MSZ, Institute for Medical Radiation and Cell Research, University of Würzburg, Würzburg 97078, Germany  
Biocenter, Div. Cell Biology, Medical University of Innsbruck, A-6020 Innsbruck, Austria

We have previously shown that p14 is an essential regulator of growth factor receptor (EGF-R) / MAP Kinase signaling (Teis et al., *Dev. Cell*, 2002). p14 functions as an adaptor which localizes the MP1-MAPK signaling module to a particular sub-cellular compartment, namely to late endosomes (Wunderlich et al, *J Cell Biol*, 2001).

Recent structural and bioinformatical analysis indicate a potentially role of p14 in endosomal membrane transport (Kurzbauer et al., *PNAS*, 2004). The overall topology of the individual MP1 and p14 proteins is almost identical having a central 5-stranded  $\beta$ -sheet sandwiched between a 2-helix and a 1-helix layer. Formation of the p14/MP1 heterodimer proceeds via  $\beta$ -sheet augmentation and yields a unique, almost symmetrical complex with several potential protein binding sites on its surface. Mutational analysis allowed identification of the p14 endosomal adaptor motif, which seems to orient the complex relative to the endosomal membrane. Two highly conserved and hydrophobic protein binding sites are located on the opposite ‘cytoplasmic’ face of the p14/MP1 heterodimer and might therefore function as docking sites for the target proteins MEK1 and ERK1. Furthermore, detailed sequence analyses revealed that MP1, p14 together with profilins define a novel protein superfamily of small subcellular adaptor proteins, named ProflAP.

Excitingly, siRNA mediated p14 depletion, not only results in defective MAP kinase signaling from endosomes (Teis et al., *Dev. Cell*, 2004) but additionally blocks the activated EGF-R in a peripheral endosomal compartment. Thus the characterization of p14’s function in endosomal membrane transport of the activated EGF-R could be a key to understand how space and time are co-ordinated in EGF-R/ERK signaling.

In a reversed genetics approach we are investigating this possible role of p14 in *Drosophila melanogaster*. The p14 deletion is capable of suppressing the rough eye phenotype caused by the oncogenic mutants of Ras and Raf, respectively. On the other hand, overexpression of p14 in the eye leads to hyperplasia during eye disc development, reminiscent of the phenotype of a Raf hypermorph (Hampoelz et al., manuscript in preparation). Meanwhile we have also generated an inducible p14  $-/-$  allele in mice. These mice are lethal during early embryogenesis and we are presently investigating crosses with tissue specific deleter strains.

Together, our work provides novel insight into the molecular mechanisms used to generate positional information within signaling cascades of the activated EGF-R, thereby allowing an understanding of the interplay of space and time to generate a specific biological response.

*This work was supported by the Austrian Genome Program (GEN-AU), Vienna, Austria and by the Special Research Program “Cell Proliferation and Cell Death in Tumors” (SFB021, Austrian Science Fund).*

## Prerequisites for the characterization of PKD 2 overproduction in cultivated pancreatic cancer cells using high-pressure freezing.

Holger Krisp<sup>a</sup>, Götz von Wichert<sup>b</sup>, Thomas Seufferlein<sup>b</sup>, Jasmine Eismann<sup>b</sup>, Paul Walther<sup>a</sup>

<sup>a</sup>Z.E. Elektronenmikroskopie, University of Ulm, 89069 Ulm, Germany

<sup>b</sup>Dept. of Internal Medicine I, University of Ulm, 89071 Ulm, Germany

The protein kinase D family consists of three isoforms: PKD1/PKDC $\mu$ , PKD2 and PKD3/PKC $\nu$ . Several reports identify PKD as a regulator of cell proliferation and apoptosis, proposing a role in carcinogenesis. Moreover, PKD appears to be an important regulator of very different intracellular signalling pathways [1]. Therefore the PKD family has been detected in pancreatic cancer and awaits its functional characterization in these tumours [2]. High PKD 2 expression is particularly found in pancreatic cancer cells. The PKD enzymes have been implicated in the organisation of the Golgi apparatus, regulating the fission of vesicles from the trans-Golgi network (TGN).

In this preliminary study, PKD 2 was overexpressed by transfection of pancreatic cancer cells (AR42J and BON) using GFP as a marker. These cells were then analysed in the LM (Fig. 1). Afterwards, the cells were immobilized by high-pressure freezing in order to capture the dynamic membrane fission events. A special freeze-substitution protocol was used to optimise membrane visibility [3] (see also Buser et al., in this issue). After plastic embedding and thin sectioning, samples were imaged in the TEM (Fig. 2).

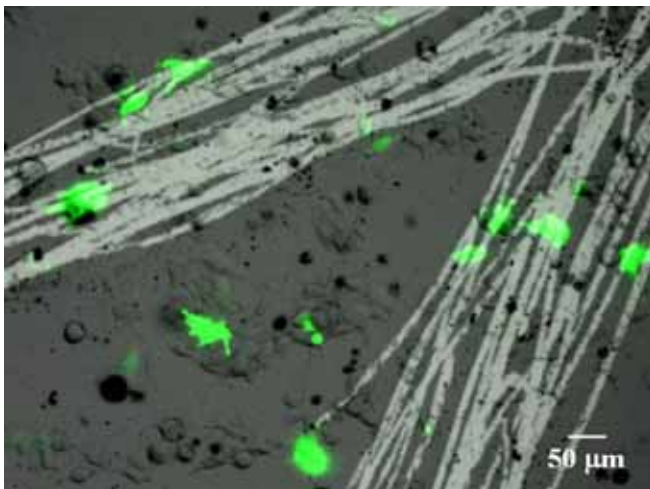


**Fig. 1:** PKD2 transfected BON cells with a green fluorescent protein Marker (GFP) as control vector for PKD 2 expression. Scratches in the sapphire substrate served as orientation-help for the subsequent analysis of the proceeding thin section in the TEM.

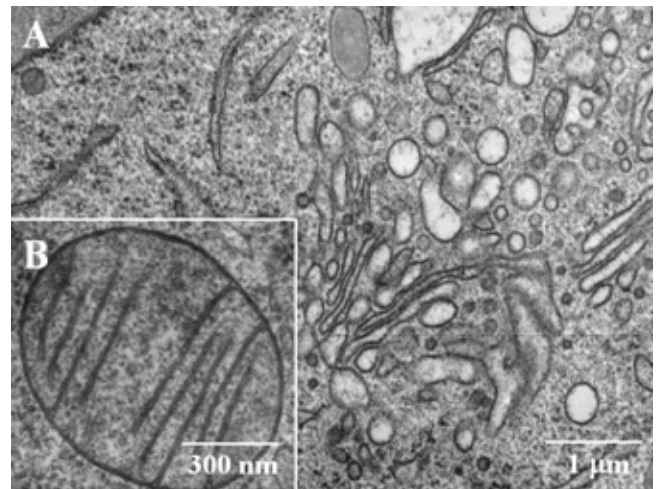


**Fig. 2:** Thin section of a high-pressure frozen AR42J cell. (A) Golgi apparatus and (B) Mitochondrion. The Golgi apparatus is surrounded by a large number of vesicles.

### References:

[1] Rykx, A., De Kimpe, L., Mikhalap, S., Vantus, T., Seufferlein, T., R. Vandenheede, J. & Van Lint, J., FEBS Letters (2003) 81-86.

[2] Yeaman, Ch., Inmaculada Ayala, M., R. Wright, J., Bard, F., Bossard, C., Ang, A., Maeda, Y., Seufferlein, T., Mellman, I., James Nelson, W. & Malhotra, V., Nature cell biology Vol. 6 No. 2 (2004) 106-112.

[3] Walther, P. & Ziegler, A., J. Microsc. 208 (2002) 3-10.

## Dynamics of Endocytic Pathways Investigated with High-Resolution 3D Microscopy

Permsin Marbet and Lukas Landmann

Structural Cell Biology, DKBW Centre for Biomedicine, University of Basel Medical School, Mattenstrasse 28, CH - 4058 Basel

According to current textbooks, traffic between endocytic compartments is mediated by small carrier vesicles. This model is hard to reconcile with the “rapid vesicular pathway” which in hepatocytes translocates internalized compounds to the apical cell pole in very short time intervals. We, therefore, reexamined endocytic pathways in isolated rat hepatocytes couplets (RHCC) and in liver cells in situ by 3D imaging techniques. Serial thin sections of liver cells which have endocytosed the fluid-phase marker HRP for various time intervals were reconstructed and demonstrated that early and late endosomes but less so lysosomes gave rise to numerous tubular protrusions. Confocal image stacks were analyzed for colocalization (Imaris, Bitplane, Zurich) after deconvolution (Huygens software packet, SVI, Hilversum) [1, 2]. RHCC that have internalized dextran for various time intervals demonstrated that fluorescence was associated with a tubulovesicular network extending from the basolateral up to the apical cell pole. EEA1, which is a marker of the early endosomal compartment, was associated with a vesicular component that colocalized with endocytic marker in the basolateral part of the cell after 1 min of endocytosis but was redistributed to all regions after longer time intervals. Asialoglycoprotein (ASGP), a ligand with lysosomal destination, was found in vesicles that immunoreacted successively with EEA1, rab7, and lamp3. In contrast, polymeric immunoglobulin A (pIgA), a marker for transcytosis, was translocated from EEA1-positive vesicles to rab11-positive tubules, and finally to rab11-positive vesicles in the apical region. Receptor for ASGP dissociated from its ligand shortly after internalization and was translocated to the tubular reticulum for recycling, whereas receptor for pIgA traveled together with its ligand to the apical plasma membrane. Thus, tubules show the characteristics of the common or sorting endosome, while apical rab11-positive vesicles correspond to the subapical compartment/apical endosome. Taken together, our data support a model for the endocytic apparatus that consists of a continuous reticulum which provides transport along the recycling and transcytotic routes. Suspended in this meshwork are vesicles that can move readily along the tubules and, initially, constitute early endosomes. Subsequently, they acquire immunologic properties of late endosomes and lysosomes, respectively. Transport mediated by small carrier vesicles seems to take place at the basolateral and apical plasma membrane only.

[1] L. Landmann, "Deconvolution improves colocalization analysis of multiple fluorochromes in 3D confocal data sets more than filtering techniques", *J. Micr.* **208**, 134-147 (2002).

[2] L. Landmann and P. Marbet, "Colocalization analysis yields superior results after image restoration", *Micr. Res. Techn.* **64**, 103-112 (2004).

## **Intra-Golgi transport. A way to a new paradigm?**

Alexander A. Mironov, Alberto Luini and Galina V. Beznoussenko

Department of Cell Biology and Oncology, Consorzio Mario Negri Sud, 66030 Santa Maria Imbaro (Chieti), Italy.

The morphofunctional principles of intra-Golgi transport are, surprisingly, still not clear, which is in marked contrast to our advanced knowledge of the underlying molecular machineries. Recently, the conceptual and technological hindrances that had delayed progress in this area have been disappearing, and a cluster of powerful morphological techniques has been revealing new glimpses of the organization of traffic in intact cells. The depletion from COPI-dependent vesicles of 14 different cargoes and most Golgi enzymes studied so far has argued against both the vesicular and cisterna maturation models of intra-Golgi transport. On the basis of the results obtained in our laboratory, we will discuss here the new concepts around the present models of intra-Golgi transport. The most plausible model of intra-Golgi transport could be the following: after the arrival of a cargo domain at the intermediate compartment/*cis*-Golgi network, this cargo domain recruits Ykt6 from the cytosol. This arrival of cargo at the Golgi complex induces the fusion of COPI vesicles with the cisternae, leading to the restoration of the ability of the cisternae to fuse with each other, and inducing the formation of intercisternal connections. The membranes of cargo-free domains of the *cis*-Golgi network are transformed into the most *cis* cisternae, and membranes from the endosomal TGN are converted into the most *trans* clathrin-positive cisternae, replacing the ER cisternae on the *trans* side of a medial cisternal stack. The cargo domain next fuses with one of the medial cisternae, and then with the newly formed *trans*-most cisterna. The last fusion step stimulates the maturation of post-Golgi carriers and their subsequent departure.

## **Immuno-electron tomography studies on COPII coated vesicle formation from the endoplasmic reticulum**

Dagmar Zeuschner<sup>1</sup>, Willie Geerts<sup>2</sup>, JeanLuc Murk<sup>1</sup>, Elly van Donselaar<sup>1</sup>, Jan Slot<sup>1</sup>, Hans Geuze<sup>1</sup>, Bram Koster<sup>2</sup>, Judith Klumperman<sup>1</sup>

<sup>1</sup>Dept. of Cell Biology & Inst. of Biomembranes, UMC Utrecht, The Netherlands.

<sup>2</sup>Molecular Cell Biology, Inst. of Biomembranes, Utrecht University, the Netherlands.

Transport from the endoplasmic reticulum (ER) to the Golgi complex requires the COPII coat complex to facilitate sorting of cargo molecules. COPII coats have been implicated in vesicle formation, but alternatively they may form sub-domains on the ER to collect proteins for large, pleiomorphic carriers that are not COPII coated. To establish whether COPII-coated membranes can form bona-fide vesicles or remain connected to the ER we have developed a combination of immunogold labeling and 3D-electron tomography. 3D-reconstructions of ER-exit sites labeled for COPII show the existence of ER-associated coated buds as well as different types of free, COPII-coated transport carriers. These COPII-coated carriers are rounded ~50 nm diameter vesicles or partially coated, crescent-shaped membranes up to ~130 nm long. Similar structures are seen in cells that are chemically fixed or by high pressure freezing. Using a novel ‘rehydration method’ that allows for the preparation of immunogold labeled cryosections of high-pressure frozen cells, we confirmed the existence of these two types of carriers. Double-labeling of COPII with Sec22p in 3D unequivocally showed the presence of this SNARE protein in the two types of COPII coated carriers. We conclude that COPII is involved in the formation of fusion-competent vesicles and larger membranes. Similar studies are presently carried to characterize COPI- and clathrin-coated membranes. *Supported by the Dutch Society for Scientific Research (NWO: FOM/ALW 805.47.051).*

## **Glycoprotein E is Involved in Coordinating Envelopment of Bovine Herpesvirus 1**

E. M. Schraner<sup>1</sup>, C. Senn<sup>2</sup>, K. Bienkowska- Szewczyk<sup>3</sup>, M. Müller<sup>4</sup> and P. Wild<sup>1</sup>

<sup>1</sup>Electron Microscopy, Institutes of Veterinary Anatomy and of <sup>2</sup>Virology, University of Zürich, CH-8057 Zürich, Switzerland, <sup>3</sup>Department of Molecular Virology, University of Gdansk, Poland, <sup>4</sup>Laboratory for Electron Microscopy, Institute of Applied Physics, Swiss Federal Institute of Technology, CH-8092 Zürich

Envelopment of bovine herpesvirus 1 (BoHV-1) and other Alpha-herpesviruses (unpublished data) follows two diverse pathways. *Nuclear envelopment* [1] includes budding of capsids through the inner nuclear membrane into the perinuclear space acquiring tegument and envelope that contains proteins for preventing membrane fusion. Virions are then transported via RER cisternae directly into the Golgi complex for packaging into transport vacuoles that deliver their content to the cell periphery. *Cytoplasmic envelopment* [2] includes exit of capsids to the cytoplasm via impaired nuclear pores. Capsids can approach the outer nuclear membrane, membranes of RER and Golgi complex at any side where they induce budding. Budding of capsids at Golgi membranes of narrow cisternae leads to virions within concentric transport vacuoles that contain proteins considered likely to prevent fusion of the envelope with the vacuolar membrane. Budding at any of the intracellular membranes is the essential step in formation of virus particles comprising capsid, tegument proteins, and an envelope in which glycoproteins are embedded.

Envelopment is probably a highly orchestrated process involving many viral proteins for its control. One of these proteins is glycoprotein E (gE). In order to clarify the significance of gE in envelopment we investigated the effect of deletion of gE or of its ectodomain or endodomain. Electron microscopy of high-pressure frozen and freeze-substituted MDBK cells infected with BoHV-1 gE deletion mutants revealed time dependent variation in virus morphology. At 24 hours of infection spherically shaped wild type virions (wt) measured 130 to 190 nm in diameter peaking at 150 nm (40%). Virions of all deletion mutants measured 130 to 260 nm peaking at 190 nm (30 to 35%). In addition 9 (7%) of a total of 137 wt virions were pleiomorphic. Pleiomorphic virions were found in 13 to 19 % of the gE deletion mutants. 4% of the gE deletion mutants contained 2 capsids whereas double capsids were not encountered in wt virions. At 40 hours of infection, the number of pleiomorphic virions and that of virions containing 2 and more capsids was obviously increased. There was no striking difference in viral morphology between the different deletion mutants. Aberrant viral formation found at the sites of envelope origin indicate that gE is involved in budding possibly in the phase of fission of the envelope from nuclear membranes, RER membranes and Golgi membranes.

### References

- [1] P. Wild et al., *Micron* 33 (2002) 327
- [2] P. Wild et al., *J Virol* 79 (2005) 1071

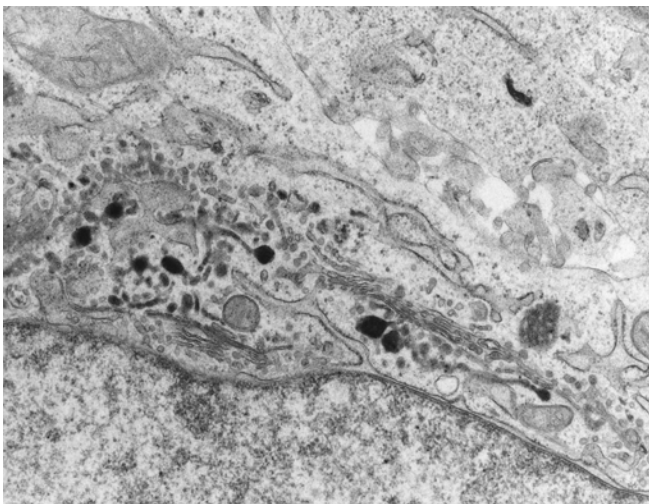
## Cytochemical Inactivation of Early and Late Endosomal Compartments A Novel Technique for Analyses of the Endocytosis System

Monika Vetterlein, Elfriede Scherzer, Josef Neumüller, Claudia Meißlitzler-Ruppitsch, Adolf Ellinger, and Margit Pavelka

Department of Cell Biology and Ultrastructure Research, Center for Anatomy and Cell Biology, Medical University of Vienna, A-1090 Vienna, Schwarzspanierstraße 17, Austria

The endocytic pathways of internalized molecules involve various early and later endosomal compartments, from where molecules and membranes are sorted to different destinations. Such routes include recycling pathways to the plasma membrane, traffic to lysosomal organelles, and transport to the Golgi apparatus and the endoplasmic reticulum. We worked out a novel technique that allows to immobilize and inactivate certain organelles and compartments along the endocytic routes in living cells, making use of the cross-linking processes that occur during peroxidase-catalysed oxidation and polymerisation of diaminobenzidine (DAB). The method is adapted from procedures used earlier for cell fractionation (1) and immunolabeling (2). The use of differentiated time protocols and kinetic studies permit to investigate, how the cells handle this situation and, how neighbored compartments, and organelles to be visited later along the endocytic routes are influenced.

We used endocytosis into HepG2 hepatoma cells of peroxidase-labelled wheat germ agglutinin (WGA-HRP). After WGA-HRP-internalization for various periods (10-60min), the cells grown on glass coverslips are transferred into HEPES buffered growth medium, cooled to 4°C and incubated in DAB for 30 min in the presence of H<sub>2</sub>O<sub>2</sub>. Afterwards, the cultures are rewarmed, either fixed immediately, or post-incubated in growth medium at 37°C for various periods ranging from 10min up to 18 hours, prior to fixation and embedding for electron microscopy.



Depending on the time point, at which the DAB reaction is performed and the cross-linking processes take place, either early endosomes, or later endosomal compartments, including Golgi-associated organelles and endocytic trans Golgi networks (TGN, 3), are immobilized and functionally inactivated. The cross-linked DAB-reaction products are visible in the electron microscope, thus permitting to localize the inactivated compartments. In the figure, an example is presented showing immobilized endocytic TGN.

Our results revealed that the cell responses depend on both the WGA-internalization times and the post-incubation periods. Inactivation of certain parts of the endosomal system influence the organization of

the Golgi apparatus leading to a disassembly of the Golgi stacks. New Golgi apparatus are built after prolonged periods of post-incubation.

### References:

- [1] P.Courttoy et.al. (1984). *J.Cell Biol.*98: 870-876.
- [2] W. Stoorvogel et al.(1996). *J.Cell Biol.* 132, 21-33
- [3] M.Vetterlein et al.(2002). *Histochem. Cell Biol.*117:143-150

## High Temporal Resolution Microscopy sheds Light on Herpesvirus Envelopment

P. Wild<sup>1</sup>, C. Senn<sup>2</sup>, E. M. Schraner<sup>1</sup>, K. Bienkowska<sup>3</sup>, P. Walther<sup>4</sup>, U. Ziegler<sup>5</sup> and M. Müller<sup>6</sup>

<sup>1</sup>Electron Microscopy, Institutes of Veterinary Anatomy and of <sup>2</sup>Virology, University of Zürich, CH-8057 Zürich, Switzerland, <sup>3</sup>Department of Molecular Virology, University of Gdansk, Poland, <sup>4</sup>Electron Microscopic Unit, University of Ulm, D-89069 Ulm, Germany, <sup>5</sup>Institute of Anatomy, University of Zürich, <sup>6</sup>Laboratory for Electron Microscopy, Institute of Applied Physics, Swiss Federal Institute of Technology, CH-8092 Zürich

Capsids of herpesviruses bud through the inner nuclear membrane acquiring both the viral envelope and tegument. On the basis of slowly fixed material, the idea was borne that the envelope derived from the inner nuclear membrane is inserted into the outer nuclear membrane by fusion with it releasing both capsid and tegument into the cytoplasm. The final envelope is speculated to originate at the *trans* Golgi network, a process referred to as wrapping. [1]. However, fusion of the viral envelope with the outer nuclear membrane has never been shown. Instead virions are transported from the perinuclear space into RER cisternae and membrane compartments devoid of ribosomes [2] ruling out fusion of the envelope with membranes of compartments virions are transported through.

The fact that membrane bound processes are difficult to capture in conventionally fixed material we investigated envelopment of bovine herpesvirus 1 and herpes simplex virus 1 by electron microscopy employing cryo-fixation followed by freeze-substitution or freeze etching, and by confocal microscopy. Examination of cells at various times post infection revealed that the process taking place at the outer nuclear membrane has nothing common with membrane fusion. It rather is identical to the process taking place at the inner nuclear membrane and is thus considered to represent budding capsids from the cytoplasm into the perinuclear space. Careful examination of the nuclear periphery revealed impaired nuclear pores through which capsids gain direct access to the cytoplasm. Nuclear pore complexes are probably disassembled and its components become distributed within the cytoplasm as revealed by confocal microscopy. The Golgi complex showed two distinctly different processes of virus-membrane interaction: One is identical to the packaging process in the secretory pathway, the other is a budding process referred to as wrapping.

The results imply envelopment via two diverse pathways. *Nuclear envelopment* includes budding of capsids through the inner nuclear membrane into the perinuclear space acquiring tegument and envelope that contains proteins for preventing membrane fusion. Virions are then transported via RER cisternae directly into the Golgi complex [3] for packaging into transport vacuoles that deliver their content to the cell periphery. *Cytoplasmic envelopment* includes exit of capsids to the cytoplasm via impaired nuclear pores [4]. Capsids can approach the outer nuclear membrane, membranes of RER and Golgi complex at any side where they induce budding. Budding of capsids at Golgi membranes of narrow cisternae leads to virions within concentric transport vacuoles that contain proteins considered likely to prevent fusion of the envelope with the vacuolar membrane. Envelopment is probably a highly orchestrated process involving many viral proteins for its control. One of these proteins is glycoprotein E localized at the viral envelope. Glycoprotein E seems to be responsible together with other (glyco) proteins for maintaining size and shape of virus particles.

### References

- [1] H. Granzow et al., J Virol 75 (2001) 3675      [2] L.M. Stannard et al., Arch Virol 141 (1996) 505  
[3] P. Wild et al., Micron 33 (2002) 327      [4] P. Wild et al., J Virol 79 (2005) 1071

## **Tumor-induced Angiogenesis: Lessons from Morphology and Molecular Biology**

Seyedhossein Aharinejad

Laboratory for Cardiovascular Research, Center for Anatomy and Cell Biology, Medical University of Vienna, Vienna, Austria

Angiogenesis is crucial in tumorigenesis. The tumor vasculature expands primarily by sprouting angiogenesis that is governed by vascular endothelial growth factor (VEGF) and Angiopoietin (Ang) family. We have shown that colony stimulating factor-1 (CSF-1) promotes extracellular matrix (ECM) remodeling, and facilitates thereby angiogenesis and tumor growth. The intussusceptive microvascular growth (IMG) constitutes an additional concept in angiogenesis. However, its underlying molecular mechanisms are unclear. We monitored angiogenesis over time in an established human embryonic tumor model using intravital video microscopy (IVM). Serial sections served to demonstrate vascular morphology. Expression of angiogenic genes, their receptors, and ECM-modifying enzymes was assessed by real time RT-PCR. CSF-1 blockade was performed by intratumoral injection of small interfering RNAs (siRNAs) directed against CSF-1. While sprouting prevailed throughout the tumor growth, IMG occurred in late tumor stages. IMG involved intravascular tissue structures, tissue pillars, and intraluminal folds; and emerged from sinusoidal veins. Vascular sprouting during the angiogenic switch was associated with upregulated VEGF-A and matrix metalloproteinase (MMP)-9, with low intercapillary distance and high functional and total microvascular length in early tumor stages. IMG correlated with decreased vascular sprouting, Ang and MMP-2 upregulation, and was suppressed following CSF-1 blockade. These data suggest that the angiogenic switch selectively involves sprouting, regulated by VEGF-A and MMP-9, while IMG is regulated by Ang and CSF-1-mediated MMP-2. IMG might act as a mechanism to compensate for the mismatch between the tumor growth and angiogenic response. Thus, angiostatic therapy requires specific molecular inhibitors matched to the tumor stage-dependent gene expression profile.

## Comparison of the Structure of the Renal Vascular System in two Caudata Species

Hans Ditrich

Institute for Zoology, Althanstr. 14; A-1090 Vienna, AUSTRIA

Unlike in mammals, the structure of non-mammalian kidneys is largely determined by the renal vascular system. Thus, kidney morphology strongly correlates with the environment of a given species, as the latter directly affects the functional demands imposed on the excretory system [e.g., 1]. Many amphibian species encounter a rather drastic change in their environmental water supply during metamorphosis. The structure of the metamorphosing kidney has already been studied in frogs [e.g., 2], however, such data on caudata species (salamanders and newts) are fragmentary.

In this study, the kidney structure in the salamander (*Salamandra salamandra*) and in both, neotenus and experimentally metamorphosed axolotls (*Ambystoma mexicanum*) was investigated using SEM of critical-point-dried tissue (Fig. 1) and microvascular corrosion casts, conventional TEM and LM of paraffin and plastic sections.

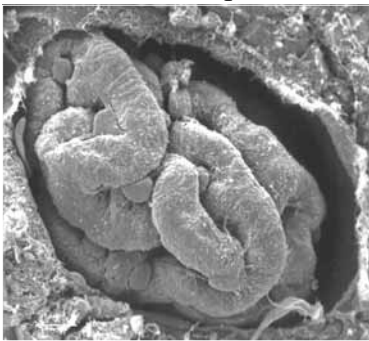


Fig. 1: Critical point dried glomerulus of a neotenus axolotl. bar = 20µm

The general structure of the kidney vascular system is quite similar in both species. The main differences found with our methods in comparing fully aquatic (neotenus) axolotls with their metamorphosed counterparts and salamanders were variations in glomerular and interstitial volume. Thus, conversion of the kidney for living in a terrestrial, albeit humid habitat results in a decrease in glomerular (filtration) surface of over  $\frac{1}{3}$  in the axolotls [3]. The corresponding values in the salamanders were about 10% lower than in aquatic axolotls, but exceeded those in the experimentally metamorphosed animals. However, it should be noted, that the overall filtering surface, i.e., the number of functional glomeruli per kidney, appears to be lower in salamanders.

In both species, the glomeruli were comparatively large and strongly ovoid in shape (Fig. 1). The podocytes showed a rather simple branching mode and the glomerular basal membranes were quite thick, compared to higher vertebrates. However, it should be taken into account that the caudata circulatory system works at relatively low pressures. Therefore no high filtration pressures can be generated at the glomerular filtering membranes. It may be concluded, that this fact is functionally compensated to some extent by larger filtering surfaces.

### References:

- [1] Ditrich H.: Renal Structure and Function in Vertebrates. Science Publ. Inc., Enfield (2005)
- [2] Ditrich H., A. Lametschwandtner: Glomerular development and growth of the renal blood vascular system in *Xenopus laevis* (Amphibia: Anura: Pipidae) during metamorphic climax. J. Morphol.: **213**; 335-340 (1992)
- [3] Ditrich H., H. Splechna: The vascular structure of the kidney of the neotenus axolotl and its metamorphosed counterpart. J. Morphol.: **211**; 55-62 (1992)

# Quantification of the Layer Specific Vascular Density using anti-Collagen Fluorescence Immunohistochemistry in the Primate Striate and Extrastriate Cortex

A.L. Keller, B. Weber, and N.K. Logothetis

MPI for Biological Cybernetics, 72076 Tübingen, Germany

**Introduction:** Non-invasive functional neuroimaging methods such as functional magnetic resonance imaging (fMRI) have become indispensable tools for the neurosciences. The underlying principle of the most frequently used methods is the brain's local, dynamic regulation of blood flow. The correct interpretation of the neuroimaging results requires an in-depth understanding of the structural and functional neurovascular coupling underlying this regulation. The structural coupling, among others, presumes a close match between the vascular density and the steady-state metabolic activity of a given region (e.g. a tangential or laminar subdivision). Here we studied the layer and area specificity of vascularization of V1, V2, V3, V4 and V5 in macaques. **Methods:** Formalin-fixed frozen sections (60  $\mu\text{m}$ ) of 4 animals (*M. mulatta*) were processed for double fluorescence microscopy. Sections were incubated with anti-collagen type IV to stain for vessels and DAPI to stain for cell nuclei. Layer and area specific regions of interest were determined via the DAPI stain and when necessary verified with consecutive Nissl and myelin stains. The anti-collagen images were median-filtered and thresholded to yield binary vessel images from which the length density [ $\text{mm}/\text{mm}^3$ ], surface density [ $\text{mm}^2/\text{mm}^3$ ], volume fraction [ $\text{mm}^3/\text{mm}^3$ ], and mean diameter [ $\mu\text{m}$ ] of the vessels were computed. **Results:** The staining procedure yielded vessel-specific images of high quality and reproducibility within and between animals. Fig 1 shows the average values for V1. The vascular density was highest in layer IVc- $\beta$  ( $761.5 \pm 41.1 \text{ mm}/\text{mm}^3$ , mean  $\pm$  sd of 4 animals) and lowest in layer I ( $512.9 \pm 27.7 \text{ mm}/\text{mm}^3$ ). The average vessel diameter in V1 was  $9.54 \pm 0.48 \mu\text{m}$ . In the extrastriate visual areas examined the vascular density was generally lower, and the difference between layer IV and the remaining layers was less prominent in comparison to V1. The length density in V2 was  $590.1 \pm 29.2 \text{ mm}/\text{mm}^3$  in layer IV and  $514.8 \pm 32.0 \text{ mm}/\text{mm}^3$  in layer I. As a further example, in V5  $599.8 \pm 52.1 \text{ mm}/\text{mm}^3$  was measured in layer IV and  $507.4 \pm 71.2 \text{ mm}/\text{mm}^3$  in layer I. **Conclusion:** V1 is clearly different from all extrastriate areas analyzed with respect to the laminar vessel distribution and the overall vascular density. Differences between extrastriate areas were negligible. The influence of differences in vascularization on the neuroimaging signals remains largely unknown. However, our findings suggest caution when response patterns are compared between V1 and extrastriate areas.

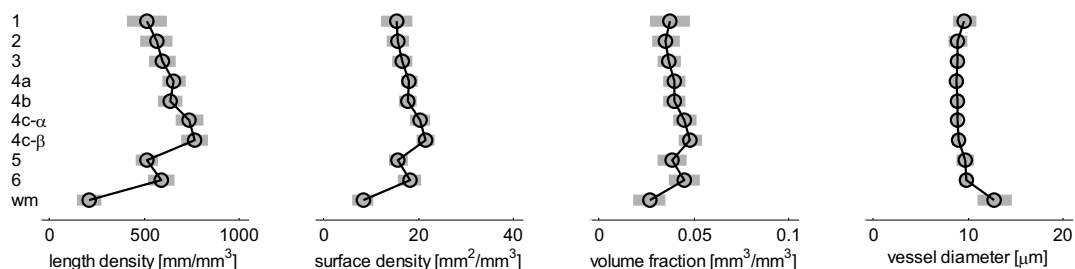


**Figure 1:** Layer specific (layer 1-6; wm=white matter) cortical vascularization in the macaque striate cortex (n=4). The black lines show the means and the gray shaded areas represent standard deviations.

## **Weibel Palade Bodies In Close Association With *Trans*-Golgi Network In Progenitor Endothelial Cells**

J. Kosiuk, M. Vetterlein, M. Pavelka, J. Neumüller

Center for Anatomy and Cell Biology, Dept. for Cell Biology and Ultrastructural Research, Medical University of Vienna, Schwarzschanierstrasse 17, A-1090 Vienna, Austria

**Objective:** Biogenesis, storage and exocytosis of von Willebrand factor (vWF) are characteristics and main functions of endothelial cells. Although vWF plays a key role in hemostasis and inflammation, the details of intracellular transport, polymerization and packing into Weibel Palade bodies (WPBs) are poorly understood. WPBs are endothelial-specific regulated organelles, which serve as storage compartments for vWF multimeric forms, which are organized into parallel proteinaceous tubules that can be demonstrated in the electron microscopy (EM). In case of blood vessel injury, the WPBs are recruited to exocytose their content. In preliminary investigations, we showed that endothelial progenitor cells (EPC) already contain organelles similar to WPBs. We are interested to examine intracellular localization of WPBs in such cells in respect to the spatial organization and functional connection with the *trans*-Golgi network (TGN) by usage of the electron tomography.

**Material and Methods:** For our studies we used lines of early hematopoietic CD133-positive cells obtained from human umbilical cord blood. Cells were cultivated on fibronectin (FN)-coated culture vessels in medium 199 containing the cytokines basic fibroblast growth factor (bFGF), epidermal growth factor (EGF) and vascular endothelial growth factor (VEGF). The cells were fixed with glutaraldehyde and reduced osmium tetroxide, dehydrated in alcohol and embedded in Epon resin. The specimens were cut in 200-300nm semi-thin sections for electron tomography and in 70nm ultra-thin sections for conventional EM, for control the cells' stage of maturation. For ultrastructural studies and tomography, we used a TECNEI 20 transmission electron microscope with an acceleration voltage of 80kV and 200kV, respectively. Digital micrographs of tilt series from -65° to +65° allow to collect a sufficient amount of data for reconstruction, by the usage of Inspect3D software. For further processing we used AMIRA software.

**Results and Discussion:** In our studies, we were able to identify the WPB's by their characteristic microtubular structures measuring 12 to 14 nm in diameter. We observed a close spatial relation of WPBs to the Golgi complex, as it has been described in mature endothelial cells [1]. Furthermore, WPB's are in close association with extended trans Golgi membranous structures. WPB's proved to be connected with TGN. In the close vicinity of WPB we noticed, organized in parallel, microtubules of the cytoskeleton. Enlarged parts of TGN contain a material of higher electron density and organization similar to WPB's. In this study we were able to characterize the differentiation of EPC's into mature endothelial cells.

### **References:**

- [1] Michaux G, Cutler DF. How to roll an endothelial cigar: the biogenesis of Weibel-Palade bodies. *Traffic*. 2004 Feb; 5(2):69-78. Review.

## **Scanning Electron Microscopy of Vascular Corrosion Casts and its Contribution to Microvascular Research**

Lametschwandtner A., Stöttinger B., Bartel H. and B. Minnich

University of Salzburg, Department of Organismic Biology, Vascular and Muscle Research Unit, Hellbrunnerstrasse 34, A-4020 Salzburg, Austria (Europe)

The cardiovascular system is one of the first systems to develop. It transports oxygen and nutrients to and removes carbon dioxide, metabolites and waste products from the cells of the body. When fully developed it consists of arteries, arterioles, capillaries, venules and veins which actively and passively change their diameters to adapt their transport capacity according to given needs. Blood vessels form a hierarchically arranged three-dimensional tree-like network enabling an optimal supply of tissues and organs which may dramatically change under pathological conditions.

There are many methods to study the cardiovascular system from the macroscopic to the subcellular level, from its first occurrence (vasculogenesis), its enlargement (angiogenesis), its remodelling and its regression under different physiological and pathological conditions. Here we focuss to SEM of vascular corrosion casts only. Since the pioneering paper of Murakami [1] this technique has tremendously contributed to our knowledge and understanding of the microvascular anatomy of tissues and organs under normal and pathological conditions. Enhanced knowledge of physico-chemical properties of present day injection media together with technical improvements in injection techniques enable the injection of minute blood vessels like vasa vasorum and give excellent castings [2]. Upon SEM inspection vascular casts reveal characteristic endothelial cell nuclei and borderline imprints which allow a clear identification of arterial, venous and capillary vessels, of imprints of intimal cushions, sphincters, venous valves, as well as of wall components (vascular smooth muscle cells, pericytes).

Presently, the technique has been successfully applied to study fully differentiated vascular beds as well as growing (angiogenesis) and regressing systems under normal, experimental and pathological conditions. We will particularly focuss on the potentials which SEM of vascular corrosion casting offers in the study of two means of angiogenesis, i.e. sprouting and non-sprouting angiogenesis (=intussusceptive microvascular growth, IMG) and its facets intussusceptive arborization (IAR), intussusceptive branching remodeling (IBR) and intussusceptive pruning (IPR) [3]. If vascular corrosion casts are analyzed by 3D-morphometry they allow to accurately measure vessel diameters, intervascular and interbranching distances, and branching angles [5]. These data serve to characterize and test individual arterial bifurcations/venous mergings as well as entire vascular networks (trees) of tissues and organs in respect to their underlying design/optimality principles .

### References:

- [1] Murakami T.: Arch histol Jpn 32 (1971) 445.
- [2] Lametschwandtner A., Minnich B., Kachlik D., Setina M. and Stingl, J.: Anat Rec 281 (2004) 1372.
- [3] Djonov V. and A.N. Makanya: In: Clauss M. and G. Breier (Eds.) Mechanisms of angiogenesis. Birkhäuser, Basel-Boston-Berlin 2004; 17.

## **Cultured Human Arterial and Venous Endothelial Cells Derived from the Same Vascular Bed Differ in their Phenotypic and Genotypic Characteristics**

Lang I<sup>a</sup>, Hiden U<sup>b</sup>, Pabst MA<sup>a</sup>, Dohr G<sup>a</sup>, Desoye G<sup>b</sup>

<sup>a</sup>Institute of Cell Biology, Histology and Embryology, Medical University, 8010 Graz, Austria

<sup>b</sup>Clinic of Obstetrics and Gynecology, Medical University, 8036 Graz, Austria

Primarily, arteries and veins are defined by the direction of blood flow and by anatomical and functional differences, but little is known about the heterogeneity of endothelial cells lining these two types of vessels so far. Although differences in fluid dynamics and microenvironment within the circulatory system may play a role in determining the characteristic structure of an artery or vein, recent evidence suggests that the identity of arterial and venous endothelial cells is established before the onset of circulation by genetic mechanisms during embryonic development [1].

In our study we examined arterial and venous endothelial cells from the same vascular bed of well defined origin. This excludes the admixture of different vessel types and the problems of organ-specific heterogeneity. The endothelial identity of the cells was carefully proofed by staining for the classical endothelial markers von Willebrand factor, Ulex europaeus lectin and QBEND10. The cells internalized acetylated low-density-lipoprotein and did not show immunoreactivity with markers for macrophages, smooth muscle cells and fibroblasts.

Despite same cell culture conditions, human arterial and venous endothelial cells differ in their phenotypic and genotypic characteristics. Human venous endothelial cells showed a mesenchyme-like phenotype with spindle-shaped morphology growing in swirling patterns until confluence. They strongly expressed mesenchyme homeobox 2 and the mesenchymal stem cell protein DSC54. The juvenile phenotype of the venous endothelial cells strengthens the hypothesis that venous endothelial cells may represent a constant source of progenitors at later stages of embryonic development and in the adult that could transdifferentiate into arterial cells by vascular mediators [2]. In contrast, human arterial endothelial cells exhibited an epithelial-like phenotype with polygonal-shaped morphology and the classical cobblestone pattern at confluence. Arterial endothelial cells showed the expression of the artery-associated genes *hey-2*, *ephrin B1* and *Notch 4*.

These data support evidence for the phenotypic diversity of human arterial and venous endothelial cells. An understanding of these differences and recognition of the anatomic variations could enhance the insight into vascular biology that may open new therapeutic approaches with selective advantage for unique targets.

### References:

[1] Lawson ND, Scheer N, Pham VN, Kim CH, Chitnis AB, Campos-Ortega JA, Weinstein BM *Development* 128 (2001) 3675-3683.

[2] Harvey NL, Oliver G, *Curr Opin Gen Develop* 14 (2004) 499-505.

[3] Acknowledgements: The excellent technical assistance of Elisabeth Bock and Nicole Prutsch is gratefully acknowledged.

## **Morphodynamics of Mammalian Ovary Microvasculature. A Review by SEM of Vascular Corrosion Casts.**

Guido Macchiarelli

Department of Experimental Medicine, University of L'Aquila, 67100, L'Aquila, Italy.

Ovarian microvascular (MV) changes accompany development and atresia of follicles (FL), ovulation, formation and regression of corpora lutea (CL). Several factors, secreted by follicular, connective and endothelial cells following gonadotropin stimulation and under oocyte coordination, regulate these changes by promoting and suppressing angiogenesis (1). Scanning electron microscopy of vascular corrosion casts (SEMcc) was used in different animal models in order to identify structural changes related to ovarian capillary angiogenesis and regression (2). Correlated functional evaluations were performed by applying morphological, histochemical and biomolecular techniques. In small rodents, gonadotropin-primed ovaries showed rapid formation of several thin capillary networks, arranged in baskets of different size supplying developing FL. After ovulation intensive capillary sprouting and small vessels growth sustained CL formation (3). In immature hypothyroid rats, administration of eCG+hCG+T4 was followed by intensive angiogenesis and by mRNA expression of VEGF, TNF- $\alpha$ , bFGF, TGF $\beta$ -1, whereas in absence of T4 atretic FL were predominant and showed a poor MV network, rich of degenerating capillaries. In hCG-treated rabbits, early FL showed a massive sprouting angiogenesis. In this model, preovulatory FL and pregnant CL showed dilation and permeabilization of inner thecal capillaries followed by intussusceptive angiogenesis and consequent vessel duplication (4,5). MV growth of rabbit pseudopregnant CL lasted 2 weeks and was rapidly followed by capillary regression caused by angiogenesis arrest (5) as observed in atretic FL (4). In pigs, preovulatory FL capillaries were either thin and dilated, as a consequence of the contemporary expression of sprouting and intussusceptive angiogenesis. They showed many post-capillary constrictions, testifying the activation of mechanisms regulating follicular blood flow (6). In cows, dominant FL presented a multilayered MV network arranged in several layers. Atretic FL were poorly vascularized and showed in the outer theca numerous thin capillaries that corresponded to endothelial apoptosis figures as seen in correlated studies with TUNEL technique (7). It is concluded that ovarian healthy angiogenesis, although species dependent, is always essential for mammalian FL and CL development, whereas angiogenesis dysfunction regulates FL atresia and CL regression.

### References

- [1] Motta PM, Nottola SA, Familiari G, Makabe S, Stallone T, Macchiarelli G: *Int Rev Cytol* 223: 177-288 (2003).
- [2] Macchiarelli G: *J Reprod Dev*, 46: 207-225 (2000)
- [3] Macchiarelli G, Nottola SA, Ohtani O, Kikuta A, Murakami T, Motta P. In: Fujita H, Murakami T, Motta PM.: *Scanning Electron Microscopy of Vascular Corrosion Casts. Methods and Applications.* ( Kluwer Academic Press, Boston) pag.: 245-259 (1992)
- [4] Macchiarelli G, Nottola SA, Vizza E, Familiari G, Kikuta A, Murakami T, Motta PM: *Arch Histol Cytol*, 56: 1-12 (1993)
- [5] Nottola SA, Macchiarelli G, Motta PM: *Cell Tissue Res*, 288: 353-363 (1997)
- [6] Jiang JY, Macchiarelli G, Miyabayashi K, Sato E: *Cell Tissue Res*, 310: 93-101 (2002)
- [7] Jiang JY, Macchiarelli G, Tsang BK, Sato E: *Reproduction*. 125: 211-23 (2003)

## **Morphological Techniques for the Demonstration of Capillary Sprouts in the Early Corpus Luteum.**

Albert Ricken and K. Spänzel-Borowski

Institute of Anatomy, University of Leipzig, D-04103 Leipzig, Germany

Capillary sprouts grow from the vascularized thecal layer of a ruptured preovulatory follicle into the avascularized granulosa layer. This process transforms the follicular structure into a corpus luteum. It is a well-vascularized endocrine gland which undergoes cyclic growth and regression of the microvascular bed. Since the morphology of capillary sprouting and of lumen formation is difficult to detect at early stages, we studied the steps of development in corpora lutea of different species and by using different techniques. At the light microscopical level, the immunostaining for the factor VIII related antigen, a specific endothelial-cell marker, and for the adhesion molecule CD49, a member of the integrin family, revealed capillary sprouts which invaded the luteinizing granulosa layer of a periovulatory follicle obtained from the cow ovary. At the scanning electron microscopical level, blood vessel corrosion casts depicted capillary sprouts in a concentric arrangement before rupture of the preovulatory follicle, as noted in superovulated ovaries of golden hamsters. Otherwise sprouts pointed to the centre of the antrum after follicular rupture. This resulted in a spoke-wheel-like pattern of the microvascular bed in the fully developed corpus luteum. At the ultrastructural level, the developing sprouts were differentiated from luteal cells by a HRP (horseradish peroxidase) - positive basal membrane, a finding that depends on the intravenous injection of the enzyme before death of the hamsters. Additionally, a HRP-positive line delineated an interdigitating intercellular space of compact capillary sprouts. Retractions of the interdigitations gave rise to the capillary lumen. Interestingly, microvascular endothelial cells derived from the bovine corpus luteum and maintained in long-term culture, spontaneously formed tubules which represented an inside-out model with the extracellular matrix in the centre and the apical cell membrane directed towards the medium. We conclude: To understand the behaviour of capillary sprouting, different morphological techniques are wanted.

## Compartmentalization of Lipid Droplet Biogenesis

Robenek, MJ<sup>1</sup>, Troyer, D<sup>2</sup>, Severs, NJ<sup>3</sup>, Robenek, H<sup>2</sup>

<sup>1</sup>Department of Medicine, Heinrich-Heine-University, Moorenstr. 5, D-40225 Düsseldorf, <sup>2</sup>Leibniz-Institute for Arteriosclerosis Research, Westfälische Wilhelms-University, Domagkstr. 3, D-48149 Münster, <sup>3</sup>National Heart and Lung Institute, Imperial College, Dovehouse Street, London SW3 6LY, UK

Lipid droplets are currently recognized as indispensable and metabolically active organelles rather than being mere storage depots for hydrophobic neutral lipids. They partake in cell signalling, intracellular vesicle trafficking and most obviously lipid homeostasis. Lipid droplets appear also to be involved in several important human diseases, including atherosclerosis, diabetes and obesity. Recent studies have highlighted the importance of specific proteins that associate with lipid droplets [1-5]. In animal cells, lipid droplet-associated proteins include the structurally related members of the so-called PAT family proteins, named after perilipin, adipophilin and the tail-interacting protein of 47 kDa (TIP47), and the caveolins. Virtually nothing is known about the mechanisms by which such proteins are targeted and incorporated into lipid droplets or how lipid droplets themselves are actually assembled.

We used freeze-fracture and appropriate marker antibodies to determine the specific distributions of the PAT family proteins and caveolin-1 and the particular compartments they occupy in macrophages and adipocytes. Our findings show that PAT family proteins and caveolin-1 are not restricted to the lipid droplet surface as previously maintained, but also clearly pervade the droplet core. We found that perilipin and caveolin-1 co-localize in lipid droplet cores of adipocytes, and adipophilin and TIP47 co-localize in lipid droplet cores of macrophages. We demonstrate unequivocally that the PAT family proteins, in common with caveolin-1, are integral plasma membrane components. Adipophilin could be localized in ER membranes and the outer nuclear membranes of macrophages and perilipin in ER membranes and the outer nuclear membranes of adipocytes. These findings suggest that plasma membranes as well as ER and nuclear membranes are associated with lipid accumulation and possibly with the transit of PAT family proteins to the lipid droplet.

### References

- [1] Robenek, MJ et al. FASEB J 17, 1940-1942 (2003)
- [2] Robenek, MJ et al. FASEB J 18, 866-868 (2004)
- [3] Robenek, H et al. JLR, in press (2005)
- [4] Robenek, H et al. JBC 280, 5789-5794 (2005)
- [5] Robenek, H et al. JBC, in press (2005)

This work was supported by the SFB 492.

# Capillary Remodeling Permits Alveolarization after Completion of Microvascular Maturation: A 3D View of Postnatal Lung Development Using X-ray Tomographic Microscopy

Johannes C. Schittny<sup>1</sup>, Sonja I. Mund<sup>1</sup>, and Marco Stampanoni<sup>2</sup>

<sup>1</sup>Institute of Anatomy, University of Bern, Baltzerstrasse 2, CH-3012 Bern, Switzerland

<sup>2</sup>Swiss Light Source, Paul Scherrer Institute, CH-5232 Villigen, Switzerland

Alveolarization, the formation of new alveolar septa, is essential for survival, because most of the gas-exchange surface is formed by this process. Currently, it is believed that new septa may only be formed early during postnatal lung development (days 4 - 14 in mice). During alveolarization one leaflet of the double capillary network inside the existing septa folds up and gives rise to a new double capillary network within the newly forming septa. Afterwards the double layered capillary network of all alveolar septa is reduced to a single layered one (microvascular maturation, days 14 - 21 in mice). The current paradigm states that further alveolarization is now excluded.

We challenged this paradigm by measuring the length density (length per volume) of the free edges of the alveolar septa. With this new method we were able to show that the anlage of new septa takes place between days 4 - 7 and between days 21 - 36 in mice (**Fig. 1**). Therefore, a second phase, the phase of **late alveolarization**, has to be postulated.

The question, how new septa may fold up during late alveolarization, remained open. We studied vascular casts (Mercox, day 21) using a X-ray Tomographic Microscope (Materials Science beamline, Swiss Light Source, Paul Scherrer Institute, X-ray wavelength of 1 Å, nominal resolution of 0.7 μm). In 3D-visualizations of the alveolar capillary network we observed up-foldings of the capillaries which represent the formation of new alveolar septa (**Fig. 2a**). Looking at the up-foldings from the opposite side of their septa, we observed local duplications of the capillary network (**Fig. 2b**).

We conclude [1] that a second, late phase of alveolarization takes place after microvascular maturation is completed, and [2] that the required double layered capillary network is formed by a local duplication of the existing single layered network. Clinically, the discovery of late alveolarization may represent the basis for the development of new treatments for degenerative lung diseases and for premature born babies.

**Fig. 2.** 3D-visualization of the capillary network of a single alveolus (mouse lung, postnatal day 21). Dashed line, up-folding (**a**) and duplication (**b**, backside of **a**) of the capillary network during late alveolarization; dotted line, entrance of an alveolus.

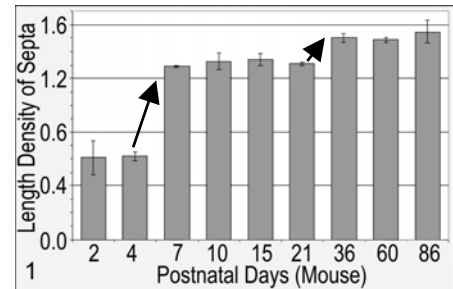
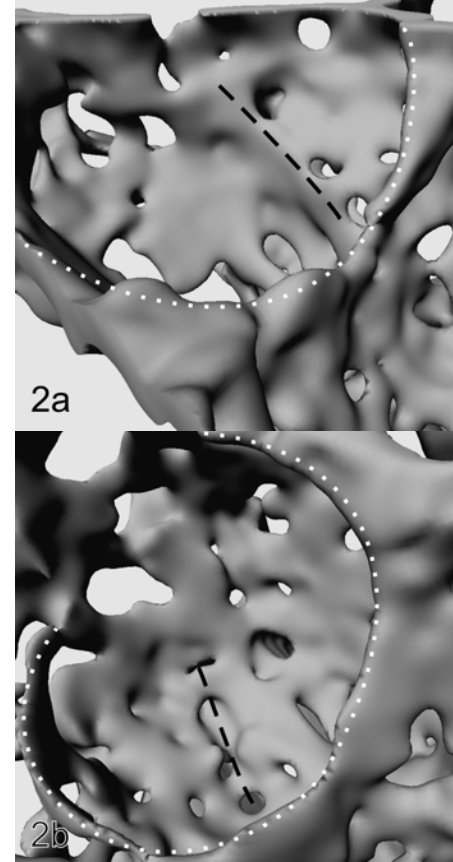


**Fig. 1.** An increase (↗) of the length density represents the anlage of new alveolar septa.



## **Epithelial and Vascular Dynamics of Rat Endometrium as Studied with SEM and Corrosion Casts.**

Udo M. Spornitz

Dept. of Electron Microscopy, Institute of Anatomy, University of Basel, CH 4056 Basel, Switzerland,

The rat endometrial cycle comprises four stages each of which, i.e. proestrus, estrus, diestrus I, and diestrus II lasts approximately 24 hours. Towards the end of the rats lifespan the cycle length may increase to about 6 days. During these individual stages characteristic morphological features are present which allow easy identification [1]. One of the outstanding features of estrus is the presence of pseudoglands, i.e. numerous depressions (pits) of the surface epithelium which resemble glandular orifices. They are formed through necrosis and apoptosis of the endometrium, they do not however penetrate the underlying basallamina. Apoptosis can clearly be detected on the basis of nuclear fragmentation and the marginalization of chromatin. Scanning electron microscopic detection of alkaline phosphatase shows a maximum during estrus and a minimum during diestrus II [2]. During early pregnancy the alkaline phosphatase activity decreases to zero on day 5 i.e. the actual day of blastocyst adhesion [3]. During the immediate postpartum period again the alkaline phosphatase activity is very low and the rat could become pregnant again. This stage is called postpartum diestrus. Shortly after this stage has been passed the rat then enters postpartum estrus, during which the alkaline phosphatase activity becomes rather high again. This in turn goes along with the fact that the rat can not become pregnant. The absence or presence of alkaline phosphatase activity can thus be taken as a marker for the relative receptivity of the animal. Underlying all these dynamical alterations during such a short period as the endometrial cycle is a rapid change in vascular architecture and presumably function [4]. Particular the capillary network seems to be constantly remodeled from one cycle to the next. The spacing of smaller areas almost free from capillaries apparently corresponds well with the spacing of the pseudoglands formed between proestrus and estrus. Not only the capillary network seems to undergo constant remodeling but also the afferent and efferent vessels in the area of the mesometrium are constantly changing. Apparently two mechanisms are involved in these rapid changes: 1. The capillary network is regulated through precapillary sphincters. 2. The vascular network is in fact constantly remodelled.

[01] Spornitz, UM., Socin, CD. and Dravid, AA Estrous stage determination in rats by means of scanning electron microscopic images of uterine surface epithelium. *Anat. Rec.* 254: 116 - 126(1999)

[02] Spornitz, UM., Dravid, AA., Winkelmann, A.: Scanning electron microscopic demonstration of surface and subsurface enzymes in rat endometrium during the estrous cycle. *Scanning* Vol. 20, 3 (1998)

[03] Winkelmann, A. and Spornitz, UM., Alkaline phosphatase distribution in rat endometrial epithelium during early pregnancy: A scanning electron microscopic study. *Acta Anat.* 158: 237 – 246 (1997)

[04] Spornitz, UM., and Bartuskova, I.: Dynamics of rat endometrium as studied with SEM and vascular corrosion casts. *Microsc. Microanal.* 8, 228 – 229 (2002)

# High Resolution Analyses of Cerebral Blood Vessels and Blood Flow

B. Weber

MPI for Biological Cybernetics, 72076 Tübingen, Germany

**Introduction:** The hemodynamic response following neural activation is the basis for most functional neuroimaging methods, including functional magnetic resonance imaging (fMRI). Consequently, in order to correctly interpret the results of neuroimaging experiments both the functional and the structural neurovascular coupling must be well understood. The degree and density of cortical vascularization should be compared with high resolution maps of blood flow changes induced by neural activation. In this presentation, methods will be described that try to elucidate this coupling using *ex-vivo* and *in-vivo* approaches.

**Methods:** *Ex-vivo* experiments: Formalin-fixed frozen sections of brain tissue (macaque monkey) were processed for anti-collagen type IV fluorescence immunohistochemistry to stain for vessels. Digital image processing was applied to compute the length density [ $\mu\text{m}/\mu\text{m}^3$ ], surface density [ $\mu\text{m}^2/\mu\text{m}^3$ ], volume fraction [ $\mu\text{m}^3/\mu\text{m}^3$ ], and mean diameter [ $\mu\text{m}$ ] of the vessels. Scanning electron microscopic analyses of intravascular polymer fillings and synchrotron-based micro-CT (using a voxel size of 1.4  $\mu\text{m}$ ) have been performed using monkey and rat tissue and the results were compared with the data obtained from the histological methods. *In-vivo* experiments: Laser speckle contrast imaging was applied in the rat barrel cortex and blood flow changes in response to single vibrissa deflection were recorded with sub-second and sub-millimeter resolution.

**Results:** *Ex-vivo* experiments: The immunohistochemical staining procedure yielded vessel-specific images of high quality and reproducibility within and between animals. The vascular density is in close relationship with the steady-state metabolic demand of the particular region, as can be seen in the high vascular density of layer IV (the layer with the highest cell density) in all visual cortices of the macaque monkey. The quantification of the synchrotron-based micro-CTs confirms the histologically obtained results and renders a true 3D-analysis possible. *In-vivo* experiments: Laser speckle contrast imaging provides blood flow maps with a high signal-to-noise ratio, making single trial analysis feasible. The spatial resolution of the method is excellent as neighboring cortical columns could be differentiated.

**Conclusion:** Several high resolution approaches to study structural and functional aspects of the cortical vasculature have been successfully implemented. The influence of differences in vascularization on the neuroimaging signals is of utmost importance but remains largely unknown. Future work will involve modeling approaches on the basis of the three dimensional vascular architecture (obtained from synchrotron-based micro-CT) to understand the basic mechanisms that are used by the brain to locally regulate the blood flow. Precise *in-vivo* measurements of the flow changes (obtained from laser speckle contrast imaging) will in turn be necessary to validate these modeling results.

## Typical and peculiar characters of degeneration in Cirripedia (Crustacea)

Adam S., Gruber D. & Klepal W.

Cell Imaging and Ultrastructure Research Unit, Faculty of Life Sciences, University of Vienna, Althanstraße 14, A-1090 Wien, Austria. [www.univie.ac.at/zoologie/ultra](http://www.univie.ac.at/zoologie/ultra)

Some Cirripedia Thoracica of the northern hemisphere degenerate and shed their penis annually after the copulatory period. It is the aim of this study to follow the sequence of events during degeneration in *Chthamalus stellatus* (Poli) and in *Semibalanus balanoides* (L.). The morphological alterations in tissues, cells and organelles of both species will be described and the occurrence of peculiar structures will be emphasized.

First signs of degeneration are noticed at the tip of the penis, beginning in the connective tissue and longitudinal nerves, followed by the longitudinal muscles and epithelia. The cytoplasm and the cell organelles in some of the small nerve fibers, in the innermost longitudinal muscles, in the epithelial cells of the ductus ejaculatorius and in those underlying the penis cuticle condense and appear dark. This results in shrinkage and separation of the cells. Other characters observed in both species are autophagic vacuoles, multilamellar bodies, swelling of RER and phagocytosis, all typical of autophagic cell death [1].

Apart from that in the longitudinal muscles of *Semibalanus balanoides* crystals are seen occasionally [2]. In *Chthamalus stellatus* large mitochondria are conspicuous. They are found between the strands of circular muscles near the penis tip (Fig. 1a). At least some of their cristae are tubular. In the longitudinal muscles are some large mitochondria with cristae changing from the lamelliform to the straight tubular type. The tubules in regular array are 25-30nm in diameter and studded with particles, arranged in rows, about 14nm apart. The distance between the tubules is 30 to 45nm (Fig. 1b). This kind of mitochondria is usually found in cells producing steroid hormones [3]. Their size, number and arrangement of cristae, indicate inactivity. It is also known that changes

in the mitochondria are often the primary event preceding dystrophic alterations. Both apply to the muscles in the degenerating penis.

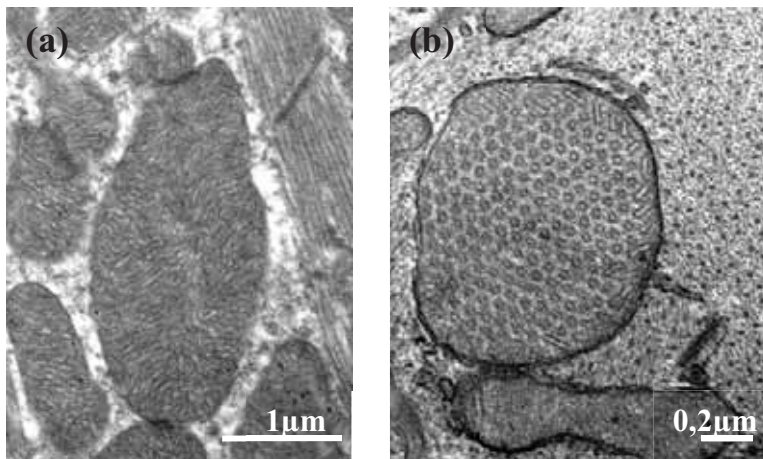


**Figure 1:** Large mitochondria (a) between circular muscles, densely packed with partly tubular cristae, (b) in longitudinal muscles, with cristae changing from the lamelliform to the straight tubular type.

### References

- [1] P. Clarke, *Anatomy and Embryology* 181, 195-213 (1990)
- [2] C. Rentenberger, H. P. Karnthaler & W. Klepal, LS5, in this volume (2005)
- [3] B. Picheral, *J. Microscopie* 7, 115-134 (1968)

## **Identification and location of bone-forming cells within cartilage canals on their course into the secondary ossification centre (SOC)**

Blumer MJF, Longato S, Richter E, Lazarescu D, and Fritsch H

Division of Functional and Clinical Anatomy Department of Anatomy, Histology & Embryology, Medical University of Innsbruck, Müllerstraße 59, A-6020 Innsbruck, Austria

In this study we examined the cartilage canals of the chicken femur in different developmental stages after hatching (D 2, 5, 7, 8, 10, 17, and 28). To obtain a detailed picture of the cellular and molecular events within and around the canals the femur was investigated by means of three-dimensional reconstruction, light microscopy, electron microscopy, and immunohistochemistry (VEGF, type I and II collagen, periostin, and tissue non-specific alkaline phosphatase).

Cartilage canals were extensions of the perichondrium and its mesenchymal cell layer into the hyaline cartilage of the distal epiphysis. The canals formed a complex network during embryonic development [1]. Shortly after hatching a secondary ossification centre (SOC) was visible and some cartilage canals penetrated into it where they ended blind. With these canals mesenchymal cells were transported into the SOC. The growth of the vascularized canals was promoted by vascular endothelial growth factor (VEGF). As the development progressed the SOC increased in size and adjacent canals were successively incorporated into the ossification centre [2]. Outside the SOC the mesenchymal cells of the cartilage canals expressed type I collagen and periostin and thus these cells have the properties of preosteoblasts. Within the SOC bone matrix was formed around the blind end of cartilage canals after the process of endochondral bone formation. Here calcified cartilage matrix was resorbed by chondroclasts and replaced by an osteoid layer which started to mineralize. The osteoid layer was lined by osteoblasts which derived from the mesenchymal cells of the canals, contained numerous matrix vesicles and labelled strongly for tissue non-specific alkaline phosphatase. Our immunohistochemical data provide evidence that this enzyme was only up-regulated in osteoblasts/preosteocytes. It was not synthesised by preosteoblasts and osteocytes.

In conclusion, our results indicate that during growth of the femur the cartilage canals supply the SOC with vessels and mesenchymal cells which express bone specific proteins depending on their position. Outside the SOC the canals mesenchymal cells have the characteristics of preosteoblasts which further differentiate into osteoblasts and osteocytes respectively when the canals are incorporated into the SOC.

### References:

[1] Blumer MJF, Fritsch H, Pfaller K, Brenner E (2004) Cartilage canals in the chicken embryo: ultrastructure and function. *Anat Embryo* 207:453-462

[2] Blumer MJF, Longato S, Richter E, Pérez MT, Konakci KZ, Fritsch H (2005) The role of cartilage canals in endochondral and perichondral bone formation: are there similarities between these two processes? *J Anat* 206:359-372

## Multiple Types of Programmed Cell Death

P.G.H. Clarke

DBCM, University of Lausanne, Rue du Bugnon 9, 1005 Lausanne, Switzerland

Although the attempt to classify cell death into different types is more than 100 years old, and numerous schemes have been proposed, during the last two decades of the 20th century most researchers accepted a simple dichotomy of apoptosis versus necrosis. Apoptosis, involving nuclear condensation and clumping of chromatin, accompanied by more moderate condensation of the cytoplasm and blebbing of the plasma membrane, was held to depend on active cellular processes, whereas necrosis, involving cellular swelling and cytoplasmic vacuolation, was held to be essentially passive, due to loss of cellular homeostasis. Since apoptosis was held to be the only active form of cell death, the term was frequently considered synonymous with programmed cell death. Already in the 1980's there was evidence that this dichotomy was too simple, and there now seems to be increasing agreement on this point. I shall review evidence for at least 3 types of programmed cell death.

**Type 1, apoptosis.** This type is too well known to require detailed exposition, but use of the term varies. Many authors now redefine apoptosis to include only caspase-mediated cell death with an apoptotic morphology, whereas others use purely morphological criteria (and some go to the other extreme of ignoring morphology). There is debate on whether DNA cleavage should be a criterion.

**Type 2, autophagic cell death.** Although ultrastructural evidence has long been available for massive (macro)autophagy in dying cells, it was unclear whether the autophagy was actually mediating the cell death. Scepticism was based on the facts that moderate autophagy occurs even in healthy cells, and that enhanced autophagy can be protective in situations such as amino acid starvation. A death-mediating role was initially deduced from the observation that most of the cytoplasm and even parts of the nucleus could be engulfed in autolysosomes. This was supported by numerous reports since 1992 that inhibitors of autophagy such as 3-methyladenine protected cells against cell death with an autophagic morphology, but unfortunately the inhibitors were not specific for autophagy. Conclusive evidence for a death-mediating role of the autophagy was provided in 2004 by 2 papers showing that inhibition of the autophagic pathway with RNAi interference of autophagy genes (Atg5, 6 or 7) blocked autophagy and the associated cell death.

**Type 3, cell death with "empty" cytoplasmic vacuoles.** This includes a variety of subtypes, perhaps even "programmed necrosis", but I shall focus on type 3B ("cytoplasmic cell death" or "paraptosis"), which is characterized by swelling of the perinuclear space and of organelles. Type 3B has frequently been described *in vivo* during development. Mechanistic studies have been few, but have indicated roles for caspase-9, MEK2, JNK1, and CDK5.

**Mixed types of cell death.** Multiple pathways of cell death can occur in a single cell, for example caspase-3 can be activated in parallel with autophagic mechanisms, and the cell death then has a mixed apoptotic-autophagic morphology. For this reason, blocking a single pathway may fail to prevent the cell death. But cells often die with the pure morphology of a single type, and I shall discuss the mechanisms responsible for this.

## Early Postnatal Apoptotic Activity of Mouse Bladder Urothelium

Andreja Erman, Kristijan Jezernik

Institute of Cell Biology, Faculty of Medicine, Lipičeva 2, 1000 Ljubljana, Slovenia

On the day of birth, mouse urinary bladder urothelium is disrupted due to the intense prenatal desquamation of urothelial cells. It has been already demonstrated [1] that beside the proliferation, apoptosis is one of mechanisms of urothelial renewal, which contributes to terminally differentiated urothelium. To get better understanding of postnatal urothelial development, the role of apoptosis during the first fourteen postnatal days has been investigated by methods: immunohistochemical detection of active caspase-3, TUNEL with fluorescent nucleotide and scanning and transmission electron microscopy. Apoptotic indices were scored on the base of data of quantitative analysis, obtained by results of TUNEL reaction.

Albino CD-1 adult male mice older than 8 weeks and mouse offspring of different postnatal age (on the day of birth - day zero and at postnatal days 1, 5, 6, 7, 10 and 14) were sacrificed.

In the majority of analysed sections we detected mostly apoptotic bodies and rarely apoptotic cells. Apoptotic bodies were of different shapes and sizes, single or in groups and present in different urothelial layers. If superficial cells underwent apoptosis, apoptotic bodies extruded from the urothelium and were observed in the junctions between cells on the urothelial luminal surface. On the other side, if intermediate or basal cells underwent apoptosis, already phagocytosed apoptotic bodies in the cytoplasm of neighbouring urothelial cells were observed. This is confirmed also by previous findings [2, 3], that the fate of apoptotic bodies depends on the location of epithelial cells, which die in apoptotic manner.

Apoptotic indices revealed that apoptosis was present in the urothelium already on the day of birth and it increased to day 6, where the most intense apoptotic activity was detected during the first fourteen days after birth. After day 6, apoptosis decreased again to day 14, whereas in terminally differentiated urothelium of adult mice no apoptotic activity was detected.

The quantitative data of this study support our previous observations [1] that apoptosis is an important event of urothelial postnatal development, essential for gradual remodelling of the urothelium. It seems that the peak of apoptotic activity on postnatal day 6 coincides with the intense urothelial reorganisation, which after that day consequently induces terminal differentiation.

### References:

- [1] Erman A et al., *Histochem Cell Biol* 115 (2001), 309
- [2] Wyllie AH et al., *Int Rev Cytol* 68 (1980), 251
- [3] Potten CS et al., *Br J Cancer* 74 (1996), 1743

## Regeneration and Blastema Formation in Flatworms

Robert Gschwentner, Bernhard Egger, Katharina Nimeth, Christian Gärber, Johannes Achatz, Peter Ladurner, Isa Philipp, Roland Aufschnaiter, Willi Salvenmoser, Reinhard M. Rieger

University of Innsbruck, Institute of Zoology and Limnology, Technikerstrasse 25, 6020 Innsbruck, Austria

Flatworms (Platyhelminthes) are an excellent model system to examine regeneration. The capacity to regenerate missing body parts in some flatworms is enormous. Totipotent stem cells – called neoblasts – are responsible for the cell renewal of all cell types during development, growth, and regeneration of the animals.

In light microscopy, neoblasts are described as small, spherical cells with a prominent nucleus surrounded by a small rim of basophilic cytoplasm. Ultrastructural studies of neoblasts revealed differences in the condensed chromatin pattern and their amount of cytoplasmic organelles such as rough endoplasmic reticulum and Golgi apparatus.

Regeneration in flatworms after amputation requires the formation of a blastema which is characterized by an accumulation of undifferentiated mesodermal cells near the wound that subsequently grows and differentiates into missing parts. We identified the contribution of neoblasts in the blastema formation by DIC-light microscopy, TEM and immunocytochemical methods. To label neoblasts we have applied the marker 5-Bromo-2'-deoxyuridine (BrdU) for labeling of neoblasts in S-phase and an antibody against the phosphorylated form of the histone H3 to label mitotic cells.

The regeneration capability and the blastema formation of the two flatworms *Macrostomum lignano* (Macrostomorpha) and *Convolutriloba longifissura* (Acoela) were examined. We found a clearly defined blastema 24 h to 48 h after injury in both animals. Additionally, we found mitotic stages in the blastema which is in contrast to observations on planarian flatworms (Tricladida) where no mitotic stages are located in the blastema itself. The high efficiency of cell proliferation in regeneration of missing body parts of *M. lignano* is shown by observation on the fate of labeled neoblasts in pulse-chase experiments.

The extraordinary stem cell system of flatworms and the formation of a regeneration blastema leading to organ differentiation may contribute the understanding of regeneration phenomena in this basal bilaterian group as well as in higher taxa.

This work was supported by FWF-Grant P16618-B03 and P15 204.

## Connections determine long-term fate – migration and adhesion of human adult stem cells to their niche

Anthony D. Ho, Werner Franke

Abteilung Innere Medizin V, Ruprecht-Karls-Universität Heidelberg, Abteilung Cell Biology, DKFZ, Heidelberg

Stem cells can be isolated from embryonic, fetal or adult tissues. Parallel to the progress made in embryonic stem cell research, adult stem cells, especially those derived from the bone marrow, have also been shown to exhibit developmental potentials heretofore not considered possible. Knowledge gained from blood stem cell transplantation has shown that adult stem cells are able to migrate to sites where they are needed - a phenomenon that is designated as "homing." Once settled in a niche after homing, surrounding cells in the microenvironment play a major role in defining their long-term fate. We have demonstrated that symmetry of divisions and self-renewal capacity of blood stem cells are governed by direct contact with the cellular microenvironment. In the bone marrow, direct contact with mesenchymal cells increased the absolute number of blood stem cells undergoing asymmetric divisions and with self-renewing capacity. To characterize the interactions between stem cells and cellular determinants we have analyzed the molecular composition of these interactions using a panel of antibodies specific for various components of tight junctions, gap junctions, adherens junctions and desmosomes by immunofluorescence microscopy, protein biochemical methods, RT-PCR, as well as with electron microscopy. We made two fundamental observations that are completely novel and of key importance for stem cell biology. In addition to the typical *puncta adherentia* junctions we have noted the occurrence of another type of adhering junctions. These consist of slender, villiform-to-vermiform cell protrusions of up to several micrometers, tightly inserted into invaginations of neighboring cells of *recessus penitus* type. This novel type of adhering junction is comparable to other junctions of the *adhaerens* category and bear similarity to those described in primary mesenchymal stem cells of day 7 to 8.5 mouse embryos. This discovery opens up another dimension for characterization of stem cells and indicates that adult stem cells communicate with each other through junctions and junction complexes. Characterization of and identifying the role of such cell-cell contacts in specific differentiation stages will be of fundamental significance for understanding the molecular mechanisms of plasticity potential of stem cells.

## Cryopreservation of Caco-2 Human Colon Cancer Cells in Fraunhofer Micro-Cryosubstrates: SEM and Block-Face- SEM for Study of Cell Differentiation After Thawing.

A. Katsen-Globa<sup>a</sup>, R. Malpique<sup>b</sup>, F. Ehrhart<sup>a</sup>, P. M. Alves<sup>b</sup>, H. Zimmermann<sup>a</sup>

<sup>a</sup>Fraunhofer IBMT, Ensheimer Str. 48, 66386 St. Ingbert, Germany,

<sup>b</sup>IBET /ITQB, Estacao Agronómica Nacional, Apartado 12, 27801-901 Oeiras, Portugal

Cryopreservation can store different biotechnologically and medically relevant cells but current cryovials are not suitable for all cell types. Miniaturized cryosubstrates have been biologically evaluated at IBMT [1]. Now we have expanded the use of micro-substrates for Caco-2 colon carcinoma cells that can differentiate spontaneously after long cultivation. One of the signs of differentiation, a brush border organization, can be investigated with scanning- (SEM) and

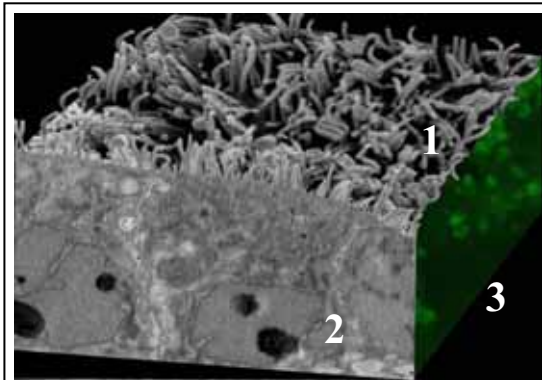


**Fig.1.** Combined SEM (1), block-face-SEM (2) and IL-8 immunostaining (3) of the same cell preparation cultivated after cryopreservation.

transmission-electron microscopy (TEM) [2]. In this work we propose a method combining immunostaining, SEM and block-face-SEM of cross- section of the same cells after cryopreservation.

Caco-2 cells were cryopreserved in suspension using conventional cryovials (1 ml) and micro-cryosubstrates (25  $\mu$ l net volume) and stored in liquid nitrogen. Addition of cryoprotectant (DMSO) before freezing was done manually or by a dispenser system [1]. Immediately after thawing, fluorescent viability tests were performed and the cells cultivated on Thermanox slides for up to 17 days. After cultivation Interleukin-8 (IL-8)-immunostaining was performed. Then the cells were

fixed and treated with heavy metals, dehydrated, critical point dried and coated. After SEM examinations the cells were embedded in epoxy resin, cross-sectioned with ultramicrotome and then a block-face preparations were coated with carbon and studied in ESEM in BSE- mode. The best results (up to 90% viability) were obtained by cryopreservation of Caco-2 cells in Fraunhofer micro-cryosubstrates with 5% DMSO automatically added. Like the controls, cryopreserved cells could express IL-8 (immunostaining) and organize a brush border (SEM and block-face-SEM, see Fig. 1) after 17 days of cultivation. SEM and block-face-SEM images show the apical surface of cells coated with a highly ordered, dense array of microvilli. The block-face preparations also show cell contact features such as tight junctions and desmosomes typical for these cells. Cell impregnation with heavy metals provides high contrast making the use of block-face SEM comparable with standard TEM. The presented method can be used for evaluation of function, morphology and ability of differentiation after cryopreservation of adherent cells. Experiments using adult stem cells are in progress.

### References:

- [1] Zimmermann H., Katsen A.D. In Proc. MICROtec., VDE Verlag (Berlin), (2003), 535-539.
- [2] Peterson M:D., Mooseker M.S. J. of Cell Science, 105, (1993), 445-460.
- [3] Grants: 03N8707 / 16SV1366/0 by BMBF and NMP4-CT-2004-500039 by EU.

## **Characterization of the Totipotent Stem Cell System of the Flatworm *Macrostomum lignano***

Peter Ladurner<sup>1</sup>, Daniela Pfister<sup>1</sup>, Georg Kuales<sup>1</sup>, Robert Gschwentner<sup>1</sup>, Katharina Nimeth<sup>1</sup>, Bernhard Egger<sup>1</sup>, Zbyszek Adamski<sup>2</sup>, Willi Salvenmoser<sup>1</sup>, Reinhard Rieger<sup>1</sup>

<sup>1</sup>University of Innsbruck, Institute of Zoology and Limnology, Technikerstrasse 25, Austria

<sup>2</sup>Adam Mickiewicz University, Institute of Experimental Biology, Electron Microscope Laboratory, ul. Grunwaldzka 6; 60-780 Poznań, Poland

Flatworms possess a totipotent stem cell system. Stem cells - called neoblasts - can differentiate into all cell types including germ cells and are responsible for physiological cell renewal, development, growth and the extraordinary regeneration capacity of most flatworm species. We are characterizing the stem cell system of *Macrostomum lignano* using a molecular, ultrastructural and histological approach. We have identified successive stages of differentiating neoblasts by electron microscopy according to the condensed chromatin pattern and the cytoplasmic differentiation. Changes in the condensed chromatin pattern during neoblast differentiation was monitored by electron microscopical serial sectioning. Successive stages of differentiating neoblasts labeled with BrdU exhibited distinct differences in the distribution of immunogold particles within condensed chromatin or euchromatin regions.

Neoblasts can be identified also by light microscopy in live animals, in single cell preparation, and by labeling of proliferating cells using 5'-bromo-2'-deoxyuridine (BrdU). Short BrdU pulses revealed bands of labeled cells along the lateral sides of the animals. Few proliferating cells were present anterior to the eyes and along the median axis. In pulse-chase experiments neoblast proliferation, migration and differentiation was observed. Cell cycle parameters were obtained by double labeling with BrdU (S-phase neoblasts)/phosphorylated Histone H3 (mitoses) combined with different pulse chase times. These approaches revealed a rapid cell turnover with more than 54% of all S-phase cells entering mitosis after 4 hours and over 88% after 24 hours, respectively. Continuous BrdU exposure for 14 days showed a replacement of about 1/3rd of all epidermal cells. Starvation and feeding experiments demonstrated the enormous plasticity of the stem cell system and an extreme reduction of mitosis after 30 days of starvation and a dramatic increase in the number of mitoses after induction by feeding. Neoblast specific molecular markers (*piwi*, *MCM*, *PCNA*) and germ line specific markers (*vasa*, *pumilio*, *nanos*) are used to study expression and function of neoblasts.

The unique stem cell system in Platyhelminthes may help to understand the mechanisms of stem cell regulation in development, growth and regeneration in these primitive bilaterians and higher organisms including humans.

Supported by FWF 15204 (R.R) and FWF 18099 (P.L).

## **How Human Cord Blood Derived Stem Cells Differentiate Into Early Matured Endothelial Cells. A Confocal And Electron Microscopic Study Including Electron Tomography**

J. Neumüller\*, M. Vetterlein\*, S.E. Neumüller-Guber\*\*, J. Kosiuk\*, J. Huber\*\*\*, M. Pavelka

\*Center for Anatomy and Cell Biology, Dept. for Cell Biology and Ultrastructural Research, Medical University of Vienna, Schwarzschanerstrasse 17, A-1090 Vienna, Austria, \*\*Dept. of Clinical Virology, \*\*\*Department of Gynecologic Endocrinology and Reproductive Medicine, both Medical University of Vienna, Währinger Gürtel 18-20, A-1090 Vienna, Austria.

**Objective:** Endothelial progenitor cells (EPCs) derived from human cord blood have a high potential in repair of damaged blood vessels. However, the origin and the stage of differentiation of EPCs is still a matter of discussion. The maturation stages are characterized by a reorganization of membranous compartments such as RER, Golgi complex as well as endocytic and exocytic vesicles. Just matured endothelial progenitor derived cells (EPDCs) form Weibel-Palade bodies (WPBs) which serve as storage compartment for the von Willebrand Faktor (vWF). In case of vessel injury, WPBs are delivered from the cells by exocytosis and the released vWF plays a role in platelet adhesion and aggregation. WPBs are cut off from the Trans Golgi Network (TGN). They are characterized by parallel microtubular structures containing among other proteins vWF in a multimeric form. We are interested in morphological and immunological characterization of the transition of stem cells into endothelial progenitor cells and EPDCs in respect of a possible therapeutic use. **Material and Methods:** In our *in vitro* model, the differentiation started from early hematopoietic CD133-positive cells. Cells were cultivated on fibronectin (FN)-coated culture vessels in culture medium 199 containing the cytokines bFGF, EGF and VEGF. Under these conditions, the cells adhered to the FN coat and started to differentiate. Every week, cultures were either fluorolabeled with monoclonal antibodies against the cell surface receptors CD31, CD34, CD54, CD106, VEGF-R2 as well as against intracellular vWF and investigated by confocal microscopy or prepared for electron microscopy and electron tomography (reconstructions of tilt series from -65° to +65° and 3D modeling revealing the spatial organization of the complex membrane structures of WPBs bodies in connection with the TGN). **Results and Conclusion:** The first cell clusters contained extended Golgi complexes with many ministacks and an abundant TGN. WPB-like organelles were localized close to the TGN and orientated along microtubules of the cytoskeleton and often interconnected. However, they did not yet contain the parallel microtubular structures found in mature WPBs. Bundles or branched mitochondria could also be detected in EPDCs. During maturation, more and more cells formed mature rod shaped and tubulated WPBs in remarkable number which also could be demonstrated by laser confocal microscopy after staining with an anti-vWF antibody. A striking feature of EPDCs was the formation of blood vessel-like structures also containing WPBs. Confocal microscopy showed a cell surface staining for CD133 and for the VEGF-R2 in EPCs which disappeared during maturation while CD34 persisted. During the differentiation, the adhesion molecules CD34, CD54 and CD106 were present in early matured cells but disappeared after further maturation. In conclusion, we emphasize that EPDCs, after the transition through several stages of maturation as EPCs, are highly active cells in respect to a significant formation of WPBs and a strong proliferative and angiogenic capacity. We postulate that these features would be appropriate for the repair of injured blood vessels.

## **Regeneration and Cellular Dynamics in the Basal Bilaterian *Macrostomum lignano***

Katharina T. Nimeth, Bernhard Egger, Robert Gschwentner, Willi Salvenmoser, Martina Hrouda, Ursula Rostek, Martina Gleirscher, Daniela Pfister, Georg Kuales, Peter Ladurner, Reinhard M. Rieger

University of Innsbruck, Institute of Zoology and Limnology, Technikerstr. 25, 6020 Innsbruck, Austria

Cell turnover and regeneration in *Macrostomum lignano* are based on totipotent stem cells (neoblasts), which may be a primitive trait among bilateral symmetrically animals.

Platyhelminthes have a high capability of regeneration. After amputation *M. lignano* features posterior and also very restricted anterior regeneration. Double labeling of mitoses (anti-phos-H3) and S-phase cells (anti-BrdU) illustrates the high efficiency of cell proliferation in the neoblast system. Our investigations revealed a fast response to amputation, with first increase of S-phase cells and a delayed rise of mitoses.

All cell renewal is accomplished by the totipotent stem cells (neoblasts). Tissue maintenance is achieved by a balance between cell proliferation and apoptosis. We have demonstrated programmed cell death using (1) terminal deoxynucleotidyl transferase-mediated dUTP nick end labeling (TUNEL), (2) specific binding of phosphatidyl-serine to fluorescent labeled annexin V and (3) identification of apoptotic stages by ultrastructure.

Our results demonstrate the possibility for detailed analysis of cellular dynamics of a basal bilaterian stem cell system in tissue maintenance and regeneration.

Supported by FWF Grants P15 204 (R.R.), P16 618 (R. R.) and P18 099 (P. L.)

# Structural Characterization of a Biomolecular Nanocrystal Developed in the Crustacean *Semibalanus balanoides* (L.) Using TEM Methods and Fourier Transform Image Analysis

C. Rentenberger<sup>a</sup>, H. P. Karnthaler<sup>a</sup> and W. Klepal<sup>b</sup>

<sup>a</sup> Institute of Materials Physics, University of Vienna, Boltzmannngasse 5, A-1090 Wien, Austria. [www.univie.ac.at/Materialphysik/EM](http://www.univie.ac.at/Materialphysik/EM)

<sup>b</sup> Cell Imaging and Ultrastructure Research Unit, Faculty of Life Sciences, University of Vienna, Althanstraße 14, A-1090 Wien, Austria. [www.univie.ac.at/zoologie/ultra](http://www.univie.ac.at/zoologie/ultra)

Every year, after the copulatory period, the marine crustacean *Semibalanus balanoides* (Linné) degenerates its copulatory organ. In the course of this process the morphological structure changes in all tissues involved. A variety of obligatory alterations, and occasionally also crystals, are seen in the longitudinal muscles [1, 3]. It was the aim of this study to characterize the structure of such a biomolecular crystal. In order to analyse its morphology and crystal structure it is necessary to examine the crystal along the different axes of the unit cell. Therefore the thin sections were mounted in a rotation holder and studied using a Philips CM200 transmission electron microscope (TEM) equipped with a goniometer stage allowing  $\pm 60^\circ$  tilt.

Tilting experiments reveal that the morphology and the crystal structure of the 3-dimensional biomolecular crystal are related to each other. Figure 1(a) shows the shape and the periodic structure of the biocrystal when projected along the c-axis; the facets are parallel to low index planes. From the selected area diffraction (SAD) pattern and from the Fourier transform (cf. Fig. 1(b)) of the image of the crystal three parameters of the reciprocal space ( $a^*$ ,  $b^*$ ,  $\gamma^*$ ) can be deduced. For the calibration in real and reciprocal space the lattice spacing of crystalline bovine liver catalase was used [2].

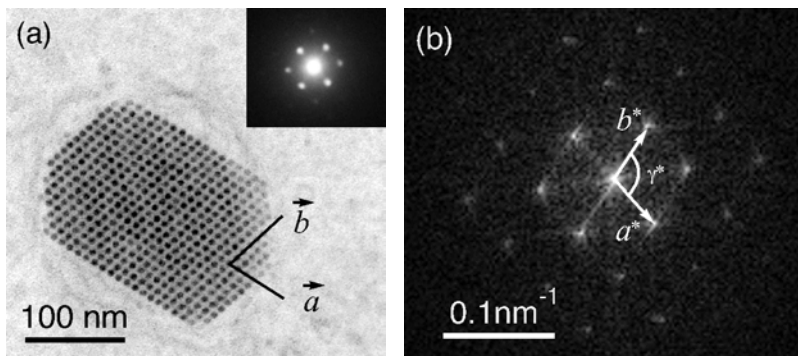


Figure 1: (a) TEM bright-field image of a biomolecular crystal showing its periodic structure; the corresponding SAD pattern is shown in the inset. (b) Fourier transform of (a); the reciprocal lattice parameters  $a^*$  and  $b^*$  correspond to the spacing of the end on lattice planes.

Using the full set of parameters obtained from the analysis of the nanocrystal projected along the three axes of the unit cell the lattice parameters are:  $a = 9.8 \pm 0.5 \text{ nm}$ ,  $b = 9.2 \pm 0.4 \text{ nm}$ ,  $c = 8.1 \pm 0.2 \text{ nm}$ ,  $\alpha = 79.8^\circ$ ,  $\beta = 87^\circ$ ,  $\gamma = 76.2^\circ$ . This leads to the conclusion that the crystal structure is triclinic (Laue group  $\bar{1}$ ) and that the crystal contains  $25 \times 19 \times 14$  unit cells.

## References

- [1] W. Klepal and D. Gruber (in preparation).
- [2] N. G. Wrigley, J. Ultrastructure Research 24, 454 (1968).
- [3] Technical help by Daniela Gruber is gratefully acknowledged.

## **Role of stem cells in the flatworm *Macrostomum lignano* as shown by immunogold labeling of S-phase neoblasts**

Willi Salvenmoser<sup>1</sup>, Bernhard Egger<sup>1</sup>, Katharina Nimeth<sup>1</sup>, Zbyszek Adamski<sup>2</sup>, Andreas Bode<sup>1</sup>, Peter Ladurner<sup>1</sup> and Reinhard Rieger<sup>1</sup>

<sup>1</sup> Institute of Zoology and Limnology, University of Innsbruck, Technikerstrasse 25, A-6020 Innsbruck, Austria

<sup>2</sup> Adam Mickiewicz University, Faculty of Biology, Institute of Experimental Biology, Electron and Confocal Microscope Laboratory, ul. Grunwaldzka 6; 60-780 Poznań, Poland

Stem cell research has become one of the main topics in medical and biological sciences. Stem cells in flatworms, called neoblasts, are considered to be totipotent and are responsible for growth, cell maintenance and regeneration. The flatworm *Macrostomum lignano* is a suitable organism to study stem cell behaviour because of its small size, transparency, stainability and regeneration capacity. For instance, 5-Bromo-2'-deoxyuridine (BrdU) can be easily incorporated, and therefore neoblasts in S-phase can be labeled in pulse experiments and their movement and differentiation traced in pulse-chase and continuous labeling experiments.

Different types of neoblasts can be classified by their location in the animal. The majority of S-phase neoblasts are distributed in two mesodermal bands along the lateral nerve cords. A comparably small number of neoblasts can be found in the gastrodermis. Gonadal stem cells are located in the testes and ovaries. The epidermis and the anterior- and posterior-most regions appear free of S-phase cells in BrdU pulse experiments. BrdU-labeled cells migrate into these areas in pulse-chase or continuous labeling experiments. Three different stages (1-3) of neoblasts in all locations can be distinguished based on the distribution of condensed chromatin in the nucleus and the content of cytoplasm.

In hatchlings, an immunogold analysis after a 30 minute BrdU pulse showed that the somatic S-phase neoblasts near the rostrum (an S-phase cell-free region in front of the eyes) appear to be at stage 1 or 2 and are in close proximity to the nervous system. After a 4 hours continuous BrdU application, neoblasts in that region may have divided: one BrdU-positive cell remains stationary in stage 1 or 2, its daughter cell apparently migrates towards the rostrum and was labeled as a stage 3 neoblast or as a cell already showing signs of differentiation. The daughter cells were found in a distance of 8 to 10 µm compared to the stationary cell, in a precisely defined area of the cross sections. Hence, one can speak of “corridors” where neoblasts proliferate and start to migrate.

Neoblasts are also involved in regeneration by forming new cells and tissue. After amputating the caudal tail plate, about 3.000 cells need to be regenerated to replace the amputated structures. Early regeneration (2h, 4h, 8h), blastema formation (24h, 48h) and late regeneration (72h) processes could be observed. The number of S-phase cells in the entire animal increased during 2 hours to 24 hours after amputation, and it decreased after 48 hours of regeneration. We are now implementing immunogold labeling of S-phase cells during blastema formation and differentiation.

Supported by FWF 16618-B03 (R.R), FWF 15204 (R.R) and FWF 18099 (P.L)

## Automated Sub-Diffraction Optical Nanometry of Cell Nuclei

U. Spöri<sup>a</sup>, H. Mathée<sup>a</sup>, D. Baddeley<sup>a</sup>, Ch. Wagner<sup>a</sup>, S. Martin<sup>b</sup>, A. Pombo<sup>b</sup>, C. Wotzlaw<sup>c</sup>, J. Fandrey<sup>c</sup>, C. Cremer<sup>a,d</sup>

<sup>a</sup>Applied Optics and Information Processing, Kirchhoff-Institute for Physics, University of Heidelberg, D-69120 Heidelberg, Germany

<sup>b</sup>Clinical Sciences Centre, Medical Research Council, London W12 0NN, UK

<sup>c</sup>University Hospital, University of Duisburg-Essen, D-45122 Essen, Germany

<sup>d</sup>The Jackson Laboratory, Maine 04609, USA

Many approaches to understand cellular processes and the functional nuclear architecture require the use of sophisticated imaging techniques. Thus, it is highly desirable to further develop light optical methods for the analysis of biological nanostructures and their dynamics in the interior of three-dimensionally conserved cells. In particular, important structural parameters such as topology, i.e. the mutual positions and distances, as well as the sizes of the constituting subunits are to be considered. In the low energy range, this has become possible by the development of novel methods of far-field light fluorescence microscopy.

Experimental results, supported by "Virtual Microscopy" computer simulations, indicated that using "Point Spread Function (PSF) Engineering" approaches with a suitably modified PSF, even at the fluorescence photon count number typical for single molecule fluorescence emission, a size discrimination limit of a few tens of nanometers with a precision in the ten nanometer range have become feasible [1]. For example, Spatially Modulated Illumination (SMI) approaches [2] have been used to measure the diameter of individual fluorescent BioMolecular Machines (BMMs) down to a few tens of nanometer inside of fixed cells, corresponding to about 1/10 of the excitation wavelength used [3]. This "SMI-nanosizing" technique is based on the analysis of the small perturbations of the SMI-diffraction image correlated with the object size.

Potential applications include the size measurement of nuclear macromolecular complexes [3], of individual small gene regions, of the thickness of metaphase chromosomes, or of membrane protein complexes. The potential of such "light nanoscopy" approaches extends to the "in situ" analysis of cellular protein-protein and protein-nucleic acid interactions, at a SMI-colocalization volume about two orders of magnitude smaller than the illumination or observation volume, respectively, in a confocal laser scanning microscope using a high numerical aperture objective lens [4]. Experimental SMI measurements of fluorescent labeled objects inside of cryosections and 3D conserved cells were performed using 458nm and 488 nm excitation. The nanosizing data shown comprise results of 3D extension analysis of the erythropoietin gene, transcription factory analysis, protein cluster analysis, and gene expression/compaction analysis.

### References:

- [1] A.V. Failla, A. Cavallo, C. Cremer, *Appl. Opt.* **41** (2002) 6651-6659
- [2] B. Albrecht, A.V. Failla, A. Schweitzer, C. Cremer, *Appl. Opt.* **41** (2002) 80-87
- [3] S. Martin, A.V. Failla, U. Spöri, C. Cremer, A. Pombo, *Mol. Biol. Cell* **15**, (2004) 2449-2455
- [4] U. Spöri, A. V. Failla, C. Cremer, *J. Appl. Phys.* **95** (2004) 8436-8443

## Effects of Curcumin on Apoptosis in “In Vivo” Solid Ehrlich Ascites Tumor Model in Balb-C Mice

Elif Ilkay Taskin<sup>a</sup>, Ibrahim Firat<sup>b</sup>, Burak Kuscu<sup>c</sup>, Tuncay Altug<sup>a</sup>, Husniye Dogruman<sup>a</sup> Fatma Oguz<sup>d</sup>, Funda Onar<sup>e</sup>, Melek Ozturk<sup>f</sup>, and Mehmet Gurtekin<sup>d</sup>

<sup>a</sup> Department of Morfology, Veterinary Medicine Faculty, Istanbul University, 34840 Istanbul/Turkey

<sup>b</sup> Department of Pathology, Veterinary Faculty Medicine, Istanbul University, 34840 Istanbul/Turkey

<sup>c</sup> Tehnical Manager, Intervet 34396 Istanbul/Turkey

<sup>d</sup> Department of Medical Biology, Istanbul Faculty of Medicine Istanbul, Istanbul University, 34310 Istanbul//Turkey

<sup>e</sup> Department of Histology-Embriyology , Istanbul Faculty of Medicine, Istanbul University, 34300 Istanbul/Turkey

<sup>f</sup> Department of Medical Biology, Cerrahpasa Faculty of Medicine, Istanbul University 34300 Istanbul/Turkey

“This work was supported by the Research Fund of The University of İstanbul.

Curcumin (diferuloylmethane) is the yellow pigment in turmeric (*Curcuma longa L*) tahat is widely used as a spice, food coloring (curry) and preservative [1]. Curcumin has shown a wide range of pharmacological properties including anti-inflammatory, anti-tumor promoter and anti-oxidant effects [2].

In this study the development and quantity of apoptosis in tumor tissue of solid ehrlich ascites tumor (EAT) model developed balb-c mouse by applying 100 mg/kg curcumin in different time periods were investigated. For this reason 54 Balb-c female mice, constituted in vivo tumor by subcutaneous injection of  $3 \times 10^6$  EAT cells, were divided into 3 experimental and 3 control groups. Using gavage method 100 mg /kg curcumin solved in 9% alcohol was applied to experimental groups, 9% alcohol was applied to control groups in different time intervals.

Long and short diameters measurement, and Terminal deoxyribonucleotydil transferase-mediated dUTP-digoxigenin Nick End Labeling (TUNEL) and hematoxylin-eosin staining were applied to the extracted tumors of all groups and findings were supported with electron microscopic (TEM) evaluations.

In long and short diameter measurement of acquired tumors no significant results were obtained ( $p > 0.05$ ). In microscopic evaluations different results were obtained from cell count of all groups. More apoptotic cells were determined in experimental group 2 ( $p < 0.001$ ) and 3 ( $p < 0.05$ ) than their control groups. According to statistical analysis, there was no significant difference between experimental group 1 that received longest-term curcumin and control 1 ( $p > 0.05$ ). All these results showed that the long-term 100mg/kg applications of curcumin do not have any effect on amount of apoptosis.

### References:

- [1] Mazumder A., Raghavan K., Weinstein J., Kohn K., Pommier Y. Biochemical Pharmacology. (1995).49;8.1165-1170.
- [2] Ahsan S. and Hadi S.M. Cancer Letters (1998).124-23-30.
- [3] acknowledgements.

## **Effects Of Human Gonadotrophin And Growth Hormon On Ovary In Immature Rat. Light And Electron Microscopic Study**

Tanfer Toparlak, Selma Yilmazer, Onur Toparlak, Melek Öztürk

Istanbul University, Cerrahpasa Faculty of Medicine Department of Medical Biology, Istanbul , Turkey

Ovulation problems and a infertility are seen in 15-25 % of the female. To stimulate ovulation with gonadotrophins is a common method of therapy. In this study the effect of both together or separately application of growth hormon(GH) and human menaposal gonadotrophin(hMG) on the ovarian morphology was evaluated by light and electron microscopy.

In the study 32 ,21 days old, immature female albino rats were used. four groups, each cansisting of 8 rats. 1 Group control, buffered with phosphate s.f., 2 .group ; 0,0033 IU/day GH, 3.group ; 0,125 IU/day hMG, 4.Group combined s.c. application of (0,0033 IU/day GH + 0,125 IU/day hMG.) The samples obtained at the end of the study were examined by light and electron microscopy.

In hMG group the amount of the primary follicles ( $p<0,05$ ) and Graafian follicle ( $p<0,01$ ) were significantly decreased whereas a significant increase of the amount of the secondary follicels was observed. Corpus luteum was significantly increased in comparison to the control group. A great number of degeneration follicles and multinuclear follicle cells were observed .In GH applicated group the amount of the primary follicles ( $p<0,001$ ) and secondary follicles ( $p<0,05$ ) were significantly decreased, whereas Graafian follicles significantly increased ( $p<0,001$ ). Both GH and hMG applicated group showed a high increase of all types of follicles ( $p<0,001$ ), but the decrease of corpus luteum was not found in significant. Under electron microscopy the hMG group showed in comporison to the control group atretic follicles with ultrastructural characteristic..In GH+hMG group especially cleavaged and multinuclear oocytes were a common finding. In some of the memrana granulosa cells with phagocytic activity increased nuclear distortion and nucleus memrane dilatation were observed in GH group.

As a result GH and hMG application stimulates folliculogenesis and ovulation, but causes also a consequent degenerative changes.

## **Qualitative Analysis of c-myc Gene Domain using Confocal and Spatially Modulated Illumination Microscopy**

C. Batram<sup>a</sup>, D. Baddeley<sup>a</sup>, C. Boxler<sup>a</sup>, S. Stein<sup>a</sup>, J. Schwarz-Finsterle<sup>a</sup>, C. Cremer<sup>a</sup>

<sup>a</sup>Applied Optics and Information Processing, Kirchhoff Institute for Physics, University of Heidelberg, Im Neuenheimer Feld 227, 69120 Heidelberg, Germany

The qualitative analysis of cellular structures is crucial for an improved functional understanding of molecular biological questions and requires even more powerful (light) microscopic techniques. Therefore, for advanced light microscopy with a biological focus the application of Confocal Laser Scanning Microscopy (CLSM) is presently the standard method for three dimensional analysis of cellular “macro“structures. To analyse cellular nanostructures new microscopic techniques have to be applied, such as Spatially Modulated Illumination (SMI) Microscopy. This novel microscopic technique offers a size resolution limit in the order of a few tens of nm.

With the help of Fluorescence in situ Hybridization (FISH), gene regions are routinely labelled, detected and evaluated. This presentation introduces the application of the CLSM and SMI-Microscopes for the qualitative analysis of the c-myc gene domain in human lymphocytes, both in metaphase spreads and interphase nuclei. The present results suggest that the difference in volume of this c-myc gene domain is not highly significant.

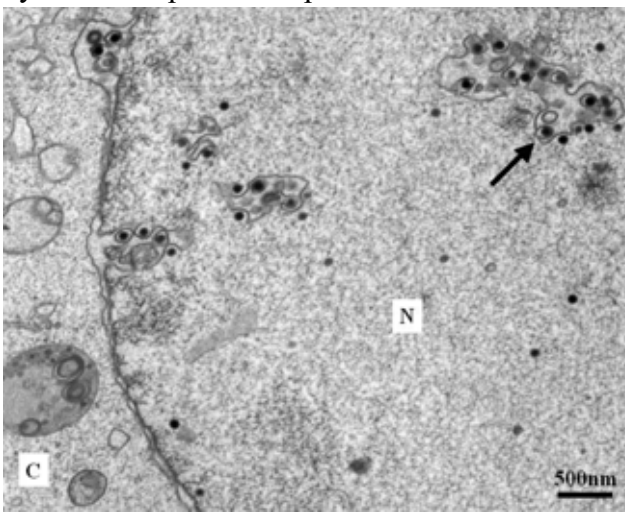
## High-pressure Freezing Electron Microscopy Reveals Tubular Invaginations of the Inner Nuclear Membrane during Cytomegalovirus Egress

Christopher Buser<sup>a,b</sup>, Pamela Häberle<sup>b</sup>, Thomas Mertens<sup>b</sup>, Paul Walther<sup>a</sup>, and Detlef Michel<sup>b</sup>

<sup>a</sup>Z.E. Elektronenmikroskopie, Universität Ulm, 89081 Ulm, Germany

<sup>b</sup>Abteilung Virologie, Institut für Mikrobiologie, Universität Ulm, 89081 Ulm, Germany

Murine cytomegalovirus (MCMV) is a member of the betaherpesviridae family and consists of a 220 kb double stranded DNA genome enclosed by an icosahedral capsid, a proteinaceous tegument layer and a lipid envelope. Due to the structural complexity of cytomegaloviruses the general steps



of virion morphogenesis are only partially understood. These steps include nuclear capsid formation, primary envelopment/deenvelopment at the nuclear membranes, cytoplasmic tegumentation/envelopment and virion release (reviewed in [1]). For further analysis of the egress pathway of MCMV, 3T3 murine fibroblasts were allowed to grow over 3mm sapphire disks and infected. At 48 hours post infection the cells were high-pressure frozen with a Compact HPF-01 (Wohlgend Engineering, Sennwald, CH), freeze-substituted in acetone containing osmium tetroxide, uranyl acetate and 5 % water [2] and embedded.

By thin- and serial sectioning and stereo imaging of thick sections, we were able to visualize deep tubular infoldings of the inner nuclear membrane that were involved in primary envelopment of the nucleocapsids (arrow; N: nucleus, C: cytoplasm). The outer nuclear membrane was unaffected by these structural alterations and the general perinuclear architecture remained intact. We propose that the local depolymerisation of the nuclear lamina [3] is not used to create individual budding sites for viral capsids but to induce the infolding of the inner nuclear membrane, thus creating an enlarged surface area available for primary envelopment. Additionally, due to the tubular shape of the invaginations and the absence of obstacles in the perinuclear space (e.g. chromatin), the movement of enveloped particles to the nuclear periphery might be more efficient. To our knowledge this structural modification has not been described before and may serve to enhance and facilitate the production and release of progeny virus from the nucleus.

Addition of water to the substitution solution [2] greatly increased the visibility and/or retention of cellular structures, especially membranes. This effect was proportionally increasing with water content until no further improvement could be seen after addition of 5%. Interestingly, up to 20% water could be added without visibly affecting the ultrastructure.

### References:

- [1] T. C. Mettenleiter, *J Virol* 76 (2002) 1537-47
- [2] P. Walther and A. Ziegler, *J Microsc* 208 (2002) 3-10
- [3] W. Muranyi, J. Haas, M. Wagner, G. Krohne and U. H. Koszinowski, *Science* 297 (2002) 854-7

## Ultrastructure of Primordial and Primary Human Ovarian Follicles after Enzymatic Isolation by Collagenase and Liberase™.

A. Camboni<sup>a-b</sup>, M.M. Dolmans<sup>b</sup>, B. Martinez-Madrid<sup>b</sup>, A. Van Langendonck<sup>b</sup>, J. Donnez<sup>b</sup> and S.A. Nottola<sup>a</sup>.

<sup>a</sup>Dept. of Human Anatomy, University La Sapienza, 00161 Rome, Italy

<sup>b</sup>Dept. of Gynecology, Saint-Luc's Hospital, Catholic University of Louvain, 1200 Brussels, Belgium

Frozen-thawed ovarian tissue transplantation now constitutes a possible option for restoring fertility in young cancer patients after the sterilizing effects of chemotherapy and radiotherapy.

Unfortunately, the possibility of reintroducing tumor cells into cancer patients by ovarian tissue autografting cannot be excluded. To avoid this problem, isolated human follicles may be grafted, as the follicular basal lamina precludes transfer of malignant cells. The most promising strategy involves harvesting and grafting primordial and primary follicles, the most abundant follicular stages in the ovary at any age. These follicles are more resistant to cryoinjury than mature follicles. Furthermore, grafting of isolated follicles may allow faster angiogenesis and could limit ischemic and reperfusion damage. Transplantation of frozen-thawed isolated primordial follicles has been successfully achieved in mice [1], yielding normal offspring. In the literature, human ovarian follicles are usually enzymatically isolated by collagenase. However, this technique does not appear to yield entirely healthy follicles [2]. Our purpose was to evaluate the effects of collagenase and Liberase™ enzymatic treatments on the morphology of primordial and primary human ovarian follicles, analyzing and comparing the ultrastructure of these isolated follicles by light and transmission electron microscopy (LM/TEM). Eight human ovarian biopsies were processed for follicle isolation by collagenase or Liberase enzymatic digestion. One hundred and nine isolated human follicles (collagenase: N= 68; Liberase: N= 41) were fixed and processed for LM and TEM. By LM, intact follicles, as well as follicles with an incomplete follicular wall, were found in both groups. Areas of detachment between the follicular cells and oocyte were occasionally detected in intact collagenase-isolated follicles. By TEM, intact follicles from both groups were surrounded by a discontinuous basal lamina. Numerous connective tissue fibers were observed on the outer aspect of the residual basal lamina of Liberase-isolated follicles. With regard to the intrafollicular compartment, collagenase-isolated follicles showed more ultrastructural signs of regression than Liberase-isolated follicles. In particular, large confluent patches of heterochromatin were more frequently encountered in the nuclei of follicular cells from the collagenase-isolated group. As revealed by LM, focal discontinuities at the oolemma-follicular cell interface were also often detected in the same group of follicles. In addition, irregularities in the nuclear profile of the oocyte were more evident in collagenase-isolated follicles than Liberase-isolated follicles. Finally, among the oocyte organelles, clusters of lipid droplets, small vacuoles and myelin-like structures were mostly found in the oocytes of collagenase-isolated follicles. In conclusion, this study demonstrates that Liberase treatment allows significantly better preservation of follicle integrity than the traditional collagenase treatment. *Funds from MIUR (Italy) and FNRS (Belgium).*

[1] Carroll and Gosden, Hum Reprod. 1993; 8:1163-7

[2] Abir et al. Fertility and Sterility 2001; 75:141-146

## The Ultrastructure of Pre-60S Ribosomal Particles

Bohumil Maco<sup>a</sup>, Tracy A. Nissan<sup>b</sup>, Kyriaki Galani<sup>b</sup>, David Tollervey<sup>c</sup>, Ueli Aebi<sup>a</sup>, and Ed Hurt<sup>b</sup>

<sup>a</sup>M.E. Müller Institute for Structural Biology, University of Basel, 4056 Basel, Switzerland

<sup>b</sup>Biochemie-Zentrum der Universität Heidelberg, 69120 Heidelberg, Germany

<sup>c</sup>Wellcome Trust Centre for Cell Biology, University of Edinburgh, EH9 3JR Edinburgh, Scotland

Ribosome biogenesis which takes place in the nucleolus is a highly dynamic and regulated multistep process of synthesis, processing and modification of pre-rRNAs, assembly with ribosomal proteins as well as with non-ribosomal factors forming the pre-ribosomal particles [1-3].

Tandem affinity purification (TAP) of Rix1 (a marker of the late pre-60S ribosomal intermediate located in the nucleoplasm) revealed its association with the non-ribosomal proteins Rea1 (a dynein-related AAA-type ATPase), Ipi1, and Ipi3 [2, 4].

To determine the ultrastructure of the late pre-60S ribosomal particles at the electron microscopy (EM) level, we prepared negatively stained specimens. Accordingly, pre-60S particles that were affinity purified via TAP-tagged Rix1, Ipi1, and Ipi3 bait proteins exhibited predominantly a tadpole-like structure composed of a globular “head” domain (~15 nm in diameter) and an extended “tail” domain (~25-30 nm in length) with an overall length of ~45 nm. Interestingly, this pre-60S ribosomal particle is strikingly different from the morphology of the mature 60S ribosome.

EM of antibody cross-linked particles allowed us to identify the specific location of Rea1 and ribosomal proteins Rpl3 and Rpl10 within the Rix1 pre-ribosome structure. The non-ribosomal protein Rea1 is localized within the tail domain, whereas the ribosomal Rpl3 and Rpl10 proteins comprise part of the head domain of the pre-60S ribosomal particles.

In vitro treatment with ATP induced dissociation of Rea1 from the pre-60S particle indicating that Rea1 and the Rix1 complex could mediate ATP-dependent remodelling of the 60S subunits and subsequent export from the nucleus into the cytoplasm.

### References:

- [1] Baßler et al., Mol Cell 8 (2001) 517-529.
- [2] Nissan et al., EMBO J 21 (2002) 5539-5547.
- [3] Tschochner H and Hurt E, TIBS 13 (2003) 255-263.
- [4] Nissan et al., Mol Cell 15 (2004) 295-301.

## Electron Tomography of *C. elegans* Meiotic Spindles

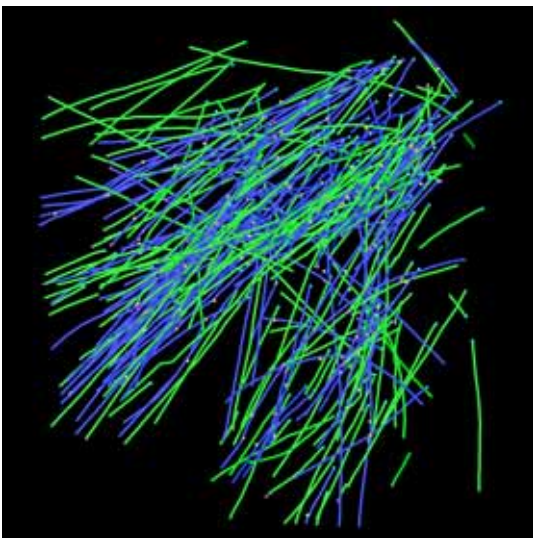
Eileen T. O'Toole<sup>a</sup>, Martin Srayko<sup>b</sup>, Jana Mäntler<sup>b</sup>, and Thomas Müller-Reichert<sup>b</sup>

<sup>a</sup>Boulder Laboratory for 3-D Electron Microscopy of Cells, University of Colorado, Boulder, CO 80309, USA

<sup>b</sup>Max Planck Institute of Molecular Cell Biology and Genetics, Electron Microscopy Facility, 01307 Dresden, Germany

Pole-proximal ends in female meiosis are arranged in acentrosomal spindle poles that lack typical centrosome components. We were interested in applying tomographic reconstruction to visualize the organization and end morphology of microtubules in *C. elegans* meiosis.

For the preparation of whole worms, we have applied a combination of methods, including high-pressure freezing and freeze substitution (HPF/FS) [1]. Material prepared by HPF/FS was subsequently thin-layer embedded, allowing us to select worms prior to serial sectioning [2]. To obtain high-resolution 3-D structure data, serial 300 nm thick sections containing meiotic spindles were imaged in an IVEM (TECNAI F30, FEI), and tilted images were collected about two orthogonal axes. Tomographic reconstructions were calculated using back projection algorithms and combined using the method of Mastronarde [3].



Electron tomographic reconstruction allowed us to trace individual microtubules in 3-D and to identify pole-proximal microtubule ends in wild-type specimens (Fig. 1: 3-D model built from three, 400nm thick sections containing microtubules arranged in a short, barrel-shaped half spindle). Spindle microtubules are not focused at a particular region of the meiotic chromosomes. Analysis of the tomograms revealed that the majority (about 90%) of pole-proximal microtubule ends are open and the three-dimensional models show a statistical distribution of these open, pole-proximal ends within the spindle. Strikingly, 20-40% of the spindle microtubules showed evidence of fragmentation. Visualizing spindles from a katanin-like protein (i.e. MEI-1) loss-of-function mutant [4], tomograms reveal disorganized spindles and no evidence of microtubule fragmentation.

These results are thought to reflect: first, chromatin-induced nucleation or capture of microtubules and second, microtubule-severing activity required in meiotic spindles to keep microtubules short.

### References:

- [1] E.T. O'Toole et al., *J. Cell Biol.* (2003) 451-456.
- [2] T. Müller-Reichert et al., *J. Microsc.* (2003) 71-80.
- [3] D.N. Mastronarde, *J. Struct. Biol.* (1997) 343-352.
- [4] M. Srayko et al., *Genes Dev.* (2000) 1072-1084.

## **Involvement of Nuclear Lamins A/C in the Formation and Maintenance of Nuclear Speckles**

Raska I.<sup>1,2</sup>, Vecerova J.<sup>1,2</sup>, Koberna K.<sup>1,2</sup>, Malinsky J.<sup>1</sup>, Soutoglou E.<sup>3</sup>, Sullivan T.<sup>4</sup>, Stewart C.<sup>4</sup>, and Misteli T.<sup>3</sup>

<sup>1</sup>Institute of Cell Biology and Pathology, 1st Faculty of Medicine, Charles University in Prague; <sup>2</sup>Department of Cell Biology, Institute of Physiology, Academy of Sciences of the Czech Republic, Prague; <sup>3</sup>National Cancer Institute, National Institute of Health, Bethesda; <sup>4</sup>Laboratory of Cancer and Developmental Biology, National Cancer Institute, Frederick

The existence of the nuclear skeleton is a subject of intensive debate the issue of which is not yet settled. Importantly in this respect, recent results have indicated [1,2,3] that lamins A/C provide a structural scaffold of nuclear domains, termed nuclear speckles, that are highly enriched in splicing factors. To further substantiate these findings [4], we characterized nuclear speckles both in normal mouse embryonic fibroblasts (+/+ cells) as well as in cells with knock-outed gene for lamin A/C (-/- cells). By means of electron microscopy and immunofluorescence microscopy of splicing factors, we showed that morphology of nuclear speckles was the similar in +/+ and -/- cells. The results of the FRAP analysis of recombinant splicing factors with GFP demonstrated that their association with speckles was highly dynamic and was the same in +/+ and -/- cells. We also showed that the apparent association of lamins A/C with nuclear speckles was rather due to a cross reactivity of the given anti-lamin A/C antibody. Our results thus demonstrate that the formation and maintenance of nuclear speckles is independent of the presence of lamin A/C, and argue against an essential role of lamins A/C in the speckle morphology [5].

### References:

1. Jagatheesan G. et al. (1999). *Journal of Cell Science* 112, 4651-4661.
2. Muralikrishna B. et al. (2001). *Journal of Cell Science* 114, 4001-4011.
3. Kumaran R.I. et al. (2002) *Journal of Cell Biology* 159, 783-793.
4. Vecerova et al. (2004). *Molecular Biology of the Cell* 15, 4904-4910.
5. This work was supported by grants from the Grant Agency of the Czech Republic 304/04/0692, the Ministry of Education, Youth and Sports MSM0021620806 and LC535, the Wellcome Trust 075834, and the Academy of Sciences of the Czech Republic IAA5039103.

## **Effects of Human Gonadotrophin and Growth Hormone on Ovary in Immature Rat: Light and Electron Microscopic Study**

Tanfer TOPARLAK, Selma YILMAZER, Onur TOPARLAK, Melek ÖZTÜRK

Istanbul University, Cerrahpasa Faculty of Medicine, Department of Medical Biology, Istanbul, Turkey

Ovulation problems and a infertility are seen in 15-25 % of the female. To stimulate ovulation with gonadotrophins is a common method of therapy. In this study the effect of growth hormone (GH) and human menaposal gonadotrophin (hMG) on the ovarian morphology was evaluated by light and electron microscopy [1,2,3,4].

In the study, 32 immature female albino rats ( 21 days old ) were studied in four groups of 8 rats. Group 1; control animals treatment with phosphate buffered subcutaneously (s.c), group 2;GH treatment 0,0033 IU/day s.c, group 3; hMG treatment 0,125 IU/day s.c , group 4; combined treatment of GH and hMG (0,0033 IU/day GH + 0,125 IU/day hMG s.c. The tissue samples obtained at the end of the study were prepared for light and electron microscopic examinations.

In hMG group the amount of the primary follicles ( $p<0,05$ ) and Graafian follicle ( $p<0,01$ ) were significantly decreased whereas a significant increase of the amount of the secondary follicels was observed. Corpus luteum was slightly increased in comparison to the control group. A great number of degeneration follicles and multinuclear follicle cells were observed.

In GH applicated group the amount of the primary follicles ( $p<0,001$ ) and secondary follicles ( $p<0,05$ ) were significantly decreased, whereas Graafian follicles significantly increased ( $p<0,001$ ). Both GH and hMG applicated group showed a high increase of all types of follicles ( $p<0,001$ ), but the decrease of corpus luteum was not found in significant. Under electron microscopy the hMG group showed in comparison to the control group atretic follicles with ultrastructural characteristic. In GH+hMG group cleavaged and multinuclear oocytes were common findings. In some of the granulosa cells with phagocytic activity, increased nuclear distortion and nucleus membrane dilatation were observed in GH group.

As a result GH and hMG application stimulates folliculogenesis and ovulation, but causes also a consequent degenerative changes

### REFERENCES.

1. Deveron JB, Hseueh AJW: Endocrinology, 118:888-90,1986.
2. Hamburg R, Eshel A, Abdallah I, and Jacobs HS: Clinical Endocrinology, 25:113-117,1998.
3. Hseueh AJW, Welsh TH, Jones PBC :Endocrinology, 108:2002,1981.
4. Jacobs HS ,Hamburg R, Owen E, Eshel HI. West C: Gynec ,33:267-270,1988.

## **ELECTRON TOMOGRAPHY OF THE *AGROBACTERIUM* DNA TRANSFER COMPLEX IN TRANSIT THROUGH THE PLANT NUCLEAR PORE**

E. Zimmerman, E. Shimoni\* and M. Elbaum

Dept. of Materials and Interfaces, \*Electron Microscopy Unit, Weizmann Institute of Science, 76100 Rehovot, Israel

*Agrobacterium tumefaciens* causes the crown gall disease in plants by a unique mechanism involving interkingdom gene transfer and efficient genetic transformation of the host. Single-stranded transfer DNA (T-DNA, or the T-strand) travels to the plant cytoplasm with a single copy of the virulence protein VirD2 bound at its 5' end. A second bacterial protein, VirE2, interacts stoichiometrically with the T-DNA to form a protein-DNA complex. The interaction is cooperative and sequence independent. We have previously characterized the structure of this complex *in vitro* by electron microscopy and 3D image processing [1]. It forms a hollow solenoidal shape with outer diameter of 15.7 nm. In the plant, VirE2 is thought to have a number of important roles in the transformation process, including protection of the ssDNA from cytoplasmic nucleases and adaptation to the host nuclear import machinery. An understanding of VirE2-ssDNA nuclear import will have broad implications to normal cell function and pathogenesis, as well as direct relevance to artificial gene delivery. We present here tomographic reconstructions of individual tobacco nuclear pores with the VirE2-ssDNA complex in transit. This affords both the first 3D structural view of the plant nuclear pore, and a first view of the nuclear transport process with a structurally defined substrate in passage.

[1] Abu-Arish A, Frenkiel-Krispin D, Fricke T, Tzfira T, Citovsky V, Wolf SG, Elbaum M. (2004) Three-dimensional reconstruction of *Agrobacterium* VirE2 protein with single-stranded DNA. *J Biol Chem* 279(24):25359-63.

## Application of FIB lift out preparation for a TEM study of the *in situ*-interaction between CaF<sub>2</sub>-like precipitates and dental enamel surfaces

L. Berthold <sup>a\*</sup>, J. Schischka <sup>a</sup>, A. Cismak <sup>a</sup>, M. Petzold <sup>a</sup>, J. Wohlfart-Zhou <sup>b</sup>, H.-G. Schaller <sup>b</sup>

<sup>a</sup> Fraunhofer-Institut für Werkstoffmechanik, Heideallee 19, D-06120 Halle (Saale), Germany, \* [bert@iwmh.fhg.de](mailto:bert@iwmh.fhg.de)

<sup>b</sup> Universitätspoliklinik für Zahnerhaltungskunde und Parodontologie der Martin-Luther-Universität Halle-Wittenberg, Große Steinstraße 19, 06108 Halle (Saale)Germany

The aim of the present investigation was to evaluate Focused Ion Beam-based lift out techniques for the TEM sample preparation of dental enamel specimen. The developed methodical approach formed the basis for a microstructural investigation of the effect of fluoride on the dental enamel microstructure under *in situ* conditions.

The samples consisted of different human dental enamel slabs derived from three different patients that were treated *in vitro* with an amine fluoride (Olaflur; 1000 ppm fluoride; pH 4.7; 60 min). This treatment resulted in an intensive precipitation of a CaF<sub>2</sub>-like material at the sample surface. Similar precipitates are assumed to be formed if fluoride-containing dentifrices are applied to the tooth surface, acting as reservoir in time between dentifrice application. Therefore, the dissolution of the CaF<sub>2</sub>-like material under oral conditions and its interaction with dental enamel are considered as essential factors affecting the cariostatic effect of fluorides. The fluoridated specimens were subsequently attached to orthodontic appliances and worn *in situ* by four different volunteers without further fluoride treatment. After 1, 3 and 10 days the sample surface microstructure was investigated using Transmission Electron Microscopy (TEM), Selected Area Electron Diffraction (SAED) and nanospot X-ray Analysis (XEDS) in cross-section. Un-treated samples and fluoridated specimens treated *in vitro* by demineralization/remineralization cycling served as control groups.

Focused Ion Beam (FIB) Milling has been used to prepare electron transparent specimens from dental enamels. A TEM specimen with a nominal dimension of 5µm wide by 20µm long by ~150nm thick is machined from a bulk sample using an FIB device. The electron transparent specimen slice is lifted-out of the bulk sample using a modified glass rod attached to a micromanipulator arm. The specimen is then placed onto a formvar-coated copper grid for TEM analysis. Although of the brittle and nanocrystalline microstructure of the dental enamel specimens, an effective and reliable ion beam preparation procedure was developed replacing time-expensive traditional procedures using face to face bonds or approaches based on the wire shadow method.

For samples worn *in situ* for three and ten days, the TEM investigations allowed to assess the stability, adhesion and chemical composition of the CaF<sub>2</sub>-like precipitates under oral conditions. In addition, the study revealed changes of the microstructure of the dental surface, in particular showing the formation of a fluoride-rich surface layer with about 1 µm depth immediately beneath the remaining CaF<sub>2</sub> surface deposits.

The model used illustrates directly the efficacy of CaF<sub>2</sub>-deposits formed after topical treatment as a fluoride-releasing reservoir and its effect on enamel microstructure under oral conditions. The observed formation of a F<sup>-</sup>-rich surface layer can contribute to understand the role of topical fluoride treatments for caries prevention and protection against erosion in more detail.

The support of GABA International AG Münchenstein, Switzerland, is gratefully acknowledged.

# Quantitative Evaluation of Filling Restorations of Human Teeth Using Three Dimensional Scanning Electron Microscopy (3-D SEM)

W. Dietz<sup>a</sup>, S. Meineber<sup>b</sup>, U. Kraft<sup>b</sup>, I. Hoyer<sup>b</sup> and E. Glockmann<sup>b</sup>

<sup>a</sup>Centre of Electron Microscopy, University of Jena, 07740 Jena, Germany

<sup>b</sup>Department of Conservative Dentistry, University of Jena, 07740 Jena, Germany

Clinical and micromorphological investigations of the surface and marginal behaviour of new dental filling materials is of importance in the therapeutical dentistry [1]. The SEM evaluation of those restorations is well established [2] and frequently executed according to the classification of Gaengler et al. [3]. However, the results are affected by the individual assessment of the examiner.

The aim of this study was to enhance the objectivity of those evaluations by means of 3-D SEM.

Four different filling materials (e.g. the composite InTen-S/AdheSE (1) or Amalcap (2), Vivadent, Germany) had been placed (40 fillings). The occlusal parts of the fillings were examined directly (baseline) and after 6, 12 and 24 months. Two-stage-replicas were taken from the patients teeth, gold sputtered and investigated in the SEM Philips 515 using a four-quadrant backscattered electron (BSE) imaging (point electronic, Germany) and the topographical software MeX (Alicona, Austria).

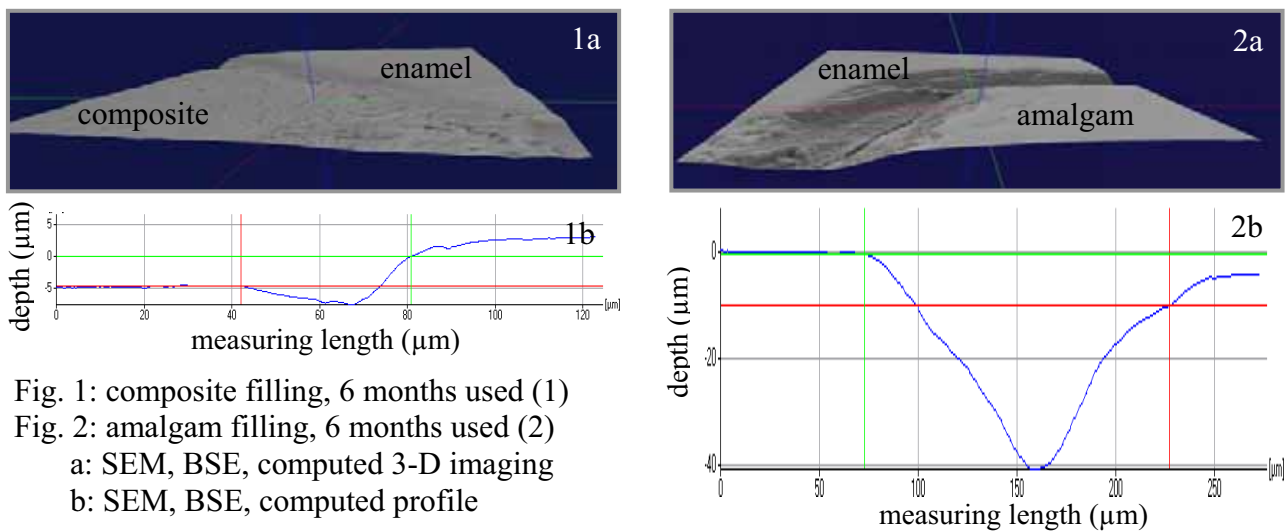


Fig. 1: composite filling, 6 months used (1)

Fig. 2: amalgam filling, 6 months used (2)

a: SEM, BSE, computed 3-D imaging

b: SEM, BSE, computed profile

In cases of composite (1) and amalgam (2) fillings the measurements showed an abrasive material loss of about 5 μm after 6 months use (Fig. 1) or e.g. 40 μm deep marginal gaps in the amalgam restoration (Fig. 2). BSE based 3-D imaging has proved to be an objective evaluation aid. The abrasion gradient of one and the same filling is testable under in vivo conditions, however, different materials have to be compared with each other under identical experimental requirements. Additionally, the impression preparation should consider the ancillary conditions of the imaging system.

## References:

[1] J.F. Roulet, B. Salchow and M. Wald, *Dent. Mater.* 7 (1991) 44.

[2] W. Dietz, R. Montag, I. Hoyer, U. Kraft, P. Gaebler, M. Voigt, *Europ. J. Cell Biol.* 78 (1999) 35.

[3] P. Gaengler, I. Hoyer, R. Montag and P. Gaebler, *J. Oral Rehabil.* 231 (2004), 991

# The Use of Silver Diamine Fluoride (SDF) in Arrest of Caries Treatment – a Scanning Electron Microscopical and X-Ray Microanalytical Study

W. Dietz<sup>a</sup>, J. Schneider<sup>b</sup>, B. Monse-Schneider<sup>c</sup> and R. Heinrich-Weltzien<sup>b</sup>

<sup>a</sup>Centre of Electron Microscopy, Friedrich-Schiller-University of Jena, 07740 Jena, Germany

<sup>b</sup>Department of Preventive Dentistry, Friedrich-Schiller-University of Jena, 07740 Jena, Germany

<sup>c</sup>Health and Nutrition Center, Department of Education, Cagayan de Oro, Philippines

Untreated dental caries in children is one of the most prevalent childhood diseases in many low-income and middle-income countries worldwide. The financial and manpower resources of most countries limit traditional treatment strategies to cope this disease. More cost effective interventions are required. SDF ( $\text{Ag}(\text{NH}_3)_2\text{F}$ ) is used as a chemical agent for the arrest of caries treatment in order to prevent the onset and progression of dental caries.

The aim of the present study was to assess the effect of SDF on carious enamel and dentine of differently progressed lesions by use of scanning electron microscopy and X-ray microanalysis.

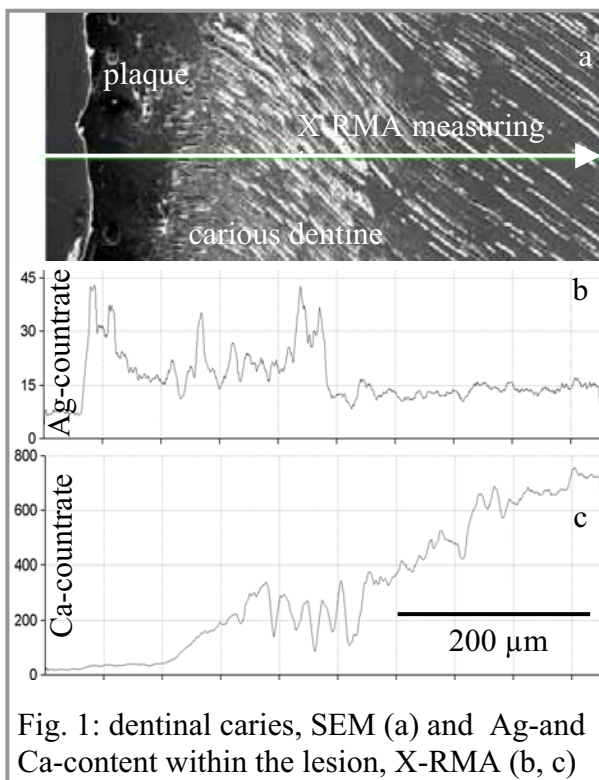


Fig. 1: dentinal caries, SEM (a) and Ag- and Ca-content within the lesion, X-RMA (b, c)

Occlusal carious lesions of 20 deciduous and 20 permanent molars were visually scored using the diagnostic criteria proposed by Ekstrand et al [1]. 38% SDF solution (Saforide, 44,800 ppm  $\text{F}^-$ ; Bee Brand Med. Dent. Comp. Ltd, Japan) was applied to the occlusal lesions, followed (after 1 min) by application of tannic acid (concentrated black tea solution, 60 min,  $37^\circ\text{C}$ ) as silver precipitant. The specimens were split in two across the occlusal lesions, air-dried and carbon evaporated. The elements silver, fluorine and calcium were detected and localised (Philips SEM 515, EDAX DX4).

The caries free occlusal enamel revealed silver within the first  $10\ \mu\text{m}$  while fluorine could be estimated only at the surface. In uncavitated whitish and brownish discoloured fissures (criteria 1, 2) silver was detected up to a depth of  $150\ \mu\text{m}$  and fluorine up to  $10\ \mu\text{m}$ , respectively. In cavitated lesions (criteria 4) silver was proved up to the front of the dentinal lesions (Fig. 1), but fluorine was detectable only below the surface of the lesions.

This study enlightens the morphological reaction of SDF in carious enamel and dentinal lesions. The results suggest that the antibacterial effective silver infiltrates the carious demineralised hard tissue, especially the dentine. Traces of fluorine are available directly under the enamel surface facilitating remineralisation processes.

## References:

[1] KR. Ekstrand, DNJ.Ricketts, EAM. Kidd Caries Res 31, (1997) 224-31

## Combination of SEM and PIXE study of the *in vivo* biocompatibility of implants at the bone interface

G. Guibert<sup>a</sup>, F. Munnik<sup>a</sup>, T. Zehnder<sup>a</sup>, Ph. A. Buffat<sup>b</sup>, D. Laub<sup>b</sup>, L. Faber<sup>c</sup>, J.D. Langhoff<sup>d</sup>, B. Von Rechenberg<sup>d</sup>, I. Gerber<sup>e</sup>, S. Mikhailov<sup>a</sup>

<sup>a</sup>CAFI CH-2400 Le Locle, Switzerland

<sup>b</sup>EPFL CIME. CH-1015 Lausanne, Switzerland

<sup>c</sup>DePuy ACE, CH-2400 Le Locle, Switzerland

<sup>d</sup>MSRU Universität Zürich CH-8057 Zürich, Switzerland

<sup>e</sup>Institute of Cell Biology, ETH Hoenggerberg, CH-8093 Zürich, Switzerland

The combination of Scanning Electron Microscopy (SEM) and Particle Induced X-ray Emission (PIXE) is a powerful method to study the bone-implant interface *in vivo*. These are complementary techniques allowing the avoidance of errors caused by artefacts in the analysis.

The objective of this study is the comparison of the behaviour of different types of screw implanted in the cortical bone of sheep for several months. The interest focussed on metallic trace element release and particle localisation [1][2]. The screws underwent five different surface treatments to improve their corrosion resistance and biocompatibility. The interface between the implant and the bone is observed with these two complementary techniques.

SEM advantages are a great range of magnification, depth of field of the image and high resolution near nm. Irradiation with a proton beam induces the emission of characteristic X-rays (PIXE) that identify and quantify the elements in the material from Na to U. PIXE advantages are a great sensitivity for trace element detection (near  $\mu\text{g/g}$ ), elemental mapping in 2D (PIXE) or 3D (RBS) and a large sampling depth. Maps provide chemical distribution of the elements in bone.

No particles of titanium are detected in the top surface with SEM whereas PIXE detected their presence. This indicates that the titanium particles are localised deeper in the bone and not on the surface, eliminating a possible pollution artefact. Elements coming from the alloys (Ti, V, Al...) have been detected and we have studied their *in vivo* behaviour. The bone around the alloy screws is characterised by trace elements (Zn, Sr, Fe...) and the major elements (Ca, P, K...). The Ti average concentration is similar for all samples except for 4, which is more polluted ( $\approx 200 \mu\text{g/g}$ ). Titanium grains are observed near the implant and their size can reach  $10 \mu\text{m}$ . Grains move towards the bone tissue. New bone is formed around the implant and it can reach several hundred  $\mu\text{m}$  thickness. A higher concentration of  $[\text{Zn}]/[\text{Ca}]$  is observed in this region. Zn is an essential element in this bone growth and new bone is less dense than old bone [3].

Great sensitivity, simultaneous multi-element analysis with micrometric and nanometric resolution make ion beam and electron beam analysis a powerful combination for biological and biomedical analysis.

### References:

[1] T. Hanawa. Mat. Science and Eng. 24 (2004) p745-752.

[2] Y. Okazaki et al. Biomaterials 26 (2005) p11-21.

[3] M. Yamaguchi. The journal of trace elements in experimental medicine. 11 (1998) p119-135.

Acknowledgements: This work is performed in the framework of the CTI project 5263.1HES and supported by DePuy ACE, Le Locle.

## High Resolution SEM imaging – Problems and Some Solutions

Iolo ap Gwynn

The University of Wales Bioimaging Laboratory, Institute of Biological Sciences, The University of Wales, Aberystwyth, Ceredigion, Wales, SY23 3DA

Obtaining optimal high resolution images from an SEM, especially with biological samples, depends not only on suitable specimen preparation but also on choosing the most appropriate set of microscope operating conditions for the specimen being studied and the information required. Assuming that good specimen preservation has been achieved, then a suitable coating must usually be applied. For high resolution secondary electron imaging, a combination of low accelerating voltage (1-3kV) and thin (circa 2-4nm) coating of Pt/Pd or Cr usually gives good results, especially when using a field emission SEM. However, under such conditions exposure of the specimen to the electron beam results in immediate deterioration of the image obtainable – with severe loss of resolution, due to contamination being resolved. For some work it is necessary to live with such limitations, and attempt to optimise the coating structure. Some of these problems can be avoided by reverting to backscattered electron imaging. Specimen preparation and coating in particular, needs to be done in a different way in order to optimise such imaging. Examples are shown of some of the advantages and disadvantages of the different approaches, especially when applied to the study of collagen in the extracellular matrix (Fig 1).

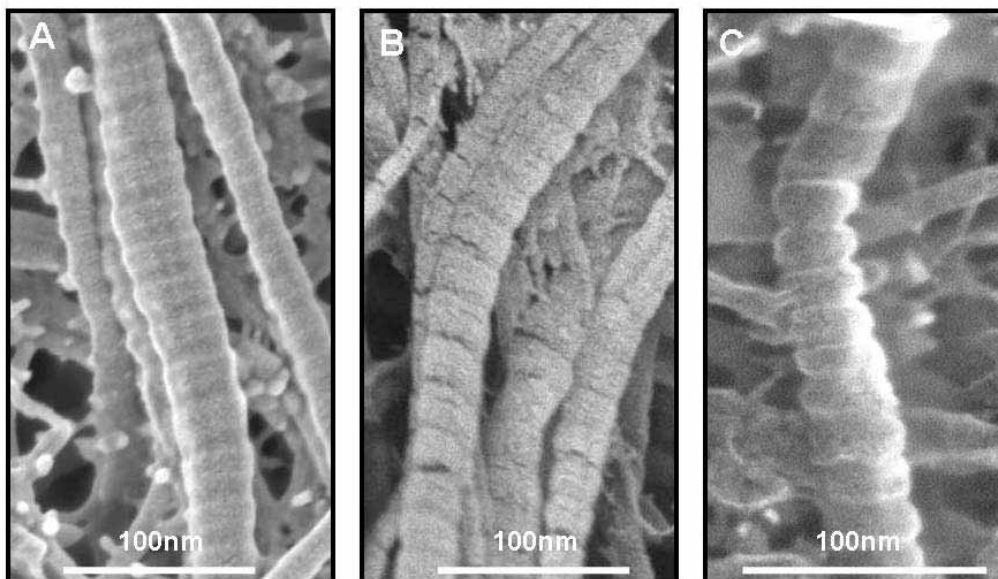


Fig. 1. Field emission SEM images of collagen from rabbit articular cartilage. A. Secondary electron image taken at 1kV accelerating voltage with 4nm Pt/Pd (4:1) coating. B. Backscattered electron image taken at 3kV accelerating voltage, utilising the Hitachi s-4700 ExB filter to eliminate secondary electrons. Specimen coated as for A. C. Backscattered electron image taken at 30kV, using an AuTrata YAG detector, after applying 60nm C to the already applied Pt/Pd coating, as used in A and B.

## Studying bacterial adhesion to biomaterials

L G Harris<sup>a</sup>, and R G Richards<sup>a</sup>

<sup>a</sup>AO Research Institute, AO Foundation, 7270 Davos Platz, Switzerland.

A common cause of implant associated infections is *Staphylococcus aureus* [1]. Several different techniques have been used to study the adhesion of *S. aureus* to biomaterials [2]. Non-contact profilometry, AFM and SEM can be used to characterise the biomaterial surface (Fig. 1).

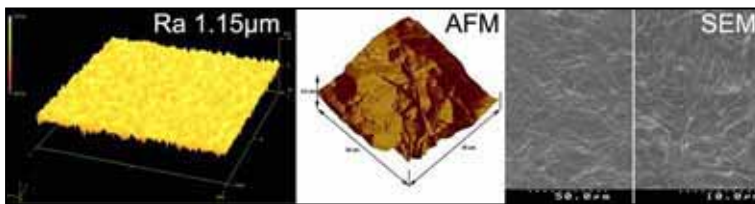


**Fig. 1. Examples of profilometry, AFM and SEM results.**

TEM has been used to visualise bacteria cell wall and contents (Fig. 2). However this technique requires a small specimen, and an implant cannot be used because of sectioning. Low-voltage SEM with SE and BSE detectors have been used to study the adhesion of *S. aureus* to the biomaterials [2]

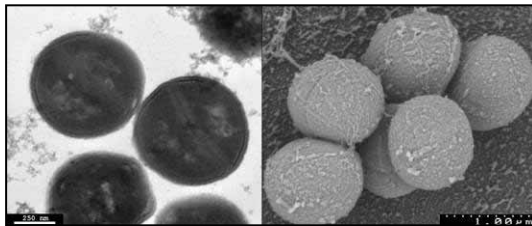
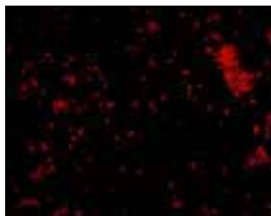


(Fig. 2). This method has disadvantages: 1) bacteria have to be fixed, so cannot distinguish between the live and dead; 2) difficult to quantify the adhesion; and 3) samples have to be dehydrated, which can damage the bacteria cell wall and polymer surfaces.

**Fig. 2. TEM and SEM images of *S. aureus*.**



To quantify the adhesion of bacteria to a surface, adherent live bacteria have been stained with a fluorescent stain, imaged with a fluorescent microscope (FM), and then quantified using an image analysis programme [2]. This method works well with metal surfaces (Fig. 2), however polymer surfaces tend to auto-fluoresce and the general resolution is low.

**Fig. 2. FM image of *S. aureus* adhering to a biomaterial surface**

An alternative to the above method is flow cytometry, which allows live and dead adherent bacteria to be quantified using fluorescent stains. The disadvantage of this technique is the fact that the bacteria have to be de-attached from the surface prior to quantification.

To conclude, a variety of methods can be used to study bacterial adhesion to a biomaterial. However they all have limiting factors, hence several of them have to be performed to fully evaluate if a surface inhibits or encourages bacterial adhesion. The main disadvantage of all these techniques is time resolution.

### References:

[1] Barth E, Myrvik QM, Wagner W, Gristina AG. *Biomaterials* 1989; 10:325-328.

[2] Harris LG, Tosatti S, Wieland M, Textor M, Richards RG. *Biomaterials* 2004; 25:4135-4148.

Acknowledgment: Thanks to Osian Meredith for profilometry and AFM images.

## Detection of silver sulphide deposits in the skin of patients with argyria after long term use of silver containing drugs

Ludwig Jonas, Catrin Bloch, Regina Zimmermann

Electron Microscopic Centre in the Department of Pathology, Department of Dermatology and Venerology, Medical Faculty, University of Rostock, D-18055 Rostock, Germany

Argyria is a rare illness of humans, resulting by long-term use of silver containing drugs with accumulation of silver in the skin and other tissues. The skin of sun exposed areas as face, neck and hands has a slate-grey discolouration because of silver sulphide deposits in the skin. In the last 20 years, there were fourteen patients with the typical symptoms of argyria. In the paraffin sections there were visible brown to black pigmentations in histiocytes, fibroblasts and multinucleated giant cells inside subcutis and corion. The pigments were concentrated around sweat glands, hair follicles, and blood vessels, which showed a slight vasculitis. In transmission electron microscope (TEM) we observed electron dense deposits inside lysosomes and residual bodies of phagocytes (Fig.1) as well as outside the cells in the connective matrix. These deposits were identified by elemental analysis in TEM and electron energy loss spectroscopy (EELS) or scanning electron microscopy (SEM) and energy dispersive x-ray microanalysis (EDX), containing silver and sulphur. Therefore, they seem to consist of silver sulphide. The pathogenesis of argyria is assumed as following [1]: uptake of silver ions from the gut, transport of stable  $\text{Ag}^+(\text{I})$  complexes into the skin, binding of silver to the amino acid cystein, accumulation of  $\text{Ag}^+$  cystein complexes at connective matrix proteins, photolytic destruction of cystein by uv radiation, precipitation of silver ions by nascent  $\text{SH}^-$  ions and forming of  $\text{Ag}_2\text{S}$ . The list of silver containing drugs [2] such as Targophagin® pills was strongly reduced in the past. Argyria is a harmless discoloration. Nevertheless, there were attempts to treat this cosmetic negative illness by chelators, but they were without success.

1. V. Stadie and W.C. Marsch; Die Argyrose - eine heute fast vergessene Dyschromie. JDDG 2004,2: 119 - 122.
2. D. Voigt; Akt. Dermatol. 1985; 11: 2 - 8.

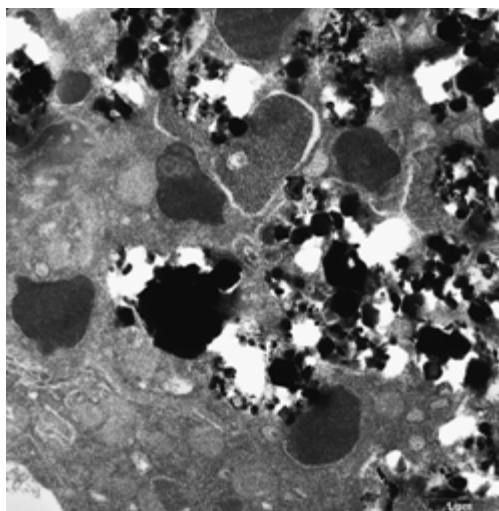


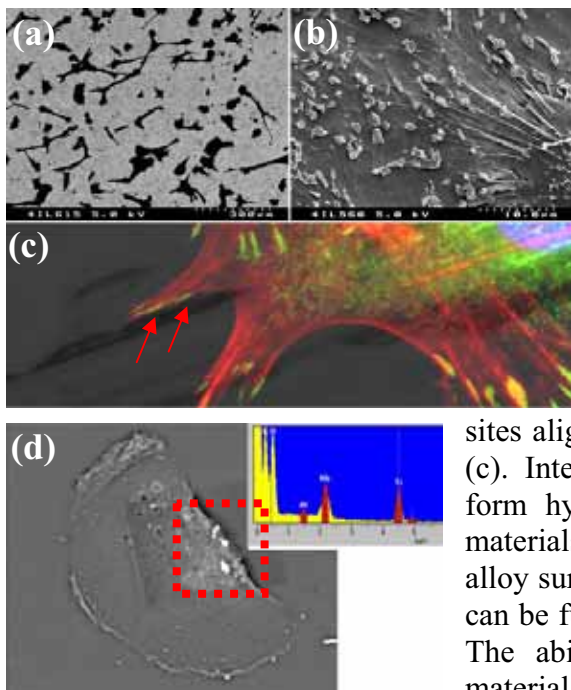
Fig.1: Argyria; electron dense deposits inside a phagocyte of the subcutis.

## Utilisation of microscopy techniques to investigate cell-biomaterial interactions

D O Meredith<sup>a</sup>, and R G Richards<sup>a</sup>

<sup>a</sup>AO Research Institute, AO Foundation, 7270 Davos Platz, Switzerland.

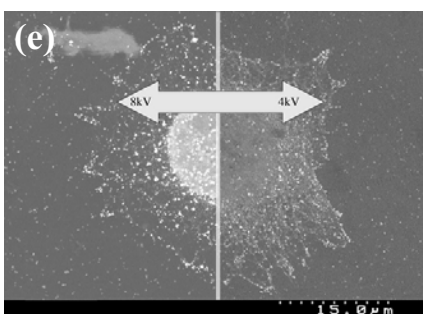
Biomaterial research benefits greatly from visual representation of both the material and biological interaction towards it. However, the opaque and robust properties of metals limit the use of light microscopy to reflected and fluorescence modes, and higher resolution microscopy to SEM.



A combination of SEM and Fluorescence Microscopy (FM) proves useful in illustrating differences in cell behaviour on metals. The versatility of SEM modes can differentiate organic and inorganic material (a) while magnification flexibility can visually demonstrate cell numbers (low mag) to cell morphology and surface feature interaction (b) (high mag). Multiple labelling possibilities for FM can simultaneously demonstrate the interaction of numerous intracellular components relative to the surface; for example fluorescently labelled adhesion

sites aligning to metal surface detail captured by reflected light (c). Interpretation of these images provides multiple cues to form hypothesis and follow-up investigations related to the materials and topography. For example, cells on the titanium alloy surfaces observed to endocytose particles from the surface can be further investigated using SEM in BSE and X-ray mode. The ability of BSE to differentiate organic and inorganic material identified ingested metal particles in cells removed

from the surface. X-ray microanalysis confirmed the particles originated from the surface (d) [1].



SEM's versatility is also an essential factor in designing investigative experiments, for instance biomaterial adhesion variations due to the cell cycle. We have designed a double label of cell adhesion and cell phase identification that can be resolved using different beam accelerating voltages (e) [2].

These examples demonstrate the versatility of FM and SEM microscopy methods for both observational and investigative purposes on opaque substrates, and illustrate that a combination

of different methods and instrument modes can synergistically enhance the information gained in biomaterials investigation.

[1] Meredith, D.O., Eschbach, L., Riehle, M.O., Curtis A.S.G., Richards, R.G. J Bio Mat Res. A. (in press) 2005. [2] Meredith, D.O., Owen G.Rh., ap Gwynn, I., Richards, R.G., Exp Cell Res. 293(1), pp. 58-67, 2004

## Additional hydration methods for observation of wet samples in ESEM.

V.Neděla, R.Autrata,

Electron Optics, Institute of Scientific Instruments ASCR, 61264 Brno, Czech Republic

Environmental scanning electron microscope (ESEM) enables observation of non-conductive and water containing samples free of charging artefacts. Higher pressure of the water vapour creates optimum condition for the detection of SE by the gaseous secondary electron detector (GSED) and ensures hydration of the water containing samples.

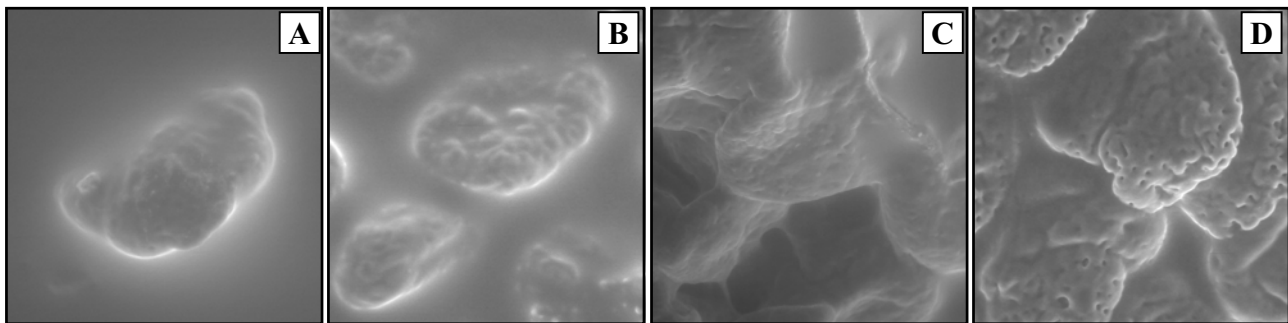


**Fig 1.:** Sample of small intestine, GSED,  $P = 900\text{Pa}$ ,  $T = 5^\circ\text{C}$  after 25min in ESEM,  $F.\text{View}=50\mu\text{m}$   
a) embedded into a cooled agar plate; b) placed on a cooled agar plate; c) placed on a cooled holder with water vapour blowing up to specimen surface; d) placed on a cooled specimen holder.

Some methods that enable to create and to retain high relative humidity in the specimen chamber, e.g. hydration system [1], cooled specimen holder (peltier stage), blowing water vapour by a capillary up to specimen [2], utilize of agar [3,4], were published. However, problems with imaging of biomedical samples in „wet mode“, connected with contrast effects, resolution, magnification etc. have not been removed fully. The most serious difficulty remains in initialization of the pumping process and the initial irrigation process, during which the wetness is insufficient and the sample begins to dry. To prevent the influence of the dehydration within the initial pumping process, utilization of agar as the mean for additional hydration is advantageous. What is important, the sample must be embedded into agar, that it is surrounded with agar from all sides (excluding the position of beam impact). The specimen of small intestine could be observed without dehydration up to 25min (Fig.1a). If the sample is only put on the agar plate, slight changes of surface structure, caused by dehydration, can be observed (Fig.1b). For comparison, the result of the method with water vapour blowing up to sample surface is shown (Fig.1c). Hydration conditions with the flooding of water vapour into the sample chamber have been preserved in all additional methods. Fig.1d shows surface changes of the same sample if no additional methods have been used.

### References:

- [1] Cameron R.E., Donald A.M., *Journal of microscopy*, vol.173 (1994) 227-237.
- [2] Lange L.A., Sujata K., Jennings H.M., *Ultramicroscopy*, vol.37 (1991) 234-238
- [3] Sanger P., Ritter M., Hohenberg H., *Microscopy and Microanalysis*, vol.9 (2003) 494-495.
- [4] Neděla V., Autrata R.: *Fine mechanics and optics* vol.4 (2004) 112-114.
- [5] This work was supported by Grant Agency of the Czech Republic, grant No. 102/05/0886.

## Cell biological processes in articular chondrocyte-grafts – An *in vivo* study of a clinically applied tissue engineering method for cartilage defect treatment.

Nürnberg S.<sup>a</sup>, Resinger C.<sup>a</sup>, Schnettler R.<sup>b</sup>, Meyer C.<sup>b</sup>, Wilke I.<sup>c</sup>, Barnewitz D.<sup>c</sup>, Klepal W.<sup>d</sup>, Vécsei V.<sup>a</sup>, and Marlovits S.<sup>a</sup>

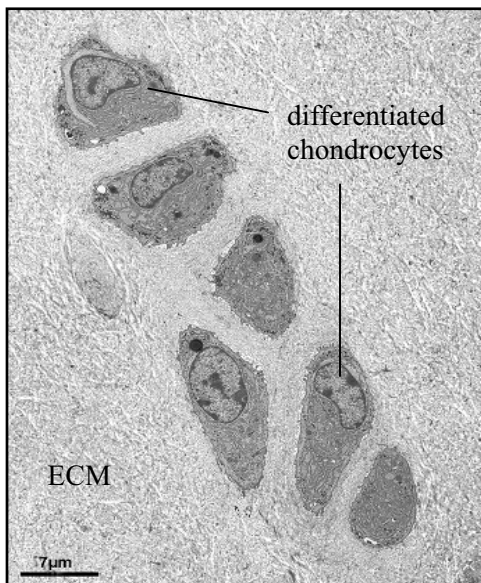
<sup>a</sup>Medical University of Vienna, Department of Traumatology, 1090 Vienna, Austria

<sup>b</sup>University of Giessen, Clinic and Polyclinic for Traumatology, 35385 Giessen, Germany

<sup>c</sup>Research Centre for Medical Technics and Biotechnology, 99947 Bad Langensalza, Germany

<sup>d</sup>University of Vienna, Cell Imaging and Ultrastructure Research, 1090 Vienna, Austria

Hyaline cartilage is necessary for diarthrotic joint movement. If traumatized it fails to regenerate and poses clinical problems resulting from the limited regeneration potential of articular cartilage. Tissue engineering by matrix associated chondrocyte transplantation (MACT) is a new option in articular cartilage defect treatment. It deals with the insertion of chondrocytes into the defect in a carrier-associated form. The present study was performed to examine *in vivo* development of the implanted cell-carrier constructs in an appropriate horse animal model. Samples were investigated by light- and electron microscopy.



Twelve weeks after transplantation the grafts are well integrated into the defect. Differentiated as well as fibrous tissue has been established. Chondrocytes in fibrous regions form intense contact to the collagen fibers. In differentiating transplant areas the newly synthesized collagen fibers are oriented perpendicular to the joint surface as in native cartilage. In transitional regions of dedifferentiated to differentiated tissue the progression of regeneration becomes evident. Cells round up, extend microvilli and accumulate intermediate filaments, glycogen and lipid droplets (see figure). Degeneration processes accompany tissue transformation: Necrosis as well as active cell death lead to local areas of cell decay. Neighboring chondrocytes cleared up the cell debris. Degrading scaffold fibers become integrated into the newly synthesized extracellular matrix (ECM).

This study demonstrates the differentiation process of chondrocytes *in vivo*. Since the initially developing cell-matrix construct does not entirely fulfill the final demands of a differentiated tissue, reorganization processes are going on. The appearance of passive and active forms of cell death suggests that different mechanisms participate in the tissue modification process. It becomes evident that chondrocytes are able to phagocytose cell debris and to perform distinct orientation of the collagen fibrils in the extracellular space. Good adhesion of the transplant is mediated by a tendon-like mechanism in the fibrous regions.

This study was supported by the EU (FA 735 A 01 04) and the Lorenz-Boehler-Society (10/04).

## Double knock-out Mice lacking Laminin $\alpha 4$ and Type XV Collagen show Abnormal Basement Membranes in Sciatic Nerves

Karolina Rasi<sup>1</sup>, Raija Sormunen<sup>2</sup>, Merja Niemelä<sup>1</sup>, Raija Soininen<sup>2</sup> and Taina Pihlajaniemi<sup>1</sup>

<sup>1</sup>Collagen Research Unit, Biocenter Oulu and Dept. Medical Biochemistry and Molecular Biology, University of Oulu, FI 90220 Oulu, Finland

<sup>2</sup>Biocenter of Oulu, University of Oulu, FI 90220 Oulu, Finland

**Introduction:** Type XV collagen is localized in basement membrane (BM)/stromal interface of many tissues, especially capillaries and skeletal muscle cells but also in Schwann cell BMs. Laminins, heterotrimeric glycoproteins composed of  $\alpha$ ,  $\beta$  and  $\gamma$  chains are essential components of BMs. The laminin  $\alpha 4$  chain is expressed in the same tissues as type XV collagen. Double knock-out mice lacking both type XV collagen and laminin  $\alpha 4$  were generated by breeding *Lama4*<sup>-/-</sup> and *Coll15a1*<sup>-/-</sup> mice. In this study, sciatic nerves of these mice were analysed.

**Methods:** Sciatic nerves of transgenic mice and wild type littermates were compared using histological, immunohistochemical, conventional transmission electron microscopical (TEM) and high pressure freezing and freeze-substitution methods.

**Results and discussion:** Lack of the laminin  $\alpha 4$  chain alone and together with collagen XV results in delayed and abnormal myelination of peripheral nerves. Bundles of naked (unsegregated to nonmyelinated) axons were found in adult *Lama4*<sup>-/-</sup> mice, the defects being more severe in double knock-out mice. *Coll15a1*<sup>-/-</sup> mice showed polyaxonal myelination. Both *Lama4*<sup>-/-</sup> and double knock-out mice showed dispersed and multilayered BMs around Schwann cells while BMs in *Coll15a1*<sup>-/-</sup> mice appeared similar to wild type.

Our results show that lack of both laminin  $\alpha 4$  and type XV collagen leads to structural changes in basement membranes affecting axonal myelination of peripheral nerves.

## Improving Imaging of Biomaterials and interfaces with FESEM

R G Richards

AO Research Institute, AO Foundation, 7270 Davos Platz, Switzerland.

Optimal imaging of biomaterials and interfaces with an SEM, requires full use of the range of the accelerating voltages and detectors available (1-7). The accelerating voltages are determined while imaging the specimen and cannot be assumed that one voltage optimal for one specimen can be applied for all. BSE imaging of biomaterials normally provides an image of high atomic number material that is located on or within the sample. Beam energies of 10kV and above can cause radiation damage to specimens. For imaging surface detail, the application of lower voltages with less beam penetration and spread is required (1-7). Low voltage BSE imaging allows specimens that normally charge, locally affecting SE detection, to be imaged without such distortions. As the interaction volume decreases, the SE signal becomes more sensitive to surface layers of hydrocarbon contamination produced during interaction of the primary beam with the specimen. BSE, being higher energy than SE, are affected to a much lesser extent by this. However, for obtainment of maximum information from a specimen, the use of a range accelerating voltages is advocated.

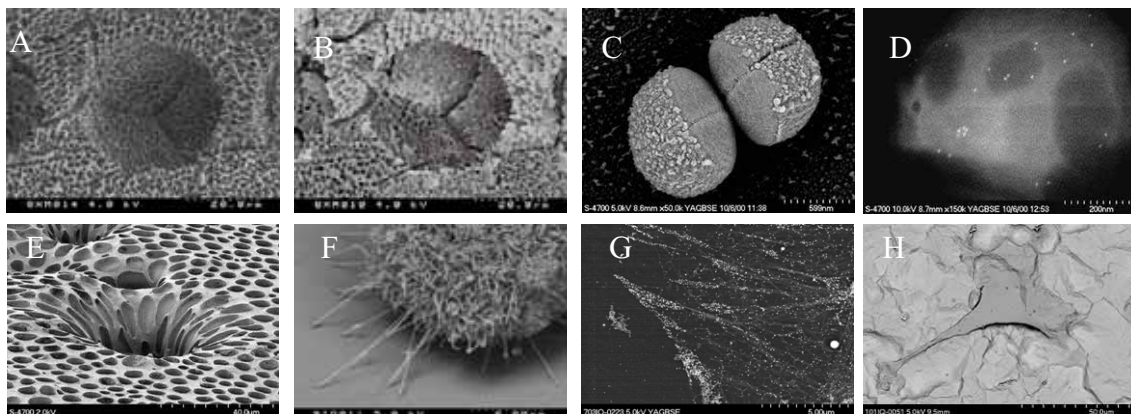


Figure 1: a) Structured and etched titanium surface observed with low voltage SE and b) BSE imaging; c) *Staphylococcus aureus* bacteria, (BSE), d) 5 nm immunogoldlabelled adhesins on the *S.aureus* surface (BSE); e) Biodegradable porous membrane, (BSE); f) Cultured fibroblast displaying intact filopodia attaching to plastic surface, indicating good sample fixation (BSE); g) immunogold labelled (vinculin) and gold enhanced cell adhesion site (BSE); h) Osteoblast growing on an anodised titanium surface (BSE).

**References:** 1Richards RG, ap Gwynn I (1995) *J Microsc* 177:43-52; 2 Richards RG, Owen GRh, ap Gwynn I (1999) *Scanning Microsc*.13 (1), 55-60. 3Richards RG, Wieland M, Textor M (2000) *J.Microsc*.199 (2) 115-123. 4Richards RG, Stiffanic M, Owen GR, Riehle M, Ap Gwynn I, Curtis AS (2001) *Cell Biol Int* 25:1237-49 5 Owen GRh, Meredith DO, ap Gwynn I, Richards RG (2001) *Cell Biology International*. 25 (12) 1251-1259. 6 Owen GRh, Meredith DO, ap Gwynn I, Richards RG. (2002) *J.Microsc*. 207 (1) 27-36. 7 Baxter L, Frauchiger V, Textor M, ap Gwynn I, Richards RG (2002) *Eur Cell Mater* (4) 1-17.

**Acknowledgments:** Thanks to current and past members of Interface Biology group, AO Research Institute for use of their samples to image.

# SEM-Analysis of diamond-bonded burs after grinding of dental enamel and ceramics

Fredy Schmidli<sup>a</sup>, Marc Jakubzik<sup>b</sup>, Carlo P. Marinello<sup>a</sup>, Heinz Lüthy<sup>a</sup>

<sup>a</sup>Dental School, University of Basel, Hebelstrasse 3, CH-4056 Basel

<sup>b</sup>Gebr. Brasseler GmbH & Co. KG, Topenhager Weg 25, D-32657 Lemgo

## Introduction

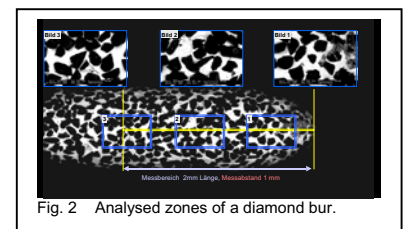
Abrasive instruments like diamond-bonded burs (Fig. 1) have different grinding effects depending on the properties of the materials which are being worked on (wear, surface roughness, removal of surface material, contamination, etc.). In dentistry diamond-bonded burs are mainly used for grinding tooth structures. The fabrication of synthetic human dental enamel being not possible, the long-term aim of this study was to look for a ceramic, similar in its characteristics to enamel, in order to examine the grinding effect on it. In the following SEM-study, however, first results are presented concerning the superficial contamination of the burs after material grinding.



## Materials and methods

Human dental enamel as well as 2 commercialized ceramics, a glass ceramic (Macor, Corning Glass) and a feldspathic ceramic (Mark II, Vita Zahnfabrik) were grinded with diamond-bonded burs (D 107, Gebr. Brasseler) on an especially designed test set-up (adjustable grinding speed, pressure on the material, water cooling rate, contact angle of the bur). The surfaces of the used burs were examined in ESEM Philips 30 in BSE-mode at different magnifications (100, 200 and 500x) on 3 specific zones, on 2 sides (Fig. 2).

The measuring of the contamination on the burs by the removal of the material after grinding was performed using a computerized image analysis equipment (Leica QWin) on a surface of 0.08mm<sup>2</sup> per zone.

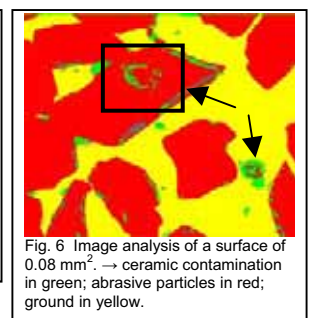
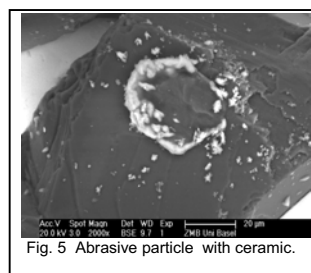
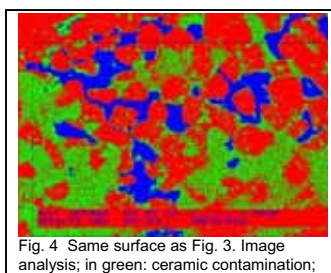
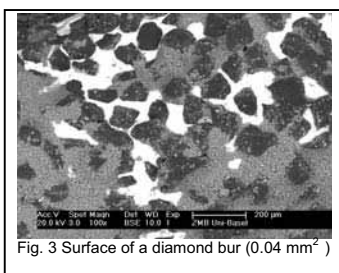


## Results and discussion

The results showed that the contamination with enamel was 5 to 8% of the total analysed surface, with the glass ceramic 43% and with the feldspathic ceramic 3 to 10%. Examples of ceramic contamination are shown in Fig. 3 and 4 on a surface of 0.4 mm<sup>2</sup>, in Fig. 5 on a abrasive particle and in Fig. 6 on a surface of 0.08 mm<sup>2</sup>. The measuring accuracy has to still be verified. Nevertheless, one can proceed in using this technique for measuring material contamination on diamond-bonded burs after grinding.

## Conclusion

In the course of this study, it was shown that the used glass ceramic had very similar characteristics to natural dental enamel regarding the diamond-bonded bur contamination.



## Mineralisation of Gelatine: Model System for Enamel

Paul Simon<sup>a</sup>, Petr Formanek<sup>b</sup>, Caren Göbel<sup>a</sup>, Harald Tlatlik<sup>a</sup>, Jana Buder<sup>a</sup>, and Rüdiger Kniep<sup>a</sup>

<sup>a</sup>Max-Planck-Institut für Chemische Physik fester Stoffe, 01187 Dresden, Germany

<sup>b</sup>Triebenberg Laboratory, Institute of Structure Physics, Dresden University, 01062 Dresden,

By means of the model system apatite-gelatin we aimed to find out the basic principles of self-organisation and pattern formation in the course of the morphogenesis of a biologically and medically relevant nano-composition *in vitro* at *in vivo* conditions without participation of living cells. The selection of this system proved to be exceedingly lucky since the combination apatite gelatine was optimised by evolution with respect to its remarkable coaction on the nanometer and sub-nanometer scale [1]. The organic part (~ 2.3 wt-%) is important for the morphogenesis of the biomimetic composite, which resembles strikingly the *in-vivo* formation of tooth or bone. The focus of the present work will be the inner architecture and real structure of the central hexagonal prismatic composite seeds which hold the potential for subsequent fractal morphogenesis [2]. We report here not only on structures in sections perpendicular to the hexagonal axis of the seeds but also account for the third dimension of these particles.

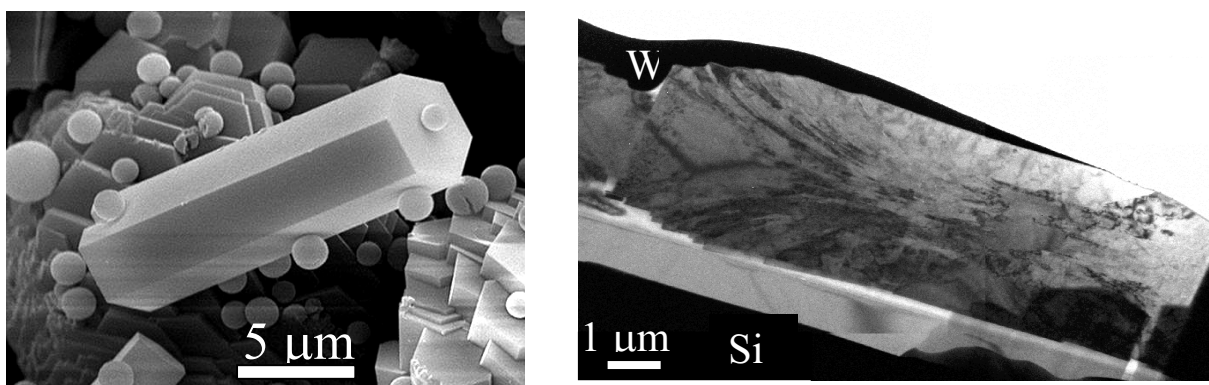


**Fig. 1:** (a, left) SEM image of hexagonal prismatic seed and (b, right) TEM micrograph of longside focussed ion beam cut.

The elongated hexagonal prismatic seeds of apatite-gelatin-composites with an aspect ratio of about 4:1 consist of rod shaped subunit along [001] (Fig. 1a, left). By high-resolution microscopy on cross sectional focussed ion beam prepared samples we identified calcified triple helices acting as nucleation cores and thus to be responsible for the observed nano-scaled pattern of the composite seed.

### References:

[1] S. Busch, H. Dolhaine, A. Du Chesne, S. Heinz, O. Hochrein, F. Lacri, O. Podebrad, U. Vietze, T. Weiland, R. Kniep, *Eur. J. Inorg. Chem.*, 10 (1999) 1643-1653.

[2] P. Simon, W. Carrillo-Cabrera, P. Formanek, C. Göbel, D. Geiger, R. Ramlau, H. Tlatlik, J. Buder, R. Kniep, *J. Mater. Chem.* 14, (2004) 2218-2224.

## The *Porcellio scaber* Model for Biomineralisation: Structure, Assembly and Function of the Organic Matrix in Amorphous CaCO<sub>3</sub> Deposits.

Andreas Ziegler and Helge Fabritius

Central Facility for Electron Microscopy, University of Ulm, Albert Einstein Allee 11, 89069 Ulm, Germany. [andreas.ziegler@medizin.uni-ulm.de](mailto:andreas.ziegler@medizin.uni-ulm.de)

Amorphous calcium carbonate (ACC) is thought to act as a precursor for the formation of crystalline CaCO<sub>3</sub> modifications. The terrestrial isopod *Porcellio scaber* forms large three-layered CaCO<sub>3</sub> deposits consisting of spherules and a glassy homogeneous layer. Electron diffraction and synchrotron high-resolution X-ray diffraction has shown that the deposits are fully amorphous. The deposits serve as transitory reservoirs to store and recycle cuticular CaCO<sub>3</sub> during molting of the mineralised cuticle of the animal. Since ACC is unstable in vitro biogenic ACC is stabilized by organic components. We used low voltage FEREM to analyse the architecture of the organic matrix at the nano-scale (Figure 1A). Sagittal surfaces of the specimens were knife polished in an Ultramicrotome using a diamond knife to obtain flat smooth faces. To minimise artefacts due to EDTA treatment this face was decalcified for 5 minutes in a medium containing 0.1 mol L<sup>-1</sup> EDTA and 2.5% glutaraldehyde [1]. The stabilisation of ACC within the spherules is not homogeneous leading

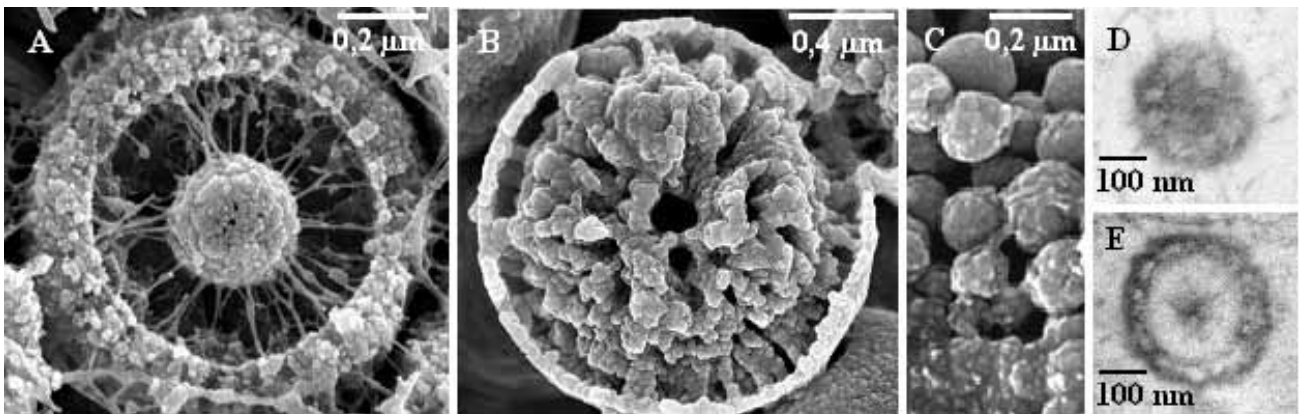


Figure 1. Structure of the organic matrix (A) and naturally degrading spherule (B) of an ACC deposit (2 nm platinum, rotary shadowed 1,5 KV). (C) growing spherule. (D, E) matrix assembly.

to a high inner surface in naturally degrading specimens (Figure 1B) facilitating the quick mobilization of calcium and carbonate ions for the mineralisation of the new cuticle [2]. Spherules form by agglomeration of 10-30 nm large ACC particles (Figure 1c). TEM analysis of high-pressure frozen and freeze substituted samples indicate that the assembly of the matrix occurs concomitant to spherule growth (Figures 1 D, E). We conclude that components of the organic matrix occur already in the initial particles to stabilize ACC and that the assembly of the organic matrix occurs by rearrangement of matrix elements within the growing spherules.

### References:

- [1] Fabritius H, Walther P, Ziegler A, Journal of Structural Biology (2005) 150:190-199.
- [2] Fabritius H and Ziegler A, Journal of Structural Biology A (2003) 142:281-291.
- [3] Supported by the DFG (Zi 368/4-2) within “Principles of Biomineralisation” (SPP 1117).

# Trace Element Analysis in Presolar Stardust Grains via Spectroscopic XANES-PEEM and Full-Field XPS-Imaging (nanoESCA)

P. Bernhard, J. Maul, H. J. Elmers, G. Schönhense, S. Merchel<sup>#</sup>, Ch. Sudek\*, U. Ott\*

Institut für Physik, Johannes Gutenberg-Universität, D-55128 Mainz, Germany

<sup>#</sup> Bundesanstalt für Materialforschung, D-12489 Berlin, Germany

\* Max-Planck-Institut für Chemie, D-55128 Mainz, Germany

Small grains of presolar origin have been found embedded in primitive meteorites [1]. They carry important information on the nucleosynthetic processes in stars and on the formation and incorporation of minor and trace elements in the grains. Isotope abundances can vary dramatically from the solar abundances, in some cases by orders of magnitude as measured by mass spectrometry [1-3]. The present work aims at non-destructive fast screening as basis of a subsequent (destructive) mass spectrometric study. We looked at a fraction from the Murchison meteorite that consists essentially of  $\mu\text{m}$ -sized SiC grains originating from red giant stars on the asymptotic branch (AGB stars). Trace elements located in certain grains have been detected via local XPS spectra using the full-field imaging “nano-ESCA” instrument [4]. Its key feature is the correction of the analyser’s spherical aberration ( $\alpha^2$ -term) yielding ultimate chemical sensitivity and high transmission up to 1.6 keV start energy. Small area spectra as well as energy filtered images in the binding-energy range 0-750 eV were taken for samples of SiC grains. Our energy resolution of 110 meV along with a spatial resolution in the 100 nm range allowed a detailed analysis of 3d and 4d lines of various transition metals and several rare earth elements besides the Si and C lines [5]. In a second experimental run, we measured the X-ray absorption near edge structure (XANES) of several K and L edges in a photoemission electron microscope (PEEM). Analogous to ELNES, XANES yields information on the chemical surroundings of the respective elements; an example is given in Fig. 1. The fingerprint-like XANES features measured on certain grains, allow a “spectral unmixing” of the image stacks yielding the lateral distribution of the detected elements, here Al (b) and O (c). Besides corundum (e.g. grain 1) we observe different Al species (3) as well as different oxygen-rich grains (2). Owing to the lower background in XPS, the sensitivity is higher for nanoESCA. Significant core level shifts give access to the chemical state of the trace elements.

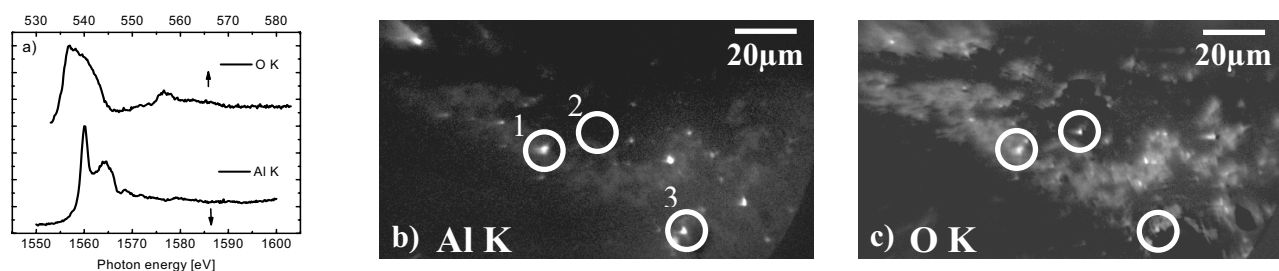


**Fig. 1:** XANES features (a) of selected microareas as denoted in the Al (b) and O image (c).

We thank M. Escher, N. Weber, M. Merkel (FOCUS GmbH), B. Krömker, D. Funnemann (OMICRON GmbH) for their help with the nanoESCA and the BESSY staff for good cooperation.

[1] U. Ott, *Nature* **364** (1993) 25-33,

[2] E. Zinner, *Annu. Rev. Earth Planet. Sci.* **26** (1998) 147-188

[3] S. Amari et al., *Meteoritics* **30** (1995) 679-693, [4] M. Escher et al., *J. Phys.: Cond. Matt.* **17** (2005) S 1329-1338

[5] U. Ott et al., *Lunar and Planetary Science* **36** (2005) 1294

## **HfO<sub>2</sub> high k gate oxides by VEELS and HREM band gap, dielectric constant, chemistry and structure.**

M. Cheynet<sup>1</sup>, S. Pokrant<sup>2</sup>, F., Tichelaar<sup>3</sup>, J.L. Rouvière<sup>4</sup>

<sup>1</sup> LTPCM, UMR-CNRS 5614, ass. INPG UJF-BP75 38402 St. Martin d'Hères, France

<sup>2</sup> Philips Semiconductors, 860 rue Jean Monnet, 38926 Crolles, France

<sup>3</sup> National Center for HREM, Rotterdamseweg 137, 2628 AL Delft, Nederland

<sup>4</sup> SP2M-DRFMC Avenue des Martyrs 38000 Grenoble France

With the downscaling of the next generations of MOSFET, SiO<sub>2</sub> gate thickness will become too small to prevent leakage current resulting to tunnel effects. Among high k oxides, the IV-B metal oxides and particularly the hafnium dioxide (HfO<sub>2</sub>) exhibit the most attractive properties to replace SiO<sub>2</sub>: good compatibility with polysilicon, high dielectric constant ( $k \geq 22$ ) and relatively wide band gap ( $E_g > 5.7$  eV). Although high k gate oxide layers are thick (3-5 nm) in comparison to conventional gate oxides (below 2 nm), their properties are badly described by bulk parameters and can be far from that expected ones, because the interfaces contribution becomes non-negligible and because chemical and structural modifications can occur across the film. Thus, to progress in the process and optimize the devices, chemical and structural properties of gate oxides have to be monitored in parallel to physical properties at the same scale.

In this work, we performed Valence Electron Energy-Loss Spectroscopy (VEELS) and High Resolution Electron Microscopy (HREM) in STEM and TEM mode respectively, to investigate HfO<sub>2</sub> thin films deposited on Si/SiO<sub>2</sub> substrate by either Chemical Vapour Deposition (CVD) or Atomic Layer Deposition (ALD) and covered with poly-Si, poly-Ge or poly-Al<sub>2</sub>O<sub>3</sub> sub-layer. For each HfO<sub>2</sub> film, band gap energy ( $E_g$ ) and dielectric constant ( $k$ ) are deduced from low-loss spectra. The variations observed are interpreted on the basis of the chemical profiles established from VEELS line-scans and of the structural properties determined from HREM imaging.

## **Probing Electron States at Surfaces, Interfaces and Nanostructures with Spatially-Resolved EELS**

Christian Colliex, Mathieu Kociak, Jaysen Nelayah, Odile Stéphan and Dario Taverna

Laboratoire de Physique des Solides (CNRS UMR 8502), Bldg. 510, Université Paris Sud, 91405 Orsay (France)

The coupling of a narrow probe of high-energy electrons (100 keV) in a STEM (Scanning Transmission Electron Microscope) instrument with an efficient PEELS (Parallel Electron Energy Loss Spectroscopy) system is quite well suited to the exploration of the structural, chemical and electronic properties of individual nanostructures and interfaces. Major technical improvements have opened the field of spectrum-imaging and chrono-spectroscopy. As a consequence, spatially resolved analysis at the subnanometer level has become currently accessible. Furthermore the high rate of EELS spectrum acquisition (up to 100 Hz) is a prerequisite for performing dynamic studies.

These possibilities have been used for mapping the composition of nano-objects, to the limit of single-atom identification. Furthermore, the detailed study of the EELS fine structures enables the investigation of the unoccupied electron density of states, and therefore of the local environment and bonding properties at specific atomic sites. The collective behavior of the electron gas is also modified by the presence of surfaces. The interaction of the incident electron beam with the involved bulk and surface plasmon modes can be monitored in a typical near-field approach, providing direct access to the local electronic properties of a nano-object.

These possibilities have been used for addressing many situations encountered in model nano-objects of simple geometries (nanotubes, nanowires, nanobubbles, nanoparticles, quantum dots...) and in interfaces, multilayers, ultra-thin foils and tunnel junctions. A couple of typical situations will be described, emphasizing the need of theoretical refinements for optimizing the extraction of useful information out of the large data-sets provided by the spectrum-imaging technique : influence of the metallic surface and of associated “Begrenzung“ effects for determining the pressure within embedded Helium bubbles, measurement of the optical band gap in individual BN nanotubes...

These examples demonstrate how far the field of application of spatially-resolved EELS nowadays covers many types of sub-nm physical parameters measurements, far beyond its widely accepted use as an elemental mapping tool.

# Electron Energy Loss Spectroscopy of Rare Earth-Transition Metal Compounds and Their Hydrides $\text{ReMn}_2(\text{H}_2)$ (Re=Gd,Er) Aided With *Ab Initio* Calculations Using WIEN2k

T. Galek<sup>1,2</sup>, C. Hébert<sup>1</sup>, D. Eyidi<sup>1</sup>, P. Schattschneider<sup>1</sup> and H. Figiel<sup>2</sup>

<sup>1</sup>Inst. für Festkörperphysik, TU Wien, Wiedner Hauptstrasse 8-10, A-1040 Wien, Austria.

<sup>2</sup>Fac. of Physics and Applied Computer Science, AGH University of Science and Technology, Al.Mickiewicza 30, PL-30059 Cracow, Poland

Electron Energy-Loss Spectroscopy (EELS) in a Transmission Electron Microscope EELS is a versatile tool for the study of solids and is under constant development. Especially EELS in the low-loss region up to 50 eV is under a scope nowadays. EELS in the low-loss region gives informations about the electronic structure of valence states of atoms and molecules in solids, a property responsible for chemical bonding, phase transitions, as well as optical, electrical and magnetic properties of materials.

The rare earth-transition metal compounds easily absorb hydrogen, which is causing many changes in their physical properties, in particularly structural and magnetic ones. Hydrogen introduced into the bulk influences the electronic structure of the material. The  $\text{ErMn}_2$  and  $\text{GdMn}_2$  and their hydrides are interesting for basic and applied research. The bulk material of  $\text{ReMn}_2\text{H}_x$  (Re=Gd,Er) can absorb up to  $X=4.3$  hydrogen per formula unit [1,2].

The WIEN2k program makes use of Density Functional Theory and the family of (Linearized) Augmented Plane Wave (L)APW methods to calculate the electronic structure and a variety of other properties, useful for the study of solid materials [3]. The LAPW method is one of the most accurate methods nowadays and it is used worldwide with many successes on its account.

Specimens were prepared from series of powders of pure  $\text{GdMn}_2$ ,  $\text{ErMn}_2$  and hydrogenated  $\text{GdMn}_2\text{H}_2$ ,  $\text{ErMn}_2\text{H}_2$  compounds. Powders were embedded in epoxy resin and cut with an ultramicrotome. Despite the brittleness of the material a number of sufficiently thin cuts of grains with an average thickness of about 100 nm were obtained. A series of Low Energy-Loss (LEL) spectra up to 50 eV were acquired. Differences in pure and hydrogenated samples were found. The main peak of the LEL spectrum is shifted, for hydrogenated specimens it is about 2 eV higher for both compounds. The interpretation of this effect and other features in the LEL spectrum in investigated materials is aided by *ab initio* calculations using the WIEN2k code. We found that the number of free electrons per volume unit increased for hydrogenated samples as it was expected.

## References:

- [1] J. Żukrowski et al. J. of Magnetism and Magnetic Materials 238 (2002) 129-139
- [2] H. Figiel et al. J. of Alloys and Compounds 368 (2004) 260-268
- [3] K. Schwarz, P. Blaha Computational Materials Science 28 (2003) 259-273
- [4] Support from the European Commission (Contr. Nbr. ENK5-CT-2001-00543) is acknowledged

## Fingerprinting Mineral Phases by EFTEM

U. Golla-Schindler<sup>1</sup>, R. Hinrichs<sup>2</sup>, and A. Putnis<sup>1</sup>

<sup>1</sup> Institut für Mineralogie, University of Muenster, Germany

<sup>2</sup> Instituto de Geociências, Universidade Federal do Rio Grande do Sul, Porto Alegre, Brazil

Energy filtered TEM offers opens the possibility of new applications in the field of Mineralogy. One excellent technique to determine the oxidation states of different mineral phases is to investigate the ELNES (Electron Loss Near Edge Structure). This was done using conventional EELS as well as the technique of spatial resolved EELS, which enables the precise study of the energy shift.

Especially for iron oxide minerals the near edge structure of the O-K edge [1] and the Fe L-edge can be used to determine the oxidation state, the iron oxide phase, and additionally the chemical composition qualitatively as well as quantitatively [2,3]. This work deals with the identification of iron bearing minerals in two systems. The possible candidates for the iron-oxide phases are FeO,  $\alpha$ -Fe<sub>2</sub>O<sub>3</sub> (hematite),  $\gamma$ -Fe<sub>2</sub>O<sub>3</sub> (maghemite), Fe<sub>3</sub>O<sub>4</sub> (magnetite),  $\alpha$ -FeO(OH) (goethite).

The first investigated materials were colloidal magnetic iron-based nanoparticles. Their structure is supposed to consist of an oxidized rim and iron core [4,6]. Fingerprinting the ELNES of the O K-edge two possible candidates for the iron oxide phase of the rim are Maghemite and Magnetite. Quantitative analysis of the EELS spectrum yields a chemical composition consistent with maghemite. HRTEM studies confirm the crystalline structure of the rim and core. Additionally the lattice fringes of the rim fits the maghemite structure.

The second batch of analysis examined minute iron oxide minerals in alkali feldspars of granitic rocks. It has long been supposed, that the clouded pink-red feldspars in granites owe their colour to hematite inclusions [5], but optical petrography and microprobe analysis can't resolve the fine structure in many cases. Using TEM and EELS these precipitates can be analysed. Fingerprinting the ELNES of the O K-edge yields that the iron oxide phase of the small precipitates consists of hematite. This can be confirmed by the comparison of experimentally taken and calculated diffraction patterns. Additionally the technique of spatially resolved EELS enables to study precisely the energy shift of the O K-edge for the different adjacent minerals.

The investigations were performed using two different TEM's. A conventional JEOL 3010 operating at 297 kV equipped with a LaB<sub>6</sub> cathode, postcolumn Gatan Imaging Filter and a 1 K slow-scan CCD camera and a LIBRA 200FE operating at 200 kV, equipped with a field emission gun, a 4 K slow-scan CCD Camera and a corrected 90° in-column Omega energy filter.

### References

- [1] C. Colliex, T. Manoubi and C. Ortiz, *Physical Review B* **44** (1991), p.11402
- [2] U. Golla and A. Putnis, *Phys. Chem. Minerals* **28** (2001), p.119
- [3] U. Golla-Schindler, G. Benner and A. Putnis, *Ultramicroscopy* **96** (2003), p.573
- [4] S. Veintemillas-Verdaguer, et al. *J. Mag. Res. Imaging*, submitted
- [5] Boone, G.M., *Am.J. Sci.* **267** (1969) pp.633-668
- [6] We thank S. Veintemillas-Verdaguer for the iron based nanoparticles, and acknowledge the support from a Alexander von Humboldt fellowship.

## Magic Angle in EELS - the Sequel

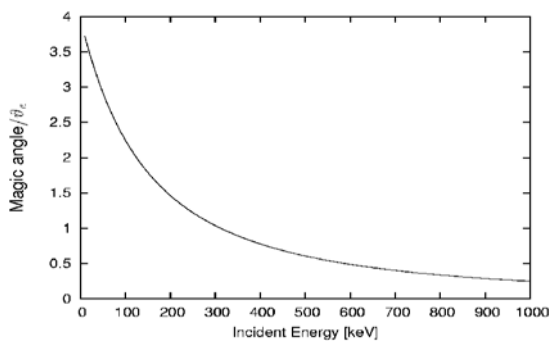
C. Hébert, H. Franco, P. Schattschneider

Institute for Solid State Physics, Vienna University of Technology, Wiedner Hauptstraße 8-10  
A-1040 Wien, Austria.

For the identification of phases with anisotropic crystal structure by fingerprints such experimental conditions should be used in which the anisotropy effects are canceled. The collection angle at which this happens is called “Magic Angle”. Much theoretical work has been devoted to the determination of Magic Angle conditions, and a discrepancy of a factor of more than 2 between theory and experiment could only be resolved very recently by using a fully relativistic Bethe's theory [1,2]. Here, we investigate some consequences of this finding.

The dielectric formalism, necessary for the description of the low-loss region can also be used for the modeling of a core loss spectrum. We show how the relativistic treatment of the dielectric formalism works and leads to the same result as the fully relativistic Bethe theory.

Practical consequences of the energy dependence of the magic angle are investigated showing that for high acceleration voltages the parallelity of the beam plays a key role while for lower acceleration voltages the contributions coming from Bragg-diffracted beams can become very important, especially for materials with large cell parameters.



Magic angle in units of  $\theta_e = \Delta E / (2\gamma T)$  as a function of the kinetic energy of the probe electron.  $\theta_e$  becomes very small at high energy. Experiments at 120 and 200 kV confirm the theoretical values of 2.05 resp 1.46  $\theta_e$  for the MA.

### References

- [1] B. Jouffrey, P. Schattschneider & C. Hébert., *Ultramicroscopy* 102 (2004)61;
- [2] P. Schattschneider, C. Hébert, H. Franco & B. Jouffrey, *Pys. Rev. B* in press
- [2] This research was supported by the European Commission, contract nr. 508971 (CHIRALTEM).

## Lifetime of Hot Electrons in Copper Obtained from Low- Loss EELS

C. Hébert, A. Satz, P. Schattschneider

Institute for Solid State Physics, Vienna University of Technology, Wiedner Hauptstraße 8-10  
A-1040 Wien, Austria.

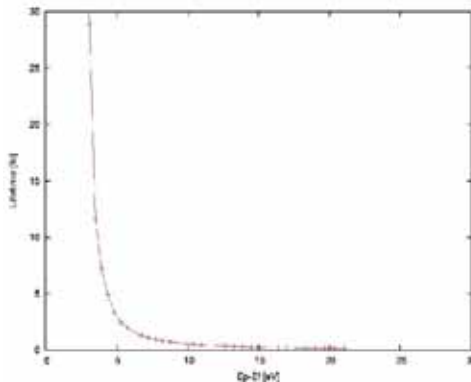
Electron dynamics in solid materials plays a key role in a variety of physical and chemical phenomena. Low energy excited electrons (up to 10-20 eV) have a finite lifetime which can be attributed to the e-e inelastic scattering. This lifetime can be directly or indirectly observed in numerous analytical methods (e.g photoelectron spectroscopy, direct and inverse photoemission spectroscopy but also in electron energy loss near edge structure analysis).

The lifetime  $\tau$  of the excited electron is energy dependent and directly related to the loss function [1] :

$$\frac{1}{\tau} = \frac{e^2}{\hbar\pi^2} \int d^3\vec{q} \cdot \frac{1}{q^2} \cdot \text{Im} \frac{-1}{\epsilon(\vec{q}, \omega)}$$

Integration is performed over all kinematically possible values of  $q$ .

The loss function can be obtained experimentally as a function of energy  $E=\hbar\omega$  for different values of momentum transfer  $q$  by an angular resolved acquisition of the low loss spectrum.



The figure on the left represents the lifetime of hot electrons in copper as a function of the energy above Fermi level.

For the experiment a thin micro-crystalline layer of copper was used. The values retrieved for the lifetime are in the right order of magnitude, however remaining problems need to be solved:

- The calculated lifetime from the EELS spectra starts at 2.5 eV because of the removal of the zero loss peak.
- A cut-off of the loss function at 30 eV was used since multiple scattering could not be removed properly.

- The Loss function was set to zero for  $E < 2.5$  eV which is not valid for a metal.

It should be possible to improve the energy resolution in our measurements in order to obtain values for the lifetime for approximately 1 eV above Fermi level. We are trying to reduce multiple scattering by using a thinner sample and by applying deconvolution methods.

This is a promising method for the determination of lifetime of electrons in solids. An interesting point is that we are able to obtain lifetimes at much higher energies than by conventional direct methods using femto-second lasers.

References:

[1] D Pines and P Nozières, The theory of quantum liquids, 1998.

## STEM and ELNES investigations of Cu-rich layers and nanostructures formed on VSe<sub>2</sub> crystal surfaces by metal deposition

S. Hollensteiner<sup>a</sup>, W. Sigle<sup>b</sup>, E. Spiecker<sup>a</sup> and W. Jäger<sup>a</sup>

<sup>a</sup>Technische Fakultät, Christian-Albrechts-Universität zu Kiel, 24143 Kiel, Germany

<sup>b</sup>Max-Planck-Institut für Metallforschung, 70569 Stuttgart, Germany

The early stages of ultra high vacuum Cu deposition onto initially smooth surfaces of layered VSe<sub>2</sub> crystals are characterized by the formation of nanostructure networks and of nearly contiguous thin Cu-rich surface layers. Transmission electron microscopy (TEM) investigations revealed that these nanostructures may have lateral dimensions within the range of ~ 10 nm up to a few hundred nanometers [1]. The larger nanostructures (> 100 nm) could be identified as nanorooftops consisting of parallel strands of crystalline tiles [2]. Analyses of microscopic structure of the thin surface layer revealed the presence of a copper-rich crystalline intercalation phase [2,3]. In order to contribute to an understanding of the microscopic nature of the observed surface phenomena, high-angle annular dark field imaging in scanning transmission electron microscopy (STEM, Fig.1a) has been combined with energy-dispersive X-ray spectroscopy (EDX) and electron loss near-edge structure measurements (ELNES) in electron energy loss spectroscopy (EELS) in spatially resolved measurements. The EDX measurements reveal a largely uniform copper distribution across the surface. The ELNES analyses of the Cu L<sub>2,3</sub> ionization edges (Fig.1b) reveal that the electronic structure of copper is modified with regard to metallic copper, which is indicative of an electron transfer to the substrate material. The V L<sub>2,3</sub> edges exhibit a change in the L<sub>2,3</sub> white line intensity in comparison to spectra obtained for pure VSe<sub>2</sub> crystals indicating that the electronic structure of the V has been modified towards a more metallic character. The comparison with the microstructure analyses [1-3] shows that electronic charge transfer from the copper adsorbate to the substrate surfaces takes place during the formation of Cu-rich intercalation phases in near-surface layers.

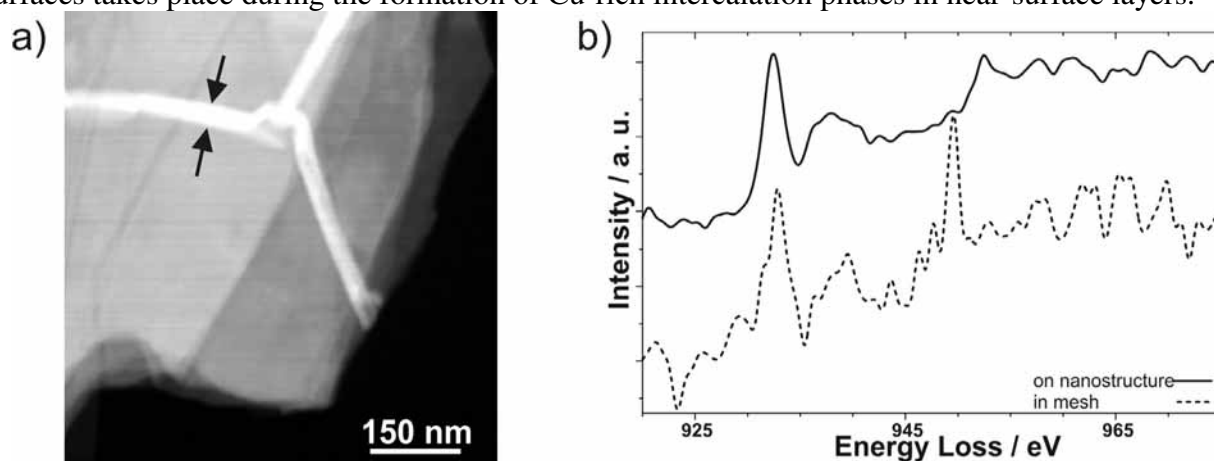


**Fig. 1:** a) High-angle annular dark field STEM image depicting linear nanostructures (brightest contrast) and cleavage steps. b) ELNES of Cu L<sub>2,3</sub> ionisation edges in EELS spectra taken from the nanostructure and from mesh region in between nanostructures.

[1] S. Hollensteiner et al., *Mat. Sci. Eng. C* 23 (2003), 171.

[2] E. Spiecker, et al., *Microsc. Microanal.*, (2005) in press.

[3] S. Hollensteiner et al., *Applied Surface Science* 241 (2005) 49.

[4] Financial support by the DFG (contract FOR 353/1-2) is gratefully acknowledged.

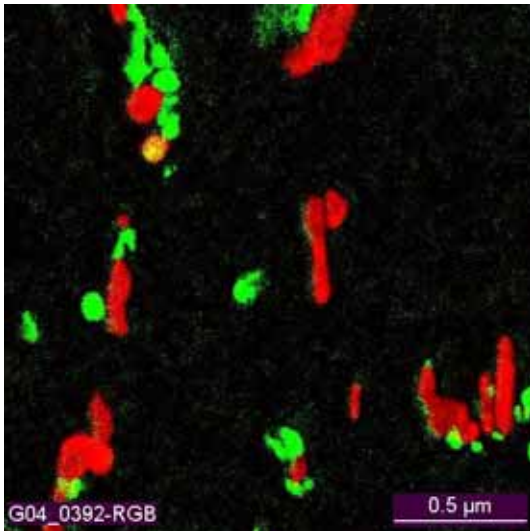
# The Influence of Annealing Conditions on the Precipitation Characteristics of a Martensitic 9-12 wt% Cr Steel

Florian Kauffmann, Christina Scheu, Herbert Ruoff and Karl Maile

Staatliche Materialprüfungsanstalt, Universität Stuttgart, 70569 Stuttgart, Germany

New ferritic-martensitic 9-12 wt.% Cr steels have been developed in recent years for the usage in steam power plants. The aim of this development is to enhance the creep properties and thermal resistance of the material. By this, higher steam temperatures and pressures could be realized in the power plants, and thereby the thermal efficiency could be increased and the CO<sub>2</sub> emission decreased.

This goal can be achieved by optimizing the microstructural features, especially the subgrain size and the precipitation size and distribution. Small precipitations with a high precipitation density and especially a high thermal stability are of great benefit for the creep properties. Several research programs focus on an optimized alloy composition for this purpose, but the present work takes a different approach. We have systematically studied the influence of the normalization and the tempering temperatures on the initial precipitation state of a 11.5 wt.% Cr steel. The normalization temperature has been varied between 1030 °C and 1090 °C, the tempering between 740 °C and 830 °C.



The precipitates have been characterized with a method combining GIF imaging, EDX spectra and diffraction measurements for the identification of the particle types. The size distribution is determined separately for each particle type by digital image analysis. Details on the applied method can be found in [1].

The picture on the left shows a GIF image of one annealing state of the investigated alloy. 10 such images have been used for each annealing state. The presence of chromium is indicated by the red color, the particles have been identified as M<sub>23</sub>C<sub>6</sub>. Green indicates vanadium and a MX particle type. The yellow particle contains both, Cr and V, and has been identified as an M<sub>2</sub>X type. Our study demonstrates that the fraction of these different

particles, and thereby the long-time creep properties of the material, can be significantly influenced by the annealing conditions of the alloy.

References:

[1] C. Scheu, F. Kauffmann, G. Zies, K. Maile, S. Straub and KH. Mayer, Z. Metallkd. 96 (2005).

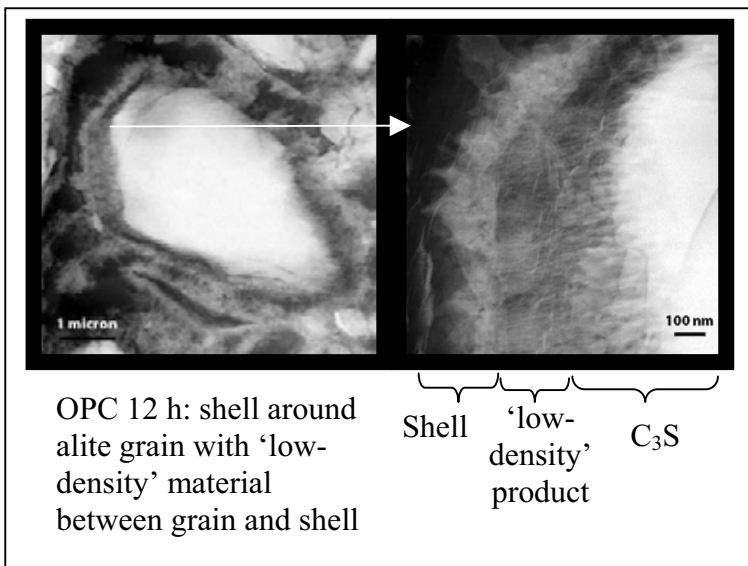
## Microstructural Studies of Early Age Hydration of Ordinary Portland Cement (OPC) using TEM

Prakash C. Mathur<sup>1</sup>, Emmanuel Gallucci<sup>1</sup>, Karen L. Scrivener<sup>1</sup>, Pierre A. Stadelmann<sup>2</sup>

<sup>1</sup> Laboratoire de Matériaux de Construction (LMC), Ecole Polytechnique Fédérale de Lausanne, CH-1015 Lausanne, Switzerland

<sup>2</sup> Centre interdisciplinaire de microscopie électronique (CIME), Ecole Polytechnique Fédérale de Lausanne, CH-1015 Lausanne, Switzerland

The study aims to characterize the microstructures of both standard and special cementitious materials. The hydration of cement is complex; hydration and strength development are mainly controlled by reaction of calcium silicates that has been exhaustively studied. Nevertheless the impact of minor phases – aluminates, ferrites and sulphates/alkalis can be very significant and is much less understood. During hydration hydrates from both silicates and aluminate containing phases interact and become intermixed on the sub-micron scale, this poses a challenge to characterization of the materials. Special cements have different chemistries – notably calcium aluminate used alone and in blends. Blending with Portland Cements and Calcium Aluminates has been shown to have a radical impact the microstructure and properties but these effects are not well understood. Initial microstructural studies have shown complex fine mix of hydrates, which needs to be characterised.



Analytical transmission electron microscope, due to its accuracy in chemical analysis and the ability to achieve high image resolution, is being used to study the above mentioned aspects. Stress has been given to obtain accurate quantitative chemical analysis.

[1] The project is funded by the Swiss National Foundation.

[2] Guidance of Ms. D. Laub (CIME, EPFL) regarding TEM specimen preparation is gratefully acknowledged.

## **Concentration and Modulus Gradients at the Interface Between an Amine-Cured Epoxy and the Thermoplastic PVP**

M. Munz and E. Schulz

Federal Institute for Materials Research and Testing (BAM), Div. VI.2  
Unter den Eichen 87, D-12205 Berlin, Germany

*(document could not be printed due to password protection)*

## **Analytical Imaging: Complementary Methods To Microscopy**

Confocal Raman Microscopy and EDX-Mapping, two essential methods in Drug Development

Kurt Paulus

NOVARTIS Pharma AG, WKL-127.3.58, 4002 Basel

Due to the progress in the development of lasers and computers, new technologies can extend tremendously the possibilities of traditional microscopy in the field of pharmaceutical drug development.

Coupled to a Scanning-Electronmicroscope, EDX-mapping at high magnifications can be used to locate the active pharmaceutical ingredient (API) with specific atoms within solid delivery systems. It could be demonstrated, that differences in the molecular dispersion of the API in the dispersion medium depend on the pharmaceutical formulation, the specific properties of the API, and the type of polymers.

Confocal Scanningmicroscopes, coupled with a Raman Spectrometer, allow an exact inspection of tiny volumes ( $>0.02 \mu\text{m}^3$ ), and thus, chemical imaging beneath the surface. The high-end systems have a high lateral resolution, limited only by diffraction (laser  $\lambda/2$ ) and store a complete Raman Spectrum with each scanned pixel. Beside the distribution of API in solid delivery systems like microparticles or inhalation formulations, it could be shown further, that identification of low amounts of polymorphic modifications on single particles could easily be performed.

Consequently both of these powerful methods contribute significantly to the pharmaceutical development.

## Characterization of Doped ZnO Films by Means of Analytical TEM/EELS

Herbert Schmid and Werner Mader

Institut für Anorganische Chemie, Universität Bonn, 53117 Bonn, Germany

ZnO films doped with various 3d transition metals (TM) show novel combinations of properties and are considered as promising candidates for spintronic applications. Depending on the oxidation states of TM-substituents on  $\text{Zn}^{+2}$  lattice sites and the possible formation of nanosized clusters of secondary phases, either weak ferromagnetic or paramagnetic behaviour could be expected. Mn and Fe doped ZnO thin films ( $\text{Mn}_x\text{Zn}_{1-x}\text{O}$  and  $\text{Fe}_x\text{Zn}_{1-x}\text{O}$ ;  $x \approx 0.05$ ) were grown on c-plane sapphire substrates by pulsed laser deposition. Thin specimens of doped ZnO films were prepared in cross-section by standard methods and characterized by analytical TEM methods (Philips CM 30 TEM/STEM with EDS and EELS attachments). Lattice imaging and electron diffraction experiments revealed that single crystalline Mn-ZnO films (film width  $d \approx 1 \mu\text{m}$ ) grow epitaxially on c-plane sapphire substrates with orientation relationships:

$$[0001]_{\text{film}} \parallel [0001]_{\text{substrate}}, \text{ and } \{11\bar{2}0\}_{\text{film}} \parallel \{03\bar{3}0\}_{\text{substrate}}.$$

Thus, both c-planes and close-packed directions of the anion sublattice coincide in epitaxial Mn-ZnO and sapphire substrate (rhombohedral structure in hexagonal notation). Residual stresses are relieved by the formation of dislocations in the epitaxial film; compositional inhomogeneities or secondary phases were not observed in this material. Lattice spacings of the Mn-ZnO film as measured by SAD are (within measuring errors  $\pm 0.0005\text{nm}$ ) identical to those of pure zincite (ZnO); the sapphire substrate with known lattice spacings was used as internal calibration standard. Doping with Fe on the other hand resulted in the formation of a strongly textured polycrystalline Fe-ZnO film with preferential orientation of the majority of crystallites similar to above orientation relationship. An angular misorientation in the range of  $\pm 4^\circ$  (FWHM) about the  $[1\bar{1}00]$  zone axis was measured by profiling the intensity distributions within diffraction rings in SAD patterns.

The oxidation states of Mn and Fe in doped ZnO films were derived by quantitative EELS analysis. It is well established that ELNES features such as (i) the absolute energy shift of ionization edges, (ii) the normalized total intensity, and (iii) the intensity ratio of white lines in core-loss spectra from 3d and 4d TM oxides vary with d-electron occupancy. For absolute energy measurements by means of the voltage scan module (Gatan 666 PEELS), the system was calibrated on the Ni-L<sub>3</sub> white line maximum ( $\Delta E = 853.2 \text{ eV}$ ) in NiO. Calibration curves of white line intensity ratios ( $L_3/L_2$ ) vs. 3d-occupancy were established from transition metal compounds of known oxidation states ( $\text{MnO}$ ,  $\text{Mn}_3\text{O}_4$ ,  $\text{Mn}_2\text{O}_3$ ,  $\text{MnO}_2$ ;  $\text{FeTiO}_3$ ,  $\text{Fe}_3\text{O}_4$ ,  $\text{Fe}_2\text{O}_3$ ). A Hartree-Slater function was used to model the intensity due to transitions into the continuum. Step onsets were set at peak maxima and step height ratio 2:1 in accordance with the multiplicity ratio of the initial 2p states. After subtraction of both the background and continuum, total white line intensities were integrated over 4 eV windows centred at peak maxima. The measurements revealed that Mn-L<sub>2,3</sub> ELNES features in Mn-doped ZnO correspond well with those in MnO, whereas Fe-L<sub>2,3</sub> ELNES in Fe-doped ZnO rather correspond to those of trivalent hematite ( $\alpha\text{-Fe}_2\text{O}_3$ ). This suggests that depending on processing conditions, Mn<sup>+2</sup> substitutes for Zn in the doped structure, whereas Fe<sup>+3</sup> rather may form oxide nanoclusters due to the electric charge imbalance on  $\text{Zn}^{+2}$  lattice sites resulting in strongly textured polycrystalline films.

# High Resolution ELNES Characterization of Chemical Bonding in Low Dielectric Constant Materials for Interconnect Isolation

H. Stegmann<sup>a</sup>, T. Walther<sup>b</sup>, E. Quandt<sup>b</sup>, E. Zschech<sup>c</sup>, and D. Schmeisser<sup>d</sup>

<sup>a</sup>Carl Zeiss Nano Technology Systems GmbH, Carl-Zeiss-Str. 56, D-73447 Oberkochen, Germany

<sup>b</sup>Center of Advanced European Studies and Research (caesar), Ludwig-Erhard-Allee 2, D-53175 Bonn, Germany

<sup>c</sup>AMD Saxony LLC & Co. KG, Wilschdorfer Landstr. 101, D-01109 Dresden, Germany

<sup>d</sup>Brandenburg Technical University, Department of Applied Physics/Sensorics, Konrad-Wachsmann-Allee 1, D-03046 Cottbus, Germany

Low dielectric constant materials for on-chip interconnect isolation are locally degraded by plasma treatment steps used in the patterning process. Characterization of chemical bonding in the affected regions with nanometer resolution is becoming a critical task for manufacturing process optimization. Electron energy-loss near edge structure (ELNES) analysis in a TEM with monochromated field-emission source provides such chemical bonding analysis [1].

In organosilicate glass (OSG) materials, substitution of oxygen in SiO<sub>2</sub> by methyl groups (-CH<sub>3</sub>) lowers the permittivity significantly. The use of OSG in the on-chip interconnect process reduces signal delay, power dissipation and cross-talk noise [2]. However, plasma processing for resist strip, trench etch and post-etch clean modifies permittivity, water absorption, and stiffness in near-surface regions (< 20 nm) of these materials. As the interconnect line spacing of ultra large scale integrated circuits is being further reduced, the effective electrical and mechanical properties of the structured material are increasingly affected. Compositional analysis alone is not sufficient to study these effects [3]. Chemical bonding characterization on a nanometer scale is necessary to understand the correlation between process parameters and material properties.

In this study, electron energy-loss spectra recorded at 0.15 eV energy resolution using a monochromated TEM with In-column Corrected OMEGA filter are compared for as-deposited and plasma-treated amorphous OSG materials. The C-K ELNES reveals modified bonding of the C atoms in the plasma-treated samples. The results are compared to synchrotron X-ray absorption near edge structure (XANES) analyses that provide complementary information on a micron scale with comparable energy resolution.

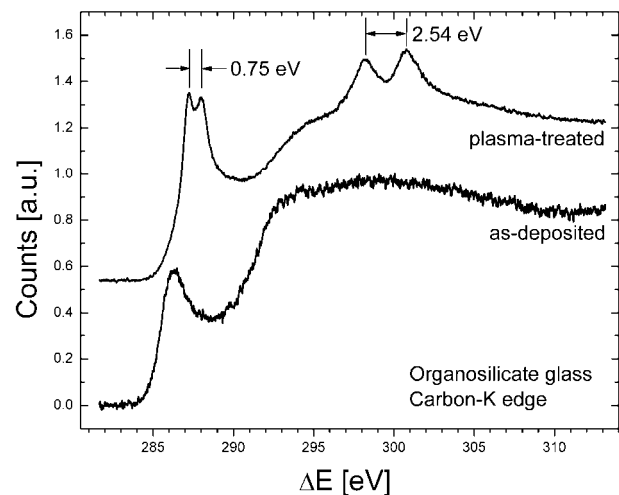


Fig.: EELS carbon-K edge recorded from an OSG dielectric film as-deposited and after plasma treatment, specimen thickness  $\approx$  50 nm.

## References:

- [1] H. Stegmann, E. Zschech, *Proc. 2005 Int. Conf. Char. Metrol. ULSI Technol.*, in press.
- [2] K. Maex et al., *J. Appl. Phys.* 93 (2003) 8793-8841.
- [3] F. Iacopi et al., *Mat. Res. Soc. Symp. Proc.* 812 (2004) 19.

# Integrated Mineralogical and SEM/EDX Analysis: An Innovative Tool For The Identification And Source Apportionment Of Deposited Dust

Cristina Trimbacher<sup>1</sup> & Hassan Neinavaie<sup>2</sup>

<sup>1</sup> Umweltbundesamt, Department Heavy Metals, Electron Microscopy, Spittelauer Laende 5, 1090 Vienna, Austria, <sup>2</sup> Geologische Bundesanstalt, Neulinggasse 38, 1031 Vienna, Austria

## Introduction

Due to exceedings of the limit values for lead (Pb) and cadmium (Cd) in deposited dust, as regulated in the Austrian Air Quality Act, measurements have been carried out in an industrial region in Austria in winter 2003/2004. Analysis with integrated mineralogical and SEM/EDX techniques in five selected samples of deposited dust (Bergerhoff method) and four material samples of the locations have been performed. The main objective was to identify the sources of Cd and Pb, as there are several industrial plants settled in that region.

## Method

Polished thin- and cross sections were prepared for mineralogical analysis, using reflected and transmitted light microscopy, as well as XRFA and EDX for semi-quantitative analysis of selected particulate pollutants. By means of scanning electron microscopy (SEM) and energy-dispersive X-ray microanalysis (EDX) structure, size and elemental composition of the particles were analysed. This methodology has already been introduced in previous studies [1, 2].

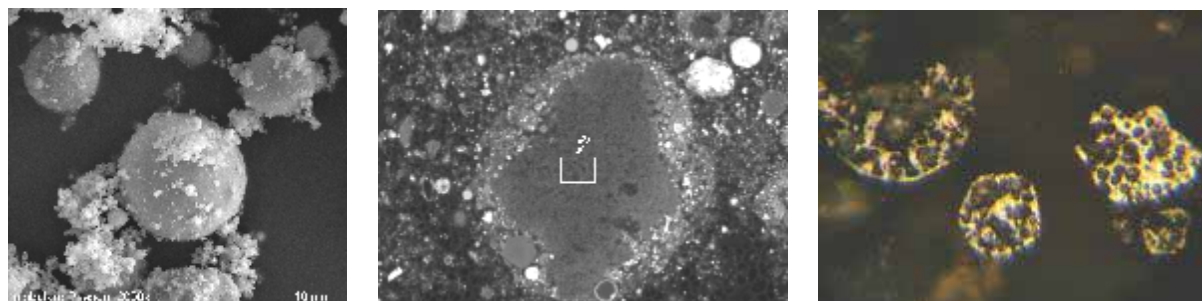
## Results

Pb-rich particles were identified in all five dust samples and could be related to an industrial plant in the area. (metallic Pb, Pb-Sulfate, PbO<sub>2</sub>-Chlorides, Pb-Silicates). Additionally, C-S-rich cenospheric particles (traces of Ni and V) and partly melted plastics from combustion processes could be attributed to the same source (see figure 1c). No Cd-rich particles could be found in the dust samples. Therefore material samples taken directly from the industrial premises were analysed. The source of cadmium could be clearly identified: 0.2 to 0.85% Cd was found in Pb-rich particles in filter dusts (see figures 1a and 1b).

## References

[1] Neinavaie, H., Pirkl, H. & Trimbacher, C. (2000): Herkunft und Charakteristik von Stäuben. UBA-BE-171, Umweltbundesamt Wien.

[2] Trimbacher, C. & Neinavaie, H. (2002): Studie zur Ermittlung der Herkunft von Stäuben an sechs ausgewählten Messpunkten in Graz. UBA-BE-210, Umweltbundesamt Wien.



Figures: 1a, SEM-micrograph of spherical Pb-Silicates of a filter dust sample (Mag: 2000x). 1b, XRFA-micrograph of a filter sample showing a PbO<sub>2</sub>-Chloride particle with 1.5% Cd. 1c, micrograph of a polished cross section of four C-S-rich cenospheric particles.

## Combining imaging with local spectroscopy in an energy-filtered TEM/STEM

T. Walther<sup>a</sup>, J. Simon<sup>b</sup> and H. Stegmann<sup>c</sup>

<sup>a</sup>Center of Advanced European Studies and Research, Ludwig-Erhard-Allee 2, 53175 Bonn, Germany

<sup>b</sup>Institut für Anorganische Chemie der Universität Bonn, Römerstr. 164, 53117 Bonn, Germany

<sup>c</sup>Carl Zeiss Nano Technology Systems GmbH, Carl-Zeiss-Str. 56, 73447 Oberkochen, Germany

The investigation of nano-structures relies strongly on the capabilities of sub-nm scale imaging and local electron energy-loss spectroscopy (EELS) which can be performed simultaneously in a modern transmission electron microscope (TEM) with an energy filter. Here, an overview on different ways to perform EELS or energy-filtered transmission electron microscopy (EFTEM) is presented [1]. Recent advances in both instrumentation and method development are described, including the first useful lattice image obtained in a new monochromated and Cs-corrected (S)TEM instrument.

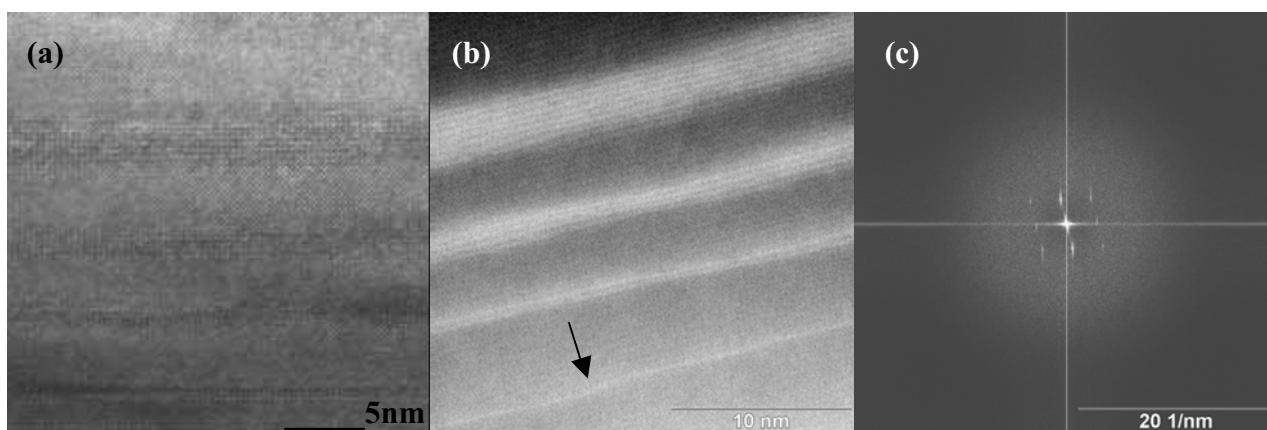


Fig.1: HREM image of a  $\text{SrTiO}_3/\text{La}_{2/3}\text{Ca}_{1/3}\text{MnO}_3$  multilayer obtained with a Philips CM300UT (a); ADF *Z-contrast* image of the same multilayer structure from the new monochromated and Cs-corrected Zeiss Libra200FE CRISP (b). The monochromator slit was set to 0.30eV FWHM, and 25mrad convergence angle yields  $\sim 8\text{pA}$  probe current. The arrow marks a single atomic step in the La/Ca sub-lattice. The Fourier transform of (b) indicates transfer at 0.39nm and also 0.28nm (c).

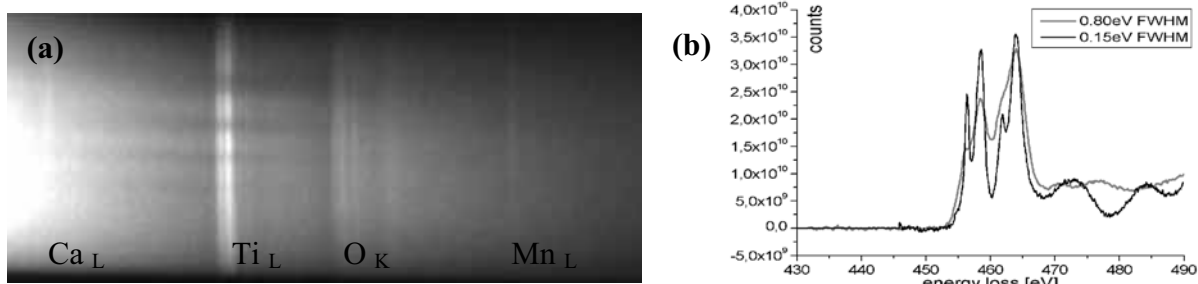


Fig.2: Energy-loss spectroscopic profiling with 0.8eV resolution [2] shows a weak splitting of the Ti  $L_3$ -edge on which the energy filter was focused. With monochromator on and in image mode, the improved resolution of 0.15eV FWHM clearly reveals the splitting of the Ti  $L_3$  and the  $L_2$  line (b).

### References:

[1] T. Walther, *Z. Metallkd.* 96 (2005) 429-437.

[2] T. Walther, *Proc. EMC 2004*, Antwerp, Belgium, 1 (2004) 33-34.

## **New approach to the quantitative analysis of low loss transmission electron energy loss spectroscopy measurements**

W. de la Cruz<sup>a</sup>, C. Rojas<sup>b</sup>, C. Mansilla<sup>b</sup>, V. Rico<sup>b</sup>, J. Ferrer<sup>c</sup> and F. Yubero<sup>b</sup>

<sup>a</sup> Centro de Ciencias de la Materia Condensada, UNAM, A. Postal 2681, 22800 Ensenada, B.C., Mexico

<sup>b</sup> Instituto de Ciencia de Materiales de Sevilla (CSIC-USE) . C/ Américo Vespucio s/n E-41092 Sevilla. Spain

<sup>c</sup>Centro Nacional de Aceleradores (CSIC-USE). C/ Tomas A. Edison s/n E-41092 Sevilla Spain

We have revised the standard approximations [1] used for the quantitative analysis of thin films from low loss transmission electron energy loss spectroscopy measurements. We have performed a critical analysis of the momentum dispersion of the dielectric description of the material. In particular, we have focussed our study in dependence of the complex dielectric function, the electron transport properties (i.e., inelastic mean free path) and the thickness of the analysed thin films on the momentum dispersion of the energy loss function. This momentum dependence is incorporated according to the model developed by Ding *et al.* [2], that is commonly used in the determination of inelastic electron mean free paths within the surface science community [3]. Thus, it is found that, the momentum dispersion in the description of the electron energy losses has a minor influence for the determination of dielectric properties of the film, but it may affect up to a factor 2 in the evaluation of inelastic mean free paths, and consequently in the absolute thickness of the film. We present some experimental analysis where the optical properties of Au, and several oxides (SiO<sub>2</sub>, Ta<sub>2</sub>O<sub>5</sub> and Sm<sub>2</sub>O<sub>3</sub>) are determined. As a result of this study, we have developed a new user friendly software to quantitatively describe transmission electron energy loss spectroscopy measurements. We named it OPTEELS, because it is specially developed for determination of Optical Properties from low loss TEELS measurements. Among other features, it allows evaluation of dielectric properties of thin films in the ~4-100 eV energy range, differential inelastic scattering cross section at the primary energy of the incident electrons used in the electron microscope and absolute determination of thin film thicknesses both with the standard zero-momentum transfer approximation [1] and momentum dispersion within Ding *et al.*[2] model. Special care was taken to force the energy loss function to fulfil the standard Kramers-Kronig relations. Thus, OPTEELS is specially designed for expansion of the optical properties of thin films obtained either by UV-Vis spectroscopy, ellipsometric methods or bibliographic sources to the far UV and soft X-ray energy regions. We expect that this user-friendly and freely available (for non commercial use) software package became a useful tool to easily and self-consistently determine dielectric properties of material in the so-called low loss region of TEELS spectra.

[1] R.F. Egerton, *Electron Energy-Loss Spectroscopy in the Electron Microscope*, (1986) Plenum Press, New York, pp410

[2] Z-J Ding and R. Shimizu, *Surface Science* 222(1989) 313-331

[3] S. Tanuma, C.J. Powell, D.R. Penn, *Surf. Interface Anal.* 20 (1993) 77

## HACDF Electron Tomography: A First Example

O.G. Abrosimov<sup>a</sup>, A.L. Chuvilin<sup>b</sup>, and U. Kaiser<sup>b</sup>

<sup>a</sup>Laboratory of Structural Methods of Investigations, Boreskov Institute of Catalysis, Novosibirsk 630090, Russia

<sup>b</sup>Materialwissenschaftliche Elektronenmikroskopie, University of Ulm, Ulm D-89069, Germany

The suitability of conventional TEM for electron tomography in materials science is limited by the so-called projection requirement. This limitation is overcome by STEM HAADF [1], EFTEM [2], and ADF TEM with Cs-corrector [3]. Recently [4], a new technique called High Angle Centered Dark Field (HACDF) was introduced, which achieves this goal without expensive STEM HAADF, FEG or Cs-corrected instruments, but instead within a conventional TEM. The resolution of this technique is about 1 nm.

In this work we investigate the use of the HACDF technique for three-dimensional reconstruction of the shape of nanosized catalytic particle. A standard JEOL JEM-2010 instrument was used. A special tip for the standard JEOL holder and special grids were developed in order to extend the accessible tilt angle range to  $\pm 72^\circ$ . The specimen used was catalytic filamentous carbon, formed by CVD method from methane  $\text{CH}_4$  on a metal catalyst (Ni-Cu alloy) at a temperature of  $625^\circ\text{C}$ . The metal particles in this sample are well faceted. Weighted Back-Projection algorithm was used for tomographic reconstruction. Crystal faces of the particle could be successfully determined from the surface model produced.

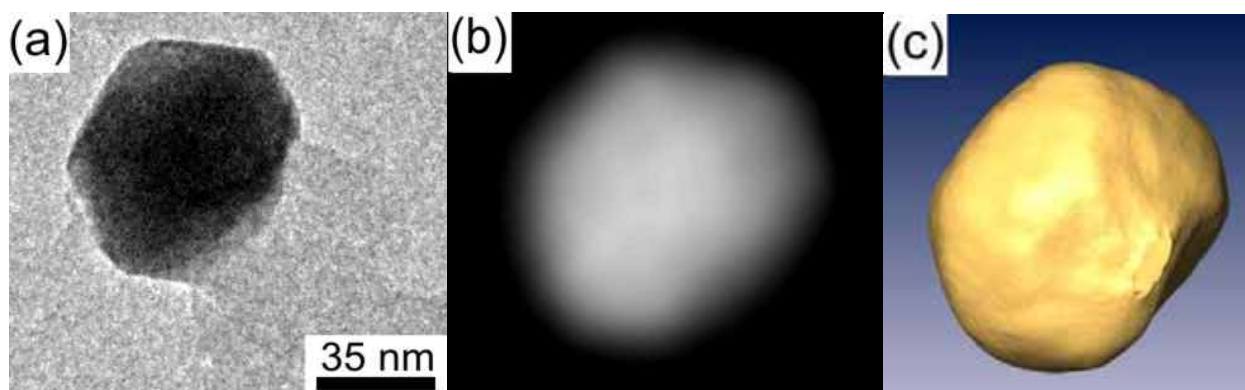


**Fig. 1:** (a) Bright field image of the Ni-Cu alloy catalyst particle; (b) HACDF image of the particle; (c) Surface model of the reconstructed particle.

References:

[1] P.A. Midgley, M. Weyland, *Ultramicroscopy* 96 (2003) 413-431.

[2] G. Möbus, R. C. Doole, B. J. Inkson, *Ultramicroscopy* 96 (2003) 433-451

[3] S. Bals, B. Kabius, M. Haider, V. Radmilovic, C. Kisielowski, *Solid State Communications* 130 (2004) 675-680.

[4] U. Kaiser, A. Chuvilin, *Microsc. Microanal.* 9 (2003) 36-41.

# Quantitative And Chemical Study Of Nano-Objects By HRTEM, HAADF And Associated Techniques

Thierry EPICIER, Rachid EL BOUAYADI and Daniel ARAUJO

GEMPPM, umr CNRS 5510, INSA de Lyon, Bât. Blaise Pascal, F-69621 Villeurbanne Cedex

The development of nanotechnologies demands more and more detailed structural and chemical characterisation at a nanometric level. Transmission Electron Microscopy (TEM) and associated techniques (HRTEM, EDX, EELS, EFTEM, STEM-HAADF) appear to be ideal tools to achieve such a goal. The present contribution will overview some recent studies on nano-particles and nano-objects of significant interest for a large variety of industrial applications.

In a first part, HRTEM and nano-analytical approaches will be illustrated through different examples: (i) Pd-Sn nano-colloïds [1], (ii) metallic h.c.p. Ni nano-particles (see figure 1), (iii) Si-based nanowires and nanocables, e.g. SiO<sub>2</sub>, SiC, Si<sub>3</sub>N<sub>4</sub>@BN, SiC@BN [3].

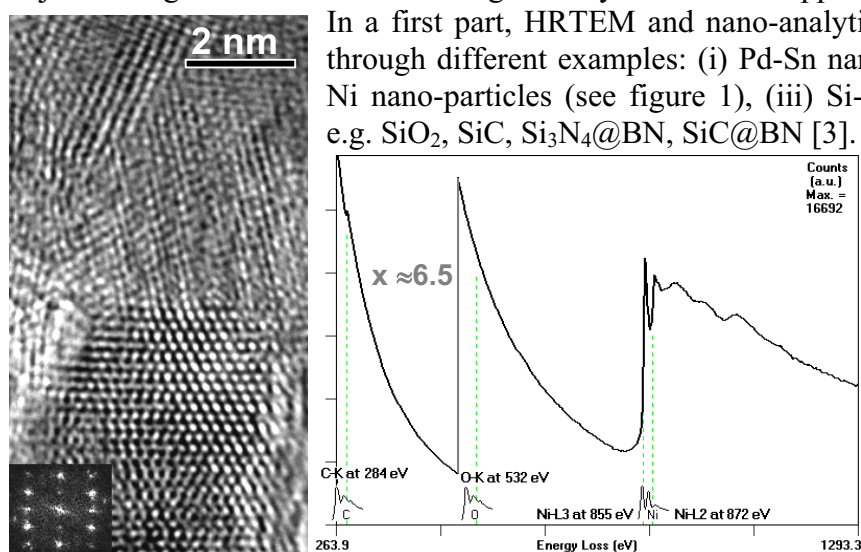


**Figure 1:** study of Ni nanoparticles [2]. The HRTEM micrograph (*left*) shows an h.c.p. (with  $a = 0.244$  nm and  $c = 0.396$  nm) nano-crystal viewed along the  $[2-1-10]$  zone-axis, as revealed by the diffractogram. EELS analysis (*right*) confirms the metallic nature of the particles through the absence of any significant oxygen (*JEOL 2010F*).

In a second part, attention will be focussed on quantitative HAADF at a nanometric resolution. On the basis of the incoherent scattering involved in HAADF, the contrast of the images can be computed from simple geometrical models. Comparisons between simulations and experimental images will be presented in the case of precipitation studies: (i) AlN and TiN precipitates in steels, (ii) (Cu,Ag) co-precipitation in silicon (see figure 2), (iii) Al<sub>3</sub>(Zr,Sc) core-shell particles in Al [4].

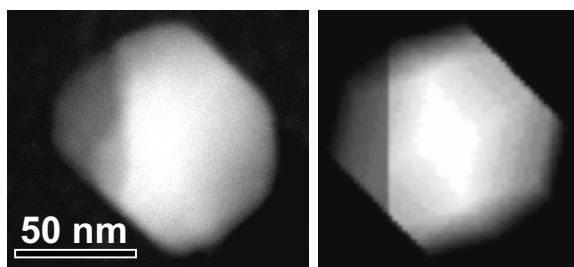


**Figure 2:** experimental (*left*) and simulated (*right*) HAADF image of a Cu-Ag precipitate in silicon. The simulation has been performed according to a geometrical model assuming a particle with a truncated octahedral shape, with an ideally planar interface between pure copper at the left-hand side of the precipitate and pure silver at the right-hand side (*JEOL 2010F*).

[1] HOLDERER O., EPICIER T., ESNOUF C., FUCHS G., *J. Phys. Chem. B.*, **107**, 8, 1723-1726, (2003)

[2] S. ILLY S., TILLEMENT O., MACHIZAUD F., DUBOIS J.M., MASSICOT F., FORT Y., GHANBAJA J., *Phil. Mag. A*, **79**, 5, 1021-1031, (1999).

[3] SAULIG-WENGER K., CORNU D., CHASSAGNEUX F., FERRO G., EPICIER T., MIELE P., *Solid State Communications*, **124**, 157-161, (2002).

[4] the CLYME (Consortium Lyonnais de Microscopie Electronique) is greatly acknowledged.

## Electron Irradiation of Carbon Nanotubes in the Electron Microscope

F. Banhart<sup>a</sup>, J.X. Li<sup>a</sup>, M. Terrones<sup>b</sup>, and A. Krasheninnikov<sup>c</sup>

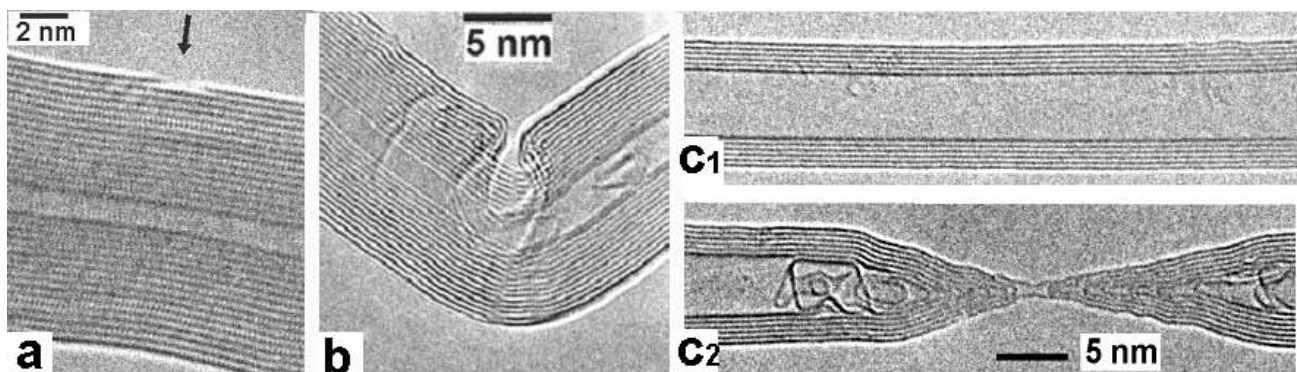
<sup>a</sup>Institut für Physikalische Chemie, Universität Mainz, 55099 Mainz, Germany

<sup>b</sup>Advanced Materials Dept. IPICYT, 78216 San Luis Potosi, Mexico

<sup>c</sup>Lab. of Physics, Helsinki University of Technology, 02015 Helsinki, Finland

The structure and morphology of carbon nanotubes can be modified by irradiation with energetic electrons [1]. This is achieved in the focused electron beam of a TEM. Modern TEMs with field emission guns allow the irradiation of nanotubes with beams of less than 1 nm in diameter and, hence, to modify structures on an atomic scale. To avoid the agglomeration of radiation defects and gradual destruction of nanotubes, a high mobility of interstitial atoms has to be ensured; therefore irradiation and imaging are carried out at high specimen temperatures.

Knock-on displacements of carbon atoms lead to the formation of interstitials, vacancies, and dangling bonds. The controlled formation of these point defects is the key to 'nanoengineering' of tubes or related carbon particles. Several alterations of the structure and morphology of nanotubes were achieved. Examples for single-wall tubes are the merging of parallel or crossing tubes and the formation of molecular junctions between tubes. Multi-wall tubes can be tailored under the electron beam by removing graphene layers locally (fig. a), bending the tubes by a pre-defined angle (fig. b), local transformation of the tubes into spherical 'onions', or the controlled collapse of tubes [2, 3]. Bundles of single-wall tubes can be transformed into multi-wall tubes and, conversely, multi-wall tubes into single-wall tubes under electron irradiation [2]. Furthermore, the injection of carbon atoms into the inner hollows of tubes can be achieved by applying an electron beam [3]. The morphological evolution of nanotubes under the beam shows that nanotubes act as pipelines for the effective diffusion of free carbon atoms (fig. c<sub>1</sub> before, fig. c<sub>2</sub> after irradiation).



### References:

[1] F. Banhart, *Philos. Trans. A* **362** (2004) 2205.

[2] J.X. Li and F. Banhart, *Nano Lett.* **4** (2004) 1143.

[3] F. Banhart, J.X. Li, and A.V. Krasheninnikov, *Phys. Rev. B*, in the press.

## Characterization of Au Gold Nanoparticles

Barbora Bártová<sup>a</sup>, Antonín Gemperle<sup>a</sup>, Juliana Gemperlová<sup>a</sup> and Miroslav Šlouf<sup>b</sup>

<sup>a</sup>Institute of Physics, ASCR, Na Slovance 2, 182 21 Prague 8, Czech Republic

<sup>b</sup>Institute of Macromolecular Chemistry, ASCR, Heyrovského nam. 2, 162 06 Prague 6, Czech Republic

Gold nanoparticles are used as a calibration particles for dynamic light scattering experiments. They scatter light quite intensively due to extremely high difference in refractive index between common solvents and Au, which is their advantage. The colloidal solutions of Au nanoparticles with pre-calculated size were prepared by controlled reduction of H[AuCl<sub>4</sub>] water solution [1, 2].

Two series of Au nanoparticles (30 and 80 nm) dispersed on an evaporated carbon foil were studied by transmission electron microscopy. Most of the particles were composed of two or more crystallites. The mutual disorientation of the crystallites was determined from spot patterns. SAD patterns were taken from particles of 80 nm in size using Jeol 1200EX with 0.7 mm selected area diameter. This gave rise to the rather strong diffuse background from the carbon foil. Reflections up to 531 could be registered. The error in orientation determination in this case is larger as compared to Kikuchi line evaluation and may attain up to 5°. The evaluation of diffraction patterns is further complicated by the size effect, which may influence angular relations between the two crystals. It was believed that the crystallites are in twinning orientation. The evaluation of diffraction patterns from 3 particles shows appreciable deviations, approximately 20°, from twin orientation in all three cases. When the deviation is higher than 10 - 15° from expected coincidence, other low  $\Sigma$  coincidences must be considered. The mutual orientations correspond better to  $\Sigma$ 11 in two cases and to  $\Sigma$ 7 in one case. Small particles (30 nm) have a well defined five fold symmetry with common grain boundary node.

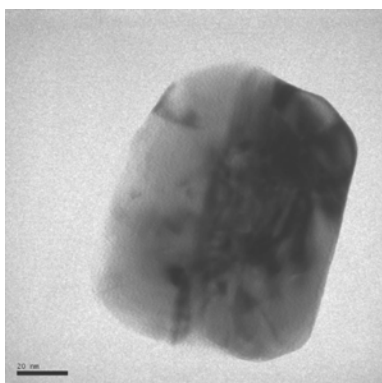


Fig. 1: Au nanoparticle (80 nm)

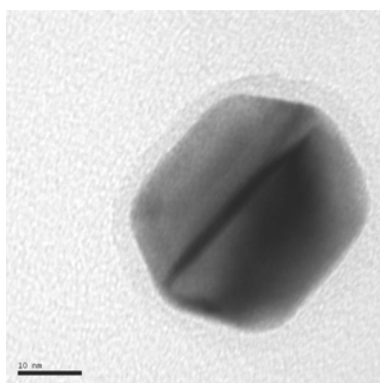


Fig. 2: Au nanoparticle (30 nm)

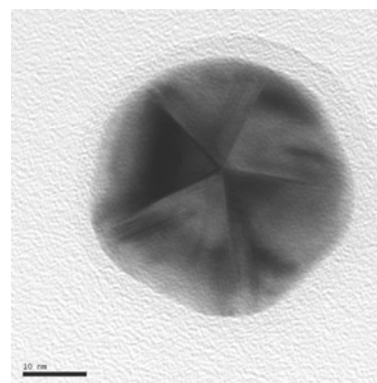


Fig.3: Au nanoparticle (30 nm)

### References:

[1] J. Turkevich, P. C. Stevenson & J. Hillier, *Disc. Faraday Soc.*, 11 (1951) 55-75

[2] M. Šlouf, R. Kužel & Z. Matěj: *Materials Structure*, 11 (2004) 166-168

[3] Authors acknowledge financial supports of GACR (106/04/1118) and GAAV (AVOZ4050913).

## Magnetic Nanocrystals in Semiconductors

Johannes Biskupek<sup>a</sup>, Ute Kaiser<sup>a</sup>, Hannes Lichte<sup>b</sup>, Andreas Lenk<sup>b</sup>, Masa Kawasaki<sup>c</sup>, Nikolai Sobolev<sup>d</sup>, Oliver Picht<sup>e</sup>, Elke Wendler<sup>e</sup>, Werner Wesch<sup>e</sup>

<sup>a</sup> Materialwissenschaftliche Elektronenmikroskopie, Universität Ulm, 89069 Ulm, Germany

<sup>b</sup> Institut für Strukturphysik, Technische Universität Dresden, Dresden, 01069, Germany

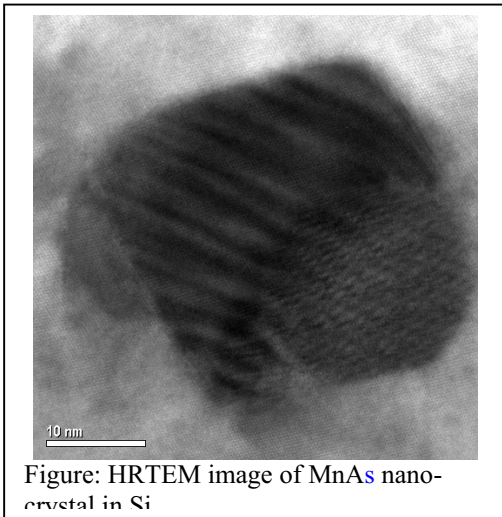
<sup>c</sup> Electron Optics Applications Department, JEOL High-Tech Co Ltd, Tokyo 196-0022, Japan

<sup>d</sup> Departamento de Física, Universidade de Aveiro, 3810-193 Aveiro, Portugal

<sup>e</sup> Institut für Festkörperphysik, Friedrich Schiller Universität Jena, 07407 Jena, Germany

The growth of magnetic nanocrystals inside a semi-conducting matrix is aimed at the development of new devices for data information storage and high sensitive magnetic sensors [1]. As properties of nanostructured materials may differ from their bulk materials in terms of magnetic anisotropy, magneto-resistance, Curie-temperatures and susceptibility [2, 3], careful characterization on the nanometer scale is required. Theoretical studies propose ferromagnetism for transitional metal-doped SiC and Si [4, 5] with impurity concentrations above 3%.

Nanocrystals formed after high-fluence (up to  $10^{17}\text{cm}^{-2}$ ) cobalt ion implantation into 4H-SiC and after co-implantation of high-fluence manganese and arsenic ions into Si followed by rapid thermal annealing (1600°C for SiC, 1300°C for Si) were studied using analytical transmission electron microscopy. High resolution (TEM) and energy filtered (EF)-TEM revealed the nanocrystal shapes, orientations to the matrix, sizes and compositions. Z-Contrast imaging (HAADF) showed the distribution of the nanocrystals within the matrix.



Nanocrystals in SiC are between 20 to 40nm in diameter and are mostly silicides while a few are of pure cobalt. Electron holography using Lorentz microscopy and subsequent electron phase reconstruction showed magnetic single domain cobalt nanocrystals that are randomly oriented at room temperature [6]. Magnetic flux and magnetization of the single particles could be determined.

For the case of co-implantation of Mn and As into Si, HRTEM investigations have shown the formation of two types of nanoclusters: small ones, consisting of two separate phases with a diameter of 10–20 nm and larger ones with a diameter of about 70 nm. Using EFTEM-imaging, the former were shown to consist of Mn and As, whereas the latter contain Mn only. Ferromagnetic resonance (FMR) spectra revealed the existence of

magnetic particles with the hard magnetization axis oriented along the four  $\langle 111 \rangle$  axes of the Si crystal and a smaller anisotropy in the perpendicular plane.

[1] Pokrant S, Herwig C, Hihara T, and Becker J A, *Eur. Phys. Journ.* **D 9** (1996), 509

[2] Leslie-Pelecky D L and Rieke R D, *Chemistry of Materials* **8** (1996), 177

[3] Shi J, Gider S, Babcock K, Awschalom D D, *Metals and Semiconductors Science* **271** (1996), 937

[4] Miao M S and Lambrecht W R L 2003. *Phys Rev B* **68** (2003), 125204

[5] Shaposhnikov V L and Sobolev N A, *J. Phys.: Condens. Matter* **16** (2004), 1

[6] Biskupek J, Kaiser U, Lichte H, Lenk A, Pasold G, Witthuhn W, *Magnetism and Magnetic Materials* 293 (2005) 394

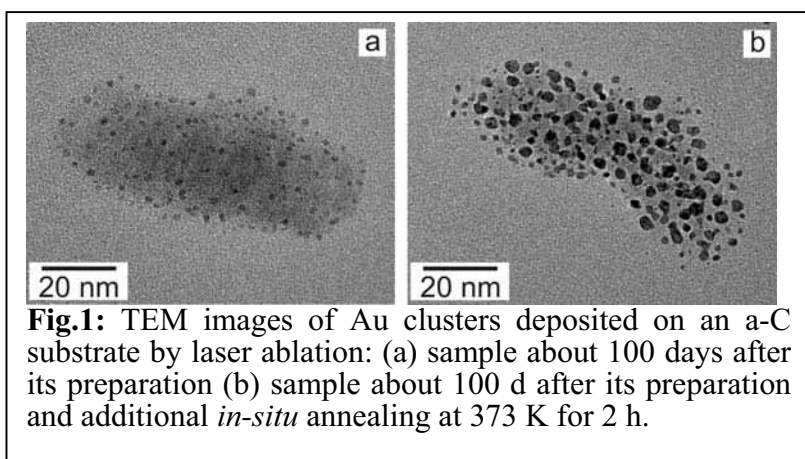
# Dynamics of Gold Clusters on Amorphous Carbon Films Induced by Annealing in a Transmission Electron Microscope

Matthias Wanner<sup>a</sup>, Ralph Werner<sup>b</sup>, and Dagmar Gerthsen<sup>a</sup>

<sup>a</sup>Laboratorium für Elektronenmikroskopie, Universität Karlsruhe (TH), D-76128 Karlsruhe, FRG

<sup>b</sup>Institut für Theorie der Kondensierten Materie, Universität Karlsruhe (TH), D-76128 Karlsruhe, FRG

Investigations concerning the stability of arrays of nanoparticles deposited on a substrate are of considerable interest with regard to potential applications in catalysis, nanoelectronics or nanooptics. In technical applications the temporal behaviour of the particle size distribution and the interaction of particles with a substrate needs to be well understood because it affects the functional properties of the particles. In particular at elevated temperatures, a strong effect on the particle sizes must be expected. In the present work we have studied the change of the size distribution of Au clusters induced by in-situ annealing in a transmission electron microscope.



The primary samples were prepared by depositing Au clusters on amorphous (a)-C films. The Au clusters were collected from the primary beam of a laser vaporization cluster source as outlined in detail elsewhere [1]. Starting from statistically distributed Au clusters, “islands” are formed within a few months after storage at room temperature, which consist of Au clusters with sizes < 4 nm embedded in a thin Au film (Fig.1a) which are described

elsewhere [2]. If the temperature is increased in the transmission electron microscope two different processes can be clearly distinguished that lead to the coarsening of the cluster size distribution (Fig.1b): cluster coalescence and (contact-free) Ostwald ripening. The degree and rate of the coarsening are found to depend on the underlying surface (Au film or amorphous carbon) and the exposure to the high-flux high-energy electron beam, which can be estimated to lead to high-temperature excursions in a cluster on a  $10^{-12}$  sec time scale. The experimental findings are confirmed by Monte-Carlo simulations using the many-body Gupta potentials in order to calculate the Au/Au interaction. Moreover, the results of MC simulations suggest an electron-beam induced formation of a “quasi two-dimensional gas” of small highly mobile Au species on the Au film, which promotes Ostwald-ripening.

## References:

[1] P. Weis, O. Welz, E. Vollmer, M. M. Kappes, J. Chem. Phys. 120 (2004) 677.

[2] W. Werner, M. Wanner, G. Schneider, D. Gerthsen, Phys. Rev. B, accepted.

[3] This work was supported by the Center for Functional Nanostructures (CFN) funded by the Deutsche Forschungsgemeinschaft (DFG).

# Investigation of Mechanisms of Electron Emission from Silver Cluster Films under Laser Excitation by means of Photoemission Electron Microscopy

A. Gloskovskii, D.A. Valdaitsev, M. Cinchetti, S.A. Nepijko, G. Schönhense

Institute of Physics, Johannes Gutenberg University, Staudingerweg 7, D-55128 Mainz, Germany

The irradiation of granular thin metal films (TMFs) by short laser pulses leads to electron emission, although their work function  $\Phi$  is larger than the energy of the exciting quanta. Following [1], in the case of weak optical fields  $\omega \gg eE/\sqrt{2m\Phi}$  multiphoton photoemission is the main emission mechanism and the photocurrent  $j \sim I^n \sim (E^2)^n$ , while in the case of the strong fields  $\omega \ll eE/\sqrt{2m\Phi}$  the optical field mechanism exhibits a  $j \sim E^2 \exp(-a/E)$  dependence. Here  $\omega$  is the frequency of the laser,  $I$  – laser peak intensity,  $E$  – optical field strength,  $m$  and  $e$  are the mass and the charge of the electron,  $n = \Phi/(\hbar\omega + 1)$ ,  $a$  is a constant. Therefore, a transition interval between these mechanisms should be expected at  $E \sim 2.8 \cdot 10^7$  V/cm for bulk silver ( $\Phi=4.8$ eV). In the TMFs the transition can occur at lower powers due to the field enhancement on rough surfaces [2]. FOCUS PEEM [3] was used to visualize the emission from TMFs under fs-laser ( $\lambda=800$  nm) excitation. The wedge-like Ag/Si sample consisting of five 20 $\mu$ m wide Ag stripes with a mass thickness from 0.1 (stripe 1) to 20 nm (stripe 5) and bulk silver was prepared in UHV. An SEM image of the 4<sup>th</sup> and 5<sup>th</sup> stripes that exhibit a much higher photoemission current than the others is shown in Fig. 1. The PEEM image (Fig. 2) shows that the 5<sup>th</sup> stripe emits rather homogeneously, whereas areas with strongly enhanced intensity (hot spots) are seen on the 4<sup>th</sup> stripe. The deviation from the  $j \sim I^n$  dependence for the hot spots and 5<sup>th</sup> stripe starts already at 300mW corresponding to  $E=10^6$  V/cm. Besides, the power law of the hot spot photocurrent is higher than that of the 5<sup>th</sup> stripe. The positive deviation of the  $n$  value may be attributed to a large deviation of the electron gas and the lattice from thermal equilibrium that leads to thermally assisted multiphoton photoemission [4].

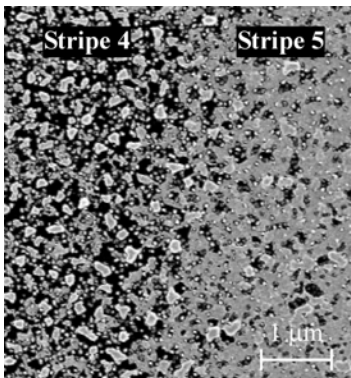


Fig. 1: SEM image of the interface between 4th and 5th stripe (mass thickness 10 and 20 nm respectively).

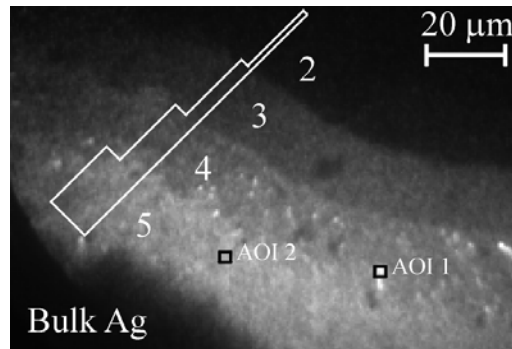


Fig. 2: PEEM image of Ag TMFs (stepped wedge) under fs-laser excitation at 800nm.

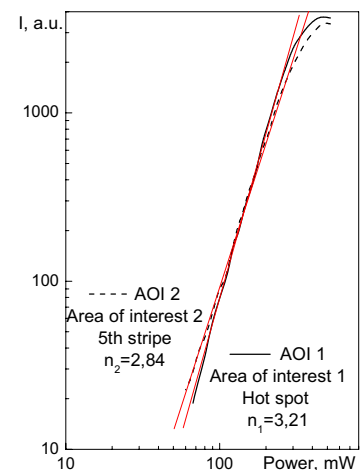


Fig. 3: The dependence of the photocurrent on laser intensity from different areas of interest on SMFs marked in Fig. 2.

- [1] L.V. Keldysh, JETP 20 (1965) 1307
- [2] B. J. Messinger et al., Phys. Rev. B 24 (1981) 649
- [3] C.M. Schneider, G. Schönhense: Rep. Prog. Phys. 65 (2002) R1785
- [4] R. Yen et al., Appl. Phys. Lett. 40 (1982) 185

## Transmission Electron Microscopy Applied To The Characterization Of $Gd_2O_3 : Eu^{3+}$ Nanoparticles Obtained By Spray Pyrolysis

Gómez L. S<sup>a</sup>; Rabanal M.E.<sup>a</sup>; Khalifa A<sup>a</sup>, Torralba JM<sup>a</sup>, Mancic L.<sup>b</sup>, Milosevic O.<sup>b</sup>

<sup>a</sup> Materials Science Department. Universidad Carlos III de Madrid, Avda de la Universidad 30, 28911 Leganés, Madrid, Spain

<sup>b</sup>Institute of Technical Sciences of SASA, K.Mihajlova 35/IV, 11000 Belgrade, Serbia&Montenegro

Gadolinium and europium nitrate solutions (Gd:Eu=0.09:0.01 at%) were ultrasonically aerosolized and fed into a high-temperature (700 °C) tubular flow reactor to control the aerosol decomposition. During the decomposition, the aerosol droplets undergo evaporation/drying, precipitation and thermolysis in a single-step continuous process. Spherical, hollow, agglomerate-free, submicron-sized “secondary” composed of “primary” nanoparticles with the crystallite sizes below 20nm have been obtained. The “as-prepared” sample were additionally thermal treated at high temperature (800, 900 and 1000 °C) during 12h. The nanoparticle morphology, crystalline and chemical structure were studied by XRD, SEM, TEM and EDS.

TEM studies have been applied in order to characterize this system. For that purpose, TEM samples were prepared by ultrasonic dispersion of a small powder portion in acetone and disposing this suspension on a carbon coated cooper grid. The low magnification bright field images (Fig. 1) allowed to identify the structure and growing of primary nanoparticles through the collision/coalescence mechanisms. HRTEM allowed to determine the presence of domains locally affected by Moires Frames (Fig 2 and 3). The crystallite size can be resolved with HRTEM images, as well, showing them the increase with thermal treatment temperature. The selected area electron diffraction patterns allowed to determine the presence of a polycrystalline material with two different phases in as- prepared samples (Fig. 4). The main corresponds to the  $Gd_2O_3 : Eu$  ( $a \sim 10,80\text{\AA}$ ), with symmetry Ia3 (SG =206) and the secondary phase (marked with arrows) corresponds to the faint rings of a  $Gd_2O_3:Eu$  ( $a \sim 5,64\text{\AA}$ ) with symmetry Fm3m (SG= 225). After thermal treatment only the Ia3 phase is present. Image calculation confirms the presence of the Ia3 phase by HRTEM.

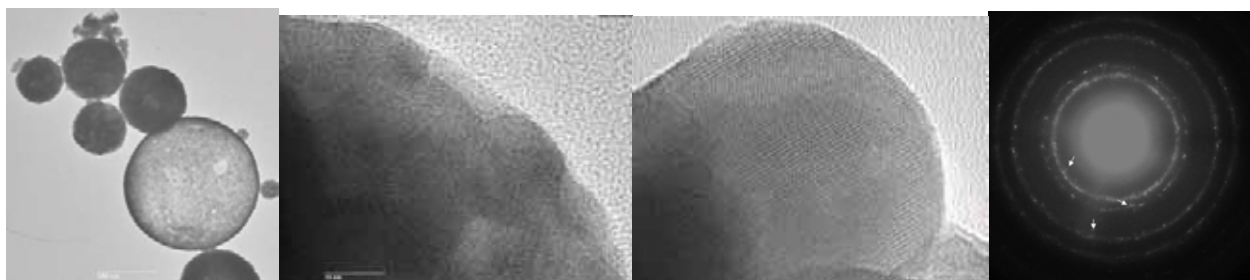


Fig. 1

Fig.2

Fig. 3

Fig.4

## Twin Configuration of Silver Nanoparticles Embedded in Glass

H. Hofmeister<sup>°</sup>, M. Dubiel\*, K.-D. Schicke<sup>°</sup>

<sup>°</sup>Max Planck Institute of Microstructure Physics, Weinberg 2, D-06120 Halle, Germany

\*Physics Department, University of Halle, Friedeman-Bach-Platz 6, D-06099 Halle, Germany

Structural characterisation of silver nanoparticles, embedded in glass by various routes of fabrication, using high resolution electron microscopy was aimed at revealing the specific details of twin faults that turned out to be an essential structural feature. The variety of particle forms, comparable to those supported on oxide carriers, comprises single crystalline particles of nearly cuboctahedron shape, particles containing single twin faults, and multiply twinned particles containing parallel twin lamellae, or cyclic twinned segments arranged around axes of fivefold symmetry.

Nearly spherical silver nanoparticles have been fabricated either by silver/sodium ion exchange or by  $\text{Ag}^+$  ion implantation of commercial soda-lime silicate float glass [1,2]. The glass prepared for electron microscopy by mechanical polishing and ion beam etching has been finally coated by a conducting carbon layer. This way, embedded Ag nanoparticles well below 10 nm size have been obtained where by HREM imaging of lattice plane fringes near Scherzer defocus (JEM 4010, 400 kV) and diffractogram analysis characteristic structural features have been worked out.

Besides single crystalline nanoparticles, above 5 nm size twinned species have frequently been observed for both fabrication routes. Parallel twinning is distinctly favoured by ion implantation whereas cyclic twinning preferably occurs upon ion exchange processing. The more twin planes are involved in the particle composition, the more complicated is the interpretation of lattice fringe patterns due to superposition of several twin segments, except the twin planes have co-zonal orientation and are imaged end-on as shown in Figure 1.

[1] M. Dubiel, S. Brunsch, W. Seifert, H. Hofmeister, G.L. Tan, *Europ. Phys. J. D* 16 (2001) 229.

[2] M. Dubiel, H. Hofmeister, G.L. Tan, K.-D. Schicke, E. Wendler, *Europ. Phys. J. D* 24 (2003) 361.

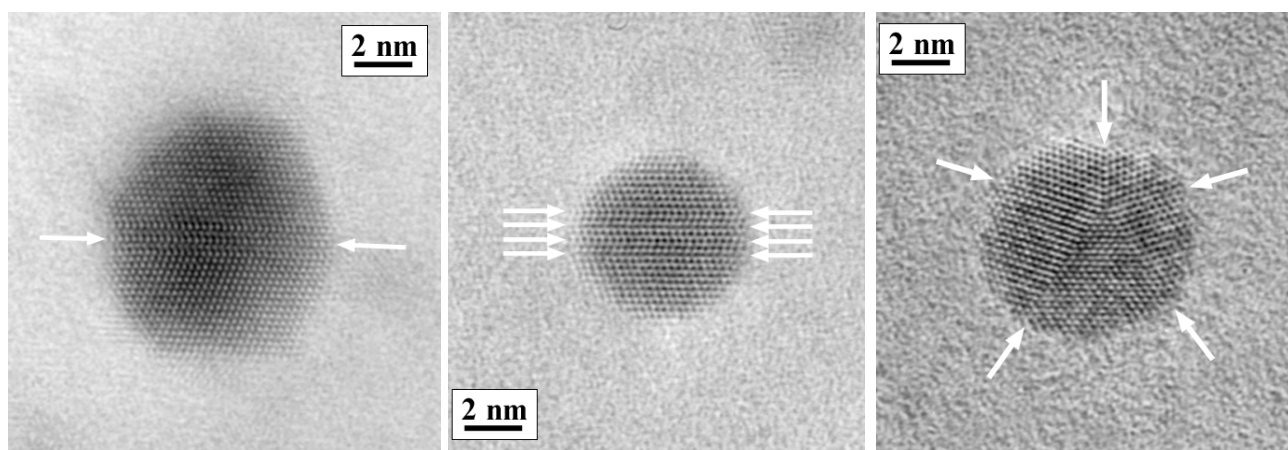


Figure 1: Single twin (left), parallel twin lamella (centre) and cyclic twin segments (right) in Ag nanoparticles of  $\langle 110 \rangle$  orientation. The twin boundaries are marked by arrows.

## Lattice Contraction and Surface Stress of Metal Nanoparticles

H. Hofmeister<sup>°</sup>, P.-T. Miclea\*, M. Steen<sup>°</sup>

<sup>°</sup>Max Planck Institute of Microstructure Physics, Weinberg 2, 06120 Halle

\*I C O P, University of Paderborn, Warburger Str. 100, 33098 Paderborn

Nanoparticles with free surface may exhibit, because of their large surface-to-volume ratio, a considerable lattice contraction caused by the surface stress  $f$ . For spherical fcc metal particles of compressibility  $K$ , the lattice contraction is given by  $\Delta a = -2aKf/3r$  as function of the radius of curvature  $r$ . Thus,  $f$  may be calculated from the size-dependent lattice contraction determined by means of high-resolution electron microscopy (HREM).

Nearly spherical metal nanoparticles have been fabricated on nanosphere silica substrate of nearly uniform size, surface configuration, and shape using a simple impregnation technique [1,2]. The silica spheres coated by metal nanoparticles have been prepared for electron microscopy examination on holey carbon-coated copper grids. This way, Ag and Au nanoparticles of 1 to 10 nm sizes have been obtained on the surfaces of silica nanospheres where by HREM imaging near Scherzer defocus (JEM 4010, 400 kV) the spacings of {111}, {200} and {220} lattice plane fringes could be measured relatively free of deterioration as indicated in Figure 1.

For both metals mainly single crystalline nanoparticles of nearly cuboctahedron shape, 2 to 10 nm in size, have been found. Above 5 nm they frequently contained twin faults. The evaluation of lattice plane spacings revealed a linear relation between lattice contraction and inverse particle radius from which the surface stress was determined to 2.55 N/m for Ag and to 3.88 N/m for Au. Experimental or calculated values reported in the literature for both metals are between 1.18 – 6.4 N/m. Extrapolation to disappearing surface curvature yields lattice spacings deviating less than 1% from the respective bulk value.

[1] H. Hofmeister, P.-T. Miclea, W. Mörke, *Particles & Particle Syst. Charact.* 19 (2002) 359.

[2] P.-T. Miclea, H. Hofmeister, *Mol. Cryst. Liq. Cryst.* 417 (2004) 135

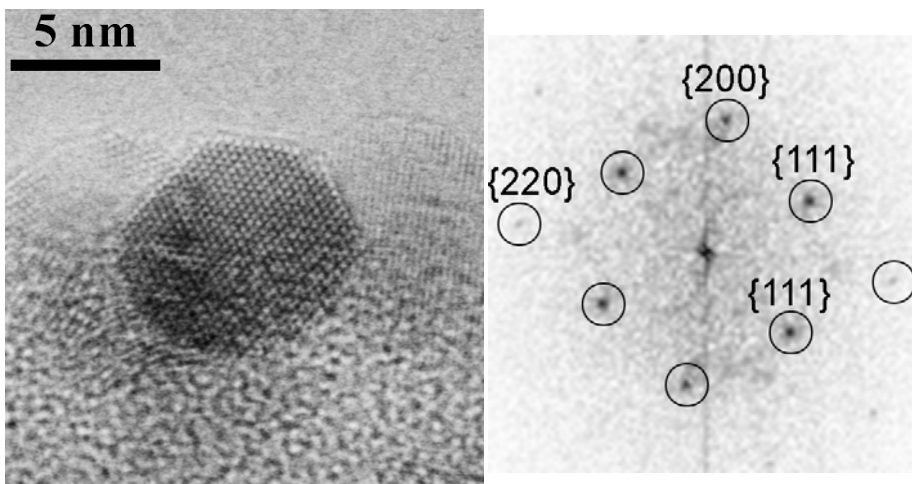


Figure 1: Au nanoparticle in  $\langle 110 \rangle$  orientation on silica nanosphere (HREM image, left) and corresponding diffractogram (right) whose reflections (marked by circles) have been used for measuring of lattice plane spacings in dependence on particle size.

## FIB-Nanotomography: Closing the Gap between Nano- and Microstructural Imaging in 3D-Microscopy

L. Holzer, Ph.Gasser, B. Münch

3D-Mat group, Section 135, Empa Materials Science and Technology, CH-8600 Dübendorf, Switzerland

Three-dimensional (3D) imaging represents the basis for a reliable quantification of granular and porous microstructures. Therefore, the development of high-resolution tomography techniques is of major importance for many materials science disciplines. Nevertheless, there is a remarkable gap in 3D-Microscopy between EM-Tomography, that operates with nm- or molecular-resolution, and conventional tomography, which exhibits resolutions above the  $\mu\text{m}$ -scale.

In this paper, we present a novel serial sectioning procedure for 3D analysis using a dual-beam FIB (focused ion beam) (Holzer et al., 2004), which has the potential to bridge the above mentioned gap in 3D-microscopy. A very narrow and reproducible spacing between the imaging planes is achieved by using drift correction algorithms in the automated slicing procedure. The spacing between the planes is nearly of the same magnitude as the pixel resolution on the SEM-images. Consequently, the acquired stack of images can be transformed directly into a 3D data volume with a voxel resolution of  $6 \times 7 \times 17 \text{ nm}$ . First applications of FIB-nanotomography for the study of porous and granular textures in modern ceramic and cementitious materials are discussed. The computational procedures for quantification are discussed in a separate contribution (Münch et al., 2005).

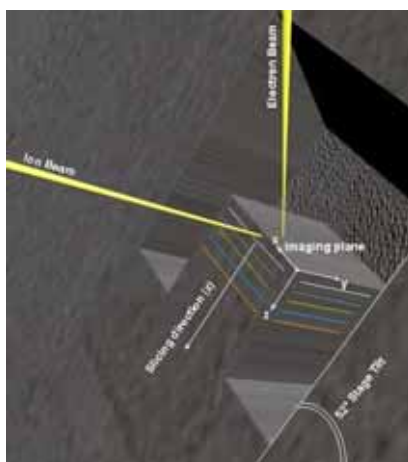


Fig. 1: Geometrical relationships for serial sectioning in dual beam FIB. The imaging plane (x-y) is parallel to the ion beam (y). SE-images are acquired under an angle of  $52^\circ$  using the SEM-column.

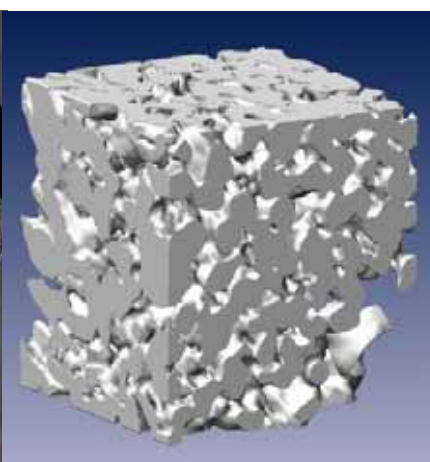


Fig. 2: Surface visualization of a nanoporous BaTiO<sub>3</sub> sample. Cube dimensions:  $1.6 \times 1.8 \times 1.7 \mu\text{m}$   
Voxel resolution:  $6 \times 7 \times 17 \text{ nm}$

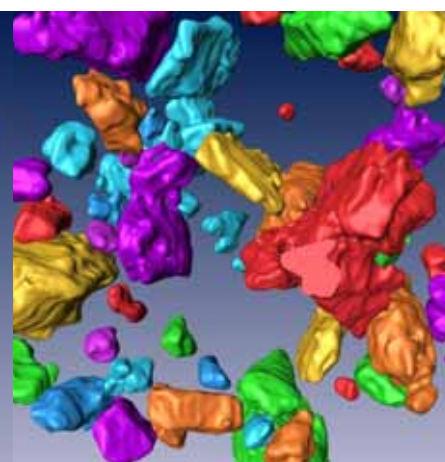


Fig. 3: 3D shape of particles in a cement powder (selected objects)  
Analyzed volume  $21 \times 17 \times 4 \mu\text{m}$   
Voxel resolution:  $30 \times 38 \times 30 \text{ nm}$   
Nr. of particles in volume: 2'439

Holzer, L., Indutnyi, F., Gasser, P., Münch, B. & Wegmann, M., 2004. 3D analysis of porous BaTiO<sub>3</sub> ceramics using FIB nanotomography. *Journal of Microscopy*, **216**(1), 84-95.

Münch, B., Gasser, P. & Holzer, L., 2005. Quantitative particle analysis based on FIB-nanotomography. In: *Microscopy Conference, 6. Dreiländertagung*, pp. this vol., SSOM, Davos, Switzerland.

# High-Resolution TEM Characterization of Precious Metal Nanoparticles Synthesized on Porous Substrates Using Supercritical Carbon Dioxide Approach

Dafei Kang<sup>a</sup>, Ying Zhang<sup>b</sup>, Carl D. Saquing<sup>b</sup>, Can Erkey<sup>b</sup>, and Mark Aindow<sup>a</sup>

<sup>a</sup>Department of Materials Science and Engineering, Institute of Materials Science, University of Connecticut, Storrs, CT 06269, U.S.A.

<sup>b</sup>Department of Chemical Engineering, Environmental Research Institute, University of Connecticut, Storrs, CT 06269, U.S.A.

The synthesis of nanoscale composite materials has gained a great deal of attention due mainly to their unique physical and chemical properties, which render them desirable for an array of potential applications [1-2]. Particularly, metal nanoparticles of uniform and tailorable size and composition incorporated into an appropriate porous support can be used in areas as diverse as catalysis, microelectronics, electrochemistry, and magnetics [3-5]. The special properties exhibited by these materials in such applications show strong dependence on the size, spatial distribution and specific concentration of the metal clusters within the host porous matrix, as well as the properties of the support.

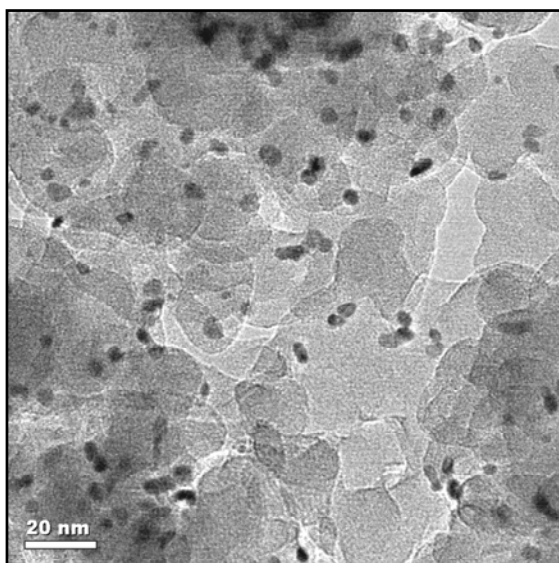


Figure 1. TEM micrograph showing Pt nanoparticles (5.0 wt%) of uniform size dispersed on a silica aerogel substrate.

We present here an HRTEM study of two kinds of precious metal nanoparticles (Pt and Ru) synthesized on two mesoporous host materials (silica aerogel and carbon aerogel, respectively). The metal nanoparticles of various loadings were produced *in-situ* via the thermal reduction of their precursors which were impregnated into the host via a novel supercritical carbon dioxide deposition route. A high-resolution JEOL 2010 FasTEM transmission electron microscope operating at 200kV was used to examine these heterogeneous structures with special attention on the morphology and size of the incorporated metal particles as their loadings were varied. An example is shown in figure 1. Other TEM techniques such as electron diffraction and energy dispersive X-ray spectrometry were also used for the comprehensive characterization of the nanocomposites. The results suggested that the supercritical carbon dioxide method is particularly efficient for the production of metal nanoparticles with very uniform size and high dispersion in porous matrix.

## References:

- [1] J. Aiken, R.G. Finke, *J. Mol. Catal. A—Chem.* (1999) 145.
- [2] C.B. Murray, C.R. Kagan, M.G. Bawendi, *Annu. Rev. Mater. Sci.* 30 (2000) 545.
- [3] A.Y. Stakheev, L.M. Kustov, *Appl. Catal. A* 188 (1999) 3.
- [4] C. Castro, J. Ramos, A. Millan, J. Gonzalez-Calbet, F. Palacio, *Chem. Mater.* 12 (2000) 3861.
- [5] L.L. Beekroft, C.K. Ober, *Chem. Mater.* 9 (1997) 1302.

## Titanium Disulfide Fullerene-like Nanoparticles

Alexander Margolin<sup>#</sup>, Ronit Popovitz-Biro<sup>#</sup>, Ana Albu-Yaron<sup>#</sup>, Alexander Moshkovich\*, Lev Rapoport\* and Reshef Tenne<sup>#</sup>

<sup>#</sup> Department of Materials and Interfaces, Weizmann Institute, Rehovot 76100, Israel

\* Department of Science, Holon Academic Institute of Technology, P.O. Box 305, Holon 58102, Israel

TiS<sub>2</sub> nanoparticles with nested fullerene-like structure, were obtained from the gas-phase reaction of TiCl<sub>4</sub> and H<sub>2</sub>S, using a vertical reactor. TEM, HRTEM and EFTEM were applied for the characterization of the collected product. The product was found to contain high fraction of *IF*-TiS<sub>2</sub> phase (~80%) and a rather narrow size distribution (60-100nm). The observed nanoparticles have no or very small hollow core and consist of 50-90 molecular sheets with quite a perfect spherical shape and low density of defects (Figure 1). A careful inspection of the nanoparticles did not reveal spiral growth mode of the molecular layers but a quasi-epitaxial, layer-by-layer, mode could be deciphered. In several cases the cores of the observed TiS<sub>2</sub> nanoparticles were found to be made of a number of tiny spherical *IF* nucleation centers, which were stacked together and enveloped by the peripheral layers, into a single spherical moiety. The present synthesis of *IF*-TiS<sub>2</sub> may be envisaged as a homogeneous nucleation of the fullerene-like structures from embryonic clusters, formed in the vapor phase, in contrast to the heterogeneous nucleation of *IF*-WS<sub>2</sub> (MoS<sub>2</sub>) on the surfaces of the respective oxide templates[1,2]. Excellent tribological results were obtained when small amounts of the *IF*-TiS<sub>2</sub> nanoparticles were added to a lubricating fluid, suggesting a major role for rolling friction in this case.

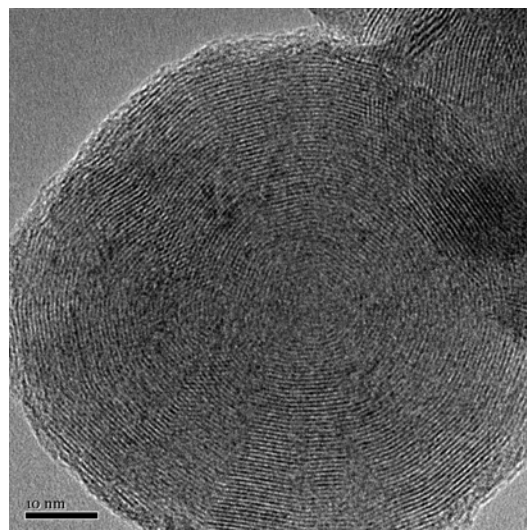


Figure 1. TEM image of a typical *IF*-TiS<sub>2</sub> nanoparticle, produced in a vertical reactor. The interlayer distance is 5.8 Å.

### References

- [1]. Feldman, Y.; Lyakhovitskaya, V.; Tenne, R. *J. Am. Chem. Soc.* **1998**, *120*, 4176.
- [2]. Zak, A.; Feldman, Y.; Alperovich, V.; Rosentsveig, R.; Tenne, R. *J. Am. Chem. Soc.* **2000**, *122*, 11108.

## HRTEM and EELS Investigations on Diesel Engine Soot Nanoparticles

J.-O. Müller, D. S. Su, R. E. Jentoft, R. Schlögl,

Fritz-Haber-Institute of the Max-Planck Society, Department for Inorganic Chemistry, Faradayweg 4-6, 14195 Berlin, Germany

The emitted particulate matter of diesel engines is subject to increasing criticism for being a serious threat to air quality and a potential risk to public health. These particles are widely distributed throughout the troposphere and even the stratosphere. The physical and structural properties of environmental carbons and fine dust particles have been investigated with increasing interest in the recent time. Monitoring the physico-chemical properties of emitted soot particles is of great importance in pollution control [1, 2]. Here we report on the correlation of microstructure and reactivity of soot and carbon black investigated by HRTEM, EELS and TG. The nanostructure of the soot and carbon black depends on their origin and affects the physical and chemical properties. Spherical primary particles consisting of a disordered core embedded in shells of layered graphene systems with radial symmetry are observed. The graphene layers are bent due to incorporation of non-hexagonal defects in the graphite structure. HRTEM images reveal fullerene-like clusters or molecules on the surface of the primary particles (Fig. 1a). EELS measurements (under the so called magic-angle-conditions) of the carbon-K-ionization edge reveal differences in the electronic structure of the particulates due to the hybridization ( $sp^2$  and  $sp^3$ ) of carbon atoms (Fig. 1b). It is observed that different bonding properties of the soot will lead to a different oxidation behavior (Fig. 1c). The correlation of bulk structure and surface reactivity [3] will be presented.

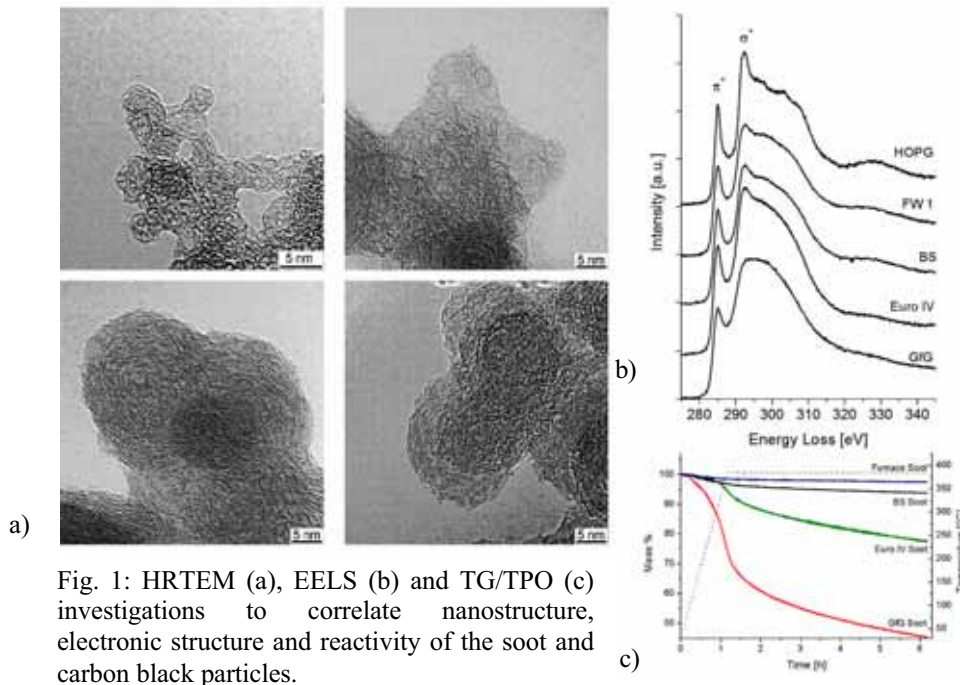


Fig. 1: HRTEM (a), EELS (b) and TG/TPO (c) investigations to correlate nanostructure, electronic structure and reactivity of the soot and carbon black particles.

- [1] D.S. Su, J.-O. Müller, R.E. Jentoft, D. Rothe, E. Jacob, R. Schlögl, *Topics in Catalysis* 30/31(2004) 241
- [2] D.S. Su, R.E. Jentoft, J.-O. Müller, D. Rothe, E. Jacob, C.D. Simpson, Z. Tomovic, K. Müllen, A. Messerer, U. Pöschl, R. Nießner, R. Schlögl, *Catalysis Today* 90 (2004) 127
- [3] J.-O. Müller, D.S. Su, R.E. Jentoft, J. Kröhnert, F.C. Jentoft, R. Schlögl, *Catalysis Today* 102-103 (2005) 259

## Quantitative Particle Analysis Based on FIB-Nanotomography

B. Münch, Ph.Gasser, L.Holzer

3D-Mat group, Section 135, Empa Materials Science and Technology, CH-8600 Dübendorf, Switzerland

Common particle analysis as it is established for the assessment of loose powders from cements and ceramics is usually achieved by particle size analyzers based on laser diffraction (e.g. Malvern Instruments, Beckman Coulter), or by analysis of 2D images from microscopy, alternatively. An outstanding new technique is introduced by the new methodology of FIB nanotomography [1] providing a true 3D approach which enables to measure volumes of a sufficient size for recording and analyzing granular textures at a resolution in the sub- $\mu\text{m}$  range. While common 2D methods suffer from serious constraints by being restricted to projected or cross sectional imaging data only, FIB nanotomography allows to acquire the complete 3D particle shape information.

Providing particle counting statistics from such volumetric data however requires especially adapted evaluation procedures. Tight particle packing is inevitable in order to achieve a sufficiently large particle count from a sample volume of limited extension due to the long data acquisition times of a few hours. In contrast, increasing problems regarding to 3D particle identification and segmentation are encountered and must be overcome by convenient image processing techniques.

Limited sample size moreover intensifies the problem of truncated particles at boundary section planes. The associated flaw of the resulting particle size characteristics is remarkable and requires an appropriate statistical remedy.

The accuracy of such preprocessed particle size distributions is checked by means of numerical modelling and calibrated by assessing monosized spherical  $\text{SiO}_2$  particles with FIB nanotomography.

The novel approach for particle analysis is applied to miscellaneous grain size fractions of ordinary portland cement, which had been separated from the cement powder by air classification. The particle size distributions acquired in such a way are compared with the results from the traditional methods mentioned above.

Though the new methodology shows to be rather time-consuming, the resulting data allow a more objective estimation of the particle size distribution than conventional approaches. Due to its complexity in sample preparation and measuring cost it is not suitable for routine particle analysis processes. Nevertheless, the novel technique holds a big potential of assessing a real 3D insight into morphological details of granular textures in the sub- $\mu\text{m}$  range enabling physical modelling of real particle interaction.

[1] L. Holzer, Ph.Gasser, B. Münch, "FIB nanotomography: filling the gap between molecular- and micrometer-resolution in 3D microscopy", this volume

## Characterization of the Core-Shell Structure in Intermetallic Nanoparticles Extracted from Ni-base Alloys

Giancarlo Pigozzi, Debashis Mukherji, and Gernot Kostorz

ETH Zürich, Institute of Applied Physics, 8093 Zürich, Switzerland

Nanostructured materials, in particular nanoparticles, have attracted recent attention as they are finding applications in chemistry, bio-medicine, electronics and materials engineering. Nanoparticles of nickel aluminides and silicides discussed here are produced by an electrochemical extraction process [1]. Intermetallic-phase precipitates of  $\text{Ni}_3\text{Si}(\text{Al})$  and  $\text{Ni}_3\text{Al}$  in the two-phase Ni-base alloys Ni-13.5Si-2Al and Ni-15.5Al were extracted by selectively dissolving the matrix phase. The precipitate morphology and size (20 to 100 nm) were controlled in the bulk alloy by isothermal aging. The structure of the nanoparticles varies with electrochemical extraction parameters - sometimes a core-shell structure is found (Fig. 1).

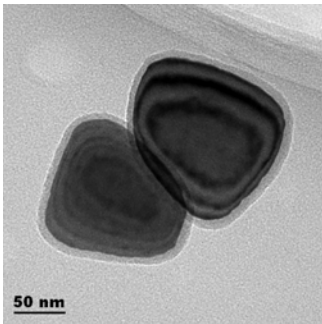


**Fig. 1**

The characterization of the core-shell structure of the nanoparticles is an important issue in order to understand how they are formed and whether they are related to the synthesis process. Extracted particles were analyzed by electron diffraction in a transmission electron microscope. Imaging plates, which allow a large dynamical intensity range to be recorded, were used to record Debye-Scherrer diffraction rings. Energy-dispersive X-ray fluorescence spectroscopy (EDX) in the electron microscope (Fig. 2) was used to analyze the core-shell composition.

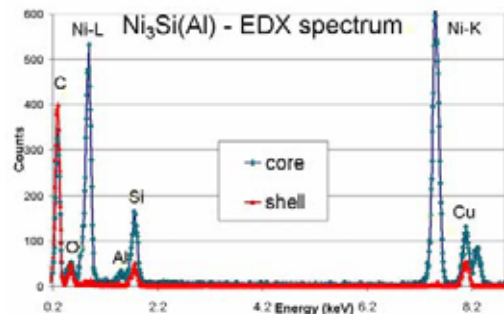


**Fig. 2**

### References:

[1] D Mukherji, R Müller, R Gilles, P Strunz, J Rösler and G Kostorz, *Nanotechnology* **15** (2004) 648.

## **The influence of support materials on the morphology and properties of Pt-Sn containing catalysts**

M.-M. Pohl, J. Radnik, D.-L. Hoang, S. Farrage, H. Lieske, D. Herein, U. Dingerdissen

Institut für Angewandte Chemie Berlin-Adlershof e.V.,  
Richard-Willstätter-Str.12, 12489 Berlin, Germany

The support materials strongly influence the size, shape, structure, composition and catalytic properties of bimetallic particles. It was the aim of this study to get a better understanding of these effects. Therefore the behaviour of Pt-Sn particles on  $\text{Al}_2\text{O}_3$ ,  $\text{MgO}$ ,  $\text{ZrO}_2$  and  $\text{MgO/ZrO}_2$  before and after reduction were studied by TEM, XRD and XPS.

The supports were calcined at  $500^\circ\text{C}$ , impregnated with  $\text{H}_2\text{PtCl}_6$  and  $\text{SnCl}_2$  followed by a second calcination step at  $500^\circ\text{C}$ .

By TEM it was found that the metal arrangement on the surface is influenced both by the support and the pretreatment. On Alumina after calcination Pt and  $\text{SnO}_2$  is found separated but in close position. Reduction leads to alloying with  $\text{PtSn}_2$  phases which could be detected by EDX and high resolution. For  $\text{ZrO}_2$  supports no evidence for either Sn or Pt containing particles was found. The metals were found by EDX as traces on the surface. Reduction did not change the morphology.

$\text{MgO}$  leads to small particles in the range of 1 to 2 nm. After reduction the particle size increases up to slightly. Due to the particle size it was impossible to analyze single particles by EDX.

The  $\text{MgO/ZrO}_2$  support mainly consists of  $\text{Mg}_2\text{Zr}_5\text{O}_{12}$  and some remaining  $\text{MgO}$ . The mixed oxide phase showed as  $\text{ZrO}_2$  no evidence for particles but continuously traces of Sn and Pt while on the minor  $\text{MgO}$  phase after reduction clearly alloyed Pt/Sn particles were found.

Additional XPS measurements were carried out. There were found significant differences for the reducibility of Pt and Sn depending of the support. While on  $\text{Al}_2\text{O}_3$  for Pt and Sn reduction was found, Zr containing supports only reduce Pt. On  $\text{MgO}$  no complete reduction was found.

This study shows clearly the influences of the oxidic support material on morphology and reduction behaviour of metal particle containing catalysts. This can be the explanation for the differences of the catalytic activity of these catalysts.

### **Acknowledgement:**

The financial support by the Federal Ministry for Education and Research of the Federal Republic of Germany, the EU and the federal state of Berlin is gratefully acknowledged.

## Gold nanoparticles – synthesis, characterization and influence of various additives on their size and shape

Katharina Riegler<sup>a</sup>, Michael Rogers<sup>a</sup>, Bernhard Schaffer<sup>a</sup>, Gerald Kothleitner<sup>a</sup>, Ferdinand Hofer<sup>a</sup>

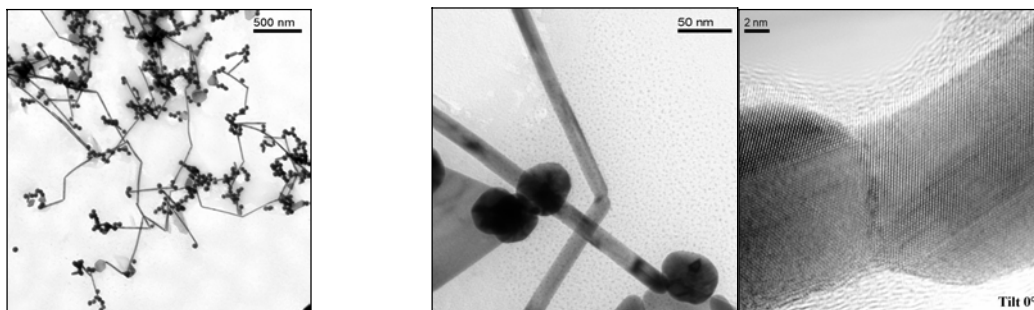
<sup>a</sup>Institute for Electron Microscopy, Graz University of Technology, Steyrergasse 17, 8010 Graz, Austria

In the synthesis of metal nanoparticles the control over the shape and the size is one of the most important tasks, since almost every property within the nanometer size regime is size and shape dependent. Hence, the particle formation control is the most important step in designing new materials with tailored properties.

This work focuses on the fabrication of gold nanoparticles (nanorods, nanoprisms, nanospheres) by wet-chemical synthesis. In particular, the influence of changes in the reaction conditions of common preparation methods like the reduction of  $\text{HAuCl}_4$  in a boiling sodium citrate solution [1] or the seed mediated growth method [2] was investigated.

In the seed mediated growth method, nanorods of uniform size and shape were synthesized in the presence of rod-like micellar templates. The dependence of the gold nanorod's diameter on the nature of the used surfactant and the effect of the electrolyte sodium chloride on the aqueous micellar solution was investigated.

The presence of  $\text{NaCl}$  in the preparation of gold nanorods with the surfactant CTAB modified the self-assembly of the nanorods. At a specific concentration, the nanorods were not only aligned head-to-head to each other, but had indeed grown together and thus formed a network-like structure.



TEM and HRTEM images showing gold nanorods synthesized in the presence of  $\text{NaCl}$

The synthesis of gold nanoparticles by the reduction of a  $\text{HAuCl}_4$  solution using sodium citrate as reducing agent was studied in terms of the addition of different additives and the influence of the reaction rate on the size and shape distribution profile of the produced nanoparticles.

The nanoparticles were characterized via TEM, EFTEM, HRTEM, SAED and SEM, which enabled a rapid and efficient investigation and provided the background for a detailed study of the structure and morphology of the gold particles.

### References:

- [1] Turkevich J., Stevenson P.C., Hillier J., Discuss. Faraday Soc. (1951) **11** 55
- [2] Murphy C.J., Jana N.R, Adv. Mater. (2002) **14** 80-82
- [3] The authors thank the “Sonderforschungsbereich Elektroaktive Stoffe” for financial support

# Mesoporous Pure and Cr-doped WO<sub>3</sub> Synthesized by Hard SiO<sub>2</sub> Templates For Gas Sensing: image simulation and 3D reconstruction

Emma Rossinyol<sup>a</sup>, Jordi Arbiol<sup>a</sup>, Andreu Marsal<sup>a</sup>, Francesca Peiró<sup>a</sup>, Albert Cornet<sup>a</sup>, Joan Ramon Morante<sup>a</sup>, Bozhi Tian<sup>b</sup>, Dongyuan Zhao<sup>b</sup>.

<sup>a</sup>Electronics Department, University of Barcelona, C/ Marti Franques 1, Barcelona 08028, Spain

<sup>b</sup>Molecular Catalysis and Innovative Materials Laboratory, Department of Chemistry, Fudan University, Shanghai 200433, China

Nanostructured mesoporous materials present a large and controllable pore size and high surface area. These properties are the most important to tailor the sensitivity of a semiconductor oxide to be used as gas sensor, offering simple implementation, low cost and good reliability for real-time

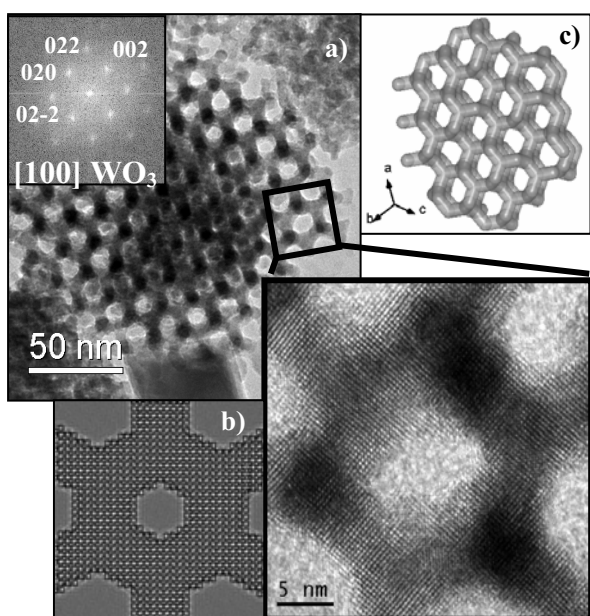


**Fig. 1:** HREM image of mesoporous WO<sub>3</sub> (a) and image simulation (b) according to a Ia3D cubic structure (c).

control systems in front of other gas sensor devices. For the preparation of ordered nanostructured oxides arrays, a hard template method has been used, with mesoporous SiO<sub>2</sub> as template [1]. In the present work we focus our attention to HRTEM characterisation of nanostructured WO<sub>3</sub>, widely used for the detection of NO<sub>2</sub>, important for monitoring environmental pollution resulting from combustion or automotive emissions. Crystalline mesoporous WO<sub>3</sub> has been obtained from both SBA-15 (2D hexagonal structure) and KIT-6 (3D cubic structure) templates, with a particle size about 8-10 nm and high surface area. The nanoparticles observed in SBA-15 replica, are randomly oriented in the mesostructured framework. The presence of a mixture of monoclinic and triclinic phases and the existence of typical undisplaced, displaced and uncoupled domains for KIT-6 replica are discussed in view of TEM, XRD and Raman [2]. TEM BF images of a WO<sub>3</sub> gyroidal aggregate have been obtained at large tilt angle range, from 60° to -60°, with every 2D TEM micrograph acting as a projection slice for a final 3D reconstruction [3]. Atomic modeling and image simulation (EMS software) have been also accomplished. Finally electrical characterization of the sensor response in front of different gases has been performed and Cr has been added as a catalytic additive in order to increase the sensitivity of the material to NO<sub>2</sub>.

## References:

- [1] E. Rossinyol, J. Arbiol, A. Marsal, F. Peiró, F. A. Cornet, J.R. Morante, B. Tian and D. Zhao, Proceedings of the SPIE Conference 5838, Sevilla (2005), to be published
- [2] L. Solovyov, V. I. Zaikovskii, et al., J. Phys. Chem B **106**, (2002)12198-12202
- [3] 3-D animation: [http://nun97.el.uib.es/~arbiol/discdos/nanopart/web/Tomo/Model\\_2.html](http://nun97.el.uib.es/~arbiol/discdos/nanopart/web/Tomo/Model_2.html)

## Structural Investigations of Silver Nanowires by HRTEM and SAED

H. Sauer<sup>a</sup>, L. Chen<sup>b</sup>, X. Bao<sup>b</sup> and D.S.Su<sup>a</sup>

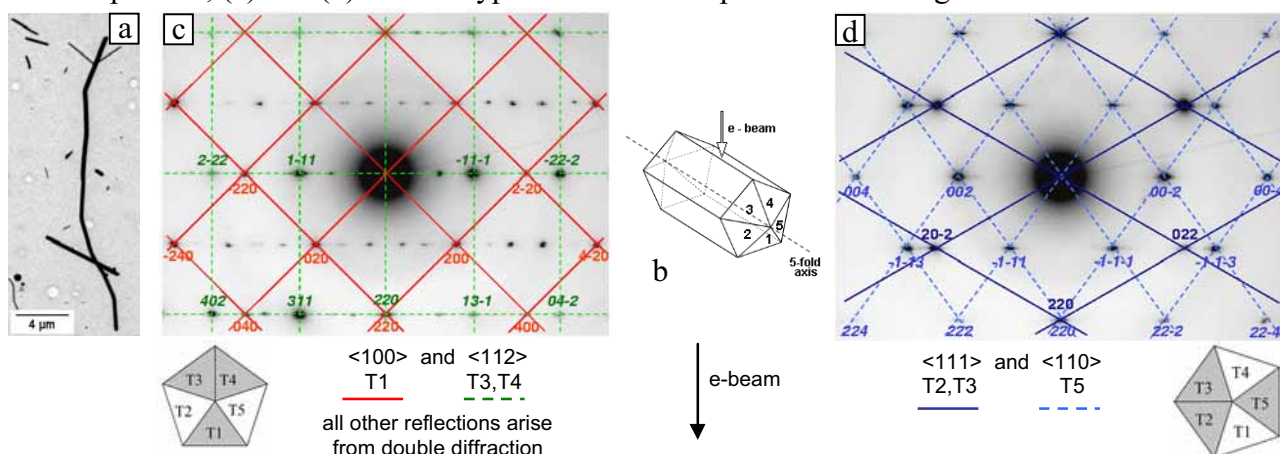
<sup>a</sup>Inorganic Chemistry, Fritz-Haber-Institute (Max-Planck-Society), D-14195 Berlin, Germany

<sup>b</sup>Dalian Institute of Chemical Physics, Chinese Academy of Sciences, 116023 Dalian, P.R.China

Silver nanowires with diameters of 60 - 300 nm and lengths of up to 20  $\mu\text{m}$  (Fig.1a) were prepared via a two step solution-phase method [1]. In the first step silver nitrate is reduced with ethylene glycol which acts as both solvent and reducing agent. The silver nanoparticles formed at this initial stage serve as seeds for the subsequent growth of wire-like Ag structures during simultaneous addition of further  $\text{AgNO}_3$ /ethylene glycol- and PVP/ethylene glycol solution in a second step. The PVP (poly vinyl pyrrolidone) probably controls the growth rates of different crystallographic faces and directs the evolution of wires and rods. The nanowires are coated with a carbonaceous layer with a thickness of 1-3 nm.

HRTEM imaging and SAED showed two different characteristic patterns which could not be explained by a single crystalline structure. They are consistent with the structure of truncated decahedra [2]. These penta-twinned structures consist of five distorted tetrahedral subunits T1-T5 arranged around the common, elongated  $[110]$  fivefold axis, giving rise to five  $\{111\}$  twin boundaries (Fig.1b). Rotation about the longitudinal axis of a wire by means of the tilting stage of the microscope revealed that these two characteristic images and/or diffraction patterns (Fig.1c, d) both had a rotational periodicity of  $36^\circ$  and were separated by a rotation angle of  $18^\circ$  from each other, making the determination of the structure unambiguous. For both orientations of the nanowire with respect to the electron beam the different tetrahedral subunits from which the diffraction spots originate are indicated.

Fig.1 (a) Image of a long Ag nanowire and some nanorods, (b) schematic drawing of a pentagonal rod-like particle, (c) and (d) the two types of diffraction patterns of the Ag nanowires.



### References:

- [1] Y. Sun and Y. Xia, *Adv. Materials* **14** (2002) 833
- [2] I. Lisiecki et al, *Phys. Rev. B* **61** (2000) 4968

## Combined TEM and *in situ* EXAFS Investigations of Ag Nanoparticles in Glass

Reinhard Schneider<sup>a,b</sup>, Manfred Dubiel<sup>a</sup>, Herbert Hofmeister<sup>b</sup>, and Klaus-Dieter Schicke<sup>b</sup>

<sup>a</sup>Martin Luther University Halle-Wittenberg, Department of Physics, D-06108 Halle, Germany

<sup>b</sup>Max Planck Institute of Microstructure Physics, D-06120 Halle, Germany

Glasses with embedded metal nanoparticles are of interest because of their specific optical properties that can be adjusted through the average particle size and the size distribution. An Ag particle/glass composite was produced by ion exchange of soda-lime glass (about 150  $\mu\text{m}$  thick, 1.8 %  $\text{Fe}_2\text{O}_3$ ) in a  $\text{NaNO}_3/\text{AgNO}_3$  (0.05 %) melt at 330  $^\circ\text{C}$  for 195 h [1]. Generally, the generation of Ag particles results from the reduction of ionic  $\text{Ag}^+$  by  $\text{Fe}^{2+}$  ions, subsequent diffusion of silver atoms, their nucleation, and growth. In order to get a deeper insight into these elementary processes of particle generation *in situ* EXAFS experiments (Ag-K edge at 25.514 keV, beamline X1 at HASYLAB) were performed at 550  $^\circ\text{C}$  for 8 h, where significant structural changes could be observed after heat treatment (cf. Fig. 1c).

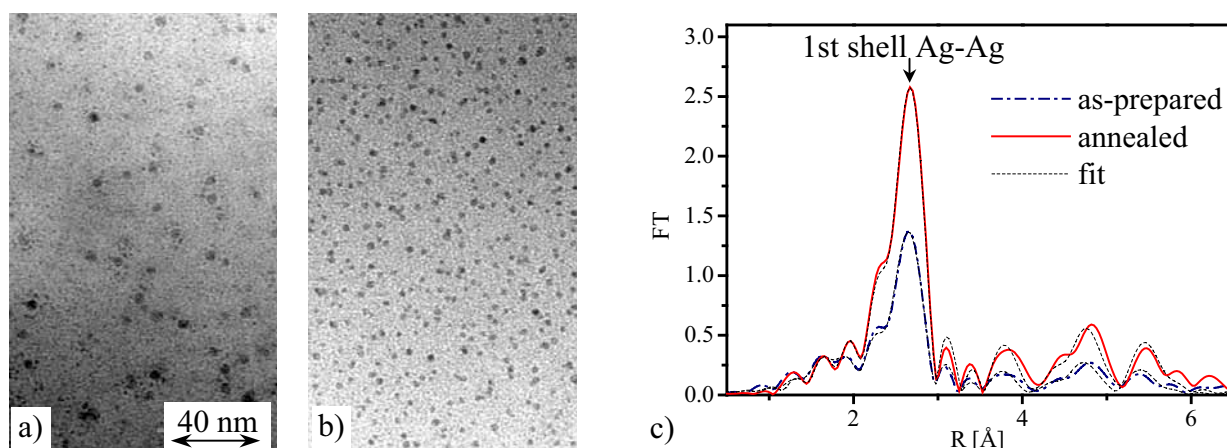


Fig. 1. TEM BF images of the a) as-prepared sample, b) the annealed one, and c) Fourier transforms of EXAFS oscillations obtained at 10 K and corresponding fits.

In detail, in the as-prepared sample (A) the nearest Ag-Ag distance  $R$  amounts to 2.8541  $\text{\AA}$  at 10 K, the coordination number  $N_{\text{Ag-Ag}}$  is about 3.1 and the Debye-Waller factor is 0.0037  $\text{\AA}^2$  (respective values of bulk silver are:  $R = 2.8753 \text{\AA}$ ,  $N_{\text{Ag-Ag}} = 12$ ,  $DW = 0.0027 \text{\AA}^2$ ). After 8 h heat treatment the parameters of the composite have changed to  $R = 2.8784 \text{\AA}$ ,  $N_{\text{Ag-Ag}} = 5.6$ , and  $DW = 0.0034 \text{\AA}^2$ , indicating a more distinct Ag-Ag neighbourhood. These findings are conform with those of TEM inspections (200 kV TEM Philips CM 20 FEG) exhibiting an increased number of Ag particles after annealing (B). Typical results of particle size (A: 1.5-6.5 nm; B: 1.5-5 nm), its distribution, and the area density (A:  $4.8 \cdot 10^{15} \text{ m}^{-2}$ ; B:  $1.6 \cdot 10^{16} \text{ m}^{-2}$ ) can be retrieved from the TEM cross-section images (Figs. 1a,b), showing in each case regions near the glass surface. Obviously, the thermal treatment predominantly promoted nucleation processes, thus leading to an increase of the number of particles. Furthermore, the decreased maximum particle size after heating hints to structural rearrangements.

[1] The funding of this project by the DFG in the SFB 418 is gratefully acknowledged.

## **Pt/C catalysts for the oxygen reduction reaction: Correlation of carbon support morphology and catalytic activity**

B. Tesche, B. Spliethoff, H. Schulenburg and M. T. Reetz

Max-Planck-Institut für Kohlenforschung, Kaiser-Wilhelm-Platz 1, D-45470 Mülheim an der Ruhr, BRD

### **Introduction:**

A great deal of recent research has centered around the preparation of nanosized transition metal colloids in the zero-valent state for fuel cells. The most common methods involve the reduction of appropriate metal salts in the presence of stabilizers which prevent undesired formation of insoluble bulk metal. Less is known concerning the respective metal oxides in the form of nanosized particles.

### **Results:**

We showed that the synthesis of carbon supported platinum oxide and platinum alloys is possible without stabilizing surfactants if the hydrolysis is carried out in presence of carbon black (instant-method). A number of such materials were prepared, including PtO<sub>2</sub>/C which was reduced to Pt/C. In polymer electrolyte membrane fuel cells (PEMFCs) carbon supported platinum catalysts are used as catalysts for oxygen reduction. For that application it is desirable to possess Pt/C or Pt-alloy/C catalysts with high metal loadings and small particle sizes so that high current densities and low platinum costs for the fuel cells can be achieved. Following immobilization using the instant method, the materials were tested as electrocatalysts. The electrocatalyst derived from Printex XE2 turned out to be exceptionally active. Detailed HRTEM and HRSEM studies showed that the unloaded supports are very different, Vulcan XC72 has a smooth surface, while Printex XE2 is characterized by a rough surface. Moreover, under operating conditions the Pt-nanoparticles agglomerate significantly more in the case of Vulcan XC72, in contrast to the electrocatalyst derived from Printex XE2. Thus rough surfaces prevent extensive undesired Pt-particle growth.

### **Conclusion:**

Our studies show that variation in the type of carbon black used in the immobilization of Pt-nanoparticles has a profound influence on the ease of Pt-loading and on the respective electrocatalytic properties [1].

[1] M.T. Reetz, H. Schulenburg, M. Lopez, B. Spliethoff and B. Tesche, *Chimia* **2004**, 58, No. 12, 896-899

# TEM Imaging of Neutron Irradiation Induced Pinning Defects in MgB<sub>2</sub> Single Crystals

B. Birajdar<sup>a</sup>, M. Eisterer<sup>b</sup>, J. Karpinski<sup>c</sup>, H. W. Weber<sup>b</sup>, and O. Eibl<sup>a</sup>

<sup>a</sup> Institute of Applied Physics, University of Tübingen, Auf der Morgenstelle 10, D-72076 Tübingen, Germany

<sup>b</sup> Atomic Institute of the Austrian Universities, 1020 Vienna, Austria

<sup>c</sup> Solid State Physics Laboratory, ETH-Zurich, Switzerland

MgB<sub>2</sub> single crystals with a superconducting transition temperature ( $T_c$ ) of 38.3 K were irradiated by thermal neutrons (energy  $<0.55$  eV) with a fluence of  $4 \times 10^{20} \text{ m}^{-2}$ . As a consequence  $T_c$  decreased to 35.0 K while superconducting transition width ( $\Delta T_c$ ) was doubled.

The effect of thermal neutron irradiation on the microstructure of MgB<sub>2</sub> single crystals is studied using a LEO 912 TEM equipped with an Omega spectrometer. The crystals were crushed in ethanol and the tiny crystallites suspended on a carbon foil. TEM bright and dark-field images of thermal neutron irradiated crystallites, were acquired under two beam conditions

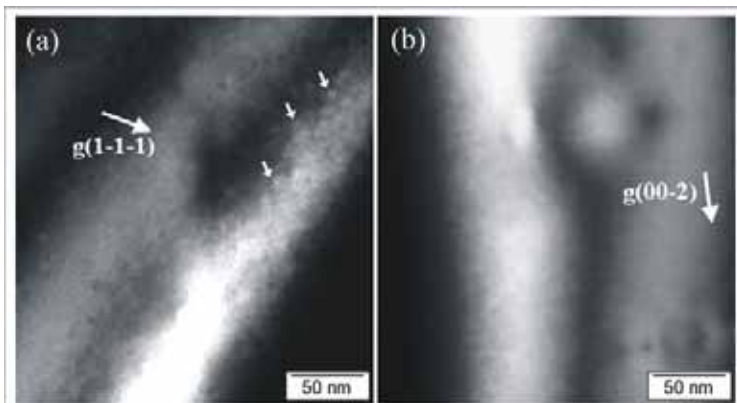


Fig. 1 : TEM dark field images of thermal neutron irradiated (a) & non-irradiated (b) MgB<sub>2</sub> crystallites, under two-beam conditions.

using an energy slit aperture of width 20 eV to filter the elastically scattered electrons. Defects, (indicated by arrows) of size less than 7.5 nm are seen superimposed to the contrast of the thickness fringes in dark field image of thermal neutron irradiated crystallites (Fig. 1(a)), while no such defects are seen in the dark field-images of the non-irradiated crystallites (Fig. 1(b)). The defects show a weak diffraction contrast because of the relatively large

extinction distances of Bragg reflections in MgB<sub>2</sub> and the  $1/r^3$  dependence of strain fields of small defects. Only  $\{0\ 0\ 2\}$ ,  $\{1\ 1\ 0\}$  and  $\{1\ 0\ 1\}$  Bragg reflections which have small extinction lengths yielded sufficient contrast in the images. The density of visible defects was inhomogeneous and varied between  $\sim 10^{16}$  to  $0 \text{ cm}^{-3}$  for different thermal neutron irradiated crystallites which explains the increase in  $\Delta T_c$  of thermal neutron irradiated crystals. These visible defects might be formed by clustering of point defects produced by thermal neutron capture reaction. Their size is comparable to the coherence length of MgB<sub>2</sub> ( $\sim 5$  nm) and can effectively pin the magnetic vortices, and thus enhance the critical current density.

In addition, long straight dislocations are found in the basal plane with line vector  $\langle 100 \rangle$ . The Burgers vector of these dislocations was found to be  $\langle 100 \rangle$ .

# HRTEM Investigation of GdScO<sub>3</sub>/BaTiO<sub>3</sub> Multilayer

M. Boese<sup>a</sup>, M. Luysberg<sup>a</sup>, J. Schubert<sup>b</sup> and T. Heeg<sup>b</sup>

<sup>a</sup>Ernst Ruska-Centrum für Mikroskopie und Spektroskopie mit Elektronen / Institut für Festkörperforschung, Forschungszentrum Jülich, D-52425 Jülich, Germany

<sup>b</sup>Institut für Schichten und Grenzflächen ISG 1-IT and CNI, Forschungszentrum Jülich

The properties of thin epitaxial perovskite films can differ from corresponding bulk properties owing to the presence of lattice strain at the film interfaces. We used aberration corrected HRTEM to achieve a high accuracy in the determination of the orientational relationship and the measurement of strain for thin perovskite multilayers of BaTiO<sub>3</sub> and GdScO<sub>3</sub>, where the nominal lattice parameters are affected in a pm range. The BaTiO<sub>3</sub> and GdScO<sub>3</sub> multilayers were deposited on SrRuO<sub>3</sub>/SrTiO<sub>3</sub> (100) by pulsed laser deposition. The HRTEM investigation was carried out in the 200 kV Cs corrected microscope in Jülich [1]. For the quantification, we used the phase of the exit plane wave function (EPWF), reconstructed from focus series [2,3]. A numerical fine tuning of the EPWF was applied to reduce the residual point-spread due to parasitic two-fold astigmatism and axial coma in the experiment. The phase of the aberration corrected EPWF is shown in Fig. 1. The zone axis of the scandate layer could be identified by comparison of the simulated and the reconstructed phase. Due to the tilting of the ScO<sub>6</sub> octahedra in the orthorhombic structure of GdScO<sub>3</sub> (space group Pnma) the O and Gd atoms are shifted from their positions compared to the BaTiO<sub>3</sub> atomic columns. Fig. 1 shows a [010] zone axis. The orientation relationship referring to the SrTiO<sub>3</sub> substrate is [010]GSO || [010]STO and [101]GSO || [001]STO. Different zone axes were found in the multilayer. The other observed orientation relationship is a in plane 90 degrees rotation: [10-1]GSO || [010]STO and [010]GSO || [001]STO. Not observed is the (010) plane of GSO parallel to (100) STO. This is caused by a bad lattice coincidence of the distorted scandate lattice and the titanate. The phase analysis of the complex-valued Fourier amplitudes belonging to the in-plane lattice planes (analogous to the geometrical phase analysis in ref. [4]) shows a 4 pm smaller lattice parameter of the scandate {101} planes compared to the titanate. The introduction of different layer orientations is assumed to be responsible for lattice relaxation in the multilayered stack.

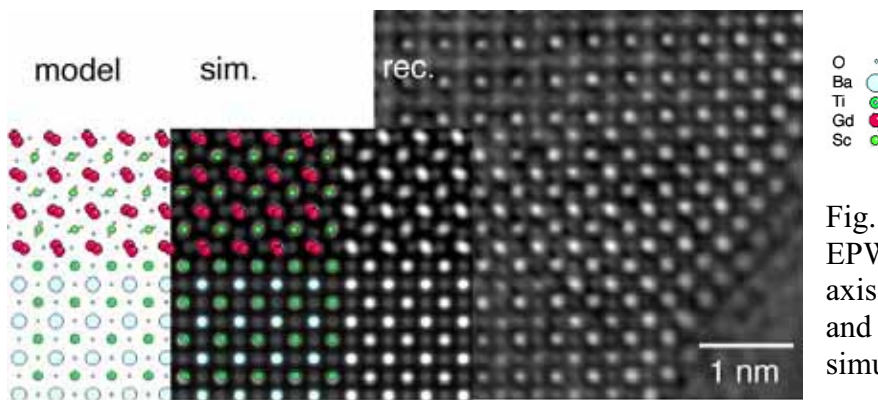


Fig. 1: Reconstructed phase of the EPWF, Scandate layer in [010] zone axis between two titanate layers (top and bottom), with atomic model and simulated phase

- [1] M. Lentzen, B. Jahn, C.L. Jia, K. Tillmann, K. Urban, Ultramicroscopy 92 (2002), 233-242
- [2] W. Coene, A. Thust, M. Op de Beeck, D. Van Dyck, Ultramicroscopy 64 (1996), 109-135
- [3] A. Thust, W. Coene, M. Op de Beeck, D. Van Dyck, Ultramicroscopy 64 (1996), 211-230
- [4] M.J. Hytch, E. Snoeck, R. Kilaas, Ultramicroscopy 74 (1998), 131-146

## FIB-Structuring of Photonic Elements

Victor Callegari, Philipp M. Nellen, Rolf Brönnimann, Urs Sennhauser

Empa, Swiss Federal Laboratories for Materials Testing and Research,  
Electronics/Metrology Laboratory, Dübendorf, CH-8600 Switzerland  
Phone: +41 – 44 – 823 4874 E-mail: [victor.callegari@empa.ch](mailto:victor.callegari@empa.ch)

The purpose of this work is to design and FIB-mill Fresnel lenses with the highest possible precision with regard to the initial design. We adapt a sophisticated scanning strategy which is the result of a computer simulation. This results in a controllable, reproducible physical sputtering process using the focused ion beam.

Investigations showed that different beam scanning strategies yield completely different shapes of milled structures. These shapes can differ significantly from the design. Beyond a material-dependent threshold, the sputtered depth becomes nonlinear with respect to the ion dose. Nonlinear behavior is due to redeposition of sputtered material and reflection of ions impinging with grazing angles of incidence [1]. These phenomena occur especially in high aspect ratio structures.

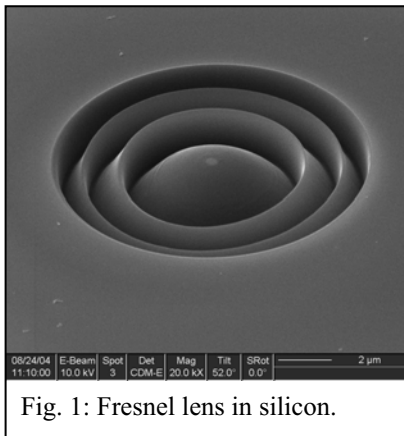


Fig. 1: Fresnel lens in silicon.

Fresnel lenses were milled on glass fiber tips for direct use and on silicon to be used as a print master (Fig. 1). Significant improvement over prior results [2] is obtained. Depths of 2  $\mu\text{m}$  are easily achieved in silicon with good agreement between design and final lens-shape. Redeposition is controlled with the new scanning technique (Fig. 2). Problems that need to be addressed are the shape of the outer part of the lens, which is concave rather than convex (Fig. 2). This is due to the angle-dependent sputtering yield.

While the majority of ions is contained within one or two central Gaussians, a non-negligible quantity of ions is contained in the beam skirts. These decrease only exponentially with distance from the beam center, resulting in non-negligible overlaps of the ion dose distributions. The increased ion dose mills away the sharp peaks, which are thus truncated with respect to the design (Fig. 2).

Our further investigations focus on improving the sputtering simulation to obtain a better milling strategy and thus sharper peaks. Gas-enhanced etching will increase the milling-speed.

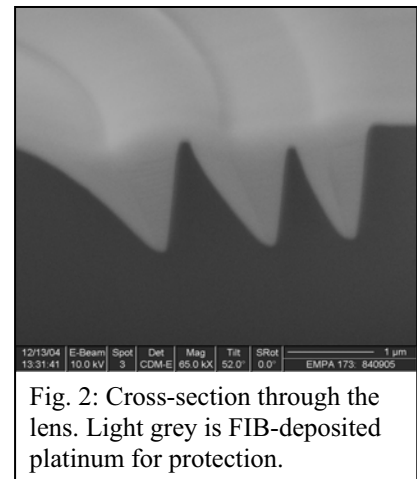


Fig. 2: Cross-section through the lens. Light grey is FIB-deposited platinum for protection.

### References:

- [1] H. Yamaguchi, A. Shimase, S. Haraichi and T. Miyauchi, J. Vac. Sci. Technol. B 3 (1) (1985), 71-74
- [2] Yongqi F., Ngoi K. A. B., Ong N. S., Microelectronic Engineering 54 (2000) 287-293

**Cr particle refinement in Cu alloy by ECAP**  
**M.Dadras<sup>(1)</sup>, N. Golay<sup>(1)</sup>, E.Vincent<sup>(2)</sup> and N.F.de Rooij<sup>(1)</sup>**

1- Service for microscopy and Nanoscopy, Institute of Microtechnology,  
University of Neuchatel, Jaquet-Droz 1, 2007 Neuchatel, Switzerland.

2- Swissmetal Boillat, 2732 Reconvillier, Switzerland

**Abstract-**

*Cu-Cr alloy deformed by Equal Channel Angular Pressing (ECAP). Cr presents very low solubility in Cu. Microstructural heterogeneity after ECAP in the studied sample. Cr having dendrite structure in as received material becomes filamentary after three passes. In maximum deformed region of the sample the Cr filament having the size of about 20nm obtained.*

**Introduction:**

Equal Channel Angular Pressing (ECAP) permits to obtain ultra fine grain and improving the mechanical properties. One of the advantageous of this method is to refining the microstructure without limitation of starting microstructure size in comparison with classical methods such as drawing and rolling. Deformation plane and direction is different in FCC structure in comparison with BCC structure. During deformation, the presence of different crystallography structure influence refinement of microstructure.

**Material and Procedure:**

The sample used for pressing is Cu-Cr alloy. The die has “L” shaped channel with inner angle of intersection of channel at 90°. The microstructural evolution and texture analysis is studied by using SEM, TEM and AFM and EBSD.

**Results and Discussion:**

Studied alloy presents a copper matrix with Cr particles (fig.1). Figure 2 presents the Cr dendrite obtained after dissolution of Cu matrix. “A” route method was used between the passes. After three times deformation by ECAP, figure 3 presents the surface structure of the sample. Heterogeneity of deformation is observed. Figure 4 presents the Cr dendrite obtained after dissolution of Cu matrix in the case of the sample deformed 3 times by ECAP. Figure 4 shows the Cr filament in this sample in the region of maximum deformation.

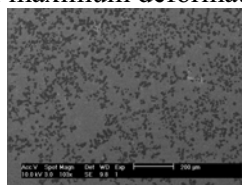


Figure 1: As received Cu Cr alloy



Figure 2: Cr particles in Cu matrix



Figure3: Sample after 3 passes

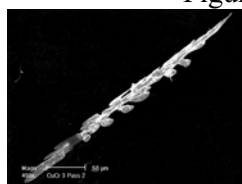


Figure4: Cr dendrite after 3 passes



Figure 2: TEM micrographie of Cr

# Microstructural Evolution Of Cu Alloys During ECAP: Approach For Nanofilament Formation

Prakash E.Thoppay, M.Dadras, M. Leboeuf, N.F.de Rooij

Service for microscopy and Nanoscopy, Institute of Microtechnology,  
University of Neuchatel, Jaquet-Droz 1, 2007 Neuchatel, Switzerland.

## Abstract-

Ag wt70% - Cu wt30% hypoeutectic alloy deformed by Equal Channel Angular Pressing (ECAP). Microstructural refinement observed after 3 passes. The study was focused more on the eutectic lamella structure. The Cu lamella width decreases from 100-150nm to 30-50nm in as prepared material and in 3 passes deformed material respectively.

## Introduction:

Interesting microstructural evolution and obtaining the ultra-fine grained (UFG) materials (d is of 100–500 nm) are in focus of many investigations during last decade. Equal Channel Angular Pressing (ECAP) gives the possibility to produce UFG specimens. The sample used for pressing is Ag70wt%- Cu wt30%. The die has a L shaped channel in the middle with inner angle of intersection of channel at 90 degrees and outer angle with 20 degrees (fig.1). The microstructural evolution is studied by using SEM, TEM and AFM. Texture evolution studied by EBSD.

## Results and Discussion:

Studied alloy presents a hypoeutectic structure having the silver phase and eutectic structure (fig.2). Cu lamella width measured about 100-150nm. After 3 passes heterogeneity in material is observed between the top and the bottom of the sample. The study was focused on refinement of eutectic lamella structure. The region of middle bottom of the sample showed better microstructural refinement. Figure 3 presents the microstructure of this region after 3 passes. Study of the deformed eutectic structure by TEM showed Cu nanofilament having the width between 30-50nm (fig. 4).

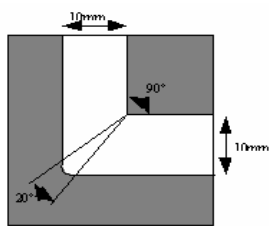


Figure 1: Schematic of ECAP die

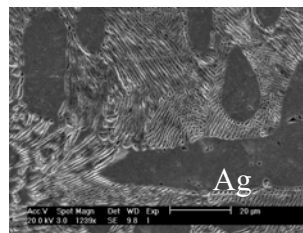


Figure 2: As received material

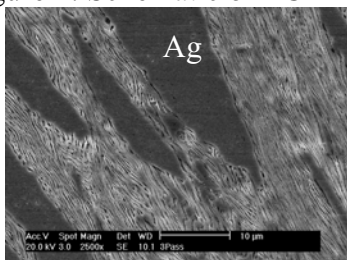


Figure3: Sample after 3 passes(SEM)

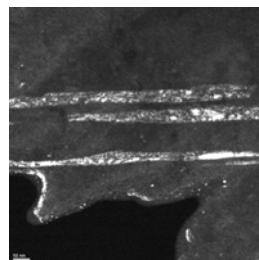


Figure4: Sample after 3 passes(TEM)

## SFM in Controlled Vapour Environment as a Tool to Observe Induced Morphology Changes of Polymer Nanostructures at Interfaces in Real Time

Marat Gallyamov<sup>a</sup>, Krystyna Albrecht<sup>b</sup>, Ahmed Mourran<sup>b</sup>, Alexei Khokhlov<sup>a</sup>, and Martin Möller<sup>b</sup>

<sup>a</sup>Physics Department, Lomonosov Moscow State University, 119992 Moscow, Russia

<sup>b</sup>DWI an der RWTH Aachen e.V., Pauwelsstrasse 8, 52056 Aachen, Germany

Morphology conversions of adsorbed polymer nanostructures can be stimulated by an exposure to different vapours [1]. The controlled rate of such transformations is sufficiently slow to allow the real-time following by in situ scanning force microscopy (SFM). Recently we reported on reversible reorganisations of self-assembled nanostructures formed by perfluoroalkyl-alkanes in vapours of selective and nonselective solvents, as observed by SFM [2]. The same approach allowed us to visualise step-by-step coil-to-globule conformational transitions of individual adsorbed polymer chains in different vapours [3]. Here we present real-time SFM-observations of vapour-induced structural transformations of ultrathin block-copolymer films on a mica substrate. Coadsorption of small molecules from vapour phase modifies the interaction of the adsorbed polymer chains with the substrate and stimulates their reorganisation. Thus, the adsorbed polymer film is forced to minimise the occupied surface area by the coadsorbed ethanol molecules, which, being amphiphilic, are more effective in the interface energy reduction. To the contrary, the coadsorbed water film stimulates spreading of the amphiphilic polymer chains and extension of the adsorbed polymer film [4].

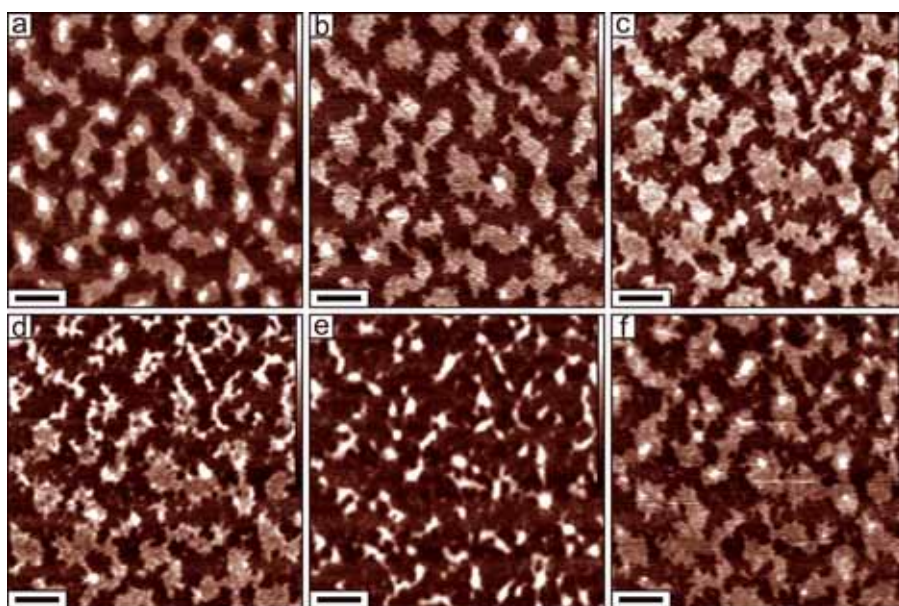


**Fig. 1:** Sequence of SFM micrographs demonstrating successive transformations of the ultrathin P2VP<sub>960</sub>-*b*-PEO<sub>1680</sub> film on mica in a vapour environment; a) as deposited by dip-coating; b,c) polymer spreading after 30 (b) and 45 (c) min exposure to water vapour; d,e: partial collapse after 15 (d) and 30 (e) min exposure to ethanol vapour; f: continued reextension in water vapour (30 min exposure). Bar size: 150 nm, height scales: 2-3 nm.

### References:

- [1] Y. Xuan, J. Peng, L. Cui, et al., *Macromolecules* 37 (2004) 7301.
- [2] A. Mourran, B. Tartsch, M. Gallyamov, et al., *Langmuir* 21 (2005), 2308.
- [3] M. O. Gallyamov, B. Tartsch, A. R. Khokhlov, et al., *J. Microsc.*, 215 (2004) 245.
- [4] M.O.G. acknowledges the support from the Alexander von Humboldt Foundation (Return Fellowship), NATO Public Diplomacy Division (grant CBP.NR.RIG.981306, Security through Science Programme), and Russian Foundation for Basic Research (project no. 04-03-32297a).

## **Features of Application of Microscopy Methods for Researches of Geological Materials**

Yevgeny A. Golubev

Institute of Geology, Russian Academy of Sciences, 54, Pervomaiskaya St., 167982, Syktyvkar, Russia

Among products of geological processes are frequently found of noncrystal solid metacoloids (further – colloids), which substance is in a heterogeneous state. The size of disperse particles can vary from units of nanometers up to hundreds micrometers. Similar substances are rather characteristic for a hypergene zone where mulling of substances is provided by such agents as superficial and subsoil waters, physical and chemical destruction, rhythmic processes etc. The role of colloids is important in formation of ores of hydrothermal deposits. In a nature in a colloidal form were encountered are simple substances (ex. gold, silver, carbon), oxides (ex. silica), and also aluminosilicate, phosphates, sulfides, hydrocarbons. The disperse phase of natural colloidal is considered as the form of supermolecular constitution. Dependence on a geological finding conditions and processes of formation make interesting researches of supermolecular structures especially by way of reception of the quantitative structural information.

For studying of supermolecular structures the most effective are methods of direct observation. Due to appeared to the present time to high-resolution probe microscopic (SPM) methods difficulties with visualization nanometrical structural elements of metastable natural substances are removed [1, 2]. We applied scanning tunneling and atomic force (AFM) microscopes. Almost all from the listed substances are not conductors, and in work basically method AFM was used. As with rare exception the form natural isolation of colloids is directive, determined either by superficial or gravitational forces, or a form of a filled space. Therefore the basic method of analysis supermolecular structures is morphological analysis having internal fracture.

SPM were visualized by various supermolecular structures, mainly globular and fibrous, the size of particles varied from 10 nm up to several microns. In the paper features of interpretation of SPM-images of a surface of natural substances, determined first of all by difficult composition. This identifies necessity of the element control of surfaces studied presence of the cementing gel complicating direct observation of structural elements etc. In our study the element analysis of researched surfaces was determined with an energy-dispersive X-ray microanalyser "Link", established on SEM JSM 6400 (Jeol).

It is known, that disperse supermolecular constitution actively influences physical and chemical properties of substances and provide to substances special qualities in colloidal (disperse) state. Existing ordered supermolecular structures can be of interest and as original models for fundamental studying processes of crystallization. There is relation between of the specified properties of mineral substances with various methods of the structural-morphological analysis considered on SPM-images and quantitative parameters describing supermolecular structure is considered.

### References:

- [1] Golubev Ye.A., Abstract of MC2003, for Ref. see Microscopy & Microanalysis, 2003, Vol. 9 (Suppl. 3), pp. 304-305.
- [2] Golubev Ye.A., Kovaleva O.V., Filippov V.N., Abstract of MC2003, for Ref. see Microscopy & Microanalysis, 2003, Vol. 9 (Suppl. 3), pp. 306-307.

# SEM/TEM Investigations of Tungsten/Tungsten-Carbide/Carbon and MoS<sub>2</sub> Multilayers/Nanocomposites

M. Gubisch; Th. Kups; H. Romanus; L. Spiess

Department of Material Engineering, Center for Micro and Nanotechnologies, Technical University Ilmenau, 98693 Ilmenau, Germany

In research project, nanomeasuring machine, promoted by German research foundation SFB 622, the group will build a machine, which should measure in a range of 450 x 450 mm with accuracy of 1 nanometer and below. The materials for the movement systems need a very small and well established surface, must withstand abrasive wasting, should be hard and must manufacture productive.

Composite layers of tungsten-carbon, tungsten carbide-carbon and tungsten carbide-MoS<sub>2</sub> were prepared by rf- and dc-sputtering with and without bias on Si<sub>3</sub>N<sub>4</sub>-covered silicon and steel (90MnCrV8). The layers were investigated with complex analytical electron microscopy (scanning and transmission electron microscopy in different detectors mode, energy dispersive X-Ray analysis and electron energy loss spectroscopy), atomic force microscopy, with electrical methods and X-Ray diffraction. The paper presents the results of the complex analytics and the electron microscopy. We show that it is possible sometimes to get comparable results with simple BSE-detection mode in SEM such as PEELS or TEM, figure 1.

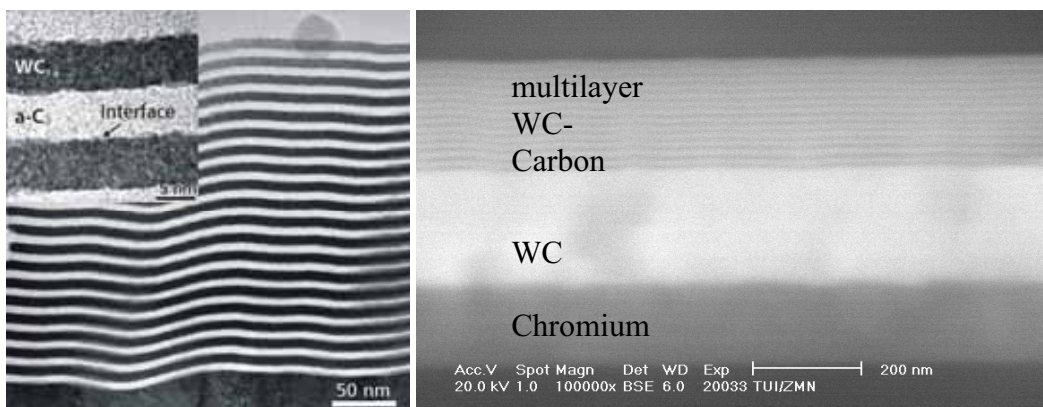


Figure 1:  
a) TEM cross section,  
b) SEM micrograph of multilayer sample (BSE-detector)

High resolution TEM investigations of WC-MoS<sub>2</sub> thin films exhibit a nanocrystalline structure depending on MoS<sub>2</sub> content and deposition parameters. In contrast, pure MoS<sub>2</sub> thin films show a structure with (002) basal planes, figure 2.

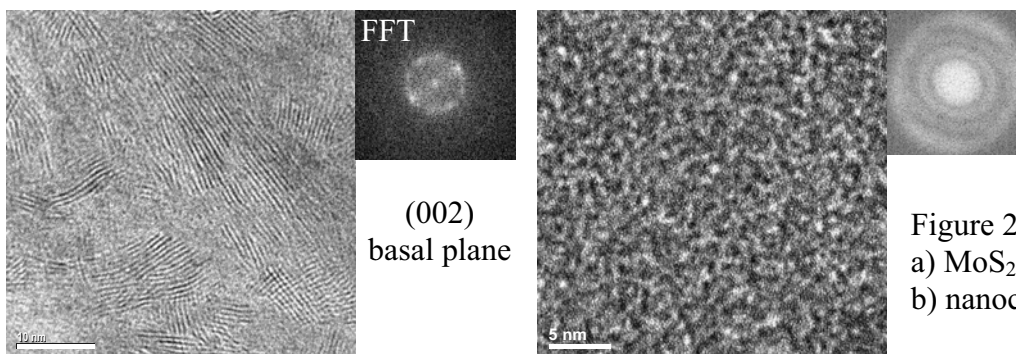


Figure 2:  
a) MoS<sub>2</sub> structure  
b) nanocrystalline WC-MoS<sub>2</sub>

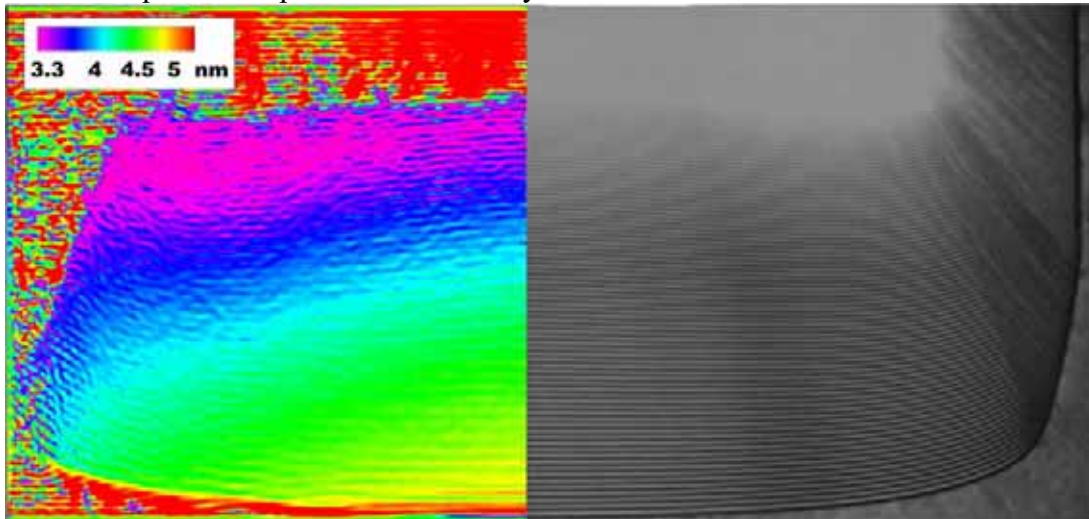
Acknowledgements: We gratefully acknowledge E. Remdt for sample preparation and the German research foundation (DFG) for financial support (SFB 622 project B3).

## Quantitative TEM characterizations of complex multilayer systems on structured silicon substrates

D. Häußler<sup>a</sup>, E. Spiecker<sup>a</sup>, W. Jäger<sup>a</sup>, M. Störmer<sup>b</sup>, C. Michaelsen<sup>c</sup>, J. Wiesmann<sup>c</sup>, G. Zwicker<sup>d</sup>

<sup>a</sup> Microanalysis of Materials, Faculty of Engineering, Christian-Albrechts-University of Kiel, 24143 Kiel, Germany; <sup>b</sup> Institute of Materials Research, GKSS Forschungszentrum Geesthacht GmbH, 21505 Geesthacht, Germany; <sup>c</sup> Incoatec GmbH, 21502 Geesthacht, Germany; <sup>d</sup> Fraunhofer Institute for Silicon Technology, 25524 Itzehoe, Germany

Advanced multilayer systems based on periodic ultrathin bilayers are used as X-ray optical components in diffractometers and spectrometers for life sciences, EUV lithography, or in microsystem technology. Artificially fabricated multilayers that exploit the effect of Bragg diffraction at long wavelengths consist of periodic bilayer stacks of, alternately, a metallic reflection layer and a non-metallic spacer layer. Filters for high-resolution spectroscopy require suitably shaped X-ray mirrors fabricated on a  $\mu\text{m}$ -scaled surface grating. Functionally decisive are the quality of the bilayer stacking period and of the interfaces which can be optimized by selecting appropriate processing parameters during layer deposition.- The structural parameters, such as layer perfection, layer periodicity and layer orientation can be characterized with high precision combining TEM bright-field imaging of specimen cross-sections and applying a geometric phase method [1] originally developed for measuring displacement fields from HREM images [2] which allows to obtain the relevant structure parameters. We applied the technique to characterize the layer growth phenomena of e.g. La/B<sub>4</sub>C multilayer systems on structured Si(100): The figure shows a BF micrograph of a multilayer region and a corresponding false-color mapping of the local bilayer period. The technique and its potential in multilayer characterizations will be described.



### References:

- [1] D. Häußler, E. Spiecker, S. Yang, W. Jäger, M. Störmer, R. Bormann, and G. Zwicker, *phys. stat. sol.* (2005), submitted.
- [2] M. J. Hytch, E. Snoeck, and R. Kilaas, *Ultramicroscopy* 74, 131 (1998).
- [3] Financial support by the ISH Innovationsstiftung Schleswig-Holstein (project grant 2004-18-HWT) is gratefully acknowledged.

## HRTEM investigations of (Si,Ge)/Si islands in combination with FEM

I. Häusler<sup>a</sup>, H. Schwabe<sup>a</sup>, R. Schneider<sup>a,b</sup>, W. Neumann<sup>a</sup>, M. Hanke<sup>b</sup>, R. Köhler<sup>a</sup>, and A. Gerlitzke<sup>c</sup>

<sup>a</sup>Humboldt-University Berlin, Institute of Physics, D-12489 Berlin, Germany

<sup>b</sup>Martin Luther University Halle-Wittenberg, Department of Physics, D-06108 Halle, Germany

<sup>c</sup>Institute of Crystal Growth, D-12489 Berlin Germany

In the investigation of self-organized (Si,Ge) islands, one of the main objectives is the determination of the composition of the islands. From the concentration and deformation profiles it is possible to arrive at indirect conclusions about the mechanisms of the self-organized growth process. For this purpose samples were grown by liquid phase epitaxy on (001) oriented Si substrates.

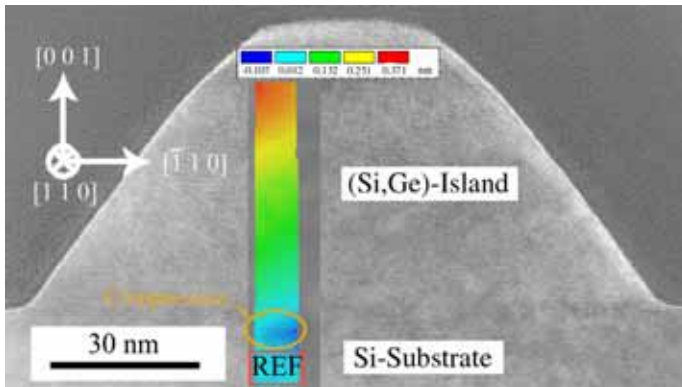


**Fig. 1:** HRTEM image of a (Si,Ge)/Si island analysed by DALI. The coloured map represents the displacement of the atom columns in [001] compared to the reference lattice

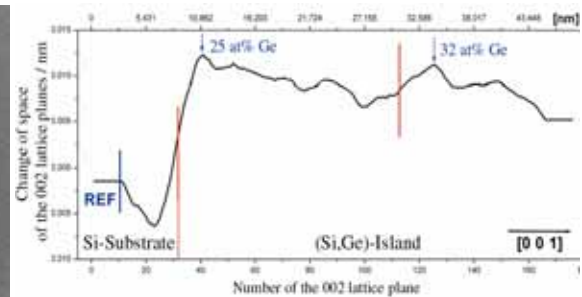


**Fig. 2:** Derivation of the displacement plot. The first maximum corresponds to a Ge content of about 25 at.%. At the midheight of the island the concentration of Ge is about 32 at.%. The values of the content are calculated by comparison with the results of FEM-computations.

Non-destructive high-resolution X-ray diffraction analysis (HRXRD) in combination with kinematical simulations (FEM) revealed a good agreement between simulation and measurement for an island model with an abrupt increase of the germanium content at about one third of the island height in the growth direction [1]. The validity of this model was investigated by using TEM. For this purpose high resolution TEM images were digitally analysed using DALI (Digital Analysis of Lattice Images [2]) for visualizing the strain distribution inside the island. A compression of the Si unit cell underneath the island and a dilatation of the (Si,Ge) unit cell, both in [001], are visible in the coloured map superimposed on Figure 1. By means of the displacement field it was possible to confirm the germanium concentration inside the island. This was done from displacement maps of simulated HRTEM images of (Si,Ge) islands obtained by a combination of FEM and the JEMS software. The analysis shows an increased Ge concentration in the top of about 32 at.% compared to a Ge content of about 25 at.% in the lower island area.

References:

[1] M. Hanke et al., Phys. Rev. B **69** (2004), 075317

[2] A. Rosenauer, U. Fischer, D. Gerthsen, A. Förster, Ultramicroscopy **72** (1998), p. 121.

## Microscopic Investigation Of Native Bitumens Constitution

Olga V. Kovaleva, Yevgeny A. Golubev

Institute of Geology, Russian Academy of Sciences, 54, Pervomaiskaya st., 167982, Syktyvkar, Russia

Supermolecular organization serves as a determining structural feature of many polymeric solid bodies. In this paper we represent results of supermolecular structure study of native bitumens. Basic supermolecular structural elements of bitumens are fibrils and globules. Visualization of the supermolecular elements was conducted by the atomic force microscope (AFM) ARIS 3500, Burleigh Instrument, USA).

The types of supermolecular structures and sizes of their initial elements have been determined. According to data received the scheme has been constructed (fig.1). This scheme qualitatively shows basic features of supermolecular structures in a carbonization row as: asphaltites → kerites → anthraxolites. Schematic images of the supermolecular constitutions are made by the contrast filter on the basis of actual AFM-images corresponding to the specified substances. Obviously, it is necessary to pay attention, that this scheme reflects only most general principles of the structures for each class of natural solid bitumens.

Therefore, main regulations of supermolecular ordering of solid bitumens are established. Asphaltites have a branchy composition and they locate randomly so that it is hard to determine a direction of the movement. Low-class kerites less mutually oriented arrangement of fibers, the fibers become longer. The oriented arrangement of the fibers are preserved in the high-class kerites, however, the fibers become shorter, and globule-like formations are observed in the general fiber mass. When referring to the high-class anthraxolites globules represent a supermolecular structure.

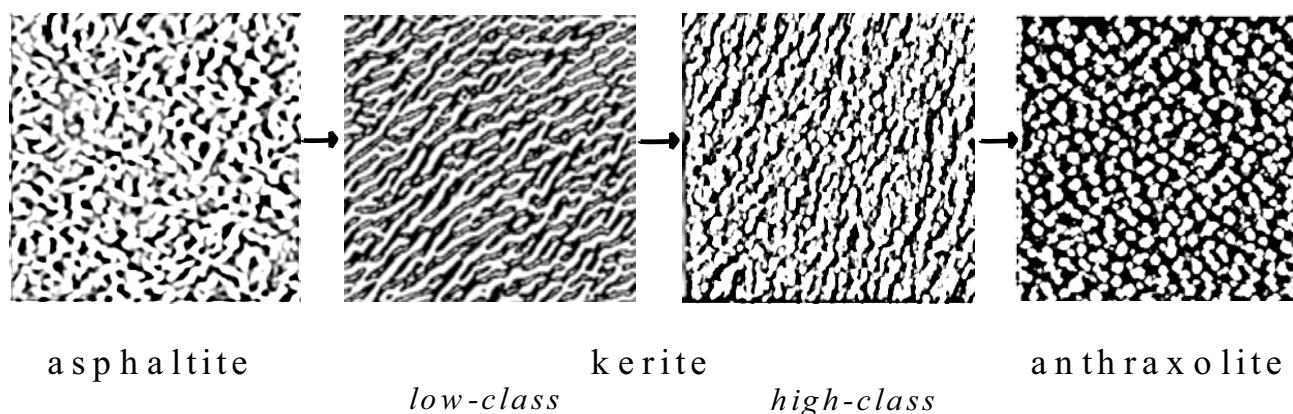


Fig. 1. The schematic snapshot of the supermolecular structure of native bitumens in a carbonization row by the AFM data.

Acknowledgements: The abstract is supported by Science School (2250.2003.5) and Program of RAS (№ 25).

## TEM-Investigation of Si(001) Modified by Pr Implantation

Arndt Mücklich, Reinhard Kögler, and Frank Eichhorn

Institute of Ion Beam Physics and Materials Research, Forschungszentrum Rossendorf e.V.

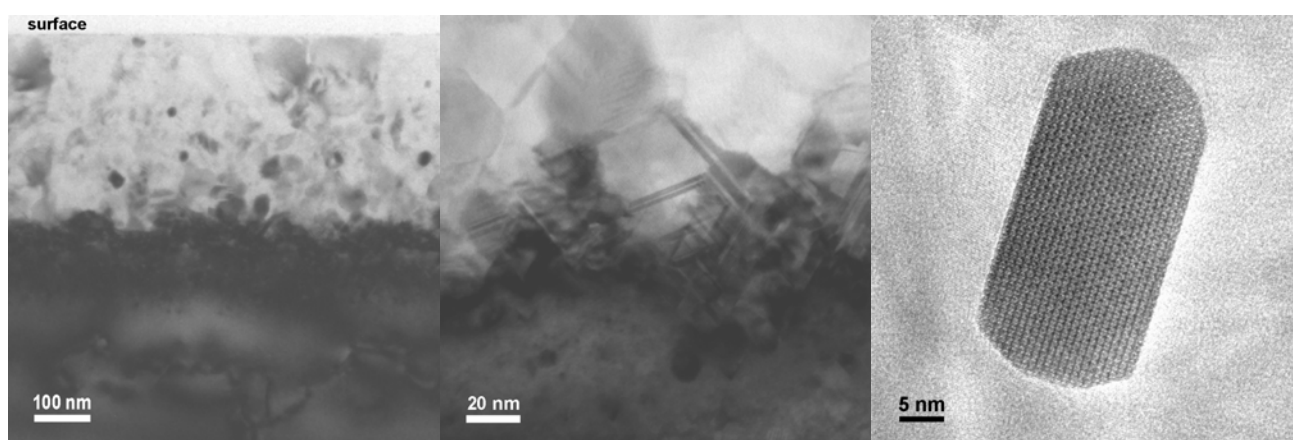
Downscaling of nanoelectronic devices requires the replacement of the common SiO<sub>2</sub> gate oxide by high-K dielectrics. Among the potential candidates Pr oxides [1] are under current discussion. Our investigation is focused on the evaluation of the compositions which are generated when Pr ions are implanted into Si.

Si(001) has been undergone a 800 keV Pr implantation ( $3.5 \times 10^{16} \text{ cm}^{-2}$ ) followed by a thermal treatment at 900°C, 1h or at 1100°C, 1h in an Ar atmosphere. Moreover, some samples were additionally implanted with oxygen at 140 keV ( $4.5 \times 10^{16} \text{ cm}^{-2}$  delivering a peak concentration of  $2.25 \times 10^{21} \text{ cm}^{-3} = 4.5 \text{ at.-%}$ ).

The Pr-implantation leads to an amorphization of the Si-surface region down to the mean projected ion range of about 300 nm. During annealing the Si-wafer recrystallized and grains 15 nm – 150 nm in size are formed (Fig. 1). In the region of the former amorphous/crystalline interface distinctive morphological features were found revealing the feasible existence of compositions being of interest (Fig. 2). Characteristic spacings larger than 0.40 nm could be identified by both diffraction and HREM (Fig. 3). They give rise to the assumption that Pr silicide and/or Pr silicate precipitates have been generated [2,3,4]. Most of the compositions which have to be taken into consideration are of low crystallographic symmetry represented by a large number of interplanar distances allowed. Thus, one of the challenges of this work consists in the scheme to give the correct indication of that compositions.

### References:

- [1] H.-J. Müssig et al., Surface Science, 504 (2002) 159-166
- [2] J. Dabrowski, V. Zavodinsky, NIC Series 20 (2003) 171-180
- [3] W. Mehr, M. Stöcker (editors), Annual Report 2003, IHP Frankfurt(Oder), 2004, 30-31
- [4] D. Schmeißer, H.-J. Müssig, J. Physics: Condensed Matter, 16 (2004) 153-160



In Figs. 1 (overview) and 2 (detail) XTEM images of Si(001) implanted with 800 keV Pr<sup>+</sup> ( $3.5 \times 10^{16} \text{ cm}^{-2}$ ) and annealed at 900°C, 1h are shown. In Fig. 3 a faceted Pr silicate precipitate can be seen.

## TEM Study of High Pressure Torsion Plastically Deformed Cu

B. Mingler, G. Steiner, H. P. Karnthaler and M. Zehetbauer

Institute of Materials Physics, University of Vienna, AT-1090 Vienna, Austria  
www.univie.ac.at/Materialphysik/EM

During the high pressure torsion (HPT) procedure the Cu samples (purity 99.9%) were subjected to a quasi-hydrostatic pressure and a torsional straining at the same time. In the present study the HPT deformation was performed at a pressure of 8 GPa at room temperature leading to shear strains up to 20000% (depending on the torsion angle, the sample thickness and the effective radius). Transmission electron microscopical (TEM) methods were used to study the evolution of the microstructure as a function of strain. TEM samples were prepared from the HPT discs (diameter: 8 mm, thickness: 0.7 mm) of the torsional plane and of planes perpendicular to it. Final thinning was done by electropolishing for the samples of the torsional plane. Samples of perpendicular planes are rather small therefore they had to be embedded in wax (hardened at  $\sim 75^\circ\text{C}$ ) before ion milling. At a strain of 120% the microstructure is dominated by a high dislocation density forming a cell structure (Fig. 1). With increasing strain (600%) the cell structure transforms to a structure consisting mainly of small subgrains ( $\sim 300\text{ nm}$  in size) separated by low angle grain boundaries (misorientations smaller than  $15^\circ$ ). At a strain of 20000% the samples prepared from the torsional plane show a high dislocation density that makes it difficult to distinguish the ultra-fine grains ( $\sim 250\text{ nm}$ ) (Fig. 2) [1]. Contrary to this samples prepared from perpendicular planes show ultra-fine grains ( $\sim 250\text{ nm}$ ) with clear high-angle grain boundaries and a reduced dislocation density (Fig. 3); in addition some larger grains ( $\sim 1\text{ }\mu\text{m}$ ) are also present in these samples. This difference in the microstructure of samples prepared in different ways is interpreted as an effect of annealing taking place during hot wax embedding. This is supported by both annealing experiments ( $75^\circ\text{C}$ ) of the bulk material and in-situ heating experiments in the TEM. It is interesting to note that the ultra-fine crystalline structure seems to develop in a random way and that no texture is developed even at very high strains indicating that grain boundary sliding is an important feature of the deformation process.

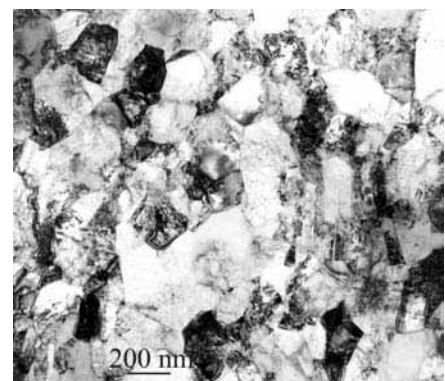
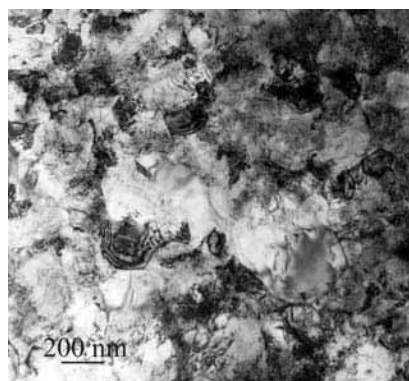
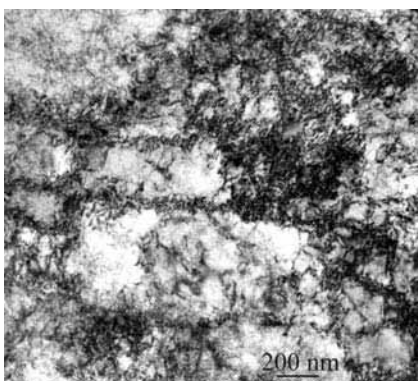


**Fig. 1:** Cu (torsional plane) HPT deformed (120%)

**Fig. 2:** Cu (torsional plane) HPT deformed (20000%)

**Fig. 3:** Cu (perpendicular plane) HPT deformed (20000%)

- [1] B. Mingler, H.P. Karnthaler, M. Zehetbauer, R.Z. Valiev, *Mat. Sci. Eng. A* 319-321, (2001) 242  
[2] Financial support by the Austrian FWF (project P17095-N02) is acknowledged.

## Bi<sub>2</sub>Te<sub>3</sub>: Superlattices and Structural Modulations in Bulk Materials

N. Peranio<sup>a</sup>, O.Eibl<sup>a</sup>, and J. Nurnus<sup>b</sup>

<sup>a</sup> Institut für Angewandte Physik, Universität Tübingen, Auf der Morgenstelle 10, D-72076 Tübingen, Germany

<sup>b</sup> Fraunhofer Institut Physikalische Messtechnik, Heidenhofstr. 8, D-79110 Freiburg, Germany

Bi<sub>2</sub>Te<sub>3</sub> is a material with a large thermopower (200 $\mu$ V/K) and thermoelectric figure of merit ZT at room temperature. Multiquantum well structures of Bi<sub>2</sub>Te<sub>3</sub> are predicted to show an enhancement of ZT [1]. The samples consisted of 1  $\mu$ m thick Bi<sub>2</sub>Te<sub>3</sub>/Bi<sub>2</sub>(Te<sub>0.88</sub>Se<sub>0.12</sub>)<sub>3</sub> superlattices (SL) with a layer thickness of 12 nm epitaxially grown on BaF<sub>2</sub> substrates by molecular beam epitaxy techniques [2]. The microstructure were investigated by transmission electron microscopy (TEM) [3]. High resolution images of the SL could be imaged with strongly excited (0,0,1)-reflections. The strong contrast is due to the interference of the (0,0,1)-reflections and the reflections of the superstructure. High resolution images with strongly excited (-1,0,5)-reflections showed a structural modulation (nns) parallel to the (1,0,10)-planes with a wave length of 10nm. This (nns) was also observed in n-type Bi<sub>2</sub>(Te,Se)<sub>3</sub> and p-type (Bi,Sb)<sub>2</sub>Te<sub>3</sub> bulk material and turns out to be of general character for Bi<sub>2</sub>Te<sub>3</sub> materials. The (nns) did not show bending due to the superlattice and vice versa. In a model for the structural modulation we assumed an ordered system of dislocation lying parallel to the (1,0,10)-planes only a few nanometers apart. There are three equivalent {1,0,10}-planes due to the trigonal symmetry of the crystal. Therefore, the structure is a superposition of the epitaxially grown superlattices (ans) and three structural modulations (nns). This model was inspected in n-type Bi<sub>2</sub>Te<sub>3</sub> bulk material. The number of (nns), the Burgers vector and the dislocation line direction were determined by stereomicroscopy. The strain field of the superimposed (nns) might also affect the thermoelectric properties yielding a one dimensional or zero dimensional behaviour and anisotropic transport coefficients in the basal plane.

References:

[1] Venkatasubramanian, R. et al., Nature, Vol. 413 (2001), pp. 597-602

[2] Lamprecht A. et. al., Proc 20<sup>th</sup> Int. Conf. on Thermoelectrics, Beijing, P.R.China (2001), pp. 335-339

[3] Peranio N. et. al., Proc 23<sup>th</sup> Int. Conf. on Thermoelectrics, Adelaide, Australia (2004), in press

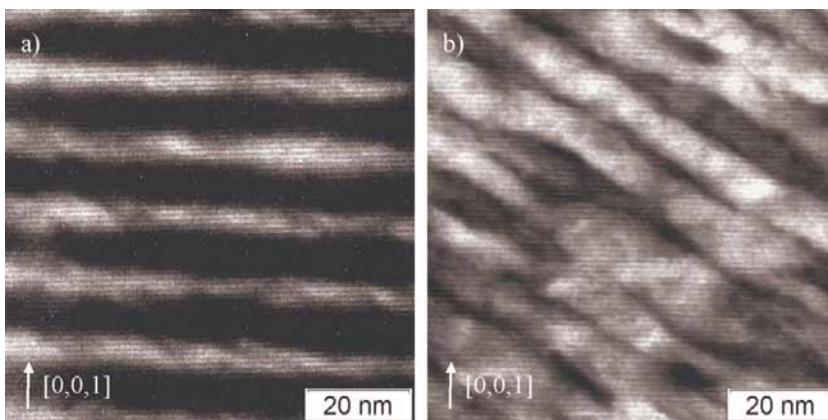


**Fig. 1:** Cross-sectional high-resolution images of the n-type Bi<sub>2</sub>Te<sub>3</sub> superlattice (ans). a) (ans) with 12nm period; (0,0,9) strongly excited and b) (nns) with 10nm wave length; (-1,0,5) strongly excited.

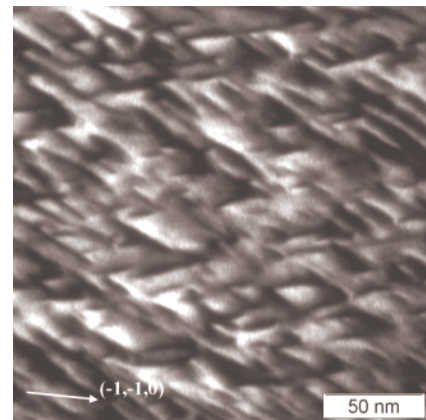


**Fig. 2:** (-1,-1,0)-dark field image of n-type Bi<sub>2</sub>Te<sub>3</sub> bulk material with two superimposed structural modulations (nns).

## Microstructure of Fe<sub>3</sub>C-Nanowires in Damascene Sabres

M. Reibold<sup>1</sup>, A.A. Levin<sup>1</sup>, D.C. Meyer<sup>1</sup>, P. Paufler<sup>1</sup> and W. Kochmann<sup>2</sup>

<sup>1</sup>Institute of Structure Physics, TU Dresden, D-01062 Dresden, Germany

<sup>2</sup>Krüllsstraße 4B, D-06766 Wolfen, Germany

Damascus steel is famous for its beauty and excellent mechanical properties. Damascus blades – originating in India - were manufactured from so-called “wootz” steel. The mystery of its excellent properties is not resolved up today. During extensive investigations in collaboration with the blacksmith A.H. Pendray, J.D. Verhoeven succeeded in revealing the technology of damascene steel [1]. Wadsworth et al. have drawn attention to both the superplastic behaviour and the excellent strength and ductility of the fine-grained microstructure (cf. [5]). Nevertheless, the correlation between microstructure on a high-resolution level and the macroscopic properties is still an open question. Therefore, the aim of our investigation is to contribute to a better understanding of the ancient technology by analysis of the microstructure of damascene steel. High-resolution electron microscopy and X-ray diffraction are eligible tools for this task. The specimens investigated by us were taken from a genuine Damascus sabre produced by the blacksmith Assad Ullah in the 17<sup>th</sup> century [2,3]. Before our analysis, two of these specimens had been heated at 400°C and 800°C, respectively. The main results are as follows: Besides ferrite and perlitic cementite (fig.1), we observed a third form of cementite forming so-called nanowires. These nanowires often arrange in colonies (fig.2) [4]. Preferably, the {010}-lattice planes of the nanowires are oriented along the longitudinal direction (fig.3). The surrounding of the nanowires often could be identified as  $\alpha$ -Fe. Between the nanowires, in many cases dislocations exist, which often tangle and pile up near the colonies (fig.4). In the specimen, heated at 400°C, we found a similar microstructure like the one in the unheated specimen (fig.5); however, the nanowires are oriented in any directions. In the specimens heated at 800°C, nanowires like in the unheated specimen, are nearly not present. Only very few nanoprecipitates were found looking like nanowires (fig.6). We mainly detected many grains of  $\alpha$ -Fe and Fe<sub>3</sub>C.

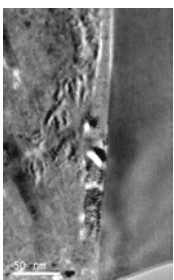


fig. 1:  $\alpha$ -Fe/Fe<sub>3</sub>C

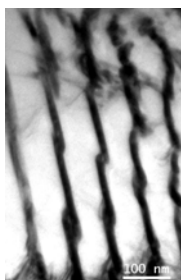


fig. 2: Nanowires

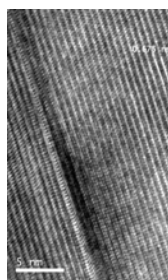


fig. 3: Detail of nanowire

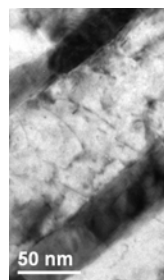


fig. 4: Dislocations

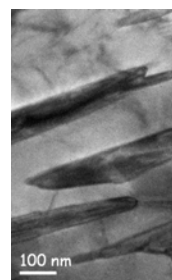


fig.5: Heated at 400°C

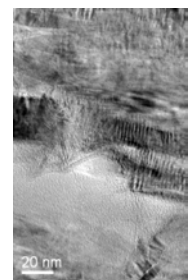


fig.6: Heated at 800°C

### References

1. J.D. Verhoeven, The mystery of Damascus blades, *Scientific American* 2001; 284(1): 74-79
2. B. Zschocke, Du damassé et des lames de damas. *Rev. De Metallurgie* 1924; 21; 635
3. R. Zeller, *Jahrbuch des bernischen Historischen Museums* 1924; 4; 24
4. W. Kochmann et al; Nanowires in ancient Damascus steel. *J. Alloys&Comp.* 2004; 372;L
5. J.Wadsworth, Ancient and modern steels and laminated composites containing steels. *MRS Bulletin* 2002; 27; 980

## **TEM-studys on nanoindents with FIB-techniques**

M. Reichelt<sup>1</sup>, Th. Weirich<sup>1</sup>, M. Bückins<sup>1</sup>, Th. Wolf<sup>2</sup>, J. Loos<sup>2</sup>, P. W. Gold<sup>2</sup> and J. Mayer<sup>1</sup>

1. Gemeinschaftslabor für Elektronenmikroskopie, RWTH Aachen, Ahornstrasse 55, D-52074 Aachen,
2. Institut für Maschinenelemente und Maschinengestaltung, RWTH Aachen, Schinkelstrasse 10, D 52062 Aachen, Germany

We investigate the tribological behaviour on the system bearing / lubricant formed by lubricants with low wear protection and high wear protection on thrust cylindrical roller bearings made of 100Cr6 steel.

Transmission Electron Microscopy (TEM) investigations reveal that the reaction layers at the rolling contact are formed by an amorphous phase with embedded nanocrystalline iron oxide particles. For a sample with good wear protection, the layer consists of an ultra-thin oxide with less than 10 nm thickness and extremely low surface roughness. In contrast, a sample with low wear protection exhibited an uneven reaction layer with a thickness varying between 0 - 130 nm and a three times higher surface roughness as the sample with high wear protection.

Furthermore, tribological mutation (tribomutation) of the steel was found in regions of about 150 - 400 nm in thickness below the surface.

The nanomechanical behaviour of the different tribological layers were investigated by a combination of nanoindentation and atomic force microscopy (AFM). The determined Young's moduli show substantial differences for the reaction layers and the tribomutation layers on the two different systems. However, they become very similar for both tribological systems with increasing penetration depth into the tribomutation layer.

On these background we study the behaviour of the layer systems under normal forces. For the investigations we indent with different forces and prepare the TEM-samples with the FIB-technique.

### **Acknowledgements**

We gratefully acknowledge the financial support of the Deutsche Forschungsgemeinschaft.

# Refinement of the austenite structure by oscillatory compression test

Kinga Rodak

<sup>1</sup>Department of Materials Science, Silesian University of Technology,  
8 Krasińskiego Str., Katowice 40-019, Poland

The processing of ultrafine grained materials by severe plastic deformation has been receiving increasing attention. Two or three most common variants of severe plastic deformation are known in the literature. However, little has been reported on the evolution of microstructure and properties of ultrafine grained materials processed via oscillatory compression [1,2]. The 0H18N9 austenitic steel was deformed at room temperature by using oscillatory compression test at constant parameters: torsion angle ( $\alpha$ ) = 10° and torsion frequency ( $f_{sk}$ ) = 1.8 Hz at strain ( $\epsilon$ ) = 4. More information about mode of oscillatory deformation is present in [3]. Studies using TEM were conducted on material extracted from the 0,8 radius in the longitudinal plane section [4].

Typical feature of austenitic steel after deformation is a banded structure indicating localized deformation in slip bands and shear bands. At a higher magnification, the detailed structure inside of

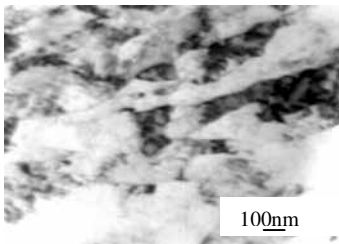


Fig. 1. TEM image of deformed material.

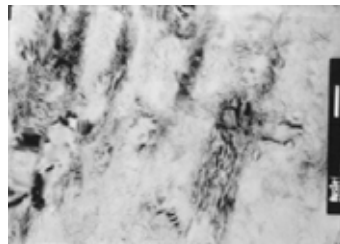


Fig.2. Fuzzy boundary fringe patterns.

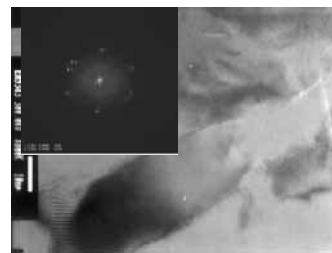


Fig.3. TEM image of subgrain boundaries.

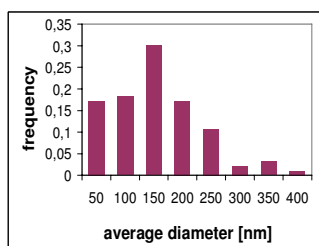


Fig.4. Subgrain size distribution

the shear band is revealed (fig.1). Microstructure consists of elongated grains, with grains about 0,1 $\mu$ m in width and about 1-2  $\mu$ m in length. These grains contain a high density of dislocation (fig.2), where many fingers are observed, leading to the description of the deformed state as one that has non-equilibrium boundaries. TEM examination in another regions of the shear bands (fig.3), show arrangement of the dislocations into cell and sub-grain boundaries. The average diameter of sub-grains was 130 nm (fig.4). The elongated grains are somewhat shortened by appearance of transverse, low-angle boundaries. Such that the microstructure tends towards an equiaxed state. Only occasionally sub-grains are misoriented by more than 15°.

## References

- [1] Rodak, K et al. *Rudy Metale*, **4**, 2004, p.184-188.
- [2] Rodak, K. *Arch. Nauki o Ma.*, **3**, 2004, p.203-209.
- [3] Grosman, F. et al. *Forming 2001* (ed. by Katedra Mechaniki i Przeróbki Plastycznej Politechnika Śląska) 2001 p. 63-68. Katowice.
- [4] Grosman, F. et al. *Forming 2003* (ed. by Katedra Mechaniki i Przeróbki Plastycznej Politechnika Śląska) 2003 p. 57-61. Katowice.

## Behaviour of EBID Pt/C Nanowires under mechanical stress

Michael Rogers<sup>a</sup>, Bernhard Schaffer<sup>a</sup>, and Gerald Kothleitner<sup>a</sup>

<sup>a</sup>Institute for Electron Microscopy, Graz University of Technology, 8010 Graz, Austria

Electron beam induced deposition (EBID) is a promising method for controlled preparation and modification of functional nanostructures, like field emitter tips or scanning probe microscopy tips [1]. A focused electron beam is scanned across the specimen surface while a precursor gas is injected into the chamber and onto the specimen. The precursor gas molecules adsorbed on the surface and near the surface are cracked by electron beam irradiation and deposit on the surface. This permits site-specific deposition of structures of very small dimensions (typically 10-100nm). The smallest achievable structural size is dependent on various factors like the type of precursor gas or the electron beam diameter. A very common precursor gas is cyclopentadienyldimethylplatinum, which is mostly used in focused ion beam (FIB) systems to deposit protective layers of platinum for transmission electron microscopy (TEM) specimen preparation. While the electronic properties like the electric resistance of Pt nanostructures prepared by both FIB-induced deposition and EBID are already known [2], there is not much knowledge about the mechanical behaviour of EBID Pt/C nanostructures. The main obstacle for obtaining information about the mechanical properties of nanostructures are the small dimensions of these structures, which make it virtually impossible to apply conventional methods like fracture tests or bending tests.

In this work a DualBeam<sup>TM</sup> FIB/SEM instrument was used to prepare Pt/C nanotips of varying diameter via EBID, with cyclopentadienyltrimethylplatinum as the precursor. The test structures were deposited on a copper TEM grid in order to allow an easy subsequent study in the analytical TEM. Testing of mechanical behaviour was achieved by application of a fine tungsten micromanipulator tip, and the process was simultaneously imaged using the electron beam. To obtain information about possible changes in morphology and chemistry after the bending process, the nanotips were investigated via energy filtering transmission electron microscopy (EFTEM).

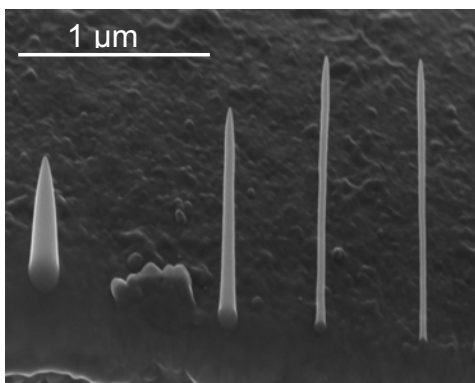


Fig. 1: Secondary electron image of Pt/C composite nanotips fabricated by electron beam induced deposition

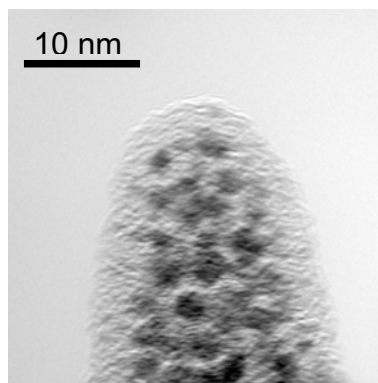


Fig. 2: TEM bright field image of an EBID Pt nanotip showing heterogeneous morphology

### References:

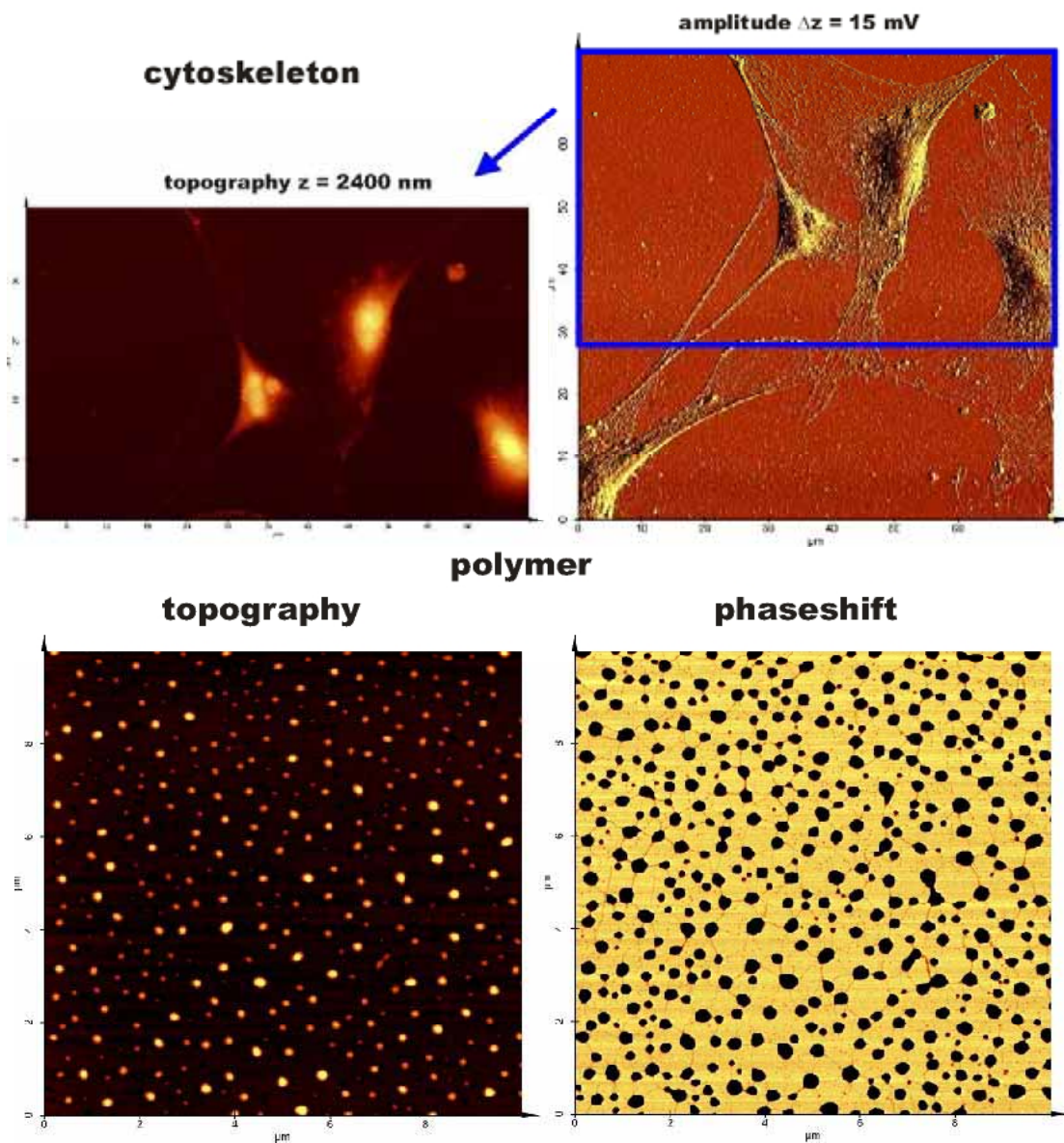
- [1] H. Koops et al., *Jpn. J. Appl. Phys.* 33(1994) 7099
- [2] L. Rotkina, J.-F. Lin, and J.P. Bird, *Appl. Phys. Lett.* 83 (2003) 4426

## AFM as a Nanomanipulation Tool for Molecular Networks: from Material Science to Life Science

Alexander Schmatulla<sup>a</sup> and Othmar Marti<sup>a</sup>

<sup>a</sup>Department of Experimental Physics, University of Ulm, 89069 Ulm, Germany

We will show the possibility of a custom built Atomical Force Microscope (AFM) as an useful tool for more than one application in life science and material science. We have analysed cytoskeleton and polymer networks. The aim is to show the nearly universal application of an AFM for scanning and nanomanipulation in life science and in material science. We will describe the different sample preparations. Moreover we show working modi and possible resolution of our AFM as well as the results and data thus obtained of scanning and nanomanipulation. Further we will compare our results with SEM images.

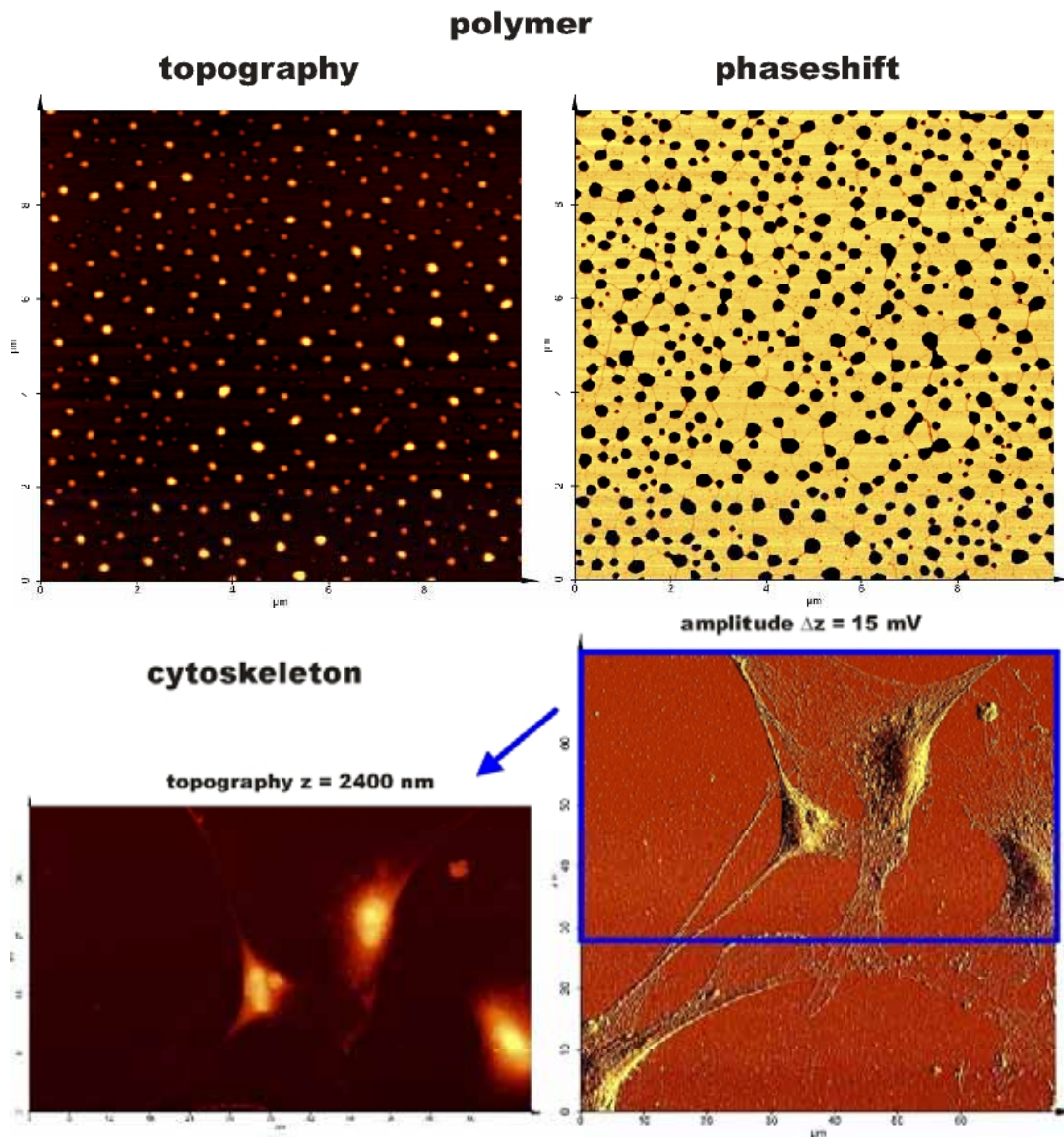


# Atomic Force Microscopy as a Nanomanipulation Tool from Material Science to Life Science

Alexander Schmatulla<sup>a</sup>, Othmar Marti<sup>a</sup>

<sup>a</sup>Department of Experimental Physics, University of Ulm, 89069 Ulm, Germany

We will show the possibility of a custom built Atomic Force Microscope (AFM) as an useful tool for more than one application in life science and material science. We have analysed cytoskeleton and polymer networks. The aim is to show the nearly universal application of an AFM for scanning and nanomanipulation in life science and in material science. We will describe the different sample preparations. Moreover we show working modi and possible resolution of our AFM as well as the results and data thus obtained of scanning and nanomanipulation. Further we will compare our results with SEM images.



## Investigations of LPE-grown $\text{Si}_{1-x}\text{Ge}_x$ Islands by Analytical TEM

Reinhard Schneider<sup>a,b</sup>, Ines Häusler<sup>a</sup>, Anne-Kathrin Gerlitzke<sup>c</sup>, and Wolfgang Neumann<sup>a</sup>

<sup>a</sup>Humboldt University of Berlin, Department of Physics, D-12489 Berlin, Germany

<sup>b</sup>Martin Luther University Halle-Wittenberg, Department of Physics, D-06108 Halle, Germany

<sup>c</sup>Institute of Crystal Growth Berlin, D-12489 Berlin, Germany

A structured (Si,Ge) layer with a germanium content of about 25 at.% grown by Low Pressure Chemical Vapour Epitaxy (LPCVD) on a (001) Si substrate was the basis layer for (Si,Ge) islands that formed by self-organisation during Liquid Phase Epitaxy (LPE) at a temperature of about 585°C. Energy-filtered TEM (three-window technique) and combined STEM/EDXS were used to image the element distribution in the transition region from the substrate over the SiGe layer up to the islands by means of a 200 kV TEM/STEM Philips CM 20 FEG.

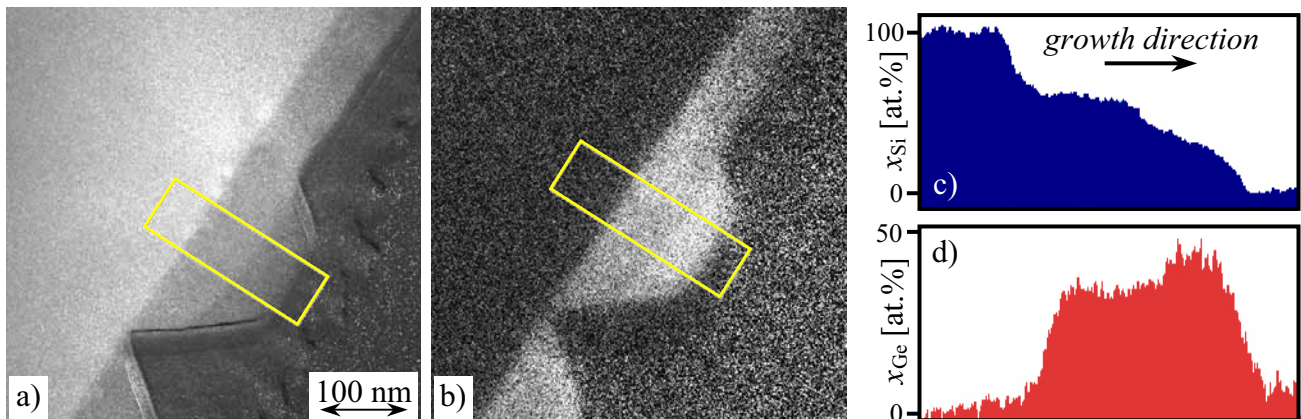


Fig. 1. Image of the element distribution in the region of a SiGe island, a) Si-L<sub>23</sub> map, b) Ge-L<sub>23</sub> map, c) corresponding profile of the Si distribution, and d) Ge profile.

The Si and Ge element maps obtained were divided by the corresponding thickness images in order to correct for thickness-dependent contributions to the net signal. Typical element distributions as recorded with the Si-L<sub>23</sub> (99 eV) and the Ge-L<sub>23</sub> (1217 eV) edge, respectively, and corrected for thickness effects are shown in Fig. 1. Obviously, the average contrast of these element maps behaves complementary. It is also clear from Fig. 1 that the Ge distribution is not uniform through the island. The region between the Si substrate to more than about half the island height exhibits a lower Ge content than at the top region of the island. The region near the substrate can be attributed to the position of the original  $\text{Si}_{1-x}\text{Ge}_x$  layer (nominal Ge content of 25 %) deposited first, whereas the adjacent one is clearly a result of island formation during the second deposition step. To reveal the variation of the element concentration in the growth direction in a semi-quantitative manner, the counts of the respective maps are drawn along a line (cf. Figs. 1c and 1d), where these signals have been integrated parallel to the substrate/layer interface to improve the signal-to-noise ratio. From the resulting Ge-L<sub>23</sub> profile an approximately 7 % higher Ge content within the uppermost island region compared to that of the underlying (Si,Ge) layer can be inferred. Up to now, it is unclear whether the more continuous transition of the element-specific signals observable at the interface between substrate and (Si,Ge) layer points to interdiffusion, which could happen during the growth process.

## Nanofold network formation on layered crystal surfaces

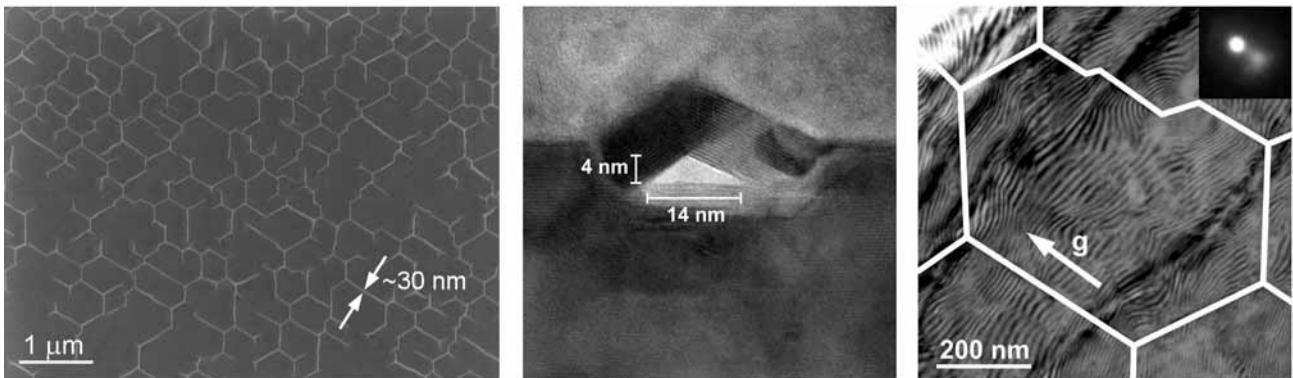
E. Spiecker<sup>a,b</sup>, S. Hollensteiner<sup>a</sup>, W. Jäger<sup>a</sup>, A. Schmid<sup>b</sup>, A. Minor<sup>b</sup>, U. Dahmen<sup>b</sup>

<sup>a</sup>Mikrostrukturanalytik, Technische Fakultät, Universität Kiel, Kaiserstr. 2, 24143 Kiel, Germany

<sup>b</sup>NCEM, Lawrence Berkeley National Laboratory, Berkeley, CA 94720, USA

Layered crystal structures possess unique properties which enable the manufacture of nanostructures. The weak van-der-Waals-like bonds between the individual layers of layered crystals, like graphite or the transition metal dichalcogenides (TMDC), allow the layers to be easily separated or shifted relative to each other. In contrast the individual layers are rather stable due to strong intralayer bonds. Thus the layers can be bent or folded on a nanometer scale without destroying their crystal structure, as shown by the structural integrity of nanotubes.

In this contribution we report on a new class of planar network nanostructures, which develop during UHV metal deposition on initially smooth surfaces of TMDCs. Using *in-situ* low-energy electron microscopy (LEEM) for dynamic observation and high-resolution transmission electron microscopy (HRTEM) for structure analysis, we have observed the rapid formation of hexagonal networks of linear “nanofolds” on top of layered VSe<sub>2</sub> crystals [1]. The scanning electron micrograph (left) shows a typical nanostructure network formed upon UHV deposition of nominally 3.4 nm of Cu onto a clean VSe<sub>2</sub> surface prepared by cleavage. HRTEM in cross-section geometry (center) shows for the first time that such surface nanostructures correspond to surface folds which contain prismatic cavities with a triangular cross section a few nanometers in size. Detailed analyses of the surface regions inside the meshes by conventional transmission electron microscopy and diffraction in plan-view geometry clearly revealed that the nanofold formation results from relaxation of compressive stresses (right, nanostructures marked by white lines) which build up during metal intercalation into a thin surface layer [1-3]. Our observations contradict an earlier model that described surface phenomena during the early stages of metal deposition onto TMDCs as resulting from the formation of surface cracks and their subsequent filling with metallic material [4].



### References:

- [1] E. Spiecker, A. Schmid, A. Minor, U. Dahmen, S. Hollensteiner, W. Jäger (submitted).
- [2] E. Spiecker, S. Hollensteiner, W. Jäger, H. Haselier, H. Schroeder, *Microsc. Microanal.*, in press.
- [3] S. Hollensteiner, E. Spiecker, W. Jäger, *Appl. Surf. Sci.* 241 (2005) 49.
- [4] R. Adelung et al., *Phys. Rev. Lett.* 74 (2001) 1303, *Adv. Mater.* 14, (2002) 1056.

This work was supported by the German Science Foundation (FOR 353/1-2) and by the U.S. DOE (DE-ACO3-76SFOO098). We thank L. Kipp from Kiel University for providing the VSe<sub>2</sub> crystals.

## Crystal Growth Related Investigations on the Zeolite Intergrowth System EMT/FAU Using SEM and AFM

Werner Stracke<sup>a</sup>, Gema González<sup>b</sup>, Ulrike Keller<sup>a</sup>, Soraya González<sup>b</sup>, Andrea Ricker<sup>a</sup>, and Rudolf Reichelt<sup>a</sup>

<sup>a</sup>Institute for Medical Physics and Biophysics, University of Muenster, Robert-Koch-Str. 31, D-48149 Muenster, Germany

<sup>b</sup>Centro Tecnológico, Laboratorio de Materiales, Instituto Venezolano de Investigaciones Científicas, km 11 Carretera Panamericana, Altos de Pipe, Caracas, Venezuela

The submicroscopic structures of the microporous crystalline zeolites are essential for their conventional use e.g. as shape-selective catalysts or ion-exchangers and, today, apart from it as sensors [1] or in microchemical systems [2]. For the structural characterization of the zeolite material a variety of high resolution (HR) microscopic and spectroscopic techniques is commonly used, e.g., HR-scanning electron microscopy (SEM), HR-transmission electron microscopy (TEM), X-ray diffraction (XRD), nuclear magnetic resonance (NMR) spectroscopy, 3-dimensional TEM. However, these methods do not allow for the precise determination of step heights in the topographic information of the surface structure.

We investigated faujasite type zeolites with hexagonal (EMT) and cubic (FAU) crystal structure, as well as the intergrowth system EMT/FAU with 50% of each by HR-SEM and atomic force microscopy (AFM). HR-SEM secondary electron micrographs revealed at moderate magnification the size, the topology and the arrangement of the crystalline “blocks” of the individual zeolite particles and, at high magnification, some fine surface features such as the location of “intercrystalline” pores (micropores) and crystal growth related structures. Step heights of the crystal growth related structures in kind of terraces are not directly accessible through SEM, but AFM proved to be a complementary microscopic technique for accomplishing this task with high precision. On the EMT/FAU intergrowth zeolite particles “block” structures with habits more similar to those of the single components were found, and habits which appear as an intermediate, too. Line profile measurements performed on the “blocks” of the first kind came to multiples of the respective smallest step height of 2.7 nm and 2.4 nm for the zeolites EMT and FAU, respectively. On an area with an “intermediate block” structure a smallest step height of 2.1 nm was found. To prove the regularity in the height of a line profile and therefore to estimate a value for the standard deviation as well as to trace a height profile in a lateral direction along a terrace step, about ten to each other equidistant line profiles were measured across a “block” edge.

In summary, these findings provide an example for the possible appearance of different types of intergrowths (e.g., [3]) pictured as regular stacking of different structurally uniform zeolite domains and overgrowing with a compositionally or structurally different zeolite phase giving an indication concerning the crystal growth mechanisms at the sub micrometer scale.

### References:

- [1] Proc. 13<sup>th</sup> International Zeolite Conference, A. Galarneau et al. (Eds.), Montpellier, France: Elsevier (2001), CD-ROM
- [2] J.L.H. Chau et al., Chem. Engineering J. 88 (2002), 187-200
- [3] A.M. Goossens et al., Eur. J. Inorg. Chem. 2001 (2001), 1167-1181

## **TEM study on the microstructures of $\text{Sr}_{0.5}\text{Ba}_{0.5}\text{NbO}_6$ thin film deposited on $\text{SrTiO}_3$ substrate**

Dong SU, Anna Infortuna, and Nava Setter

Laboratoire de Céramique, Ecole Polytechnique Fédérale de Lausanne, EPFL, CH-1015 Lausanne, Switzerland

$\text{Sr}_{0.5}\text{Ba}_{0.5}\text{NbO}_6$  (SBN50) thin films deposited on  $\text{SrTiO}_3$  (100) single crystalline substrate by Pulsed laser deposition (PLD) were studied by transmission electron microscopy (TEM). The selected area diffraction patterns of cross-section sample show different growing columns which are coherent with substrate. The detail of the interface are studied by high resolution electron images (HREM). Growing models were built and well answered experimental results, based on the relationships between SBN50 and STO.

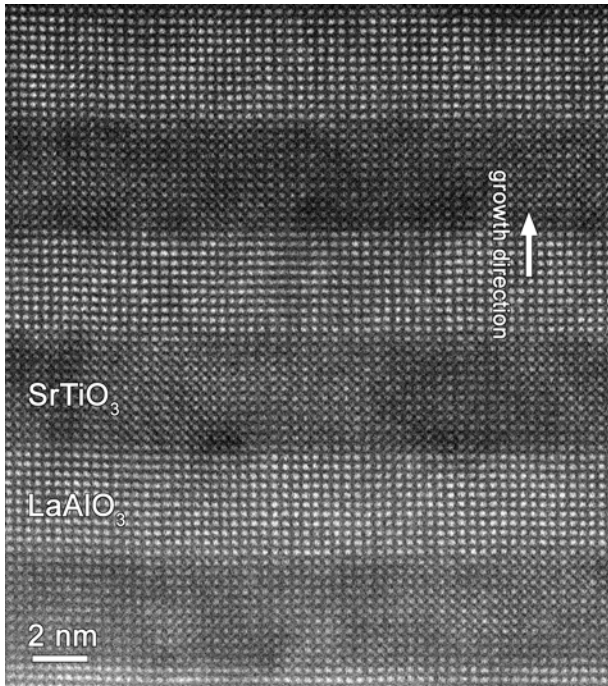
## LaAlO<sub>3</sub> / SrTiO<sub>3</sub> interface characterization

Sara Bals, Sandra Van Aert, Jo Verbeeck and Gustaaf Van Tendeloo

EMAT research group, University of Antwerp, B-2020 Antwerp, Belgium

The LaAlO<sub>3</sub>/SrTiO<sub>3</sub> system has attracted great attention because of the high mobility electron gas found at this heterointerface [1]. It is shown that the stacking of the atomic planes at the interface between the 2 insulating perovskite materials determines the sheet resistance. More specifically an insulating hole doped interface is found for the following sequence: -LaO-AlO<sub>2</sub>-SrO-TiO<sub>2</sub>-, whereas an -AlO<sub>2</sub>-LaO-TiO<sub>2</sub>-SrO- configuration yields an electron doped interface with extremely high carrier concentration, exceeding 10,000 V cm<sup>-1</sup> s<sup>-1</sup>. These observations demonstrate the need to control and characterise thin film deposition on an atomic scale.

A HAADF-STEM image of a LaAlO<sub>3</sub>/SrTiO<sub>3</sub> multilayer system (grown using pulsed laser deposition) is presented in Figure 1. It can be seen that the interfaces between the different layers appear very sharp. Although the intensity difference between the La and Sr atoms is apparent it is more difficult to visualize and distinguish the Ti and the Al atoms. Therefore we have evaluated the peak heights of the atoms at the interfaces in a quantitative manner by means of parameter estimation [2]. By comparing the error bar (95% confidence interval) corresponding to the peak height of the unknown atoms at the interface with the error bars of the surrounding Ti/Al peak heights, it has been found that the the interface at the top of every SrTiO<sub>3</sub> layer has the following sequence: -AlO<sub>2</sub>-LaO-TiO<sub>2</sub>-SrO-. At the bottom of every SrTiO<sub>3</sub> layer we determined -LaO-AlO<sub>2</sub>-SrO-TiO<sub>2</sub>- to be the stacking sequence. This means that the system is controlled in a way that an alternating sequence of n-type and p-type junctions is formed.



These results are combined with EELS data which allows us to relate the electronic configuration at the interfaces with the physical properties found.

### References:

- [1] A. Ohtomo and H.Y. Wang, Nature 427 (2004) 423.
- [2] A.J. den Dekker, S. Van Aert, A. van den Bos, D. Van Dyck, Ultramicroscopy (2005) in press.
- [3] The authors acknowledge FEI Company and B. Freitag for their permission to publish Figure 1.
- [4] S. Bals and S. Van Aert are grateful to the Fund for Scientific Research-Flanders.

## TEM Study of Carbon Nanophases Grown in Carbon-Ion Implanted Quartz

A. M. Tonejc<sup>1</sup>, I. Djerdj<sup>1</sup>, A. Tonejc<sup>1</sup>, M. Bijelić<sup>1</sup>, M. Buljan<sup>2</sup>, U. V. Desnica<sup>2</sup>, and R. Kalish<sup>3</sup>

<sup>1</sup>Department of Physics, Faculty of Science, POBox 331, 10002 Zagreb, Croatia

<sup>2</sup>Rudjer Bošković Institute, PO Box 180 Zagreb, Croatia

<sup>3</sup>Physics Department and Solid State Institute, Technion, Haifa, Israel

In this work, carbon ions were implanted into SiO<sub>2</sub> at different doses. Following annealing the samples were structurally characterized with the aid of the 200 kV high-resolution transmission electron microscopy (HRTEM) and selected-area electron diffraction (SAED). The aim of the present work was to investigate the phase composition, crystallographic parameters, morphology, average grain size and grain size distribution as a function of preparation conditions i.e. implantation dose.

The synthesis of nanocrystalline carbon structures is supported by the fact that carbon can bond in sp<sup>1</sup> (linear polymer-like), sp<sup>2</sup> (trigonal planar graphite-like) and sp<sup>3</sup> (tetrahedral diamond-like) hybridizations. The existence of three distinct nanocrystalline carbon phases has been previously reported [1]: the cubic diamond (*c*-diamond) phase with the space group *Fd3m*, and unit cell parameter  $a_0=0.356$  nm, a metastable form of diamond known as a *n*-diamond (or  $\gamma$ -carbon) with *fcc* unit cell ( $a_0=0.356$  nm) and a space group *Fm3m*, and a form of nanocrystalline carbon phase referred to as *i*-carbon in the literature [2] with the primitive cubic unit cell ( $a_0=0.432$  nm) belonging to the space group *P2<sub>1</sub>3* or *P4<sub>2</sub>32*.

The formation of carbon nanocrystals, produced by ion implantation of carbon ions into fused SiO<sub>2</sub> substrates, followed by one hour thermal annealing at 1000<sup>0</sup> C, in an Ar + 5% H atmosphere has been studied. The carbon nanocrystals formed by the implantation for a dose of  $1 \times 10^{16}$  C/cm<sup>2</sup> at 320 keV have been identified as a mixture of *c*-diamond nanophase and a modified diamond nanophase known as *n*-diamond. For a higher implantation dose,  $5 \times 10^{16}$  C/cm<sup>2</sup>, besides *n*-diamond, another solid carbon nanophase was observed, with a structure known as *i*-carbon. Following the highest implantation dose  $1 \times 10^{17}$  C/cm<sup>2</sup> the sample contained the *i*-carbon nanophase only.

A least-square refinement of SAED patterns was employed for the calculation of unit-cell parameters of identified carbon nanophases. Raman spectroscopy measurements confirmed HRTEM results in formation of carbon nanocrystals of different solid carbon phases.

[1] J. O. Orwa, S. Praver, D. N. Jamieson, J. L. Peng, J. C. McCallum, K. W. Nugent, Y. J. Li, and L. A. Bursill, *J. Appl. Phys.*, **90** (2001) 3007.

[2] B. G. Burkhard, K. Dan, Y. Tanabe, A. K. Sawaoka, and K. Yamada, *J. Appl. Phys.* **33** (1994) 5875

## Investigation of Brake Pad Samples before and after Squealing

I. Urban, I. Dörfel, M. Engelhardt, H. Rooch, W. Gesetzke, W. Österle

Federal Institute for Materials Research and Testing, Unter den Eichen 87, 12200 Berlin, Germany

Among a sequence of different investigations concerning various complex effects during brake processes we have studied features like the formation of friction layers, their microstructure and composition or the genesis of wear debris and their characterization. A further important problem is the identification of reasons for the origination of brake squeals. This phenomenon is of great interest and is not fully understood up to now [1,2].

The different friction materials were polymer matrix composites, with a large number of different constituents, used against brake discs of grey cast iron. Samples before and after squealing were considered.

Here SEM, FIB and TEM investigations are presented, which were applied among a number of other chemical and physical investigation methods (ESCA, RAMAN spectroscopy, XRF, ICP-OES, GDOES). Samples were generated in tests interrupted before and after squealing.

The following results were obtained: During a bedding procedure the surface of the brake pad gets covered by a discontinuous third body layer which is filling troughs of the surface profile and thus provides smooth contact areas [3]. Since the main component of this so-called friction layer is iron oxide, the colour-coded SEM images reveal such areas in violet, as shown in Fig. 1a. The other colours correspond to different pad constituents. After squealing the surface is rough and consequently the colours are not shown clearly (Fig. 1b). Only small smooth fragments of the friction layer are shown in blue or violet. More detailed FIB/TEM-investigations with micro-cross-sections revealed the nanocrystalline nature of the friction layer. Furthermore it appeared that at least some of the loose wear particles had the same composition and microstructure, implying that the layers were formed by re-deposition of wear particles. The thickness of layers was relatively thin and uniform before squealing, but either thick fragments or totally removed layers were observed after squealing

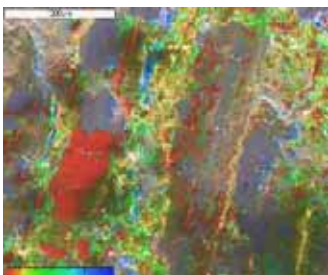


Fig.1a: SEM-Cameo before squealing

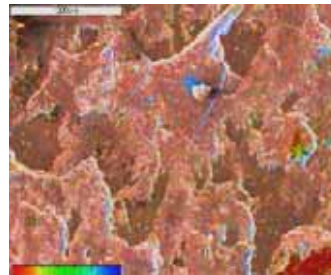


Fig.1b: SEM-Cameo after squealing

events. Furthermore coarse wear particles frequently cover the pad surface after squealing, indicating that the wear process is in an initial state after removal of the protecting friction layer.

Obviously friction layers spall off as soon as they have reached a critical thickness, which seems to be the origin of noise excitation.

[1] M. Eriksson, F. Bergmann, S. Jacobson *Wear* **232** (1999) 163-167

[2] H.A. Sherif *Wear* **257** (2004) 687-695

[3] W. Österle, I. Urban *Wear* **257** (2004) 215-226

## Nanostructured NiTi alloys studied by TEM

Thomas Waitz and H. Peter Karnthaler

Institute of Materials Physics, University of Vienna, Boltzmanngasse 5, AT-1090 Wien, Austria  
www.univie.ac.at/Materialphysik/EM

Recently bulk nanostructured NiTi shape memory alloys were made using methods of severe plastic deformation. By high pressure torsion (HPT) amorphization of NiTi was obtained in the solid state [1]. During HPT strong structural refinement and a deformation texture arise followed by amorphization caused by a shear strain instability. By annealing nanocrystalline structures were achieved by devitrification of the amorphous phase [2, 3]. Amorphous and nanocrystalline phases are studied by high-resolution transmission electron microscopy (HRTEM) in combination with TEM dark field (DF) methods and selected area (SA) diffraction.

Figure 1 shows a HRTEM micrograph of a NiTi specimen after a HPT deformation of  $\sim 40\,000\%$ . Embedded in an amorphous phase heterogeneously distributed nanocrystalline debris is encountered that has survived the HPT deformation. Most of the nanocrystals are contained in band shaped areas and show similar crystallographic orientations. Figures 2 and 3 show the structure of the nanograins after complete devitrification (after annealing at  $300^\circ\text{C}$  for about 5h, retained amorphous phase is not encountered). In the TEM dark field image of Fig. 2 nanograins showing a bright contrast have a similar orientation and are arranged in bands. The analysis was carried out placing the objective aperture over the part of the  $\{111\}_{\text{B2}}$  diffraction pattern marked by a circle (cf. Fig. 3). The texture of the nanograins is indicated by arrows. Nanocrystalline debris retained in the amorphous matrix leads to a memory effect: The HPT texture still shows up after devitrification since a preferred orientation of the nanograins is caused by the retained nanocrystals acting as nucleation sites.

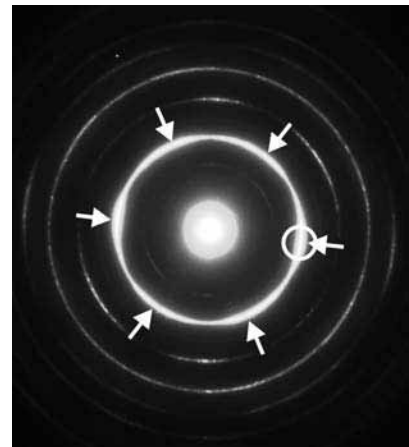
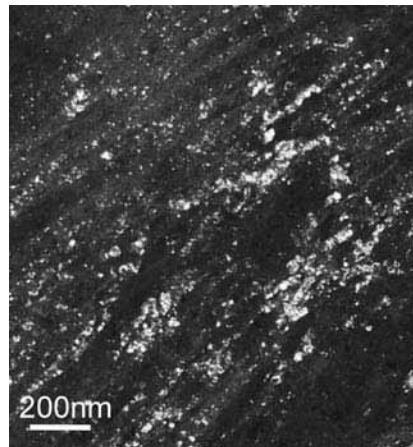
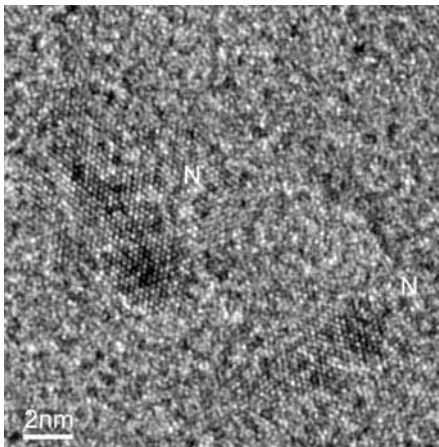


**Fig. 1:** NiTi; HRTEM image of nanocrystals marked N embedded in an amorphous matrix.

**Fig. 2:** NiTi; DF image of similar orientated nanograins contained in band shaped areas

**Fig. 3:** NiTi; SA diffraction of the nanograins that show a texture.

### References:

- [1] T. Waitz, V. Kazykhanov and H. P. Karnthaler, *Acta Mater.* 52 (2004) 137.
- [2] T. Waitz and H. P. Karnthaler, *Acta Mater.* 52 (2004) 5461.
- [3] T. Waitz, *Acta Mater.* 53 (2005) 2273.

## Characterization of electropolymerized substituted metalloporphyrins by Atomic Force Microscopy (AFM)

Xi Zheng, A. Sheila Holmes-Smith and Mahesh Uttamlal

School of Engineering, Science and Design, Glasgow Caledonian University, Cowcaddens Road, Glasgow, G4 0BA, UK

Platinum(II)metalloporphyrins have been widely employed as luminescence indicators in oxygen sensing applications<sup>1</sup>. We have been investigating improving the robustness and sensitivity of sensing polymers employing metalloporphyrin by electropolymerization of di-phenyl-di-(4-aminophenyl)-porphyrin-Pt (II) (DAPP-Pt (II)). In the electropolymerization process, the working electrode (ITO glass) is cycled between two potential values resulting in oxidation and reduction of the porphyrin molecule in solution and, in the correct conditions, polymer growth on the electrode surface. This paper describes different experimental conditions for polymer growth and the characterisation of the resulting polymer by Atomic Force Microscopy (AFM).

Cyclic voltammetry involves sweeping the potential on a working electrode, which is located in a solution containing the porphyrin monomer and electrolyte, between two limits for a predetermined number of cycles. The different electrolyte molecules investigated were sodium chloride (NaCl), lithium perchlorate (LiClO<sub>4</sub>) and tetrabutylammonium perchlorate (TBAP). Using NaCl or LiClO<sub>4</sub> resulted in poor growth of the cyclic voltammogram waves and the AFM images revealed crystals with little evidence of the layered structure expected for good polymer growth. This is a result of the small size of these electrolyte molecules giving poor polymer growth. Different potential ranges for the cyclic voltammetry were investigated using TBAP as the electrolyte. If the potential range does not include the oxidation potential of the amine reactive group of DAPP-Pt(II) (0.9 V), then no polymerization will occur. Cycling up to the oxidation potential of the Pt(II) ion, 1.4 V shows additional topographic features scattered on the surface of the AFM image. These features have a height range of 50nm to 110nm, are ~0.2 μm in diameter and are crystalline in appearance. It is reasonable to deduce these features are TBAP crystals, which have crashed out of solution at the high potential. Cycling 8 times over the potential range 0.4V to 1.2V, results in good polymer growth as shown in Figure 1. The layered structure of the polymer growth is clearly observed and the average height of each layer is about 2 nm. The AFM characterizations of these polymers show that the electrolyte, the number of cycles and the potential range plays an important role in the polymer formation. AFM images will be presented for these different experimental conditions.

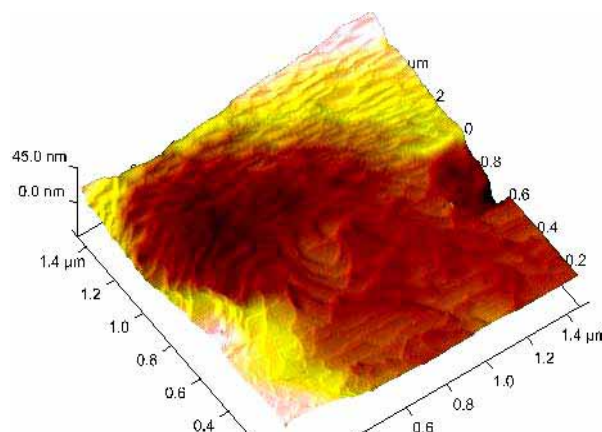


Figure 1: AFM height image of Poly DAPP-Pt (II)

[1] G.DiMarco, M.Lanza, Optical solid-state oxygen sensors using metalloporphyrin complexes immobilized in suitable polymeric matrices, *Sensors and Actuators B*, 2000, **63**:42

## Visualization of Structural State in CSD BST Thin Films

O.M.Zhigalina<sup>a</sup>, K.A.Vorotilov<sup>b</sup>, A.S.Kumskov<sup>a</sup>, O.I. Lebedev<sup>c</sup>, A.S.Sigov<sup>b</sup>, and D.H.Khmelenin<sup>b</sup>

<sup>a</sup> Institute of Crystallography, Russian Academy of Sciences, Leninskii pr. 59, 119333, Moscow, Russia

<sup>b</sup> Moscow State Institute of Radioengineering, Electronics and Automation (Technical University), Vernadskii pr. 78, 117454, Moscow, Russia

<sup>c</sup> Antwerpen University, Groenenborgerlaan 171 B-2020 Antwerp, Belgium

High-permittivity perovskite ceramic thin films have been investigated as dielectric materials for future dynamic random access memory (DRAM), monolithic microwave integrated circuits (MMIC) and microwave phase shifters for electronically erasable antennas. With respect of these applications a control of the film structural and morphological peculiarities is of crucial importance for tailoring electrical properties. [1, 2].

BST films (Ba/Sr=70/30) were prepared by chemical solution deposition (CSD) on Si-SiO<sub>2</sub>-Ti-Pt and single crystal sapphire substrates and annealed at 600-1100°C. Crystallization process was realized by different ways: layer-by-layer crystallization and one step crystallization.

The structural state of BST films was characterized by transmission electron microscopy (TEM) and high resolution electron microscopy (HREM) with Philips EM430 ST at accelerating voltage of 200 kV. The phase composition and texture were investigated by XRD analysis. EDX-mapping was carried out with CM30. The cross-sectional and plan-view samples for TEM and HREM studies were prepared by mechanical polishing, dimpling and ion milling by Ar<sup>+</sup> in Gatan 600.

TEM analysis and EDX-mapping have shown that BST-Pt-Ti-SiO<sub>2</sub>-Si heterostructures were unserviceable for the high temperature treatments due to intensive diffusion processes through Pt-Ti layers while BST-Sapphire heterostructures were more stable and exhibited an average grain size about 60 nm (Fig.1). Two crystallization mechanisms have been observed at the crystallization of perovskite BST phase: heterogeneous nucleation both on the Pt and sapphire substrates (Fig.2) and nucleation in the volume of films. The sharp texture in the part of volume was formed at the crystallization on Pt, while random oriented equalaxis grains grew on sapphire substrates.

### References:

[1] Daisure Ueda, Journal of Electroceramics, 32(1999), p.105.

[2] S.Ezhilvalavan, Tseung-Yuen Tseng, Materials Chemistry and Physics, 65 (2000), p.227.

[3] The work is supported by RFBR (Grant No 04-02-16804).

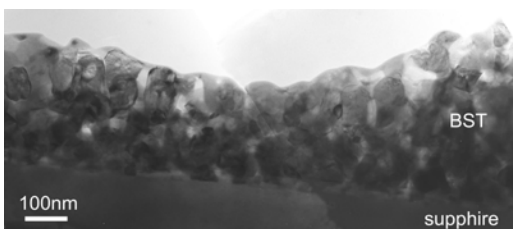


Fig.1. BST-sapphire TEM image, cross-section.

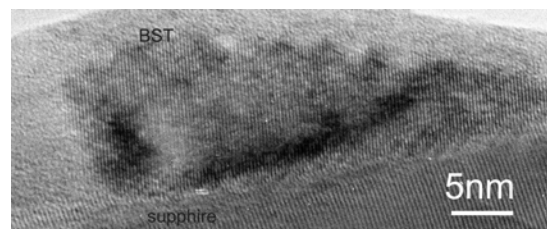


Fig.2. HREM image of heterogeneous nucleation.

# Cryopreservation of Cells Cultured on Nanostructured Surfaces Studied by Block-Face SEM in Combination with Freeze-Substitution

H. Zimmermann<sup>a</sup>, M. Laue<sup>b</sup>, S. Pflueger<sup>a</sup>, N. Puetz<sup>b</sup>, M. Zwanzig<sup>c</sup>, S. Fiedler<sup>c</sup>, P. Mestres<sup>b</sup>, A. Katsen-Globa<sup>a</sup>

<sup>a</sup> Fraunhofer IBMT, Ensheimer Str. 48, 66386 St. Ingbert, Germany,

<sup>b</sup> University of Saarland, F.2.1, 66421 Homburg, Germany

<sup>c</sup> Fraunhofer IZM, Gustav-Meyer-Allee 25, 13355 Berlin, Germany

Monolayer cryopreservation of cells on a substrate is complex. One problem is the detachment of cells during ice formation. Successful cryopreservation requires new cryobiological methods and new surfaces, such as nanostructures [1] as well as a method for studying the cell-substrate interface [2]. The distance between cell and substrate can change during cryopreservation and depends on the cell-substrate interaction and ice formation. To study these we have developed a new method for combined block-face SEM and freeze-substitution. This method has been applied to mammalian

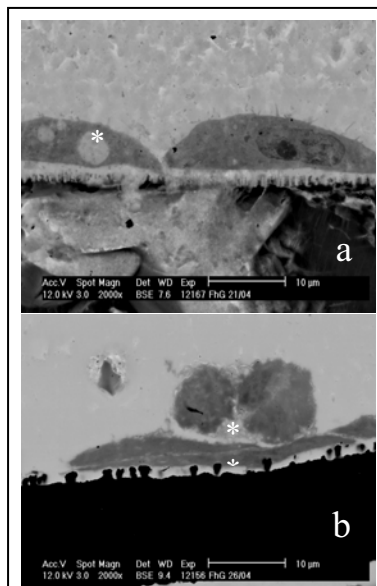


**Fig. 1.** Block-face SEM of freeze-substituted cryopreserved cells on the nanostructured substrate : a- intracellular ice (\*), b- possible intercellular ice(\*\*).

cells cryopreserved with cryoprotectants on nanostructured surfaces. L929 mouse fibroblasts were cultured on gold, silicon and carbon surfaces with specific nanotopography mounted in micro-cryosubstrates [2]. After freezing with cryoprotectants (DMSO) down to  $-80^{\circ}\text{C}$ , one half of the specimens was thawed, fixed, treated with tannic acid and heavy metals and prepared according to standard for SEM. The other half of the specimens was freeze-substituted with osmium and acetone over a period of 3 days. All were embedded in epoxy resin, cross sectioned with a diamond saw, polished and investigated in SEM as described [2].

Viability of cells after cryopreservation on nanostructured surfaces was high (up to approx. 90% on the carbon substrates), but variable (possibly due to thermal conductivity variations of the substrates). First results indicate that the cells did not detach from the substrates after thawing. We measured the distance between cell and substrate. Typical values are in the range of 50 nm. In some regions this distance can be up to 500 nm (Fig. 1a). Interestingly, the big distances seem to correlate with the existence of large intracellular ice crystal domains. Further research has to be done to clarify whether the distance is cause or symptom of intracellular ice formation. The proposed method may be also useful for identifying of intercellular ice domains (Fig. 1b) and, thus, for the improvement of cell and tissue cryopreservation in general.

## References:

- [1] Zimmermann H., Katsen A.D., Ihmig F.R., Durst C.H.P., Shirley S.G., Fuhr G.R. IEE Proc.-Nanobiotechnology, vol. 151, 2004, pp. 134-138.
- [2] Katsen-Globa A., Pflüger S., Zwanzig M., Fiedler S., Howitz S., Zimmermann H. In Proc. of Focus on Microscopy, Jena, (2005), 212.
- [3] Grants: 03N8707 by BMBF and NMP4-CT-2004-500039 by EU.

## **Oxidation of Tungsten Alloy**

A. A. ALHAZZA\*, A. AL-OMAIR\*, and K. ALHAZZA\*\*

\*Kuwait Institute for Scientific Research, Central Analytical Laboratory, P.O. Box 24885, 13109 Safat, Kuwait

\*\*Kuwait University, College of Engineering and Petroleum, Mechanical Engineering Department, P.O. Box 5969, 13060 Safat, Kuwait

Tungsten and the tungsten alloy group represent a wide range of uses extending from everyday uses to component of nuclear fusion reactors or ion drive motors in space probes. The reason for this range of use lies in the many outstanding properties of tungsten. In the W-O system, there are the stoichiometric oxides  $WO_3$ ,  $WO_{2.9}$ ,  $WO_{2.7}$ ,  $WO_2$ , and non stoichiometric structure that represent the ordered or partially ordered defect structures of the oxygen-rich oxide, in which the central W atom is octahedrally surrounded by six oxygen atoms. In  $WO_3$ , neighbouring octahedra are in contact only at the corners. Which increase oxygen deficiency (reduction, conversion to lower oxides), common edges and surfaces are progressively formed.

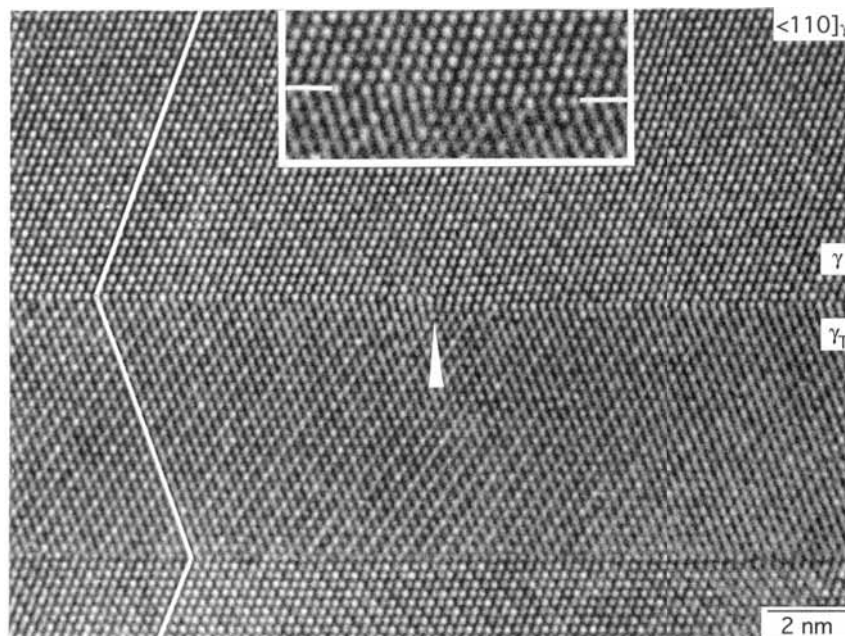
The aim of this work is to produce from a "heavy metal swarf" a homogeneous powder for recycling. The process route envisaged was a controlled oxidation, to breakdown the swarf. In the first step the microstructure of the Swarf was to be characterised using optical metallography, SEM, and XRD. This characterisation was followed by the oxidation to achieve the mechanical breakdown and to give a friable oxide. In this step a TG was planned for use to determine the temperatures for oxidation and to give some idea on the kinetics of the process. SEM and XRD were to be used to find the morphology and the type of the oxide. According to the TG results, temperatures could be selected for oxide manufacture.

# An Electron Microscope Study of Mechanical Twinning and Fracture in TiAl Alloys

F. Appel

Institute for Materials Research, GKSS Research Centre Geesthacht  
D-21502 Geesthacht, Germany

Titanium aluminide alloys based on the intermetallic phases  $\gamma(\text{TiAl})$  and  $\alpha_2(\text{Ti}_3\text{Al})$  exhibit outstanding thermo-mechanical properties, which provide good potential for application in high-temperature technologies. However, the material suffers from brittle fracture, which is the key risk to implementation. Many aspects of this behaviour can be attributed to the kinematics and dynamics of dislocation glide in  $\gamma(\text{TiAl})$ , which is generally difficult because of high Peierls stresses and non-planar core dissociation. As shown in the micrograph, deformation of  $\gamma(\text{TiAl})$  can also be provided by mechanical twinning, which provides auxiliary slip systems and plays an important role in alloy design strategies for mitigating the problems associated with the poor



damage tolerance of the material. Understanding of mechanical twinning in ordered structures is still in many ways imperfect. To some extent this is due to the atomic scale of the processes and the difficulties associated with the complexity of defect structures and constraint stresses that are developed in heavily twinned material. This imbalance of information is addressed by a high-resolution transmission electron microscopy study of twin structures in  $\gamma(\text{TiAl})$ . The major areas of the investigation are: (i) twin nucleation and propagation, (ii) effects of solutes and precipitates on the kinematics and dynamics of twin propagation, (iii) association of mechanical twinning and fracture. More details are given in [1].

[1] F. Appel, An electron microscope study of mechanical twinning and fracture in TiAl alloys, *Phil. Mag.* 85, 2005-231 (2005).

## Analytical TEM of Nb<sub>3</sub>Sn multifilament superconductor wires

M. Cantoni<sup>a</sup>, F. Bobard<sup>a</sup>, V. Abächerli<sup>b</sup>, D. Uglietti<sup>b</sup>, B. Seeber<sup>b</sup> and R. Flükiger<sup>b</sup>

<sup>a</sup>EPFL-CIME, Bat. MXC-135, Station 12, CH-1015 Lausanne

<sup>b</sup>Group of Applied Physics, University of Geneva, CH-1211 Geneva

Bronze processed Nb<sub>3</sub>Sn superconducting wires are today still considered as the best candidates for nuclear magnetic resonance (NMR) magnets operating in persistent mode at high magnetic fields. The metallurgical treatment of Nb<sub>3</sub>Sn bronze wires with additives like Ta and Ti is quite difficult to further improve because the correlation between the additive and its effect on the superconducting properties, which do not only depend on its concentration but also on the whole variety of fabrication parameters. The aim of this work is to clear up the different effects of the internal (Nb-Ta / Nb-Ti filaments) and external (Cu-Sn-Ti bronze) Ti doping method on the superconducting properties and to analyze their possible reasons [1].

Conventional techniques of specimen preparation did not lead to TEM-samples with the required large and thin areas for the analysis because of severe preferential thinning of the bronze matrix around the Nb<sub>3</sub>Sn filaments. The focused ion beam (FIB) was used to cut out lamellae of 20x5um size directly from a cable, to attach them to a TEM grid and to thin them further to electron transparency (Fig. 1). The samples obtained this way have uniform thickness and are ideally suited for EDX-Anlalysis (Fig. 2).

Scanning Transmission Electron Microscopy (STEM) in combination with Energy Dispersive X-Ray (EDX) Microanalysis was used to analyze the chemical composition of the superconducting phase. Energy filtered imaging and EELS were used to investigate and trace the additives on a nanometer scale at the grain boundaries.



Fig.1: STEM dark field image: cross-section of a single superconductor filament. The inset shows the TEM lamella prepared by FIB.

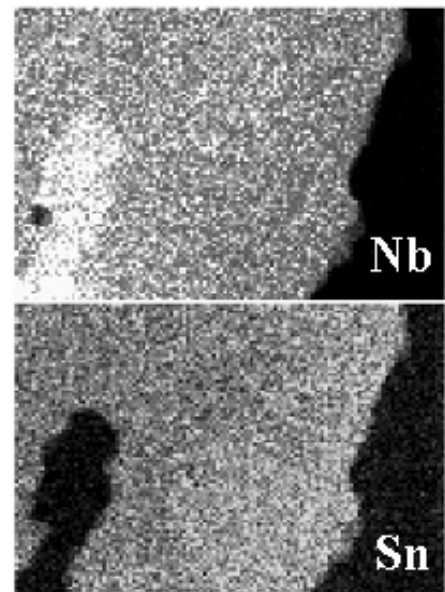


Fig. 2: EDX element maps of Nb and Sn. The remaining Nb core and a gradient in the Sn concentration are clearly recognizable.

### References:

[1] Abächerli V, Uglietti D, Seeber B, Flükiger R, Physica C 372-376 (2002), 1325-1328.

Acknowledgement: EPFL-CMI for he access to the FIB

## Antiphase Boundaries in Ni-Al-Cr Ordered Intermetallic

Elżbieta Jezierska

Warsaw University of Technology, Faculty of Materials Science and Engineering  
Wołoska 141, 02-507 Warsaw, Poland

The antiphase domain structure in Ni-Al-Cr alloy was recognized by conventional TEM and large angle convergent beam electron diffraction (LACBED) methods. The TEM samples were prepared by standard electrochemical polishing using 5% perchloric acid in acetic acid and investigated on JEOL JEM 3010 (300 keV) microscope. The distinguishing between stacking faults and antiphase boundaries (APBs) is quite complicated procedure in conventional TEM. By LACBED method the recognition of APBs is not such difficult and the results are easier to interpret [1-3]. In the case of antiphase boundary the superlattice excess line is split into two lines with equal intensity (Fig.1) on bright and dark field LACBED pattern (“bird eye” effect). This splitting can be considered as typical and used to identify APBs.

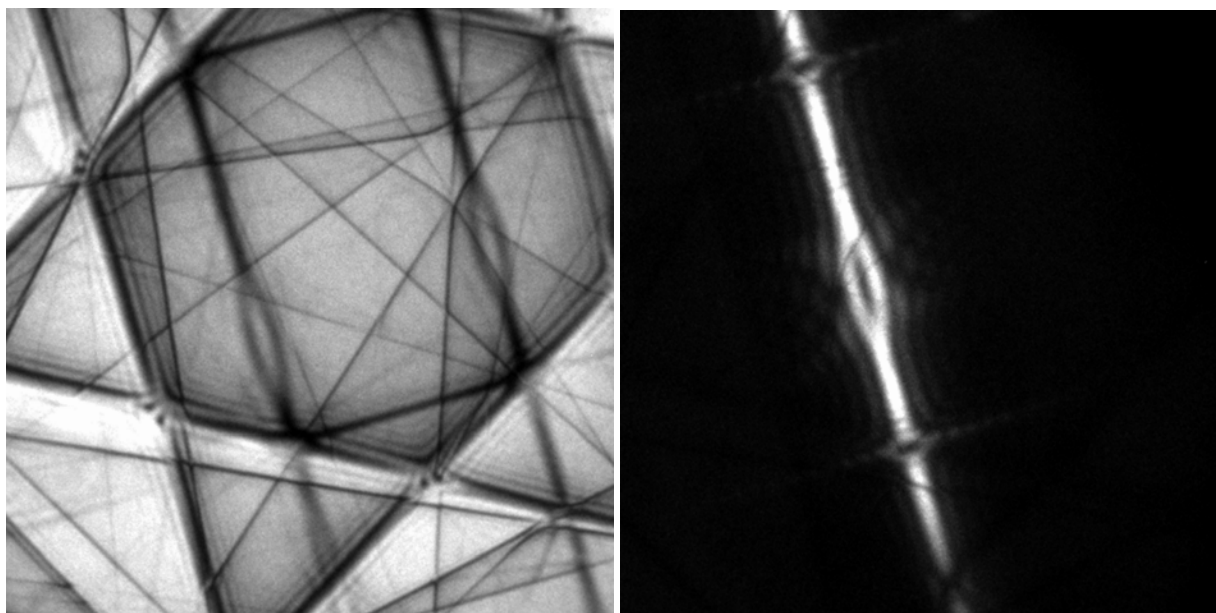


Fig. 1 Bright-field (a) and dark-field (b) LACBED patterns of APBs in Ni-Al-Cr ordered  $L1_2$  phase.

### References

1. J.P. Morniroli, Large-Angle Convergent-Beam Electron Diffraction (LACBED). Applications to Crystal Defects, SF $\mu$ , Paris (2002) 357.
2. E. Jezierska, J.P. Morniroli, Antiphase boundaries in Ni<sub>3</sub>Al ordered intermetallic – application of CBED method, Material Chemistry and Physics 81 (2003) 443-447.
3. J.P. Morniroli, M.L. No, P.P. Rodrigues, J. San Juan, E. Jezierska, N. Michel, S. Poulat, L. Priester, CBED and LACBED characterization of antiphase boundaries, Ultramicroscopy 98 (2003) 9-26.
4. The financial support from the Committee for Scientific Research is gratefully acknowledged. Thanks are due to Jean Paul Morniroli for valuable discussions and collaboration.

## ***In situ* TEM Straining of bcc Twins – Unexpected Modes of Slip Transfer**

Antonín Gemperle, Juliana Gemperlová, Niva Zárubová, Zdeněk Dlabáček

Institute of Physics ASCR, Na Slovance 2, 18221 Praha 8, Czech Republic

It has been supposed that the slip transfer across grain boundaries (GBs) basically depends on three conditions: (i) the angle between the lines of intersection of the slip planes with the GB and the angle between the Burgers vectors (BVs) must be small (high geometrical factor), (ii) the BV of the residual dislocation left in the GB should be small, (iii) the active slip plane in the second grain should have a high resolved shear stress [1]. In the previous studies on Fe-Si alloy twin bicrystals [2], one case corresponded to the transfer criteria. Other two cases were shown to be in direct contradiction to these assumptions. In the first case, slip dislocations entering the boundary splitted in three twinning dislocations and slip continued as narrow twins spreading into the second grain. In the second case, the expected favourable slip system was not active. Instead, a slip system operated with a low geometrical factor and a residual dislocation not a GB dislocation with a high energy. Its only advantage was a higher Schmid factor.

Specimens of two orientations were *in situ* TEM strained. The foil plane and load axis were  $(\bar{9}\bar{1}7)A = (\bar{1}1\bar{1}3)B$  and  $(152)A = (15\bar{2})B$  for common primary slip systems, and  $(\bar{1}7\bar{1}\bar{4})A = (\bar{3}\bar{3}\bar{4})B$  and  $(\bar{1}5\bar{3})A = (\bar{1}53)B$  for non-common primary slip systems, respectively. Common slip system transferred as twins spread along the boundary in the second grain (Fig.1). In the second case a system having small geometrical factor, small resolved shear stress and residual edge GB dislocation with large energy was initiated at the boundary (Fig.2).

Conclusions. In twin bicrystals having common primary slip systems and BV in the twin boundary plane, the slip deformation was transformed into deformation twinning in both observed cases. Cases of non-common slip systems may largely deviate from the transfer criteria. In the contribution the weight of the individual transfer conditions will be critically assessed.

### References:

- [1] T.C. Lee, I.M. Robertson and H.K. Birnbaum, Scripta Metall. 23, 789-803, 1989.
- [2] A. Gemperle, N. Zárubová and J. Gemperlová, J. Mater.Sci 40, June, 2005.
- [3] Authors highly acknowledge financial support of GA CR (Contract 202/01/0670).

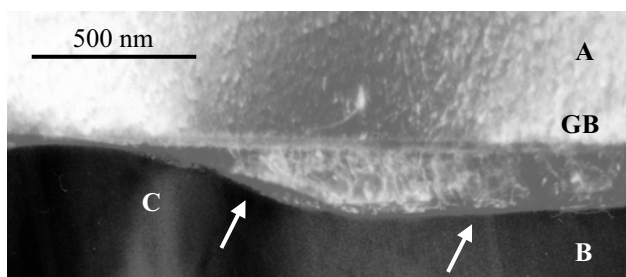


Fig.1: GB original twin boundary, newly formed boundaries marked by arrows, C contrast of crack initiation at the twin tip. DF  $\bar{1}2\bar{1}A$ .

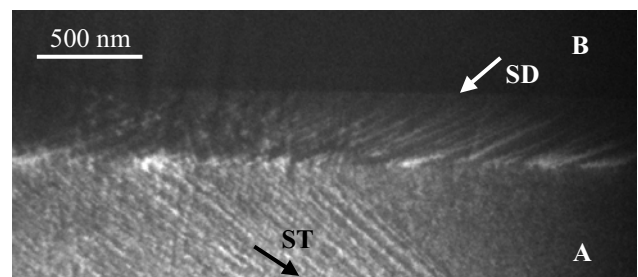


Fig.2: SD slip dislocations trapped in the twin boundary, ST slip traces of a new transferred system. DF 020 A.

## **TEM image simulations of nanometer-size Cu-based defects in Fe**

Ari Harjunmaa<sup>a</sup>, Gang Yu<sup>b</sup> and Robin Schaeublin<sup>b</sup>

<sup>a</sup>Accelerator Laboratory, University of Helsinki, 00014 Helsingin yliopisto, Finland

<sup>b</sup>Fusion Technology – Materials, CRPP, 5232 Villigen PSI, Switzerland

Nanometer-size defects in Fe, as those found in irradiated steels, are investigated with transmission electron microscopy (TEM) image simulations. The investigated defects comprise of pure Cu precipitates, pure voids, and different mixtures of both. Images of simulation cells relaxed using molecular dynamics (MD) simulations are compared with images of unrelaxed cells. Although the difference between the relaxed and unrelaxed cells themselves seems very slight, the TEM images, which are sensitive even to very small changes, show distinct differences between the two. The image contrast and defect visibility threshold for various kinds of defects is also determined as a function of defect diameter. Overall, relaxation has the expected effect of increasing contrast and thus decreasing the visibility threshold.

# Temperature Estimation Of Gas Turbine Component Service By TEM Microstructure Analysis

A. Hessler-Wyser<sup>a</sup>, F. Diologent<sup>b</sup>, M. Biel<sup>c</sup>, F. Bobard<sup>a</sup> and P.-A. Buffat<sup>a</sup>

<sup>a</sup>Interdisciplinary Centre for Electron Microscopy, Ecole Polytechnique Fédérale de Lausanne, 1015 Lausanne, Switzerland

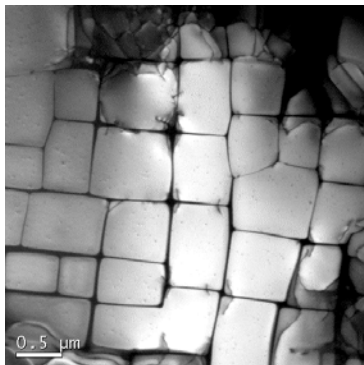
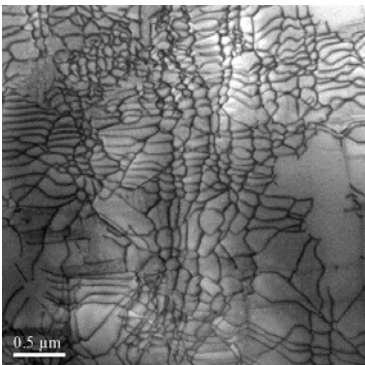
<sup>b</sup>Laboratory of Mechanical Metallurgy, Ecole Polytechnique Fédérale de Lausanne, 1015 Lausanne, Switzerland

<sup>c</sup>AGH University of Science and Technology, 30 059 Krakow, Poland

Single crystal (SC) nickel-base superalloys are currently used for the production of gas turbine (GT) blades and vanes. During service, those are subjected to the superposition of high temperature up to 1100 °C, centrifugal stresses and thermomechanical fatigue, which all together lead to the change of the blade microstructure in very complicated way. Clear understanding of the real stress pattern (temperature, pressure) acting upon the turbine blades during the operation is necessary to enhance turbine efficiency, turbine availability and lowering maintenance costs.

The Ni-base single crystal microstructure consists of cubic-shaped  $\gamma'$  particles ( $L1_2$  type) precipitated in a  $\gamma$  matrix (fcc). Quantitative description of  $\gamma/\gamma'$  parameters of nickel-base superalloys provides information concerning creep and thermomechanical behaviour of these materials during exploitation in service conditions. The aim of this study is to estimate the temperature that Ni-base single crystal superalloy components of GT are subjected to during the service with an accuracy better than  $\pm 25$  K. Up to now, the estimation of the temperature inside a component has been made by classical metallographic technique, which implies characterization of the microstructure by SEM images and TEM micrographs analysis by the threshold method [1].

In order to carry out image analysis, a new method based on the properties of the Fourier transform has been applied [2]. It allows, with a few parameters, to describe the evolution of the  $\gamma/\gamma'$  microstructure in a large range of transformation from cubical  $\gamma'$  precipitates up to strongly distorted  $\gamma'$  rafted structure. Moreover, the dislocations microstructure by TEM has been investigated, which offers unique information on the deformation mode of the material.



## References:

[1] Dubiel *et al.*, Proc. 1<sup>st</sup> Stanislaw Gorczyca Summer School on Advanced Electron Microscopy, Krakow, Poland, (2003).

[2] Epishin *et al.*, Acta Mater. **48** (2000) 4169.

[3] The authors kindly acknowledge the support of Alstom and the Swiss Innovation Promotion Agency KTI/CTI.

## SEM investigations of Mg-Ag-Nd magnesium alloy

Andrzej Kielbus

Department of Materials Science, Silesian University of Technology, 40-019 Katowice, Poland

The Mg-Ag-Nd alloys have good ambient and elevated temperature properties (high yield strength, good tensile strength and fatigue) whilst retaining good foundry characteristic. These alloys may be used up to temperatures of 200°C. They are widely used for aerospace, automotive and military applications including landing wheels and rotor heads for helicopters [1,2].

The studied samples were obtained from commercial MSR-B magnesium alloy, provided by Magnesium Electron, Manchester, UK. The alloy MSR-B containing 2.5 wt.% Ag, 2.5 wt.% Nd and 0.42 wt.% Zr. The observations were performed on HITACHI S-4200 scanning electron microscope with a cold cathode, equipped with an X-radiation detector EDS-VOYAGER of NORAN INSTRUMENTS.

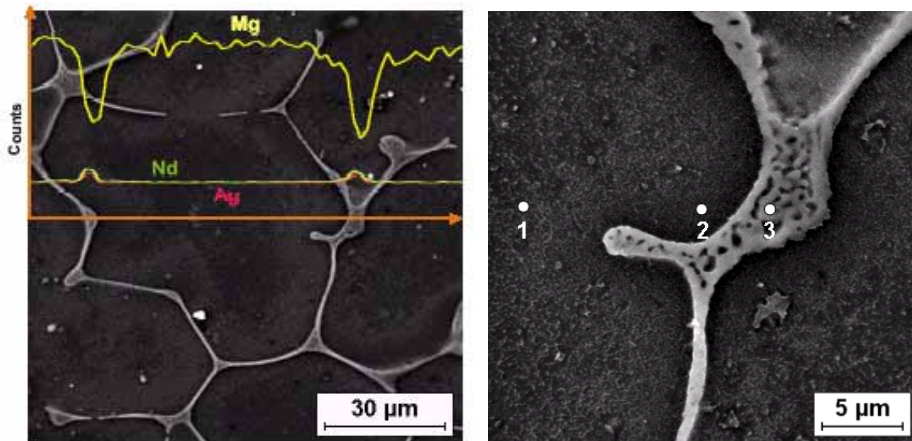


Fig.1. SEM micrographs of MSR-B as-cast structure with EDS linear analyses of Mg, Ag and Nd along the marked line.

Fig.2. SEM micrographs with EDS point analyses.

The microstructural investigations showed that this alloy is characterized by a solid solution structure  $\alpha$  with continuous eutectic on grain boundaries. The linear analyse across the grain boundary (line with arrow on fig.1) revealed that the distribution of silver changes from 0,2 at. % in the centre of grain (point 1, fig.2), by 0,89 at.% near grain boundary (point 2, fig.2), to 6,89 at. % in eutectic

precipitate (point 3, fig.2). The results of SEM and EDS quantitative analysis confirmed that almost the whole amount of neodymium entered the ternary eutectics containing apart from Mg, 8,76 at.% Nd and 6,96 at.% Ag (point 3 fig.2). The X-ray diffraction analyses showed  $\alpha$  solid solution and the eutectic compounds consisted of  $Mg_{12}Nd$  and  $Mg_{41}Nd_5$  phases with magnesium substituted by silver. Moreover, the occurrence  $AgMg_3$  has been proved. However, chemical composition of eutectic phase (8,76 at.% Nd and 6,96 at.% Ag and 85,28 %at Mg) suggested that it is rather  $(Mg,Ag)_{12}Nd$  phase.

### References

- [1] Elektron MSR-B Information from Magnesium Electron, Manchester, UK.
- [2] Avedesian M., Baker H.: „Magnesium and Magnesium Alloys.”, ASM Speciality Handbook, 1999.
- [3] The Ministry of Science and Information Society Technologies supported the present work under research project No 3 T08C 060 28.

## Study of the Intermetallic compound between Steel and Al coating layer in the Hot-Dip Aluminizing Steel

Kee-Hyun Kim<sup>a</sup>, Yong-Sug Chung<sup>b</sup>, Jong-Kyu Yoon<sup>a</sup>

<sup>a</sup>Material Science and Engineering, Seoul National University, 151-742, Seoul, Korea

<sup>b</sup>Technical Research Lab., Dongbu Steel Co. Ltd., 404-711, Incheon, Korea

The key processes of the aluminizing steel which can be used in the automobile exhaust system are the controls of Al coating and the intermetallic compounds between steel and Al coating layer. Though the intermetallic compounds affect the mechanical properties, corrosion resistance and surface quality, the studies of those have made numerous contradictory results due to the complexity of the system(Fe-Al-Si, 10 or more ternary phases). In addition, the difficulty of studying the intermetallic compounds is caused by the thin thickness and the inner layer of the alloy position[1~5]. TEM-EDX and SEM-EDS/EPMA analysis are difficult and restricted due to the thickness and position of the alloy layer. In this study, TEM and SEM analyses can not confirm the phases of alloying layer exactly. However, through the TEM, the phases could be confirmed approximately. In EPMA analysis, it only tells that which elements are involved in the formation of intermetallic compound. The technology of FIB(focused ion beam) used TEM or SEM analysis could tell the exact alloy phases. FIB lift-out technology can make the very thin in-situ specimen for TEM sample. The samples of hot-dip aluminizing steel are made by the Hot-Dip simulator. The conditions are 3s dipping time and 670°C dipping temperature with 1mm cold rolling steel sheet. The melt composition is pure Al with 10 weight percent Si(type I). In this study, the pressure of air knife is 0.3 Mpa and the thickness of Al coating layer is 20µm. The conditions are similar with the real factory processing. First of all, the hot-dip aluminizing steel is carried out by EPMA analysis. Fe atoms of steel are diffused into the Al coating layer. After the diffused Fe meet the Al atoms and surrounding Si atoms, the intermetallic compound layer is made. The Alloying layer grows broad due to the Fe atoms penetrating the layer through the grain boundary of compound[2]. In TEM and FIB analysis, the compound is thought to be FeSiAl<sub>3</sub> with monoclinic structure and FIB used analysis will be followed to confirm the compound phases. The study of the mechanical properties of the intermetallic compound should be studied for optimal coating conditions with more improved quality.

### References:

- [1] R.W. Richards, R.D. Jones, P.D. Clements, and H. Clarke, International Materials Reviews Vol.39 No.5 (1994) 191-212
- [2] T. Maitra, S.P. Gupta, Materials Characterization 49 (2003) 293-311.
- [3] K. Bouche, F. babier, A. Coulet, Materials Science & Engineering A 249 (1998) 167-175
- [4] Shigeaki Kobayashi, Takao Yakou, Materials Science & Engineering A 338(2002) 44-53
- [5] Marie-Laurence Giorgi, Jean-Bernard Guillot, Galvatch'04 Conference (2004) 703-712

## Evolution of Dislocation Boundaries in Deformed Aluminum

P. Landau<sup>1</sup>, R.Z. Shneck<sup>1</sup>, G. Makov<sup>2</sup> and A. Venkert<sup>2</sup>

<sup>1</sup>*Department of Materials Engineering, Ben-Gurion University, P.O.Box 653, Beer- Sheva, 84105, Israel*

<sup>2</sup>*NRCN, P.O.Box 9001, Beer- Sheva, 84190, Israel*

Patterning of dislocations into sub-boundaries or walls, delineating cell structures, is common to many metals during plastic deformation [1]. Cells are formed at low levels of strain in fcc metals having medium and high stacking fault energies while much higher strains are required in metals with low stacking fault energies. The internal structure of dislocation boundaries formed in aluminum at elevated temperatures is known to consist of 2-3 regular arrays of parallel dislocations that do not possess a long-range stress field [2].

Pure polycrystalline aluminum was compressed at room temperature to 3.5-70% reduction. The evolution of the internal structure of dislocation boundaries formed during room temperature plastic deformation was studied using TEM. Crystallographic analysis was performed in order to characterize the dislocation boundaries and to estimate the energetic state of the dislocation boundaries.

At low strain levels the cell structure is not fully developed. The dislocation boundaries contain irregularly undulating dislocation arrays. As strain increased the dislocation boundaries close cells and only regular, parallel dislocation arrays, consisting of 2-3 different Burgers vectors, are observed in the boundaries. This simple structure was observed both in dense dislocation walls (DDWs) and in incidental dislocation boundaries (IDBs). The only difference between the two is the dislocation density in the boundaries. As the strain level increases, dislocation boundaries containing 3 different Burgers vectors are the abundant observation.

Crystallographic analysis indicates that the dislocations are inclined by arbitrary angles to the slip plane. These boundaries were found not to fulfill the Frank-Bilby equation. This implies that they do not possess a minimum energy orientation, in contrary to boundaries formed at elevated temperatures.

It is evident that the ordering of the dislocations in the boundaries requires cross slip and mobility of the dislocations. The sufficient mobility in room temperature deformation is inspired in Al by its high stacking fault energy and low melting temperature.

It is suggested that the ordered structure reflects the fundamental driving forces for the dislocation patterning. These are mutual interactions in the boundary, tending to reduce the interaction energy among the dislocations, and the interaction with external forces or constraints, requiring the relative rotation of neighboring subgrains.

[1] D. Kuhlmann-Wilsdorf, *Mat Sci. Eng.*, A113, p. 1 (1989)

[2] D. Caillard, J. L. Martin, *Acta Metall.*, vol. 30, p. 437(1982)

## TEM Studies of B2 Ordered Fe45at%Al Deformed by High Pressure Torsion

Clemens Mangler, Christian Rentenberger, and H. Peter Karnthaler

Institute of Materials Physics, University of Vienna, Boltzmannngasse 5, AT-1090 Wien, Austria  
<http://www.univie.ac.at/Materialphysik/EM/>

It is known that B2 ordered FeAl is very brittle in a wide range of compositions. Therefore strong plastic deformation as cold rolling is usually leading to severe cracking. This occurs even in the case of the more ductile Fe25at%Al composition when the thickness is reduced by ~25% by rolling [1]. To achieve a high grade of deformation high pressure torsion (HPT) was used to carry out severe plastic deformation while avoiding fracture. During the HPT procedure a sample of polycrystalline Fe45at%Al (diameter ~8mm and thickness of ~0.8mm) was rotated 1.25 turns between two anvils under a pressure of 8 GPa at RT. From different areas of the sample (with shear strains up to 4000%) thin foils were prepared by grinding and further electro polishing in a Struers Tenupol 3 by the use of a methanol 33% nitric acid solution at -25°C. Transmission electron microscopic (TEM) investigations were carried out using a Philips CM 200 operating at an acceleration voltage of 200kV.

B2 structured FeAl deforms by the glide of superdislocations. In TEM bright field images elongated areas showing a high density of dislocations were found (cf. Fig. 1) that lead to small misorientations between neighbouring bands. The variation of contrast indicates that the change of orientation perpendicular to the bands is alternating. Because of the high density of dislocations individual ones can only be resolved in weak-beam dark-field images. The bands have an average width of about 300nm and lie parallel to a {123} plane (marked by the dashed line); this plane is one of the likely slip-planes in bcc crystals. No indication of deformation induced disordering was found, which is contrary to L1<sub>2</sub> ordered Cu<sub>3</sub>Au [2,3] where local complete disordering is observed after HPT deformation.

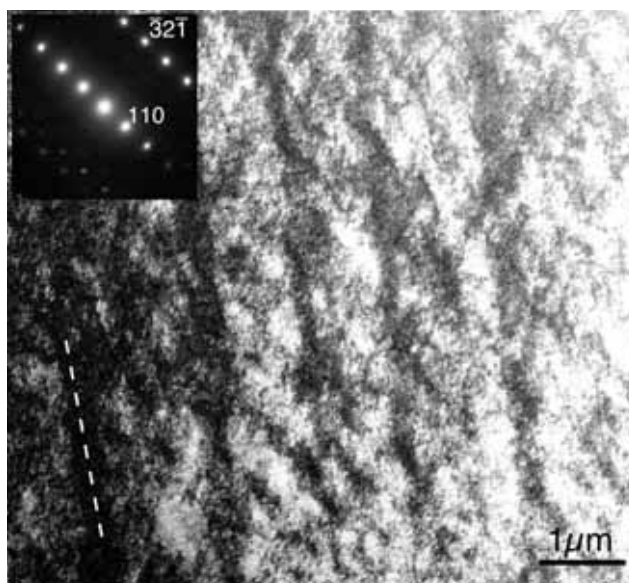


**Figure 1:** TEM bright-field image of polycrystalline HPT-deformed Fe45at%Al showing a high density of dislocations. They are arranged in bands having alternating contrast. The beam-direction is parallel to [115].

### References:

- [1] H. Hosoda, S. Miyazaki, K. Inoue, T. Fukui, K. Mizuuchi, Y. Mishima and T. Suzuki, *Journal of Alloys and Compounds* 302 (2000) 266-273
- [2] C. Mangler, C. Rentenberger, H.P. Karnthaler, *Proc. of the 6<sup>th</sup> MCM*, Pula (2003) 426
- [3] C. Rentenberger, C. Mangler and H. P. Karnthaler, *Mat. Sci. Eng. A* 387-389 (2004) 795-798
- [4] We would like to thank DI Florian Wetscher, ESI, Leoben for providing kind support to carry out the HPT deformation.

## The 475°C embrittlement in 2205 duplex stainless steel

Joanna Michalska<sup>a</sup>, Kinga Rodak<sup>a</sup>, Maria Sozańska<sup>a</sup>

<sup>a</sup>Department of Materials Science, Silesian University of Technology, Faculty of Materials Science and Metallurgy, 40 019 Katowice, Poland

Duplex austenitic-ferritic stainless steels (DSSs) offer an attractive combination of properties, particularly high mechanical strength, good corrosion resistance and castability, which have result in exploitation by the offshore oil and gas industries [1]. Duplex stainless steels are susceptible to the formation of additional phases that can influence their mechanical and corrosion properties. Long-term thermal aging in the range of 300–500°C produces an increase in hardness and tensile properties, together with a decrease in the impact properties, ductility and toughness. Degradation of mechanical properties is attributed to a spinodal reaction occurring in the ferrite phase, in which the ferrite decomposes into an iron-rich phase and an enriched chromium  $\alpha'$  phase [2,3]. This is often called 475°C embrittlement, based on the temperature at which the embrittling happens quickest. Many authors studied the effect of high temperature aging on DSSs properties, but it is little information about their performance in the presence of precipitation at low temperatures.

In this study, the effect of isothermal treatment at 475°C on 2205 duplex stainless steel has been investigated. A duplex stainless steel was aged at 475°C for different times from 100 up to 400 h. The resulting microstructural modifications were analyzed. No microstructural change was observed by light and scanning electron microscopies analysis after long-term aging. The structure consisted of white etched austenite islands and embedded in a grey etched ferrite matrix with no other secondary precipitates. The volume fraction of austenite phase measured by quantitative metallography was about 0,55. EPMA analysis revealed the concentrations of major alloying elements in ferrite and austenite. As expected, ferrite phase was partitioned with Cr, Mo and Si, while the austenite phase contained increasing Ni content. TEM bright field images revealed that aging at 475°C produced a remarkable change in the microstructure. Evolution of dislocation structure occurred in a form of cross-stitch in ferrite during aging.

The Vickers microhardness (HV0.02) of the aged specimens were measured at each condition. Vickers microhardness results shows that duplex 2205 is prone to hardening at 475°C. Average microhardness in unmodified condition were equal 260 HV0.02 for ferrite and 238 for austenite respectively. It was noticed that increase in time of aging caused gradual increase in microhardness, while the results for austenite phase were insignificantly changed.

### References:

- [1] M. Hirao, T. Ichitsubo, H. Ogi, M. Tane, *Scripta Materialia*, **48** (2003) 229.
- [2] D.Y. Kobayashi, S. Woly nec, *Materials Research*, **2** (1999) 239.
- [3] T. Kruml, J. Sopousek, *Scripta Materialia*, **35** no. 6 (1996) 689.

## TEM *in situ* Heating of Ultra Fine Grained Titanium

B. Mingler, M. Peterlechner, H. P. Karnthaler and M. Zehetbauer

Institute of Materials Physics, University of Vienna, AT-1090 Vienna, Austria  
www.univie.ac.at/Materialphysik/EM

Commercially pure titanium (CP Ti) is biologically more compatible than Ti alloys [1]; therefore it is preferentially used for medical implants. As compared to Ti alloys coarse grained (CG) CP Ti lacks of the necessary strength. Therefore ultrafine grain (UFG) sized CP Ti processed by equal-channel angular pressing (ECAP) was studied after cold rolling (CR) with transmission electron microscopy (TEM) methods. To compare the annealing response of the two-step processed material with that of the same material but cold rolled only *in situ* heating experiments were carried out.

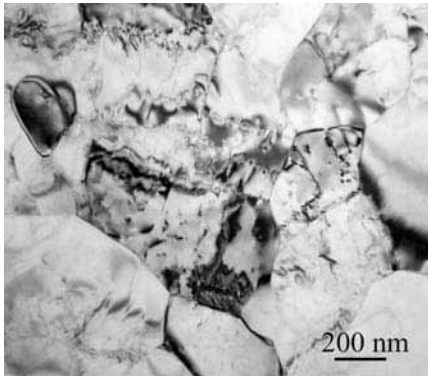


**Fig. 1:** CP-Ti; 8 ECAP passes

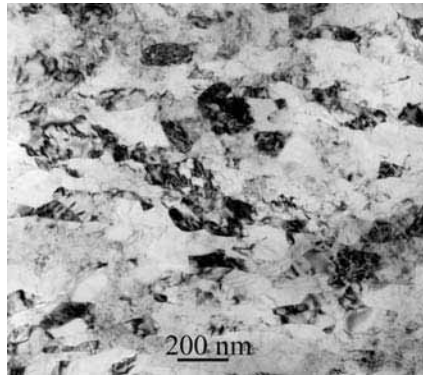


**Fig. 2:** CP-Ti; 8 ECAP passes plus CR (88%)

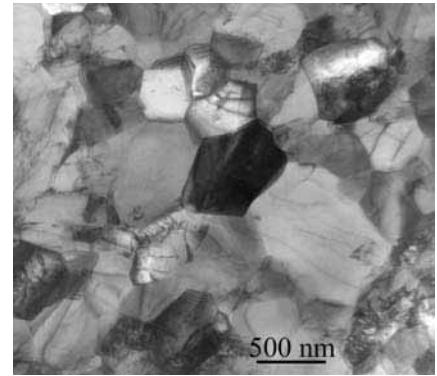


**Fig. 3:** specimen as in Fig. 2 plus *in situ* annealing at 500°C

After 8 ECAP passes the sizes of the equiaxed grains in the UFG Ti range from 300–800 nm (Fig. 1) [2]. The misorientations between adjacent grains are in many cases  $> 15^\circ$  indicating that various high angle grain boundaries are present. The dislocation density in the interior of the grains is low. With increasing strain imposed by CR on the UFG material the number of small subgrains increases; in Fig. 2 both equiaxed and elongated subgrains with sizes down to less than 100 nm are visible. The dislocation density is higher than that observed in the UFG material without CR. Only the combination of ECAP with a second processing step carried out at low temperatures like CR has the potential to increase both strength and ductility. *In situ* annealing experiments in the TEM showed that recrystallization started in CG Ti plus CR at about 450°C; contrary to this UFG Ti remains stable after CR up to about 475°C. It should be mentioned that the beginning of recrystallization is clearly visible only in thicker areas of the foil far away from the edge of the hole. During recrystallization elongated subgrains are transformed into larger equiaxed grains containing a significantly reduced dislocation density (as shown in Fig. 3).

### References:

- [1] V.V. Stolyarov, Y.T. Zhu, T.C. Lowe and R.Z. Valiev, Mater. Sci. Eng. A 303 (2001) 82.
- [2] B. Mingler, L. Zeipper, H. P. Karnthaler and M. Zehetbauer, in „Nanomaterials by Severe Plastic Deformation” (Wiley-VCH, Germany 2004) 369.
- [3] Financial support by the Austrian FWF (project P17095-N02) is acknowledged.

## Direct Observation of Gliding Dislocations in Bi<sub>2</sub>Te<sub>3</sub> Materials

N. Peranio<sup>a</sup> and O.Eibl<sup>a</sup>

<sup>a</sup> Institut für Angewandte Physik, Universität Tübingen, Auf der Morgenstelle 10, D-72076 Tübingen, Germany

Bi<sub>2</sub>Te<sub>3</sub> bulk materials are widely used for Peltier cooling devices due to their high thermoelectric figure of merit ZT. One reason for the high ZT value is the low thermal conductivity of 1W/mK. Moving dislocations are known to contribute to phonon scattering. Models predict a strong interaction between phonons and dislocations acting as oscillating strings [1]. The microstructure of p-type (Bi,Sb)<sub>2</sub>Te<sub>3</sub> was investigated by conventional transmission electron microscopy (TEM). The dislocation density is 10<sup>9</sup>cm<sup>-2</sup> and dislocations in the basal plane show a high mobility [2]. The motion was induced by heating with a focused electron beam at 120kV. External stresses were not applied. The dislocations are bowed out in the direction of motion and are pinned only at the surface. Stereomicroscopy investigations yielded edge dislocations with Burgers vector [1,1,0], line direction [-1,1,0] and (0,0,1)-glide plane. Movies showing the glide of single dislocations, and groups of dislocations were recorded and will be presented. Free standing dislocations show a high mobility in ±[1,1,0]-direction. The dislocation velocity is up to 1μm/s. Dislocation dipoles are pinned and did not glide. Dislocations arranged equidistantly within the same glide plane show a collective movement. Dislocations piled up in different glide planes are fixed and act as barriers. The motion of dislocations is due to residual shear stresses in the sample and depends on the sign of the Burgers vector. Attractive and repulsive forces of dislocations directly visualize the forces due to the elastic strain fields of the dislocations. The high mobility and density of the dislocations should be relevant for phonon scattering.

References: [1] Granato A. and Lücke K., Phys Rev. B24, (1981), pp. 6991-7006

[2] Eyidi D. et. al., Phys. Stat. Sol. (a), Vol.187, No.2 (2001), pp. 585-600

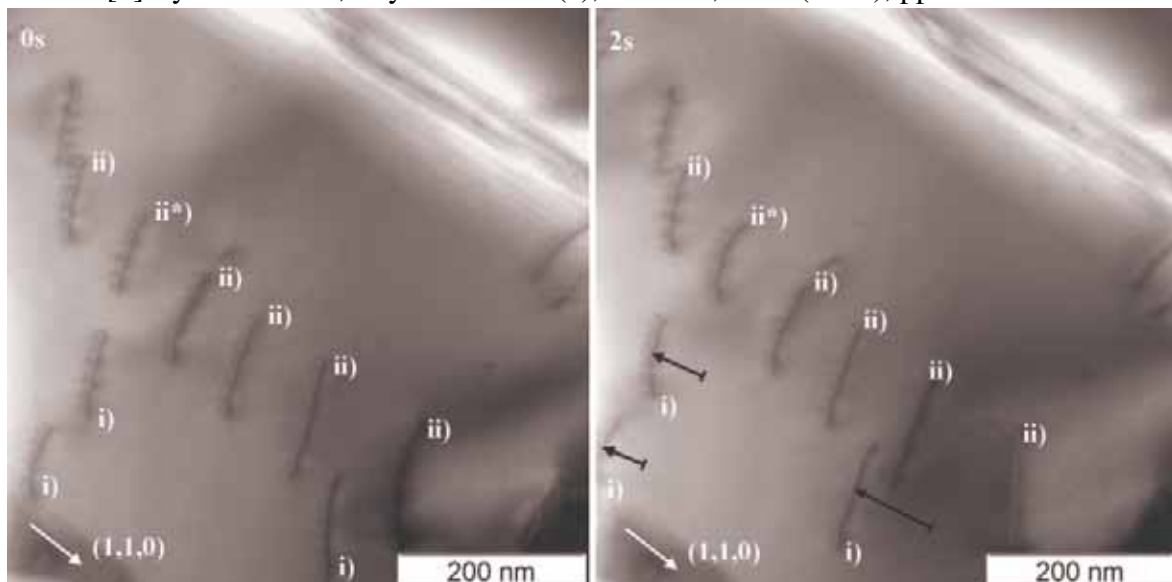


**Fig.1:** (1,1,0)-bright field images recorded before and after 2s of heating by a focused electron beam. i) free standing dislocations with a high mobility of 20-50nm/s in <1,1,0>-direction (dark arrows) ii) equidistant dislocations in the same glide plane with a distance of 80nm ii\*) dislocation pinned at the surface and bowed out by 15nm after heating.

## **An Improvement of Aluminum Alloy Properties**

Saad M Potrous

Dept. of Physics, College of Science, University of Basra, Iraq

First group of the aluminum alloy is used widely for electrical conductivity applications such as wires and cables ..etc.

In this work an impurity has been added to the 1<sup>st</sup> group of Aluminum alloy. Aluminum wires with a diameter of 10mm have been fabricated for investigation the microscopical examination, mechanical and electrical properties.

Improvements of these properties were obtained. It was found before addition of the impurity the Ultimate Tension Force of 4500N, Ultimate Strength of  $57.3 \text{ N/mm}^2$  and Elongation of 30%. These figures has been changed after addition the impurity and become as follows: the Ultimate Strength Tension Force of 6600N, Ultimate Stenght of  $84 \text{ N/mm}^2$  and Elongation of 32%.

The Electrical properties have also been changed before and after addition of an impurity. The microscopical examinations have shown an improvement of the structure of these fabricated wires.

## Microstructural investigations of extruded WE43 magnesium alloy

Tomasz Rzychoń, Andrzej Kielbus

Department of Materials Science, Silesian University of Technology, 40-019 Katowice, Poland

Precipitation hardened Mg-Y-Nd alloys (WE43, WE54) offer attractive properties for aerospace and automotive industries. They reach high specific strength, creep resistance, good castability and corrosion resistance up to a temperature of 250°. The strength of these alloys is achieved by precipitation strengthening. To find more applications in the industrial fields, it is important to use wrought magnesium alloys, for example for extrusion [1÷3].

The studied samples were obtained from commercial extruded WE43 magnesium alloy, provided by Magnesium Electron, Manchester, UK. The alloy containing 4 wt.% Y, 2.5 wt.% Nd 3.3 wt.% HRE and 0.5 wt.% Zr. Extrusion was performed at temperature of 523K. The microstructural observations were carried out using light microscope Reichert Me-F2 and scanning microscope HITACHI S3400, equipped with an X-radiation detector EDS-VOYAGER of NORAN INSTRUMENTS. Phase analyse was performed with JDX-75 X-ray diffractometer.

The microstructural investigations showed that this alloy is characterized by a solid solution structure  $\alpha$  with large particles of Y-rich phase at grain boundaries. Small particles are distributed inside the grains (Fig.1). After extrusion the alloy showed grain size of about 10÷20  $\mu\text{m}$ .

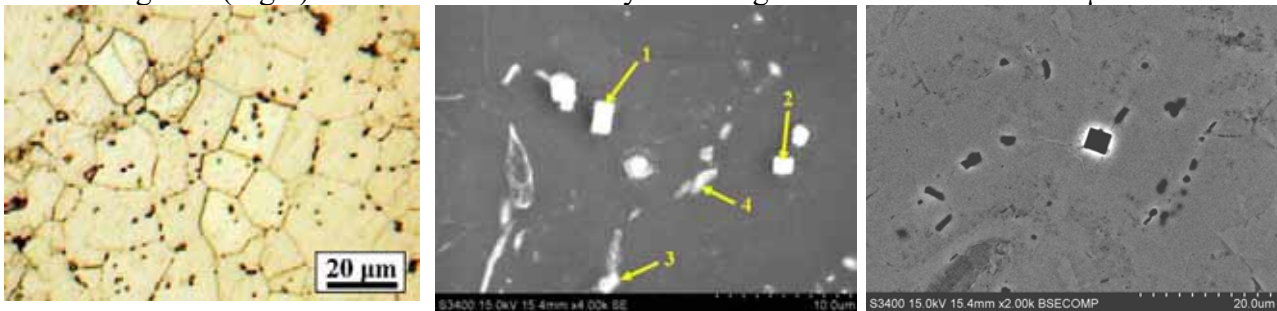


Fig.1. LM micrographs of Fig.2. Y-rich phases on  $\alpha$  matrix (points 1 and 2), SEM. Fig. 3. BSE micrograph of extruded WE43 alloy.

Fig. 2 and 3 shows the SEM and BSE microstructure images of the studied alloy. The images suggest that there are two kinds of phases which have different morphology and chemical composition. The rectangular particles (points 1 and 2) have a high yttrium content and the Mg:Y ratio is close to 1:1 and 2:1 respectively, suggesting a stoichiometry of MgY and Mg<sub>2</sub>Y. The Y concentration in the irregular phase (points 3 and 4) is significantly lower than in the rectangular particles. Moreover these particles contain of neodymium. The Y:Nd ratio is near 1:2, suggesting a phase composition close to Mg<sub>14</sub>Nd<sub>2</sub>Y. Investigations of chemical composition revealed the segregation of yttrium in the matrix.

### References:

- [1] Electron Wrought WE43 Information from Magnesium Electron, Manchester, UK.
- [2] Antion C. and others: "Hardening precipitation in a Mg-4Y-3RE alloy.", *Acta Materialia* 51 (2003), 5335-5348.
- [3] Zhang Y. and others: "Effects of yttrium on microstructure and mechanical properties of hot-extruded Mg-Zn-Y-Zr alloys," *Materials Science and Engineering A* 373 (2004), 320-327.
- [4] Greger M. and others: "Mechanical properties and fatigue of magnesium alloys", 7<sup>th</sup> International research/expert conference, Barcelona 2003
- [5] The Ministry of Science and Information Society Technologies supported the present work under research project No 3 T08C 060 28.

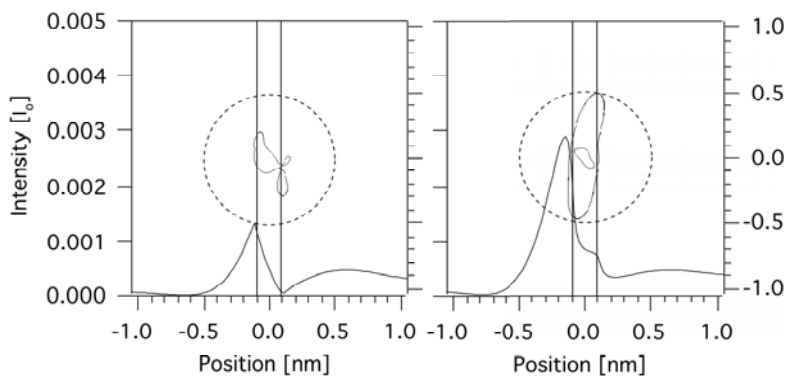
# TEM Weak Beam Spatial Resolution: Application to TiAl $1/2a\langle 112 \rangle$ Superdislocation Core

R. Schaeublin

Fusion Technology-Materials, CRPP - EPFL, Association EURATOM-Confédération Suisse, 5232 Villigen PSI, Switzerland

TEM weak beam imaging is applied to the resolution of core configuration of the locked superdislocation  $1/2\langle 112 \rangle$  in stoichiometric TiAl. The candidate core configurations are based on the decomposition of the superdislocation into 4 partial dislocations separated by stacking faults. While there is a general agreement on the bordering partials Burgers vector to  $1/6\langle 112 \rangle$  and  $1/6\langle 112 \rangle$ , there is an uncertainty on the central couple of partials forming the lock. It presents an interesting case to probe spatial resolution in weak beam when differences are subnanometric.

The interest in understanding the core structure of the central partials lies in the fact that it may cause  $1/2\langle 112 \rangle$  dislocations to be sessile [1] as confirmed by certain observations of rectilinear edge segments [2]. Recent experimental work based on weak beam TEM observations and performed independently in different groups provided contradictory conclusions [2,3]. The difficulty in TEM in



identifying the nature of partials resides in the fact that, firstly, they are separated by only 0.23 nm and, secondly, the difference between 2 configurations amounts to at most one atomic row. One faces thus an uncertainty in deciding which dissociation mode actually takes place in the crystal. It has been recently claimed that diffraction contrast under weak-beam conditions is unable to provide the

resolution adequate to that purpose [3]. It is proposed to revisit this statement by exploring weak beam image simulations under various diffraction conditions, and using contour maps of the strain field around dislocation cores, as displayed in the centre of the images. The dotted circle indicated the classical resolution limit. It appears that there is a difference in the simulated intensity profiles (continuous line). An attempt of experimental observation in the optimal diffraction condition defined by the simulations is presented. It is shown that weak beam may in principle provide sufficient spatial resolution to resolve faint differences between core configurations.

## References:

- [1] B. Inkson, *Phil. Mag. A* 77 (1998)715.
- [2] M. Kumar, S. Sriram, A.J. Schwartz, V.K. Vasudevan, *Phil. Mag. Letters* 79 (1999) 315.
- [3] C. Lang, P.B. Hirsch, D.J.H. Cockayne, *Phil. Mag. Letters* 84 (2004) 139.
- [4] Patrick Veyssi re and Mukul Kumar are thanked for fruitful discussions.

## Ni<sub>4</sub>Ti<sub>3</sub> precipitates and their effects on the Ni-Ti B2 matrix

Dominique Schryvers<sup>a</sup>, Wim Tirry<sup>a</sup>, and Zhiqing Yang<sup>a</sup>

<sup>a</sup>Electron Microscopy for Materials Science, University of Antwerp, B-2020 Antwerp, Belgium

Ni-Ti based alloys are among the most abundantly used alloys in superelastic and shape memory applications [1]. The origin of this behaviour is the martensitic transformation from a B2 cubic parent or austenite phase to a B19 monoclinic or B19' orthorhombic product or martensite phase. For practical applications the alloys undergo specific heat treatments which induce Ni<sub>4</sub>Ti<sub>3</sub> precipitates. However, although the thermo-mechanic effects of this precipitation are well documented, still many uncertainties on the micro- and nanostructural features exist. In this contribution recent results obtained by applying the geometric phase method to the deformations in the matrix, the multi-slice least-squares (MSLS) method to the atomic structure of the precipitates and EELS to the electronic structure and chemical composition of the precipitate and matrix are presented.

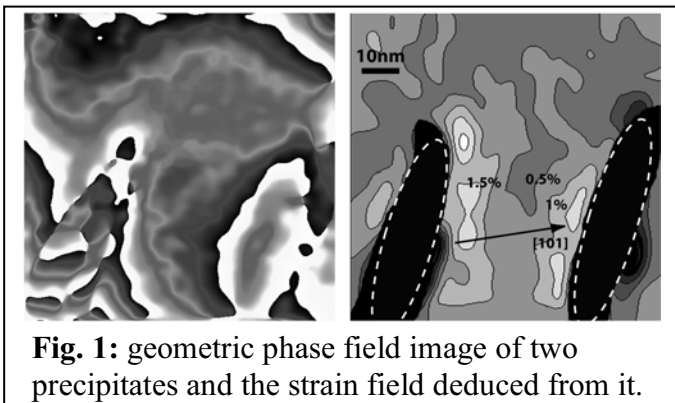


**Fig. 1:** geometric phase field image of two precipitates and the strain field deduced from it.

HRTEM imaging followed by quantitative measures of the interplanar spacings using a windowed FFT or the geometric phase method (see fig. 1) clearly shows nanoscale regions of expanded B2 lattice surrounding the lens-shaped precipitates [2]. These regions fully account for the accumulated stress in the matrix region due to the lattice contraction in the precipitate. Due to the Ni enrichment of the precipitate, a similar phenomenon appears with respect to concentration: EFTEM and EELS (and to a

lesser extend also EDX) reveal Ni depleted matrix regions next to the precipitates and fully accounting for the loss of Ni necessary to construct the precipitate [3].

As for the precipitate itself, the present simple model, only taking into account the lattice contraction and a periodic replacement of a Ti atom by a Ni one, cannot account for the actually observed intensities of the superreflections. A refinement was performed based on the basic and superreflections in the electron diffraction patterns of the [111]<sub>R</sub> and <100><sub>R</sub> zones. As a result, small shuffles are obtained enabling the mixed columns to accommodate the smaller lattice dimensions in the direction normal to the central disc of the precipitate. The new model is shown in fig. 2.

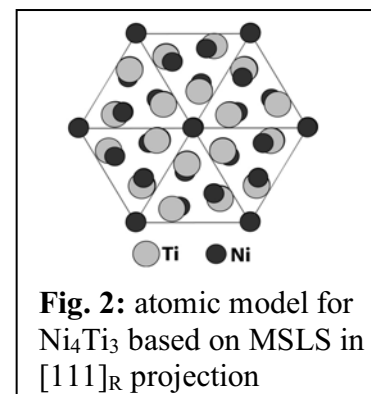


**Fig. 2:** atomic model for Ni<sub>4</sub>Ti<sub>3</sub> based on MSLS in [111]<sub>R</sub> projection

### References:

- [1] K. Otsuka, X. Ren, Progress Mater. Sc. 50 (2005) 511
- [2] W. Tirry, D. Schryvers, Acta Mater. 53 (2005) 1041
- [3] Z.Q. Yang, W. Tirry, D. Schryvers, Scripta Mater. 52 (2005) 1129.

## SEM/TEM Investigations of Nickel filled Ceramic Layers

S. Selve<sup>a</sup>, A. Knotz<sup>b</sup>, Th. Kups<sup>a</sup>, H.G. Krüger<sup>b</sup>, L. Spiess<sup>a</sup> and H. Kern<sup>b</sup>

<sup>a</sup> Department of Material Engineering, Center for Micro and Nanotechnologies, Technical University Ilmenau, 98693 Ilmenau, Germany

<sup>b</sup> Department of Metallic Materials and Composite Materials, Technical University Ilmenau, 98693 Ilmenau, Germany

The combination of ceramics and metals and the favourable manner to combine their important properties leads to new materials and applications.

With galvanic filled porous structures it is expected that the common developing tears, caused of loads, inside the ceramic layer can be avoided and the materials may resist higher mechanical loads than ordinary layers.

The aim of the present tests is to develop a surface coating for investigating the interface between the ceramic layer and galvanic embedded Nickel. Ceramic layers made by ZrO<sub>2</sub> electrophoretically for these investigations, and then sintered in an open-porous layered structure.

The starting material for the electrophoretic coating was the commercial powder zirconium oxide ZrO<sub>2</sub> with 8% Yttrium (Tosoh TZ8Y). For SEM investigations the stainless steel X5Cr17 was used as a coating substrate. Because of the low sputter rate of steel it was not used as substrate for TEM investigations. For this investigation the ceramic was coated on silicon substrate. The coating occurred at a voltage of 60 V, a coating period of up to 5 s and an electrode spacing of 3 cm in a homogenous and constant electrical field.

After the layer had dried, the sintering was carried out at a heating and cooling speed of 6 K/min in vacuum (holding time of 3 h). Additionally Nickel was galvanically embedded in the porous ceramic structure.

After sintering the layer structures were characterised by TEM (CTEM, HRTEM, EDX, EELS) and SEM. The SEM samples were broken cooled to LN<sub>2</sub> temperature to avoid the etching influence made by the etching beam.

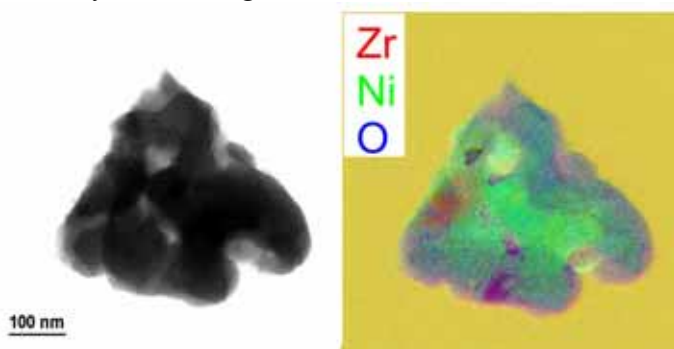


*Fig. 1 RGB-EELS map of a ZrO<sub>2</sub>-Ni Particle*

Because of the very fragile samples on Si substrate the TEM investigations were made after separating the layer from the substrate and controlled crushing of the layer (to get very small particles with the ZrO<sub>2</sub>-Particals and Ni content) and putting it on a TEM-Cu grid. The size of the resulting particles is in the range of the size of the ceramic particles of about 50-100nm.

The EELS investigations showed that the Ni is inside the porous holes of the ceramic particles. The measurement of the lattice planes obtained in HRTEM images shows ZrO<sub>2</sub> and Ni lattice planes.

acknowledgements: We are grateful for H. Romanus for the EELS measurements and E. Remdt for the sample preparation and the DFG for financial support (KE 359/7-1).

## The Microstructure Of Co And Ni Binder Phases In Graded Hard Metals And Its Influence On Corrosion Resistance

Federico Sket <sup>a</sup>, Dominique Eyidi <sup>b</sup>, José Luis Garcia <sup>c</sup>, and Anke Rita Pyszalla <sup>a</sup>

<sup>a</sup> Technische Universität Wien, Institute of Material Science and Technology, Karlsplatz 13, A-1040 Wien, Austria

<sup>b</sup> University Service Center for Transmission Electron Microscopy, Technische Universität Wien, Wiedner Hauptstrasse 8-10, A-1040 Wien, Austria

<sup>c</sup> R&D Dept., Boehlerit GmbH & Co. KG, A-8605 Kapfenberg, Austria

Hardmetals are wear resistant materials used in cutting tool applications. These materials are composed of coarse ceramic hard phases grains (Ti, WC, TaC, NbC) embedded in a tough metal binder phase (Fe, Ni, Co). In graded hardmetals, the structure is tailored in order to control the properties in the surface-near zone. This may improve the wear and corrosion resistance while sufficient toughness remains. The gradient in the graded hardmetals is obtained by a diffusion-controlled sintering process in a controlled N<sub>2</sub> atmosphere. The binder phase has a less metallic behaviour when it contains precipitates originating from interdiffusion processes between the matrix and the hard phases and this increases the corrosion resistance.

The microstructure of six hardmetals sintered in vacuum and in N<sub>2</sub> atmosphere with two different binder phases (Co and Ni) was characterized by transmission electron microscopy (TEM) techniques and X-Ray diffraction (XRD) for phase and residual stress analyses. TEM was performed in combination with energy-dispersive X-ray spectrometry (EDX) in a Tecnai F-20 operating at 200 kV to determine the fraction of Ti and W dissolved in the matrix and the amount of precipitates in the Co and Ni binder phase and the lattice defects in the binder phases.

Quantitative analysis of the phase distribution in the hardmetals reveals that the mean particle size of the different ceramic hard phases is not affected by the sintering conditions and amounts to about 1.5 μm on average. TEM studies showed additionally the presence of nanosized hard particles.

Twinning and stacking faults were found in the sample with Co binder phase and without gradient. A modulated structure in the Co matrix, is observed in Ti(C,N)-gradient sample. Electron diffraction patterns show additional spots corresponding to these effects.

High dislocation densities are found in the samples with Ni binder, both, with and without gradient. Moiré fringes originating from nanoprecipitates in the binder phase are observed in the high resolution images.

W- and Ti-contents in Co binder phase in the untreated samples are higher than in the samples treated in a N<sub>2</sub> atmosphere. The higher impurity content shifts the corrosion potential to more noble values which improve the corrosion resistance.

# Study of the Microstructure of Rapidly Solidified Al-Ni-La-Zr Alloys by Synchrotron Tomography and Transmission Electron Microscopy

M. Wollgarten<sup>1</sup>, S. Hiller<sup>1</sup>, J. Vierke<sup>1</sup>, A. Haibel<sup>1</sup>, P. Schubert-Bischoff<sup>1</sup>, K.L. Sahoo<sup>2</sup> and J. Banhart<sup>1</sup>

<sup>1</sup>Hahn-Meitner-Institut Berlin, Dep. SF 3 Materials, Glienicker Str. 100, D-14109 Berlin, Germany

<sup>2</sup>National Metallurgical Laboratory, Jamshedpur-831007, India

Ribbons of amorphous  $\text{Al}_{87}\text{La}_7\text{Ni}_5\text{Zr}_1$  were prepared by melt spinning at a wheel speed of 40 m/s. The ribbons have a thickness of about 30  $\mu\text{m}$  and a width of about 1 mm. Using the experimental setup for tomography at the BAMline of BESSY II resulted in tomograms revealing inhomogeneities preferentially close to the ribbon edges (Figs. 1a and b). However, chemical analysis of cross sections in a scanning electron microscope gave no indication for variations in chemical composition.

Synchrotron tomography maps the variation of density by measuring the X-ray transmission of a sample. However, it might be compromised by spatially varying crystallinity, which will influence the intensity of the transmitted beam due to different amounts of Bragg scattering. In order to clarify this point in the present case cross sectional samples for transmission electron microscopy were prepared from ribbons using a microtome. The way of specimen preparation is critical since heating of the sample must be avoided as it will lead to crystallization of the amorphous phase. Diffraction patterns were obtained in a Philips CM 30 operated at 300 kV. The intensity distribution was averaged along the azimuthal angle (Fig. 1c). Preliminary results show, that the intensity of the first maximum increases significantly if patterns were recorded close to the ribbon edges.

In this contribution it will be discussed whether this increase can be systematically correlated to the features observed by synchrotron tomography.

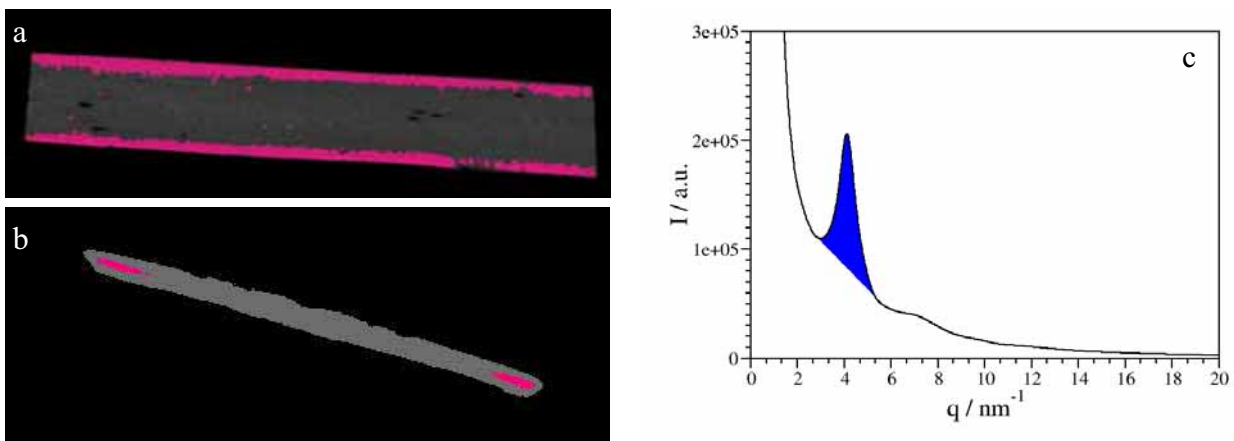
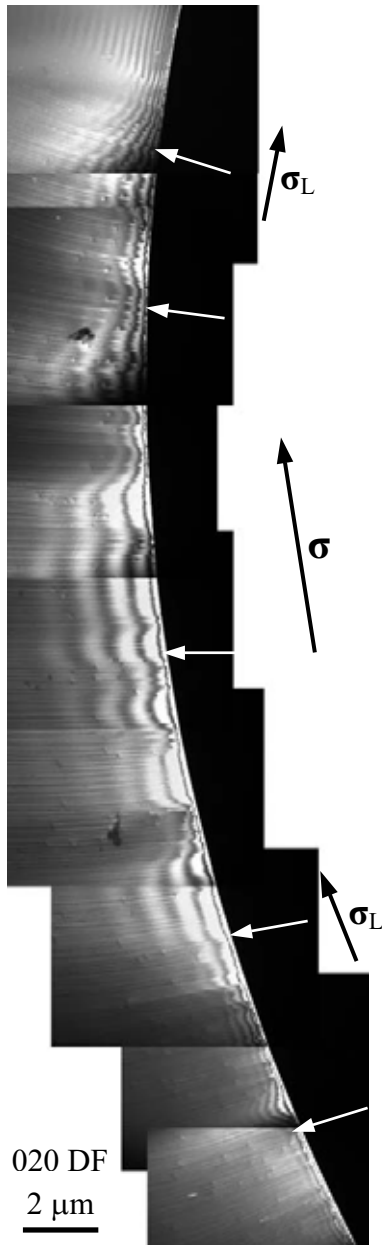


Figure 1: (a) Tomogram of a  $\text{Al}_{87}\text{La}_7\text{Ni}_5\text{Zr}_1$  ribbon. Volume parts that have at least 75% of the maximum density are colored magenta. (b) Cross sectional view of (a). (c) Electron diffraction intensity as function of the scattering vector obtained from a amorphous  $\text{Al}_{87}\text{La}_7\text{Ni}_5\text{Zr}_1$  ribbon. The peak, characteristic of the amorphous phase, is colored blue.

## Direction of Local Tensile Axis in *in situ* TEM Strained Specimens

Niva Zárubová, Juliana Gemperlová, Antonín Gemperle, Zdeněk Dlabáček

Institute of Physics ASCR, Na Slovance 2, 182 21 Praha 8, Czech Republic



*In situ* TEM straining experiment is an important tool for investigation of stress induced microscopic processes, e.g. mechanisms of plastic deformation, interactions of slip dislocations with grain boundaries, phase transformations induced by external stress etc. Uniaxial tensile stress is applied in the experiments. However, the stress distribution in the foil is strongly affected by the depression and the hole produced during the foil preparation [1]. The local direction of the tensile stress around the hole differs considerably from the direction of the external stress, and the interpretation of the results may be difficult or incorrect. The problem was illustrated by *in situ* straining experiments on Fe-Si bicrystals. In many cases the active slip systems did not correspond to the predicted ones. Instead of the primary slip system the secondary or the tertiary one, regarding the applied stress, were activated [2].

An experimental determination of the stress distribution during *in situ* TEM straining is presented here. The Figure shows a part of the plastically deformed region in an Fe-Si foil strained by the external stress  $\sigma$ . Directions of the slip traces at the edge of the hole are marked by white arrows. The determination of the direction of the local stress  $\sigma_L$  is based on the fact that in Fe-Si alloys with low Si content (bcc structure) the active slip planes at room temperature are non-crystallographic planes situated close to the planes with maximum resolved shear stress (MRSS) [3]. The active slip planes were reconstructed from the observed slip traces and the active slip vector found using the  $\mathbf{g}\cdot\mathbf{b}$  criteria. Then, the local MRSS planes were determined using the corresponding  $\psi$ - $\chi$  curve published in [3].  $\sigma_L$  lies in the plane given by the slip vector and the MRSS plane normal. At the same time,  $\sigma_L$  is parallel to the foil surface.

In agreement with the finite element calculations [1], the deviation of the local tensile axis from the external one is very small at the places where the tangent to the hole edge is parallel to the external axis. Far from this place, deviations as large as  $\pm 60^\circ$  were observed.

### References:

- [1] A. Coujou, Ph. Lours, N.A. Roy, D. Caillard and N. Clement, *Acta Metall.* 38, 825-837, 1990.
- [2] A. Gemperle, N. Zárubová and J. Gemperlová, *J. Mater.Sci* 40, June, 2005.
- [3] B. Šesták and N. Zárubová, *phys.stat.sol.* 10, 239-250, 1965.
- [4] Authors highly acknowledge financial support of GA CR (Contract 202/01/067).

## Studies of thin-film solar cells by transmission electron microscopy

Daniel Abou-Ras<sup>a,b</sup>, Debashis Mukherji<sup>a</sup>, Gernot Kostorz<sup>a</sup> and Ayodhya N. Tiwari<sup>b,c</sup>

<sup>a</sup>ETH Zurich, Institute of Applied Physics, 8093 Zurich, Switzerland

<sup>b</sup>ETH Zurich, Thin-Film Physics Group, Laboratory for Solid State Physics, Technopark, Technoparkstrasse 1, 8005 Zurich, Switzerland

<sup>c</sup>Centre for Renewable Energy Systems and Technology, Department of Electronic and Electrical Engineering, Loughborough University, Loughborough, Leicestershire, LE11 3TU, UK

Polycrystalline thin-film solar cells provide promising potential for low-cost and reliable generation of solar electricity for terrestrial and space applications. Among these solar cells, highest efficiencies of over 19% [1] have been achieved using p-type Cu(In,Ga)Se<sub>2</sub> (CIGS) as solar absorber material. To form a p-n heterojunction in the solar cell, an n-type counterpart, also referred to as “buffer layer”, to the p-type absorber is needed. In the frame of research and development of these solar cells, various n-type materials such as CdS, In<sub>2</sub>S<sub>3</sub> and ZnS, have been studied. While the effects of parameter variations (e.g., temperature, layer thickness, etc.) on the solar cell performance are easily measured externally, access to internal changes caused by these parameter variations is difficult.

Transmission electron microscopy (TEM) and its related techniques provide an important tool to study the microstructural and chemical properties of layers and their interfaces in CIGS solar cells. In the present studies, particular emphasis is placed on the interface between the CIGS absorber and the n-type buffer layer. There, lattice mismatches of these two layers and interdiffusion of elements across the interface are investigated by means of bright-field, high-resolution and energy-filtered TEM, electron diffraction and energy-dispersive x-ray spectrometry.

As an example, it has been found during the development of CIGS solar cells with In<sub>2</sub>S<sub>3</sub> buffer layers that the solar-cell performance deteriorates strongly when In<sub>2</sub>S<sub>3</sub> is deposited at substrate temperatures higher than about 230°C, independent of the deposition technique. By means of TEM and its related techniques, it was shown that within this temperature range, CuIn<sub>5</sub>S<sub>8</sub> forms instead of In<sub>2</sub>S<sub>3</sub>. Its spinel-type cubic crystal structure contains a high density of vacancies, and in addition, these CuIn<sub>5</sub>S<sub>8</sub> thin films exhibit a high density of planar defects. Vacancies and defects at the p-n junction of the solar cell provide recombination centers for the generated charges and thus may lead to the measured reduction of the solar-cell efficiency.

For more details on this field of research, please refer to, e.g., Ref. [2].

### References:

[1] K. Ramanathan, M. A. Contreras, C. L. Perkins, S. Asher, F. S. Hasoon, J. Keane, D. Young, M. Romero, W. Metzger, R. Noufi, J. Ward, and A. Duda, *Prog. Photovolt. Res. Appl.* **11** (2003) 225.

[2] D. Abou-Ras, D. Rudmann, G. Kostorz, S. Spiering, M. Powalla, and A.N. Tiwari, *J.Appl.Phys.* **97**(8) (2005) 084908.

[3] The authors are grateful to the Zentrum für Solarenergie- und Wasserstoff-Forschung and to the Institut für Physikalische Elektronik, both Stuttgart, Germany, for providing the solar-cell samples. This work was supported in part by the Swiss National Science Foundation, and also by the Swiss Federal Office of Science and Education for the EU projects PROCIS and NEBULES.

## Electron Microscopy Characterization of GaN Films by ELO on Sapphire

Y. Arroyo, P. Stadelmann

Institut Interdisciplinaire de Microscopie Electronique, Ecole Polytechnique Fédérale de Lausanne, Bâtiment MXC, Station 12, CH-1015 Lausanne, Switzerland.

The identification of structural defects in gallium nitride (GaN) is important to optimize the heteroepitaxial growth and to understand their effect on the optoelectronic properties. TEM analysis was performed on GaN specimens grown on "R" type sapphire substrates. Metal organic vapor phase epitaxy (MOVPE) was used for the buffer layer and hydride vapor phase epitaxy together with lateral overgrowth (HVPE-ELO) for the GaN layers. The GaN grows in the  $[11\bar{2}0]$  direction to the surface of layer and laterally in both  $[0001]$  and  $[000\bar{1}]$  direction.

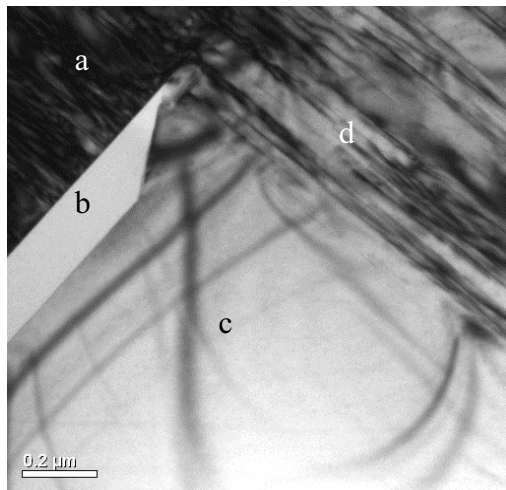


Figure 1. BF image of GaN

- a) GaN Buffer Layer
- b) SiO<sub>2</sub> Mask
- c) ELO Area
- d) Openings

The predominant defects in the microstructure of GaN layers are threading dislocations, which originate at the GaN/sapphire interface and are due their difference of lattice parameters and thermal expansion coefficients. In the SiO<sub>2</sub> mask openings the dislocations are propagating throughout the GaN film. The lateral overgrowth regions are nearly free of defects as is shown in figure 1. A high dislocations density in the range of  $10^{10}$  -  $10^{11}$  cm<sup>-2</sup> was measured in the GaN buffer and in the SiO<sub>2</sub> openings. The density is reduced in the lateral overgrowth area (above the SiO<sub>2</sub> mask) by many orders of magnitude.

A small number of dislocations were also found in middle of the lateral overgrowth area at the coalesce boundary. There are propagating to the surface of layers. Figure 1 shows bend contours in the low dislocations density area. It demonstrates that the specimen is highly distorted above the SiO<sub>2</sub> mask (at least after specimen preparation).

# Quantative TEM Analysis of the composition of InGaN/AlGaN layers – Selection of the proper imaging conditions

M.Beer<sup>1</sup>, K. Engl<sup>1,3</sup>, J. Zweck<sup>1</sup>, A. Able<sup>1</sup>, W. Wegscheider<sup>1</sup>, M. Schowalter<sup>2</sup>, A. Rosenauer<sup>2</sup>

<sup>1</sup>Institut für Experimentelle und Angewandte Physik, Universität Regensburg, Universitätstr. 31, D-93053 Regensburg, Germany

<sup>2</sup>IFP – University Bremen, Otto-Hahn-Allee 1, D-28359 Bremen, Germany

<sup>3</sup>OSRAM Opto Semiconductors GmbH, Wernerwerkstr. 2, D-93049 Regensburg, Germany

GaN based (opto-) electronic devices such as blue light emitting diodes (LEDs) and laser diodes offer a wide variety of applications e.g. for optical storage media or high resolution laser printers. To improve the performance of light emitting and electronic devices a precise knowledge of the composition and composition fluctuations of InGaN and AlGaN layers in group-III-nitride heterostructures is necessary.

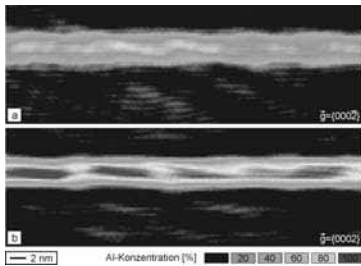


Fig. 1: Al concentration maps for tilting in (000-2) and (0002) direction

One way to study quantitatively the In/Al concentration and distribution in InGaN/AlGaN-layers is based on the linear relationship between the distances of the lattice planes and the concentration  $x$  in a ternary compound  $A_xB_{1-x}C$ . This method is implemented in the software package DALI developed by Rosenauer et al.[1]. Gerthsen et al. [2] performed finite element and multislice simulations to acquire the optimum imaging conditions for this purpose. They found the best results for (0004) two beam conditions, with the (0002) beam centered on the optic axis. For image formation only the (0000) and (0002) beams are selected. Bloch-wave calculations showed, that not only the magnitude of the tilting is important, but also the direction, i.e. tilting

in (0002) or (000-2) direction. To illustrate this, Fig. 1 shows two Al concentration maps from identical specimen areas (an AlN layer embedded in GaN). The only difference is the specimen tilt along (0002) or (000-2). Obviously, different values of the Al concentration and different characteristics for the distribution of the Al in the AlGaN layer are obtained. From the simulations it is known, that only the (0002)-tilted specimen yields the right result.

However, under standard (SA) TEM diffraction conditions, it is not possible to distinguish between tilting in (0002) or (000-2) direction. The assignment of the beams depends on the polarity of the (Al, In)GaN layer and the rotation of the diffraction pattern relative to the image. To assign the right denotation to the right spot in the diffraction pattern, shadow image analysis in an underfocused diffraction pattern [3] and CBED investigations [4] were carried out. With the aid of the shadow image, one gets knowledge of the rotation of the diffraction pattern relative to the TEM image, via comparing recorded CBED patterns with simulated CBED patterns the polarity of the (Al,In)GaN epitaxy layer can be determined.

[1] A. Rosenauer et al., *Optik* **102**, 63 (1996)

[2] D.Gerthsen et al., *phys. stat. sol (c)* **0**, No.6 1668-1683 (2003)

[3] E. Spiecker, *Ultramicroscopy*, **92**, 111 (2002)

[4] Z. Liliental-Weber et al. *Mater. Res.Soc. Symp.Proc.* **395**, 351 (1996)

## TEM Investigations of High-Quality Ge Films on Patterned Si Substrates

Eberhard Bugiel, Tobias F. Wietler, and Karl R. Hofmann

Institute for Semiconductor Devices and Electronic Materials, University of Hannover, Appelstr. 11A, 30167 Hannover, Germany, Phone: +49-511-762-4226, Fax: +49-511-762-4229, E-mail: bugiel@ihw.uni-hannover.de

Direct growth of relaxed Ge layers on patterned Si(001) substrates was achieved by using surfactant mediated epitaxy (SME) with the surfactant Sb. The Si substrates were anisotropically etched (KOH) after masking steps with SiO<sub>2</sub> so that we have had the original Si(001) surface, inclined (111) surfaces and a micro-faceted (001) surface. Large Sb flux at temperatures around 670°C resulted in all three cases in high-quality Ge films with defect densities as low as  $5 \times 10^7 \text{ cm}^{-2}$ . Fig. 1 shows a typical XTEM micrograph of an 1  $\mu\text{m}$  thick Ge layer on a patterned (001)Si substrate. We did not observe any drastic differences in the threading dislocation density between this three regions.

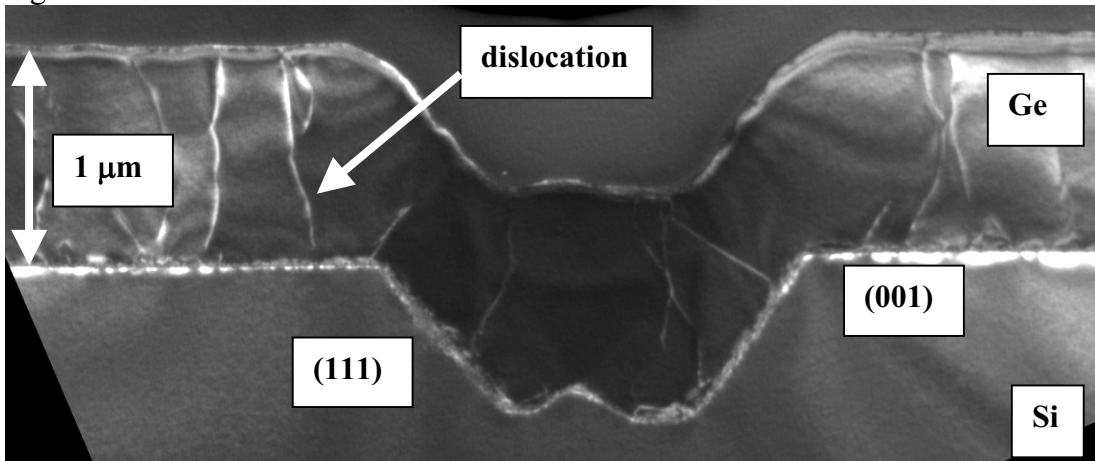


Fig. 1: Dark field XTEM micrograph of an 1  $\mu\text{m}$  thick Ge layer on a patterned (001)Si substrate.

We ascribe this to an abrupt release of strain via the formation of a regular array of 90° dislocations at the interface during the initial, micro-rough stage of growth, which occurs only under the chosen growth conditions. This dislocation array was observed in HRTEM.

High-resolution x-ray diffraction (HRXRD) measurements were performed with a diffractometer using Cu<sub>Kα</sub> radiation, a Ge(220) Bartels-monochromator, and a channel cut analyser. Strain analysis was carried out measuring reciprocal space maps (RSM) of symmetrical and asymmetrical reflexes of a 1  $\mu\text{m}$  thick Ge film grown on a Si(001) substrate by SME. A value of 0.20 % tensile in-plane strain is obtained. This can be explained considering the different thermal expansion coefficients of Ge and Si. Assuming complete relaxation of the Ge layer at growth temperature, the cooling process to room temperature induces a tensile strain of 0.21 %. The excellent agreement with the measured residual strain shows that the entire stress is compensated elastically by the Ge film. Thus, no additional dislocation generation is necessary in the cooling process.

The high growth temperature also enhances Sb segregation resulting in a low background doping level of  $3\text{-}4 \times 10^{16} \text{ cm}^{-3}$ . Hence, device application of relaxed Ge films on Si(001) grown by surfactant mediated epitaxy is feasible.

## Mapping of Dopants in Semiconductors: The PEEM Study

L. Frank<sup>a</sup>, I. Müllerová<sup>a</sup>, D. Valdaitsev<sup>b</sup>, A. Gloskovskii<sup>b</sup>, S. Nepijko<sup>b</sup>, H. Elmers<sup>b</sup>, G. Schönhense<sup>b</sup>

<sup>a</sup>Institute of Scientific Instruments, CZ-61264 Brno, Czech Republic

<sup>b</sup>Institute of Physics, Johannes Gutenberg University, D-55099 Mainz, Germany

High resolution imaging of doped areas in semiconductors with slow electrons is one of hot topics for both solid state physics and technology. Recent study employing the scanning low energy electron microscope demonstrated a high image contrast of dopants and revealed some side effects connected with charging [1]. While various versions of photoelectron spectroscopy have been widely used to examine electron states in semiconductors including dopant-related ones, only low attention has been devoted to the photoemission electron-microscopic (PEEM) imaging of these structures. The pioneering work [2,3] presented the basic dependence between the doping level and image contrast and ascribed the crucial role to local differences in the photoemission threshold, i.e. to shifts along the energy axis of the emission spectrum. The present study profits from availability of an energy-selective PEEM applied to various p- and n-type doping densities.

Specimens were prepared by standard ion implantation through patterned oxide masks with dopant concentrations between  $10^{15}$  and  $10^{19}$   $\text{cm}^{-3}$  (boron or phosphorus) in Si (100) substrates of opposite types ( $5 \times 10^{14}$   $\text{cm}^{-3}$ ). Photoemission was excited by a mercury arc lamp with and without monochromator. PEEM micrographs have been acquired over entire energy range in 40 meV steps and the spectral data points were extracted by averaging the p- and n-type areas in each frame. Example in Fig.1 concerns the p-type doping ( $10^{19}$   $\text{cm}^{-3}$ ) and reveals a contrast reversal appearing when only fastest photoelectrons are acquired. As the shift between low-energy ends of the p- and n-type spectra does not exceed 50 meV, the contrast more likely comes from local differences in absorption of hot electrons due to pair generation than from variations in the photo-threshold.

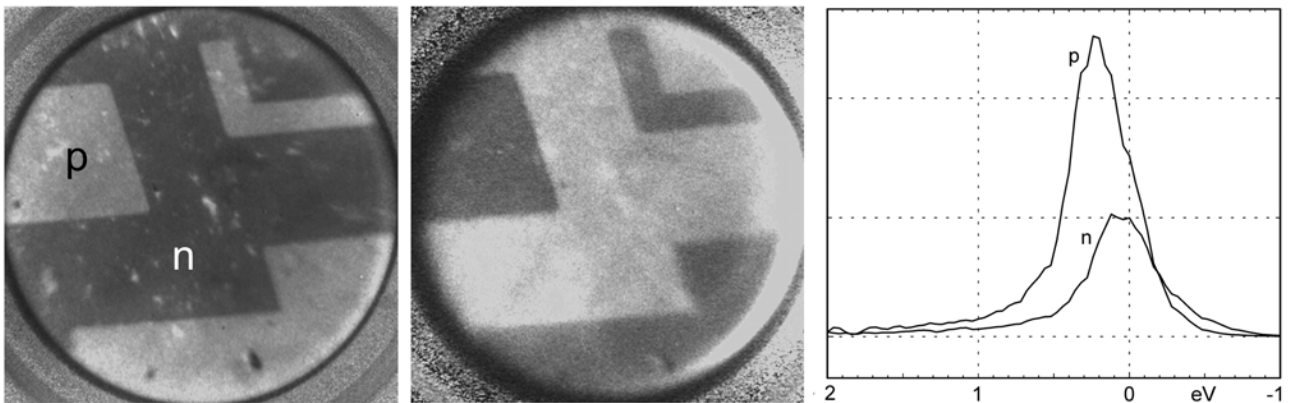


**Fig. 1:** PEEM images (viewfield 150  $\mu\text{m}$ ) taken through a high-pass energy filter set at +2.4 V (left) and  $-0.36$  V (centre); intensity vs. retard voltage curves (right).

[1] L. Frank, I. Müllerová, Ultramicroscopy, in print.

[2] V.W. Ballarotto et al., Surface Sci. 461 (2000) L570.

[3] V.W. Ballarotto et al., J. Appl. Phys. 91 (2002) 469.

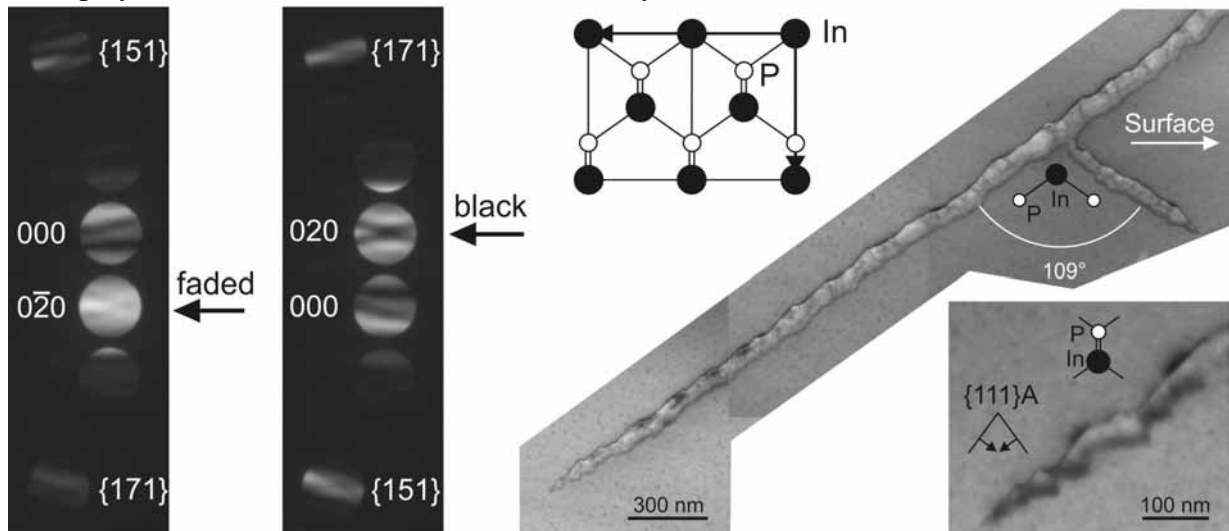
[4] The study is supported by Materialwissenschaftliches Forschungszentrum Mainz and by the GACR grant no. 202/04/281.

## Interface Polarity and Shapes of Electrochemically Etched Pores in InP

E. Spiecker<sup>a</sup>, M. Rudel<sup>a</sup>, W. Jäger<sup>a</sup>, M. Leisner<sup>b</sup>, H. Föll<sup>b</sup>

<sup>a</sup>Microanalysis of Materials and <sup>b</sup>General Materials Science, Faculty of Engineering, Christian-Albrechts-University Kiel, Kaiserstr. 2, 24143 Kiel, Germany, EU

Shapes and interfaces of pores in InP(001) samples and their relationship to the polar crystal structure have been investigated by the methods of transmission electron microscopy (TEM) and by convergent-beam electron diffraction (CBED) [1]. The pores were grown by electrochemical pore etching under etching conditions appropriate for fabricating 3-dimensional structures which are of considerable interest as photonic crystals. Characteristic for InP are the excellent self-assembling properties of pore growth along certain crystal directions forming a 3-dimensional array and pore dimensions that are appropriate for applications in the visible range. The study aims at an understanding of the factors determining shapes, interfaces and pore growth mechanisms, especially also the branching behaviour of pores during etching. The sign of the crystal polarity has been locally determined by CBED (Fig., left) with a recently developed method [2] in order to correlate these microstructural properties with the polar atomic arrangement of InP. The pores are found to grow along  $\langle 111 \rangle_A$  directions, defined as the directions pointing along the bond from an In atom to the next nearest P atom. Along the pore growth axis the pore diameters oscillate (Fig., right). The oscillation decreases with increasing distance from the pore tip while the pore diameter slowly increases. The resulting pore possesses a triangular cross section and is bounded, on the average, by  $\{112\}$  interface facets. The morphology of the pore tips can be described approximately by a chain of interconnected tetrahedrons bounded by  $\{111\}_A$ -facets (Fig., bottom right). Side-ward branching of pores is found to occur also along  $\langle 111 \rangle_A$  lattice directions (Fig., right). Hence the formation of 3-dimensional pore networks in InP(001) is governed by repeated branching of pores growing along all four equivalent  $\langle 111 \rangle_A$  lattice directions. The observations of pore growth along  $\langle 111 \rangle_A$  combined with the preferential  $\{111\}_A$  pore tip faceting show the importance of crystal polarity for the interplay of dissolution rate and interface stability.



References:

- [1] E. Spiecker, M. Rudel, W. Jäger, M. Leisner, H. Föll, *phys. stat. sol. (a)* 2005, (submitted).
- [2] E. Spiecker, C. Jäger, H. Lu, and W. Jäger, *Microsc. Microanal.* **9** (Suppl. 3), 94 (2003).

## Energy-Filtering TEM in Semiconductor Research

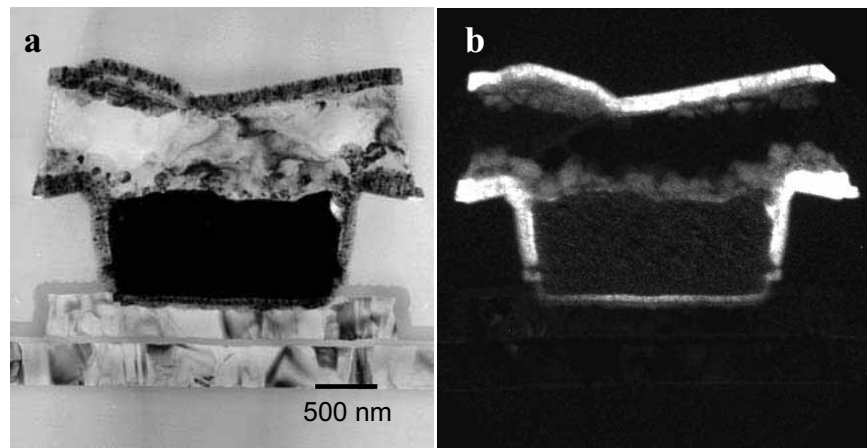
Ferdinand Hofer, Werner Grogger, Bernhard Schaffer

Research Institute for Electron Microscopy, Graz University of Technology, A-8010 Graz, Austria

Over the last decade there has been a large increase in the application of transmission electron microscopy (TEM) to semiconductor devices to evaluate and characterize new process modules and technologies and perform analyses for quality control. Most work, however, has been devoted to morphological investigations and to the analysis of the crystalline structure and crystal defects in devices which can be major yield detractors. An important reason for wider acceptance of TEM analyses is the possibility to combine it with advanced analytical methods, such as energy-dispersive x-ray spectrometry (EDXS) and the main topic of this contribution, electron energy-loss spectrometry (EELS) which can provide elemental information at nanometer resolution. A recent and major improvement in this respect is the availability of energy-filtering TEM's (EFTEM) providing exceptional advantages for semiconductor device analyses [1]. EFTEM is a powerful method for both overview and nanoscale characterisation of thin samples, applicable to most chemical elements and especially sensitive to light elements.

In this paper we outline the principles of EFTEM presenting applications where EFTEM generates unique information which cannot be provided by any other method (Fig.1) [2]. Additionally, new developments will be highlighted which concentrate on the low loss electrons such as contrast tuning for improving the material specific contrast [3], band gap studies at high spatial resolution and EFTEM spectrum imaging for the detailed analysis of local electronic properties [4].

Fig.1 TEM cross-section of an integrated circuit;  
a. TEM bright field image,  
b. EFTEM Ti  $L_{2,3}$  jump ratio image



References:

- [1] F. Hofer, P. Warbichler, in Transmission EELS in Materials Science, ed. C.C. Ahn, Wiley-VCH, Berlin (2004) 181-233.
- [2] F. Hofer, O. Leitner, W. Grogger, P. Warbichler, Solid State Technology, 3 (2000), pp.S23-S28.
- [3] B. Schaffer, W. Grogger, F. Hofer, Micron 34 (2003) 1-7.
- [4] B. Schaffer, W. Grogger, G. Kothleitner, Ultramicroscopy (in print).
- [5] The authors gratefully acknowledge financial support by the FWF, Vienna.

## Growing 1-Dimensional Semiconductor Wires inside Single-Walled Carbon Nanotubes: New Structures and Properties

John L Hutchison<sup>1</sup>, Jeremy Sloan<sup>1,2</sup>, Angus I Kirkland<sup>1</sup>, Robin Carter<sup>1</sup>, Alexis Vlandas<sup>1</sup> & Malcolm LH Green<sup>2</sup>

<sup>1</sup>Department of Materials, University of Oxford, Parks Road, Oxford OX1 3PH, UK.

<sup>2</sup>Inorganic Chemistry Laboratory, University of Oxford, South Parks Road, Oxford OX1 3QR, UK.

Single walled carbon nanotubes (SWNTs) are a relatively new form of nanostructured carbon, occurring with closely defined inner and outer diameters. They offer a novel route to growing spatially confined structures within their empty central channels. In an extensive programme at Oxford, a wide range of essentially 1-dimensional crystals have been grown within SWNTs and their structures characterized by ultra-high resolution electron microscopy techniques. Because of their narrow diameters, SWNTs behave as weak phase objects: ideal specimens for HREM, which was carried out using a 300 kV FEGTEM instrument (JEOL 3000F). Accurate projected atom positions were obtained from restored phases, performed using 20-member, through-focal series [1].

Insertion of guest materials into SWNTs is relatively straight-forward, involving refluxing a mixture of SWNTs and a molten salt, which is then drawn into the SWNTs by capillary attraction. For successful filling of carbon nanotubes by a molten salt, two criteria must be fulfilled: the surface tension of the melt must be less than 200 mN.m<sup>-1</sup> to allow wetting, and its melting temperature should be <ca. 900° C, to prevent damage to the nanotube itself.

We have succeeded in filling SWNTs with compound semiconductors including HgTe, CdTe, InSb etc.[2] and we will present examples of the novel structures that are formed in these confined spaces.

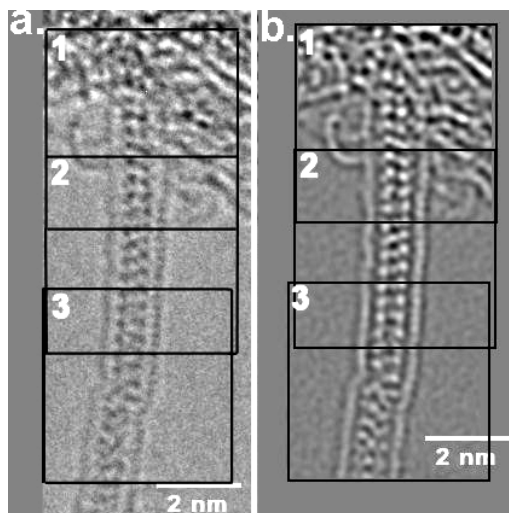


Fig. 1 shows an example of a SWNT filled with HgTe. Numbered boxes are used for subsequent image analysis. (a) is recorded close to Scherzer focus and shows the nanotube walls and guest atom columns (in this case only two atoms along the beam direction) with dark contrast. (b) shows the restored phase, with atoms now revealed with bright contrast. The contrast in the upper half of the nanotube differs from that in the lower part, evidence of the HgTe adopting a twisted 1-D structure. From the projected atomic positions, and maintaining realistic bond lengths and co-ordinations we have been able to derive a number of novel 1-D structures for some of these materials. These will be presented and discussed in detail. Optical properties are also being measured to probe the effects of spatial confinement [3].

1. R.R.Meyer, A.I.Kirkland & O. Saxton *Ultramicroscopy* **92** (2002) 89.
2. A.Vlandas et al. *Proc. EMC 2004 (Antwerp) Vol 1* (2004) 345.
3. We are grateful to the EPSRC, the Royal Society and the Leverhulme Trust for support.

# Electron Tomographic Characterization of $\text{ErSi}_2$ and $\text{Ge}_x\text{Si}_{1-x}$ Nanoparticles Prepared by Doping of 4H-SiC

Ute Kaiser<sup>a</sup> and Christian Kübel<sup>b</sup>

<sup>a</sup> Universität Ulm, Zentrale Einrichtung Elektronenmikroskopie, Albert Einstein Allee 11, 89069 Ulm, Germany

<sup>b</sup> Fraunhofer Institut – IFAM, Wiener Straße 12, 28359 Bremen, Germany

Small semiconductor or transition metal crystals embedded in a semiconducting matrix are nanostructured systems with interesting new properties in fields such as optics and spintronics. Ge nanocrystals embedded in SiC are, for instance, a promising system for optically active quantum dots. In addition to their size, composition and strain, their electronic structure strongly depends on their shape [1]. We have studied the 3D structure of  $\text{Ge}_x\text{Si}_{1-x}$  and  $\text{ErSi}_2$  nanocrystals formed after high dose Ge and Er ion implantation in 4H-SiC, respectively, using HAADF-STEM tomography. Nanoparticles with a diameter of 1-25 nm could be imaged in 3D. Their shape and faceting were analyzed for particles with diameters starting from 5 nm.

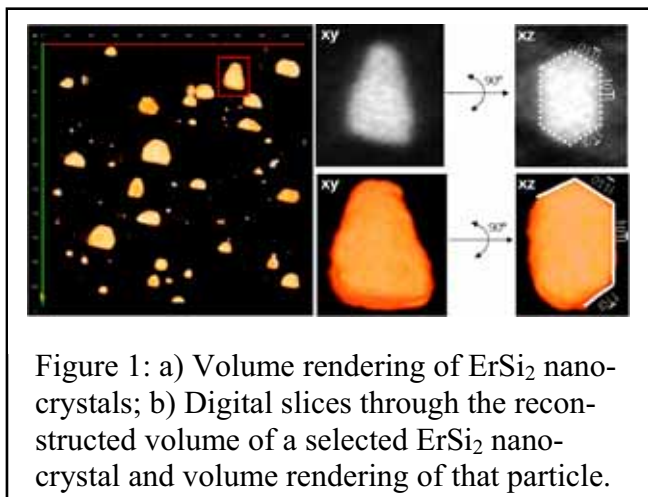


Figure 1: a) Volume rendering of  $\text{ErSi}_2$  nanocrystals; b) Digital slices through the reconstructed volume of a selected  $\text{ErSi}_2$  nanocrystal and volume rendering of that particle.

In 2D, the nucleation, growth and structure of these clusters and nanocrystals have already been studied by Kaiser and coworkers using HRTEM and Z-contrast imaging [2-4]. Viewed along the  $[11-20]$  SiC projection, the  $\text{ErSi}_2$  nanocrystals exhibit a characteristic hill-like shape with a well-defined flat base along the  $(0001)$  SiC basal plane [2]. Further faceting of these nanocrystals only becomes visible in 3D. It was found that their basal plane typically exhibits strong hexagonal faceting corresponding to the  $\{1-101\}$  class planes in SiC (Figure 1). Both their shape and orientation stay the same throughout most of the sample.

In contrast, the overall shape of the  $\text{Ge}_x\text{Si}_{1-x}$  particles is not as uniform as the  $\text{ErSi}_2$  particles and the orientation varies significantly with respect to the SiC matrix. This variation of the 3D-orientation confirms earlier calculations, which indicated several energy minima for a rotation of a  $\text{Ge}_x\text{Si}_{1-x}$  crystal within a SiC matrix [3]. Nevertheless, for the first time, clear similarities between the shape of the  $\text{ErSi}_2$  and  $\text{Ge}_x\text{Si}_{1-x}$  could be observed, which could lead to a new dimension in interpretation of nucleation and growth of embedded nanocrystals.

## References:

- [1] F. Bechstedt, A. Fissel, J. Furthmüller, U. Kaiser, H.-Ch. Weissker, W. Wesch, *Appl. Surf. Science* 212 (2003) 820.
- [2] U. Kaiser, D.A. Muller, A. Chuvilin, G. Pasold, W. Witthuhn, *Micr. and Microanal.* 9 (2003) 1.
- [3] U. Kaiser, J. Biskupek, D. A. Muller, K. Gärtner, Ch. Schubert, *Cryst. Res. Techn.* 37, 4 (2002) 391.
- [4] U. Kaiser, D.A. Muller, J.L. Grazul, A. Chuvilin, M. Kawasaki, *Nature Materials* 1 (2002) 102.

## Application of Electron Tomography for Semiconductor Device Analysis

Christian Kübel<sup>a,b</sup>, Tan-Chen Lee<sup>c</sup>, David Su<sup>c</sup>, Jian-Shing Luo<sup>d</sup>, Hui-Min Lo<sup>d</sup>, Jeremy Russell<sup>d</sup>

<sup>a</sup> Fraunhofer Institut – IFAM, Wiener Straße 12, 28359 Bremen, Germany

<sup>b</sup> FEI Company, Application Laboratory, Achtseweg Noord 5, 5651GG Eindhoven, The Netherlands

<sup>c</sup> Taiwan Semiconductor Manufacturing Company, Ltd., Failure Analysis Division 9, Creation Road 1, Science-Based Industrial Park Hsin-Chu, Taiwan

<sup>d</sup> Inotera Memories, Physical Failure Analysis Department, Hwa-Ya Technology Park, 667, Fuhsing 3Rd., 333 Kueishan, Taoyuan, Taiwan

The continual shrinking of semiconductor devices has resulted in commercial products with complex non-planar features and dimensions comparable to or smaller than the thickness of a typical TEM specimen. As a result, device features and defects are becoming increasingly difficult to image and accurately identify by conventional cross-section (S)TEM imaging due to geometric blurring in a single 2D projection. With the development of even smaller devices, this limitation will become even more pronounced in the next years. TEM and STEM tomography are proving to be a promising solution to this problem by offering a high-resolution 3-dimensional image of the volume of interest.

We will demonstrate the use of TEM and HAADF-STEM tomography to image the 3D structure of VIAs (Figure 1), flash memory [1] and DRAM devices including visualization of buried defects and metrology in 3D. Special attention will be paid to 1) the quality of the reconstruction and how it is affected by the ‘missing wedge’ and 2) the validity of TEM tomography to image thin oxide layers in close proximity to high atomic number materials such as a contact.

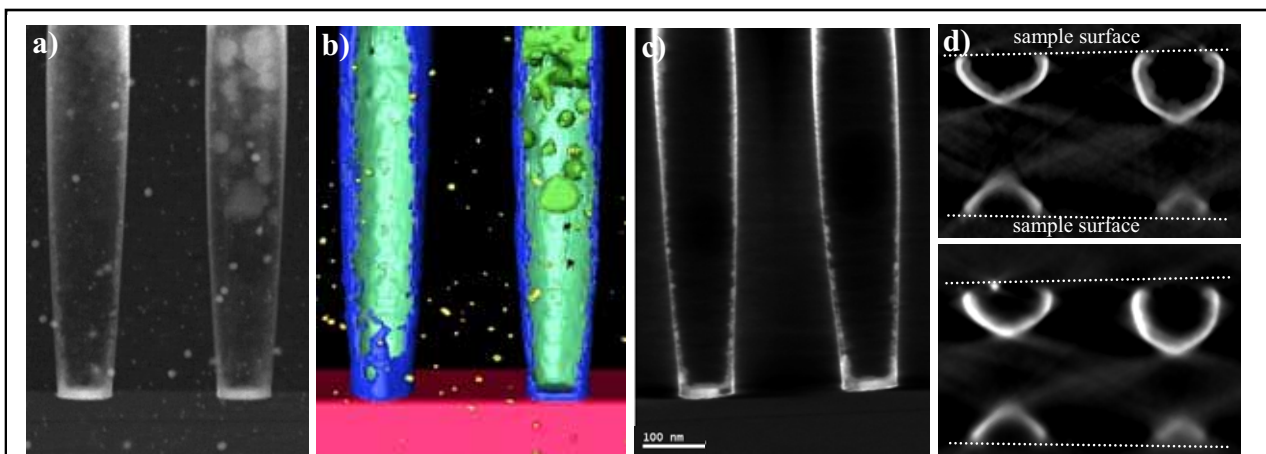


Figure 1: a) HAADF-STEM image b) Surface rendering of the 3D structure c) Slice through the reconstructed volume parallel and d) perpendicular to the TEM sample surface revealing the barrier layer thickness and variations in the copper seed coverage of an unfilled VIA.

### References:

[1] C. Kübel, A. Voigt, R. Schoenmakers, M. Otten, D. Su, T.-C. Lee, A. Carlsson, J. Bradley, *Micr. and Microanal.* 2005 in print.

## Assessment of quantum dot electronic level structure using TEM and cathodoluminescence

K. Leifer<sup>a,c</sup>, F. Bobard<sup>b</sup>, F. Michelini<sup>a,d</sup>, E. Pelucchi<sup>a</sup>, S. Watanabe<sup>a,e</sup>, B. Dwir<sup>a</sup>, and E. Kapon<sup>a</sup>

- a. Laboratory of Physics of Nanostructures, FSB, EPFL, 1015 Lausanne, Switzerland
- b. Interdisciplinary Centre for Electron Microscopy, FSB, EPFL, 1015 Lausanne, Switzerland
- c. Present address: Angstrom Laboratory, Uppsala University, 743 Uppsala, Sweden
- d. Present address: L2MP - UMR CNRS, 13394 Marseille, France
- e. Present address: Department of Physics, University of Tokyo, Tokyo, 113-0033 Japan

Precise site and size control of semiconductor quantum dots (QD) is essential to fully exploit 0-D properties in future optical and electronic QD based devices. In this paper, we study optical and structural properties of QDs that possess excellent size uniformity and position control. We demonstrate for the first time a correlation of QD energy level calculations based with QD luminescence peak positions of better than 10meV. This correlation is based on the assessment of the QD structure obtained by an optimisation of dark-field TEM techniques. The III/V semiconductor quantum dots are obtained by growth of AlGaAs/GaAs heterostructures on tetrahedral pyramid recess patterns etched in (111)B GaAs substrates using metal organic chemical vapour deposition (MOCVD) [1]. The positions of the pyramids are precisely controlled by the e-beam lithography. Due to capillarity forces, a GaAs QD is formed during growth in the pyramid centre. Since the QD shape is given by the technique of self-limiting growth, one obtains very uniform arrays of QDs using this approach.

Due to the structural perfection and reproducibility of these QDs, it is possible to extract the QD structure on one part of the sample dedicated for TEM and employ this structure as representative for another part of the sample on which CL measurements were performed. The challenge for TEM sample preparation consists in obtaining the QD structure in the part where the TEM sample is about 50nm thick. To achieve this precision, we optimised the pyramid density using e-beam lithography and sample preparation technique using tripod polishing with a final Ar ion bombardment. As result we were able to prepare the QD structure in a TEM foil of the desired thickness and with an excellent surface quality. Cathodoluminescence (CL) and angular dark-field imaging are used to obtain the QD barrier structure and chemical composition. Likewise we measured the evolution of the QD luminescence energy of ground and first excited state as a function of QD thickness. These experimental values are in excellent agreement with the theoretical predictions.

Using CL, we obtain fluctuations of the QD emission energy of only 3.8 meV. From energy level calculations[2], we deduce the thickness fluctuations of 1-3 monolayers. These very small thickness fluctuations can be attributed to the well controlled self-limited growth mode. These results show that TEM measurements on individual, buried QDs are essential for the understanding of fundamental electronic QD properties.

### References:

- [1] A. Hartmann, Y. Ducommun, K. Leifer, E. Kapon, J. Phys. Cond. Matt.11 (1999) 5901.
- [2] F. Michelini, M.-A. Dupertuis, E. Kapon, Appl. Phys. Lett 84 (2004) 4086.

# Electron Holography in Combination with FIB-based “Lift-Out” Technique: Minimum Invasive 2D-Dopant Profiling of Commercial Semiconductors

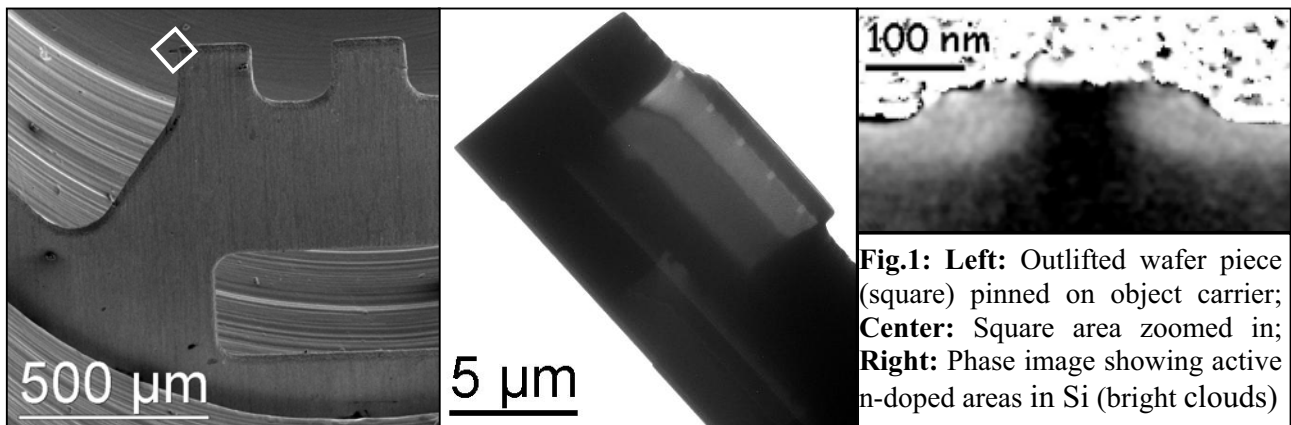
Andreas Lenk<sup>a</sup> and Uwe Mühle<sup>b</sup>

<sup>a</sup> Institute of Structure Physics, Triebenberg Laboratory, Dresden University, 01062 Dresden, Germany

<sup>b</sup> Infineon Technologies Dresden GmbH & Co OHG, Germany

The steady development of commercial semiconductors towards increasing speed of performance and simultaneously decreasing structure sizes has resulted in the application of highly doped but shallow dopant areas that guarantee enhanced functionality of microdevices. Monitoring the doping process has therefore become an important issue of physical failure analysis. Electron Holography, combined with highly efficient focussed ion beam (FIB) target preparation, is a promising method on this purpose. Several investigations have shown its capability of revealing 2D dopant distribution maps of semiconductor devices, qualitatively and quantitatively [1,2].

However, the advance in device shrinking also increases the costs of production. The industry counteracts this by using larger silicon wafers (today: 300mm diameter), resulting in a higher yield of chips per manufactured wafer. For physical failure analysis, this raises a strong requirement to find methods that limit the area destroyed by the preparation needed for analysis. To save the remaining chips, a wafer has not only to be kept as a whole entity, but it also must not leave the clean room area of the production line. Therefore, the “Lift-out” technique was developed as a new type of FIB-preparation, which allows cutting the small area of interest out of the wafer directly in the production line, leaving the wafer disc intact for further processing in production.



This work demonstrates the compatibility of the new lift-out technique with electron holography by mapping the electrically active doped areas of selected microdevices. The results of investigation at two complementarily doped field effect transistors (FET) of the 140nm device generation are shown.

## References:

- [1] W D Rau, P Schwander, F H Baumann, W Hoppner and A Ourmazd “Two-dimensional mapping of the electrostatic potential in transistors by electron holography” Phys Rev Lett **82** (1999) 2614-2617.
- [2] A C Twitchett, R E Dunin-Borkowski, P A Midgley “Quantitative electron holography of biased semiconductor devices” Phys Rev Lett **88** (2002) 238302

## Structural properties of epitaxial ZnMnSe layers

D. Litvinov<sup>a</sup>, D. Gerthsen<sup>a</sup>, B. Daniel<sup>b</sup>, and M. Hetterich<sup>b</sup>

<sup>a</sup>Laboratorium für Elektronenmikroskopie and Center for Functional Nanostructures (CFN), Universität Karlsruhe, D-76128 Karlsruhe, Germany

<sup>b</sup>Institut für Angewandte Physik and CFN, Universität Karlsruhe, D-76128 Karlsruhe, Germany

Transmission electron microscopy (TEM) was applied to study the structural properties of ZnMnSe layers which are of considerable interest as spin-aligning layers in spintronic devices. With increasing Mn-concentration, ZnMnSe occurs in different phases exhibiting the sphalerite, wurtzite or rock salt structure. We have investigated the formation of the different phases and the generation of defects as a function of the Mn-concentration which is relevant for the degree of spin alignment. The ZnMnSe layers were deposited by molecular-beam epitaxy on GaAs(001) substrates with nominal Mn-concentration between 0 % and 100 % and a layer thickness between 700 nm and 1000 nm.

The increase of the Mn-concentration is accompanied by an increase of the lattice-parameter mismatch between the substrate and the epilayer which is approximately 4 % between GaAs and pure MnSe in the sphalerite phase. The incorporation of only a few percent of Mn in the ZnSe matrix already leads to the generation of V-shaped stacking faults with a density in the order of  $10^9$  cm<sup>-2</sup>. In ZnMnSe layers with  $x_{Mn} > 25$  %, misfit dislocations with threading segments appear which extend along the [001]-growth direction and have Burgers vectors of the type  $\mathbf{b} = \frac{1}{2}\langle 110 \rangle$ . As expected from the increasing lattice-parameter mismatch, the dislocation density increases with the Mn-concentration.

Only the ZnMnSe layer with  $x_{Mn} = 31$  % contains a significant fraction of the wurtzite phase in contrast to material with lower and higher Mn-concentrations up to 43 % which consist exclusively of the sphalerite phase. The transformation between the sphalerite and wurtzite phase was analyzed in detail by applying conventional and high-resolution TEM in combination with selected area electron diffraction. It is observed, that the sphalerite Zn<sub>0.69</sub>Mn<sub>0.31</sub>Se layer contains twins with a crystallographic orientation where the {111} planes of the epitaxially grown ZnMnSe layer serve as mirror planes. The twinned areas are strongly strained, which leads to the formation of a high density of stacking faults. As a result, the structure is locally transformed into the wurtzite structure. The pure MnSe layer exhibits a grain-like structure and contains a mix of the sphalerite and rock salt phases. A similar phase mix was observed in thin MnSe layers with nominal thicknesses above 6 monolayers which were grown on ZnSe [1].

References:

[1] D. Litvinov, A. Rosenauer, D. Gerthsen, B. Daniel, and M. Hetterich, Appl. Phys. Lett. **85** (2004) 751.

[2] We are grateful for the financial support of the DFG Center for Functional Nanostructures at the University of Karlsruhe (Germany) within project A2.

## Dislocation formation in Si<sub>1-x</sub>Ge<sub>x</sub> virtual substrates by He implantation and annealing: Relaxation Mechanism and Strain Transfer into Si cap layers

M. Luysberg<sup>a</sup>; N. Hueging<sup>a</sup>; L. Houben<sup>a</sup>; K. Urban<sup>a</sup>; St. Lenk<sup>b</sup>; D. Buca<sup>b</sup>; B. Hollaender<sup>b</sup>; H. Trinkaus<sup>b</sup>; S. Mantl<sup>b</sup>, M. Morschbacher<sup>c</sup>; P. Fichtner<sup>c</sup>, R. Loo<sup>d</sup>; M. Caymax<sup>d</sup>; R. Carius<sup>e</sup> and P. Schäfer<sup>f</sup>

<sup>a</sup> Institute of Solid State Research and cni-Center of Nanoelectronic Systems for Information Technology, Research Center Juelich, 52425 Juelich, Germany.

<sup>b</sup> Institute of Thin Films and Interfaces and cni-Center of Nanoelectronic Systems for Information Technology, Research Center Juelich, 52425 Juelich, Germany.

<sup>c</sup> University Federal do Rio Grande do Sul, Porto Alegre, Brazil.

<sup>d</sup> IMEC, Kapeldreef 75, B-3001 Leuven, Belgium.

<sup>e</sup> Institute of Photovoltaics, Research Center Juelich, 52425 Juelich, Germany.

<sup>f</sup> Infineon Technologies AG, Otto-Hahn-Ring 6, 81739, München, Germany

The great industrial and scientific interest in elastically strained Si devices arises from significantly enhanced carrier mobilities. Epitaxial growth of a Si cap layer onto strain-relaxed Si<sub>1-x</sub>Ge<sub>x</sub> buffer layers results in a tensile strain due to the larger lattice constant of Si<sub>1-x</sub>Ge<sub>x</sub>. The Si cap layer can be sufficiently strained if (i) the strain in the Si<sub>1-x</sub>Ge<sub>x</sub> buffer layer grown onto a Si (100) substrate is relaxed and if (ii) the thin Si cap layer shows no strain relaxation. In our contribution we will address both issues: the relaxation mechanism of the Si<sub>1-x</sub>Ge<sub>x</sub> layers and the efficient strain transfer into a Si cap layer.

In order to induce the strain relaxation of the Si<sub>1-x</sub>Ge<sub>x</sub> buffer layers with Ge contents of 19 to 27 at %, misfit dislocations are introduced through He implantation into the Si substrate and subsequent thermal treatment. He<sup>+</sup> ions are implanted with doses between 7x10<sup>15</sup> and 1.5x10<sup>16</sup> cm<sup>-2</sup>. The He<sup>+</sup> energy is chosen such that the implantation depth equals twice the Si<sub>1-x</sub>Ge<sub>x</sub> layer thickness. Annealing at 700 to 850°C results in the formation of He precipitates underneath the Si<sub>1-x</sub>Ge<sub>x</sub>/Si interface and a dense misfit dislocation network [1]. By ex-situ and in-situ TEM the different stages of precipitate and dislocation formation can be monitored [2]. He precipitates formed in the initial stages are unambiguously identified as internal dislocation sources. Quantitative TEM contrast analysis yields pressure values of up to 13 GPa inside the precipitates, involving shear stress values within the Si matrix beyond the critical value for dislocation nucleation. Employing this “Juelich Process”, i.e. He implantation and annealing, high degrees of relaxation up to of 80% are achieved in the Si<sub>1-x</sub>Ge<sub>x</sub> buffer layers.

Strain transfer from the relaxed SiGe buffer to the Si cap layer is successful for thin Si cap layers. Measurements of the strain by Raman spectroscopy and analyses of the dislocation structure show, that the strain transfer is efficient for Si layers thinner than 8 nm [3]. Thus, the “Juelich Process” is suitable for the fabrication of strained Si devices.

### References:

- [1] M. Luysberg, D. Kirch, H. Trinkaus, B. Holländer, S. Lenk, S. Mantl, T. Hackbarth, H.J. Herzog and P.F.P. Fichtner, *J. Appl. Phys.* **69** (2002), 4290.
- [2] N. Hueging, M. Luysberg, K. Urban, D. Buca, S. Mantl, *Appl. Phys. Lett.*, **86** (2005) 042112.
- [3] D. Buca et al. *App. Phys. Lett.* **85** ( 2004) 2499.

## **TEM on Silicon-based Material: a Short Insight into a Nearly Infinitely Wide Field of Research**

E. Müller<sup>a,b</sup>, M. Borgström<sup>c</sup>, H. von Känel<sup>d</sup>, D. Grützmacher<sup>a</sup>

<sup>a</sup>Laboratory for Micro- and Nanotechnology, Paul Scherrer Institute, CH-5232 Villigen, Switzerland

<sup>b</sup>Laboratory for Solid State Physics, ETH Zürich, CH-8093 Zürich, Switzerland

<sup>c</sup>Institute for Quantum Electronics, ETH Zürich, CH-8093 Zürich, Switzerland

<sup>d</sup>INFM and L-NESS, Dipartimento di Fisica, Politecnico di Milano a Como, Via Anzani 2, I-22100 Como, Italy

Silicon, the most important material for electronic applications, is known to be one of the most perfect materials which can be grown. As such it could also be considered as one of the most boring materials for transmission electronmicroscopic investigations, which is mainly used for many reference measurements because it is so well defined and well known. As a basic material in electronic devices, however, it is used in combination with a large amount of other materials for a wide variety of technologies. Therefore nearly all phenomena, which might be interesting for TEM investigations in the field of anorganic materials, can be treated on Si-based materials. Typically, almost every TEM-technique is required for the investigation of these phenomena. Out of this almost infinitely wide field of research, a selection of examples will be discussed as e.g. silicides, nanostructures, novel oxides, growth on prestructured material and self-alignment.

## HRTEM Investigation of the Intermediate Layer Formed During MOCVD Growth of ZnO on GaAs

J.H. Neethling<sup>a</sup>, H. Kirmse<sup>b</sup>, W. Neumann<sup>b</sup>, C. Weichsel<sup>a</sup>, P.R. Berndt<sup>a</sup> and A.W.R. Leitch<sup>a</sup>

<sup>a</sup>Physics Department, PO Box 77000, Nelson Mandela Metropolitan University, Port Elizabeth, 6031, South Africa

<sup>b</sup>Humboldt-Universität zu Berlin, Institut für Physik, AG Kristallographie, Newtonstr. 15, 12489 Berlin, Germany

ZnO is a promising compound with potential application in UV light emitters and window materials for display and solar cells [1]. The interest in the growth of ZnO on GaAs substrates increased after Ryu *et al.* reported that As diffusion from the substrate into the ZnO layer resulted in the formation of p-type ZnO [2]. The ZnO layers for this investigation were grown by metal-organic chemical vapour deposition (MOCVD) on Si-doped ( $3 \times 10^{18} \text{ cm}^{-3}$ ) GaAs (001) substrates. A 100 nm thick ZnO buffer layer was first grown at 350 °C followed by a 2.5  $\mu\text{m}$  thick ZnO layer grown at 450 °C. High resolution TEM and EDX were used to investigate the ZnO/GaAs interface for evidence of interdiffusion and the replacement of Ga by Zn in the substrate, as was observed in the case of InP exposed to Zn [3].

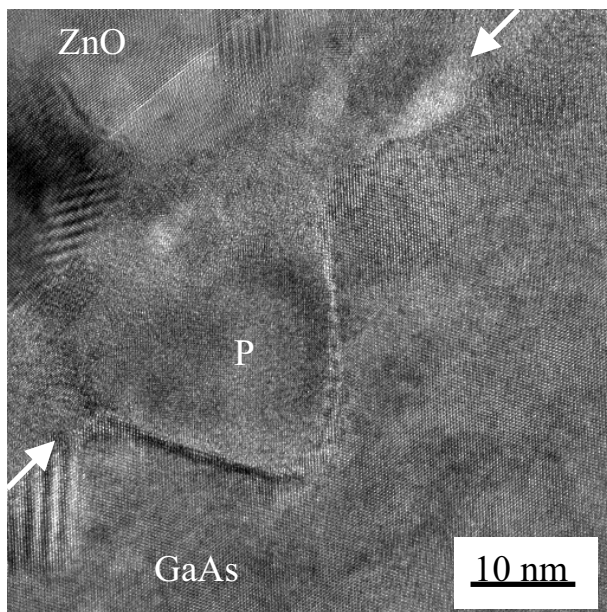


**Fig. 1:** HRTEM image of the ZnO/GaAs interface (arrowed) showing an inverted pyramid (P) in the GaAs substrate.

HRTEM of the interface (indicated by arrows) shows inverted pyramids (indicated by P) in the GaAs substrate as can be seen in Fig. 1. The material in the pyramid still exhibits some degree of crystallinity, as revealed by the presence of lattice fringes in certain regions with the same orientation as the substrate. Nano-probe EDX line scans across the inverted pyramids and intermediate layer revealed a reduction in Ga content compared to the substrate, and increase in Zn, from the bottom of the pyramid to the interface. The reduction of Ga content in the pyramid correlates with a much higher Ga than As content in the intermediate layer. This indicates that the Zn has partially replaced the Ga in the inverted pyramids formed in the GaAs. The replaced gallium then diffused to the intermediate layer. The intermediate layer is amorphous. On this amorphous layer, the ZnO started to appear in the form of columnar grains.

### References:

- [1] D.C. Look *Mater. Sci. and Eng. B* **80** (2001), 383.
- [2] Y.R. Ryu *et al. J. Crystal Growth* **216** (2000), 330.
- [3] D. Eger *et al. J. Electron. Mater.* **16** (1987), 63.

## TEM study of deformation mechanisms of semiconductors during nanoscratching

M. Parlinska-Wojtan<sup>a</sup>, R. Gassilloud<sup>b</sup>, S. Meier<sup>c</sup>, H. Michler<sup>b</sup>,

<sup>a</sup> Oberflächen und Magnetismus, EMPA, Ueberlandstr. 129, Dübendorf, Switzerland

<sup>b</sup> [Werkstofftechnologie](#), EMPA, Feuerwerkerstr. 39, Switzerland

<sup>c</sup> Elektornik und Messtechnik, EMPA, Ueberlandstr. 129, Dübendorf, Switzerland

Polished n-type InP{100}, n-type GaAs{100} and p-type Silicon{100} wafers were scratched in the <110> direction at constant load and velocities varying between 10  $\mu\text{m/s}$  and 10 mm/s using a MTS Nano-Indenter XP equipped with a rounded Berkovitch diamond tip with an curvature radius of approximately 2.4  $\mu\text{m}$ . The investigated semiconductors illustrate the variety of effects that occur during scratching observed by conventional and high resolution transmission electron microscopy (TEM) in cross-sectional lamella prepared by focused ion beam (FIB) technique. These effects range from the nucleation of dislocations, to the formation of slip bands and highly defected areas associated to semiconductor plasticity observed in all tree semiconductors. Additionally in the Silicon sample the generation of new nanocrystalline phase with a very sharp interface to the crystalline material was observed. HRTEM observations confirmed the presence of equiaxed nanocrystals of 5 nm. Eventually, the creation of atomically sharp cracks below the scratch is observed, when scratching at higher load using a sharp diamond tip. Such cracks can extend in the substrate behind the plastically deformed area. Another important aspect of scratching at high load is the generation of surface particles or chips, which are likely to be linked to a non-reproducible process.

# Grain boundaries and domain structures of ferroelectric barium titanate investigated by TEM

Michael Rössel, Mihail Dan Croitoru, David Moser, Jörg Ihringer, Oliver Eibl

Universität Tübingen, Institut f. Angewandte Physik, Auf der Morgenstelle 10, D-72076 Tübingen

Polycrystalline BaTiO<sub>3</sub> exhibits a PTC (positive temperature coefficient) effect and is used for various devices. The electrical resistivity is strongly determined by the microstructure of the material. At the ferroelectric Curie temperature (393 K) BaTiO<sub>3</sub> shows a dramatic increase of resistivity (Fig. 1) The domain structure plays a crucial role for the PTC-effect, compensating space charges at the grain boundaries. Especially the microstructure of the domains, the orientation of the polarization and the contact point of the domains at the grain boundaries are of interest.

Samples were characterized by X-ray powder diffraction (XRD) in a temperature range between 190 K and 420 K including the orthorhombic-to-tetragonal and tetragonal-to cubic phase transition. The domain structure was imaged by SEM and AFM. Grain boundaries and domains were investigated by diffraction contrast under two-beam and many beam diffraction conditions in the TEM. Straight and faceted grain boundaries (Fig. 2a) and domains with a size of about 60 nm (Fig. 2b) are observed. These grain boundaries consist of planar sections with low indexed crystallographic planes and a predominantly simple domain structure and curved sections, yielding a complicated arrangement of 90°-domains which can be identified by delta fringe pattern [1].

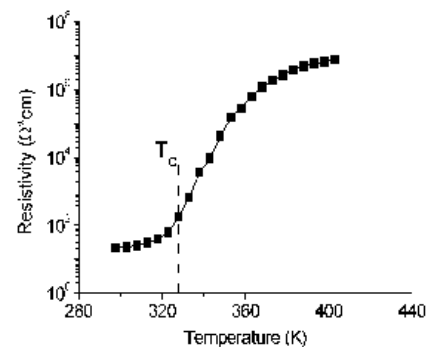


Fig.1: Typical resistivity vs. temperature curve of our samples.

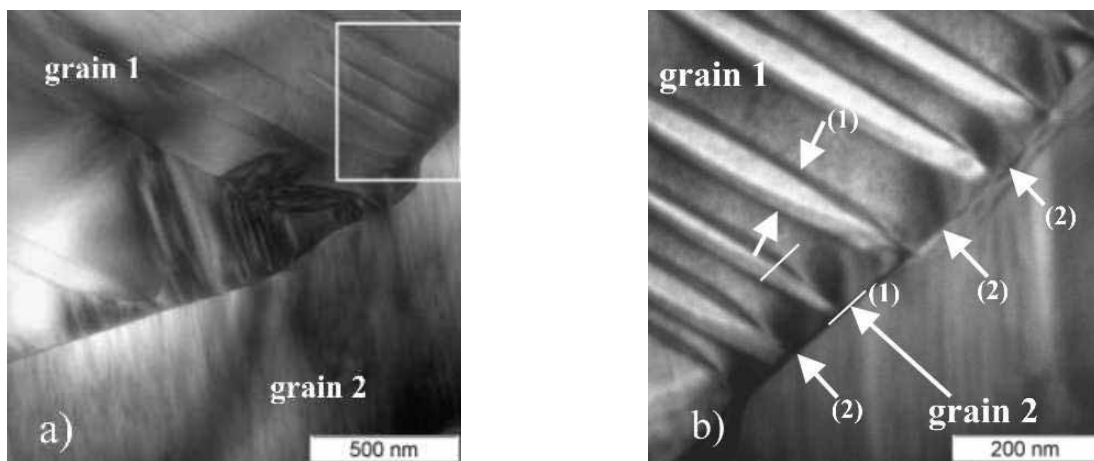


Fig.2 a) TEM micrograph of 90° domains at a grain boundary in ferroelectric BaTiO<sub>3</sub>. b) Domain configuration according Figure 2a. The domain width in the grain and at the grain boundaries can be measured (1) and strain fields at the grain boundaries can be imaged (2).

[1] R. Gevers, P. Delavignette, H. Blank, J. Van Landuyt, S. Amelinckx, Phys.Stat.Sol. 5 (1964) 595

## Growth of Ge on graded oxide of (Sr,Ba)TiO<sub>3</sub> and Sr(Ti,Hf)O<sub>3</sub> on (001)Si

J.W. Seo<sup>a</sup>, Ch. Dieker<sup>a</sup>, A. Guiller<sup>b</sup>, J.-P. Locquet<sup>b</sup>, J. Fompeyrine<sup>b</sup>, Y. Panayiotatos<sup>c</sup>, G. Mavrou<sup>c</sup> and A. Dimoulas<sup>c</sup>

<sup>a</sup>Institute of Physics of Complex Matter, Ecole Polytechnique Fédérale de Lausanne, 1015 Lausanne, Switzerland

<sup>b</sup>IBM Research GmbH, 8803 Rüschlikon, Switzerland

<sup>c</sup>MBE Laboratory, Institute of Materials Science, NCSR DEMOKRITOS, 153 10, Athens, Greece

High mobility materials such as Ge are emerging as potential silicon replacement in CMOS. With the recent achievements to grow complex oxides epitaxially on Si [1,2], Ge can be integrated as channel by overgrowing an epitaxial oxide on Si. One of the challenges is to accommodate the lattice mismatch between Si and Ge of about 4%, which can be achieved for instance by grading the lattice constant in the intermediate insulating oxide layer. A second challenge is the subsequent growth of Ge on the oxide because the competition between kinetic and thermodynamic surface energetic effects during growth does not allow obtaining two-dimensional films with a flat surface morphology and high crystalline quality. In this contribution we studied the growth of Ge on graded

oxides of (Sr,Ba)TiO<sub>3</sub> and Sr(Ti,Hf)O<sub>3</sub> grown on (001) Si by molecular beam epitaxy.

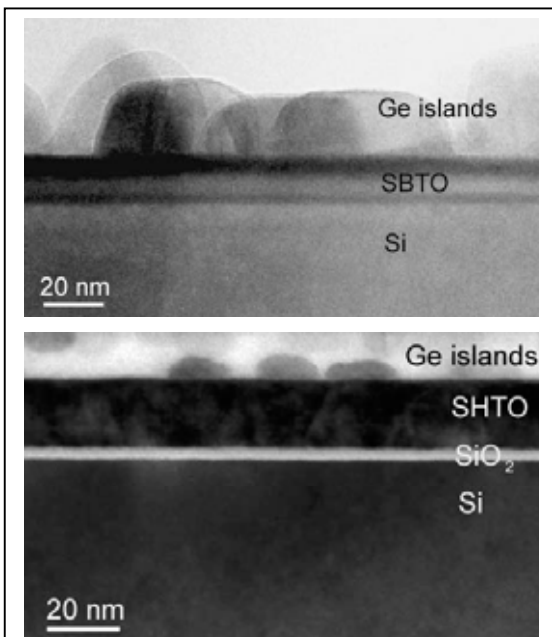


**Fig. 1:** Ge grown on graded oxide of (top) (Sr,Ba)TiO<sub>3</sub> (SBTO) and (bottom) Sr(Hf,Ti)O<sub>3</sub> (SHTO). By using Sb surfactant (bottom) a better coverage of the surface was achieved.

By means of EDX line scans we found that the compositional grading was achieved. The oxide film was epitaxial but was defective and strained. Ge deposited on the oxide formed crystalline islands with an average diameter of 50 nm. We have not observed a significant difference between both graded oxide systems. The crystallographic orientation of the islands predominately remained the same within one island however the epitaxial relationship between the oxide and Ge islands was not uniformly preserved. In order to avoid the Ge clustering, a surfactant material with a low surface free energy such as Sb and Se was applied. In the case of Sb surfactant, flattening of islands was observed with the aspect ratio (width to height) increasing from 2.2 to 2.9. Moreover Ge islands revealed preferentially (001) orientation.

### References:

- [1] R.A. McKee et al., Phys. Rev. Lett. 81 (1998) 3014.
- [2] G. Norga et al., Materials Research Society Symp. Proc. 786 (2004) E7.3.1-8.

[3] This work is supported by the European project IST-ET4US-2048 "Epitaxial Technologies for Ultimate Scaling". We also acknowledge the Centre Interdépartement de Microscopie Electronique CIME of the EPFL for access to electron microscopes.

# TEM Investigation of Dislocation Characteristics in MOVPE Grown InGaN/GaN Multiple Quantum-Well Heterostructures on SiC and Al<sub>2</sub>O<sub>3</sub> Substrates

M.Soda<sup>1,2,3</sup>, M.Beer<sup>2</sup>, J. Zweck<sup>2</sup>, E.Zanoni<sup>1</sup>, M. Peter<sup>3</sup>, S. Bader<sup>3</sup>, K. Engl<sup>3</sup>, U. Zehnder<sup>3</sup>, G. Brüderl<sup>3</sup>, U. Strauss<sup>3</sup> and V. Härle<sup>3</sup>

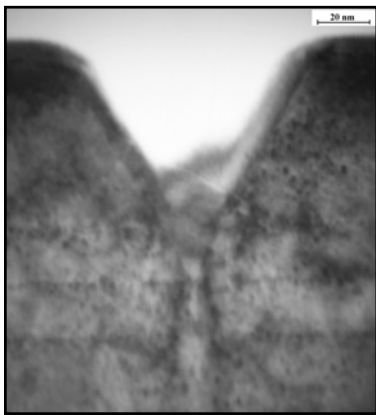
<sup>1</sup>Department of Information Engineering, University of Padua, Via Gradenigo 6/B, 35131 Padova, Italy

<sup>2</sup>Institut für Experimentelle und Angewandte Physik, Universität Regensburg, Universitätstr. 31, D-93053 Regensburg, Germany

<sup>3</sup>OSRAM Opto Semiconductors GmbH, Wernerwerkstr. 2, D-93049 Regensburg, Germany

GaN based Optoelectronic devices such as blue light emitting diodes (LEDs) and laser diodes offer a wide variety of applications e.g. for optical storage media or high resolution laser printers. To achieve high performance and lifetime of such devices high crystalline quality and low defect density is required.

One commonly reported morphological feature of InGaN/GaN quantum-well heterostructures is the so called V-defect that consists either of a threading dislocation or of a stacking mismatch boundary terminated by a pit in the specimen surface in the shape of an inverted hexagonal pyramid with (10-11) sidewalls [1]. Such defects may cause a loss of interface abruptness between individual quantum wells within the multiple-quantum well stack. How this defect affect the properties of GaN based optoelectronic devices is not completely understood [2][3]. Particularly important is the behaviour of the InGaN quantum wells in the proximity of the V-defect.



The structure of the test samples consists of four InGaN/GaN layers at the top of an n-doped GaN bulk substrates grown either on SiC or Al<sub>2</sub>O<sub>3</sub> substrates. We investigated size and origin of the V-defects with high resolution TEM. The correlation between V-defects and the threading dislocation types was carried out by weak beam imaging.

Our cross section investigations show that almost all threading dislocations end with a V-defect independent of their Burgers - vector. Size and depth of the V-defects are independent of the threading dislocation type from which they originate. No V-defects in relationship with stacking mismatch boundaries were found. It has become evident, that V-defects originate not only from dislocations with a screw component, but from pure edge dislocation, too, even if in smaller percentage.

From our plan-view images we obtain the confirmation that almost every V-defect is in relationship with a threading dislocation. We found that the formation effects of V-defects are independent of the substrates SiC and Al<sub>2</sub>O<sub>3</sub>.

[1] H.K. Cho, J.Y. Lee, G.M. Yang, C.S. Kim, *Appl. Phys. Lett.* **79**, 215 (2001)

[2] Y.S. Lin *et al.*, *Appl. Phys. Lett.* **77**, 2988 (2000)

[3] H. Takahashi, A. Ito, T. Tanaka, A. Watanabe, H. Ota, and K. Chikuma, *Jpn. J. Appl. Phys., Part 2* **39**, L569 (2000)

# Formation of compositionally ordered dots in strained GeSi alloy during in situ electron irradiation at ARM1300s

S.A. Song<sup>a</sup>, Y.M. Kim<sup>b</sup>, L.I. Fedina<sup>c</sup>, A.K. Gutakovskii<sup>c</sup> and A.V. Latyshev<sup>c</sup>

<sup>a</sup> AE Center Samsung Advanced Institute of Technology, POB 111 Suwon, 440-600, Korea.

<sup>b</sup> Div. of Nano-Material and Environmental Science, Korean Basic Science Institute, P.O. BOX 41, Taejeon, 305-333, Korea

<sup>c</sup> Lab. of Electron Microscopy and Submicron structure, Institute of Semiconductor Physics, 630090, pr. Lavrentjeva 13, Novosibirsk, Russia

Order-disorder transitions have been observed in several semiconductor systems. These phase transitions have potential applications due to changes in the band gap [1]. Alloy ordering in single-crystal GeSi alloy films grown by molecular beam epitaxy has been attributed mostly with surface Ge segregation during nonequilibrium growth [2]. Here we present the formation of well shaped compositionally ordered dots of 5-7 nm of size within initially strained Ge<sub>0.2</sub>Si<sub>0.8</sub> alloy of 10 nm thick grown on (100)Si wafer after electron irradiation at ARM1300S operated at 1250 KeV at increased temperature between 250-450°C (Fig.1). The microscope is characterized by excellent point-to-point resolution of 1.2Å which allows in principle the atoms within dumbbells to resolve or at least to make ones chemically sensitive. From Fig.1 one can see that the contrast of atomic columns in ordered dots is varied not only at each doubled layers, but also within columns. Simulations of HREM images were performed with multislice program MUSLI (Chuvilin et al 2005). Various ordered GeSi dots were constructed within 43Åx42Åx42Å supercell of Si and optimized by Mm<sup>+</sup> force field (HyperChem program). Simulated HREM images for (2xN) and (2x2) type of ordering are inserted in Fig.1 with corresponding simulated diffraction patterns which are similar to experimental diffraction patterns from single dots (FFT not shown). Based on extensive image simulations the mechanism of new (2x2) ordering including the possibility of (2x2x2) type is discussed.

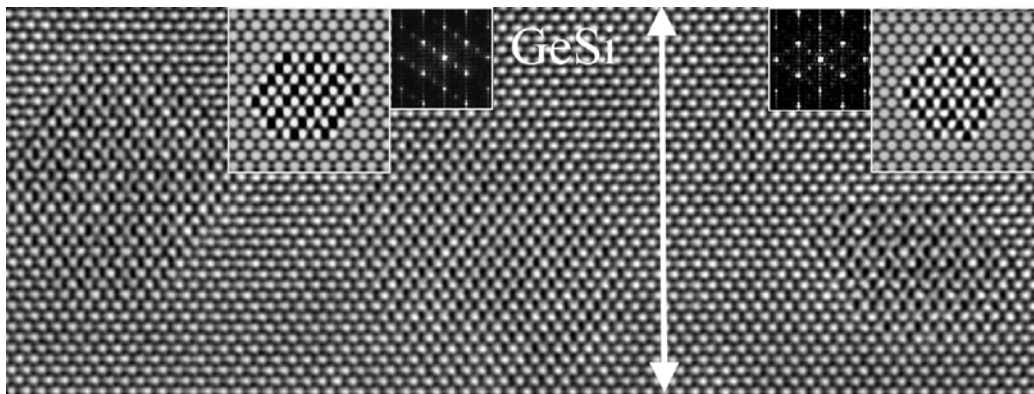


Fig.1 HREM image of ordered QDs in strained Ge<sub>0.2</sub>Si<sub>0.8</sub> alloy forming by in situ electron irradiation at 1250 KeV at 450°C. Inserted

frames are simulated HREM images and diffraction patterns corresponding to (2xN) ordering (left frames) and (2x2) ordering (right frames). Crystal thickness is 253Å, defocus value (-810Å).

References:

[1] N. Ikarashi, A. Oshiyama, A. Sakai, T. Totsumi, Phys. Rev. B **51** (1995), 14786.

[2] T. Suzuki, A. Gomyo, J. Appl. Phys **27** (1988), 2098.

[3] A. Chuvilin A, U. Kaizer Ultramicroscopy, 2005 (in press).

[4] Authors gratefully acknowledge the use of the 1.3MV High Voltage Electron Microscope at KBSI, Taejeon, Korea, SAS and LIF thank to Dr. Young-Joong Kim for HVEM access.

# Quantification of the N content in Ga(NAs) and (GaIn)(NAs) by dark field TEM and refined structure factor calculation

K. Volz, T. Torunski, O. Rubel, W. Stolz  
Material Sciences Center, Philipps University Marburg, Germany

The theoretically predicted and experimentally observed large bandgap bowing of mixed III/V nitrides as a function of nitrogen content has led to tremendously increasing research activities in the growth and characterisation of the novel (Ga(In))(NAs), as wavelengths, which are relevant for telecommunication applications can be achieved using this material system. As one deals with a metastable material system, phase separation effects as well as local atomic ordering might play an important role. Hence, nanoanalytical quantification of the composition of this class of material systems is indispensable.

To be able to quantitatively characterise dilute N containing III/V semiconductors, we have studied systematically the nitrogen content in (Ga(In))(NAs)/GaAs quantum wells by (002) dark field transmission electron microscopy. The nitrogen contents derived from this analysis, when assuming that all the atoms occupy their unperturbed position in a virtual crystal, significantly deviate from the nitrogen contents we derive for the same samples by other methods, e.g. high resolution X-ray diffraction and dynamical simulation of those XRD patterns. The nitrogen causes a significant local strain in the crystal and can accordingly displace the neighboring atoms dramatically. We show that, if the structure factor of the crystals is recalculated, taking these static displacements of the Ga atoms into account [1], the composition derived from the TEM analysis with that from XRD is in perfect agreement (see figure 1). It is hence necessary for tetragonally distorted crystals which have mixed sublattices containing atoms with different covalent radii to take these static displacements into account when quantification of the composition from dark field TEM images is aimed for.

[1] F. Glas, Phil. Mag. 84(20) (2004), 2055.

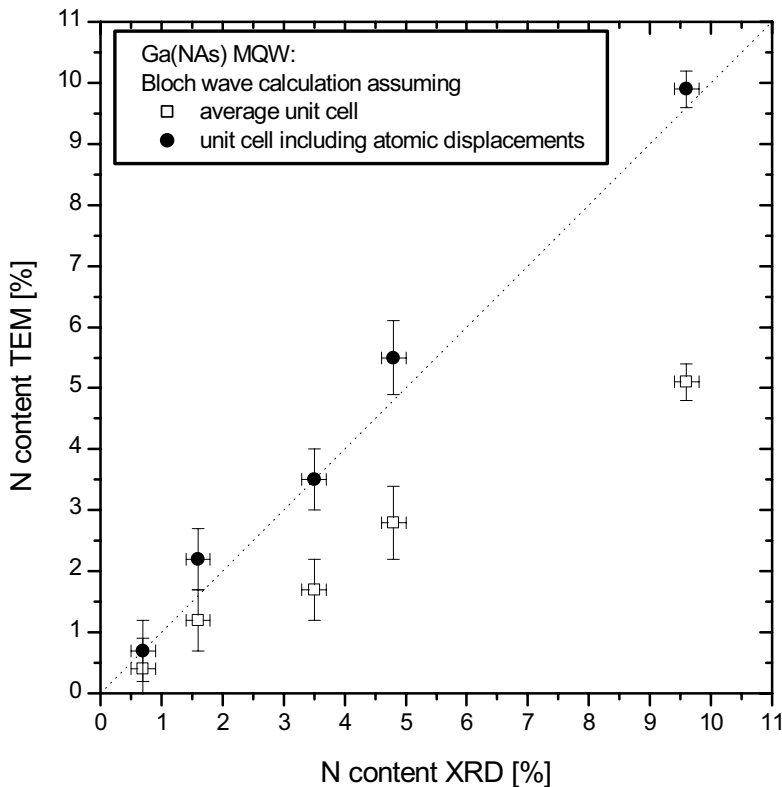


Figure 1: Comparison of the N content in Ga(NAs)/GaAs quantum wells derived from TEM and XRD analysis, respectively. The filled and open symbols correspond to structure factors calculated taking static atomic displacements into account and disregarding them, respectively.

## SEM Observation of Multilayer Semiconductor Structures Using Different Detection Modes

Petr Wandrol<sup>a</sup>, Jiřina Matějková<sup>a</sup>, and Rudolf Autrata<sup>a</sup>

<sup>a</sup>Dep. of Electron Optics, Institute of Scientific Instruments AS CR, 61264 Brno, Czech Republic

Manufacturing of semiconductor devices especially chips is a very exact process susceptible to errors and therefore the detailed inspection and failure analysis is necessary. One of the non-destructive testing instruments is the Scanning Electron Microscope (SEM). The negative charging of the specimen is the main difficulty in the observation and imaging of semiconductor structures in the SEM. The influence of the semiconductor specimen charging on the quality of image provided by different detection systems was the goal of this contribution.

The multilayered semiconductor structures were observed in the field emission SEM JSM 6700F equipped with three detection systems. First was the Everhart-Thornley (ET) detector which is standardly used in most of SEMs. Second was the in-lens [1] detection system located in the objective lens of JSM 6700F. Both of above mentioned detectors collect the secondary electrons (SE) and provide the topographical contrast of the specimen. The planar YAG backscattered electron (BSE) detector [2] that is placed tightly under the pole piece was applied for the true material contrast observation.

The image of the in-lens SE detector is most influenced by the charging (see Fig. 1) because of low energy of the SE1, which are affected by the negative surface charge. The ET detector provides an image of reasonable quality with lower charging artefacts (see Fig. 2) because the SE3 and BSE contribute to its signal. The charging effect in SEM is best suppressed by the YAG-BSE detector (see Fig. 3) thanks to the high energy of BSE, which penetrate through the surface layer. Another possibility of charging elimination is the use of a low voltage SEM or a low vacuum SEM.

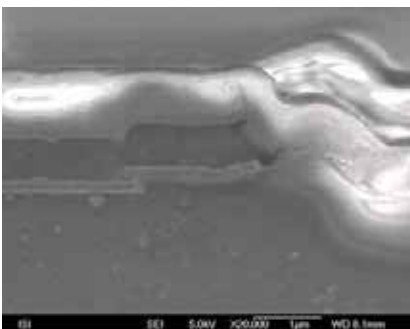


**Fig. 1:** In-lens SE image of multilayer structure. Strong charging effect.

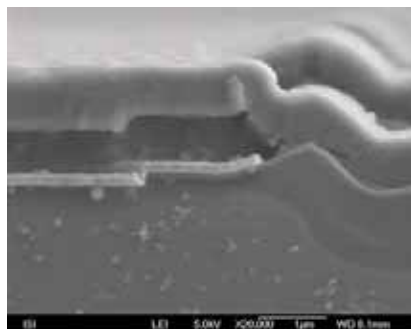


**Fig. 2:** ET SE image of multilayer structure. Low charging artefacts visible.

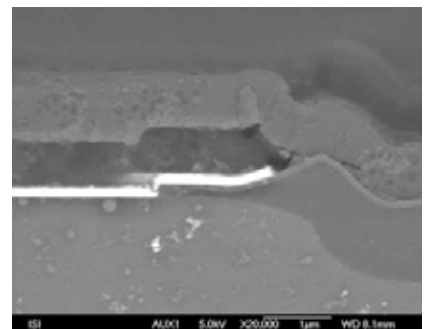


**Fig. 3:** YAG BSE image of multilayer structure. No charging artefacts.

### References:

- [1] Kazumori, H.: Jeol News Magazine (2002), p. 44-47
- [2] Autrata R., Schauer P.: In Proceedings of 13<sup>th</sup> European Microscopy Congress (2004), p. 75-76
- [3] This work is supported by the Grand Agency of the Czech Republic, grant no.102/05/0886

## TEM-Study on durability tested Anode-Supported SOFCs with LSCF Cathodes

Wilfried Assenmacher<sup>a</sup>, Werner Mader<sup>a</sup>, Andreas Mai<sup>b</sup>, Michael Becker<sup>c</sup>, Frank Tietz<sup>b</sup>, Ellen Ivers-Tiffée<sup>c</sup>, Detlev Stöver<sup>b</sup>

<sup>a</sup>Institute for Inorganic Chemistry, University Bonn, Römerstr. 164, 53117 Bonn, Germany

<sup>b</sup>Institute for Materials and Processes in Energy Systems (IWV), FZ Jülich, 52425 Jülich, Germany

<sup>c</sup>Institut für Werkstoffe der Elektrotechnik (IWE), Adenauerring 20, D-76131 Karlsruhe, Germany

Mixed ionic electronic conducting perovskites, like (La,Sr)(Co,Fe)O<sub>3-δ</sub> (LSCF), lead to significantly higher power densities compared to pure electronic conducting (La,Sr)MnO<sub>3-δ</sub> perovskites when used as cathodes for Solid Oxide Fuel Cells (SOFC) [1,2]. Former endurance tests with LSCF cathodes under a constant load of 0.5 A/cm<sup>2</sup> at 800 °C showed a performance loss of 0.9 to 1.5 % per 1000 h [3] compared to approx. 0.5 % for (La,Sr)MnO<sub>3-δ</sub>-cathodes. For this reason, the degradation of anode-supported SOFCs with LSCF-cathodes has been studied in detail. In this study, anode supported cells with YSZ electrolytes, Ce<sub>0.8</sub>Gd<sub>0.2</sub>O<sub>2-δ</sub> (CGO) buffer layers and La<sub>0.58</sub>Sr<sub>0.4</sub>Co<sub>0.2</sub>Fe<sub>0.8</sub>O<sub>3-δ</sub>-cathodes were investigated. After the initial testing, each cell was tested under one constant operation condition selected from the combinations of temperature, current density and oxygen partial pressure on cathode side for a period of 1000 h. The cells showed a power drop, characterized by impedance spectroscopy per 1000 h of 2 % at 700 °C / 0.6 A/cm<sup>2</sup>, and 4 % at 800 °C / 0.6 A/cm<sup>2</sup>, respectively. This degradation is mainly caused by an increased polarisation resistance.

TEM investigations (EELS, ESI, EDS) on cross sections prepared by FIB of the YSZ/cathode region of as prepared and tested cells were performed to reveal differences in composition, micro structure and/or crystal structure of the different samples. Observed differences in the samples are:

- Increasing amount of segregations of SrZrO<sub>3</sub> at the interface of the electrolyte and the CGO-interlayer with operating time;
- Formation of an interdiffusion zone between YSZ and CGO;
- Formation of CoO in the cathode by Sr-loss.

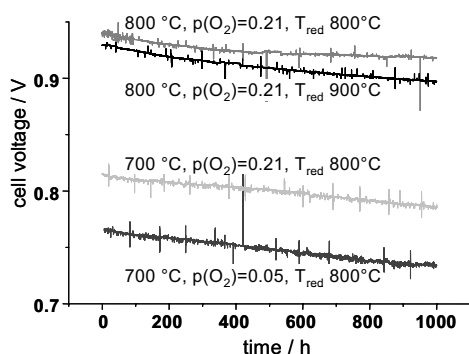


Figure 1: Cell voltage drop of different cells operated at 0.6 A/cm<sup>2</sup>.

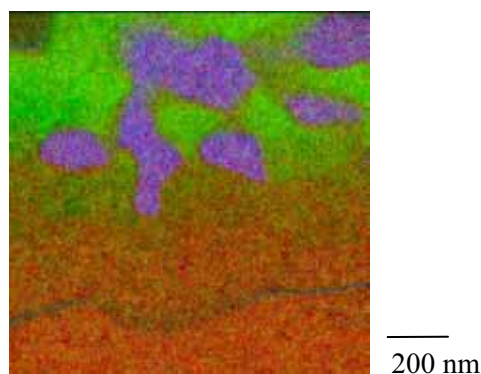


Figure 2: ESI Elemental-maps of Sr (blue), Zr (red) and Ce (green) as coloured overlay from the cathode/electrolyte interface of an as prepared SFOC, showing a formation of SrZrO<sub>3</sub> grains.

[1] A. Mai, V.A.C. Haanappel, S. Uhlenbruck, F. Tietz, D. Stöver, *Solid State Ionics*, submitted.

[2] B. Rietveld, P. Nammensma, J.P. Ouweltjes, N. Dekker, in *5th European Solid Oxide Fuel Cell Forum*, J. Huijsmans, Editor, p. 716 - 720, European Fuel Cell Forum, Oberrohrdorf, Switzerland (2002).

## Analytical TEM Study on the Evolution of Perovskite-Type Oxides in Soft Chemical Synthesis

Armin Feldhoff, Julia Martynczuk, Haihui Wang

Institute of Physical Chemistry and Electrochemistry,  
Faculty of Natural Science, University of Hanover,  
Callinstr. 3-3A, D-30167 Hanover, Germany

Membranes for the oxygen separation from air require functional ceramics that offer both, high electrical and high ionic conductivities as well as a good phase stability under reducing atmospheres. That can be constructed into the ceramic by a proper tailoring of grains and grain boundaries [1,2]. Some perovskite-type oxides  $ABO_{3-\delta}$  offer the possibility to vary their relevant properties over a wide range by the partial substitution of A and B site cations by other metal cations with different valencies. Perovskite phases of the type  $(Ba,Sr)(Zn,Fe)O_{3-\delta}$  turned out to be very suitable base materials according to the above mentioned requirements [1-3]. To obtain ceramics with improved functionality, it is crucial to get insight into the whole ceramic processing from molecular precursors to crystalline powders and further on to sintered materials. Here, we focus on the evolution of perovskite-type oxides in a soft chemical synthesis route. In a modified citrate process the nitrates  $Ba(NO_3)_2$ ,  $Sr(NO_3)_2$ ,  $Zn(NO_3)_2$ , and  $Fe(NO_3)_2$  are dissolved in a buffer solution of  $EDTA-NH_3 \cdot H_2O$  and citrate acid that keeps the pH value at around 6 and thus avoids precipitation. With the evaporation of water, a dark purple gel is obtained that is heated at around 120 - 150 °C for several hours followed by a calcination at temperatures between 500 and 950 °C. A major challenge is to obtain phase pure perovskite-type oxides with variable cationic ratios. To get insight into several steps of the phase formation, intermediates taken from solution, gel and the calcination process are analyzed by high-resolution (HRTEM) and analytical transmission electron microscopy including energy-dispersive X-ray spectroscopy (EDXS) and electron energy-loss spectroscopy (EELS) as well as selected area electron diffraction (SAED).

### References

- [1] H. Wang, C. Tablet, G. Grubert, A. Feldhoff, J. Caro, Investigation of phase structure, sintering and permeability of perovskite type  $Ba_{0.5}Sr_{0.5}Co_{0.8}Fe_{0.2}O_{3-\delta}$  membranes, *Journal of Membrane Science* (in press).
- [2] H. Wang, C. Tablet, A. Feldhoff, J. Caro, A novel cobalt-free oxygen permeable membrane based on the perovskite-type oxide  $Ba_{0.5}Sr_{0.5}Zn_{0.2}Fe_{0.8}O_{3-\delta}$ , *Advanced Materials* (in press).
- [3] H. Wang, G. Grubert, C. Tablet, J. Caro, Sauerstoff transportierende Oxidkeramiken mit kontrolliertem Sauerstoff-Fluss und Verfahren zur Herstellung der Oxidkeramiken, Anmeldung am Europäischen Patentamt durch die Universität Hannover, *EP 04020506*.

## TEM Investigations of Hydrothermally Treated Zircons

U. Golla-Schindler, T. Geisler, and A. Putnis

Institut für Mineralogie, University of Muenster, Germany

The investigated material was a partially metamict zircon from Sri Lanka, which was used for a hydrothermal experiment (gold capsuled experiment at 617 °C for 72 h and 1 kbar with 2 M CaCl<sub>2</sub>) [1]. Under these conditions sharply bounded reaction fronts penetrate into the zircon, resulting in a reaction rim and an unreacted core. The nature of the structural and chemical changes induced by the hydrothermal treatment, as well as the mechanism of the alteration has been investigated by defining the nature of the reaction interface by TEM.

One problem for TEM investigation of interfaces is the specimen preparation. The new FIB technology offers the opportunity to prepare site specific TEM foils. This enables the preparation of a FIB prepared lamella which includes the reaction front, i.e. the interface between the rim and the unreacted core. Fig. 1 (a) shows an SEM image of the investigated zircon and the position of the TEM lamella cut out [2].

CTEM investigations yield a sharp interface in the range of some nm shown in Fig. 1 (b). The diffraction pattern of the rim and core are identical apart from the sharpness of the diffraction spots. For the unreacted part of the zircon the diffraction spots are slightly blurred. These results indicate a topotactic exchange mechanism and a structural recovery due to less diffuse scattering from the amorphous parts in the rim. Due to the small concentration variations introduced by the hydrothermal experiments, the study of chemical changes is complicated. EDX spectra yield a significant change in the amount of Ca. With an EDX-linescan we obtained an chemical interface in the range of 50 nm, which is blurred by the probe size and the interaction volume of the electrons in the sample. Additionally we found in the rim an increase in porosity with increasing distance to the reaction front. Fig. 1(c) shows the small pores, which increases in size with increasing distance to the reaction front.

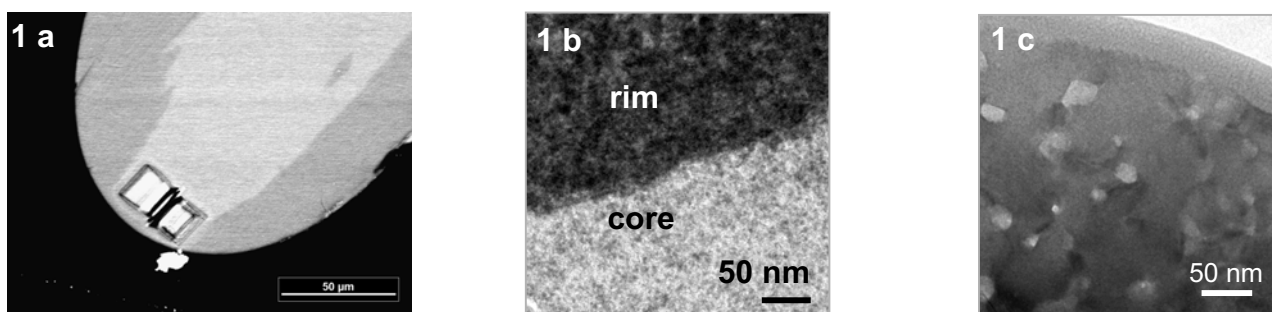


Fig. 1 (a) shows a SEM image where the rim and the position of the TEM Lamella is clearly visible (b) shows the TEM image of the interface (dark part rim, bright core) and (c) the increased porosity (bright parts) in the rim

### References

- [1] T. Geisler-Wierwille et al, *American Mineralogist* **88** (2003), p. 1496
- [2] We thank the FEI Company and the Carl Zeiss NTS GmbH for the FIB specimen preparation

## Superstructure and Domains in $\text{La}_{0.4}\text{Sr}_{0.6}\text{CoO}_{2.71}$

C.Gspan<sup>a</sup>, W.Grogger<sup>a</sup>, I.Letofsky-Papst<sup>a</sup>, F.Hofer<sup>a</sup>, E.Bucher<sup>b</sup> and W.Sitte<sup>b</sup>

<sup>a</sup>Research Institute for Electron Microscopy, Graz University of Technology, A-8010 Graz, Austria

<sup>b</sup>Department of Physical Chemistry, University of Leoben, A-8700 Leoben, Austria

Due to their high ionic conductivities, strontium-substituted lanthanum cobaltites  $\text{La}_{1-x}\text{Sr}_x\text{CoO}_{3-\delta}$  (LSC) have potential applications as high temperature fuel cell cathodes, gas separation membranes or oxygen sensors. Different  $\text{La}_{0.4}\text{Sr}_{0.6}\text{CoO}_{3-\delta}$  powders were investigated, which were synthesized by the glycine nitrate process [1]. The ionic conductivity from this heavily Sr doped material shows a maximum at a  $\delta$  value of 2.77 [2].

Two powders with different oxygen concentrations were compared in this study: LSC ( $3-\delta \approx 3$ ) and LSC+ ( $3-\delta = 2.71$ ). Investigations with XRD, TEM and SAED reveal that there are significant differences between these two samples. An additional weak peak at low  $2\Theta$  value of the LSC+ sample can be observed in x-ray powder diffraction. Another difference between LSC and LSC+ is the occurrence of domains in LSC+ samples, which can be seen in bright field and dark field images (Fig.1). Compared to that of LSC, the electron diffraction pattern of LSC+ shows additional reflections in the [100] zone axis (Fig. 2). Many papers try to explain these superreflections [3,4,5]. However, all these explanations are not able to make the superstructure reflections “visible” in an electron diffraction simulation. Investigation of LSC+ by using CBED (Fig.3) shows that the point group is  $4/mmm$  with a tetragonal crystal system. This result leads to a perfect agreement between electron diffraction simulation and the experiment (superstructure). Also the additional peak in the XRD can be explained using this symmetry.

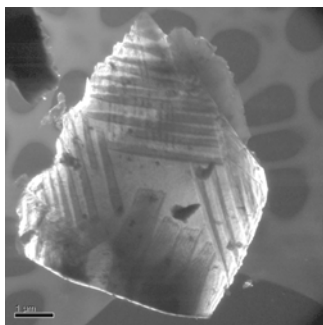


**Fig. 1:** Dark field image

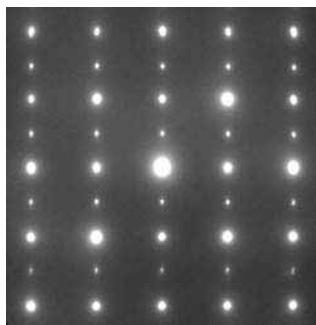


**Fig. 2:** SAED from LSC+  
in [100]



**Fig. 3:** CBED from LSC+  
in [100] (or [010])

References:

- [1] L.A.Chick, L.R.Pederson, G.D.Maupin, J.L.Bates L.E.Thomas, Mater. Let. 10 (1990) 6
- [2] E.Bucher, W.Sitte, I.Rom, W.Grogger, F.Hofer, Solid State Ionics 152-153 (2002) 417
- [3] Z.L.Wang, J.Zhang, Physical Review B54 (1996) 1153
- [4] S.Malo, A.Maignan, Inorg. Chem. 43 (2004) 8169
- [5] Z.L.Wang, J.Bentley, N.D.Evans, Micron 31 (2000) 355
- [6] We gratefully acknowledge financial support by the *Fonds zur Förderung der wissenschaftlichen Forschung, Vienna, Austria* within the Special Research Program *Electroactive Materials*

# Electron Energy-Loss Near-Edge Structure of Transition Metals in Crystalline, Disordered, and Amorphous Matter

Thomas Höche

Leibniz-Institut für Oberflächenmodifizierung e.V., Permoser Straße 15, D - 04318 Leipzig, Germany

Based on thorough crystal-structure analyses of  $\text{Ba}_2\text{TiSi}_2\text{O}_8$  (fresnoite),  $\text{Ba}_2\text{TiGe}_2\text{O}_8$ , and  $\text{Sr}_2\text{TiSi}_2\text{O}_8$  by either neutron, X-ray, or electron diffraction [1,2], the inherent structural flexibility and composition-dependent crystal-chemical driving forces are identified to be responsible for the occurrence of incommensurate structural modulations in fresnoite framework structures. Large-amplitude modulations are proved to provoke characteristic distortions of co-ordination polyhedra, which are sensitively reflected in the electronic structure and can thus be detected by electron energy-loss spectroscopy in the transmission electron microscope.

Consequently, in weakly modulated  $\text{Ba}_2\text{TiSi}_2\text{O}_8$ , both  $\text{Ti-}L_{2,3}$  electron energy-loss near-edge structure (ELNES) and O-K ELNES exhibit very distinct peaks while by contrast, the corresponding ELNES spectra of  $\text{Ba}_2\text{TiGe}_2\text{O}_8$  and  $\text{Sr}_2\text{TiSi}_2\text{O}_8$  (both are very strongly modulated) are significantly broadened (Fig. 1).

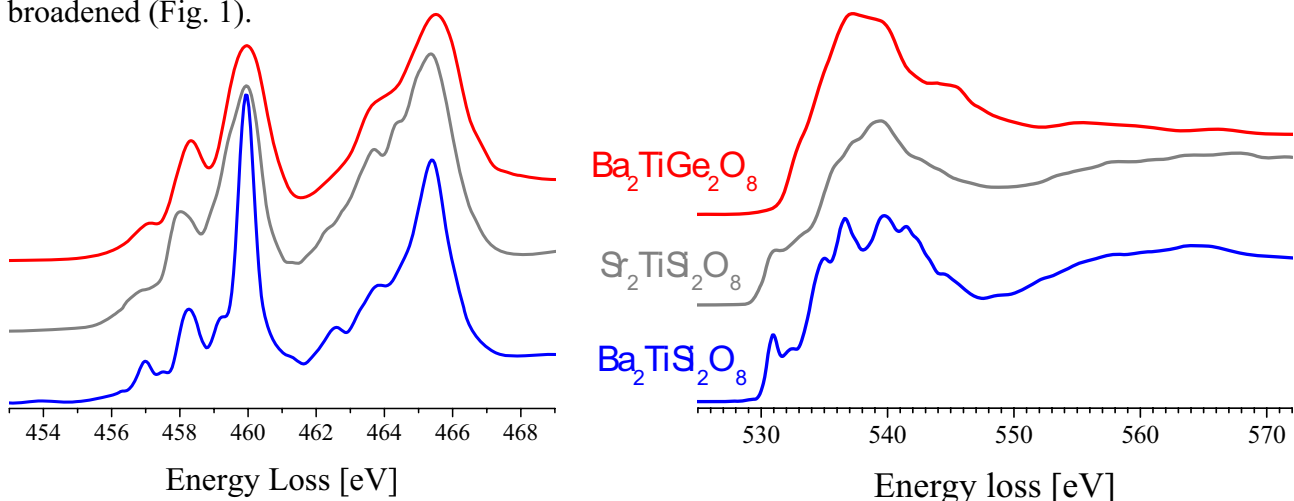


Fig. 1  $\text{Ti-}L_{2,3}$  and O-K ELNES of the fresnoite-type compounds  $\text{Ba}_2\text{TiSi}_2\text{O}_8$ ,  $\text{Ba}_2\text{TiGe}_2\text{O}_8$ , and  $\text{Sr}_2\text{TiSi}_2\text{O}_8$  (recorded at  $\sim 0.4$  eV spectral resolution in a VG STEM HB501 + Enfina).

In fresnoitic glasses ( $2 \text{ BaO-TiO}_2-2 \text{ SiO}_2$ ,  $2 \text{ BaO-TiO}_2-2 \text{ GeO}_2$ , and  $2 \text{ SrO-TiO}_2-2 \text{ SiO}_2$ ) the superposition of tetrahedrally, pentahedrally, and octahedrally co-ordinated Ti environments can be analysed on the basis of the  $\text{Ti-}L_{2,3}$  ELNES [3]. Moreover, it is revealed that the Ti co-ordination in amorphized  $\text{Ba}_2\text{TiSi}_2\text{O}_8$  (obtained by  $\text{Ar}^+$  ion irradiation) is i) depth dependent (due to the different interaction mechanisms at various depths) and ii) clearly different from the corresponding glass.

## References:

- [1] T. Höche, S. Esmailzadeh, R. Uecker, *et al.*, *Acta Cryst. B* 59 (2003) 209.
- [2] T. Höche, W. Neumann, S. Esmailzadeh, *et al.*, *J. Solid State Chem.* 166 (2002) 15.
- [3] T. Höche, P. A. v. Aken, M. Grodzicki, *et al.*, *Phil. Mag.* 84 [29] (2004) 3117.
- [4] Contributions by P. van Aken (Darmstadt) und F. Heyroth (Halle) are gratefully acknowledged.

## Crystal Structure Determination via Experimental and Calculated ELNES

Kathrin Hofmann and Barbara Albert

Institute of Inorganic and Applied Chemistry, University of Hamburg, Martin-Luther-King-Platz 6, 20146 Hamburg, Germany

Evidence of the presence or absence of carbon in boron-rich solids is usually difficult to achieve with conventional methods such as X-ray or neutron diffraction, but essential for the characterisation of such compounds. Carbon has a great influence upon the electronic situation and thus the physical properties of boron rich materials.

Electron energy loss spectroscopy (EELS) is a unique tool to detect carbon next to boron and study its influence on the electronic structure. This is made possible by the detailed analysis of the fine structure of the  $B_K$ - and  $C_K$ -ionisation edges (ELNES) and their calculation on the basis of the density functional theory (Wien2k, TELNES) [1,2]. With this, a differentiation of competing atomic arrangements is possible, because the calculations are based on structural models. The ELNES relates to the density of unoccupied electronic states (DOS) and thus to systematic changes in the electronic structure.

For the diboride-dicarbides of calcium and beryllium reasonable structure models consistent with physical properties and X-ray powder data could be derived and confirmed by this method.  $CaB_2C_2$  crystallises in a layered structure with condensed four- and eight-rings of alternating boron and carbon atoms [3,4].  $BeB_2C_2$  was first discovered by Markovskii et al. in 1966 [5]. Although the authors obtained the compound in the form of single crystals it was not possible to solve the crystal structure by conventional methods alone, because of the presence of light atoms only. We have now addressed this problem with a powerful combination of modern techniques: the above mentioned method of the detailed analysis of the  $B_K$ - and  $C_K$ - ELNES, and high-resolution X-ray powder data.  $BeB_2C_2$  crystallises in a layered structure of condensed hexagonal sheets of alternating boron and carbon atoms. These sheets are arranged along the crystallographic c-axis in a way that they resemble the structure of graphite, an arrangement that had not before been found in ternary compounds [6].

[1] P. Blaha, K. Schwarz, J. Luitz, WIEN2k, A Full Potential Linearized Augmented Plane Wave Package for Calculating Crystal Properties, 1999

[2] M. Nelhiebel, P.-H. Louf, P. Schattschneider, P. Blaha, K. Schwarz, B. Jouffrey, Phys. Rev. B59 (1999) 12807; C. Hébert-Souche, P.-H. Louf, P. Blaha, M. Nelhiebel, J. Luitz, P. Schattschneider, K. Schwarz, B. Jouffrey, Ultramicroscopy 83 (2000) 9

[3] B. Albert, K. Schmitt, Inorg. Chem., 38 (1999) 6159

[4] K. Hofmann, B. Albert, ChemPhysChem 10 (2002) 896

[5] L. Ya. Markovskii, N. V. Vekshina, Yu. D. Kondrashev, I. M. Stroganova; J. Appl. Chem. 39 (1966) 10

[6] K. Hofmann, B. Albert, submitted for publication

## Characterisation of Optically Anisotropic Grandite by Electron Microscopy

F. Kern<sup>1</sup>, U. Golla-Schindler<sup>1</sup>, K. Pollok<sup>1</sup>, A. G. Shtukenberg<sup>2</sup>, A. Putnis<sup>1</sup>

<sup>1</sup>Institut für Mineralogie, University of Muenster, Germany

<sup>2</sup>Department of Crystallography, Saint-Petersburg State University, Russia

We studied a grandite from Mali consisting of two areas, a brown and a colourless part, which are more or less birefringent. The examination with optical methods yield stronger birefringence for the brown part. The colourless part is nearly isotropic.

Grandites with optical anomalies have been investigated before and there have been many suggestions, regarding the origin of the birefringence. Various causes may be possible: ordering of Fe<sup>3+</sup>- and Al – cations on the octahedral sites or ordering of Ca – and Fe<sup>2+</sup> - cations or impurities of Mg<sup>2+</sup> or Mn<sup>2+</sup> on the dodecahedral sites, a non-cubic distribution of OH-groups, mismatch strain in the lattice and as a consequence, a reduction of the symmetry.

We analysed the parts which appeared isotropic and anisotropic with the microprobe (JEOL JXA 8600 MX) and with the SEM (JEOL 6300F). The two areas can easily be distinguished and are separated by a sharp interface. Fig.1 (a) shows the BSE image of the anisotropic area where parallel zonation and non – planar interfaces are visible, which could be a hint for the presence of OH – groups. The analytic measurements yield a variation of the Al and Fe content dependent on the specimen position. It is obvious, that a strong relation between Al and Fe<sup>3+</sup> does exist. The darker sections have a higher Al-content whereas the lighter parts have a higher Fe-content. Fig.1 (b) shows the isotropic and anisotropic area with the sharp interface in between. The analytic measurement obtained also a strong change of Al and Fe content at the interface. Additionally both examinations show an increase of the Mg content, when the Fe content decreases strongly. With the microprobe data it was possible to calculate the chemical composition of the different areas. The composition varies in the range: (Ca<sub>3,0-2,91</sub>, Mg<sub>0,04-0,08</sub>) (Al<sub>1,14-1,62</sub>, Fe<sup>3+</sup><sub>0,33-0,84</sub>) Si<sub>3</sub>O<sub>12</sub>.

We have just started TEM investigations to study the microstructure due to finer zonings, dislocations at interfaces and deviation from the cubic system for both areas. Additionally IR spectroscopy will enable us to detect OH groups, if they are present in the crystal.

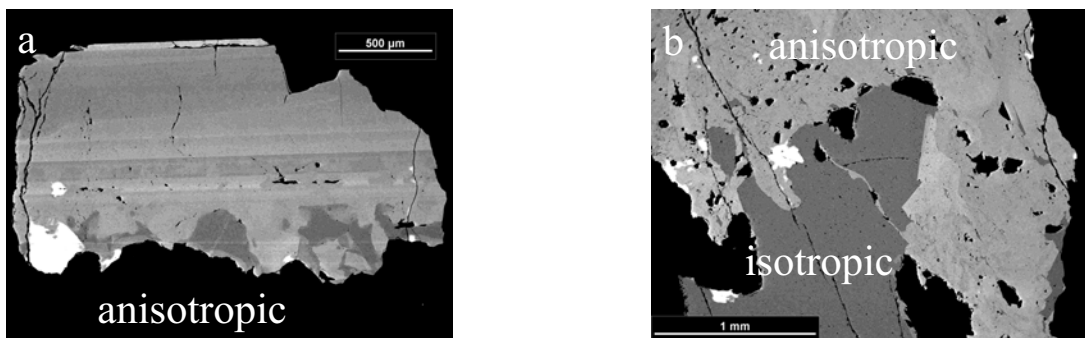


Fig. 1 BSE images of the grandite. (a) anisotropic area with zonation (b) isotropic and anisotropic area with sharp interface

## Microstructural Implications of an Electric-Field Driven Solid State Reaction

C. Korte<sup>1</sup>, B. Franz<sup>1</sup>, N.D. Zakharov<sup>2</sup>, and D. Hesse<sup>2</sup>

<sup>1</sup> Physikalisch-Chemisches Institut, Justus-Liebig-Universität, D-35392 Gießen, Germany

<sup>2</sup> Max-Planck-Institut für Mikrostrukturphysik, Weinberg 2, D-06120 Halle, Germany

Thermally induced solid state reactions have been studied both on the macroscopic and microscopic level. However, only few studies exist on the influence of external electric fields. We study the field driven, topotaxial spinel-forming solid state reaction  $\text{MgO} + \text{In}_2\text{O}_3 \rightarrow \text{MgIn}_2\text{O}_4$  by preparing epitaxial  $\text{In}_2\text{O}_3$  films on  $\text{MgO}(100)$  single-crystal substrates by PLD. The experiments were performed at  $1320^\circ\text{C}$ , applying a voltage of 100 V to Pt electrodes. Three topics were studied [1-3]:

- The reaction kinetics was analysed using linear transport theory, yielding kinetic equations including both the chemical and the electric-field related driving forces.
- The average thickness of the formed spinel phase in cross section samples was analysed by SEM, comparing field-free and field-driven experiments. A constant (linear growth law) and significantly enhanced reaction rate has been found in the field-driven case.
- (HR)TEM cross sectional investigations of the  $\text{In}_2\text{O}_3/\text{MgIn}_2\text{O}_4$  and  $\text{MgIn}_2\text{O}_4/\text{MgO}$  reaction fronts resulted in the following: Differing from the field-free case [4], the formed  $\text{MgIn}_2\text{O}_4$  films imply a mix of (100)- and (111)-oriented parts. The reason are the  $\text{In}_2\text{O}_3$  films growing with mixed (100) and (111) orientation on  $\text{MgO}(100)$  [5]. The orientation of the  $\text{MgIn}_2\text{O}_4$  product phase follows that of the  $\text{In}_2\text{O}_3$ . Corresponding large-angle (100)/(111) grain boundaries are formed in the  $\text{MgIn}_2\text{O}_4$  film. Thus, the  $\text{MgIn}_2\text{O}_4/\text{MgO}$  reaction front consists of (semi)coherent sections at the (100)-oriented  $\text{MgIn}_2\text{O}_4$  regions and other sections at the (111)-oriented  $\text{MgIn}_2\text{O}_4$  regions. The (100)/(111) grain boundaries in the  $\text{MgIn}_2\text{O}_4$  phase represent fast diffusion paths, which modify the local reaction kinetics, up to the point that the product formation is locally stopped, most probably due to an enhanced mobility of  $\text{In}^{3+}$  ions in the grain boundaries. A relatively high average  $\text{In}^{3+}$  transference

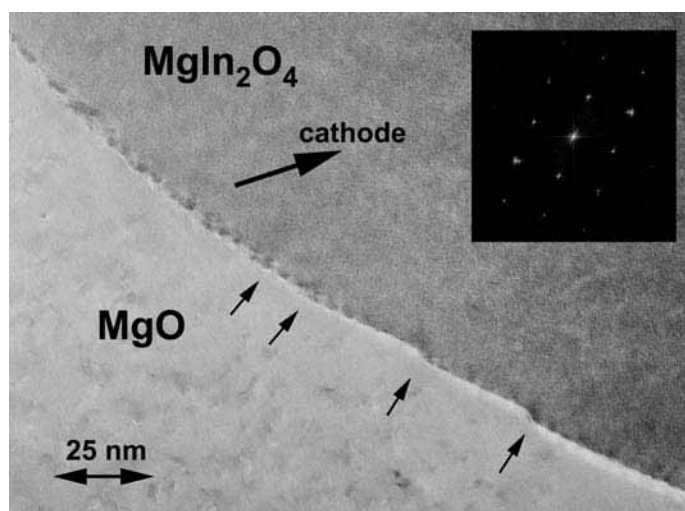


Figure 1: HRTEM-structure image (low-magnification print) of a curved section of the  $\text{MgIn}_2\text{O}_4/\text{MgO}$  reaction front. Arrows point to some ledges.

can also be affirmed by analysing the shift rates of the  $\text{In}_2\text{O}_3/\text{MgIn}_2\text{O}_4$  and  $\text{MgIn}_2\text{O}_4/\text{MgO}$  reaction fronts. As a consequence, the  $\text{MgIn}_2\text{O}_4/\text{MgO}$  reaction front is partially curved. It consists of rather plane (100)/(100) sections, where a dislocation-type interfacial reaction mechanism [4] prevails and of curved sections, where a ledge mechanism occurs (Figure 1).

[1] C. Korte, N. Ravishankar, C.B. Carter, and H. Schmalzried, *Solid State Ionics* **148** (2002) 111.

[2] C. Korte, N.D. Zakharov, and D. Hesse, *Phys. Chem. Chem. Phys.* **5** (2003) 5530.

[3] C. Korte, B. Franz, and D. Hesse, *Phys. Chem. Chem. Phys.* **7** (2005) 413.

[4] H. Sieber, D. Hesse and P. Werner, *Phil. Mag. A* **75** (1997) 889.

[5] H. Sieber, St. Senz and D. Hesse, *Thin Solid Films* **303** (1997) 216.

## High-Resolution STEM Characterization of Niobium Tungsten Oxides

Frank Krumeich and Reinhard Nesper

ETH Zurich, Laboratory of Inorganic Chemistry, CH-8093 Zurich, Switzerland

Starting with the fully oxidized phase  $\text{Nb}_8\text{W}_9\text{O}_{47}$ , the formal substitution of two  $\text{Nb}^{5+}$  by  $\text{Nb}^{4+}$  and  $\text{W}^{6+}$  results in a solid solution series  $\text{Nb}_{8-n}\text{W}_{9+n}\text{O}_{47}$  ( $0 < n < 5$ ) [1]. All these phases crystallize isostructurally in a threefold superstructure of the tetragonal tungsten bronzes [2]. The oxidation of these reduced phases at  $T_{\text{OX}} = 1200$  °C results in a separation into the thermodynamically stable phases. In contrast to that, lower oxidation temperatures lead to unusual products that contain several new structural elements and ordering varieties [3,4]. In general, these structures can be directly observed in projection along the short crystallographic axis since the metal positions are visible as dark spots in HRTEM images recorded close to Scherzer defocus. Now, an investigation of some of these samples was performed by scanning transmission electron microscopy with a high-angle annular dark field detector (HAADF-STEM) attached to a Tecnai 30F microscope. At the selected imaging conditions (Z contrast), not only the metal positions are revealed by this technique but additional information about the elemental distribution can be obtained. This has recently been demonstrated for  $\text{Nb}_8\text{W}_9\text{O}_{47}$  [5].

In this contribution, we report on the investigation of the oxidation product of  $\text{Nb}_4\text{W}_{13}\text{O}_{47}$ . At  $T_{\text{OX}} = 1200$  °C,  $\text{Nb}_4\text{W}_7\text{O}_{31}$  and  $\text{WO}_3$  are formed according to the phase diagram. In segregations of  $\text{WO}_3$ , which appear at  $T_{\text{OX}} = 1000$  °C as well [2], the brightness of the metal positions is higher than in the bronze-type  $(\text{Nb},\text{W})\text{O}_x$  matrix (Fig. 1). Additionally, planar defects that consist of uncommon edge-sharing pentagons of  $(\text{Nb},\text{W})\text{O}_6$  octahedra occur in the matrix.

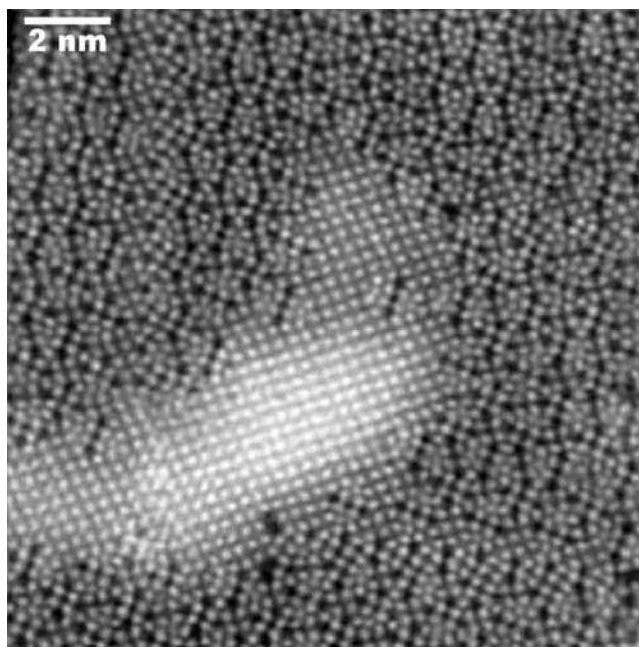


**Fig. 1:** HAADF-STEM image of  $\text{Nb}_4\text{W}_{13}\text{O}_{47}$  oxidized at 1000°C showing a segregation of  $\text{WO}_3$  and planar defects.

### References:

- [1] F. Krumeich, A. Hussain, C. Bartsch, and R. Gruehn, *Z. anorg. allg. Chem.* **621** (1995) 799.
- [2] F. Krumeich, M. Wörle, and A. Hussain, *J. Solid State Chem.* **149** (2000) 428.
- [3] F. Krumeich, *J. Solid State Chem.* **119** (1995) 420.
- [4] F. Krumeich, C. Bartsch, and R. Gruehn, *J. Solid State Chem.* **120** (1995) 268.
- [5] A. I. Kirkland, W. O. Saxton, *J. Microsc.* **206** (2002) 1.

## Electron Microscopy in Solid State Sciences – A Web Tutorial

Frank Krumeich, Anke Zürn, and Reinhard Nesper

ETH Zurich, Laboratory of Inorganic Chemistry, CH-8093 Zurich, Switzerland

In the last years, the internet has established a unique means to provide and to distribute useful information about electron microscopy. In particular, this opportunity is being exploited by the manufacturers of electron microscopes and equipment. Besides that, useful information about various electron microscopy methods can be found widely distributed in the internet. Different methods for teaching are utilized, ranging from short, rather superficial introductions to comprehensive treatments. For example, the basics of transmission electron microscopy including the operation of magnetic lenses are explained and demonstrated in nice animations as a part of Goodhew's Matter project [1]. A detailed treatment of TEM theory is provided as a lecture script by H. Kohl [2]. Other web pages are focused, e.g., on image simulation [3] or EELS and EFTEM [4]. However, as far as we know, there exists no web page that informs about all electron microscopy methods which are employed for the investigation of inorganic materials. Our new microscopy page has been designed to fill this gap [5].

The aim of this site [5] is to give advanced students a survey of the electron microscopy methods applied in our laboratory. An introduction into the electron-matter interactions underlying these methods is followed by a treatment of the signals arising from that and the information about structure, composition and elemental distribution that can be retrieved from these signals. For this purpose, there are two central pages from which the others can be reached: (i) *Methods*: list of methods with links to their explanation. (ii) *Interactions*: a scheme showing the most important signals arising when electrons hit the sample. From here, pages providing explanations of the underlying basic physics as well as examples for applications are linked. In general, the intention of this site is to give a general idea what electron microscopy methods offer for the characterization of materials rather than to provide a comprehensive treatment of theory and physics.

### References:

- [1] [www.matter.org.uk/TEM](http://www.matter.org.uk/TEM)
- [2] [www.uni-muenster.de/Physik/PI/Kohl](http://www.uni-muenster.de/Physik/PI/Kohl)
- [3] [cimesg1.epfl.ch/CIOL/ems.html](http://cimesg1.epfl.ch/CIOL/ems.html)
- [4] [www.felmi-zfe.tugraz.at](http://www.felmi-zfe.tugraz.at); [tem.atp.tuwien.ac.at/EELS](http://tem.atp.tuwien.ac.at/EELS)
- [5] [www.microscopy.ethz.ch](http://www.microscopy.ethz.ch)

## HRTEM Study on the Ordered Structure of the Metastable $\text{Ge}_2\text{Sb}_2\text{Te}_5$

Y.J. Park<sup>a</sup>, J.Y. Lee<sup>a</sup>, and Y.T. Kim<sup>b</sup>

<sup>a</sup>Department of Materials Science and Engineering, Korea Advanced Institute of Science and Technology, Daejeon 305-701, Republic of Korea

<sup>b</sup>Semiconductor Materials and Devices Laboratory, Korea Institute of Science and Technology, Seoul 136-791, Republic of Korea

The  $\text{Ge}_2\text{Sb}_2\text{Te}_5$  thin films deposited by sputtering method on  $\text{SiO}_2/\text{Si}$  (100) substrates were annealed through a rapid thermal annealing process at 200°C in  $\text{N}_2$  ambient condition for 1 minute and investigated by a HRTEM in order to precisely reveal the ordered structure of the metastable rock-salt structure of  $\text{Ge}_2\text{Sb}_2\text{Te}_5$  on an atomic level. The NaCl-type structure model in the space group  $Fm\bar{3}m$  of the metastable  $\text{Ge}_2\text{Sb}_2\text{Te}_5$  was proposed by Yamada *et al.*, and he supposed that the 4(*a*) site is wholly occupied by Te only, and the 4(*b*) site is randomly occupied by Ge, Sb and some vacancies with different probabilities depending on the actual compositions of  $\text{Ge}_2\text{Sb}_2\text{Te}_5$  [1].

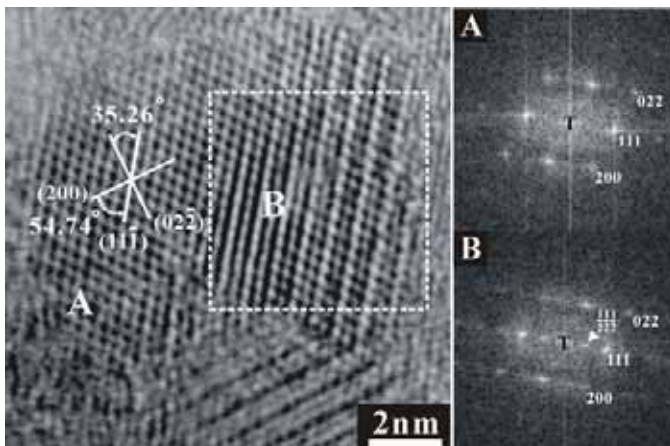


**Fig. 1:** HRTEM image (left) and fast-Fourier transformed image (right) of metastable  $\text{Ge}_2\text{Sb}_2\text{Te}_5$ .

Fig. 1 shows a HRTEM image and fast-Fourier transformed (Gatan Digital Micrograph) image of the metastable  $\text{Ge}_2\text{Sb}_2\text{Te}_5$ . Within the identical grain, the Ge and the Sb atoms are randomly placed to show fcc structure with uniform point resolution in region A, just as Yamada *et al.*, had proposed. However, in region B, the  $\{111\}$  periodically show different intensity. This implies that in the  $\{111\}$ , different atomic layers are orderly being formed. In other words, compared with Sb, Ge has larger difference of atomic number with respect to Te and if the Ge and the Sb atoms stack on separate  $\{111\}$  the close-packed plane periodically while causing the

inter-planar intensity difference of the Te basis can occur. As can be seen from the Fig. 1, it clearly depicts the diffraction spots which reveal the superlattice reflections in region B.

In the Te-based fcc lattice of the metastable  $\text{Ge}_2\text{Sb}_2\text{Te}_5$ , the Ge atom and the Sb atom settle on a specific plane where  $\{111\}$  the close-packed plane have double period along the  $\langle 111 \rangle$  orientation forming the ordered structure which has similar stacking structure as the stable  $\text{Ge}_2\text{Sb}_2\text{Te}_5$ , thereby facilitating the phase transition [2].

### References:

- [1] N. Yamada and T. Matsunaga, *J. Appl. Phys.* 88 (2000) 7020.
- [2] Y.J. Park, J.Y. Lee *et al.*, *J. Appl. Phys.* 92 (2005) 093506.

## Processes of Dissolution of Crystals by Atomic Force Microscopy Data

Natalya N. Piskunova

Institute of Geology of Komi SC of Ural Branch of the Russian Academy of Sciences, 167982, Syktyvkar, Komi Republic, Russia

Character of crystalline surface (100) of  $KH_2PO_4$  crystal (KDP) in almost equilibrium solution has been studied during *in situ* experiments by atomic force microscopy of crystal growth. At first crystal surface is not visibly changing. Calibration of scanning force wherein probe with radius of rounding is 10 nm pressing in the middle of the area during 550 msec resulted in occurrence of a pit on the crystal. This is stipulated by steep dependence of dissolution upon temperature for crystals of potassium dihydrogen phosphate. Little increase of temperature at a point of short-term pressure of style rather rapidly induces local dissolution on the surface and occurrence of the first pit in the third minute of observation. The seventh minute of observation resulted in occurrence of such six pits. Square pits extend towards  $\langle 101 \rangle$  and arise in chain line spreading towards  $\langle 101 \rangle$ . Surrounding surface is not changing. During the eighth minute of observation no new pits occur, after 8 minutes of the experiment the available pits are not growing. In accordance with Heinman theory to form succeeding pits in chain line towards  $\langle 101 \rangle$ , takes efforts to penetrate little energetic barrier, and the pits freely arise until local saturation is recovered.

With atomic-force microscopy we have studied other cases of dissolution on the surface of a crystal growing in the solution, including early AFM-experiments in the directed solution flow [1].

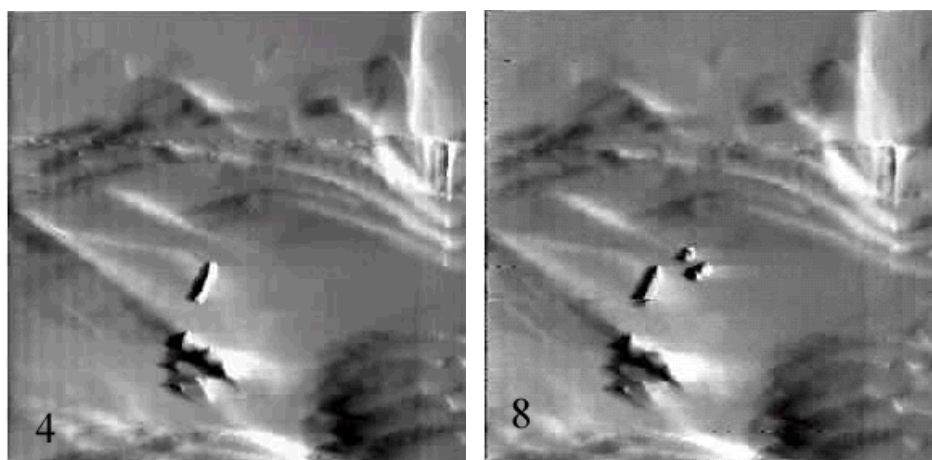


Fig. 1. Dynamics of surface dissolution (100) of  $KH_2PO_4$  (KDP) crystals during 2.7 min. Local dissolution close to equilibrium. Image size 14×14 mcm.

### References:

- [1] Piskunova N.N. Acta Cryst. A58 (Supplement), 2002. C. 168.
- [2] This work was supported by RFBI (project №05-05-65112a).

## Incommensurate Metal Chains in Subnitrides – an ED Study on $\text{Ca}_7\text{N}_4\text{Ag}_x$

R. Ramlau, P. Höhn, and R. Kniep

Max-Planck-Institut für Chemische Physik fester Stoffe, 01187 Dresden, Germany

Ternary nitrides of the general formula  $(\text{Ca}_7\text{N}_4)\text{M}_x$  with  $M = \text{Ga}, \text{In}, \text{Tl}, \text{Ag}$  exhibit particular features. The Ca-N substructures are isotypic to each other. They are build-up of  $\text{NCa}_6$  octahedra which are condensed to 1-dimensionally infinite blocks. The blocks, on their part, are corner sharing and form a 3-d framework comprising large channels parallel to the blocks [1, 2].

The Ca-N substructure can be unambiguously refined from x-ray powder-diffraction data (space group  $Pbam$ ,  $a = 1.145$  nm  $b = 1.206$  nm,  $c = 0.366$  nm) and is described as an electronically balanced subnitride  $(\text{Ca}_3^{2+}\text{Ca}_4^{1.5+}\text{N}_4^{3-})^0$ . The determination of the  $M$  sites, however, was not possible. It was supposed, that the metal atoms form equidistant chains along the central axis of each channel, with absolutely no order relation from chain to chain (channel to channel) [3].

HREM and ED seemed to be promising tools to obtain more information about the positions of the  $M$  atoms in the chains. All representatives of the  $(\text{Ca}_7\text{N}_4)\text{M}_x$  family readily hydrolyze when exposed to air and, therefore, have to be prepared and transferred to the electron microscope under inert gas atmosphere. Enormous difficulties arose, and –until now– only the title compound was amenable to ED experiments. Selected-area ED patterns were registered for the [100], [110], and [010] zones.

In all the three zones continuous diffuse lines can be discerned besides the Bragg reflections of the subnitride (and of some hydrolyzation product). Reconstruction in 3-dimensional reciprocal space results in sheets of diffuse intensity  $\mathbf{G} \pm \varepsilon \cdot \mathbf{a}^* \pm \eta \cdot \mathbf{b}^* \pm \gamma \cdot \mathbf{c}^*$ ,  $\varepsilon, \eta$  continuous,  $\gamma = 1.357$ , which appear

as first-order "satellites" to the subnitride Bragg-reflections  $\mathbf{G} = [hkl]^*$ . That means that the Ag chains are incommensurate to the subnitride structure. The distance of Ag atoms in the chains is  $d(\text{Ag}-\text{Ag}) = 270(5)$  pm and the composition of the compound  $x = 1.36$ , which is in good agreement with the originally weighted-in quantities and the results of chemical analysis.

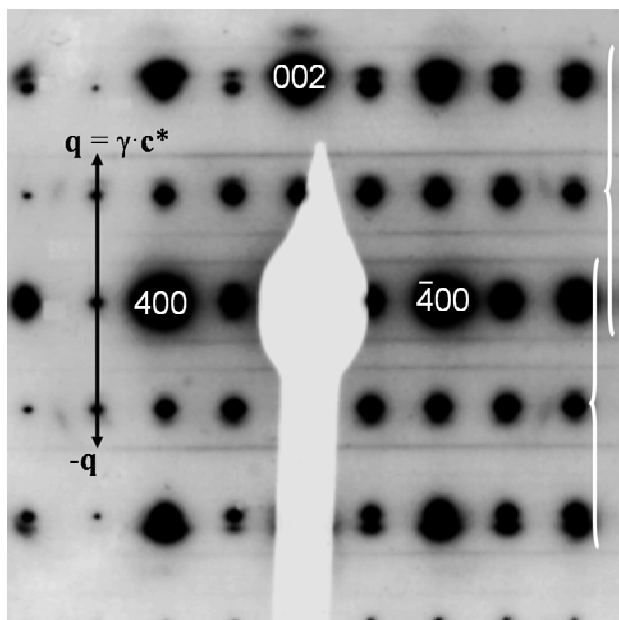


**Fig. 1:**

Selected-area ED of  $(\text{Ca}_7\text{N}_4)\text{Ag}_{1.36}$  in [010] orientation showing diffuse lines  $\mathbf{G} \pm \varepsilon \cdot \mathbf{a}^* \pm \gamma \cdot \mathbf{c}^*$  ( $\varepsilon$  continuous,  $\gamma = 1.357$ ) as first-order satellites to the Bragg reflections  $\mathbf{G} = [hkl]^*$ . Very weak second-order satellite lines are also present.

### References:

- [1] J. Jäger, Thesis, TU Darmstadt 1995.
- [2] M. Ludwig, Thesis, TU Darmstadt 1998
- [3] P. Höhn *et al.*, *Z. Anorg. Allg. Chem.* **630** (2004), 1704.